

AD-A255 697



AGARD-LS-182

AGARD-LS-182

AGARD

ADVISORY GROUP FOR AEROSPACE RESEARCH & DEVELOPMENT

7 RUE ANCELLE 92200 NEUILLY SUR SEINE FRANCE

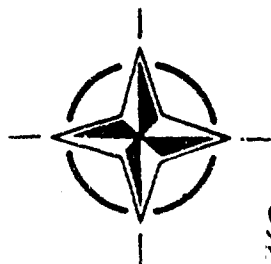
AGARD LECTURE SERIES 182

Fundamentals and Special Problems of Synthetic Aperture Radar (SAR)

Les Aspects Fondamentaux et
les Problèmes Spécifiques aux
Radars à Ouverture Synthétique (SAR)



This material in this publication was assembled to support a Lecture Series under the sponsorship of the Avionics Panel of AGARD and the Consultant and Exchange Programme of AGARD presented on 5th—6th October 1992 in Bad Neuenahr, Germany, 8th—9th October 1992 in Gebze-Kocaeli (near Istanbul), Turkey and 26th—27th October 1992 in Ottawa, Canada.



NORTH ATLANTIC TREATY ORGANIZATION

Published August 1992

Distribution and Availability on Back Cover

40th
Anniversary
Year

7 RUE ANCELLE 92200 NEUILLY SUR SEINE FRANCE

Fundamentals and Special Problems of Synthetic Aperture Radar (SAR)

Accession For

1944-1945	1
1946-1947	2
1948-1949	3
1950-1951	4
1952-1953	5
1954-1955	6
1956-1957	7
1958-1959	8
1960-1961	9
1962-1963	10
1964-1965	11
1966-1967	12
1968-1969	13
1970-1971	14
1972-1973	15
1974-1975	16
1976-1977	17
1978-1979	18
1980-1981	19
1982-1983	20
1984-1985	21
1986-1987	22
1988-1989	23
1990-1991	24
1992-1993	25
1994-1995	26
1996-1997	27
1998-1999	28
2000-2001	29
2002-2003	30
2004-2005	31
2006-2007	32
2008-2009	33
2010-2011	34
2012-2013	35
2014-2015	36
2016-2017	37
2018-2019	38
2020-2021	39
2022-2023	40
2024-2025	41
2026-2027	42
2028-2029	43
2030-2031	44
2032-2033	45
2034-2035	46
2036-2037	47
2038-2039	48
2040-2041	49
2042-2043	50
2044-2045	51
2046-2047	52
2048-2049	53
2050-2051	54
2052-2053	55
2054-2055	56
2056-2057	57
2058-2059	58
2060-2061	59
2062-2063	60
2064-2065	61
2066-2067	62
2068-2069	63
2070-2071	64
2072-2073	65
2074-2075	66
2076-2077	67
2078-2079	68
2080-2081	69
2082-2083	70
2084-2085	71
2086-2087	72
2088-2089	73
2090-2091	74
2092-2093	75
2094-2095	76
2096-2097	77
2098-2099	78
2100-2101	79
2102-2103	80
2104-2105	81
2106-2107	82
2108-2109	83
2110-2111	84
2112-2113	85
2114-2115	86
2116-2117	87
2118-2119	88
2120-2121	89
2122-2123	90
2124-2125	91
2126-2127	92
2128-2129	93
2130-2131	94
2132-2133	95
2134-2135	96
2136-2137	97
2138-2139	98
2140-2141	99
2142-2143	100
2144-2145	101
2146-2147	102
2148-2149	103
2150-2151	104
2152-2153	105
2154-2155	106
2156-2157	107
2158-2159	108
2160-2161	109
2162-2163	110
2164-2165	111
2166-2167	112
2168-2169	113
2170-2171	114
2172-2173	115
2174-2175	116
2176-2177	117
2178-2179	118
2180-2181	119
2182-2183	120
2184-2185	121
2186-2187	122
2188-2189	123
2190-2191	124
2192-2193	125
2194-2195	126
2196-2197	127
2198-2199	128
2200-2201	129
2202-2203	130
2204-2205	131
2206-2207	132
2208-2209	133
2210-2211	134
2212-2213	135
2214-2215	136
2216-2217	137
2218-2219	138
2220-2221	139
2222-2223	140
2224-2225	141
2226-2227	142
2228-2229	143
2230-2231	144
2232-2233	145
2234-2235	146
2236-2237	147
2238-2239	148
2240-2241	149
2242-2243	150
2244-2245	151
2246-2247	152
2248-2249	153
2250-2251	154
2252-2253	155
2254-2255	156
2256-2257	157
2258-2259	158
2260-2261	159
2262-2263	160
2264-2265	161
2	

DTIC QUALITY INSPECTED 3

North Atlantic Treaty Organization
Organisation du Traité de l'Atlantique Nord

92 9 23 035

92-25718 203
290

The Mission of AGARD

According to its Charter, the mission of AGARD is to bring together the leading personalities of the NATO nations in the fields of science and technology relating to aerospace for the following purposes:

- Recommending effective ways for the member nations to use their research and development capabilities for the common benefit of the NATO community;
- Providing scientific and technical advice and assistance to the Military Committee in the field of aerospace research and development (with particular regard to its military application);
- Continuously stimulating advances in the aerospace sciences relevant to strengthening the common defence posture;
- Improving the co-operation among member nations in aerospace research and development;
- Exchange of scientific and technical information;
- Providing assistance to member nations for the purpose of increasing their scientific and technical potential;
- Rendering scientific and technical assistance, as requested, to other NATO bodies and to member nations in connection with research and development problems in the aerospace field.

The highest authority within AGARD is the National Delegates Board consisting of officially appointed senior representatives from each member nation. The mission of AGARD is carried out through the Panels which are composed of experts appointed by the National Delegates, the Consultant and Exchange Programme and the Aerospace Applications Studies Programme. The results of AGARD work are reported to the member nations and the NATO Authorities through the AGARD series of publications of which this is one.

Participation in AGARD activities is by invitation only and is normally limited to citizens of the NATO nations.

The content of this publication has been reproduced directly from material supplied by AGARD or the authors.

Published August 1992

Copyright © AGARD 1992
All Rights Reserved

ISBN 92-835-0683-9



*Printed by Specialised Printing Services Limited
40 Chigwell Lane, Loughton, Essex IG10 3TZ*

Abstract

The Lecture Series will cover the field of airborne and spaceborne SAR with respect to its technical realization in order to convey the participants' ideas and know-how on SAR, on its capabilities and on the technology necessary for the successful construction and application of airborne and spaceborne SAR systems.

The basic principles of SAR will be explained and its peculiarities, ambiguities and special effects will be highlighted especially in comparison with airborne and spaceborne Radar with Real Aperture (RAR). The influence of speed and altitude variations, lateral motions on respective compensation possibilities will be presented.

The antenna is a system related SAR component. Therefore, the influence of the antenna parameters on specification and capabilities of SAR will be considered. Polarization effects and multi-polarization SAR are presently key-points for SAR development and SAR application as well as questions on absolute SAR calibration. The advantages, necessities and limits of these topics will be included.

Digital SAR processing is for SAR indispensable. Theories and special algorithms will be given along with basic processor configurations and different processing techniques on hardware and software bases.

The simulation of SAR-systems as well as SAR-products will also be a topic of the Lecture Series. This includes the simulation of SAR-techniques and SAR-components as well as the simulation of SAR images. Special SAR-methods like squint-, stretch- and spotlight-techniques for example will be presented in addition to the inverse SAR-techniques using the motion of targets instead of the motion of the radar. A presentation of the state of the art giving examples of presently planned and up to now realized airborne and spaceborne SAR with its application foreseen will conclude the Lecture Series.

The Lecture Series should appeal to technically and technologically oriented engineers concerned with development of SAR and to scientists, who have to work with SAR for different applications as well as to students of both specialities who have already attained a high degree of knowledge in techniques and of remote sensing applications.

This Lecture Series, sponsored by the Avionics Panel of AGARD, has been implemented by the Consultant and Exchange Programme.

Abrégé

Ce cycle de conférences traitera du domaine des SAR aéroportés et spatioportés du point de vue de leur réalisation technique. Les conférenciers mettront à profit leur compétence pour présenter leurs idées concernant les SAR, leurs possibilités, et les technologies qui sont à utiliser pour réussir l'industrialisation et la mise en oeuvre des systèmes SAR aéroportés et spatioportés.

Les principes de base de ces systèmes seront exposés, ainsi que leurs particularités, ambigüités et spécificités, en particulier par rapport aux radars aéroportés et spatioportés à ouverture réelle (RAR). L'influence des déplacements latéraux ainsi que des variations de vitesse et d'altitude sur les possibilités respectives de compensation sera également présentée.

L'antenne est un composant du système des SAR. Par conséquent, l'influence des paramètres d'antenne sur les spécifications techniques et les capacités des SAR sera prise en considération. A l'heure actuelle, les effets de polarisation et de multipolarisation SAR doivent être considérés comme des points clé pour le développement et les applications des SAR, de même que leur étalonnage absolu. Les avantages, les nécessités et les limites de ces données seront examinés.

Le traitement numérique est indispensable aux SAR. Des théories et des algorithmes spécifiques seront proposés, ainsi que des configurations de processeur de base et différentes techniques de traitement sous les aspects matériel et logiciel.

La simulation des systèmes SAR et des produits SAR constitue un autre sujet de ce cycle de conférences. Ce sujet comprend la simulation des techniques et des composants SAR, ainsi que la simulation de l'imagerie SAR. Des méthodes spécifiques au SAR, telles que le déport antenne (squint) les impulsions étalées (stretch) et le mode télescope par exemple, seront présentés en complément des techniques SAR inverses faisant appel aux mouvement des cibles au lieu du mouvement du radar. Le cycle de conférences se terminera par une présentation de l'état de l'art dans ce domaine, avec des exemples de systèmes SAR aéroportés, spatioportés existants et projetés et des applications prévisibles pour lesquelles ils ont été conçus.

Ce cycle de conférences est susceptible d'intéresser les ingénieurs travaillant sur le développement des SAR et les scientifiques appelés à travailler avec les SAR pour diverses applications ainsi que les étudiants ayant déjà des connaissances avancées dans les deux domaines des techniques en question ainsi que des applications en télédétection.

Ce cycle de conférences est présenté par le Panel AGARD d'Avionique; et organisé dans le cadre du programme des Consultants et des Echanges.

List of Authors/Speakers

Lecture Series Director: Dr Wolfgang Keydel
DLR
Institut für Hochfrequenztechnik
8031 Oberpfaffenhofen
Germany

AUTHORS/SPEAKERS

Dr John C. Curlander
Jet Propulsion Laboratory
4800 Oak Grove Drive
Pasadena, CA 91109
United States

Dr Anthony Freeman
Jet Propulsion Laboratory
4800 Oak Grove Drive
Pasadena, CA 91109
United States

Mr Jean-Philippe Hardange
Thomson-CSF
178, Boulevard Gabriel Péri
92242 Malakoff Cedex
France

Mr David Hounam
DLR
Institut für Hochfrequenztechnik
8031 Oberpfaffenhofen
Germany

Dr Herwig Öttl
DLR
Institut für Hochfrequenztechnik
8031 Oberpfaffenhofen
Germany

Dr R. Keith Raney
RADARSAT Project Office
Canadian Space Agency
110 O'Connor St, Suite 200
Ottawa, Ontario K1A 1A1
Canada

Contents

	Page
Abstract	iii
Abrégé	iv
List of Authors/Speakers	v
	Reference
Basic Principles of SAR by W. Keydel	1
SAR Peculiarities, Ambiguities and Constraints by W. Keydel	2
Motion Errors and Compensation Possibilities by D. Hounam	3
The Real Aperture Antenna of SAR, A Key Element for Performance by H. Öttl	4
Polarization Effects and Multipolarization SAR by A. Freeman	5
Radiometric Calibration of SAR Systems by H. Öttl	6
SAR Simulation by D. Hounam	7
Multi-Frequency Multi-Polarization Processing for Spaceborne SAR by J.C. Curlander and C.Y. Chang	8
Inverse Synthetic Aperture Radar J.-P. Hardange	9
Special SAR Techniques and Applications by R.K. Raney	10
Review of Spaceborne and Airborne SAR Systems by R.K. Raney	11
Bibliography	B

BASIC PRINCIPLES OF SAR

by

W. Keydel

Deutsche Forschungsanstalt für Luft- und Raumfahrt e.V.
 Institut für Hochfrequenztechnik
 8031 Oberpfaffenhofen
 Germany

SUMMARY

The basic principles of SAR will be explained. Equations for geometric and radiometric resolution and their inter-relations will be given in addition to a range equation. The difference between focussed and unfocussed SAR and the conception of beam sharpening will be explained.

1. RESOLUTION, KEY TO REMOTE SENSING

For remote sensing purposes the resolution of the respective sensor is one of the main factors. Resolution in the wide sense is defined as the degree to which a sensor can discriminate two closely spaced targets, having similar properties (geometry, colour, velocity, etc.) However, angular resolution is a matter of dominant concern. It is defined as the minimum angular separation between two items which can be distinguished by a system.

Note that for all systems using electromagnetic waves, the laws of optics apply. The angular resolution of an optical system is principally limited by both the aperture diameter and the turbulence of the wave propagation medium (i.e. the earth's atmosphere). Quantitatively the angular resolution of an aperture of a given size l is found by the ratio of wavelength λ over this size.

$$r = \frac{\lambda}{l} \quad (1)$$

The human eye, for example, is an optical system, the resolution r of which is limited by the pupil diameter. Under mean illumination with a wavelength of about 5×10^{-4} mm the pupil diameter varies between 1 mm and 8 mm and an angular resolution power between about 2 arc minutes and 10 arc seconds results. The mean resolution power of 1 arc minute corresponds to a ground resolution of 3 m for a distance of 10 km. (This value can be experienced (approximately!) by looking down to the ground from an aircraft). For optics with diameters roughly a factor 100 larger and at altitude of about 100 km, a resolution power in the order of 10 cm results. This corresponds excellently to values known or guessed for military satellites which are now operational.

Diffraction limiting laws of optics apply to microwave remote sensing systems, too. Here, the antenna is the lens of the system and the antenna aperture, the diameter or length determines the aperture size. The antenna diameter l determines the so-called antenna pattern. The halfpower beamwidth of this pattern determines of conventional radars the angular resolution following in good approximation equation (1). In order to obtain the same resolution as the human eye in the visible region tremendous antenna diameters are required. A wavelength of 5 cm for instance (corresponding to 5 GHz) would require an antenna diameter of 175 m. This illustrates the principal disadvantage of conventional microwave systems in orbital application. However, these disadvantage can be

overcome by the here considered Synthetic Aperture Radar (SAR) techniques.

2. The SYNTHESIS OF AN APERTURE [1 to 5]

Radar techniques are principally one dimensional measurements. For image-construction the second dimension has to be added. This is done principally by moving the radar platform of side looking systems in aircrafts or satellites. The geometric range resolution of such systems is dependent on the bandwidth which estimates the shortest processed pulse length. The azimuth resolution is dependent on the antenna aperture l which determines the half power beamwidth of the radar beam.

The basic idea of the synthetic aperture radar (SAR) is the construction after data collection of a very long antenna along the flight path (here assumed as strongly linear) by means of data processing. Along the flight path are the measuring points for amplitude, phase and frequency of the backscattered signal. In this way the real antenna acts as individual elements of the large (synthetic) array antenna. The stored echos are combined through data processing, and the SAR image is produced.

The Fig. 1 and 2 show the geometry and the respective terminology of SAR.

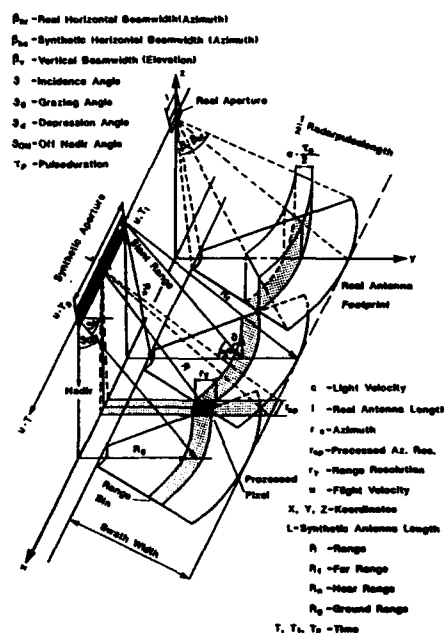


Fig. 1 Geometry and terminology for SAR in 3-dimensional representation.

Due to the inherent velocity u of the radar, the frequency of the received signal is Doppler shifted against the transmitted frequency. For a target seen under small angles β against the cross-track direction (less about 30°) these Doppler frequency is:

range bin, holds an other synthetic aperture and these synthetic aperture increases with increasing distance as well as the geometric resolution of any optical aperture decreases with increasing distance. The range independence of the resolution is a reason for the possibility to extend SAR results gained with airborne systems to spaceborne systems.

As already mentioned the construction of the synthetic aperture for a SAR can be considered as the artificial construction of an array by means of computer techniques. The signals will be stored correctly with respect to amplitude, phase and the appropriate positions. During the image processing procedure the stored signals will be added up correctly and processed to a SAR-image. However, it will be a difference between a real array aperture length and a synthesized aperture of the same length. Whilst for a conventional array the one way beamwidth β_h estimates the resolution, for a synthetic array due to the coherent illumination the two way beamwidth has to be taken into account, since the beamforming phaseshift is introduced on both the paths to and from the target. Therefore, for the azimuth beamwidth of a synthetic array, a factor 1/2 must be included in the formula (1) for the one way pattern.

The time during which a point target is illuminated by the radar beam is called the dwelltime T_D (11).

The required dwelltime for a specified azimuth resolution is:

$$T_D = \frac{\lambda R}{r_a \cdot u} \quad (14)$$

An illumination time T_D can be provided with an oneway antenna beamwidth

$$\beta_{ha} = \frac{1}{R_0} \quad (15)$$

There is principally a need for some phase compensation during the whole dwelltime. The distances R_0 of the far end of the synthetic aperture to a point target are larger as the distance of the middle R_0 (Fig. 1). A so-called unfocussed SAR ignores these differences. This case limits the observation angle to the area, where the differences in distance are smaller than $\lambda/16$, which is identical with $\pi/4$ radian in phase

$$|R_e - R_0| \leq \frac{\lambda}{16} \quad (16)$$

If this focus condition is fulfilled the occurring degradations and the reduction of the result is not very large in comparison with the ideal case. However, the dwelltime is not as large as it could be and the resolution is degraded as well as the maximum aperture length. From fig. 1 results with $R_e + R_0 = 2R_0$:

$$\left(\frac{\lambda}{2}\right)^2 = R_e^2 - R_0^2 = 2R_0(R_e - R_0) \quad (17)$$

The limitation (16) leads to the maximum aperture length of a unfocussed SAR:

$$L_{un} \leq \sqrt{\frac{1}{2} R_0 \lambda} \quad (18)$$

This aperture is responsible for the resolution obtainable and leads to

$$r_{aun} = \sqrt{\frac{1}{2} R_0 \lambda} \quad (19)$$

In the focussed case the incoming phase and ampli-

tude signals must be stored as well as in the unfocussed case. But before the addition of the various signals a phase correction equalizing the phase difference $R_e - R_0$ has to be made. Fig. 3 shows the impulse response for a point target for different phase errors (30° , 90° , 150°). The signal degradation with increasing error evidently can be seen.

The consideration of SAR as a synthesized array leads to the same equations and results with respect to resolution, synthetic aperture length etc. as the Doppler consideration does. However, the meaning of focussed and unfocussed becomes more understandable in the case of the synthetic aperture consideration. Also the name SAR becomes here more evident.

3. THE PHASE INFORMATION, KEY TO SAR [1 to 5]

3.1 THE PHASE REFERENCE

The range R between the platform and a point target can be written:

$$R^2 = R_0^2 + (u \cdot t)^2 \quad (20)$$

u = flight velocity and t = observation time (the maximum observation time is the dwelltime), R_0 is the shortest distance between platform and target. With $R + R_0 = 2R_0$ follows:

$$R - R_0 = \frac{1}{2} \cdot \frac{u^2 t^2}{R_0} \quad (21)$$

To this oneway range difference corresponds a phaseshift

$$\varphi = 2\pi \frac{R - R_0}{\lambda} = \pi \frac{u^2 t^2}{\lambda R_0} \quad (22)$$

The two way phase change will be twice:

$$\varphi = 2\pi \frac{u^2 t^2}{\lambda \cdot R_0} \quad (23)$$

This equation is very important as a reference function for digital SAR processing. The phase shift is a quadratic function of time. This is the so-called phase history of a point target, the phaseshift versus time is a parabola.

To the quadratic phase function of time belongs a linear frequency shift. The Doppler shift f_D of the signal due to the inherent constant platform motion is given by

$$\omega_D = 2\pi f_D = \frac{d\varphi}{dt} = 4\pi \frac{u^2 t}{\lambda R_0} \quad (24)$$

For a transmitted signal $V_t = V_1 \sin(2\pi ft)$ the received signal has the form

$$V_r = V_2 \sin(2\pi ft + 2\pi f_D \cdot t) \quad (25)$$

$$V_r = V_2 \sin\left[2\pi\left(f + \frac{2u^2 t}{\lambda R_0}\right)t\right]$$

This is strongly equivalent to a linear frequency modulation. The received signal of a SAR is linearly frequency modulated. This modulation will be considered as a code which designates all points with respect to their azimuth angle during flight time. The steepness of the so-called chirp is

$$\frac{2u^2}{\lambda R_0}$$

The bandwidth required for this linear modulation results from the dwell time T_D :

$$B_{f_D} = 2 \frac{u^2}{\lambda R_0} T_D . \quad (26)$$

3.2 DEPTH OF FOCUS

Under the assumption that a maximum phase error of $\lambda/8$ may be allowed at the end of the aperture the so-called "Depth of Focus" (DOF) can be defined. DOF is the accuracy with which a given quadratic phase reference function must be matched to the considered range, it defines the number of different reference functions required over the whole swath considered. It holds per definitionem:

$$DOF = 2\Delta R_0 . \quad (27)$$

The maximum allowed one way phase error caused by improper positioning of the phase reference function can be written as $|\Delta R - \Delta R_0| = \lambda/8$. From (20) follows:

$$\frac{dR}{dR_0} = \frac{R_0}{R} = \frac{\Delta R}{\Delta R_0} = \frac{R_0}{\sqrt{R_0^2 + (\frac{L}{2})^2}} = 1 - \frac{1}{8} \left(\frac{L^2}{R_0^2} \right) , \quad (28)$$

$$|\Delta R - \Delta R_0| = \Delta R_0 \frac{1}{8} \left(\frac{L}{R_0} \right)^2 = \frac{\lambda}{8} ,$$

$$DOF = 2\Delta R_0 = 2\lambda \frac{L^2}{R_0^2} . \quad (29a)$$

With (12) results

$$DOF = \frac{8 r_a^2}{\lambda} . \quad (29b)$$

The depth of focus becomes smaller as r_a is made smaller. This is a very important fact for image processing. For example, if $\lambda = 5$ cm, $r_a = 3$ m the DOF is about 1.44 km and, therefore, the processing of a 4.3 km swath requires 3 different reference functions. For a resolution of 50 cm under the same conditions the DOF is 40 m and 10 references are required. This increases the processing complexity. Fig. 3 and Fig. 4 show the influence of focussing effects on SAR images exemplarily.

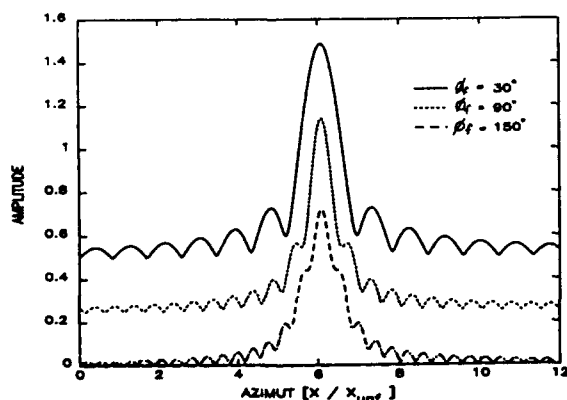


Fig. 3 Point target impulse response degradation for unfocussed processing with different phase deviations (30°, 90°, 180°).

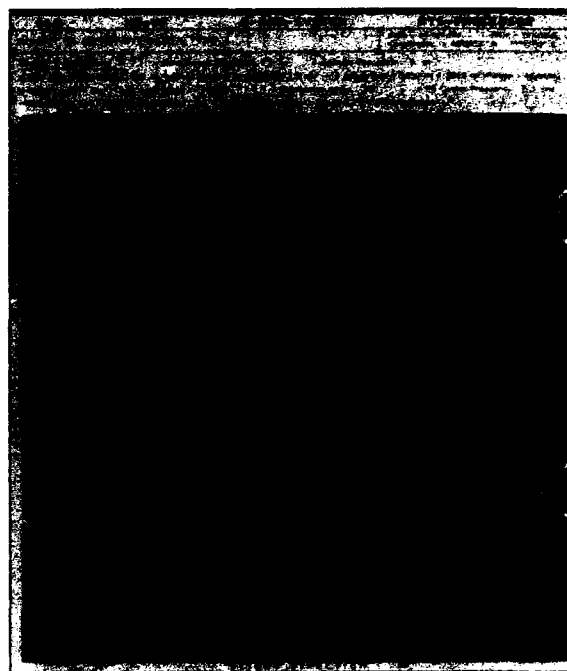


Fig. 4 Example for focus influence of an image quality. The lower image is unfocussed (errors result from velocity) the upper image is focussed.

4. HIGH RESOLUTION IMAGING BY USING THE PHASE REFERENCE FUNCTION

The phase of the received signal (25) contains the required information on an observed target. These information can be extracted by a quadratic demodulator which eliminates the terms with the carrier frequency and leaves the so-called "inphase component I" and the "quadrature component Q" and a joint amplitude factor A containing amplitude or signal to noise informations on the target.

$$I(t) = A \cos(2\pi \left(\frac{u^2 t}{\lambda R_0} \right) t) , \quad (30)$$

$$Q(t) = A \sin(2\pi \left(\frac{u^2 t}{\lambda R_0} \right) t) .$$

Therefore, the complex signal relevant for the information on the target is (with $A = 1$):

$$S_a = I(t) + jQ(t) = \exp(j 2\pi \left(\frac{u^2 t}{\lambda R_0} \right) t) \quad (31)$$

Herein, the target is positioned at $t = 0$ (where $f_D = 0$!) on the variable t , the dwelltime runs from $-T_D/2$ to $+T_D/2$. The further information can be obtained by correlation with a known reference function s_r for a point target. The appropriate reference function for a point target at this location is the same as (31). The output of the correlator is:

$$S_o = \int_{-T/2}^{+T/2} S_a(t) \cdot S_r^*(t+t_r) dt , \quad (32)$$

$$S_o = e^{-j 2\pi \frac{u^2 t_r^2}{\lambda R_0}} \int_{-T/2}^{+T/2} e^{-j 2\pi \frac{u^2 t_r}{\lambda R_0} t} dt ,$$

$$S_o = e^{-j 2\pi \frac{u^2 t_r^2}{\lambda R_o}} \cdot \frac{T_a}{2} \operatorname{sinc}\left(\frac{\pi u^2 T_a}{\lambda R} t_r\right) \quad (33)$$

The sinc function in (33) delivers the image of the point target. Remarkable are the sidelobes. The correlator output has a maximum for $t_r = 0$, when the reference function and the target aligned with each other. Fig. 5 shows the unprocessed amplitude of a point target as well as it gives the processed image of a point target in azimuth direction.

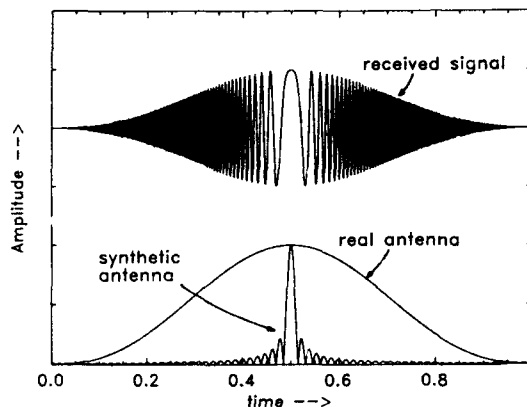


Fig. 5 Amplitude of a pulse response (upper curve) from a point target and SAR-processed impuls response of a point target (lower curve) following (33) in comparison with point target response for a real aperture radar.

5. MODULATION PRINCIPLES FOR RANGING

The main considerations up to now went into direction of the azimuth resolution capability of SAR, which is obviously the main advantage: The azimuth resolution of SAR can be equivalent to the resolution of optical systems, despite of the fact that small antenna apertures will be used. However, the range resolution should have the same order in order to produce high quality imagery. The range resolution r_y of a pulsed radar is equal to half of the pulslength r_p .

$$r_y = \frac{r_p}{2} \quad (34)$$

High resolution would require extremely short pulses and this would require extremely small bandwidth. However, this would entail considerable technological problems and would rapidly lead to the border of SAR possibilities. A solution is here to use pulse compression-methods [1]. There are mainly two methods: the commonly used frequency chirp modulation and the digital pulse code modulation with Barker or Pseudo-Noise codes respectively. Both methods require large time bandwidth products and are well developed for RAR with ranging tasks. However, it should be mentioned here, that the principles of SAR can be considered without special ranging procedures. But looking at the results of the previous Doppler shift considerations during the azimuth measurements a SAR uses principally a linear frequency modulation for azimuth coding, which is formally identical with the frequency modulation principle for ranging. For both, ranging and azimuth measuring the same receiver unit (and the same processor) can be used and this is the main reason why always the FM-chirp for ranging will be considered in connection with SAR in the literature.

6. POWER CONSIDERATIONS AND FADING STATISTICS

Principally, radar uses information on electromagnetic waves characterized with amplitude E , phase φ , frequency f , the polarization which characteri-

zes the vector character and the signal delay time τ . The received radar signal is of the kind of

$$\vec{E}_r = \sum_{i=1}^N \vec{E}_i e^{j(\omega_i t_1 + \varphi_i)} \quad (35)$$

Here is N the total number of scatterers contributing to the signal, \vec{E}_i the vector-field scattered by the i th scatterer, \vec{E}_r the totally received field, $\omega_i = 2\pi f_i$ the circular frequency and $t_1 = t + \tau_i$ the observation time with the respective delay time τ_i . The radar receiver in connection with the data processing part has the task to transform this complex signal into an observable signal proportional to $|\vec{E}_r|^2$ and to extract the information on distance, velocity, behaviour, shape, quality and other quantitative aspects of the observed target. $|\vec{E}_r|^2$ is equivalent to the observed power.

A very important part plays the term "coherency" which will be used for techniques, instruments and for scattering mechanisms as well. Coherency means the phase stability and the statistical behaviour of the phase of electromagnetic waves over the observation time. For complete incoherent scattering - this means if there are many independent scatterers within the beam and for a pure statistical phase distribution between the scattered signals - the performance of radar can be described with good validations by the radar equation.

6.1 THE RADAR EQUATION FOR SAR

The radar equation is given by Hall for a point target (which consists per definitionem of one single scatterer) [1]:

$$S/N = \frac{P_{ave} G^2 \lambda^2 \sigma \cdot T_D}{(4\pi)^3 (k T_o F) R^4 \cdot L_{tot}} \quad (36)$$

Herein is: P_{ave} = average transmitted power, G = antenna gain, λ = wavelength, σ = radar cross-section, R = distance radar-target, k = Boltzmann constant, T_o = noise reference temperature usually 290 K, F = receiver noise figure, L_{tot} all losses.

For the dwelltime T_D Results from (11) and (12):

$$T_D = \frac{\lambda \cdot R}{2 r_a u} \quad (37)$$

This leads to the SAR equation for point targets:

$$S/N = \frac{P_{ave} G^2 \lambda^3 \sigma}{(4\pi)^3 R^3 (k T_o F) \cdot 2u \cdot r_a \cdot L_{tot}} \quad (38)$$

For area targets the radar cross section per unit area σ_o has to be taken into account:

$$\sigma = \sigma_o \cdot r_a \cdot r_y, \quad S/N = \frac{P_{ave} G^2 \lambda^3 \sigma_o r_y}{(4\pi)^3 R^3 (k T_o F) \cdot 2u \cdot L_{tot}} \quad (39)$$

Remarkable is here the dependence of the cube of the range even for point targets. This is a significant difference to real aperture radar. This equation holds if all scatterers within the resolution cell $r_a \cdot r_y$ are independent that means for incoherent summation of the backscattered power. Fig. 6 shows as an example the image of an oilspill on the seasurface taken with a SAR in C-Band.

Fig. 7 shows the signal to noise ratio as a function of range [7]. The dependence of R^3 and of the antenna diagram becomes evident as well as the so-called amplitude line-echo (ALE) which results from



Fig. 6 SAR image of an oilspill on the sea surface taken with DLR E-SAR, C-band [7].

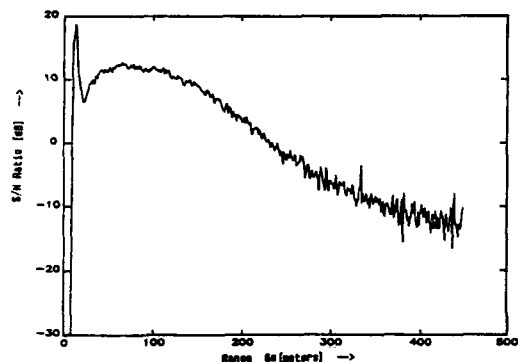


Fig. 7a Signal to noise ratio over the whole scene in Fig. 6 as a function of range. (660 m flight altitude, 30 deg depression angle [7].) The Altitude line echo (ALE) clearly can be identified.

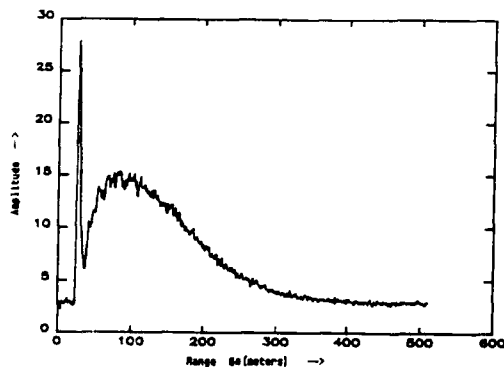


Fig. 7b Signal intensity curve of Fig. 7a as a function of range integrated over 50 s. (660 m flight altitude, 30 deg depression angle.)

reflections directly underneath the aircraft. This curve can be used for image correction.

Fig. 8 gives the signal intensity curve of Fig. 7 after correction. The image in Fig. 6 is corrected (!) by using the results of Fig. 7.

6.2 SPECKLE STATISTICS

However, equation (35) shows the statistical nature of the radar response signal due to the target and scatter statistics. Normally complex radar targets like cars, trees and areas etc. have not only one

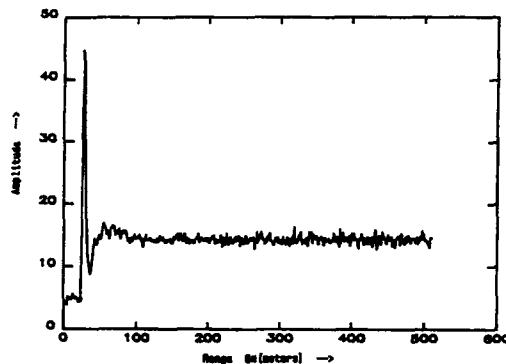


Fig. 8 Signal intensity curve of the image in Fig. 6 after radiometric correction using the curve in Fig. 7b. (660 m flight altitude, 30 deg depression angle.)

but many scattering centers which contribute to the radar response signal; individual scattering centers may be seen with very high resolution systems (exceptions are very simple targets only like spheres, corners, cylinders, plates). Fig. 9 shows as an example the distribution of such centers on a car [8].

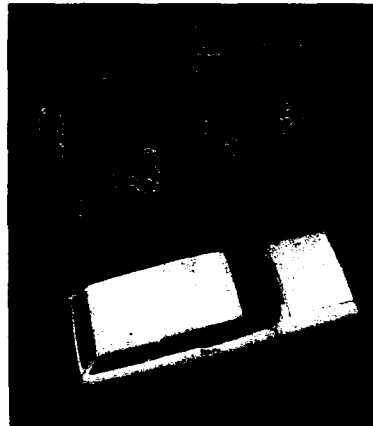


Fig. 9 Distribution of reflection centers on a car in a twodimensional representation. Resolution is about 15 cm x 15 cm (measurement Graf, DLR [2]).

Under the assumption of statistical distributed amplitudes E_1 and phases ϕ_1 (35) becomes a statistical phasor the quality of which is dependent on the respective distribution functions. For uniformly distributed phases ϕ_1 and Rayleigh distributed amplitudes results an exponential distribution for the amplitude square of (35). That means in general if homogeneous areas of the earth are illuminated by a coherent radar the backscattered signal amplitudes of the single observations (pixels) are statistically distributed and this is the reason for the speckle typical for each radar image also for images of very homogeneous areas. There is no possibility to characterize a radar target by measurement of one pixel only. Principally this speckle can be reduced by image averaging with the use of multi looks for instance, this reduces the standard deviation proportional to the root of the look number and smoothes the speckle. Speckle can be seen in all the radar images presented here.

The Rayleigh distribution for the envelope V_r belonging to (35) is

$$P(V_r) = \frac{V_r}{\sigma_v^2} \exp\left(-\frac{V_r^2}{2\sigma_v^2}\right) \quad \text{for } 0 \leq V_r. \quad (40a)$$

The phase is uniformly distributed

$$P(\varphi) = \frac{1}{2\pi} \quad \text{for } 0 \leq \varphi \leq 2\pi. \quad (40b)$$

Mean value \bar{V}_r and the second moment $\overline{V_r^2}$ of (40a) are:

$$\bar{V}_r = \sqrt{\frac{\pi}{2}} \sigma_v, \quad \overline{V_r^2} = 2\sigma_v^2 \quad (41)$$

The variance is by definition:

$$\text{Var}(V_r) = \overline{V_r^2} - \bar{V}_r^2 = 0.429 \sigma_v^2 = \overline{V_{ac}^2}.$$

The variance represents the fluctuation of the registered voltage around the mean value, this is principally an inherent noise and it can be written as a mean squared AC component $\overline{V_{ac}^2}$. Together with (41) one obtains the inherent signal to noise ratio S_{nr} for Rayleigh fading

$$S_{nr} = \frac{\bar{V}_r^2}{\overline{V_{ac}^2}} = 3.66 \hat{=} 5.6 \text{ dB}.$$

This occurs, even in the absence of any other additional noise. That means, the Rayleigh fading is equivalent to addition of noise that results in a signal-to-noise ratio of 5.6 dB, even if the ratio of the average signal level to actual noise is very high. Thus, the best equivalent signal-to-noise ratio that can be obtained when Rayleigh fading exists is 5.6 dB. This is the reason that fading distributions are so important in radar problems. One often would like to have a high signal-to-noise ratio, but the effective signal-to-noise ratio cannot exceed 5.6 dB unless multiple independent fading samples are added together, regardless of the ratio of the mean received power to the thermal-noise power in the system [5].

The measured signal P_r which is considered in (36) is the power, which can be written as

$$P_r = V_r^2 = S.$$

From distribution (40) for V_r results the exponential distribution for P_r :

$$P(P_r) = \frac{1}{2\sigma_v^2} \exp\left(-\frac{P_r}{2\sigma_v^2}\right) \quad \text{for } 0 \leq P_r. \quad (42)$$

For the mean value \bar{P}_r and the second moment $\overline{P_r^2}$ holds

$$\bar{P}_r = 2\sigma_v^2, \quad \overline{P_r^2} = 8\sigma_v^4 = 2\bar{P}_r^2.$$

With these results the Rayleigh distribution (40) can be rewritten:

$$P(V_r) = \frac{V_r}{\bar{P}_r} \exp\left(-\frac{V_r^2}{2\bar{P}_r}\right). \quad (43)$$

Fig. 10 shows as an example the histogrammes of Fig. 7 [7].

If N independent pixel values are added than follows from the laws of probability theory that the mean value of the sum is identical with the mean value of the single element whereas the variance for the sum of N independent samples is the variance of the single sample divided by N . That means for the case of a linear detector if N numbers of samples are averaged and if V_{r1} is the envelope voltage of the i th sample than is the average received voltage V_L :

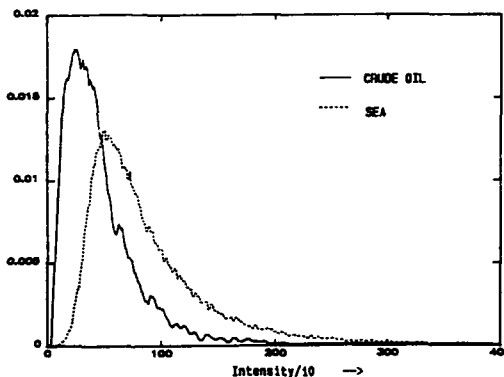


Fig. 10 Histogram of the filtered SAR image of Fig. 6. (Oil slick A2, 660 m flight altitude.) Both curves follow a Rayleigh distribution.

$$V_L = \frac{1}{N} \sum_{i=1}^N V_{r1}.$$

For the mean holds principally

$$\bar{V}_L = \bar{V}_r = \sqrt{\frac{\pi}{2}} \sigma_v.$$

But for the variance one obtains

$$\overline{V_{Lac}^2} = \frac{\overline{V_{ac}^2}}{N} = \frac{0.429 \cdot \sigma_v^2}{N}.$$

With these results for the optimum equivalent S_{nr} results instead of (41):

$$S_{nr} = 3.66 \cdot N. \quad (44)$$

The maximum obtainable signal to noise ratio increases rapidly with increasing N .

The time T during which a point target remains within the real beam is the time for observing this fading signal. This time can be obtained from the consideration of the extension of the footprint in flight direction which is the azimuth ground-resolution r_a of the real antenna.

$$r_a \beta_{hr} \cdot R = vT. \quad (45)$$

The number N_{az} of independent samples in azimuth direction is the product of bandwidth and observation time.

$$N_{az} = \Delta f_D \cdot T, \quad (46)$$

$$N_{az} = 2 \frac{\beta_{hr}^2 R}{\lambda}.$$

This leads to the simple equation

$$N_{az} = \frac{r_a}{1/2}. \quad (47)$$

The equations (46) and (47) are very fundamental. They apply to SLAR and to SAR as well. Equation (47) shows the possible tradeoff which can be made between large resolution and small r_a and high specle reduction (large N).

The number N_r of independent samples in range direction results from considerations of range resolution. The slant range resolution for a pulse

radar r_y is given by:

$$r_y = \frac{c \cdot \tau_p}{2} = \frac{c}{2B}$$

If N_y returns with that resolution will be averaged than a poorer resolution will result. Therefore, the number of independent rangepixels is proportional to the reduced range resolution r_{yred} .

$$N_y = \frac{r_{yred}}{r_y}$$

The equivalent pulselength τ_{peq} associated with N_y averaged returns is:

$$\tau_{peq} = N_y \cdot \tau_p$$

Using these results, one can express the number of independent range samples:

$$N_y = \frac{r_{yred}}{r_y} = \frac{\tau_{peq}}{\tau_p} = \frac{B}{B_{eq}} \quad (48)$$

In (48) is B_{eq} the equivalent bandwidth which belongs to τ_{peq} .

The total number of independent samples is given by:

$$N = N_{az} \cdot N_y \quad (49)$$

Equation (48) shows as well as equation (47) in connection with (45) the possible tradeoff between high geometrical resolution and high speckle reduction which corresponds to high radiometric resolution. Radiometric resolution describes the possibility to consider two areas with two different speckles (or medium grey tones) as different. One possibility is to take the mean values \bar{X}_1 and \bar{X}_2 of the probability density functions of the pixels of those two fields and use the ratio of both mean values for a measure of the separability:

$$r_{rad} = \frac{\bar{X}_2}{\bar{X}_1} \quad (50a)$$

$$r_{rad} = \frac{\bar{X}_1 + \Delta X}{\bar{X}_1} \quad (50b)$$

This ratio is called radiometric resolution. For SAR the angular resolution is closely connected to the radiometric resolution. The radiometric resolution is the minimum brightness contrast necessary for the discrimination of two targets. The radiometric resolution in radar images is dependent on the image statistics, the speckle. Therefore, by increasing the integration time (i.e. the observation time of a certain area represented through the number of looks on it) the speckle will decrease, the radiometric resolution increases (the image becomes sharper), but the angular resolution decreases.

Fig. 11 shows the processed radar answer of a point target with different geometric resolution (8.94 m and 11.4 m). The decrease of the sidelobes with increasing resolution is evident. A quality measure is the peaksidelobe ratio PSRLR as well as the integrated sidelobe ratio ISLR which are defined as follows:

$$PSLR = \frac{\text{power within the sidelobes}}{\text{power within the main beam}}$$

$$ISLR = \frac{\text{power within the sidelobes}}{\text{power within the total diagramm}}$$

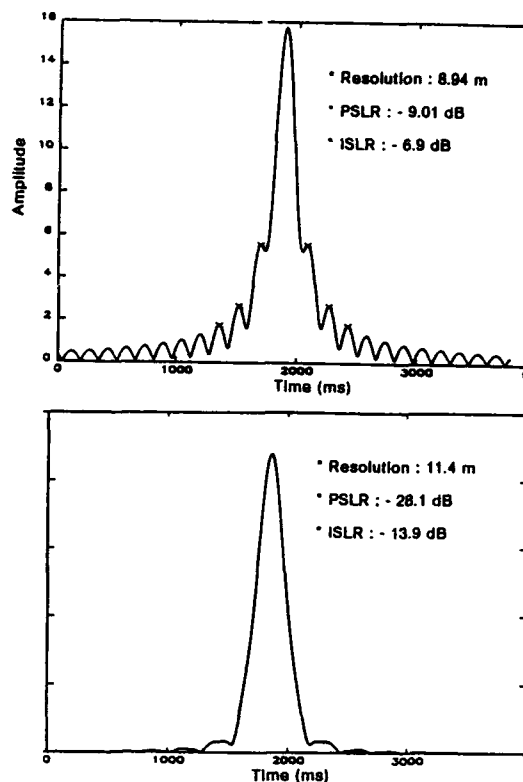


Fig. 11 Impulse responses (2dimensional image) of a point target showing the interconnection of resolution and siderlobe level.

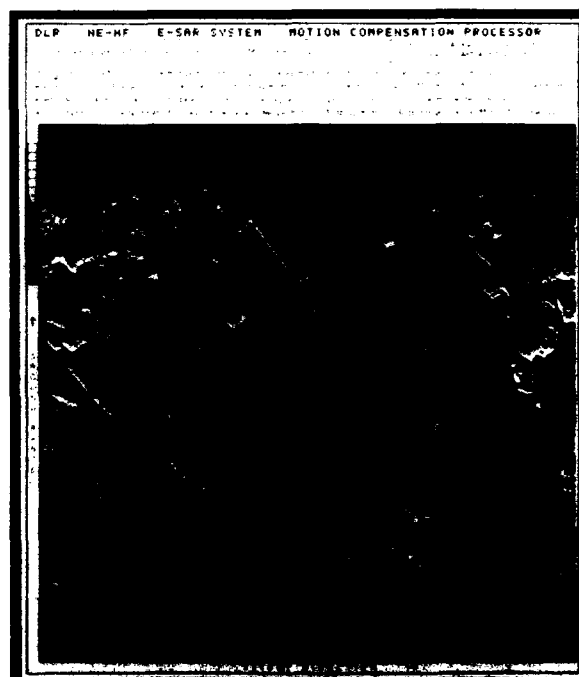


Fig. 12 SAR image of DLR-Research Center and airfield in Oberpfaffenhofen taken at 5 cm wavelengths from an aircraft at 914 m altitude. Scene dimension 2700 m x 3510 m, resolution 2 m x 3 m (azimuth x range), 8 looks.

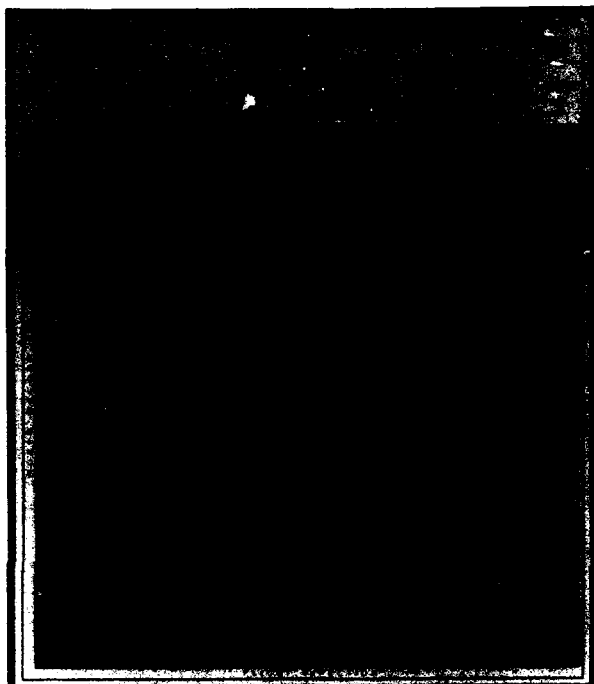


Fig. 13 SAR image, part of the airport in Oberpfaffenhofen. The scene corresponds to a section of the image in Fig. 12. Scene dimension is $826 \text{ m} \times 1079 \text{ m}$, ground resolution $0.5 \text{ m} \times 2 \text{ m}$ (azimuth \times range), 1 look. The aircraft on the platform in the middle will be enlarged represented in Fig. 14 (Moreira, DLR).

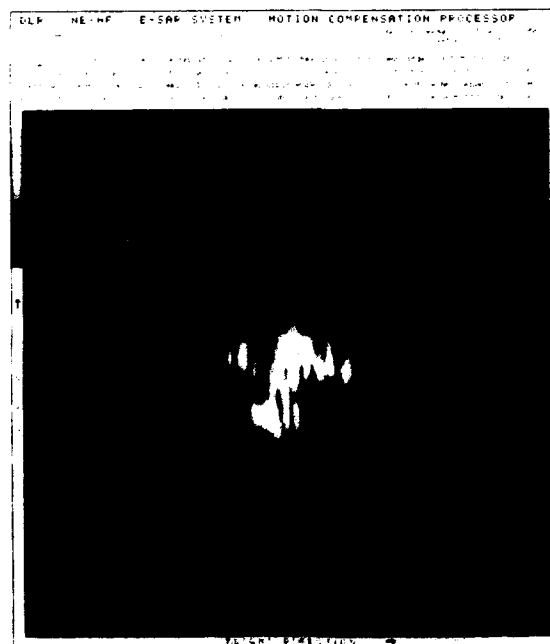


Fig. 14 Enlargement of the aircraft on the dark platform in the upper left corner of Fig. 13. Scene dimension is $60 \text{ m} \times 60 \text{ m}$, ground resolution is $0.5 \text{ m} \times 2 \text{ m}$ (azimuth \times range). The unsymmetry in the resolution pixels caused by the unsymmetrical ground resolution area clearly can be seen. The aircraft is probably a Do 228; this is a conclusion of a geometrical evaluation of the aircraft image in comparison with the well known real dimensions. The different reflection centers typical for radar imaging as well as the speckle clearly can be seen (Moreira, DLR).

In Fig. 12, 13 and 14 this tradeoff between geometric and radiometric resolution as well as the influence of the speckle is illustrated. The images from the DLR-Dornier airport at Oberpfaffenhofen have been taken by the airborne SAR of the DLR at 5 cm wavelength [9, 10, 11]. Fig. 12 shows an 8 look image with low speckle and high contrasts. This image with its dimensions of $2.700 \text{ m} \times 3.510 \text{ m}$ (range \times azimuth) has a resolution of 2 m in range and 3 m in azimuth; with its many details it is comparable to a real photography. Fig. 13 shows enlarged a part of Fig. 12: the scene dimension is 828 m in range and 1.079 m in azimuth. This one look image has an azimuth resolution of 0.5 m and a range resolution of 2 m . (The resolution in range here can not be increased due to the limited bandwidth of the system.) The increase of the speckle against the 8 look image in Fig. 12 is evident. Impact of high resolution becomes clear by looking at the large black platform in the upper left corner. There an aircraft clearly can be seen. This aircraft together with its background is shown enlarged in Fig. 14 with the same resolution. The image size corresponds here to $60 \text{ m} \times 60 \text{ m}$. The differences in range and azimuth resolution are evident. This same image was used for estimation of the dimensions of the aircraft. A comparison with the known dimensions of a DO 228 aircraft leads to the conclusion, that the image shows with a high degree of probability a DO 228. The estimated dimensions (with the real values of a DO 228 in parenthesis) are: Total length 14.3 m (15.04), total wingspread 16.3 m (16.97 m), wingspread of the elevator unit 7.7 m (6.45 m). This points out, that for airborne SAR a resolution in the order of dm is the present state of the art [12, 13]. However, for spaceborne SAR the present state of the art is poorer due to different reasons (atmospheric turbulences, power limitations, data-rates). Present spaceborne SAR principally can have a ground resolution power in the order of one or a few meters.

7. SAR IMAGES

7.1 IMAGE GEOMETRY

SAR-pictures are different from normal photographs in many details. They look like an aerial photograph although taken from a sidelooking perspective. This side looking perspective leads to shadow-effects and to the well-known characteristic plasticity of SAR-pictures. The shadows can be used for height estimation of trees, rocks, and other shadow producing elements in a SAR image as in Fig. 22 for example.

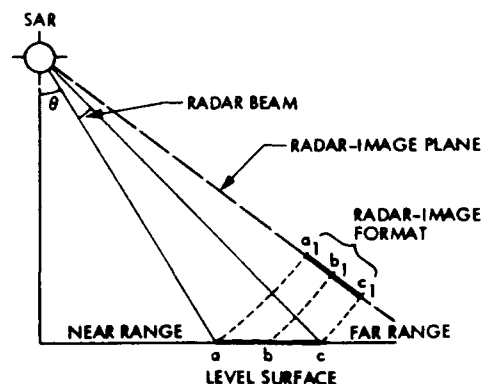


Fig. 15 Radar-image format showing slant-range presentation a_1 b_1 c_1 relative to ground-range abc , assuming a level surface long-dashed line represents radar-image plane. Look angle is inclination of the radar beam off vertical [14].

An uncorrected SAR image is always a so called slant range image it represents basically the distance from the radar to each of the respective surface elements in the scene. Therefore, in its raw stage it shows some geometric distortion due to the differences between slant range and ground range explained in Fig. 15 [14]. Fig. 16, 17 and 18 show raw data a slant range image as well as a finally processed image of the same scene.

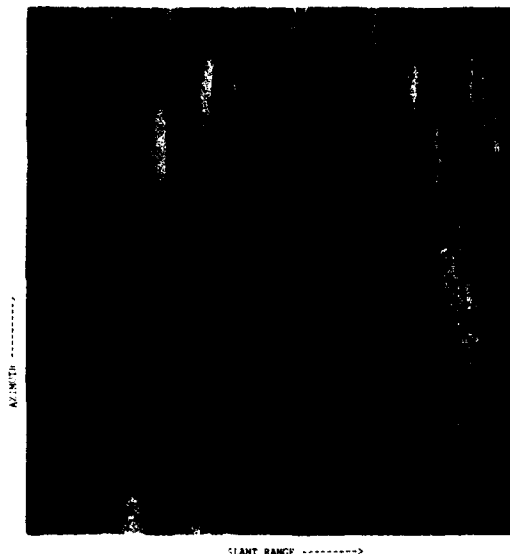


Fig. 16 Raw data: RCM corrected, range compressed image before the azimuth processing.

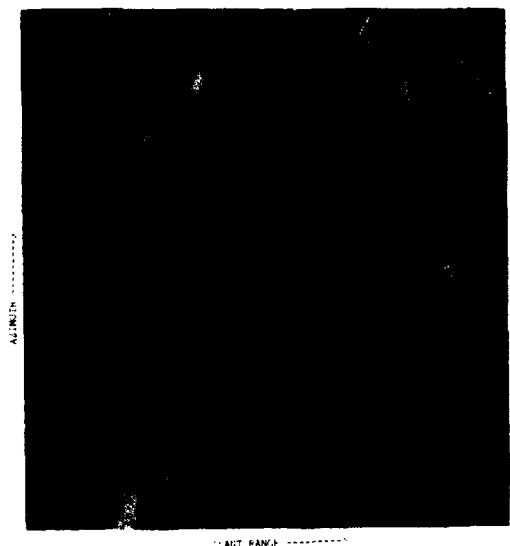


Fig. 17 Slant range image processed from raw data in Fig. 16. Azimuth processed image including the partially processed region.

A further set of geometric relief displacements that is characteristic of all imaging radars is the apparent variation in length of equal terrain slopes when the respective slope lengths are imaged at different incidence angles. The displacements result in foreshortening, layover, and shadowing. These effects are feature-dependent and cannot be easily corrected.

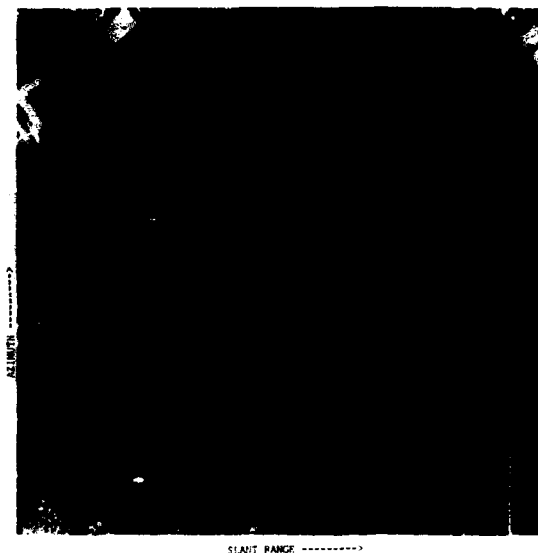


Fig. 18 Azimuth processed image - only the totally focussed region. Processed from raw data in Fig. 16 and slant range image in Fig. 17.

Foreshortening [14]

Slopes inclined toward the radar appear compressed relative to slopes inclined away from the radar. The effect is illustrated in Fig. 19. The foreshortening factor F is approximately:

$$F = \sin(\theta - \alpha)$$

where the look angle θ is the angle between the vertical plane and a line that links the imaging-radar antenna to a feature on the ground, and is the slope angle of the surface. Alpha is positive (α^+) where the slope is inclined toward the radar (foreslope), and negative (α^-) where the slope is inclined away from it (backslope).

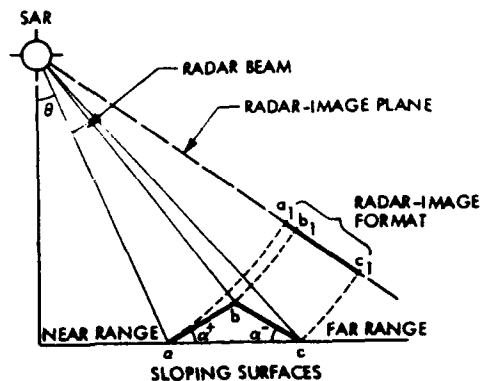
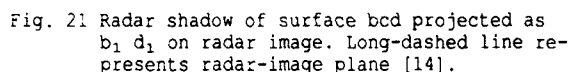
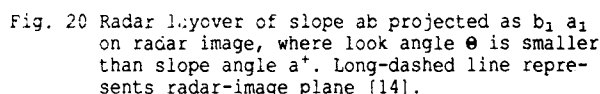


Fig. 19 Radar foreshortening of slope ab , which is projected as $a_1 b_1$, relative to slope bc , which is projected as $b_1 c_1$, showing look angle θ , foreslope angle α^+ , backslope angle α^- . Long-dashed line represents radar image plane.

Layover [14]

Layover is an extreme case of foreshortening that occurs when the look angle θ is smaller than the foreslope α^+ ($\theta < \alpha^+$). This is illustrated in Fig. 20. In this case, a mountain is laid over on its side.



Shadowing is essentially the opposite of foreshortening. Slopes inclined away from the radar are in shadow when the look angle θ plus the backslope angle α are greater than 90° [$(\theta + \alpha) > \pi/2$]. Shadows are caused by ground features that obstruct the radar beam and prevent illumination of the area behind them. This effect occurs on Seasat SAR images whenever the backslope in the radar viewing direction exceeds about 70° . It is shown diagrammatically in Fig. 21. Fig. 22 shows clearly the shadows of different features.

8.1 PRINCIPAL CONSIDERATIONS

The SAR is mounted on a platform moving at a constant velocity. The PRF must be sufficiently high to avoid azimuth ambiguities. This criterion requires that the radar platform displacement cannot exceed one-half the antenna size between successive transmit pulses.

```

graph TD
    PG[PULSE GENERATOR] -- PRF 1.009 --> WG[WAVEFORM GENERATOR]
    WG --> HPA[HIGH POWER AMPLIFIER]
    HPA --> ANT[ANTENNA]
    ANT --> LNA[LOW NOISE AMPLIFIER]
    LNA --> MIX[MIXER]
    SO[STABLE OSCILLATOR] --> MIX
    MIX --> QD[QUADRATURE DEMODULATOR]
    QD -- I --> AD1[A/D]
    QD -- Q --> AD2[A/D]
    AD1 --> 2DM[2D MEMORY]
    AD2 --> 2DM
    2DM -- I --> RP[REALTIME PROCESSOR]
    2DM -- Q --> RP
    RP --> MON[MONITOR]
    RP --> ST[STORAGE]
  
```

A typical SAR transmitter is designed to overcome limitations of peak power in components and to satisfy stringent azimuth and range resolution requirements. High resolution in azimuth requires stringent phase stabilities from pulse-to-pulse and over the integration time. High range resolution requires wide RF bandwidths. To meet the signal-to-noise ratio and target detection requirements correlation principles and pulse code modulations can be used respectively with special wave forms.

Electronic circuits using a voltage controlled oscillator can provide the desired transmit pulse. The output from the high power amplifier passes through a circulator and is radiated by the radar antenna. The received signal passes through the same circulator, is amplified (and normally pulse

compressed). (the pulse compression circuit can use a frequency dispersive delay line which converts a wideband linearly swept FM long pulse into a short pulse signal with same bandwidth.) The phase of the short pulse is measured by the phase coherent detector, and the resultant signals are delivered to the signal processor.

8.2 THE DLR E-SAR AS AN REALISATION EXAMPLE

The DLR airborne experimental synthetic aperture radar system E-SAR, designed and manufactured at the DLR Institut fuer Hochfrequenztechnik, is a research tool to elaborate SAR related problems concerning both system performance and data analysis. The instrument is installed on board a DLR Dornier DO 228 aircraft, which is a small STOL aircraft (STOL: short take-off and landing), offering the advantages of low costs and operation from airstrips in any part of the world.

All SAR results shown here have been obtained with this instrument.

Since the beginning of 1989 the E-SAR system has been flown many times in preparatory campaigns for the European Remote Sensing Satellite ERS-1. The German/Italian X-SAR, which will fly with SIR-C on three Shuttle Radar Lab missions, and the French Radar 2000, both spaceborne SAR projects, are supported with E-SAR image data.

Applications

The E-SAR is a high-resolution SAR operating in L-, C- and X-band with either horizontal or vertical polarization. Although being developed mainly for use by the research community, commercial lease opportunities are as well anticipated. The sensor is versatile, with many options for flight and radar configurations and image products. It provides the opportunity to image areas, whether flat or mountainous terrain, ocean or ice, with excellent image quality. It can be used for monitoring resources, renewable such as agriculture and forestry, or nonrenewable such as geological resources. Changing characteristics such as urban growth, deforestation or ocean waves also can be monitored.

The System Platform

A Dornier DO 228 aircraft equipped with modern navigation systems like a laser inertial reference system (IRS) and a GPS receiver carries the E-SAR sensor. Its maximum take-off weight equals 5980 kg. The maximum operating altitude above mean sea level (MSL) is 8000 m. The maximum cruising speed is about 440 km/h. For SAR operation the nominal ground speed of the aircraft is 70 m/s, which corresponds to 252 km/h.

The On-board Segment

The radar sensor is a modular designed system, which contains three different RF-segments in L-, C- and X-band. Pulse generation and I/Q-detection are located in the IF-section. A single digital conversion and recording system is used to store the SAR raw data on high density digital tape (HDDT) formatted in the SAR 580 HDDT format.

The On-ground Segment

The ground segment consists of the following units:

- Radar Raw Data Transcription

A SAR 580 High Density Tape Transcription system (HTS) transcribes the raw data from HDDT to computer compatible EXABYTE (Video 8) tapes. A further data transfer to conventional CCTs is possible. This operation

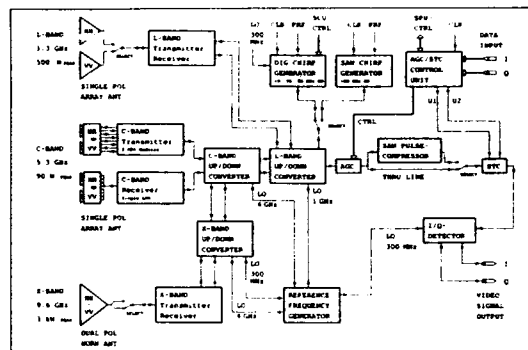


Fig. 24 E-SAR sensor system blockdiagram (RF-electronics).

RF centre frequency, L-band:	1.3 GHz
C-band:	5.3 GHz
X-band:	9.6 GHz
IF centre frequency:	300 MHz
System bandwidth:	120 MHz
SAW chirp, signal bandwidth:	100 MHz
expanded pulse length:	4.98 μ s
compressed (analogue) pulse length:	17 ns
Digital chirp, signal bandwidth, narrow swath mode:	90 MHz
wide swath mode:	50 MHz
super wide swath mode:	18 MHz
expanded pulse length:	5.0 μ s
Antenna gain, L-band:	14 dBi
C-band:	17 dBi
X-band:	17.5 dBi
Antenna 3 dB beamwidth, azimuth, L-band:	18 Deg
C-band:	19 Deg
X-band:	17 Deg
elevation, L-band:	35 Deg
C-band:	33 Deg
X-band:	30 Deg
Transmit peak power, L-band:	500 W
C-band:	90 W
X-band:	2500 W
Receiver noise figure, L-band:	8.5 dB
C-band:	4.0 dB
X-band:	4.5 dB
Receiver dynamic range with AGC/STC:	≥ 40 dB
Nominal pulse repetition frequency (PRF):	952.38 Hz
Variable PRF range:	± 30 %
Quantization (I or Q):	6 bit
A/D converter dynamic range (at 35 MHz):	25 dB
Sampling rate, narrow swath mode:	100 MHz
wide swath mode:	60 MHz
super wide swath mode:	20 MHz
Echo buffer memory capacity (I or Q):	2560 words
Nominal data rate on high density tape:	28 MBPS
Maximum recording time per tape (14 inch tape reel):	15 min
Spatial resolution, range and azimuth, narrow swath mode:	2.5 m \times 2.5 m
wide swath mode:	4.5 m \times 4.5 m
super wide swath mode:	11.5 m \times 11.5 m
Number of statistically independent looks:	8
Radiometric resolution (8 looks):	< 2 dB
Geometric distortion:	less than one resolution cell

Table 1 E-SAR specifications.

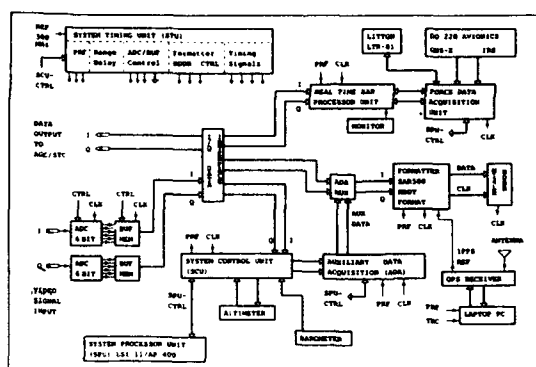


Fig. 25 E-SAR sensor system blockdiagramm (digital electronics).

also converts the SAR 580 HDDT format into the SAR 580 video signal CCT format and provides the full data rate in a single channel transcription mode.

- E-SAR Standard SAR Processing

The E-SAR standard SAR processor consists of three basic modules, auxiliary data processing, off-line motion compensation and focused multi-look SAR processing. The development was carried out in DLR. The processor output is calibrated and available in form of a standard image product.

Motion Compensation

The DO 228 aircraft is fairly sensitive to air turbulence and, therefore, not very well suited for carrying a SAR sensor. A SAR is a coherent system and flight instability causes phase errors, which, in turn, defocus and distort the image geometrically. This problem can be overcome by measuring the dynamic behaviour of the platform and correcting the SAR data, either on board the aircraft or on ground. Two methods for compensating platform motions are implemented with the E-SAR, one using an inertial Measurement Unit (IMU), the other, the "Reflectivity Displacement Method (RDM)", extracting true forward velocity and Line-of-Sight (LOS) accelerations out of the radar raw data. This guarantees that the E-SAR achieves good image quality with high spatial and radiometric resolution.

9. REFERENCES

- [1] Skolnik, M.I. Radar Handbook. McGraw Hill Book Company, 1970.
- [2] Hovanessian, S.A. Introduction to Synthetic Array and Imaging Radars. Artech House, Inc., 1980.
- [3] Tomiyasu, K. Tutorial Review of Synthetic Aperture Radar (SAR) with Applications to Imaging of the Ocean Surface. Proc. of the IEEE, Vol. 66, No. 5, May 1970, pp. 563-583.
- [4] Kowaly, J.J. Synthetic aperture radar. The Artech radar library. Artech House, Inc., 1976.
- [5] Ulaby, F. Moore, R.K. Fung, A.K. Microwave Remote Sensing Active and Passive. Vol. II Radar Remote Sensing and Surface Scattering and Emission Theory. Addison-Wesley Publ. Comp. Advanced Book Program/World Science Division Reading, Mas., 1982.
- [6] Elachi, Ch. Spaceborne Radar Remote Sensing Applications and Techniques. IEEE, New York, 1987.
- [7] Moreira, A. Entwurf und Ergebnisse des DLR-Echtzeit-Azimuthprozessors für das E-SAR-System. DLR-FB 89-30.
- [8] Graf, G. High Resolutin Imaging of Radar Targets with Microwaves. Conf. Proc. Military Microwaves '78, London/Engl., 25.-27.10.78. Microwave Exhibitions and Publ. Ltd., pp. 295-302.
- [9] Horn, R. C-Band SAR Results Obtained by an Experimental Airborne SAR Sensor. Proc. IGARSS, IEEE, 1989, pp. 2213-2216.
- [10] Moreira, J. Estimating the Residual Error of the Reflectivity Displacement Method for Aircraft Motion Error Extraction from SAR Raw Data. ICCO Intern. Radar Conf., May 7-10, Arlington, USA, 1990, pp. 70-75.
- [11] Moreira, J. A New Method of Aircraft Motion Error Extraction from Radar Raw Data for Real Time SAR Motion Compensation. 12th Canadian Symposium on Remote Sensing, IGARSS '89, Vancouver, Canada, 10-14 July 1989. Proc. IGARSS, IEEE, 89, pp. 2217-2220.
- [12] Keydel, W. Microwave Sensors for Remote Sensing of Land and Sea Surfaces. Geo Journal 24.1, 1991, pp. 7-25.
- [13] Keydel, W. Verification Using Spaceborne Microwave Imaging. IEEE, Technology and Society Magazine, Dec. 1990/Jan. 1991, pp. 53-61.
- [14] Ford, J.P. Blom, B. Daily, D. Elachi, X. Seasat Views North America, the Caribbean and Western Europa with Imaging Radar. JPL-Publication 80-67, 1980.

SAR PECULIARITIES, AMBIGUITIES AND CONSTRAINTS

by

W. Keydel

Deutsche Forschungsanstalt für Luft- und Raumfahrt e.V.

Institut für Hochfrequenztechnik

8031 Oberpfaffenhofen

Germany

ABSTRACT

A synthetic aperture radar (SAR) is basically a coherent scatterometer that employs a coherent real aperture radar with highly sophisticated data evaluation and image processing capabilities. Therefore, the coherence of the system is very important; furthermore, the keypoints for SAR are data storage, evaluation and processing. These facts entail peculiarities of SAR and special ambiguities which are different from those arising with real aperture radar (RAR). The objective of this paper is to point out the special peculiarities and ambiguities of SAR in comparison to the corresponding properties of RAR. Main topics in this connection are: basic peculiarities like range dependency of signal to noise ratio, azimuth resolution and influence of platform velocity. Furthermore, range and azimuth ambiguities, pulse repetition frequency limitations, velocity effects and phase errors influence on SAR-image that cause motion compensation problems. All these effects will be explained together with different contrast-equations between the target and clutter signals of SAR and RAR.

1. INTRODUCTION

A Synthetic Aperture Radar is essentially a coherent scatterometer or real aperture radar with sophisticated data evaluation and image processing. Important is the coherence of the system. However, storage, evaluation and processing of the data are the key points for SAR. The use of a synthetic aperture in connection with extremely high range resolution methods like pulsecompression requires a high degree of coherency and frequency stability. This holds also if pulse compression techniques for scatterometer will be used. However, the combination of synthetic apertures with pulse compression entails requirements for frequency adjustable oscillators for example and other high sophisticated components and this makes evident: SAR requires extreme effort not only with respect to software but also to hardware.

These facts entail peculiarities of SAR and special ambiguities which are different from those arising with real aperture radar (RAR). The objective of this paper is to point out the special peculiarities and ambiguities of SAR in comparison with similar facts of RAR. Basic peculiarities like range dependence of signal to noise ratio, azimuth resolution and influence of platform velocity. Furthermore, range and azimuth ambiguities, pulse repetition frequency limitations, velocity effects and phase errors influence SAR-images and cause motion compensation problems.

2. BASIC SAR-PECULIARITIES IN COMPARISON WITH REAL APERTURE RADAR

For complete incoherent scattering, this means if there are many independent scatterers within the antenna beam and for a pure statistical phase distribution between the scattered signals the performance of radar can be described with a good validation by the radar equation. The decisive factor is here the signal to noise ratio. For the detection of a point target not only the radar signal itself but also its background, the clutter, and the respective contrast between signal and clutter is most important. However, each imaging radar measures and uses the clutter as primary signal. Therefore, the clutter to noise ratio, C/N, is for imaging radars decisive, whereas for point target estimation the contrast between signal and clutter, S/C as well as the signal to noise contrast S/N is essential.

Table 1 shows the different equations for area and point-targets and for real and synthetic apertures and the respective contrasts. For contrast computation the losses in all equations have been assumed as identical and equal. However, this is normally not the case and it shall be remarked that normally special system losses are dependent on the special applied techniques; but for simplicity it shall be allowed here to take all losses out of consideration in order to reach the simple compa-

	Point Target	Area Target	Contrast
Real Apertur (RAR)	$(S/N)_{\text{real}} = \frac{P_{\text{ave}} G^2 \lambda^2 \sigma}{(4\pi)^3 R^4 (kT_0 F) \cdot B f_p \tau_p \cdot L_{\text{tot}}}$	$(C/N)_{\text{real}} = \frac{P_{\text{ave}} G^2 \lambda^3 \sigma_0 \cdot r_y}{(4\pi)^3 R^3 (kT_0 F) f_p L_{\text{tot}}}$	$(S/C)_{\text{real}} = \frac{\sigma \cdot l}{\sigma_0 \cdot R \cdot \lambda \cdot r_y \cdot B \cdot \tau_p}$
Synthetic Aperture (SAR)	$(S/N)_{\text{SAR}} = \frac{P_{\text{ave}} G^2 \lambda^3 \sigma}{(4\pi)^3 R^3 (kT_0 F) \cdot 2u \cdot r_a \cdot L_{\text{tot}}}$	$(C/N)_{\text{SAR}} = \frac{P_{\text{ave}} G^2 \lambda^3 \sigma_0 r_y}{(4\pi)^3 R^3 (kT_0 F) 2u \cdot L_{\text{tot}}}$	$(S/C)_{\text{SAR}} = \frac{\sigma}{\sigma_0 r_y \cdot r_a}$
Improvement Factor	$(S/N)_{\text{SAR}} / (S/N)_{\text{real}} = \frac{B \cdot \tau_p \cdot \lambda \cdot R \cdot f_p}{r_y \cdot 2u}$	$(C/N)_{\text{SAR}} / (C/N)_{\text{real}} = \frac{f_p \cdot l}{2u}$	$(S/C)_{\text{SAR}} / (S/C)_{\text{real}} = \frac{B \cdot \tau_p \cdot R \cdot \lambda}{r_a \cdot l}$

Table 1 Radar- and contrast equations for real aperture radars and SAR.

rison and contrast equations in table 1.

(C/N) = received clutter to noise ratio, (S/N) = received signal to noise ratio, P_{ave} = average transmitter power, G = antenna gain, λ = wavelength, R = distance, σ = radar cross section, σ_0 = radar cross section per unit area, k = Boltzmann constant, $T_0 = 290$ K, B = receiver bandwidth, F = receiver noise figure, f_p = pulse repetition frequency, τ_p = pulselength, L_{tot} = losses, u = SAR-velocity, l = real azimuth diameter of SAR antenna, r_y = ground range resolution, r_a = processed azimuth resolution.

Table 1 shows for point and area targets as well the peculiarities of SAR against conventional radar. It shows evidently the importance of the pulse repetition frequency PRF and platform velocity. For the point target case the dependence of azimuth, resolution, bandwidth, pulselength, wavelength and distance becomes evident while for area targets the real aperture length plays an important part. Especially the expressions in the "Improvement-Factor-Line" and in the "Contrast-Row" show factors, which are most important for a comparison between RAR and SAR.

In order to increase the understanding of table 1 it should be mentioned, that there are basically two SAR-techniques called the focussed and the unfocussed techniques.

Table 2 compares the maximum azimuth resolution and maximum synthetic aperture length for imaging radars with real aperture, focussed and unfocussed synthetic aperture for a real azimuth antenna-length 1.

Real Aperture Radar

max. synthetic aperture length	1
azimuth resolution	$\lambda \cdot R / l$

Unfocussed SAR

max. synthetic aperture length	$\sqrt{(\lambda \cdot R)}$
azimuth resolution	$1/2 \sqrt{(\lambda \cdot R)}$

Focussed SAR

max. synthetic aperture length	$\lambda \cdot R / l$
azimuth resolution	$1/2$

Table 2 Comparison of RAR, focussed and unfocussed SAR.

Fig. 1 represents the maximum azimuth resolution of different radar systems versus height for a 10 m antenna length l typically used for spaceborne SAR as it is installed on ERS-1 for instance.

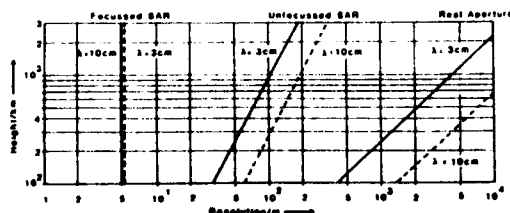


Fig. 1 Azimuth-resolution of radar systems versus height, real antenna length 10 m, incidence angle: 45°.

The following basic peculiarities of a SAR, especially of a focussed SAR, in comparison with a conventional real aperture radar (RAR) result from table 1:

1. The maximum-azimuth resolution is independent of wavelength and distance.
2. A better azimuth resolution can be reached with smaller real antennas and not with larger antennas as it is the case with RAR and optical systems respectively.
3. The S/N for a SAR is inversely proportional to the platform velocity.
4. The S/N for point target detection is inversely proportional to the third power of range and inversely proportional to the processed azimuth resolution.
5. The S/C for point targets is independent of distance R .

3. AMBIGUITIES

Ambiguities play an important part in all radar considerations. For all pulse-Doppler radars ambiguities exist due to the periodical structures of the signals. This illuminates the fact, that the pulse repetition frequency PRF, f_p , will be the decisive factor. However, ambiguities can also be responsible for the choice of the basic radar frequency. The principal Doppler frequency system received with periodically pulsed Doppler radar for moving configurations is shown in Fig. 2 schematically.

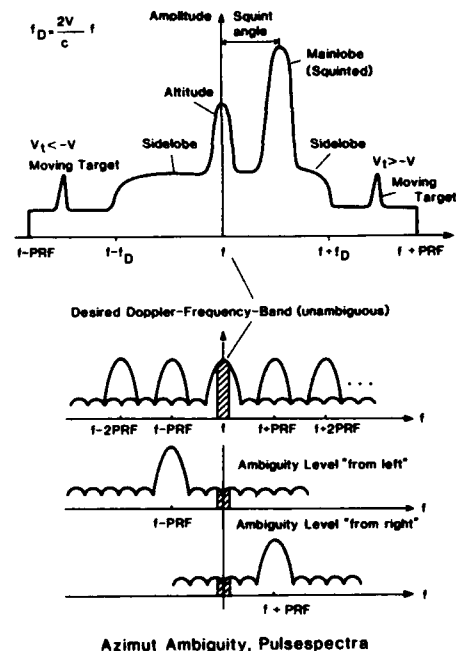


Fig. 2 Scheme of a pulse spectrum and of azimuth ambiguities caused by PRF.

3.1 BASIC AMBIGUITY CONSIDERATIONS FOR RAR

The distance between main spectral lines corresponds strongly to PRF and, therefore, holds for the unambiguous Doppler range

$$f_{Dunamb} \leq \frac{f_p}{2} \quad (1)$$

The Doppler frequency f_D results from the relative velocity u_x between radar and radar target following the relation $f_D = 2 u_x / c f$.

This leads to the unambiguous range for the velocity

$$u_{\text{unamb}} \leq \frac{c}{4} \frac{f_p}{f} \quad (2)$$

The unambiguous range for the distance measurement R_{unamb} is given by

$$R_{\text{unamb}} \leq \frac{c}{2} \frac{1}{f_p} \quad (3)$$

(This holds for a periodically pulsed radar and for small τ_p .)

A combination of (2) and (3) leads to the ambiguous product

$$u_{\text{unamb}} R_{\text{unamb}} \leq \frac{c^2}{8} \cdot \frac{1}{f} \quad (4)$$

This equation shows that the choice of frequency for a pulse doppler radar limits principally the possibility for the simultaneous measurement of distance and velocity of a radar target. On the other side a frequency limit is fixed if the unambiguous values of u_{unamb} and R_{unamb} are given. Example:

$$u_{\text{unamb}} = 300 \text{ m s}^{-1}, R_{\text{unamb}} = 40 \text{ km},$$

$$\text{frequency requirement: } f \leq 1 \text{ GHz.}$$

These relations derived for a simple RAR hold principally for SAR also. The equations show the importance of the PRF for all radar considerations. In fact, the PRF is the central radar parameter for SAR. The appointment of PRF has deep going consequences for the whole SAR, and the discussion of PRF limitations is widely identical with the discussion of the ambiguities. Range ambiguities will result if the PRF is too high, following in principle equation (3). Azimuth ambiguities will result if the PRF is too low, so that the reflected signal phase changes by 2π radians or more between two successive pulses. However, the SAR ambiguities are not only controlled by the waveform (represented by PRF for instance) but also by the antenna pattern.

3.2 AZIMUTH AMBIGUITIES FOR SAR

Basic equation for azimuth ambiguity consideration is equation (1), which gives a lower limit for the PRF and which is identical with the requirement of the sampling theorem. f_D is the maximum considered doppler frequency:

$$f_D = \frac{2u}{\lambda} \sin\beta = \frac{2u}{\lambda} \beta \quad (5)$$

u is the platform velocity of the SAR and β the angle against the antenna mainlobe direction. (Normally the mainlobe of a SAR antenna is vertical to the velocity-vector; however, squint angles are possible but not considered here for simplicity reasons.) From (1) and (5) follows for small antenna beams ($\beta < 30^\circ$):

$$4u \frac{\beta}{\lambda} \leq f_p$$

For the half power beamwidth $\beta_{\text{HP}} = 2\beta$ and because of the validity of $\beta_{\text{HP}} = \lambda/l$ follows:

$$\frac{2u}{l} \leq f_p \quad (6)$$

This equation defines the lower limit of PRF, it implies that the transmitter must be pulsed before the radar platform moves a distance equal to one half the real antenna length. The basis for the sampling theorem represented by (1) is the use of ideal low pass limitation. However, this condition is normally not fulfilled and this entails ambiguity levels within the used doppler band. This level can be minimized by increasing the PRF, that means by a so-called over-

sampling. With bandwidth $B = \Delta f_D = 2f_D$ follows from (1) the so-called oversampling ratio

$$\frac{f_p}{\Delta f_D} > 1 \quad (7)$$

Figure 2 shows the spectral parts coming from the first and second ambiguous band and contributing to the desired SAR band schematically [5].

The described ambiguity is mainly PRF conditioned. However, a main influence has the antenna pattern which is partly responsible for the spectrum shape, Fig. 2. Especially improper (that means higher) side-lobes enable the SAR to receive power from positive and negative squint angles, which is within the desired frequency band. These ambiguities are called doppler squint angle ambiguities.

Fig. 3, 4, 5 and 6 show the influence of PRF on azimuth ambiguities. Fig. 3 shows a 2-dimensional representation of a radar image of 5 corner reflectors and Fig. 4 gives the same image in 3-dimensional representation taken in X-band with a PRF of 952 kHz. Fig. 5 and 6 show the same scene taken with a PRF of 238 kHz. The ambiguities can be seen evidently.

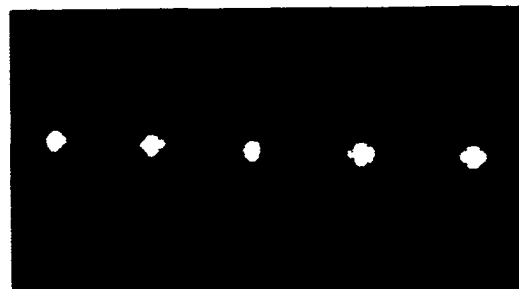


Fig. 3 SAR image of 5 corner reflectors (X-band), PRF 952 kHz.

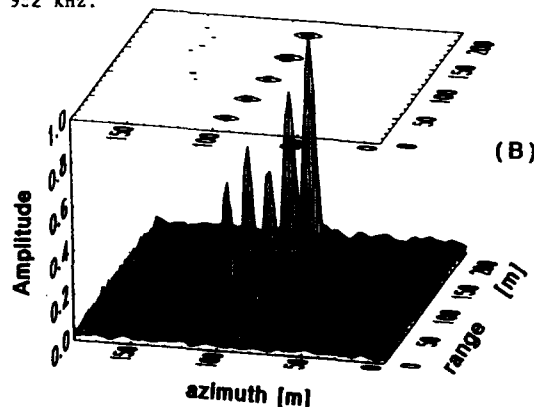


Fig. 4 3dimensional representation of the SAR image in Fig. 3, PRF 952 kHz. The contours on top represent -3 dB values.

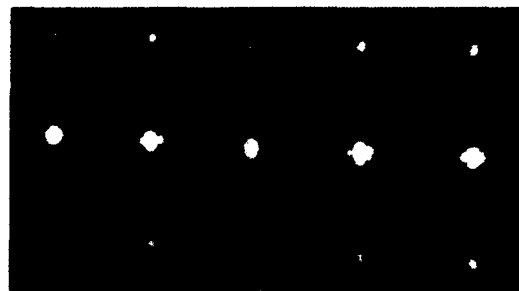


Fig. 5 SAR image of the corner reflector configuration of Fig. 3 and 4 taken in X-band with 238 kHz PRF, the azimuth ambiguities clearly can be seen.

3.3 RANGE AMBIGUITIES

In order to guarantee a range unambiguity an equation similar to (3) holds:

$$\tau_P + 2 \frac{R_{un}}{c} \leq \frac{1}{f_P}, \quad (8)$$

$$f_P \leq \frac{1}{\tau_P + 2 \frac{R_{un}}{c}}.$$

This equation defines principally an upper limit for the PRF. However, this condition cannot be fulfilled

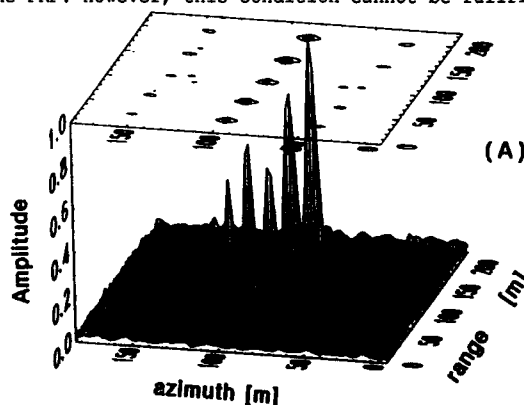


Fig. 6 3dimensional SAR image of Fig. 5. The contours on top represent the 3 dB values for the mainlobes and the -20 dB values of the azimuthal ambiguity sidelobes.

at any time, it can be incompatible with the condition for the azimuth ambiguity and in this case one makes allowance for range ambiguities and tries to suppress these ambiguous signals with proper antenna pattern design or with special processing procedures respectively. Fig. 7a shows exemplarily an X-band SAR image with ambiguities. The ambiguities are eliminated in Fig. 7b.

4. PRF-CONSIDERATIONS

It has been already mentioned, that the PRF is a decisive factor for SAR-ambiguities. However, from other point of view the PRF has deep going consequences for the effectiveness of a SAR also. The definition of PRF becomes difficult due to different other conditions and limitations which have to be fulfilled.

There are principal limitations due to azimuth ambiguities, range ambiguities, swathwidth, complete coverage. There are also unallowed PRF-bands due to geometrical variations like earth curvature, orbit eccentricity, height variations, and altitude line echos.

The ambiguity equations (6) and (8) lead to the following PRF limitations:

$$\frac{2u}{1} \leq f_P \leq \frac{1}{\tau_P + 2 \frac{R_{un}}{c}}.$$

The choice of PRF estimates the maximum swath width R_g or vice versa. Principally, an impulse needs for crossing the swath the time $\tau = 2R_g/c$. Herefrom results:

$$f_P \leq \frac{c}{2R_g}. \quad (9)$$

A pulsed radar using a single antenna is normally unable to receive during the duration of the transmission pulse, it is blind at certain slant ranges. If the



Fig. 7a SAR image of Zürich airport disturbed by sidelobe ambiguities caused by an antenna squint angle of 6.8° ($\beta_{hr} = 12^\circ$); near range 2805 m, far range 5355 m, $u = 70 \text{ m s}^{-1}$, X-VV (DLR-E-SAR measurement Horn, Moreira).



Fig. 7b SAR image of Fig. 7a, correctly processed to the squint angle 6.8° ; all ambiguities are eliminated (measurement Horn, Moreira).

viewing geometry is fixed by other reasons (given orbit height of a satellite, fixed incidence angle etc.) the PRF must be tuned to selected values. Fig. 8 shows allowed PRF-bands for a satelliteborne system with a fixed depression angle, taking into account the variation of the local orbit height [7]. The white ranges are the allowed PRF-ranges, m is the number of the respective range ambiguities. The lower limit for the PRF with respect to azimuth ambiguity is also given in Fig. 8.

The result is:

- with increasing range ambiguity decreases the respective width of the allowed PRF-bands.

This can lead to the request of switchable PRF for different purposes (shown in Fig. 9 as necessary due to ALE-influences). Substituting (9) into (6) (considering the equality in both relations) one obtains together with the maximum azimuth resolution relation an important relation between swathwidth, azimuth resolution and SAR velocity:

$$\frac{2u R_g}{r_a} = c. \quad (10)$$

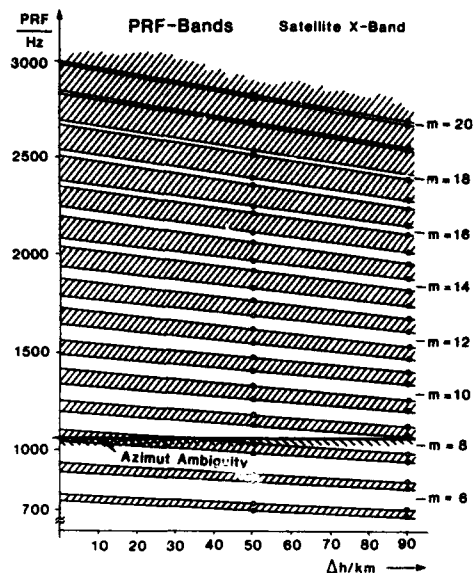


Fig. 8 Allowed PRF-bands versus altitude variations for a satellite, X-band.

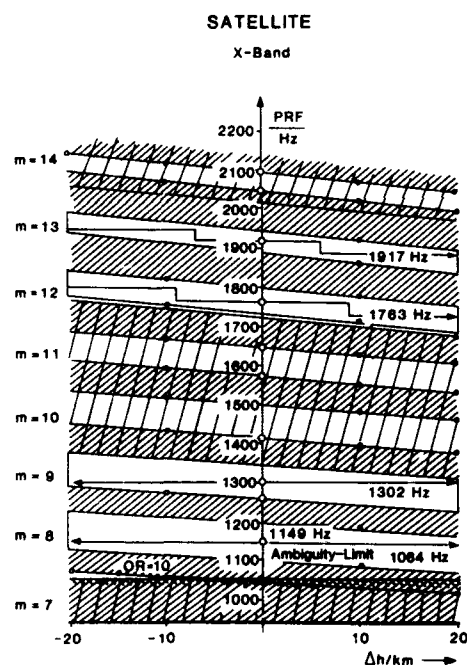


Fig. 9 PRF limitations due to altitude variations Δh , example for PRF switching.

The Altitude Line Echo

The already mentioned altitude line echo (ALE) is the radar signal coming from Nadir. The time duration of ALE is with sufficient accuracy identical with the transmitter pulse duration τ_p . ALE appears earlier than the desired swath echo. On the one side it will be more attenuated than the desired signal proportional to the sidelobe level of the antenna pointing in Nadir direction and on the other side it will be less attenuated due to the shorter distance, where ALE is resulting from. σ_0 has normally a higher value for Nadir direction than in any other directions and this will increase the ALE-signal level. Principally, the ALE can be used as a reference for geometrical calibration as well as for altitude estimation of the

platform.

For a pulsed radar ALE considerations will be identical with altimeter-considerations. An example for PRF-limitation due to ALE shows Fig. 9 in comparison with Fig. 8. For $m = 12$, the influence of ALE leads to the request of PRF-switching as mentioned in the previous section.

5. ANTENNA PECULIARITIES

Equation (6) gives a relation between the real azimuth diameter of the SAR-antenna, flight-velocity and the PRF:

$$\frac{2u}{f_p} \leq 1.$$

A minimum vertical dimension of the antenna l_{vert} will be estimated due to the necessity to focus the beam into the swath width R_g . From Fig. 2 in lesson 1 and in connection with (10) the following relation can be derived for a small half power beamwidth:

$$R_g = \frac{R \beta_v}{\sin \theta_1} = \frac{R \cdot \lambda}{\sin \theta_1 l_{\text{vert}}} \quad (11)$$

From (6) and (10) follows in connection with (1.1):

$$\frac{4uR\lambda}{c \sin \theta_1} \leq l_{\text{vert}} l_{\text{az}} \quad (12)$$

Equation (12) gives the lower bound for the antenna area.

6. PECULIARITIES AND CONSTRAINTS CAUSED BY PHASE ERRORS

Essential for the effectivity of a SAR system is its phase coherency. High quality images can be produced only if the targets phase history is observed along a precisely known radar translation. However, these phase history is normally not known exactly. Phase errors usually occur. Principally there are two different types of phase errors:

More or less deterministic errors, caused by well known geometry effects and defined instrumental influences.

Statistical errors caused by instabilities of the radar itself, of the platform or of the propagation path for example.

6.1 DETERMINISTIC GEOMETRY EFFECTS, RANGE CURVATURE

In lesson 1, Cap. 3.2 the "Depth of Focus" has been considered and in Fig. 3 an example for the influence of defocussing on a SAR image has been shown there.

The same considerations can be used for the computation of the so-called "Range Curvature Effect". The range curvature (RC) is given by

$$RC = R_a - R_o \quad (13)$$

For high azimuth resolution application a long integration time is required and image degradation may be caused if the time delay variation corresponding to (13) reaches the same order or exceeds the range resolution cell ($\tau_p/2$) for a pulse radar. From (13) follows

$$RC = \frac{1}{2} \frac{(u T_D)^2}{R_o} \quad (14)$$

$$RC = \frac{\lambda^2 R_o}{16 r_a^2} \quad (15)$$

By this the importance of r_a is evident. In comparison to r_y follows:

$$\frac{RC}{r_y} = \frac{\lambda^2 R_o}{16 r_y r_a^2} \quad (16)$$

This equation gives the number of resolution cells through which a point migrates during the formation of the synthetic aperture. Ratio values in excess of 0.3 will normally cause image degradation and this must either be avoided by design or compensated during signal processing [2].

In Fig. 10a the range curvature clearly can be seen. However, here the curvature is less enough to avoid image degradation.

Fig. 10b shows the influence of a range curvature effect together with ambiguities in the sidelobes on the pulse answer of a point target. Here, a degradation clearly can be seen.

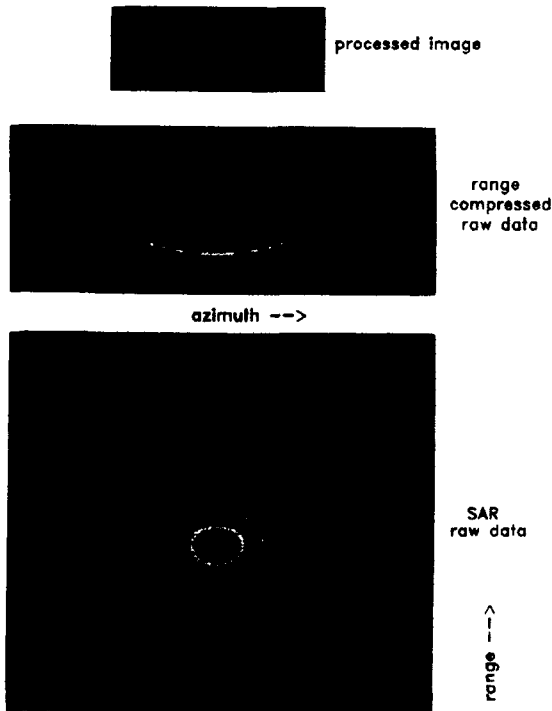


Fig. 10a The raw data received from a point target (lower image) show as well as the range compressed data the influence of range curvature.

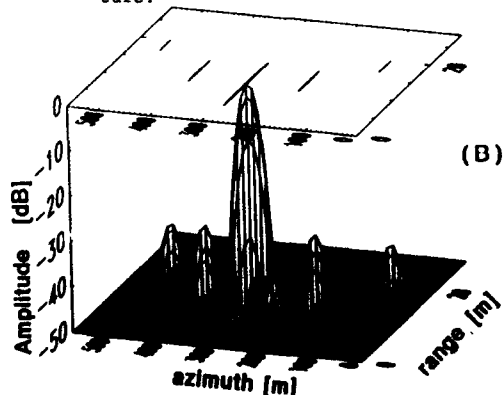


Fig. 10b Impulse response of a point target disturbed due to range migration caused by range curvature. The sidelobes are caused by ambiguity. The 2dimensional representation on top shows evidently a smearing effect (DLR-E-SAR, Horn, Moreira).

Other so-called deterministic phase changes can occur due to orbit excentricity of satellites and each rotation effect, which can normally be estimated exactly or due to antenna influences like diagramme deformation or angle switching. Both effects can be measured and estimated exactly.

6.2 PLATFORM INSTABILITY EFFECTS

Fig. 11 shows measured displacements in the line of sight of an airborne SAR, extracted by a RDM motion compensation equipment.

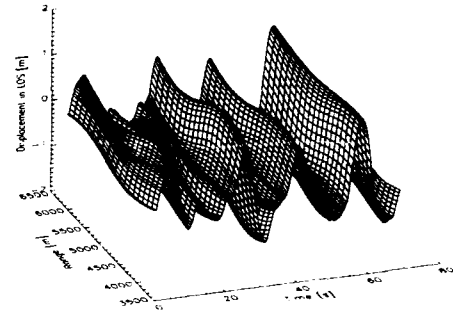


Fig. 11 SAR platform line of sight displacements extraction from SAR raw data by RDM (DLR-E-SAR, L-band, measurement Horn, Moreira).

Fig. 12 shows as an example the degradation of a point target impulse response due to turbulences up to 2 m s^{-1} (RMS 1 m s^{-1}) for an airborne SAR.

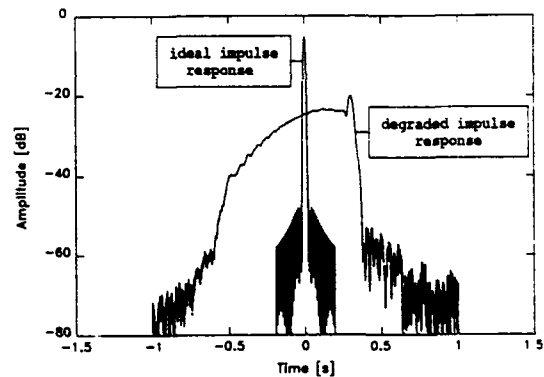


Fig. 12 C-band impulse response of a point target for DLR-E-SAR degraded by phase errors due to displacements and turbulence (RMS = 1 m s^{-1} , peak value 2 m s^{-1} , displacements between -2 m upto 4.5 m).

In principle these effects can be neutralized by motion compensation by measuring the dynamic behaviour of the platform and correcting the SAR data either on board of the aircraft or on ground. Two methods are principally possible, either the measurement using an Inertial Measurement Unit (IMU) or a procedure, which extracts the true forward velocity and line of sight changes and acceleration out of raw data called "Reflectivity Displacement Method" RDM. RDM, recently has been developed at DLR [9, 10]. This procedure has been used to exclude the errors caused by aircraft motion and velocity instabilities during the processing of the images shown here. In the DLR approach only the information in the radar signal has been used for motion compensation; principally no inertial platform or other equipment for measuring details of the aircraft motion is necessary. This method enables the estimation of deviations of the aircraft from an ideal path as shown in Fig. 11.

Obviously, phase errors caused by atmospheric and ionospheric turbulences in principle cause the same motion errors as the aircraft instabilities. Therefore, the same method can be applied for the correction of phase errors due to propagation. This implies that for spaceborne SAR the negative influence of atmospheric and ionospheric turbulences to a large extent can be neutralised when they occur [10]. This results in an increase of the resolution power and in image quality. Therefore, it seems in principle that for spaceborne SAR a dm resolution can be reached. However, special techniques are required in order to fulfill power and data requirements in this case.

The tolerable platform velocity variation Δu can be computed from (18) in lesson 1. The radar range R at the ends of a synthetic aperture (after the dwelltime T_D) is:

$$R = \sqrt{R_0^2 + \left(\frac{u T_D}{2}\right)^2}.$$

The differentiation with respect to u delivers

$$\frac{dR}{du} = \frac{u T_D^2}{4 R} = \frac{\Delta R}{\Delta u},$$

$$\Delta u = \frac{4 R}{u T_D^2} \Delta R.$$

For a tolerable range error of $\lambda/16$ follows a tolerable velocity component Δu (for $R = R_0$):

$$\Delta u = \frac{4 R_0}{u T_D^2} \cdot \frac{\lambda}{16} = \frac{u r_a^2}{R_0 \lambda}. \quad (17)$$

Remarkable is: The tolerable Δu becomes more critical if the azimuth resolution is improved.

Fig. 13 gives the measured forward velocity variations of an airborne SAR during a flight time of about 60 seconds.

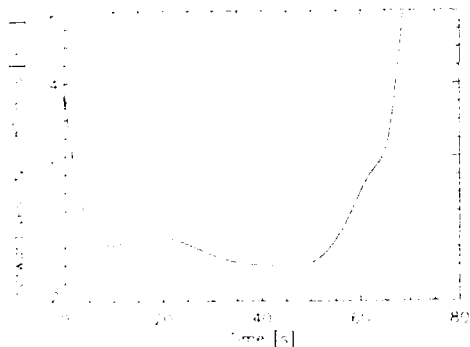


Fig. 13 Changes in forward velocity of E-SAR extracted from DLR-E-SAR raw data, L-band, by RDM (measurement Horn, Moreira).

Fig. 14 shows as an example errors in a SAR image due to a 12 % velocity variation and its corrections with a motion compensation procedure.

6.3 TARGET MOTION EFFECTS

Usually a SAR signal processor locates the position of a non-moving target in the image place where its doppler frequency is zero. If the target is moving with a radial velocity component U_{tr} , then it imposes a Doppler shift on the signal. Thus a target moving towards the radar will cause a shift Δx in target location in the flight direction of the radar (and vice versa).

If the radar is moving with a velocity U than results

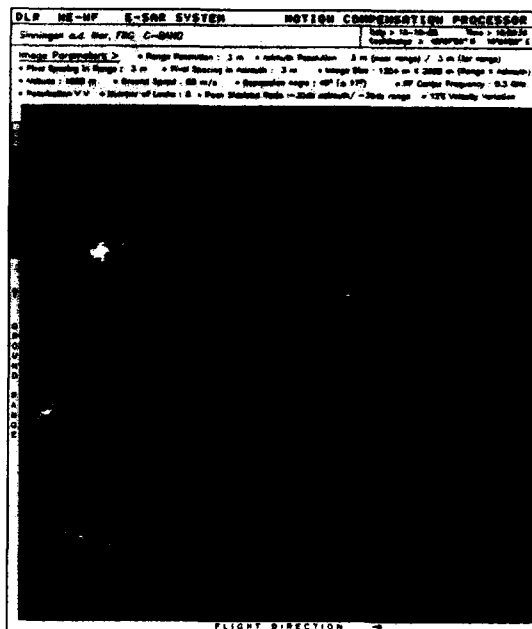


Fig. 14 Example for errors in SAR images caused by phase distortions and the effect of motion compensation. The upper image is distorted due to a 12 % velocity variation, the lower image shows the same scene after a motion compensation. Scene dimensions are 1254 m x 1344 m, ground resolution 3 m x 3 m (measurement Moreira, Horn, DLR-SAR).

for a moving target at a distance R the displacement Δx

$$\Delta x = \pm R \frac{U_{tr}}{U} \sin \theta. \quad (18)$$

The sign in (18) depends on the direction of the target velocity with respect to the radar. An example for image shift due to the radial component of target motion is shown in Fig. 15. Ships with velocity components radial to the Seasat SAR orbit plane have an image displacement. This effect can be used for the estimation of target velocities if the distance between the SAR and the targets as well as the velocity of the SAR is known.

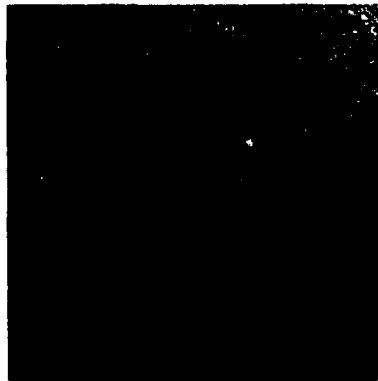


Fig. 15 SAR image of a sea surface with 2 ships taken by SEASAT. The displacement of the ships against the satellite clearly can be seen. The opposite displacement against the wakes correspondings to opposite velocity directions (processing: DLR-WT-DA). Mean displacement is about 450 m.

In addition to radial velocity, radial acceleration will also cause image distortions such as defocus in

azimuth and range, range walk etc. However, the most sensitive effect is azimuth defocus [3].

A real linear array is to be considered as flat as long as the deviations from a straight line are less than a half wavelength. For a synthetic array this for the two way case must be halved due to the phase coherency conditions. Therefore, for the line of sight deviation holds: $\Delta R \leq \lambda/4$. An acceleration d^2R/dt^2 acting for the whole dwelltime T_D corresponds to a radial position error $\Delta R = d^2R/dt^2$ (if a case constant acceleration is assumed). In the two way this coefficient also must be halved. From these considerations results with equation (14) from lesson 1:

$$\frac{d^2R}{dt^2} \leq \frac{\lambda}{2T_D^2} = \frac{2u^2 r_a^2}{R^2 \cdot \lambda} \quad (19)$$

This is the maximum tolerable acceleration a target may have in line of sight direction of a SAR or the radar platform may show vice versa. (19) is a basic equation for motion compensation. For turbulence disturbances in Fig. 12 mainly acceleration errors are responsible.

In Table 3 several sources of phase errors are listed together with the respective errors caused within SAR images. The Figures 16a to 16d show as examples the influence of different phase errors on the impuls response of a point target.

7. REALIZATION CONSIDERATIONS

Atmosphere and ionosphere produce frequency dependent distortions. These effects set an upper frequency limit due to attenuation for airborne radar (about 90 GHz) and spaceborne radar (about 15 GHz) and a lower limit for spaceborne SAR due to ionospheric granularities (about 1 GHz). The state of technology sets upper limits as well. The frequency bands available for radar surveillance are also limited due to international agreements.

Like other electromagnetic systems, radars employ radiation with polarization, the alignment (relative to vertical or horizontal) of the electric vector in the wave. Polarization on both transmit and receive is determined by the antenna. Scattering objects, such as terrain features or hard targets such as vehicles, have radar cross sections that reflect differently in response to the incident polarization.

In principle a complete description of a radar target can be given only if all like polarized and cross-polarized amplitudes and the respective phases of the radar signal are known. Such a polarimetric radar gives all possible information on a target within the relative small bandwidth of the modulated radar carrier frequency.

At present, technological limitations in the efficiency of radio frequency power generators are important design factors. The "radar equation" shows an increase of the average power necessary for higher frequency ranges. The dependence is linear: this means that an X-band SAR needs about twice as much power as a C-band SAR, and about 7 times as much as an L-band SAR. In addition, other technological difficulties increase with frequency. Phased array antennas (desirable for beam steering) are much easier to realize in lower than in higher frequency bands. In L- and C-band a realization with microstrip technology is state of the art, whereas in X-band a realization of a large microstrip antenna with sufficient efficiency for space applications seems to be extremely difficult. State of the art for X-band use slotted waveguide arrays [11, 12]. This is the main reason for the single polarization of X-SAR against the multipolarization capability of SIR-C.

The mean transmitter power determines the distance from which a radar observation to a certain target can be successfully made and, therefore, the orbit altitude of spaceborne systems is power limited.

Error Source		Image Misregistration	Image shift	Azimuth Defocus	Range Defocus	Range Walk	Azimuth	Image Mainlobe Loss	Image Sidelobe Increase
Range (altitude and cross track)	r	•							
	f		•			•			
	r			•	•			•	•
	$\frac{d^n r}{dt^n}$			•	•			•	•
Azimuth (along track)	x	•							
	f			•				•	•
	x			•			•	•	•
	$\frac{d^n x}{dt^n}$			•			•	•	•
Propagation path	$\Delta\phi$			•	•			•	•
Electronic stability	$\Delta\phi$			•	•			•	•

Table 3 Effects of phase errors caused by platform or target motions respectively (the relative motion is from relevance only), as well as caused by phase jitter $\Delta\phi$ in the propagation path and in the SAR electronic.

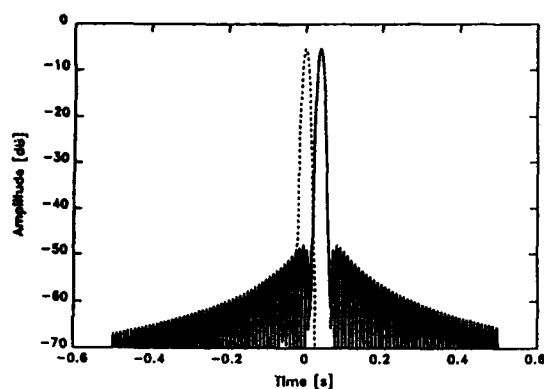


Fig. 16a Impulse response, shifted by a linear phase error.

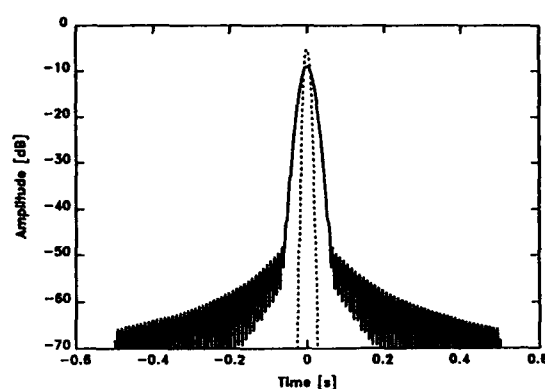


Fig. 16c Impulse response, degraded by a cubic phase error.

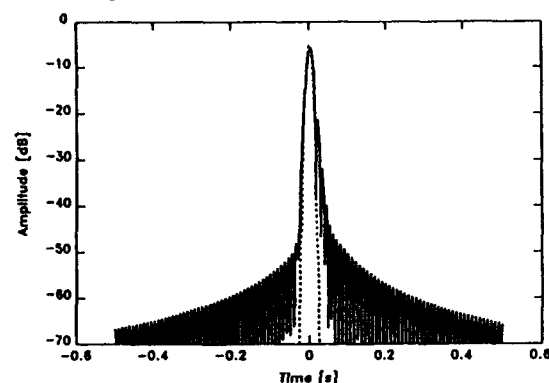


Fig. 16b Impulse response, degraded by a quadratic phase error.

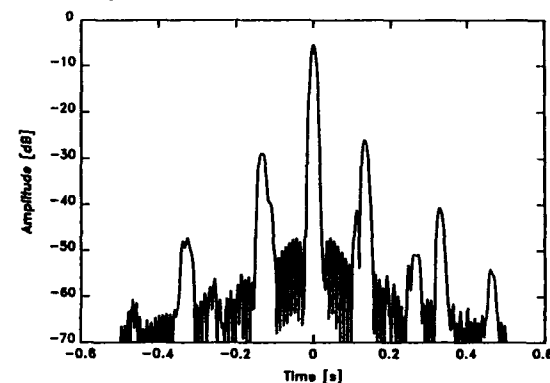


Fig. 16d Impulse response, degraded by a random high frequency phase errors.

Principally, the power required increases with the 3rd power of the radar distance. (This means a doubling of the distance, i.e. the orbit height, requires an 8-fold multiplication of the required power). A larger antenna beams more power to a required area (expressed through the so-called antenna gain) than a small one, and, therefore, a large antenna would seem to be favourable. But the ground resolution of a SAR is improved for smaller real antennas. These considerations lead to a tradeoff, which must be made carefully in order to fulfill a satellite SAR's requirements. In any case the transmitter power is a limiting element for the design of a SAR as well as the antenna. Today's state of the art are a few hundreds watt (mean power). This implies requirements for the primary power supply of a satellite. State of the art is about 6 kW to 10 kW. These requirements can be fulfilled with solar power generators and atomic generators as well. The antenna dimensions for spaceborne SAR have at present values of about $2 \text{ m} \times 15 \text{ m}$.

8. FUTURE SAR TECHNIQUES

SAR systems produce a tremendous amount of data (examples for data-recorder bitrates on the ground:

ERS-1 $\approx 102 \text{ MBPS}$, X-SAR/SIR-C $\approx 45 \text{ MBPS per channel (!)}$, DLR airborne E-SAR $\approx 28 \text{ MBPS}$). Requirements

for simultaneous high resolution and large swath widths make the data rates higher. All requirements for extensions of SAR to multifrequency and multipolarization capability respectively entail a multiplication of the data rates and this would exceed the present limitations of data handling. This seems to be a key problem in all high resolution imaging systems. Therefore, different requirements have to be fulfilled in order to handle or reduce the data stream of future systems either by means of onboard processing or with development of advanced SAR systems like spotlight SAR. One solution is to increase the data links

capacity. A reasonable goal would be 250 Mbit s^{-1} . New data transmission systems with splitted data links to data relay satellites or ground stations respectively are under preparation.

Data storage capability has to be increased also. As a first step new recorders with capabilities exceeding 100 Mbit s^{-1} are qualified for use in space. The present approach is to use more than one recorder, i.e. one recorder for each channel in multipolarization and multifrequency SAR, as on the SIR-C mission.

Image data processing capabilities also are limited. However, this processing time will decrease rapidly during the next few years and at the end of the decade real time processing with excellent image quality will be possible.

Requirements for high resolution and wide swath in continuous strip map mode are in conflict with data handling capabilities, and with requirements for a large antenna to conserve power. Therefore, new SAR techniques have to be introduced and developed which allow electronically steered beams. For this purpose the spotlight mode and Scan-SAR modes are under consideration. The length of a synthetic antenna corresponds to the section of the flight path from which one target stays within the antenna beam. This fact leads to the requirement for wide beams and, therefore, small antennas for conventional high resolution systems. The same effect, however, can be reached if a small antenna beam (from a large antenna) can be continuously pointed at the target. This allows also a longer synthetic array and, therefore, a finer azimuth resolution [11]. However, the gain of azimuth resolution entails a loss of coverage due to the fact that during the continuous spotlight illumination of one small surface

area, the sensor passes other parts of the swath which are not illuminated. Therefore, the spotlight mode can be used for the enlargement of a sector of the observed swath similar to the zooming with an optical camera. The Scan SAR Mode can be used for an extension of the swath in radial direction using more than one beam generated in a time shared manner. This method increases the swath at the expense of azimuth resolution [16 to 20]. A spotlight SAR in orbit, however, would be a rather expensive enterprise.

The combination of all modes allows variable resolution and swath widths as well; the trade-off between resolution, swath width, power etc. leads to optimised configurations.

9. REFERENCES

- [1] Skolnik, M.I. Radar Handbook. McGraw Hill Book Comp., New York, 1970.
- [2] Hovanessian, S.A. Introduction to Synthetic Array and Imaging Radars. Artech House, Inc., 1980.
- [3] Tomiyasu, K. Tutorial Review of Synthetic Aperture Radar (SAR) with Applications to Imaging of the Oceans Surface. Proc. of the IEEE Vol. 66, No. 5, May 1978.
- [4] Kovaly, J.J. Synthetic Aperture Radar. The Artech Radar Library. Artech House, Inc., 1976.
- [5] Ulaby, F.T. Moore, R.K. Fung, A.K. Microwave Remote Sensing Vol. II, Radar Remote Sensing and Surface Scattering and Emission Theory. Addison Wesley Publ. Comp., 1982.
- [6] Elachi, Ch. Bicknell, T. Jordan, R.L. Wu, Ch. Spaceborne Synthetic Aperture Imaging Radars: Applications, Techniques and Technology. Proc. IEEE Vol. 70, No. 10, Oct. 1982, pp. 1174-1209.
- [7] Schlude, F. Imaging Radar Systems. Proc. of an ESA-EARSEL Workshop held at Alpbach, Austria, 16-20 March 1981 on "Coherent and Incoherent Radar Scattering from Rough Surfaces and Vegetated Areas", ESA-SP-166.
- [8] Moreira, J. Estimating the Residual Error of the Reflectivity Displacement Method for Aircraft Motion Error Extraction from SAR Raw Data. ICCO Intern. Radar Conf., Arlington, USA, 1990, pp. 70-75.
- [9] Moreira J. A New Method of Aircraft Motion Error Extraction from Radar Raw Data for Real Time SAR Motion Compensation. 12th Canadian Symposium on Remote Sensing, IGARSS '89, Vancouver, Canada, proc. IGARSS, IEEE, 89, pp. 2217-2220.
- [10] Keydel, W. Moreira, J. Verfahren zur Extraktion von durch die Atmosphäre verursachten Phasenfehlern des Rückstreuensignals eines Abbildungsradarsystems aus Radarrohdaten. German Patent P 41 24 062.6.
- [11] Buckreuz, S. Motion Errors in an Airborne Synthetic Aperture Radar System. ETT Vol. 2, No. 6, Nov/Dec. 1991, pp. 655-664.
- [12] Keydel, W. Verification Using Spaceborne Microwave Imaging. IEEE Technology and Society Magazine, Dec. 1990/Jan. 1991, pp. 53-61.
- [13] Horn, R. C-Band SAR Results Obtained by an Experimental Airborne SAR Sensor. Proc. IGARSS 89, IEEE, pp. 2213-2216.
- [14] Moreira, A. Improved Multilook Techniques Applied to SAR and SCANSAR Imagery. IEEE Trans. on Geosc. and Remote Sensing, Vol. 29, No. 4, July 1991.
- [15] Moreira, A. A New Subaperture Approach for Real-Time SAR Processing. ETT, Vol. 2, No. 6, Nov.-Dec. 1991.
- [16] Brunner, A. Langer, E. Öttl, H. Zeller, K. Concept for a Spaceborne Synthetic Aperture Radar (SAR) Sensor Based on Active Phased Array Technology. AGARD Conf. Proc. No. 459 on High Resolution Air- and Spaceborne Radar, Papers presented at the Avionics Panel Symposium held in The Hague, The Netherlands, 8-12 Aug. 1989, pp. 23 A1 - 23 A10.
- [17] Jatsch, W. Langer, E. Öttl, H. Concept of an X-Band Synthetic Aperture Radar for Earth Observing Satellites. Journ. of Electromagnetic Waves and Applications, May 1990.
- [18] Luscombe, A. Taking a Broader View: Radarsat adds Scansar to its Operations. Proc. IGARSS '88 Symp., Edinburgh, Scotland, 13-16 Sept. 1988, pp. 1027-1032.
- [19] Raney, K. Canada's RADARSAT. Remote Sensing Yearbook 1990, (personal communication).
- [20] Luscombe, A.P. The Radarsat Synthetic Aperture Radar: A Flexible Imaging System. Proc. 11. Canadian Symp. on Remote Sensing, Waterloo, 22.-25.6.1987.

MOTION ERRORS AND COMPENSATION POSSIBILITIES

by

D. Hounam

Deutsche Forschungsanstalt für Luft- und Raumfahrt, e.V.

Institut für Hochfrequenztechnik

8031 Oberpfaffenhofen

Germany

1. SUMMARY

The synthetic aperture radar (SAR) technique relies on knowledge of the relative motion between the sensor and the target. If the flight path of the sensor is not accurately known or the SAR processor is limited in its ability to take the flight data into account, the SAR image will be degraded. Motion errors are particularly critical for SAR sensors on small, low-flying aircraft, due to turbulence, and where high spatial resolution is required.

The lecture discusses the effects of motion errors on image quality and the requirements on the sensor and processor to compensate for motion errors. The DLR airborne sensor, E-SAR, and associated image processor will be used as examples. Techniques using a priori knowledge of the flight path from independent sensors, e.g. inertial navigation systems (INS), and by extracting the flight data from the SAR data, e.g. autofocus and reflectivity displacement method (RDM), are treated.

The author would particularly like to thank J. Moreira and S. Buckreiß whose work, referenced below, was used extensively for the lecture.

2. INTRODUCTION

Every amateur photographer is familiar with the blurring of his photograph if the camera is not held steady while the film is being exposed. The action of the lens focusing the scene on photographic film results in the scene being resolved in angular units. Rotation of the camera in any plane will cause the scene to move across the film and blur the resulting image.

In contrast to this well known effect, the focusing of a SAR sensor is in principle insensitive to angular deviations. This is because the sensor resolves the scene in terms of displacements rather than angles.

In the plane orthogonal to the flight path, i.e. in the range direction, the position of a target is determined by measuring the delay of the target's echo (range delay). The spatial resolution is determined by the length and bandwidth of the transmitted pulse. If the sensor is rotated in this plane (roll angle), the influence of the antenna gain pattern may cause the strength of the echo, i.e. the image intensity, to vary but the delay and, hence the spatial resolution will remain unaffected.

Parallel to the flight path, i.e. in the azimuth direction, the scene is resolved by matched filtering the Doppler spectrum, there being a fixed correspondence between Doppler frequency and the relative position of the target on the ground. The spatial resolution is determined by the spacing of the lines of constant Doppler and the bandwidth of the matched filter. Rotation in azimuth produced by pitch and yaw will have no influence on the lines of constant Doppler nor on the matched filter characteristics. In principle, therefore, the

along-track position and spatial resolution will not be influenced, by attitude errors. However, if the antenna beam points to a different part of the Doppler spectrum than that which is processed (filtered), the image intensity will be influenced. With serious mismatch, defocusing will occur, due to distortion of the matched filter weighting function and errors in the range migration correction. Also ambiguous responses can occur. Antenna pointing needs to be known to process the SAR data, or the processor has to derive it by analysing the Doppler spectrum. The latter can be considered normal processing practice and, therefore, in the following, these effects will be neglected.

Whereas, with the above reservations, the focusing of a SAR is insensitive to angular deviations, deviations in the path of the sensor will lead to displacement and defocusing of the target in the final image. The path of the sensor does not need to be a straight line but it must be known with sufficient accuracy so that deviations can be taken into account in the processing of the SAR data to achieve a sharp image. This process is often referred to as motion compensation.

When discussing the path of a sensor, the question arises as to where the reference point within the sensor is located. Displacements of the sensor are clearly only effective on the propagation path of the radar signal. Hence, the reference point within the sensor is the phase centre of the antenna, i.e. origin of the spherical far-field wavefront. The phase centre is the point from which the antenna effectively radiates. For many antenna types, the phase centre is outside the structure of the antenna, e.g. dish antennas, where it is located behind the dish.

Hence, by the path of the sensor is understood the path of the phase centre of the antenna. If the path is not measured directly at the phase centre, roll, pitch and yaw angles need to be known to correct for the offset. Errors in these angles will then lead to degradation in image quality, further contradicting the generalisation above that the focusing of the SAR is insensitive to angular variations. For the sake of simplicity, these angular effects have been neglected below. If needed their influence can be derived from the formulas provided.

Clearly, a stable flight path greatly eases the task of motion compensation. Satellite platforms fall into this category even though in some cases, e.g. space shuttle the orbital parameters as well as the attitude can be poorly defined. The real challenge for motion compensation is presented when SAR sensors are flown on light aircraft due to the influence of air turbulence and the often frantic effort of the pilot to combat it. The airborne SAR sensor of the DLR (ESAR) is such a case [1] and will be used as an example in the following analysis. Fig. 1 shows an image of the DLR centre in Oberpfaffenhofen using this sensor which exhibits typical degradations due to motion errors. The aircraft was deliberately flown to produce motion errors which can be seen as blurring of the image (top right) and geometric distortion

of the runway and taxiways.

In the following analysis, the influence of motion errors on the azimuth imaging properties will be discussed first as this is far greater than the influence in range. The analysis closely follows the approach of Buckreus [2]. These properties are discussed in terms of the impulse response, which is the response of the SAR sensor, including processing, to a point target.

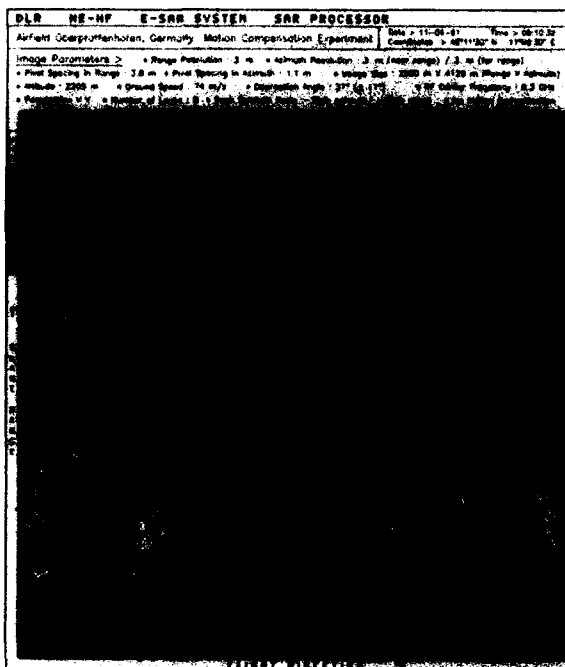


Fig. 1 SAR image of the DLR centre in Oberpfaffenhofen exhibiting strong motion errors.

2.1 Impulse Response in the Azimuth Direction

Let us consider first the azimuth channel of a SAR system, where the platform flies in a straight line (Fig. 2). The coherent integration can be expressed by the convolution of the backscattered signal $S(t)$, with a reference function $H(t)$, where $Z(t)$ is the impulse response.

$$|Z(t)| = |S(t) * H(t)| \quad (1)$$

The returned signal $S(t)$, corrupted by a phase error $\Phi(t)$ is given by

$$S(t) = A_0 \cdot e^{j\phi(t)} \cdot e^{j\Phi(t)} \quad (2)$$

where A_0 is the amplitude of the returned radar signal and $\phi(t)$ is the nominal phase history of a point target. According to the geometry (see Fig. 2) the velocity in line of sight (LOS), is:

$$V_{\text{LOS}}(t) = V \cdot \sin \Theta_A(t) \quad (3)$$

where V is the forward velocity of the aircraft and Θ_A is the angle between the LOS vector and cross-track plane (azimuth angle). For small values of Θ_A , we can put:

$$\Theta_A(t) = \frac{Vt}{\sqrt{H^2 + D^2}} \quad (4)$$

where H is the height of the sensor and D is the

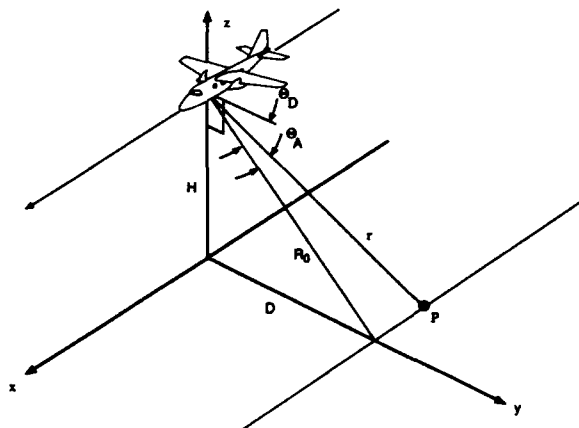


Fig. 2 SAR geometry, where P is a target on the ground, H is the altitude of the sensor, D is the distance of the target from the ground track, R_0 is the slant range at closest approach, Θ_A is the azimuth angle and Θ_D is the depression angle of the target.

distance between the target and the ground track.

Alternatively,

$$\Theta_A(t) = \frac{Vt}{R_0} \quad (5)$$

where R_0 is the range at the point of closest approach of the sensor of the target.

Integrating and defining $t = 0$ when the sensor is at the point of closest approach, we obtain the slant range r :

$$r(t) = R_0 + \frac{V^2 t^2}{2R_0} \quad (6)$$

Ignoring the constant phase expression, the two way phase change $\Phi(t)$, mentioned in Eq. (2) becomes:

$$\Phi(t) = \frac{4\pi}{\lambda} \cdot \frac{V^2 t^2}{2R_0} \quad \text{where } \lambda \text{ is the radar wavelength.} \quad (7)$$

Or,

$$\Phi(t) = -\frac{kt^2}{2}, \quad \text{where } k = \frac{4\pi \cdot V^2}{\lambda \cdot R_0} \quad (8)$$

Hence, the nominal phase modulation is a quadratic function of time, i.e. linear frequency modulation.

Let us now consider deviations from the nominal path where the platform is displaced from the nominal position A to the position A' (see Fig. 3). The range r' becomes:

$$r'(t) = R_0 + \frac{V^2 t^2}{2R_0} + \Delta x(t) \cdot \Theta_A - \Delta y(t) \cos \Theta_D + \Delta z(t) \sin \Theta_D \quad (9)$$

where $\Delta x(t)$ is the displacement in the flight direction, $\Delta y(t)$ and $\Delta z(t)$ are the displacements of the platform in y and z direction, respectively, and Θ_D is the depression angle of the target.

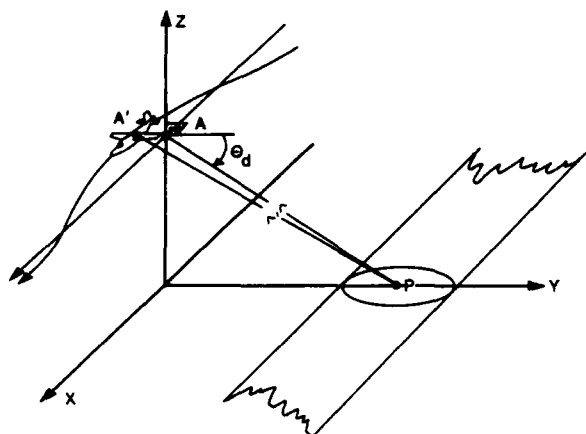


Fig. 3 Deviation from the nominal flight path, due to turbulences.

The phase error $\Phi(t)$ is, therefore:

$$\Phi(t) = -\frac{4\pi}{\lambda} [\Delta x(t) \cdot \Theta_A(t) - \Delta y(t) \cdot \cos \Theta_D + \Delta z(t) \sin \Theta_D]. \quad (10)$$

From equation (10) it can be seen that the influence of the motion errors in the x direction is independent of the depression angle Θ_D and, therefore, of the position of the target within the swath. Whereas, in the other two directions (y and z), Θ_D needs to be known. Also, it is evident that the variations of the displacements with respect to time in all three directions is reproduced in the phase error, a linear variation in the displacement manifesting itself as a linear phase error and so on.

The normalized reference function $H(t)$ from Eq. (1) is given by:

$$H(t) = W(t) \cdot T \sqrt{\frac{k}{2\pi}} \cdot e^{\frac{jkt^2}{2}}, \quad -T/2 \leq t \leq +T/2, \quad (11)$$

where T is the aperture time and $W(t)$ is a weighting function to suppress sidelobes. Often a Hamming weighting function [4] is used:

$$W_H(t) = \alpha + (1-\alpha) \cdot \cos \left[\frac{2\pi}{T} t \right], \quad \alpha = 0.54. \quad (12)$$

Using equations (1), (2), and (11), the impulse response of a point target becomes:

$$Z(t) = S(t) * H(t) = \frac{1}{T} \int_{-T/2}^{+T/2} S(t-\tau) \cdot H(\tau) d\tau. \quad (13)$$

Or,

$$Z(t) = A_0 \cdot \sqrt{\frac{k}{2\pi}} \cdot \int_{-T/2}^{+T/2} e^{-\frac{jkt^2}{2}} \cdot e^{j\Phi(\tau)} \cdot W(t-\tau) \cdot \frac{jkt(t-\tau)^2}{2} d\tau. \quad (14)$$

Taking the absolute value of $Z(t)$, we approximately obtain:

$$|Z(t)| = A_0 \cdot \sqrt{\frac{k}{2\pi}} \cdot \left| \int_{-T/2}^{+T/2} W(\tau) \cdot e^{j\Phi(\tau)} \cdot e^{-jkt\tau} d\tau \right|. \quad (15)$$

This can also be considered as the Fourier transform of the weighting function $W(t)$ modulated by

the phase error $\Phi(t)$.

If the weighting function is a rectangular window $W(t) = W_R(t)$, with

$$W_R(t) = 1 \text{ for } |t| \leq T/2 \text{ and} \quad (16)$$

$$W_R(t) = 0 \text{ for } |t| > T/2$$

and $\Phi(t) = 0$, the ideal impulse response $|Z_0(t)|$ becomes:

$$|Z_0(t)| = A_0 \cdot T \cdot \sqrt{\frac{k}{2\pi}} \cdot \left| \frac{\sin(ktT/2)}{ktT/2} \right| \quad (17)$$

It will be seen below that the phase error function $\Phi(t)$ caused by motion errors can lead to considerable distortion of the azimuth impulse response.

2.2 Impulse Response in the Range Direction

Differentiating, Eq. (10) we can obtain expressions for the angular frequency error $\dot{\Phi}(t)$, due to velocity components along the three axes.

$$\dot{\Phi}_x(t) = -\frac{4\pi \cdot V}{\lambda \cdot R_0} \cdot [\Delta x + t \cdot \dot{\Delta x}(t)], \quad (18)$$

$$\dot{\Phi}_y(t) = \frac{4\pi}{\lambda} \cdot \cos \Theta_D \cdot \dot{\Delta y}(t), \quad (19)$$

$$\dot{\Phi}_z(t) = -\frac{4\pi}{\lambda} \cdot \sin \Theta_D \cdot \dot{\Delta z}(t). \quad (20)$$

The first term in the brackets of Eq. (17) represents the frequency error resulting from the displacement in flight direction. The second term shows a linear relationship between angular frequency error and velocity component, it being proportional $V \cdot t / R_0$, i.e. the azimuth angle Θ_A . This angle is the sum of the so-called squint angle, i.e. the angular offset of the boresight of the antenna, and half the azimuth antenna beamwidth. Eq. (19) and Eq. (20) also show a linear relationship between frequency error and velocity component.

Assuming that the velocities are constant, we can now calculate the phase error Φ_P across the transmit pulse length τ_P :

$$\Phi_{Px} = \dot{\Phi}_x \cdot \tau_P, \quad \Phi_{Py} = \dot{\Phi}_y \cdot \tau_P, \quad \Phi_{Pz} = \dot{\Phi}_z \cdot \tau_P \quad (21)$$

Let us now calculate some practical values for the velocity components and the displacement in flight direction, which would each result in a linear phase error of $\pi/2$, a value which would need to be achieved to influence the impulse response. The results are given in Table 2. We will use the parameters for a typical satellite sensor (ERS-1) and airborne sensor (E-SAR) given in Table 1.

		ERS-1	E-SAR	
Velocity	V	7100	75	m/s
Closest approach	R_0	850	4	km
Wavelength	λ	0.0566	0.0566	m
Depression angle	Θ_D	20.55	45	deg
Max. azimuth angle	Θ_{Amax}	0.013	0.14	rad
Pulse length	τ	37.1	5	μ s

Table 1 Sensor parameters.

	ERS-1	E-SAR	
Δ_x	-22830	-75467	m
$\dot{\Delta}_x$	-9339	-6434	m/s
$\dot{\Delta}_y$	130	1274	m/s
$\dot{\Delta}_z$	-346	-1274	m/s

Table 2 Displacement in flight direction and velocities resulting in a phase error across the pulse of $\pi/2$.

The values in Table 2 show that the displacement and velocities necessary to influence the range impulse response are far higher than achievable with both satellite and aircraft platforms. Hence, motion errors can be considered to only influence the azimuth impulse response, and this will be concentrated on below.

3. CLASSIFICATION OF PHASE ERRORS

Let us consider a sinusoidal phase error $\Phi(t) = \Phi_0 \cos(2\pi f_0 t - \gamma_0)$ with constant frequency f_0 and constant phase shift γ_0 . The impulse response of a point target from Eq.(15) becomes:

$$|Z(t)| = A_0 \cdot \sqrt{\frac{k}{2\pi}} \times \left| \int_{-\infty}^{+\infty} W(\tau) \cdot e^{j\Phi_0 \cos(2\pi f_0 \tau)} \cdot e^{-jkt\tau} d\tau \right| \quad (22)$$

Equation (22) describes a Fourier transformation of the product of the weighting function $W(t)$ and a frequency modulated signal. This corresponds to the convolution of the Fourier transformed weighting function $W(t)$ with a Bessel function, the latter resulting from Fourier transforming the FM signal. Assuming a small amplitude of the phase error $\Phi_0 \ll 1$, the frequency modulation can be approximated by an amplitude modulation and the impulse response becomes:

$$|Z(t)| = \left| Z_0(t) + \frac{\Phi_0}{2} \cdot Z_0\left[t - \frac{2\pi f_0}{k}\right] + \frac{\Phi_0}{2} \cdot Z_0\left[t + \frac{2\pi f_0}{k}\right] \right|, \quad (23)$$

where $Z_0(t)$ is the ideal impulse response from Eq.(17). Eq.(23) shows we obtain one main impulse response and so called 'paired echoes', located at $t = \pm 2\pi f_0/k$, with their maximum being a factor $\Phi_0/2$ below the main lobe

For phase errors with frequencies above $1/T$ the paired echoes are spaced away from the main lobe and result in an increase of the sidelobe level. In general, energy from the mainlobe is transferred to the sidelobes decreasing the Integrated Sidelobe Ratio (ISLR), which corresponds to a loss of contrast in the image. The ISLR is defined as:

$$\text{ISLR} = \frac{\text{Energy of the Mainlobe}}{\text{Energy of the Sidelobes}}$$

If the frequency f_0 of the sinusoidal phase error is lower than the reciprocal aperture time $1/T$, i.e. low frequency phase errors, the paired echoes will merge with the mainlobe and cause its deformation. The low frequency phase error can be expanded into a Taylor series:

$$\Phi(t) = \frac{4 \cdot \pi}{\lambda} \left[p(0) + v(0)t + \frac{1}{2} a(0)t^2 + \frac{1}{6} \dot{a}(0)t^3 + \dots \right], \quad (24)$$

where $p(0)$ is the position error, $v(0)$ the velocity error, $a(0)$ is the acceleration error and $\dot{a}(0)$ is the derivative of the acceleration error at the beginning of the synthetic aperture.

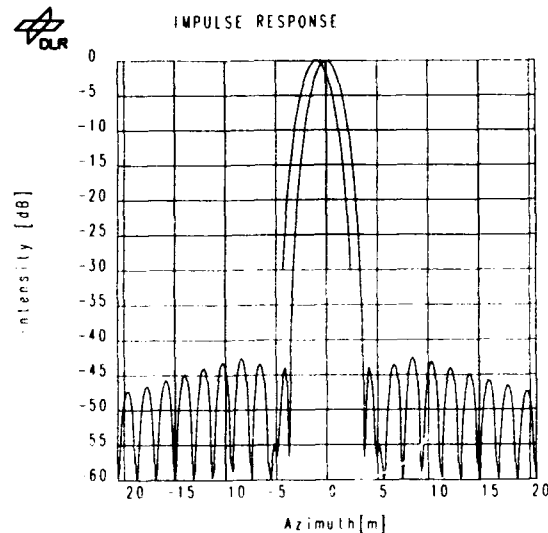


Fig. 4a Impulse response with no phase errors and the shift due to a linear error of π rad.

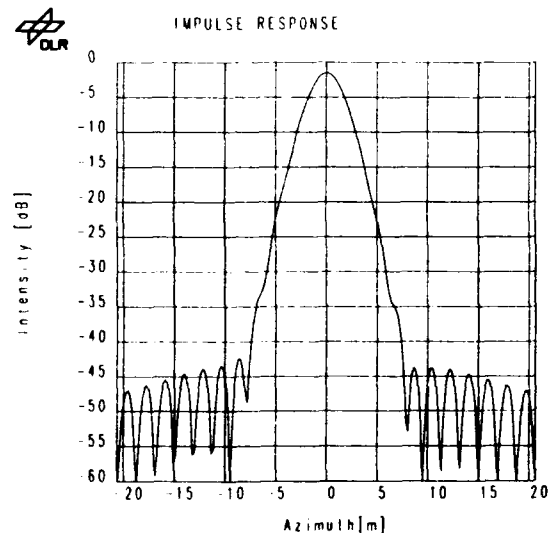


Fig. 4b Impulse response with a quadratic phase error of π rad.

Each term causes different effects on the image quality:

- The constant term has no effect on the image quality. In this case, the aircraft can be supposed to fly parallel to the nominal track and a different area is mapped.
- The linear term corresponds to a shift of the mainlobe in azimuth direction causing geometric distortions of the image.

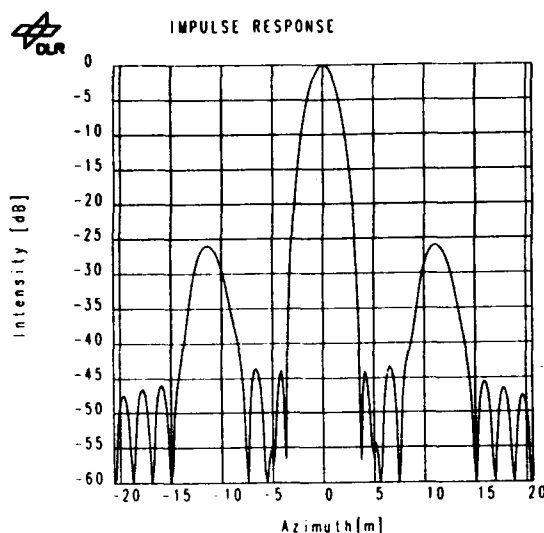


Fig. 4c Impulse response with a sinusoidal phase error of 0.1 rad amplitude and 6 cycles across the interval showing paired echoes.

- The quadratic term causes a broadening of the mainlobe, respectively a loss of geometric and radiometric resolution.
- The cubic term causes an asymmetric distortion of the mainlobe and an increase of the side-lobe level, which also leads to a degradation of the radiometric resolution and a loss of contrast.

Fig. 4 shows examples of the influence of linear, quadratic and sinusoidal phase errors on the impulse response for an airborne sensor with a nominal azimuth resolution of 2.45 m.

4. MOTION COMPENSATION REQUIREMENTS

The motion error of a platform is regarded as a stochastic process, which is assumed to be stationary and ergodic. Thus it can be described most completely by a power spectral density (PSD) [3].

The following Eq. (25) denotes the relation between the phase error PSD $G_\phi(f)$ and the PSD of the displacement of the platform from the nominal track $G_D(f)$. Within Eq. (26) and Eq. (27) the factor $(1/2\pi f)^2$ corresponds to an integration in the time domain, which enables the conversion from the acceleration PSD $G_A(f)$ to the velocity PSD $G_V(f)$ and to the displacement PSD $G_D(f)$.

$$G_\phi(f) = \left(\frac{4\pi}{\lambda}\right)^2 \cdot G_D(f), \quad (25)$$

$$G_D(f) = \left(\frac{1}{2\pi f}\right)^2 \cdot G_V(f), \quad (26)$$

$$G_V(f) = \left(\frac{1}{2\pi f}\right)^2 \cdot G_A(f). \quad (27)$$

The components of the platform motion in x, y and z direction are contributing to the total phase error PSD $G_\phi(f)$.

Using Eqs. (10) and (25), we get for the x-axis

$$G_\phi(f) = \frac{1}{12} \cdot \left(\frac{VT}{R_0}\right)^2 \cdot \left(\frac{4\pi}{\lambda}\right)^2 \cdot G_{Dx}(f). \quad (28)$$

The components in y- and z-direction are denoted as:

$$G_\phi(f) = \cos^2\theta_D \cdot \left(\frac{4\pi}{\lambda}\right)^2 \cdot G_{Dy}(f) \quad (29)$$

and

$$G_\phi(f) = \sin^2\theta_D \cdot \left(\frac{4\pi}{\lambda}\right)^2 \cdot G_{Dz}(f), \quad (30)$$

where $G_{Dx}(f)$, $G_{Dy}(f)$ and $G_{Dz}(f)$ denote the displacement PSDs of the platform in x, y, z direction.

The expected image quality can be predicted, if the power spectral density of the phase error is known. In the following, the effects of the phase errors, classified above, are expressed by means of the PSD.

4.1 Linear Phase Errors

At first we consider a deterministic sinusoidal phase error with a constant frequency f_0 and a constant phase shift γ_0 ,

$$\phi(t) = \phi_0 \cos(2\pi f_0 t - \gamma_0). \quad (31)$$

Expanded into a power series, the linear term $\phi_L(t)$ becomes

$$\phi_L(t) = \phi_0 \cdot 2\pi f_0 t \quad \text{for } \gamma_0 = \pi/2. \quad (32)$$

The phase history of a point target $\phi(t)$, corrupted by the linear phase error $\phi_L(t)$ can be denoted as

$$\phi(t) + \phi_L(t) = -\frac{kt^2}{2} + \phi_0 \cdot 2\pi f_0 t. \quad (33)$$

Thus the impulse response is shifted by the distance l , where

$$l = \frac{\lambda \cdot R_0}{2 \cdot V} \cdot \phi_0 \cdot f_0. \quad (34)$$

We can see, that the shift of the impulse response is proportional to the slope of the linear phase error, which is determined by ϕ_0 and f_0 .

Considering all frequencies contributing to the linear phase error, which are defined by $G_\phi(f)$, the variance of the shift of the impulse response σ_L^2 can be evaluated with

$$\sigma_L^2 = \left(\frac{\lambda \cdot R_0}{2 \cdot V}\right)^2 \cdot \int_0^{1/T} f^2 \cdot G_\phi(f) df. \quad (35)$$

4.2 Quadratic Phase Errors

Concerning the sinusoidal phase error denoted in Eq. (31), for $\gamma_0 = 0$, the quadratic term of the power series becomes

$$\phi_Q(t) = \phi_0 \cdot \frac{(2\pi f_0 t)^2}{2}. \quad (36)$$

At the end of the synthetic aperture when $t = T/2$, the quadratic phase error is

$$\phi_Q(T/2) = \phi_0 \cdot \frac{(\pi f_0 T)^2}{2}. \quad (37)$$

Considering all frequencies contributing to this phase error, which are described by $G_\phi(f)$, the variance σ_Q^2 of the quadratic phase error, measured at the end of the synthetic aperture results in the expression

$$\sigma_Q^2 = \frac{(\pi \cdot T)^4}{4} \cdot \int_0^{1/T} f^4 \cdot G_\phi(f) df. \quad (38)$$

The relation between the mainlobe broadening and the quadratic phase error at the end of the synthetic aperture $\Phi_Q(T/2)$ was determined empirically, by correlating a simulated backscatter signal of a point target with a Hamming weighted reference function ($\alpha = 0.54$) and is described by Eq. (39).

$$\frac{\rho_{\text{eff}}}{\rho_{\text{ideal}}} = \sqrt{1 + 0.55 \left(\frac{\Phi_Q(T/2)}{\pi} \right)^2}, \quad 0 \leq \Phi_Q(T/2) \leq \pi \quad (39)$$

The ideal resolution is denoted as ρ_{ideal} and the resolution, which is degraded by a phase error is ρ_{eff} . For example, a quadratic phase error of $\pi/2$ at the end of the synthetic aperture results in a mainlobe broadening of 6.6%.

4.3 High Frequency Phase Errors

It has already been pointed out, that phase errors with periods below the aperture time T will have an impact on the integrated sidelobe ratio or the image contrast. According to Haslam [4], the required expression is

$$\text{ISLR} = \int_{1/T}^{\infty} G_{\Phi}(f) df \quad (40)$$

4.4 The Effect of Phase Errors on Multilook SAR Images

The multilook technique was developed to reduce the speckle of SAR images. This can be achieved by dividing the synthetic aperture into overlapping subapertures, which are finally summed up incoherently. The impact of motion induced phase errors on each look can be calculated with Eqs. (35), (38), (39), (40), where the integration time of one look T_N has to be taken into consideration.

- A linear phase error has the same effect on a multilook image as pointed out in 4.2.1: Each look is shifted in the same direction by the same distance.
- A quadratic phase error causes a mainlobe broadening and a displacement of the looks from each other.

The distance d_N between the first and last look [5] is given by

$$d_N = \frac{\Delta \alpha_r \cdot T_N \cdot V}{\alpha_r} \quad (41)$$

where α_r is the nominal Doppler rate,

$$\alpha_r = \frac{2 \cdot V^2}{\lambda \cdot R_0} \quad (42)$$

and $\Delta \alpha_r$ is the deviation from the Doppler rate due to the quadratic phase error Φ_Q , which is given by

$$\Delta \alpha_r = \frac{4 \cdot \Phi_Q}{\pi \cdot T_N^2} \quad (43)$$

From Eqs. (41), (42), (43) and after replacing the look displacement d_N by its standard deviation σ_{QN} , we get:

$$\sigma_{QN} = \frac{2 \cdot \lambda \cdot R_0 \cdot \sigma_Q}{\pi \cdot V \cdot T_N} \quad (44)$$

The mean value of the resolution with N looks ρ_N , can be estimated empirically and becomes approximately

$$\rho_N = \sqrt{\rho_1^2 + \frac{\sigma_{QN}^2 \cdot 2.3}{2}} \quad (45)$$

where ρ_1 is the mean value of the resolution of one look. The looks were evaluated with a Hamming weighted reference function and finally root sum squared.

4.5 Determination of the Acceptable Motion Error

The acceptable residual motion error, which remains uncorrected, represents the required performance of the motion compensation system. The following analysis is based on the E-SAR system parameters given in Table 3 and the image quality specifications in Table 4.

• platform:	Dornier Do 228
• altitude:	1000m ... 3000m
• forward velocity (nominal):	$V = 70\text{m/s}$
• maximum slant range:	$R_0 = 6000\text{m}$
• depression angle:	$\Theta_D = 0^\circ \dots 70^\circ$
• antenna beamwidth:	$\Theta_B = 10^\circ$
• wavelength:	$\lambda_L = 0.2308\text{m}$ $\lambda_C = 0.0566\text{m}$ $\lambda_X = 0.0313\text{m}$
• aperture time:	$T_L = 15.0\text{s}$ $T_C = 3.68\text{s}$ $T_X = 2.03\text{s}$
• azimuth resolution (1 look):	$\rho = 0.66\text{m}$

Table 3 System parameters of the E-SAR.

• Integrated Sidelobe Ratio:	ISLR = -20dB
• loss of geometric resolution:	< 10%
• pixel shift:	< 50% of one resolution cell

Table 4 Required image quality.

4.5.1 Specification of the PSD for an Acceptable Motion Error

A power spectral density of the displacement of the aircraft can be specified, which expresses the allowable, residual motion error. The specified PSD of the displacement is denoted as $G_{D_s}(f)$, the measured PSD of the Dornier DO 228 aircraft is denoted as $G_{D_m}(f)$. The PSD $G_{D_s}(f)$ is split up in subdivisions, which are characterized by exponential functions, depicted as straight lines, using a double logarithmic scale (Fig. 5). For computation, Eqs. (25), (35), (38), (39), (40) were used. The coefficients and exponents of these subfunctions were adjusted numerically to achieve the requirements in Tab. 4 for L/C/X-band. $G_{D_s}(f)$ is limited to a frequency range from 0.001 Hz, which corresponds to a maximum duration of one pass of 1000 seconds or approximately 16 minutes, to an upper boundary of 2.2 Hz. Frequencies above 2.2 Hz would cause a maximum ISLR of approximately -30 dB (X-Band) and are not considered to degrade the image quality markedly. The result is given by Eqs. (46)-(50) and is also shown in Fig. 5. The exponent of the subfunction (50) was intentionally set to zero, to reduce the degrees of freedom for further computation. It is remarkable that in this case the requirements for the linear phase error turned out to be more restrictive than the requirements for the quadratic phase error. Thus only Eq. (35) was used to specify the low frequency section of $G_{D_s}(f)$.

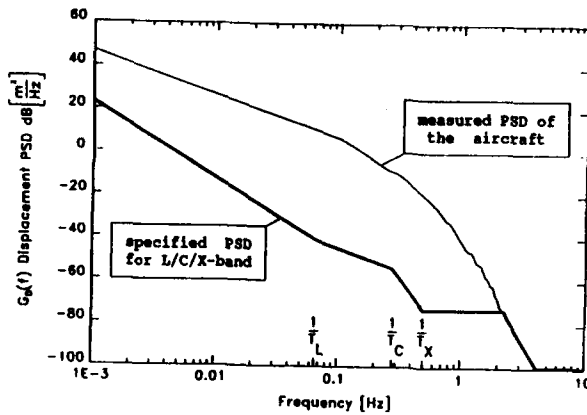


Fig. 5 The measured PSD of the motion of the DO 228 aircraft, compared to the specified PSD of the acceptable motion error.

$$G_{Ds}(f) = 6.46 \cdot 10^{-5} \frac{m^2}{Hz} \cdot (T_L \cdot f)^{-3.5}, \quad 0.001Hz \leq f \leq 1/T_L \quad (46)$$

$$G_{Ds}(f) = 3.41 \cdot 10^{-6} \frac{m^2}{Hz} \cdot (T_C \cdot f)^{-2.093}, \quad 1/T_L \leq f \leq 1/T_C \quad (47)$$

$$G_{Ds}(f) = 4.11 \cdot 10^{-8} \frac{m^2}{Hz} \cdot (T_X \cdot f)^{-7.456}, \quad 1/T_C \leq f \leq 1/T_X \quad (48)$$

$$G_{Ds}(f) = 4.11 \cdot 10^{-8} \frac{m^2}{Hz}, \quad 1/T_X \leq f \leq 2.2 Hz \quad (49)$$

$$G_{Ds}(f) = G_{Dm}(f), \quad 2.2Hz \leq f < \infty. \quad (50)$$

For easier interpretation of the specified PSD $G_{Ds}(f)$, the standard deviation σ_{Ds} of the displacement from the nominal track in line of sight of the antenna can be calculated using:

$$\sigma_{Ds} = \sqrt{\int_0^{\infty} G_{Ds}(f) df} \quad (51)$$

In this case the forward velocity of the aircraft is assumed to be constant. Thus we get a standard deviation of $\sigma_{Ds} = 0.4 m$ for the low frequency section of $G_{Ds}(f)$ for L-, C- and X-band. This means, the RMS deviation from the nominal flight path should not exceed 40 cm within 1000 seconds, to keep the RMS mainlobe shift within 33 cm.

For the high frequency section of $G_{Ds}(f)$ we get

$$\begin{aligned} \text{L-band: } \sigma_{Ds} &= 1.84mm, \quad 1/T_L \leq f \leq \infty \\ \text{C-band: } \sigma_{Ds} &= 0.45mm, \quad 1/T_C \leq f \leq \infty \\ \text{X-band: } \sigma_{Ds} &= 0.25mm, \quad 1/T_X \leq f \leq \infty. \end{aligned}$$

To obtain an ISLR of -20 dB in L/C/X-band, the RMS deviation from the flight path should not exceed 0.8 % of the used wavelength within the aperture time.

4.5.2 Simulations

In addition to theoretical examinations, the obtained results were verified by simulations, based on the Monte Carlo method. Therefore, motion errors

were derived from the PSDs of Fig. 5, and impulse responses were computed according to the E-SAR system parameters, using a Hamming weighted reference function ($\alpha = 0.54$). Typical results for C-band are depicted in Figs. 6-9. The impulse responses of Fig. 7 and Fig. 9 are normalized to the maximum of an ideal, unweighted impulse response $|Z_0(t)|$ from Eq. (16).

The required transfer function $S(f)$ of the motion compensation system is shown in Fig. 10 and is given by

$$S(f) = \frac{G_{Dm}(f)}{G_{Ds}(f)} \quad (52)$$

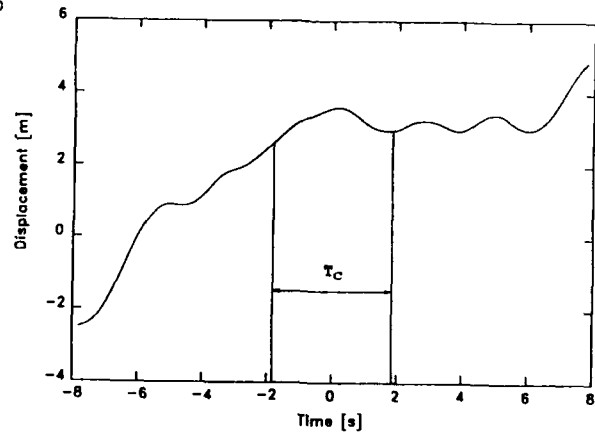


Fig. 6 Simulated motion error, derived from the measured PSD of the aircraft.

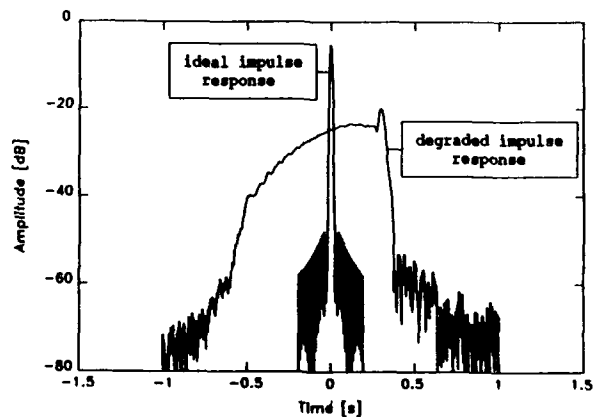


Fig. 7 Simulated C-band impulse response, degraded by phase errors due to Fig. 5, compared to an undistorted impulse response.

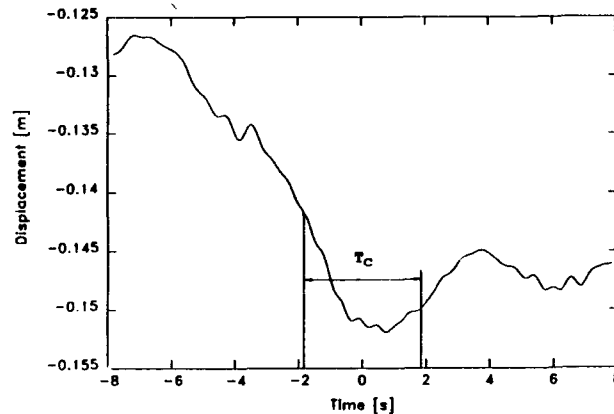


Fig. 8 Simulated motion error, derived from the specified PSD due to Eqs. (46) - (50).

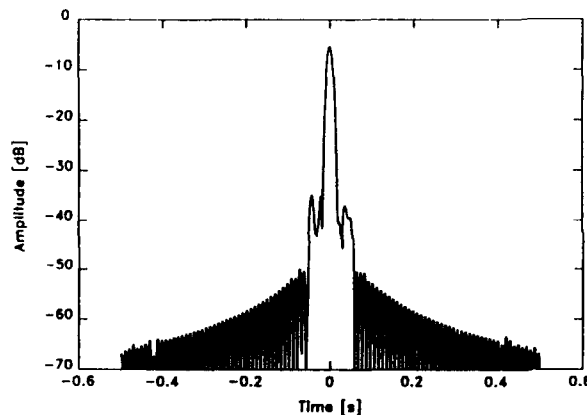


Fig. 9 Simulated C-band impulse response, corresponding to Fig. 7 with an acceptable main-lobe shift, loss of resolution and ISLR.

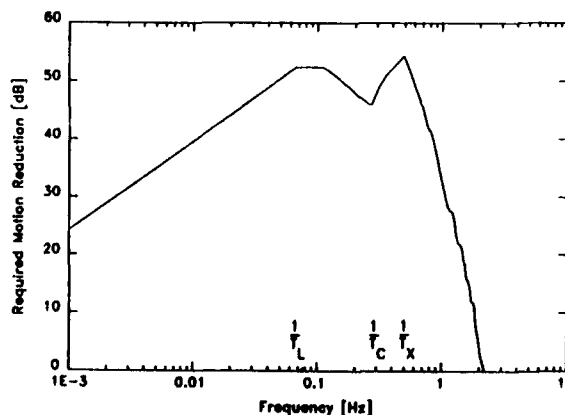


Fig. 10 Required transfer function of a motion compensation system for the E-SAR.

5. MOTION COMPENSATION METHODS

5.1 Flight Path Measurement with a Strapdown Inertial Measurement Unit (IMU)

Within a strapdown inertial measurement unit, the sensor elements are directly mounted to the aircraft frame, whereas linear motions are detected by accelerometers and for angular rate measurement, gyros are used. The following information is usually supplied by a commercial strapdown system:

- aircraft referenced accelerations,
- aircraft referenced attitude,
- inertial velocity,
- ground speed,
- heading,
- position.

To obtain this information, the following evaluations have to be made by a strapdown computer:

- compensation of the rotation of the earth and the transport rate, both being included in the gyro signal,
- compensation of the gravity, included in the accelerometer signal,
- computation of the attitude angles of the aircraft (pitch, roll and yaw), by integrating the angular rates,
- transformation of the accelerations to the earth referenced coordinate system,
- computation of the velocities by single integration,
- computation of the actual position by double integration.

5.1.1 Systematic IMU Sensor Errors

The inertial sensors may produce an output signal, although the IMU system is actually not moved. Farrell [6] already showed, that an accelerometer bias a_b leads to a quadratic phase shift and a cubic phase shift arises from a gyro drift ω_d .

The quadratic phase error $\Phi_Q(t)$ is denoted as

$$\Phi_Q(t) = \frac{4\pi}{\lambda} \cdot \frac{1}{2} \cdot a_b \cdot t^2 \quad (53)$$

and at the end of the synthetic aperture, where $t=T/2$ we get

$$\Phi_Q(T/2) = \frac{1}{2} \cdot \frac{\pi}{\lambda} \cdot a_b \cdot T^2 \quad (54)$$

Taking the E-SAR parameters for L-band, the most critical case, we obtain for a phase error of $\Phi_Q(T/2) = \pi/2$, a total accelerometer bias of $a_b = 104.6 \mu g$. The cubic phase shift $\Phi_C(t)$ is given by

$$\Phi_C(t) = \frac{4\pi}{\lambda} \cdot \frac{1}{6} \cdot g \cdot \omega_d \cdot t^3 \quad (55)$$

where g is the gravity of the earth. With $t=T/2$ we get

$$\Phi_C(T/2) = \frac{1}{12} \cdot \frac{\pi}{\lambda} \cdot g \cdot \omega_d \cdot T^3 \quad (56)$$

For an acceptable cubic phase error $\Phi_C(T/2) = \pi/8$, we obtain a total gyro drift of $\omega_d = 2.16^\circ/h$ for L-band parameters.

5.1.2 Errors from Digital Data Processing

In addition to the phase errors induced by the aircraft motion or by the inertial sensors, further errors will occur due to the imperfect solution of the motion compensation algorithms and of digital data processing artefacts.

Using a digital phase shifter, the amplitude of the phase error $\Phi(t)$ can be adjusted only in discrete steps, due to the number of available bits. The variance σ_n^2 , respectively the mean power of the quantisation noise is

$$\sigma_n^2 = \frac{\Delta s^2}{12}, \quad (57)$$

where Δs is the quantisation step width.

Quantizing 360° with N bits, we get

$$\Delta s = \frac{2\pi}{2^N} \quad (58)$$

and finally, from Eqs. (40) and (51), the ISLR, induced by the quantisation noise, becomes

$$\text{ISLR} = \sigma_n^2 = \frac{\pi^2}{3 \cdot 2^{2N}}. \quad (59)$$

5.1.3 Delayed Phase Adjusting

Within an online motion compensation system, utilising an inertial strapdown system, the computation time will cause a delayed phase correction. Thus a residual, uncorrected phase error will remain, causing an increase of the ISLR. Considering a phase error $\Phi(t) = \Phi_0 \cos(2\pi f_0 t)$, which will be corrected after a time delay Δt_d , a residual, uncompensated phase error $\Phi_{res}(t)$ will remain.

$$\Phi_{res}(t) = \Phi_0 \cos(2\pi f_0 t) - \Phi_0 \cos[2\pi f_0 (t - \Delta t_d)] \quad (60)$$

$$= 2 \cdot \Phi_0 \sin(\pi f_0 \Delta t_d) \cdot \sin[2\pi f_0 (t - \Delta t_d/2)] \quad (61)$$

The residual signal is sinusoidal too, with the phase error frequency f_0 . Its amplitude depends on the time delay Δt_d , the frequency f_0 and the amplitude of the original signal Φ_0 .

Considering all frequencies and amplitudes, defined by:

$G_\Phi(f)$, the ISLR can be evaluated using Eq. (40) as:

$$\text{ISLR} = 4 \cdot \int_{1/T}^{\infty} \sin^2(\pi f \Delta t_d) \cdot G_\Phi(f) df : \quad (62)$$

5.1.4 Sampling and Holding the Detected Motion

Within an on-line motion compensation system, the phase shifter is adjusted in time intervals Δt_s . This is equivalent to sampling and holding the phase error.

Considering a phase error $\Phi(t) = \Phi_0 \cos(2\pi f_0 t)$, the power of the residual, uncompensated phase error, $L_s(t)$ within the interval Δt_s is approximately

$$L_s(t) = \frac{1}{\Delta t_s} \int_0^{\Delta t_s} (\Phi_0 2\pi f_0 t)^2 dt = \frac{4}{3} (\Delta t_s \cdot \pi \cdot \Phi_0 \cdot f_0)^2. \quad (63)$$

Thus the ISLR, caused by sampling and holding the detected motion, becomes

$$\text{ISLR} = \frac{4}{3} (\pi \cdot \Delta t_s)^2 \cdot \int_{1/T}^{\infty} f^2 \cdot G_\Phi(f) df. \quad (64)$$

5.1.5 Flight Path Correction

Once the flight path has been determined, it has to be taken into account during the processing of the SAR data to ensure an undistorted, well focused image. The correction for the errors in the

flight-path can be performed online in the sensor or off-line in the SAR processor. Thereafter the data can be processed as if the platform moves in a straight line at constant altitude and parallel to the swath.

From the flight-path the following parameters are derived.

- The true forward velocity is used to correct the range independent phase errors by ensuring the along track samples are equidistant. This also corrects the image geometrically along track.

With on-line correction, equidistant sampling can best be achieved by controlling the PRF of the radar, i.e. the PRF is directly slaved to the forward velocity. Off-line, the same effect is obtained by interpolating the data in the along-track dimension.

- The range delay of the samples is needed to ensure the range cells are correctly aligned. On-line this is achieved by adjusting the delay of the digitised echo window. Off-line the range cells are shifted in the computer memory.
- The phase of the data in each range sample is corrected according to the true slant range to eliminate phase errors. On-line this can be achieved with a digital phase shifter. Off-line the data can be corrected by shifting the phase mathematically.

5.1.6 Example of Motion Correction using an IMU Sensor

The image in Fig. 1 was taken with the DLR airborne SAR equipped with a LITEF LTR-81 heading and altitude reference system supported by the inertial reference system of the aircraft. The aircraft was deliberately caused to yaw $\pm 2^\circ$ causing the motion errors already described.

From the recorded flight path data, the forward velocity (Fig. 11) and phase errors (Fig. 12) were derived.

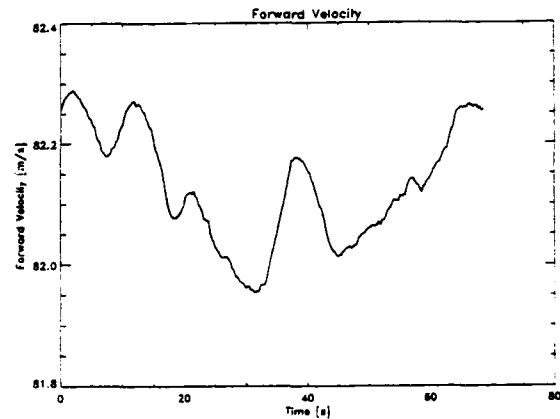


Fig. 11 Forward velocity variation for the example SAR image.

The flight data were used to correct the SAR data and the resulting image is shown in Fig. 13. The image is now well focused and the geometric distortion (runway and taxiways) has been corrected.

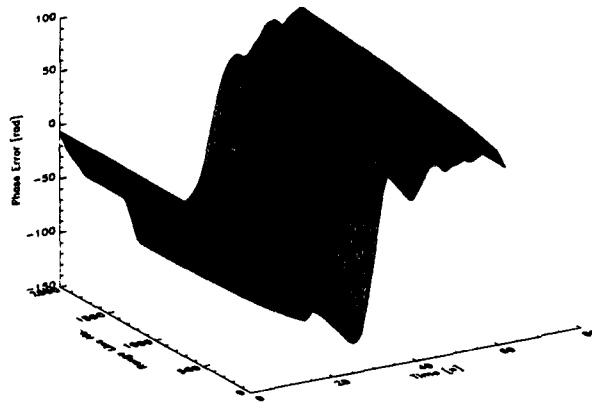


Fig. 12 Phase error profile for the example SAR image.

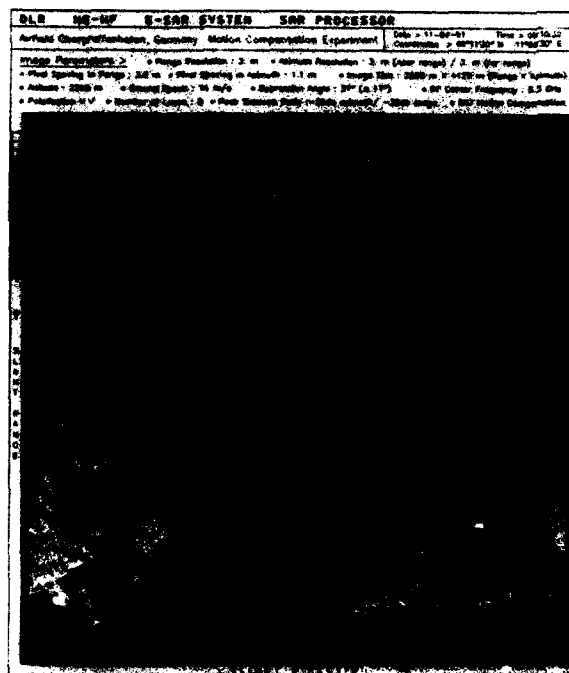


Fig. 13 The scene from Fig. 1 corrected for motion errors.

5.2 Deriving the Flight Path from the Radar Data

5.2.1 Autofocus Methods

Autofocus is a process whereby the SAR processor attempts to derive the data necessary for accurate focusing of the image from the radar data. The following methods describe typical approaches.

5.2.1.1 Look Misregistration Method

With this method the SAR data are processed to obtain a two-look image. The azimuth processing is performed with an assumed Doppler rate. The prin-

ciple of the method is based on the misregistration of the looks if the Doppler rate is incorrect. An error in the Doppler represents a quadratic phase error. In Section 4.1 we have seen that the shift of the impulse response is proportional to the linear phase error.

Assuming a quadratic phase error (see Eq. 24)

$$\Phi(t) = \frac{2\pi}{\lambda} a(0) t^2 \quad (60)$$

Differentiating we obtain:

$$\dot{\Phi}(t) = \frac{4\pi}{\lambda} a(0) t \quad (61)$$

From the earlier analysis it can be shown that the relative position of the impulse response becomes:

$$s = \frac{R_0}{V} t a(0) \quad (62)$$

For two looks spaced Δt in time, the misregistration between the looks in meters is given by:

$$\Delta s = \frac{R_0}{V} \Delta t a(0) \quad (63)$$

Hence, the coefficient of the quadratic phase error $a(0)$ can be determined from the misregistration of the looks. Note that R_0 , V and Δt are all known.

The misregistration of the looks can be determined by correlating them to determine the spacing. Knowing the quadratic phase error term, the Doppler rate can be corrected.

This method works well where quadratic phase errors dominate. This is the case where the platform flight path is stable but the velocity is not known, e.g. satellite sensors. Higher order terms cannot be derived.

The method requires a preliminary processing of the image before correction can be applied.

5.2.1.2 Contrast Optimisation

This method is based on the relationship between the contrast in the image and the Doppler rate used for processing. The image (or parts of the image) is processed and the contrast is measured by calculating the ratio of the deviation/mean intensity of the image. It can be shown [7] that this ratio is directly related to the spatial resolution. This is a trial and error method for finding the optimum Doppler rate for azimuth processing and, hence, requires considerable computer effort.

5.2.2 Reflectivity Displacement Method (RDM)

This method [8, 9] of motion compensation using the SAR data is the most comprehensive and in principle is capable of correcting both high and low-frequency errors with impressive results. The technique analyses the frequency spectrum of the SAR data after range compression to derive the flight path of the sensor.

Considering the deviation from the optimum flight path in terms of a velocity component in line-of-sight V_{Los} , rather than displacements, we can write:

$$f_{Doppler} = \frac{2 V(t) \cdot \theta_A}{\lambda} - \frac{2 \cdot V_{Los}(t)}{\lambda} \quad (64)$$

Assuming the forward velocity $V(t)$ is constant during the period under consideration, we can derive the following expression for the frequency shift between two adjacent power spectra spaced Δt in time:

$$\Delta f_{\text{Doppler}} = -\frac{2 V^2(t) \cdot \Delta t}{\lambda r} + \frac{2 \dot{V}_{\text{LOS}}(t) \cdot \Delta t}{\lambda}, \quad (65)$$

where r is the range of the selected range samples. We see the frequency shift can be separated into two components, one dependent on the forward velocity and one dependent on the acceleration in line of sight.

The spectrum of the SAR data in azimuth is a convolution of the antenna pattern and the ground reflectivity function. If the antenna pattern is broad enough not to influence the ground reflectivity function or, if it can be corrected for, the frequency shift can be determined by correlating the two adjacent azimuth spectra. If Δt is much smaller than the azimuth illumination time, the frequency shift $\Delta f_{\text{Doppler}}$ can be determined very accurately.

Fig. 14 shows two such spectra for the E-SAR airborne sensor operating in L-band with a time offset Δt of 1.075 s.

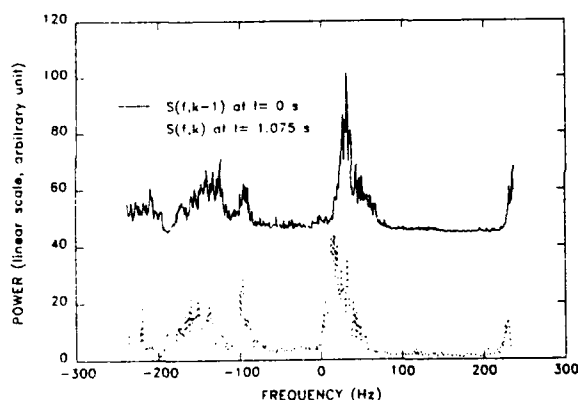


Fig. 14 Two adjacent azimuth power spectra taken with a time offset $\Delta t = 1.075$ s.

Fig. 15 shows the corresponding correlation function yielding a $\Delta f_{\text{Doppler}}$ of 12.1 Hz.

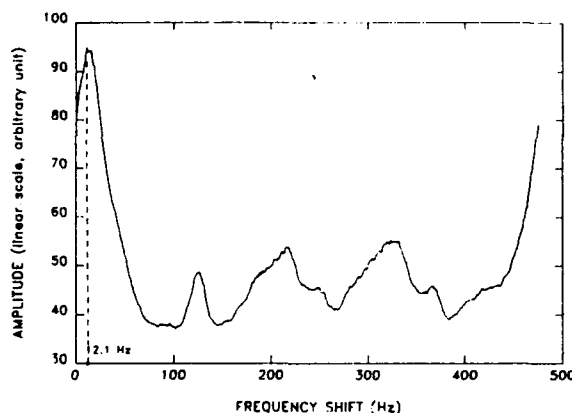


Fig. 15 Correlation of the azimuth power spectra from Fig. 14.

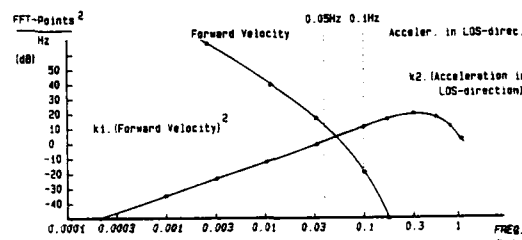


Fig. 16 Power spectral density of the forward velocity and acceleration in LOS for a DO 228 aircraft.

The next step in the RDM method is to consider the power spectral density of the forward velocity and the acceleration in LOS. Fig. 16 shows the PSD for the E-SAR aircraft, a twin-engine Dornier 228. It can be seen that the velocity variations are mainly low-frequency whereas the accelerations in LOS are mainly high frequency. This is true for most airborne platforms where the forward momentum is much higher than in other directions.

This phenomenon enables the forward velocity and acceleration influences to be separated in Eq. (65) by filtering the values of $\Delta f_{\text{Doppler}}$. For the above examples, the filter cut-off frequencies are at 0.05 and 0.1 Hz.

This procedure enables the forward velocity and acceleration to be determined. From these parameters, the necessary corrections of the SAR data can be carried out. Fig. 17 shows an example with

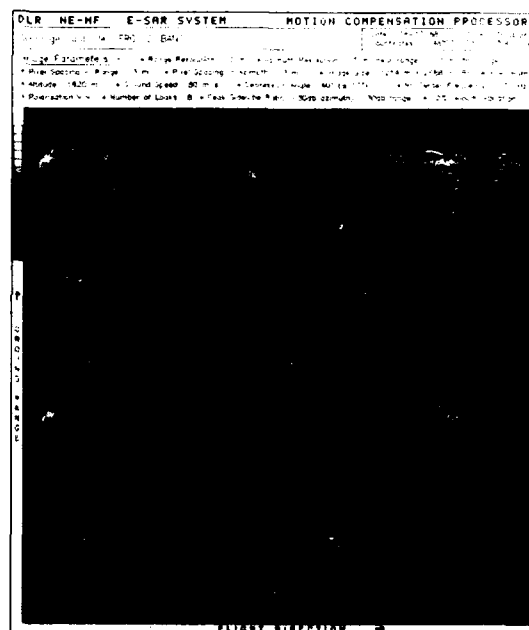


Fig. 17 Image taken in C-band with the E-SAR sensor with 12 % velocity variations. The upper image is uncorrected and the lower one corrected using the RDM method.

the E-SAR sensor operating in C-band with 12 % velocity variations. The upper image is processed with constant velocity and the lower one with the processing parameters corrected using the RDM method. The defocusing visible in the upper image is eliminated after motion compensation.

6. CONCLUSIONS

The influence of motion errors on SAR images has been discussed and the requirements for a compensation system derived.

Several methods of compensation have been discussed, the use of inertial platforms and the RDM method showing the best results.

As an alternative to using inertial platforms, it would be attractive to use the satellite navigation system GPS, being a much cheaper solution.

A GPS receiver is used in the E-SAR airborne SAR to provide absolute position of the aircraft. However, due to the deliberate errors introduced into the GPS data by the GPS operator (selective availability), the data are not accurate enough for motion compensation of the SAR data and they are only used for annotation purposes. Note, that the selective availability degradation particularly influences the velocity measurements. The use of an additional stationary GPS receiver to compensate for these errors (differential GPS) could provide an attractive method for measuring the flight path and is worth investigation.

An additional method of improving image quality was suggested by Chan, the so-called tuned auto compensator [10]. This method analyses strong point targets to identify paired echoes. From these the high-frequency phase errors can be derived. The method requires much trial and error and can, therefore, only be regarded as an augmentation of other techniques.

Table 5 summarises the capabilities of the various methods.

Method	Forward velocity	Low-frequ. errors in LOS	High-frequ. errors in LOS
Inertial measurement	yes	yes	yes
Look misregistration	either or		no
Contrast optimisation	either or		no
Tuned auto compensator	no	no	yes
RDM	yes	yes	yes

Table 5 Comparison of the capabilities of the various motion compensation methods.

7. REFERENCES

- [1] R. Horn:
C-Band SAR Results Obtained by an Experimental Airborne SAR Sensor.
IGARSS Symposium, Vancouver, Canada, 1989 July 10-44.

- [2] S. Buckreuz:
Motion Errors in an Airborne Synthetic Aperture Radar-System.
ETT-Journal Special Issue: "ETT Focus on SAR", Lfd. Nr. 2, Bd. 6, 1991, pp. 655-664.
- [3] A. Papoulis:
Probability, Random Variables and Stochastic Processes.
Internat. Student Edition, McGraw-Hill Kogakusha, Ltd. Tokyo, 1965, p. 336-384.
- [4] G.E. Haslam and B. Reid:
Motion Sensing Requirements for Synthetic Aperture Radar.
Proc. IEEE Conf. Toronto, 1983, Vol.1, pp. 126-131.
- [5] F.K. Li, D.N. Held, J. Curlander, and C. Wu:
Doppler Parameter Estimation for Spaceborne Synthetic Aperture Radars.
IEEE Trans. Geosci. Remote Sensing, Vol. GE-23, 1985, pp. 47-56.
- [6] J.L. Farrell:
Strapdown INS Requirements Imposed by SAR.
Conf. Dayton, OH, USA. 21-25 May 1984.
Proceedings of the IEEE 1984 National Aerospace and Electronics Conference.
Naecon 1984 (IEEE Cat. No. 84CH2029-7).
- [7] D. Blacknell, I.A. Ward and A. Freeman:
Motion Compensation and Geometric Distortion in Airborne SAR Imagery.
Progress in Imaging Sensors, ISPRS Symp., Stuttgart, 1-5 Sept. 1986.
- [8] J.A. Moreira:
A New Method of Aircraft Motion Error Extraction from Radar Raw Data for Real Time SAR Motion compensation.
Proc., IGARSS Symposium, Vancouver, Canada, 1989.
- [9] J. Moreira:
Motion Compensation SAR-Processing Facility at DLR.
EARSeL '90, Toulouse, France, 5-8 June 1990.
- [10] Y. Chan:
A Tuned Auto-compensator for Residual Antenna Motion in Synthetic Aperture Radar Systems.
IEEE Trans. Geosci. Remote Sensing, Vol. GE-24, Nov. 1986, pp. 1025-1027.
- [11] J.C. Kirk:
Motion Compensation For Synthetic Aperture Radar.
IEEE Transactions on Aerospace and Electronic Systems, Vol. 1. AES-11, No.3 (May 1975) pp. 338-348.
- [12] T.A. Kennedy:
Strapdown Inertial Measurement Units for Motion Compensation for Synthetic Aperture Radars.
Presented at the IEEE 1988 National Radar Conference 0885-8985/88/1000-0032, IEEE AES Magazine, Oct. 1988.
- [13] Joos D.K.:
Inertialnavigation in der Strapdown Technik.
Special Issue. Ortung und Navigation.
Journal 2/1983.

THE REAL APERTURE ANTENNA OF SAR, A KEY ELEMENT FOR PERFORMANCE

by

H. Öttl

Deutsche Forschungsanstalt für Luft- und Raumfahrt e.V.
Institut für Hochfrequenztechnik
8031 Oberpfaffenhofen
Germany

SUMMARY

For a SAR system flying on an airborne or spaceborne platform, the real antenna must be designed in such a way so as to avoid ambiguities and achieve the envisaged resolution.

Although a SAR is, with respect to geometric azimuth resolution, independent of its distance from a target, the ground range resolution depends on the incidence angle and, of course, on the bandwidth dependent slant range resolution.

The antenna size and its half power beam width (HPBW) in azimuth and elevation define its azimuth resolution and, for a given off-nadir angle and chosen altitude, the swath width.

The minimum antenna size, measured in wavelengths, depends on the altitude, velocity of platform and chosen off-nadir angle. In real antenna design, the aperture size will be somewhat larger in order to allow for amplitude taper (at least in elevation), for electronic beam steering and possibly for beam shaping.

This paper explains the interdependence of antenna parameters with SAR system performance.

1. INTRODUCTION

Spaceborne imaging radars and, in many cases, airborne imaging radars require enormous antenna dimensions (measured in wavelengths) if real aperture systems are envisaged for ground resolutions of several metres or less. Such large apertures can neither be launched into space nor installed on high flying aircraft. Coherent RF-technology allows the composition of a synthetic aperture length in flight direction, which defines the azimuth resolution, while in the orthogonal direction (in range) resolution is achieved by the short radar pulse length or, if chirp modulated, by the compressed pulse length.

A schematic view of SAR's illumination geometry is illustrated in Fig. 1.

Each target within the footprint of the real aperture antenna will be illuminated during the time needed to fly along one synthetic aperture length, which corresponds approximately to the length of the footprint. The data taken are characterized by time, Doppler frequency and distance between the flying (or orbiting) real aperture antenna and the target (Fig. 2). These data are the input for a SAR processor which generates the SAR images.

Two steps are generally performed by a SAR processor. Firstly, the data are range compressed, that means correlated with the range reference function. Accordingly, one could imagine that this step produces as many fan beams as range bins are foreseen. The HPBW of one such fan beam in range is dependent on the slant range resolution and the incidence angle; the HPBW in azimuth is still approximately equal to the HPBW of the real aperture antenna. Secondly, azimuth compression is performed, which means that the data are correlated with

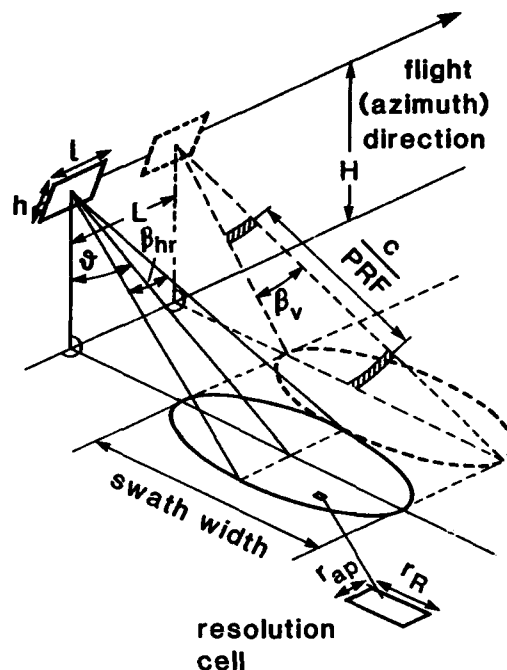


Fig. 1 Coordinate system and illumination geometry.

the azimuth reference function (Doppler function) along the synthetic aperture length. This step creates the synthetic aperture; accordingly, it reduces the azimuth HPBW of the multiple fan beams in relationship to the synthetic aperture length, resulting in a ground resolution of approximately half the real antenna length for a single look image.

It should be noted that the illustration of resolution cells created by multiple beams across range, which are sweeping along the azimuth direction, is only one possibility of describing SAR. It does not include illumination geometry, that means changing incidence angle direction and value during a flight along one synthetic aperture length.

2. GEOMETRIC RESOLUTION, ANTENNA APERTURE AND SWATH WIDTH

It is important to understand the improved along track resolution of a synthetic aperture antenna in comparison to a real aperture antenna of the same length l and same azimuth aperture taper factor a_{hr} . To explain this, we assume an antenna carrying platform passing a target. In the case of a real antenna, the target will be fully illuminated if the Doppler frequency is zero. The antenna beam, originating from the phase center of the antenna, is orthogonal to the flight direction (Fig. 3). Resolution is given by:

$$r_{ax} = \frac{H}{\cos \theta} \beta_{hr} \quad (1)$$

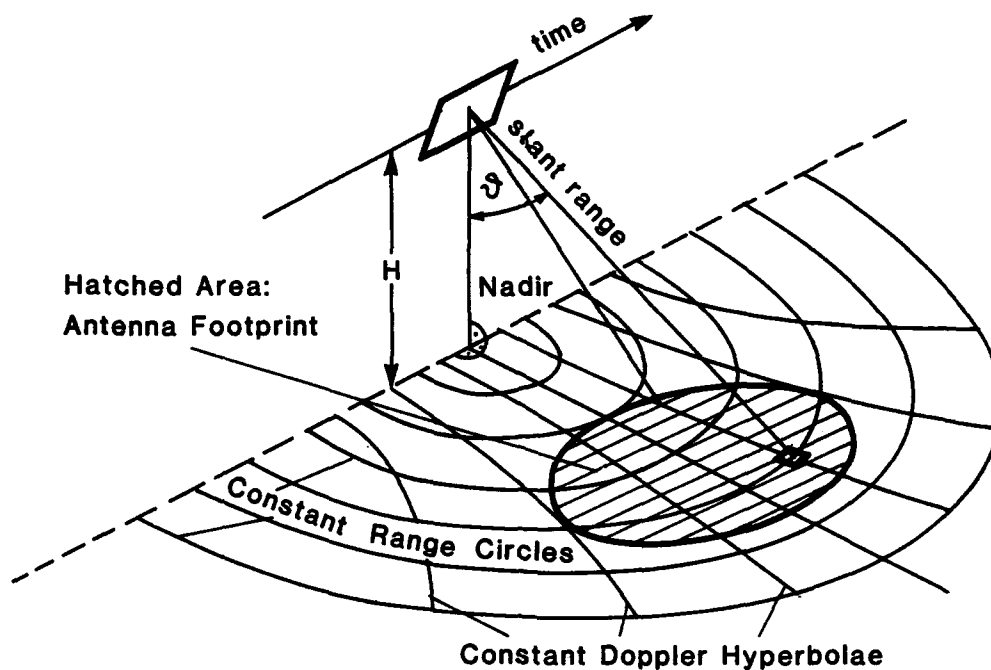


Fig. 2 Position of resolution cell within a SAR image is determined by slant range, Doppler frequency and time.

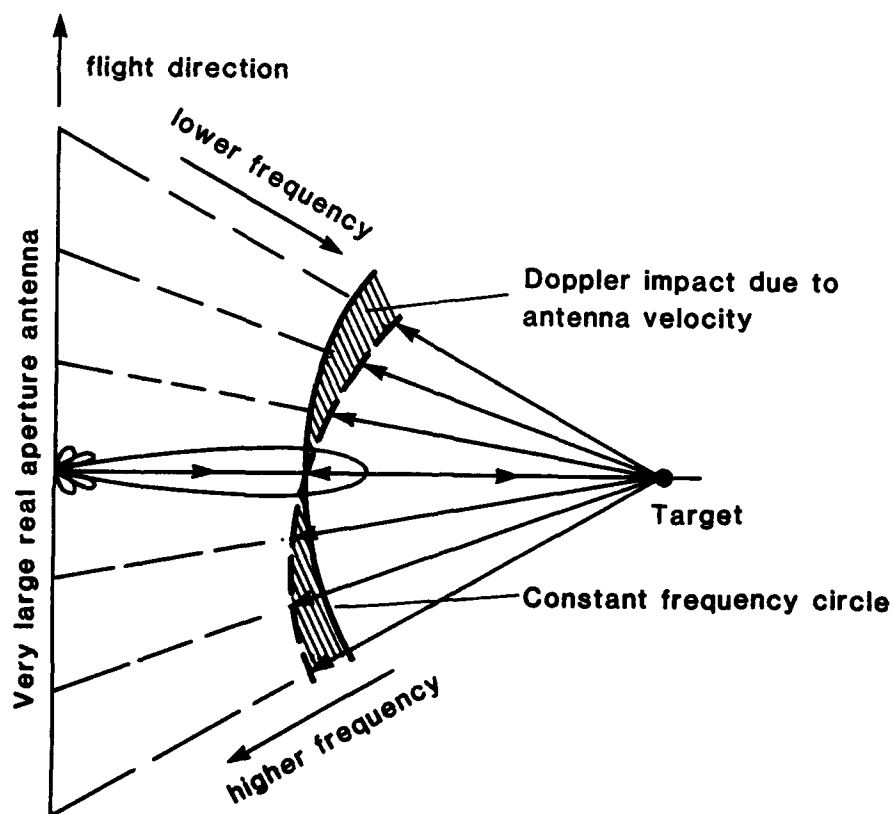


Fig. 3 Very long real aperture antenna illuminates a target. The Doppler frequency shift of the backscattered signal corresponds to the one way case.

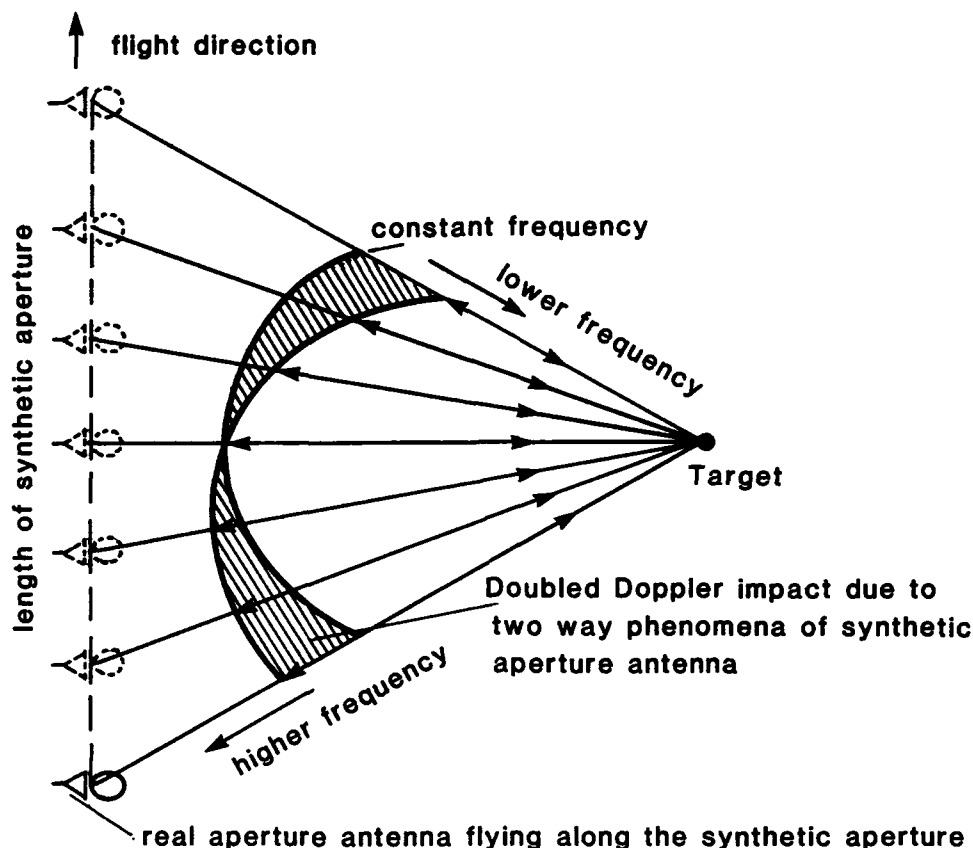


Fig. 4 Synthetic aperture antenna illuminates a target. The signal from the real aperture antenna propagating to the target undergoes already a Doppler shift; the backscattered signal is "Doppler shifted" again resulting in twice the value of the one way case.

H = altitude of antenna above ground,
 θ = off-nadir angle (= incidence angle),

$$\text{azimuth HPBW } \beta_{hr} = a_{hr} \frac{\lambda}{l}, \quad (2)$$

λ = wavelength.

The signal reflected from the target reaches the different parts of the real aperture antenna with a phase distribution corresponding to the one way distance. The Doppler frequency occurring at the different parts of the moving "long, real aperture" antenna represent also the one way case.

In the case of a synthetic aperture antenna, a small signal source (phase centre) flies along the synthetic aperture. We have, therefore, a two way case for the phase difference along the synthetic aperture (Fig. 4), which means that phase differences (or Doppler frequency) are twice the values achieved in the real aperture case of the same length. This phenomenon causes a phase change of 180° twice as fast as in the case of the real aperture antenna, meaning that the nulls of the synthetic aperture antenna main beam have a spacing which is half of the real aperture antenna.

Therefore, a synthetic aperture antenna has an along track resolution (HPBW of SAR) which is approximately twice as good as for the case of a theoretical, real aperture antenna of the same length. The along track (azimuth) resolution for a single look image is given by

$$r_{ap} = \frac{H}{\cos \theta} \beta_{hs}, \quad (3)$$

the HPBW of the synthetic aperture

$$\beta_{hs} = a_{hs} \frac{\lambda}{2L}, \quad (4)$$

a_{hs} = azimuth aperture taper factor,

L = length of synthetic aperture.
 The HPBW of the real aperture antenna which flies along the synthetic aperture (the antenna is much smaller than in the above mentioned comparison) is used for the definition of the antenna footprint. The length of the synthetic aperture is given by the length of the footprint and therefore,

$$L = r_{ar} = a_{hr} \frac{\lambda}{1 \cos \theta} \quad (5)$$

Substituting L from (4) and β_{hs} from (3) in (5) leads to

$$r_{ap} = \frac{a_{hs}}{a_{hr}} \frac{1}{2}, \quad (6)$$

which is the well known approximation for finest along track resolution. For $a_{hs} = a_{hr}$, r_{ap} corresponds to half the length l of the real aperture antenna.

However, it should be noted that in many cases the amplitude distribution in azimuth of the real aperture antenna is not tapered, resulting in $a_{hr} = 0.88$, while the sidelobe suppression achieved by the reference function of the synthetic aperture azimuth pattern (more than 40 dB below mainlobe) leads to $a_{hs} = 1.3$. Therefore, it is a realistic assumption to expect an $r_{ap} = 0.8 l$.

The swath width is a parameter which is dependent on along track resolution r_{ap} , platform velocity u and off-nadir angle θ , as will be shown below.

Flying along a synthetic aperture length covers, in the case of SAR, twice the normally encountered Doppler frequency shift f_D .

For zero offset processing (using in-phase and quadrature channels for positive and negative Doppler identification) only f_D per channel is used.

From geometric considerations (see also Fig. 1 and 2), f_D is defined by

$$f_D = \frac{2u}{\lambda} 2 \sin \frac{\beta_{hr}}{2} \quad (7)$$

For high flying platforms (satellites), β_{hr} is small and

$$f_D = \frac{2u}{\lambda} \beta_{hr} = 2a_{hr} \frac{u}{\lambda} \quad (8)$$

The Nyquist sampling theorem requires a pulse repetition frequency (PRF) equal to or higher than the f_D which is used in SAR processing per channel. Generally, a PRF of 1 to 1.3 times f_D will be chosen. Two radar pulse returns must not be received simultaneously from the illuminated footprint (instantaneous field of view, IFOV) of the real aperture antenna. Looking at Fig. 5, we notice that the slant range difference between the edges of the illuminated swath width (corresponding to β_v) is given by the slant swath width

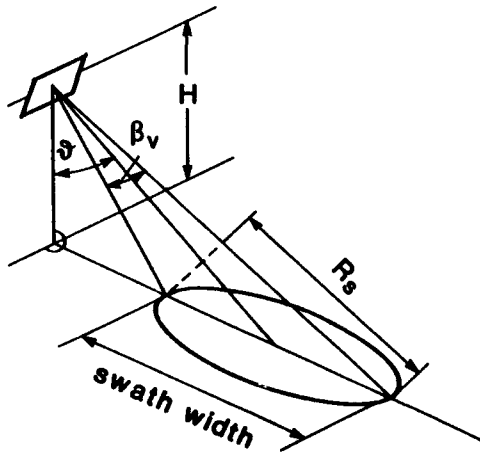


Fig. 5 Distance between two pulses must be $> 2R_s$ in order to avoid range ambiguities occurring within the IFOV. R_s = slant range swath width.

$$R_s = \frac{H \beta_v \sin \theta}{\cos^2 \theta} \quad (9)$$

The distance between two radar pulses must be $> 2R_s$, to avoid the reflected pulse from the far range edge overlapping with the reflected pulse from the near range. Therefore,

$$\frac{c}{\text{PRF}} > 2 H \beta_v \frac{\sin \theta}{\cos^2 \theta} \quad (10)$$

c = speed of light.

Substituting $a_v \frac{\lambda}{h}$ for β_v gives the antenna height h

$$h > \frac{2 \text{ PRF } a_v H \lambda \sin \theta}{c \cos^2 \theta} \quad (11)$$

a_v = elevation taper factor.

Since $\text{PRF} \geq f_D$ and $f_D = 2 a_{hr} \frac{u}{\lambda}$, the physical dimensions of the real aperture antenna are given by

$$A_p = h \lambda > 4 a_{hr} a_v \frac{u}{c} H \lambda \frac{\sin \theta}{\cos^2 \theta} \quad (12)$$

In many cases, $a_{hr} = 0.88$ (constant amplitude) while a_v will be approximately 1.3 to allow suppression of the sidelobes in the elevation plane. Furthermore, range ambiguities should also not occur within the main lobe at all (main lobe width is approximately 2 to 3 times larger than β_v).

Therefore, empirical estimations of the real antenna dimensions could be based on

$$A_p = 10 \frac{u}{f} H \frac{\sin \theta}{\cos^2 \theta} \quad (13)$$

f = SAR frequency.

It can be concluded that the estimated minimum dimensions of the real antenna enforce a trade-off between resolution and swath width. High resolution can only be achieved with a small swath width; increasing the swath width reduces resolution (Fig. 6 and Fig. 7).

3. DIRECTIVITY, GAIN, BANDWIDTH AND DUAL POLARIZATION

The remarks given below refer to spaceborne antennae, which are more difficult to realize due to their size and the associated, complicated, feeding network.

These antenna, of several square metres area, are usually designed as flat (foldable) arrays.

The directivity of such antennae is proportional to their area but depends of course on the chosen taper. Compared to constant amplitude distribution with a sidelobe level of about -13 dB, a good sidelobe suppression (in elevation) reduces directivity easily by 1 to 1.5 dB, which must be compensated by an increased antenna area.

For a rectangular, flat array antenna of length l and height h , the directivity D is given by

$$D = \frac{4\pi l h}{\lambda^2} \quad (14)$$

if an equal phase and amplitude distribution is assumed. In this case, we call $l h$ the effective antenna area

$$A_{eff} = l h \quad (15)$$

For any deviation from constant phase and amplitude distribution, the effective antenna area will be smaller than the real aperture. The relationship between the two areas is called aperture efficiency η_a . It reduces the directivity proportionally and therefore,

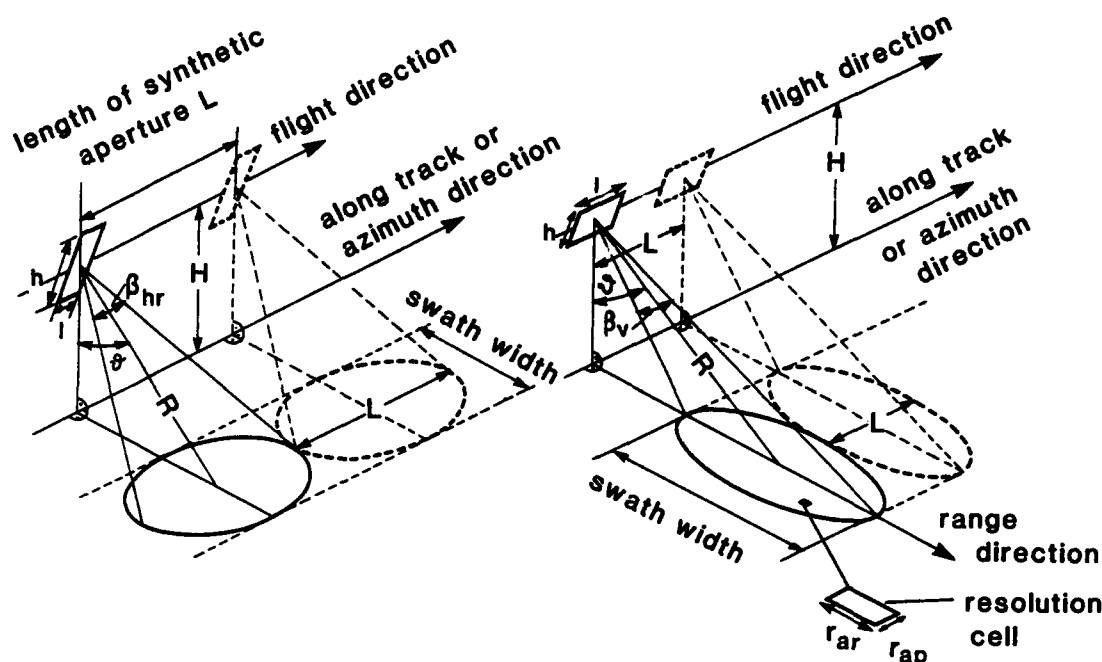


Fig. 6 High resolution corresponds to long synthetic aperture and small swath width (left side of figure) while a wide swath width enforces a short synthetic aperture and low resolution (right side of figure).

$$D = \eta_a \frac{4\pi l h}{\lambda^2} \quad (16)$$

The antenna gain G is smaller than the pattern directivity D due to internal antenna losses. This thermal efficiency, or radiation efficiency, is defined by

$$\eta_1 = \frac{G}{D} \quad (17)$$

For a passive microstrip antenna of several square metres or a waveguide array of several metres length (spaceborne SAR antenna), η_1 might be 0.5 or even lower (depending on the frequency).

Considering these high one way losses associated with such arrays, one solution would be to use an active array with distributed transmit/receive modules (T/R modules). The one way loss of such systems is much lower and leads to $\eta_1 = 0.8 - 0.9$. For lower microwave frequencies, such as L-band and S-band, light weight and volume considerations lead to microstrip arrays while for higher frequencies, such as C-band and X-band, a waveguide array might be favoured for its lower losses.

The bandwidth of the antenna should be broad enough to easily achieve the desired range resolution (chirp bandwidth). Frequencies (signals) outside the useful bandwidth should be rejected or, at least, strongly attenuated.

Typically, microstrip and wave guide arrays attain a relative bandwidth of 3% to 5%. That means, for a high slant range resolution r_R it is advisable to use higher frequency bands for the SAR. For example, a slant range resolution of 0.5 m corresponds approximately to a chirp bandwidth of 300 MHz (which is 3% of 10 GHz).

Slant range resolution r_R is defined by

$$r_R = \frac{c}{2B} \quad (18)$$

B = chirp bandwidth.

The ground resolution across track is accordingly given by

$$r_y = \frac{c}{2B \sin \theta} \quad (19)$$

Dual polarization capability has been increasingly requested in recent years in order to allow for full polarimetric SAR operation. For instance, a horizontally polarized signal pulse will be transmitted and the back scattered signal will be received in the same polarization and simultaneously in vertical polarization; then a vertically polarized signal pulse will be transmitted and the back scattered signal will be received in the same polarization and simultaneously in horizontal polarization. This sequence will be continuously repeated. Assuming that the time between 2 transmitted pulses of different polarizations is negligible, we achieve the complete polarimetric matrix of backscattered signals (scattering matrix). It

contains much more information about radar illuminated target classes than the copolarized back scattered signal of one polarization.

However, it should be noted that polarimetric SAR operation (also named "quad-pol" operation) requires doubling the PRF for a SAR with 2 receiver channels. This results in reducing the swath width to half of the single polarisation case and, accordingly, doubling the antenna height h for proper range ambiguity suppression (exception: airborne SAR is usually not affected by range ambiguity problems, due to the low altitude and smaller swath width).

The polarization ratio between copolarized and cross-polarized antenna pattern should exceed 30 dB within the HPBW's in azimuth and elevation. It

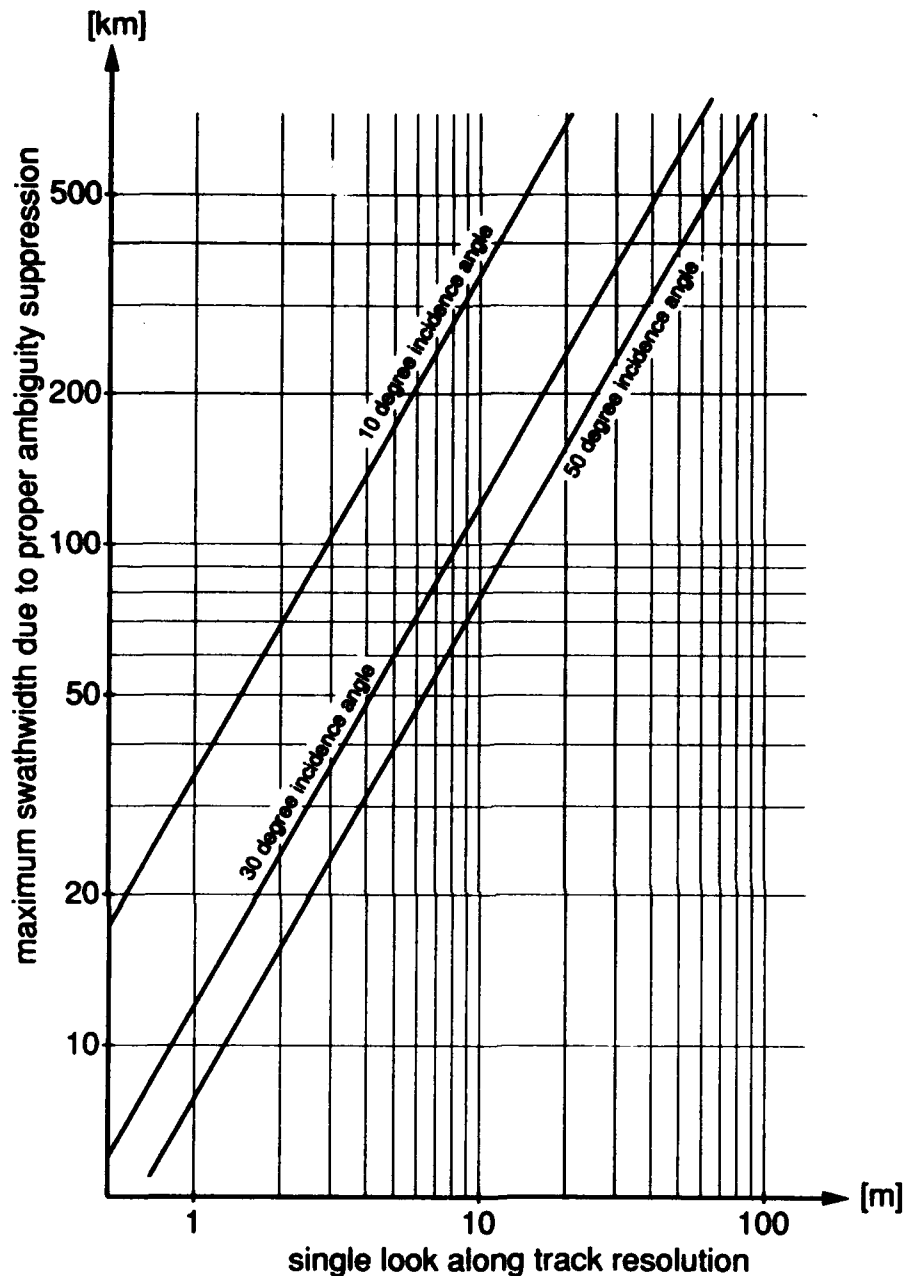


Fig. 7 Azimuth resolution r_{ap} influences proportionally the swath with; the parameter is incidence angle.

is very difficult to reach this performance for the large arrays needed for spacecraft. Screening the feeding network and accurate mechanical alignment of single radiating elements are a "must" for a good polarization ratio. The request for 30 dB is based on the facts that cross-polarization occurs in many cases in the range of 5 dB to 20 dB below the copolarized back scattered signal and that the performance of a spaceborne SAR sensor (noise floor) seldom allows a signal to noise ratio S_n of more than 20 dB.

4. ACTIVE PHASED ARRAY

For spaceborne remote sensing, a fast off-nadir angle change capability is needed

- to allow scan-SAR operation,
- to increase the number of data take opportuni-

ties and therefore reduce the revisit time intervals,

- to collect radar data under different incidence angles.

The off-nadir angle range used in various studies extends from 15° (20°) to 50° (60°) covering a data take opportunity width of about 200 km to 600 km on the ground (depending on the orbital altitude, e.g. shuttle or satellite).

For an array antenna with distributed T/R modules, only phase shifters need to be added in order to produce an active phased array antenna.

The number of T/R modules and the spacing of the radiators (or groups of radiators) fed by a single T/R module depends on the chosen phase controlled angle range.

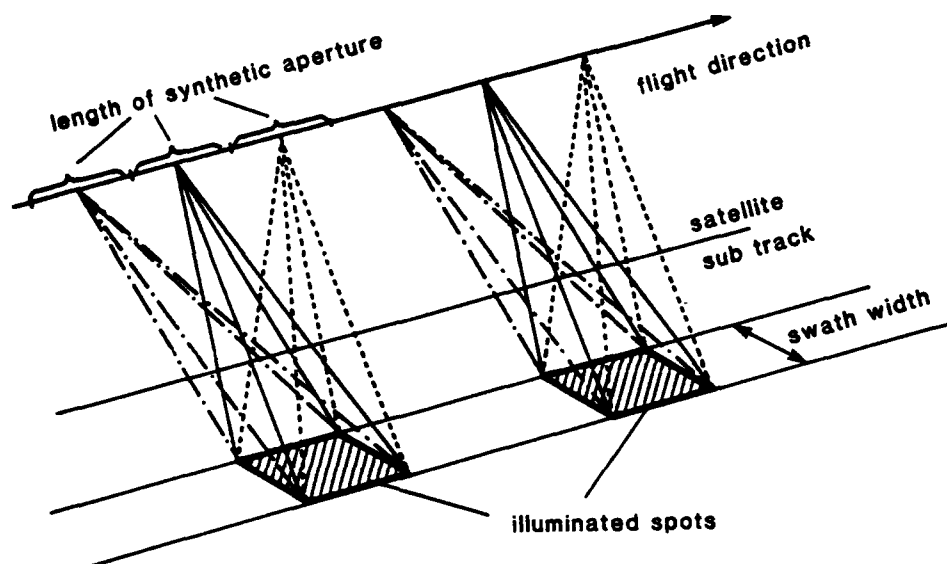


Fig. 8 Azimuth look steering mode increases the overall synthetic aperture (for multi look images with azimuth resolution r_{ap}). Only spot-wise data takes are possible in this mode.

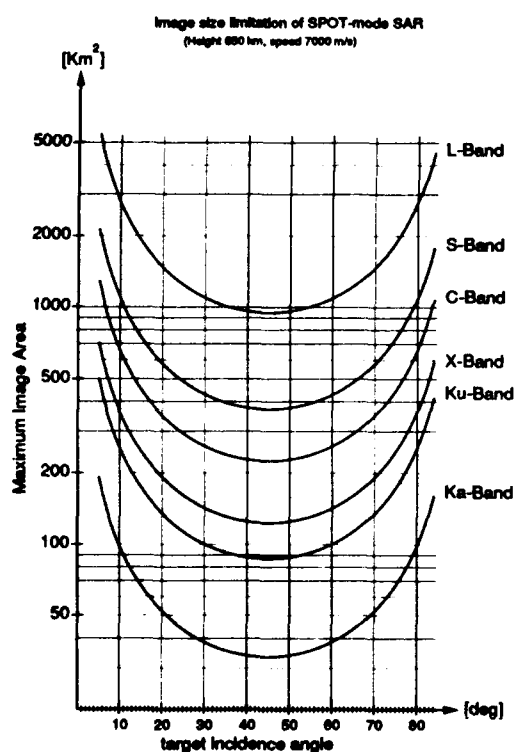


Fig. 9 Illuminated area for spot lightmode and/or azimuth look steering mode increases approximately proportionally with the wavelength.

The generation of several "main beams", which are called grating lobes, occurs if the spacing is too large. In such a case, several angles exist with equal phase distribution; it is at these angles that the grating lobes occur. Suppression of grating lobes is accomplished by satisfying

$$\frac{d}{\lambda} < \frac{1}{1 + |\sin \Delta\theta|} \quad (20)$$

d = distance between phase centres of single radiators (or groups of radiators) fed by neighbouring T/R modules,

$\Delta\theta$ = half the desired phase controlled angle range.

In case of $\Delta\theta = \pm 20^\circ$, the spacing must be less than or equal to 0.75λ . Spotlight or azimuth look steering modes require a beam which is electronically controlled by phase shifters within a small (squint) angle range. These modes allow high resolution observations of small areas (spots) by sacrificing the observational possibilities before and after each spot (Fig. 8). The required squint angle $\Delta\theta$ for such operations is seldom larger than $\pm 1^\circ$ to $\pm 2^\circ$. The spot size is frequency dependent because of the IFOV, which increases proportionally with the wavelength (Fig. 9).

Equation (20) will not be applied for squint angles of 1° to 2° in order to keep the number of T/R modules and its phase shifters small. The radiator groups in azimuth fed by a single T/R module have a high directivity, which is used to suppress the grating lobes.

There are two causes of gain reduction due to electronic beam steering. Any angle deviating from the mechanical boresight angle reduces the antenna area proportionally to $\cos \Delta\theta$ or $\cos \Delta\phi$. Furthermore, each single radiator has a pattern which usually has its maximum at the (mechanical) boresight angle. The reduced gain at other angles must be multiplied with the array factor (which represents the far field of point sources arranged in the geometric layout of our antenna). For instance, the gain loss of a well designed active phased array at $\Delta\theta = 20^\circ$ will be approximately 0.5 dB.

5. CONCLUSIONS

The real aperture antenna is a key element for SAR performance. It defines and/or influences

- the along track resolution r_{ap} by its length l ,
- the swath width by its height h ,
- the across track resolution r_R by its bandwidth B ,
- the range ambiguity suppression by its amplitude distribution in elevation (taper factor a_v),
- the required onboard power by antenna losses (thermal efficiency η_1),
- the polarimetric performance by its polarization decoupling,
- the data take opportunity, scan SAR and spotlight mode SAR by its electronic beam steering.

It is, therefore, worthwhile investing efforts in a good antenna design and accompanying technologies.

6. REFERENCES

This paper is a lecture based on principles, which have been published several times by other authors and by recent studies, in which the author was involved. The references below were used as sources, but due to the general aspect of this lecture, no special reference is given in the text.

1. Skolnik, M.I., "Radar Handbook", McGraw-Hill Book Company Inc., 1970.
2. Barton, D.K. and Ward, H.R., "Handbook of Radar Measurement", Artech House, Inc., 1984.
3. Meinke/Gundlach, "Taschenbuch der Hochfrequenztechnik", Dritte Auflage, Springer Verlag, 1968, Kapitel H. Antennen.
4. Jasik, H., "Antenna Engineering Handbook", McGraw-Hill Book Company Inc., 1961.
5. Ulaby, F.T., Moore, R.K. and Fung, A.K., "Microwave Remote Sensing", Vol. I and II, Addison-Wesley Publishing Company, 1981 and 1982.
6. Ulaby, F.T. and Dobson, M.C., "Handbook of Radar Scattering Statistics for Terrain", Artech House, Inc., 1989.
7. Colwell, R.N., Simonett, D.S. and Ulaby, F.T., "Manual of Remote Sensing", Second Edition, Vol. I, The Sheridan Press, 1983, Chapter 9 and 10.
8. Jordan, R.L., Huneycutt, B.L. and Werner, M., "The SIR-C/X-SAR Synthetic Aperture Radar System", Proc. IEEE, Vol. 79, No. 6, June 1991, pp. 827-838.
9. Jatsch, W., Langer, E., Öttl, H. and Zeller, K.H., "Concept of an X-Band Synthetic Aperture Radar for Earth Observing Satellites", JEWA, Vol. 4, No. 4, 1990, pp. 325-340.
10. Öttl, H. and Wahl, M., "X-EOS, a Multi-Mode X-Band Synthetic Aperture Radar for EOS SAR", under Publication in Proc. of ISY Conference, Munich, March 29 - April 4, 1992.

Polarization Effects and Multipolarization SAR

A. Freeman

Jet Propulsion Laboratory
Pasadena, CA 91109
USA

Introduction

Imaging radar polarimetry has excited much attention in the literature over the past few years ([1]-[6]), since NASA/JPL first demonstrated a successful SAR polarimeter system in 1985 [1]. That system was known as the CV-990 L-Band radar; NASA/JPL now have a fully operational, three-frequency polarimetric SAR flying on a DC-8 platform, which has taken part in many science data acquisition campaigns since 1988 [7]. Several other institutions have radar polarimeter systems which are operational or under development, including the University of Michigan, MIT/Lincoln laboratories, the Environmental Research Institute of Michigan (ERIM) [8], the Canada Center for Remote Sensing (CCRS), FEL-TNO in the Netherlands and the Technical University of Denmark. NASA/JPL are currently completing the construction of a two-frequency, fully polarimetric SAR system which will fly on the Space Shuttle in 1993/1994 [9]. These systems generally transmit and receive horizontally (H) and vertically (V) linearly polarized electromagnetic fields.

Imaging radar polarimeters are usually implemented using a Synthetic Aperture Radar (SAR) approach to give a high resolution image in two dimensions: range and azimuth. For each pixel in the image a polarimetric SAR gives sufficient information to characterize the polarimetric scattering properties of the imaged area (or target) as seen by the radar. Using a polarimetric SAR system as opposed to a single-polarization SAR system provides significantly more information about the target scattering mechanisms and allows better discrimination between different types of surfaces.

In these notes a brief overview of SAR polarimetry is offered. The notes are intended as a text to accompany a lecture on SAR polarimetry as part of an AGARD-NATO course. For a more in-depth treatment, the interested reader is referred to the recent review paper by Zebker and van Zyl [10] and the textbook on 'Radar Polarimetry for Geoscience Applications', edited by Ulaby and Elachi [11]. For a discussion of inverse methods to determine scattering phenomena for polarimetric radar data the interested reader is referred to the textbook on 'Inverse Methods in Electromagnetic Scattering', edited by Boerner [12]. For brevity, a discussion of the development history of polarimetric radar has not been included in these notes, nor has a comprehensive bibliography. The reader interested in more information on these topics would do well to begin by examining references [10]-[12].

Covered in the notes are: the polarization properties of electromagnetic waves; the concepts of radar scattering and measuring radar backscatter with a SAR; polarization synthesis; scattering matrix, Stokes matrix and covariance matrix representations of polarimetric SAR data; polarization signature plots; design and calibration of polarimetric SAR systems; polarization filtering for target detection; fitting a simple model to polarimetric SAR measurements of naturally occurring features; and supervised classification of polarimetric SAR data.

Polarization of Electromagnetic Waves

The polarization of any electromagnetic wave can be characterized by the ellipticity angle, χ , and the orientation angle, ψ , of the polarization ellipse, shown in Figure 1. The intensity of the wave is represented by the parameter I_0 , where

$$I_0 = a_h^2 + a_v^2 \quad (1)$$

Some commonly occurring polarization states are:

Vertical (linear) - ($\psi = 0^\circ, \chi = 0^\circ$)

Horizontal (linear) - ($\psi = 90^\circ, \chi = 0^\circ$)

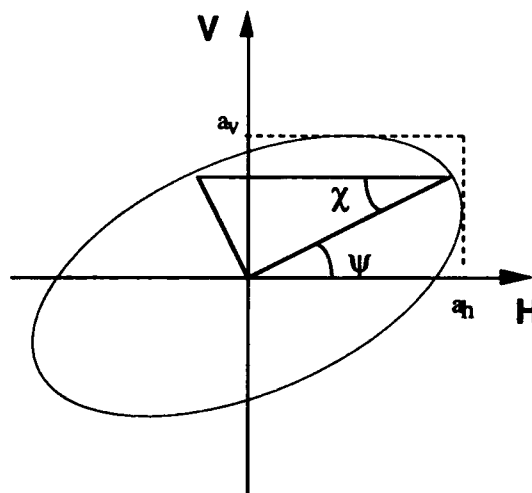
Right-hand circular - ($\chi = -45^\circ$)

Left-hand circular - ($\chi = 45^\circ$)

For the two circular polarization states above, the orientation angle, ψ , is unspecified. Another useful way of characterizing the polarization state of an electromagnetic wave is the Stokes vector,

$$\mathbf{F} = \begin{bmatrix} I_0 \\ Q \\ U \\ V \end{bmatrix} = \begin{bmatrix} I_0 \\ I_0 \cos 2\psi \cos 2\chi \\ I_0 \sin 2\psi \cos 2\chi \\ I_0 \sin 2\chi \end{bmatrix} \quad (2)$$

where I_0 , Q , U and V are the four Stokes parameters, which all have the same dimension. The Stokes



Polarization Ellipse

Fig. 1 Polarization ellipse.

parameters are related via:

$$I_0^2 = Q^2 + U^2 + V^2 \quad (3)$$

so that only three of them are actually independent.

The polarization state of an electromagnetic wave can be represented as a (unique) mapping to a point on a sphere of radius I_0 , called the Poincare' sphere, where Q , U , and V are the Cartesian coordinates of the point. The angles 2χ and 2ψ define the latitude and longitude of the point in the spherical coordinate system. The four common polarization states listed above are shown as points on the Poincare' sphere in Figure 2.

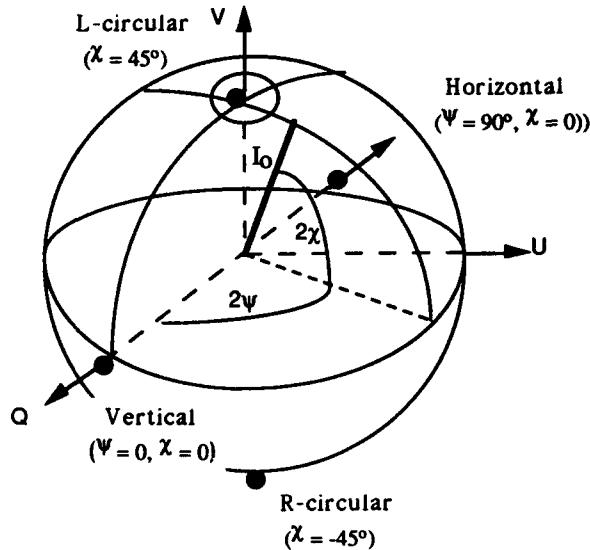


Fig. 2 Poincare' sphere.

Radar Scattering Measurements

In Figure 3 the general geometry for measurements made by a bistatic radar is illustrated. The transmitting antenna transmits an electric field whose components are expressed in terms of a local Cartesian coordinate system $(\hat{h}, \hat{v}, \hat{n})$ with origin at the transmitting antenna. We can define another Cartesian coordinate system $(\hat{x}, \hat{y}, \hat{z})$ with origin at the scatterer. The two coordinate systems are related via:

$$\hat{h} = \sin \phi_i \hat{x} - \cos \phi_i \hat{y} \quad (4a)$$

$$\hat{v} = -\cos \phi_i \cos \theta_i \hat{x} - \sin \phi_i \cos \theta_i \hat{y} + \sin \theta_i \hat{z} \quad (4b)$$

$$\hat{n} = -\cos \phi_i \sin \theta_i \hat{x} - \sin \phi_i \sin \theta_i \hat{y} + \cos \theta_i \hat{z} \quad (4c)$$

A third coordinate system $(\hat{h}', \hat{v}', \hat{n}')$ is defined with origin at the antenna which receives the electromagnetic wave which is scattered by the scatterer. This coordinate system is related to the scatterer coordinate system in a similar fashion to the above, substituting subscripts s for subscripts i in (4). This choice of coordinate systems ensures that the primed $(\hat{h}', \hat{v}', \hat{n}')$ and unprimed $(\hat{h}, \hat{v}, \hat{n})$ coordinate systems coincide for a monostatic system, i.e. when the receiving and transmitting antennas are at the same location. The radar scattering measurements made by a monostatic radar system are referred to as radar backscatter measurements.

Measuring Radar Backscatter with a SAR system

A SAR system is simply a high-resolution active microwave sensor, capable of measuring the (real or complex) radar reflectivity of a surface. SAR's usually operate as monostatic radars, mounted on a moving platform, with an antenna looking out and down towards one (or both) sides relative to the platform motion vector. Most SAR systems measure the radar backscatter using linearly polarized antennas, typically with polarizations given by the \hat{h} and \hat{v} coordinates in Figure 3. In its ideal realization, the resulting SAR image should just represent the scattering matrix element, S_{pq} , in complex representation, or the radar cross-section, σ_{pq} , in intensity, for the receive (q) and transmit (p) polarizations of the radar. The scattering matrix determines the relationship between the wave incident on the scatterer and the scattered wave. After [11], the scattering matrix is defined via:

$$\begin{pmatrix} E_h^s \\ E_v^s \end{pmatrix} = \frac{e^{jk_0 R}}{R} \begin{pmatrix} S_{hh} & S_{vh} \\ S_{hv} & S_{vv} \end{pmatrix} \begin{pmatrix} E_h^i \\ E_v^i \end{pmatrix} \quad (5)$$

where $\begin{pmatrix} E_h^i \\ E_v^i \end{pmatrix}$ is the electric field vector of the wave

incident on the scatterer, $\begin{pmatrix} E_h^s \\ E_v^s \end{pmatrix}$ is the electric field vector of the scattered wave, k_0 is the wave number of the illuminating wave, and R the (radial) distance between the scatterer and the radar antenna. A fully polarimetric SAR system would typically measure all four of the scattering matrix elements simultaneously (or near-simultaneously) as complex numbers for each pixel within the area being imaged by the SAR.

Polarization Synthesis

Knowledge of the scattering matrix allows the calculation of the backscatter intensity, or radar cross-section, for any possible combination of transmit and receive antenna polarizations (e.g. left-hand circular transmit and right-hand circular receive). This procedure is called polarization synthesis. For any given radar receive and transmit polarization, the radar cross-section (RCS) can be calculated [11] via:

$$\sigma_{pq} = 4\pi |\mathbf{q}^T \mathbf{S} \mathbf{p}^t|^2 \quad (6)$$

where \mathbf{S} is the scattering matrix defined in (1), and \mathbf{q}^T , \mathbf{p}^t are polarization field vectors for the radar receive and transmit polarizations, respectively. For linear polarizations (horizontal, h or vertical, v) note that the RCS is given by:

$$\sigma_{pq} = 4\pi |S_{pq}|^2 \quad (7)$$

In what follows we will concentrate on linear polarizations, since most SAR systems just measure linear polarizations.

Expressions (5) and (6) above represent the quantities which are directly measurable by a SAR. The units for σ_{pq} are in meters squared. Both σ_{pq} and S_{pq} are functions of spatial position $[(\hat{x}, \hat{y})$ in the scatterer coordinate frame], time (t), viewing geometry (θ_i, ϕ_i) , and radar wavelength (λ) in addition to the polarizations of the transmitted and received

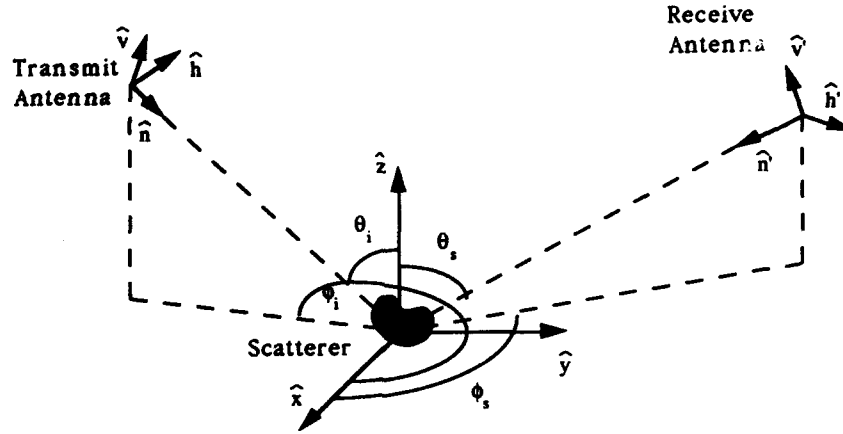


Fig. 3 Coordinate systems for radar scattering.

electromagnetic waves. If the radar backscatter measurements made by the SAR are calibrated, each image pixel value should correspond to an accurate and precise measurement of one of these quantities, and be repeatable, under the same conditions, by that or another sensor.

Stokes matrix and Covariance matrix representations

In the monostatic scattering case, it can be shown that the reciprocity principle [10], which dictates that

$$S_{hv} = S_{vh} \quad (8)$$

is generally applicable. This simplifies some of the analysis of polarimetric SAR data and quantities derived from it. For example, another useful way of representing the polarimetric scattering information contained in the scattering matrix is to construct a covariance matrix between the scattering matrix elements. Without reciprocity the covariance matrix would have to be a 4x4 matrix containing all possible cross-products between the four scattering matrix elements. With reciprocity a 3x3 covariance matrix is sufficient, i.e.,

$$C = \begin{pmatrix} S_{hh} S_{hh}^* & S_{hh} S_{hv}^* & S_{hh} S_{vv}^* \\ S_{hv} S_{hh}^* & S_{hv} S_{hv}^* & S_{hv} S_{vv}^* \\ S_{vv} S_{hh}^* & S_{vv} S_{hv}^* & S_{vv} S_{vv}^* \end{pmatrix} \quad (9)$$

The covariance matrix is also Hermitian, so that three of its elements ($S_{hv} S_{hh}^*$, $S_{vv} S_{hh}^*$ and $S_{vv} S_{hv}^*$) contain redundant information, which is already contained in three of the other elements.

Another way of representing the cross-products derived from the scattering matrix elements is in the Stokes matrix format [13]. For reciprocal scatterers the Stokes matrix M is a 4x4 symmetric matrix, with the following elements:

$$M_{11} = 0.25(S_{hh} S_{hh}^* + 2S_{hv} S_{hv}^* + S_{vv} S_{vv}^*)$$

$$M_{12} = 0.25(S_{hh} S_{hh}^* - S_{vv} S_{vv}^*)$$

$$M_{13} = 0.5 \operatorname{Re}(S_{hh} S_{hv}^*) + 0.5 \operatorname{Re}(S_{hv} S_{vv}^*)$$

$$M_{14} = 0.5 \operatorname{Im}(S_{hh} S_{hv}^*) + 0.5 \operatorname{Im}(S_{hv} S_{vv}^*)$$

$$M_{22} = 0.25(S_{hh} S_{hh}^* - 2S_{hv} S_{hv}^* + S_{vv} S_{vv}^*)$$

$$M_{23} = 0.5 \operatorname{Re}(S_{hh} S_{hv}^*) - 0.5 \operatorname{Re}(S_{hv} S_{vv}^*)$$

$$M_{24} = 0.5 \operatorname{Im}(S_{hh} S_{hv}^*) - 0.5 \operatorname{Im}(S_{hv} S_{vv}^*)$$

$$M_{33} = 0.5(S_{hv} S_{hv}^*) + 0.5 \operatorname{Re}(S_{hh} S_{vv}^*)$$

$$M_{34} = 0.5 \operatorname{Im}(S_{hh} S_{vv}^*)$$

$$M_{44} = 0.5(S_{hv} S_{hv}^*) - 0.5 \operatorname{Re}(S_{hh} S_{vv}^*) \quad (10)$$

The first element, M_{11} , in the Stokes matrix is often referred to as the total power. It is related to two of the other Stokes matrix elements via:

$$M_{11} = M_{22} + M_{33} + M_{44} \quad (11)$$

Note that it is possible to recover the covariance matrix elements from the Stokes matrix elements. It is not possible, however, to recover the original scattering matrix from either, since the overall or *absolute* phase of the scattering matrix (for example the phase of the S_{hh} term) has been lost in forming the cross-products. The *relative* phase between the scattering matrix elements is preserved in the covariance matrix and Stokes matrix formats, in terms such as the $S_{hh} S_{vv}^*$ cross-product, whose argument is the relative phase between the S_{hh} and S_{vv} terms.

It is still possible to carry out polarization synthesis on the covariance matrix and Stokes matrix format polarimetric SAR data to synthesize the radar cross section measured by a radar of arbitrary transmit and receive polarization [10]. A common technique employed on SAR measurements of radar cross section to reduce the variance due to speckle is to perform incoherent averaging or multi-looking. Using the scattering matrix data, the synthesized radar cross section would be calculated for each pixel using (6). The calculated radar cross section values would then be averaged to reduce the speckle variance. Multi-looking can also be carried out by averaging the covariance matrix or Stokes matrix elements for several pixels to produce a single composite result, then performing

polarization synthesis on the composite result [14]. The two approaches can be shown to be mathematically equivalent and give the same answers, but there is a considerable saving in computation time using the covariance matrix and Stokes matrix approach.

Example Scattering Matrices

Table 1 gives examples of some simple scattering matrices for selected man-made targets. The targets are the trihedral corner reflector and the sphere (which have the same scattering matrix), the dihedral corner reflector, the dipole and the polarimetric active radar calibrator (PARC) [15]. Only the scattering matrices for the trihedral and the sphere show no dependence on the rotation of the scatterer about the vector \hat{n} which defines the line of sight between target and radar. By rotating the dihedral, the dipole and the PARC about the line of sight it is possible to change the scattering matrix for these targets as seen by the radar. The scattering matrices corresponding to more complicated man-made targets, such as vehicles or planes, may be very different from the simple ones given in Table 1.

In Figure 4, we see a total power image of San Francisco, California which was derived from L-band (24cm) polarimetric SAR data collected by the NASA/JPL DC-8 SAR system [7]. The image is interesting because it contains three distinct types of scatterer: the man-made buildings and other structures in the urban areas; the largely vegetation covered areas in the Golden Gate Park and the Presidio (just south of the Golden Gate Bridge); and large stretches of open water in the bay and out in the ocean.

In Figure 5, an example of a useful tool for visualizing the polarimetric scattering properties of a target, known as the polarization signature plot, is shown. In this case, the polarization signature plot was calculated from a composite Stokes matrix formed from pixels in one of the urban areas in Figure 4. After [13], the polarization signature plots represent the (synthesized) response of the target to all possible like- and cross-polarized radar transmit/receive combinations. The



Fig. 4 L-band total power image of San Francisco from the NASA/JPL system.

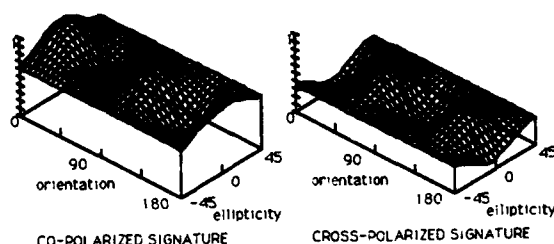


Fig. 5 Polarization signature for a predominantly urban area in the San Francisco image.

Table 1: Scattering matrices for man-made targets, normalized so that the largest matrix element is one

Target type	Scattering matrix
Trihedral , Sphere	$\begin{pmatrix} 1 & 0 \\ 0 & 1 \end{pmatrix}$
Dihedral	$\begin{pmatrix} \cos 2\alpha & \sin 2\alpha \\ \sin 2\alpha & -\cos 2\alpha \end{pmatrix}$
Dipole	$\begin{pmatrix} \cos^2 \alpha & \sin \alpha \cos \alpha \\ \sin \alpha \cos \alpha & \sin^2 \alpha \end{pmatrix}$
PARC	$\begin{pmatrix} \sin \alpha \cos \alpha & \cos^2 \alpha \\ -\sin^2 \alpha & -\sin \alpha \cos \alpha \end{pmatrix}$

[α is a rotation angle for each target type, about the line of sight to the radar.
 α -values of 0° , 45° and 90° are commonly used, in practise.]

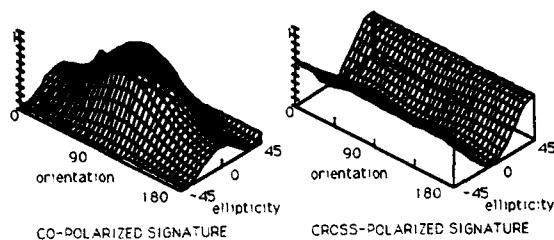


Fig. 6 Polarization signature for an ocean area in the San Francisco image.

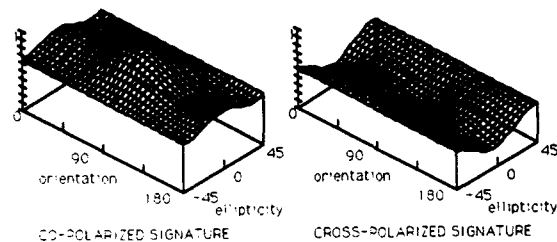


Fig. 7 Polarization signature for a vegetated area in the San Francisco image.

polarization signature plots are given as functions of orientation and ellipticity angle, and are normalized with respect to the total power. Note that the like-polarized polarization signature in Figure 5 shows a maximum response when the orientation angle is 90° or 0° (180°). This behavior, and the double-null structure visible for $(\psi = 45^\circ \text{ and } 145^\circ, \chi = 0^\circ)$ is very similar to that expected for a dihedral corner reflector with rotation angle, $\alpha = 0^\circ$. Thus the polarimetric radar backscatter from the urban area is seen to be similar to that produced by two flat plates; one flat on the ground, the other vertically upright.

The scattering matrix model for Bragg scattering from an idealized rough surface, such as wind-blown water, is:

$$S = \begin{pmatrix} a & 0 \\ 0 & b \end{pmatrix} \text{ with } a, b \text{ real, } b > a > 0 \quad (12)$$

and $\langle ab^* \rangle = ab$

i.e., a scattering matrix with zero cross-polarized return, HH and VV returns which are completely correlated and zero phase difference between the HH and VV returns. The ratio a/b and the absolute backscatter level are dependent on the surface roughness (i.e., the sea-state in this case) but need not be known a priori. Although we specify a rough surface for (12) to hold, it should not be too rough, since second order Bragg scattering can give rise to significant cross-polarized backscatter. The polarization signature corresponding to a patch of

water from the San Francisco image is shown in Figure 6. We see that the like-polarized signature shows that the VV return is greater than the HH (i.e. $b > a$) and the linear ($\chi = 0^\circ$) polarization response in the cross-polarized signature is zero for all orientation angles.

In Figure 7 we show the polarization signature plot corresponding to a largely vegetation-covered area in the Golden Gate Park from the San Francisco image. In this case we see that the cross-polarized and like-

polarized signature plots have no zero points for any orientation angle/ ellipticity angle combination. The like-polarized signature plot is similar in form to that of the water, except that the polarization signature of the vegetated area appears to sit on a 'pedestal'. The presence of such a pedestal indicates that the individual scattering, covariance or Stokes matrix measurements used to calculate the polarization signature plot for the area in question were not identical. In fact, the height of the pedestal can be related to the variance in the measurements. Note that the polarization signature plots for the water shown in Figure 6 do not have a significant pedestal, which suggests that the measurements averaged to produce those plots were fairly similar.

Design of Polarimetric SAR systems

An example of a polarimetric SAR system is NASA/JPL's DC-8 SAR system, first tested in January 1988, which operates at three frequencies (L-, C- and P-Band) and four polarizations, HH, HV, VH and VV (in this notation HV means Horizontal polarization on transmit, Vertical on receive). This system is the latest in a series of NASA/JPL synthetic aperture radar systems that have been designed, built and tested primarily by the Radar Science and Engineering Section at the Laboratory. The radar will serve as a test-bed for SIR-C with which it has similar characteristics, as well as acting as a useful science tool for the remote sensing community in its own right.

A detailed description of the NASA/JPL's DC-8 SAR can be found in [7]. A block diagram of the basic transmit/receive circuitry required for just one of the frequencies is shown in Figure 8. This basic design contains just one transmitter, two receivers and two antennas (one H, one V). In the DC-8 SAR case, the radar system generates a pulse at L-Band which is frequency shifted using a common reference oscillator to generate the P- and C-Band pulses. After amplification at each frequency, the transmitted chirp is alternately polarized by the operation of a switch to either the H or the V antennas. The antenna patterns for each of the frequencies cover approximately the same range of incidence angles, between 20° and 70° . On receive, the radar can collect both H and V channel data simultaneously at all three frequencies, the six receiver channels being entirely separate. The receivers have no Sensitivity Time Control (STC) or Automatic Gain Control (AGC), but the receiver gains can be adjusted over a 26dB range of settings. A wide instantaneous dynamic range of $\sim 45\text{dB}$ is achieved by using 8-bit analog-to-digital converters (ADC's), which are clocked together to ensure cross-channel coherence. The ADC's each operate at 45MHz and produce real data samples (not I and Q) at a sustained data rate of between 20 and 60 MBytes/second, depending on the data collection mode.

The operation of the DC-8 SAR is such that alternate H and V polarized pulses are transmitted. The return echoes are received by both the H and V receivers simultaneously. Thus for one H-polarized transmitted pulse the H- and V-polarized return echoes are recorded (HH and VV returns); the next transmitted pulse will be V-polarized and the VH and VV return echoes are recorded. This process is repeated throughout a data-take. Then the recorded return echoes undergo SAR processing (range and azimuth compression) to produce SAR images corresponding to each of the set of HH, HV, VH and VV return echoes. The SAR processing operations applied to each polarization are identical. After processing, the HH and HV images must be resampled in the azimuth dimension so that they are registered with the VH and VV images; prior to this operation the two sets of images will be misregistered by one pulse repetition interval. After registration the scattering matrix measurements can be

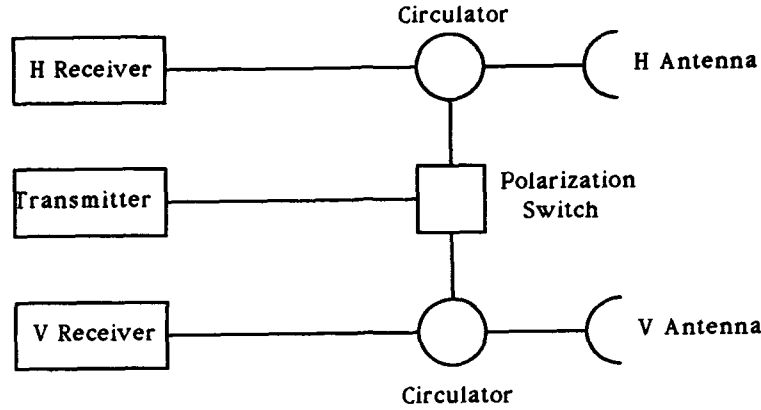


Fig. 8 Simple block diagram for a polarimetric SAR system.

considered to be spatially coincident, i.e. they correspond to the same patch of ground.

Polarimetric Calibration

Calibration of the data produced by polarimetric SAR's (e.g. [1], [16], [17]) is necessary if the data is to be used in a quantitative fashion. Goals for calibrating polarimetric SAR data are given in Table 2. The basic problem in calibrating polarimetric radar data can be seen from the following expression, after [18], for the measurements made by a polarimetric radar for which the 2×2 R and T matrix system model is valid:

$$\begin{aligned} M &= \sqrt{K_s} e^{j\phi_s} \begin{pmatrix} 1 & \delta_1 \\ \delta_2 & f_1 \end{pmatrix} \begin{pmatrix} S_{hh} & S_{vh} \\ S_{hv} & S_{vv} \end{pmatrix} \begin{pmatrix} 1 & \delta_3 \\ \delta_4 & f_2 \end{pmatrix} \\ &+ \sqrt{K_n} \begin{pmatrix} n_{hh} & n_{vh} \\ n_{hv} & n_{vv} \end{pmatrix} \\ &\equiv \sqrt{K_s} e^{j\phi_s} R^t S T + \sqrt{K_n} N \end{aligned} \quad (13)$$

where δ_1 and δ_2 are the HV and VH cross-talk or polarization impurity terms on receive, δ_3 and δ_4 are the HV and VH cross-talk terms on transmit, f_1 is the channel imbalance (amplitude and phase) between the H and V channels on receive, and f_2 is the channel imbalance (amplitude and phase) between the H and V channels on transmit. We shall ignore the radiometric calibration problem for the moment, setting $K_s = 1$, and absorbing the $\sqrt{K_n}$ factor into the individual noise matrix elements, n_{pq} . We shall also ignore the absolute phase calibration problem for now, setting $\phi_s = 0$. The polarimetric radar data calibration problem can then be stated as follows: to solve for the scattering matrix S from the measured matrix M we need estimates for the matrices R and T , which represent the radar polarimetric characteristics on receive and transmit. Ideally, R and T are identity matrices for a perfect radar polarimeter. Once we have obtained estimates for R and T they can then easily be inverted and applied to (13) to recover an estimate for S , i.e.,

$$\hat{S} = (\hat{R}^t)^{-1} \hat{M} (\hat{T})^{-1}$$

$$= S + (\hat{R}^t)^{-1} N (\hat{T})^{-1} \quad (14)$$

(provided $\hat{R} = R$ and $\hat{T} = T$, with $\hat{\cdot}$ denoting an estimate). Note that the result still has noise superimposed on it. At the complex SAR image stage (which is what polarimetric SAR scattering matrix data is), although the mean noise contribution is zero, the rms uncertainties due to noise can not be removed. After square-law detection, however, the average noise power can be subtracted off the resulting RCS measurements (though this still does not remove the rms uncertainties due to noise). Polarization synthesis, in which the target RCS, σ_{pq} , in response to a radar with transmit polarization p and receive polarization q is synthesized from the scattering matrix, involves a square-law detection step, so the noise bias term can be subtracted off the synthesized image pixel powers, provided it can be estimated.

We characterize the (complex) noise terms as having two-dimensional, zero-mean, Gaussian distributions, with the following properties:

$$\begin{aligned} \langle n_{jk} \rangle &= 0 \\ \langle n_{jk} n_{jk}^* \rangle &= \sigma_{jk}^n \\ \langle n_{jk} n_{lm}^* \rangle &= 0, \text{ for } j \neq l \text{ or } k \neq m. \\ \langle n_{jk} S_{lm}^* \rangle &= 0, \text{ for any } j, k, l, m. \end{aligned} \quad (15)$$

where σ_{jk}^n is the noise power (or noise-equivalent sigma-zero) in the polarization channel jk . We assume that the noise terms are uncorrelated with each other and with the scattering matrix (signal) terms.

An important point to note is that, in equations (13) and (14), we have not included any (x, y) dependence in any of the terms. In practice, the elements of R , T and N may vary significantly within a SAR image, especially in the across-track dimension. Depending on how quickly the elements of these matrices vary, it may be necessary to calculate them at many different points across the image. This is a strong factor in deciding what type of approach to adopt in calibrating data from a polarimetric radar (see below).

The validity of the majority of the polarimetric calibration algorithms in the literature depends on the validity of the system model above for radar polarimeters, which was first put forward in [1]. This system model contains just six relative parameters, including four cross-talk (or leakage) terms and two channel imbalance terms, one for the H,V transmitters and one for the H,V receivers. Determination of these six parameters, followed by correction for any deviations from the ideal is then sufficient to calibrate the radar data polarimetrically, so that the HH, HV, VH and VV scattering matrix measurements can be meaningfully compared.

The generally accepted polarimetric system model relies on the constancy of the system, particularly the transmitters, the receivers and the antennas. For instance, it assumes that the ratio of the power transmitted between H and V polarizations never varies, and that the receiver gains for H and V are kept

at a constant level relative to each other. This is not always the case for radar polarimeters [19]. For example, in operating the NASA/JPL system the gain of the H (or V) receiver can be switched by up to 6dB, depending on whether a like-polarized (HH or VV) or cross-polarized (VH or HV) return is expected. (As described above, the NASA/JPL system has two receivers, one for H and one for V, and alternately transmits H and V pulses). The reason for operating the radar this way is that the cross-polarized returns from natural targets are usually lower than the like-polarized returns, so the gain is increased when expecting a cross-polarized return to keep the signal level within the optimum range for the analog-to-digital converters. This gain differential should be removed during processing. The ERIM P-3 polarimetric SAR solves the same problem with a different design, having only one transmitter, one receiver and an automatic gain control (AGC), which varies the gain of the radar receiver in some pre-set fashion [8]. The AGC setting in amplitude and phase is usually different for HH, HV, VH and VV returns, which are collected in sequence. The design for the CCRS polarimetric SAR has an elaborate switching sequence for its two receivers, so that HH and VV returns go through the same receiver, and VH and HV returns go through the other receiver. In none of these cases is the 2x2 R and T matrix system model necessarily valid, unless the gain differentials between receivers are properly removed from the data.

Let us now return to the problem of estimating R and T, in order to calibrate the scattering matrix data. Expanding (13), we obtain four equations relating the scattering matrix measurements with their actual values:

$$M_{hh} = S_{hh} + \delta_2 S_{hv} + \delta_4 S_{vh} + \delta_2 \delta_4 S_{vv} + n_{hh} \quad (16a)$$

$$M_{hv} = \delta_1 S_{hh} + f_1 S_{hv} + \delta_1 \delta_4 S_{vh} + f_1 \delta_4 S_{vv} + n_{hv} \quad (16b)$$

$$M_{vh} = \delta_3 S_{hh} + \delta_2 \delta_3 S_{hv} + f_2 S_{vh} + f_2 \delta_2 S_{vv} + n_{vh} \quad (16c)$$

$$M_{vv} = \delta_1 \delta_3 S_{hh} + f_1 \delta_3 S_{hv} + f_2 \delta_1 S_{vh} + f_1 f_2 S_{vv} + n_{vv} \quad (16d)$$

These four equations contain ten unknown quantities (ignoring the noise), which are the four (complex) scattering matrix elements and six (complex) radar system unknowns (the δ 's and the f 's). Clearly, to solve

the problem, we need at least another six equations in the various terms involved. There are three approaches to obtaining the required six equations: the first is to use man-made targets with known scattering matrices; the second is to make assumptions regarding the general properties of the backscatter being measured; and the third is to make assumptions about the radar system parameters. Of course, all three of these approaches may be combined to find an appropriate solution.

The first attempts ([20] - [22]) to calibrate polarimetric radar systems used only the man-made target approach. There are only a limited set of such targets available. Table 1 lists the normalized scattering matrices for some of the more common ones. Barnes [21] and Woods [22] both used combinations of three passive devices to come up with the six additional equations required to solve the problem. In his approach, Woods [22] used a trihedral and two dihedrals, one at 0° rotation, the other at 45°. Barnes [21] also used this approach, and presented another solution using two dipoles (at 0° and 90° rotation angles) and one 45° dihedral. The dipole signatures were achieved using screened trihedral corner reflectors ([23], [24]). Three targets were found to be necessary to solve the problem because it was very difficult to obtain more than two of the required equations from each target signature. Yueh et al [25] presented a more general solution using passive targets, in which at least two must either have singular or non-singular scattering matrices, and the targets must not be the same. Whitt and Ulaby [26] showed how the problem may be solved provided just one of the three target scattering matrices is non-singular. Freeman, Werner and Shen [15] showed how three polarimetric active radar calibrator (PARC) signatures could be used to solve the problem. The sensitivity of all of these approaches to small errors in the rotation angles of the devices used was pointed out in [19].

Other authors have used assumptions about the system and the backscatter to arrive at a solution to the problem. van Zyl [27] made the following assumptions about the polarimetric radar system:

$$\begin{aligned} \delta_1 &= \delta_3 \\ \delta_2 &= \delta_4 \\ f_1 &= f_2 \end{aligned} \quad (17)$$

i.e. R - T. These are three of the required equations. van Zyl also assumed that the backscatter was reciprocal, i.e. $S_{hv} = S_{vh}$, which would at first seem to provide a fourth equation, but on further examination of equations (16b) and (16c) this makes one of them redundant, so the net number of equations does not increase. Next, van Zyl assumed that for most natural backscatter types, azimuthal symmetry holds [3], for which the like- and cross-polarized backscatter terms are uncorrelated, i.e.,

$$\begin{aligned} \langle S_{hh} S_{hv}^* \rangle &= 0 \\ \langle S_{hv} S_{vv}^* \rangle &= 0 \end{aligned} \quad (18)$$

This gave two more equations, which allow the calculation of the two cross-talk terms, δ_1 and δ_1 . These can vary significantly with incidence angle as can be seen from the plots shown in Figure 9. The solution was completed by estimating $f_1 f_2$ from the ratio of the HH and VV measurements from a trihedral. From (16a) and (16d) it is easy to see that for a trihedral, with scattering matrix as given in Table 3,

Table 2. Calibration Goals

Long and Short-Term Relative Calibration (Between passes and within an image frame)	±1 dB
Absolute Calibration (any channel)	±3 dB
Cross-frequency calibration	±1.5 dB
Polarization Amplitude Imbalance (between polarization channels)	±0.4 dB (2-way)
Polarization Relative Phase Calibration (between polarization channels)	±10° (2-way)
Polarization Cross-Talk error (isolation)	-30 dB

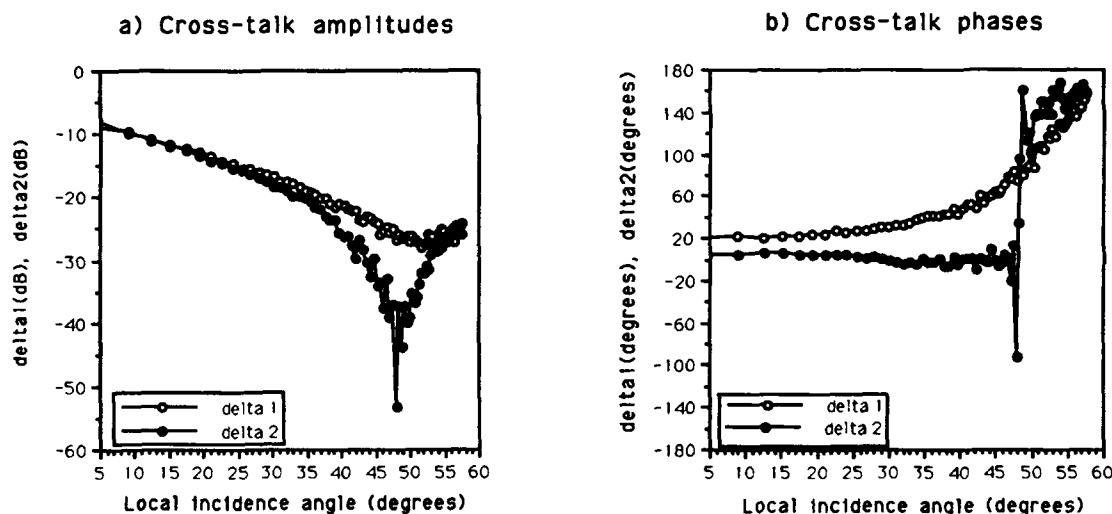


Fig. 9 Plots of cross-talk amplitude and phase for the NASA/JPL L-band polarimetric SAR system, showing variations as a function of elevation (or incidence) angle.

$$\frac{M_{vv}}{M_{hh}} = f_1 f_2 \quad (19)$$

provided second order terms in the δ 's and noise terms are ignored.

In an alternative approach, Klein [28] showed how just the assumption of backscatter reciprocity could be used to give three equations relating the system parameters, which could replace those in (30). The remainder of the equations in Klein's approach were similar to van Zyl's. This was followed by an analysis of the problem in Freeman et al [29], in which it was shown that the assumptions underlying van Zyl's and Klein's approaches were similar and that the backscatter reciprocity assumption could be used in a transformation to reduce the number of unknown

radar system terms to three. Klein and Freeman [30] showed that, if backscatter reciprocity were assumed, then only two man-made targets were necessary to solve the polarimetric calibration problem.

Sarabandi, Ulaby and Tassoudji [31] simplified the problem by assuming that all four cross-talk terms were zero, using backscatter reciprocity and an estimate of $f_1 f_2$ from a trihedral or sphere to complete the solution. Whitt and Ulaby [32] proposed that there exists a rotation of the H-V coordinate system for which $\delta_4 = 0$. Then backscatter reciprocity can be used to give three more equations and a single trihedral signature can be used to solve for $f_1 f_2$ and δ_1 , completing the solution. This approach gives a solution for which there is an arbitrary (small) rotation of the H-V coordinate system, although they are orthogonal. Sarabandi and Ulaby [33] used the simplifying

assumptions that the different pairs of cross-talk terms were equal (but not that $f_1 = f_2$). This was followed by a rotation of the H-V coordinate system such that $\delta_1 = \delta_2$, with a trihedral signature then yielding the remaining three equations.

Calibration of the phase difference between polarization channels (i.e. determination of $\arg(f_1)$ and $\arg(f_2)$ alone) using corner reflector signatures and signatures of moderately rough surfaces is addressed in [34]. An examination of the assumptions on the system and backscatter behavior required for this approach to be successful was presented in [35].

Polarization Filtering

We have seen that it is possible to synthesize the response of any target to arbitrary combinations of transmit and receive polarizations from measurements of the scattering matrix, the covariance matrix and the Stokes matrix. We have also seen from the example polarization signatures that transmit/polarization combinations exist for which the synthesized radar cross-section is maximized or minimized and that the particular combinations of transmit and receive polarizations for which the maximum and minimum RCS values are reached will depend on the type of scattering (e.g. Bragg, dihedral mechanism). Consider the problem of trying to detect an isolated target (e.g. a ship) against a clutter background (e.g. the ocean) using a polarimetric SAR. In this case we would choose the transmit and receive polarization combination which maximized the ratio of the synthesized target RCS over the average of the synthesized clutter RCS, i.e. the signal-to-clutter ratio:

$$SCR = \frac{\sigma_T}{\sigma_C} = \frac{((q(\psi_t, \chi_t)^T S_T p(\psi_r, \chi_r))^2}{((q(\psi_t, \chi_t)^T S_C p(\psi_r, \chi_r))^2} \quad (20)$$

SCR is also known as the contrast ratio. Several authors have offered mathematical solutions to this problem ([36]-[38]). The first step is to characterize the scattering properties of the target and the clutter, i.e. to determine S_T and S_C . Then the polarizations on transmit and receive which maximize the SCR have to be determined. Application of those transmit and receive polarizations to an entire image is known as polarization filtering.

Radar mapping of vegetation types

Due to the concern in the scientific community over the global warming problem, mapping of vegetation cover (and changes in vegetation cover), especially in tropical rain forest areas, using remote sensing data has received considerable attention recently. Synthetic Aperture Radar, with its ability to collect data during day or night, or in cloudy conditions, is ideally suited for monitoring the earth's remaining tropical rain forests.

In what follows, we present multi-frequency, polarimetric SAR results from a tropical rain forest site in Belize, Central America, as an example of the ability of polarimetric SAR to map different vegetation types. An image of a 10x10km area is shown in Figure 10. The area under study is dominated by old growth upland tropical rain forest. There are also small areas which have been cleared of upland forest within the last five years and allowed to re-grow. In addition, there are areas of almost pure palm forest, consisting of either cohune or botan palm trees. There are several types of wetland forests. High marsh forest has vegetation resembling the upland rain forest, but standing water is present during a large portion of the year. Bajo is another type of wetland forest which grows in areas having very poorly drained clay soils. The vegetation

is short (less than 10 meters), densely packed, and has sparse foliage. Yet another wetland forest type is swamp forest, consisting of short trees or shrubs growing in standing water. Besides forest, there are reed and sedge marshes. These are areas of herbaceous vegetation in standing water. The sedges are considerably taller than reeds (200 cm versus 40 cm). In addition to these naturally occurring vegetation types there are agricultural areas consisting of cleared areas, bare soil and various crops.

Table 3 contains typical radar backscatter measurements for the different vegetation types identified in the area imaged by the DC-8 SAR. From the table it can be seen that the very low radar cross sections correspond to open water and bare ground at all three frequencies. The upland forest spans a fairly narrow range of cross-sections. The range of radar cross sections is given in the table by the two values shown in the table. Radar cross section tends to increase as the angle of incidence decreases. If incidence angle effects are considered, the radar cross section for the upland forest is essentially constant. For other types of vegetation, at P-Band we see a steady climb in the HH cross section as the biomass of the canopy increases until we reach a plateau where the upland forest begins. The same feature is visible in the L-Band and C-Band data, but at L-Band the plateau is reached for re-growth vegetation (2-3m in height), while at C-Band the plateau is reached for farmland vegetation (<1m in height). This type of saturation of radar backscatter with biomass has been observed previously. At all three frequencies, especially C-band, we then see a secondary increase region in the HH radar cross section data. The sites corresponding to these data points may have much less biomass than the upland forest, but they have a brighter radar return. These areas generally have some feature which adds a secondary scattering mechanism in addition to the volume scatter which dominates the upland forest. One site was a rain forest area where the trees had been cut but not cleared (clear-cut in Table 3). The site had an enhanced HH polarization return due to the many tree trunks laying on the ground. Other sites with enhanced backscatter were sites with vegetation growing in standing water (reeds, sedge, high marsh forest, swamp forest, flooded Bajo). In this case the backscatter probably consists of volume scatter from the vegetation canopy plus double bounce scattering due to interaction between the vegetation and standing water. In other sites, the double-bounce mechanism may be enhanced because the vegetation understory is relatively clear (in the areas designated coffee and palm forest, for example).

A simple, three-component scattering model

We can begin to understand the phenomena which give rise to the radar backscatter characteristics seen in Table 3 and in other polarimetric SAR images of natural surfaces by using a very simple conceptual model of scattering. This model is more fully developed in [39]; here an outline is presented. We assume that scattering from a vegetation layer is a combination of volume scattering from vegetation, double bounce scattering from the ground/trunk interaction and scattering from a rough surface. For volume scattering, we assume that the return is from randomly oriented, very thin cylinder-like scatterers. The double bounce scattering component can be modeled by scattering from an upright (rotation angle = 0°) dihedral corner reflector. In the model, both surfaces in the reflector are made of dielectric material, and the two surfaces may have different dielectric constants, corresponding to trunk and ground. The trunk has Fresnel reflection coefficients R_{th} and R_{tv} for horizontal and vertical polarization, respectively. Likewise, the ground has Fresnel reflection coefficients R_{gh} and R_{gv} . For the

Vegetation Class	P-band					L-band					C-band				
	σ_{HH}	ϕ_{HHVV}	ρ	HH/VV	HV/HH	σ_{HH}	ϕ_{HHVV}	ρ	HH/VV	HV/HH	σ_{HH}	ϕ_{HHVV}	ρ	HH/VV	HV/HH
Open Water	-32.6	5.8	0.33	-6.6	-7.4	-28.7	-3.1	0.63	-7.7	-6.6	-23.7	-18.7	0.29	-2.4	-5.3
Bare Soil	-25.1	-8.8	0.75	-5.4	-9.5	-16.5	-23.7	0.75	-1.8	-10.4	-9.0	-10.0	0.76	-0.3	-8.9
Reeds	-23.0	115.3	0.72	-10.9	-10.7	-9.0	98.1	0.54	-3.3	-11.6	-0.3	135.8	0.44	2.2	-11.9
Farmland	-20.3	-12.5	0.53	-2.0	-11.5	-13.3	-18.6	0.75	-1.5	-11.7	-7.6	-1.2	0.47	0.7	-6.4
Regrowth	-15.3	20.7	0.25	-0.9	-5.8	-10.1	-22.7	0.31	-0.1	-5.5	-5.7	3.2	0.44	0.7	-6.5
Bajo	-14.5	70.8	0.21	-2.8	-5.8	-9.7	15.1	0.17	0.1	-5.6	-6.2	-2.1	0.42	-0.2	-5.6
Swamp Forest	-13.8	149.5	0.1	-0.6	-8.4	-6.9	165.4	0.06	0.4	-7.6	-2.1	2.3	0.41	1.2	-8.9
Upland Forest	-12.8	32.3	0.22	-0.8	-5.4	-9.2	7.9	0.25	0.2	-5.1	-7.4	9.0	0.46	0.0	-5.8
Upland Forest	-11.5	51.1	0.14	0.4	-6.4	-9.2	7.9	0.25	0.2	-5.1	-5.6	-4.1	0.51	0.6	-6.6
High M. F. 2	-11.0	6.4	0.16	-2.3	-5.3	-8.4	7.8	0.16	0.2	-5.2	-5.3	-1.4	0.43	0.6	-5.8
Palm Forest	-11.3	91.4	0.21	-0.1	-7.2	-8.6	48.5	0.2	0.6	-6.4	-5.0	-2.4	0.56	0.4	-7.0
Sedge	-10.3	93.6	0.18	0.5	-7.0	-8.8	-5.7	0.26	-0.2	-5.2	-6.1	-0.9	0.52	0.0	-6.3
Flooded Bajo	-9.7	75.6	0.16	0.9	-7.0	-8.6	31.4	0.22	0.6	-5.6	-6.4	-2.3	0.42	-0.9	-5.5
Coffee	-9.2	137.3	0.4	1.1	-8.8	-8.0	52.1	0.12	1.7	-7.7	-6.6	6.9	0.42	1.4	-7.0
Clear-cut	-9.0	31.0	0.32	3.0	-8.5	-7.6	6.9	0.4	2.0	-8.0	-6.0	8.3	0.55	1.4	-8.3
High M. F. 1	-8.2	-32.7	0.29	-1.6	-7.5	-4.0	-2.5	0.32	2.1	-7.8	-3.2	15.0	0.35	1.5	-7.0

- Cross section results and ratios are in dB; phase differences are in degrees
- High M. F. - High Marsh Forest

Table 3: Radar backscatter measurements from typical examples of the different vegetation classes.

Vegetation Class	P-band			L-band			C-band		
	Odd	Even	Vol.	Odd	Even	Vol.	Odd	Even	Vol.
Open Water	0.67	0.09	0.24	0.76	0.01	0.23	0.24	0.05	0.70
Bare Soil	0.77	0.03	0.20	0.65	0.07	0.27	0.56	0.01	0.44
Reeds	0.02	0.93	0.05	0.16	0.67	0.17	0.11	0.59	0.30
Farmland	0.65	0.16	0.19	0.69	0.08	0.23	0.20	0.01	0.79
Regrowth	0.14	0.09	0.76	0.08	0.05	0.87	0.19	0.02	0.78
Bajo	0.10	0.26	0.64	0.02	0.11	0.87	0.14	0.01	0.85
Swamp Forest	0.16	0.37	0.47	0.09	0.29	0.62	0.36	0.12	0.52
Upland Forest	0.04	0.12	0.84	0.02	0.03	0.95	0.16	0.01	0.83
Upland Forest	0.05	0.18	0.77	0.00	0.05	0.95	0.23	0.01	0.76
High M. F. 2	0.04	0.23	0.73	0.00	0.03	0.97	0.12	0.00	0.88
Palm Forest	0.02	0.39	0.59	0.08	0.14	0.78	0.29	0.01	0.70
Sedge	0.07	0.25	0.68	0.02	0.06	0.91	0.24	0.01	0.75
Flooded Bajo	0.05	0.21	0.73	0.00	0.00	0.94	0.17	0.02	0.81
Coffee	0.00	0.46	0.54	0.07	0.25	0.69	0.23	0.04	0.74
Clear-cut	0.30	0.07	0.63	0.29	0.06	0.65	0.37	0.04	0.59
High M. F. 1	0.30	0.19	0.51	0.24	0.07	0.69	0.19	0.05	0.76

Table 4: Backscatter mechanisms from the model fit for typical examples of the different vegetation classes.

surface scatter, we assume a first-order Bragg model (12) is adequate to describe the backscatter. For all of these three backscatter components, we assume that like- and cross-polarized returns are uncorrelated, and that the backscatter is reciprocal (HV = VH). Now, if the volume, double-bounce and surface scatter components are uncorrelated, the total second order statistics are the sum of the statistics for the individual mechanisms; i.e., the backscattered powers rather than voltages are added. Thus our model for the total backscatter is:

$$|S_{hh}|^2 = \beta^2 f_s + |\alpha|^2 f_d + f_v \quad (21)$$

$$|S_{vv}|^2 = f_s + f_d + f_v \quad (22)$$

$$|S_{hv}|^2 = f_v/3 \quad (23)$$

$$S_{hh}S_{vv}^* = \beta f_s - \alpha f_d + f_v/3 \quad (24)$$

where f_s , f_d and f_v are the surface, double-bounce and volume scatter contributions to the VV cross section, β is a real number and α is given by:

$$\alpha = \frac{R_{gh} R_{lh}}{R_{gv} R_{lv}} \quad (25)$$

This model gives us four equations in five unknowns. In general, a solution can be found if one of the unknowns is fixed. Since neither the surface or double-bounce mechanisms contribute to the HV term in the model, we can use this to estimate the volume scatter contribution directly. The volume contribution can then be subtracted off the $|S_{hh}|^2$, $|S_{vv}|^2$ and $S_{hh}S_{vv}^*$ terms, leaving three equations in four unknowns. After [40], we then decide whether double-bounce or surface scatter is the dominant contribution in the residual based on the sign of the real part of $S_{hh}S_{vv}^*$. If $\text{Re}(S_{hh}S_{vv}^*)$ is positive, we decide that surface scatter is dominant, and fix $\alpha = 1$. If $\text{Re}(S_{hh}S_{vv}^*)$ is negative, we

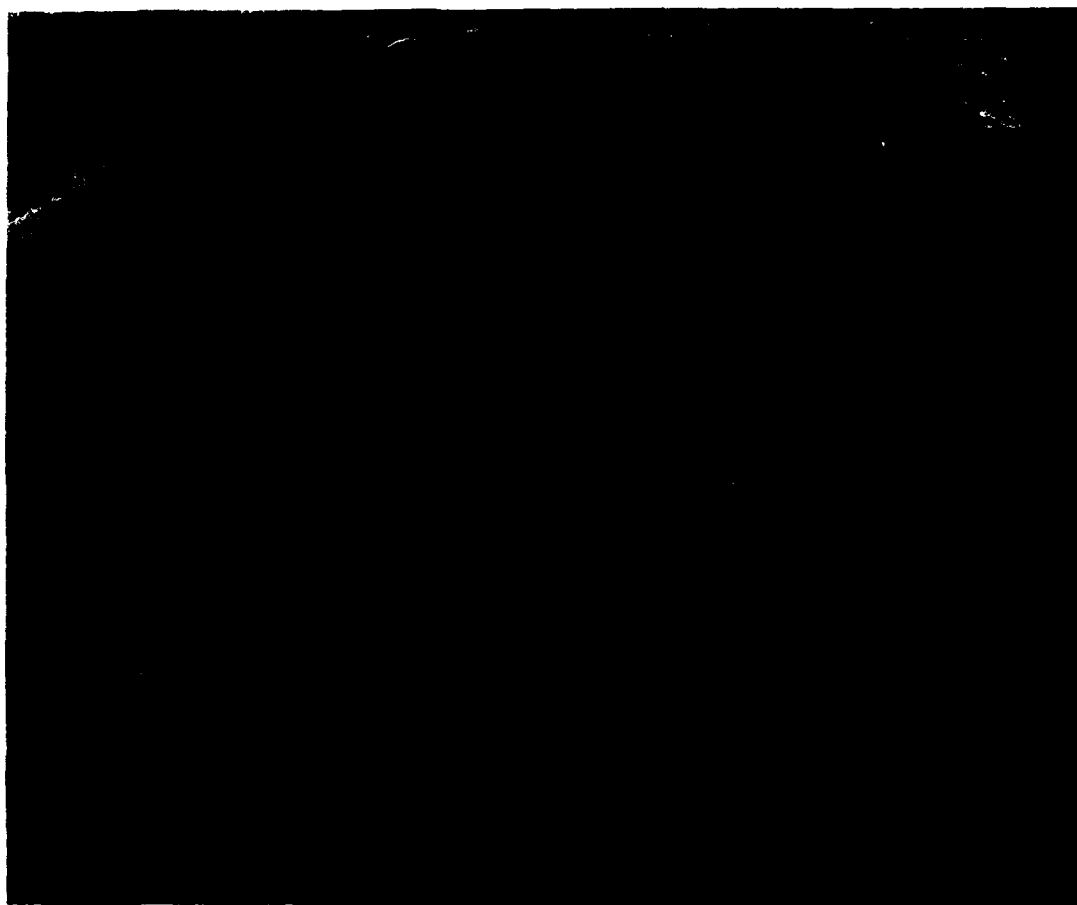


Fig. 10 P-band (68cm) NASA/JPL DC-8 SAR image of a tropical rain forest area in Belize, Central America.

decide that double-bounce scatter is dominant in the remainder and fix $\beta = 1$. Then we calculate f_s , f_d and β or α from the backscatter measurements. In Table 4 we show the fraction of the total power contributed by each of the three mechanisms (with odd - surface, dbl - double-bounce and vol - volume scatter) for the vegetation classes given in Table 3.

From Table 4, we see that the model predicts that the dominant backscatter mechanism for the upland forest is volume scatter at all three frequencies. There is a small (<20%) contribution from the double-bounce mechanism at P-Band, practically none at L-Band, and none at all at C-Band. The surface scatter is very low at P- and L-Band, but contributes ~20% of the C-Band returns. This may be caused by relatively thick branches in the upper canopy which may look like surface backscatter at that wavelength. For the lower biomass sites and the enhanced backscatter sites, we see the volume scatter percentage drop for all three frequencies, while surface and/or double-bounce components become significant. The bare soil results, for example, indicate that surface scattering is dominant at all three frequencies, while for reeds, the double-bounce term is dominant.

Supervised Classification

Polarimetric SAR data can be a very effective tool for mapping different surface cover types. Several techniques are available in the literature for

performing supervised classification on polarimetric radar data. First training sets are selected, which represent different surface types. Then the elements of the covariance matrix for each surface type can be averaged to find the average polarimetric scattering properties for each class. Kong et al [41] developed a supervised classifier in which the following vector is formed for each pixel in the image:

$$\bar{X} = \begin{pmatrix} S_{hh} \\ S_{hv} \\ S_{vv} \end{pmatrix} \quad (27)$$

then a distance measure $d_i(\bar{X})$ is calculated for each class i , where

$$d_i(\bar{X}) = \bar{X}^* (C_i)^{-1} \bar{X} + \ln |C_i| - \ln [P_a(i)] \quad (28)$$

C_j is the covariance matrix calculated for the i th class from the training set and $P_a(i)$ is the *a priori* probability that the pixel belongs in class i . The pixel under classification is classified as a member of class i if

$$d_i(\bar{X}) < d_j(\bar{X}) \text{ for all } j \neq i \quad (29)$$

This classification scheme is a maximum likelihood scheme for polarimetric radar data.

Another type of classifier is known as the minimum distance classifier. For polarimetric SAR data, a minimum distance classifier was implemented by van Zyl and Burnette. For this type of classifier the distance measure used is:

$$d_i^2(\bar{Y}) = \|\bar{Y}^* - \bar{Y}_i\|^2 \quad (30)$$

where

$$\bar{Y} = \begin{pmatrix} S_{vv} S_{vv}^* \\ S_{vv} S_{hv}^* \\ S_{vv} S_{hh}^* \\ S_{hv} S_{hv}^* \\ S_{hv} S_{hh}^* \\ S_{hh} S_{hh}^* \end{pmatrix} \quad (31)$$

i.e. a subset of the covariance matrix elements and the decision rule is that the scatterers which are represented by \bar{Y} are a member of the class i if

$$d_i(\bar{Y}) < d_j(\bar{Y}) \text{ for all } j \neq i \quad (32)$$

Acknowledgment

Part of the work described in these notes was carried out by the Jet Propulsion Laboratory, California Institute of Technology, under a contract with the National Aeronautics and Space Administration.

Bibliography

- [1] Zebker, H.A., van Zyl, J.J. and Held, D.N., Imaging Radar Polarimetry From Wave Synthesis, *J. Geophys. Research*, Vol. 92, pp. 683-701, 1987.
- [2] van Zyl, J.J., Papas, C.H. and Elachi, C., On the optimum polarizations of incoherently reflected waves, *IEEE Trans. on Antennas and Propagation*, vol. AP-35, pp. 818-825, 1987.
- [3] Borgeaud, M., Shin, R.T. and Kong, J.A., Theoretical models for polarimetric radar clutter, *J. Electromagnetic Waves and Applications*, vol. 1, pp. 67-86, 1987.
- [4] Boerner, W. M., Foo, B.-Y. and Eom, H. J., Interpretation of polarimetric Copolarization phase term in the radar images obtained by the JPL airborne L-band SAR system, *IEEE Trans. on Geoscience and Remote Sensing*, vol. GE-25, pp. 77-82, 1987.
- [5] Ulaby, F.T., Held, D.N., Dobson, M.C., McDonald, K. C. and Senior, T. B. A., Relating Polarization phase Difference of SAR signals to scene properties, *IEEE Trans. on Geoscience and Remote Sensing*, vol. GE-25, pp. 83-92, 1987.
- [6] Evans, D. L., Farr, T. G., van Zyl, J. J. and Zebker, H. A., Imaging radar polarimetry: analysis tools and applications, *IEEE Trans. on Geoscience and Remote Sensing*, vol. GE-26, pp. 774-789, 1988.
- [7] Held, D.N., et al, The NASA/JPL multifrequency, multipolarization airborne SAR system, *Proc. IGARSS '88*, Edinburgh, Scotland, pp. 345-349, 1988.
- [8] Sullivan, R. et al, Polarimetric X/L/C-band SAR, *Proc. IEEE National Radar Conf.*, Ann Arbor, MI, pp. 9-14, 1988.
- [9] Carver, K., et al, Shuttle Imaging Radar-C Science Plan, JPL Publication #86-29, 1986.
- [10] Zebker, H. A. and van Zyl, J. J., Imaging Radar Polarimetry: A Review, *Proc. IEEE*, vol. 79, No. 11, November 1991, pp. 1583-1606.
- [11] Ulaby, F.T. and Elachi, C. (ed.), *Radar Polarimetry for Geoscience Applications*, Artech House, 1990.
- [12] Boerner, W. M., et al (eds.), *Inverse Methods in Electromagnetic Scattering*, Hingham, MA: Reidel, 1985.
- [13] van Zyl, J. J., Zebker, H. A. and Elachi, C., Imaging radar polarization signatures: theory and observation, *Radio Sci.*, vol. 22, pp. 529-543, 1987.
- [14] Dubois, P.C. and Norikane, L., Data volume reduction for imaging radar polarimetry, *Proc. IGARSS '87*, Ann Arbor, MI, pp.691- 696, 1987.
- [15] Freeman, A., Shen, Y. and Werner, C.L., Polarimetric SAR Calibration Experiment Using Active Radar Calibrators, *IEEE Trans. on Geoscience and Remote Sensing*, Vol. GE-28, No. 2, March 1990.
- [16] Freeman, A., Werner, C. and Shen, Y., Calibration of Multipolarization Imaging Radar, *Proc. IGARSS '88*, pp. 335-339, 1988.
- [17] Freeman, A., Shen, Y., van Zyl, J.J. and Klein, J.D., Calibration of NASA/JPL DC-8 SAR data, *Proc. IGARSS '91*, Espoo, Finland, June 1991.
- [18] Freeman, A., SAR Calibration: An Overview, submitted to *IEEE Trans. on Geoscience and Remote Sensing*, October 1991.
- [19] Freeman, A., A New System Model for Radar Polarimeters, *IEEE Trans. on Geoscience and Remote Sensing*, Vol. 29, No. 5, pp. 761-767, September 1991.
- [20] Livingston, P.S. and Kaplan, D.J., Radar Calibration Procedure, Technical Note 1432, Naval Ocean Systems Center, San Diego, CA, November 1985.
- [21] Barnes, R.M., Antenna Polarization Calibration Using In-Scene Reflectors, Lincoln Laboratory Technical Report TT-65, Sept. 1986.
- [22] Woods, M.A., A Calibration Procedure For A Coherent Scattering Matrix Radar, Royal Signals and Radar Establishment, Memorandum 3889, May 1986.
- [23] Kennaugh, E.M., Polarization Properties of Corner Reflectors With Modified Walls, Ohio State University, Report 612-6, January 1957.
- [24] Kennaugh, E.M. and Chang, C., Design and Theoretical Performance of Reactive-Wall Corner Reflectors, Ohio State University Technical Report NOW 64-0215-D, January 1965.
- [25] Yueh, H.A., Kong, J.A., Barnes, R.M., and Shin, R.T., Calibration of Polarimetric Radars Using In-Scene Reflectors, *J. of Electromagnetic Waves & Applications*.

- [26] Whitt, M.W., Ulaby, F.T., Polatin, P. and Liepa, V.V., A General Polarimetric Radar Calibration Technique, IEEE Trans. on Antennas and Propagation, Vol. AP-39, No.1, pp. 62-67, January 1991.
- [27] van Zyl, J.J., Calibration of Polarimetric Radar Images Using Only Image Parameters and Trihedral Corner Reflector Responses, IEEE Trans. on Geoscience and Remote Sensing, Vol. GE-28, No.3, pp. 337-348, May 1990.
- [28] Klein, J.D., Calibration of Complex Quadpolarization SAR Images Using Backscatter Correlations, submitted to IEEE Trans. on Aerospace and Electronic Systems, 1989.
- [29] Freeman, A., van Zyl, J.J., Klein, J.D., Zebker, H.A. and Shen, Y., Calibration of Stokes and scattering matrix format polarimetric SAR data, accepted for publication in IEEE Trans. on Geoscience and Remote Sensing, 1991.
- [30] Klein, J.D. and Freeman, A., Quadpolarization SAR Calibration Using Target Reciprocity, Journal of Electromagnetic Waves & Applications, Vol. 5, No. 7, pp. 735-751, 1991.
- [31] Sarabandi, K. and Ulaby, F.T., and Tassoudji, M.A., Calibration of Polarimetric Radar Systems With Good Polarization Isolation, IEEE Trans. on Geoscience and Remote Sensing, Vol. 28, pp. 337-348, May 1990.
- [32] Whitt, M. and Ulaby, F.T., A polarimetric calibration technique with insensitivity to target orientation, Proc. IGARSS '90, Washington, D.C., pp. 1089-1092, May 1990.
- [33] Sarabandi, K. and Ulaby, F.T., A Convenient Technique For Polarimetric Calibration of Single-Antenna Radar Systems, IEEE Trans. on Geoscience and Remote Sensing, Vol. GE-28, No. 6, pp. 1022-1033, November 1990.
- [34] Zebker, H.A., and Lou, Y., Phase Calibration of Imaging Radar Polarimetric Stokes Matrices, IEEE Trans. on Geoscience and Remote Sensing, Vol. GE-28, No. 2, pp. 246-252, March 1990.
- [35] Sheen, D.R., Freeman, A. and Kasischke, E.S., Phase Calibration of Polarimetric Radar Images, IEEE Trans. On Geoscience and Remote Sensing, Vol. GE-27, pp. 719-731, Nov. 1989.
- [36] Ioannidids, G. A. and Hammers, D. E., Optimum Polarizations for Target Discrimination in Clutter, IEEE Trans. on Antennas and Propagation, Vol. AP-27, pp. 357-363, 1979.
- [37] Dubois, P. C. and van Zyl, J. J., Polarization filtering of SAR data, Proc. IGARSS '89, Vol. 3, pp. 1816-1819, 1989.
- [38] Swartz, A. A., Yueh, A. H., Kong, J. A., Novak, L. M. and Shin, R. T., Optimal polarizations for achieving maximum contrast in radar images, Journal of Geophysical Research, Vol. 93, No. B12, pp. 15252-15260, 1988.
- [39] Durden, S., et al, Multi-frequency polarimetric radar observations of a tropical rain forest, submitted to IEEE Trans. On Geoscience and Remote Sensing, April 1992.
- [40] van Zyl, J. J., Unsupervised classification of scattering behavior using radar polarimetry data, IEEE Trans. On Geoscience and Remote Sensing, vol. 27, pp. 36-45, 1989.
- [41] Kong, J. A., Swartz, A. A., Yueh, H. A., Novak, L. M. and Shin, R. T., Identification of Terrain Cover using the Optimum Polarimetric Classifier, Journal of Electromagnetic Waves and Applications, Vol. 2, pp. 171-294, 1988.

RADIOMETRIC CALIBRATION OF SAR SYSTEMS

by

H. Öttl

Deutsche Forschungsanstalt für Luft- und Raumfahrt e.V.
Institut für Hochfrequenztechnik
8031 Oberpfaffenhofen
Germany

1. SUMMARY

Most SAR image interpretation performed in recent years was based on data which were often insufficiently calibrated. Ground truth data were used for comparison and interpretation.

The importance of calibration was recognized by the need for reproducible data, by the introduction of multifrequency and multipolarization systems (interchannel calibration) and the long term scope of remote sensing.

Hydrologists, especially, requested an absolute calibration with tolerances of less than 1 dB. Internal calibration schemes, as well as the use of external passive and active calibrators, were introduced to achieve this goal over the wide dynamic range. The in-flight measurement of the antenna pattern by means of ground based receivers became increasingly important due to pattern changes caused by electronic beam steering and the necessity of beam alignment in case of multifrequency and/or polarimetric operation modes.

The use of radiometric corrections to compensate for near range/far range differences caused by antenna pattern and geometry of illumination will be explained in the lecture.

The impact of geocoding on radiometric levels will also be mentioned, including the phenomenon of over-/underexposing hilly regions, caused by incidence angle changes.

2. INTRODUCTION

For the Radarlab missions, SIR-C/X-SAR Science Plans [1, 2] were published which described experiment goals within the various disciplines (such as geology, hydrology, glaciology, vegetation, technology). At that time, it was not possible to guarantee SAR system performance as well as was requested by the scientific user community (selected principal investigators and co-investigators). Critical parameters were instrument stability and relative and absolute radiometric calibration. Consequently, a number of selected experiments in the field of technology are dedicated to radiometric calibration. The engineers designing and manufacturing the SAR sensors were requested to provide internal calibration loops. Means for X-SAR internal calibration are described in [3]. Similar loops were integrated in the ERS-1 [4].

An overview of the efforts and plans of five years ago was published in [5], and one year ago a workshop was dedicated to SAR calibration [6].

In 1989, the flights of NASA/JPL's airborne SAR over various European test sites were used in a calibration campaign. For this purpose, 42 trihedral reflectors, 4 dihedral reflectors, as well as a receiver prototype and an ARC prototype, were positioned on grassland and concrete surfaces within DLR's Oberpfaffenhofen test site. The corner reflectors were located in special configurations, taking into account viewing angles, spacing and

the dynamic range of radar cross-sections (RCS). Flight passes were also performed with DLR's airborne SAR.

Results concerning the transfer function between image amplitude and radar backscattering coefficient σ^0 of DLR's airborne C-band SAR were published in [7] and, with NASA/JPL's airborne SAR performance, in [8]. The latter reference describes the cross-calibration between the 2 systems as well as the polarimetric calibration of the JPL system.

The main emphasis of the lecture will be on the spaceborne sensors, because an angle dependence of σ^0 has a strong impact on image evaluation due to the large incidence angle range coverage of airborne systems.

3. RADIOMETRIC CORRECTION OF NEAR RANGE/FAR RANGE DIFFERENCES AND OF ANTENNA PATTERN INFLUENCE

Spaceborne SAR sensors usually have a half power beamwidth (HPBW) of a few degrees in elevation. Therefore, the influence of incidence angle changes on σ^0 can, in many cases, be neglected if the instantaneous field of view (IFOV) covers flat terrain. The range dependence cannot be neglected, because it affects the signal-to-noise ratio S_n by a power of 3.

A similar statement can be made for the antenna gain directional pattern $G(\theta)$, since the signal-to-noise ratio increases with the square of $G(\theta)$, as can be seen in the simplified SAR-equation below:

$$S_n = \frac{G^2(\theta) \sigma^0(\theta)}{R^3(\theta) \sin \theta} K, \quad (1)$$

$$K = \frac{P_{av} \lambda^3 a_{hs} r_R}{2(4\pi)^3 k T_o F u a_B}$$

K is assumed to be constant, because the average power P_{av} , wavelength λ , azimuth taper factor a_{hs} (of the synthetic aperture), slant range resolution r_R , Boltzmann's constant k , temperature T_o , noise figure F , platform velocity u and pulse taper factor a_B do not change with respect to the off-nadir angle θ .

In order to keep $S_n(\theta)$ seeming constant across the swath, assuming at the same time that $\sigma^0(\theta)$ is constant across the swath, the following correction function CF is required:

$$CF = \frac{R^3(\theta) \sin \theta}{G^2(\theta)} \quad (2)$$

This correction causes a relatively accurate amplitude distribution within a SAR image (across the swath) but, of course, it cannot change the real signal-to-noise ratio.

As an example for deriving CF , the X-SAR elevation pattern is used to illuminate a "flat Earth" under 40° off-nadir (Fig. 1).

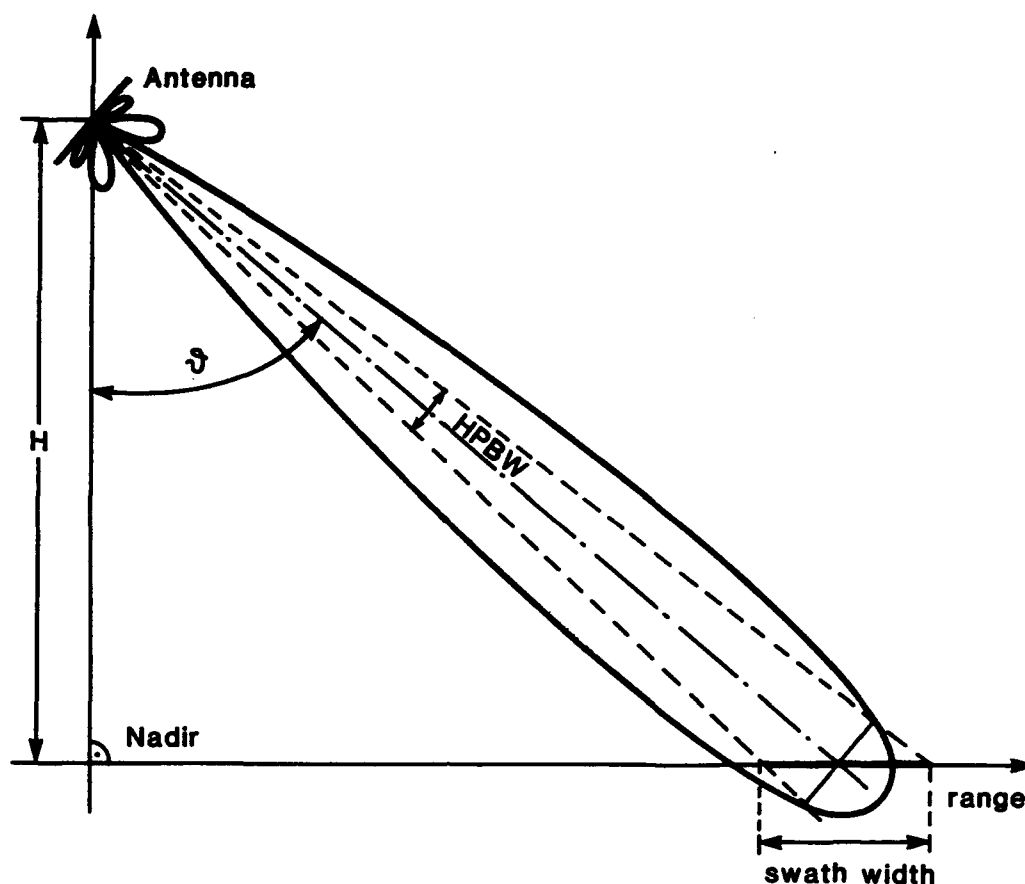


Fig. 1 Illumination geometry; swath width corresponds to HPBW.

X-SAR RADIOMETRIC CORRECTION

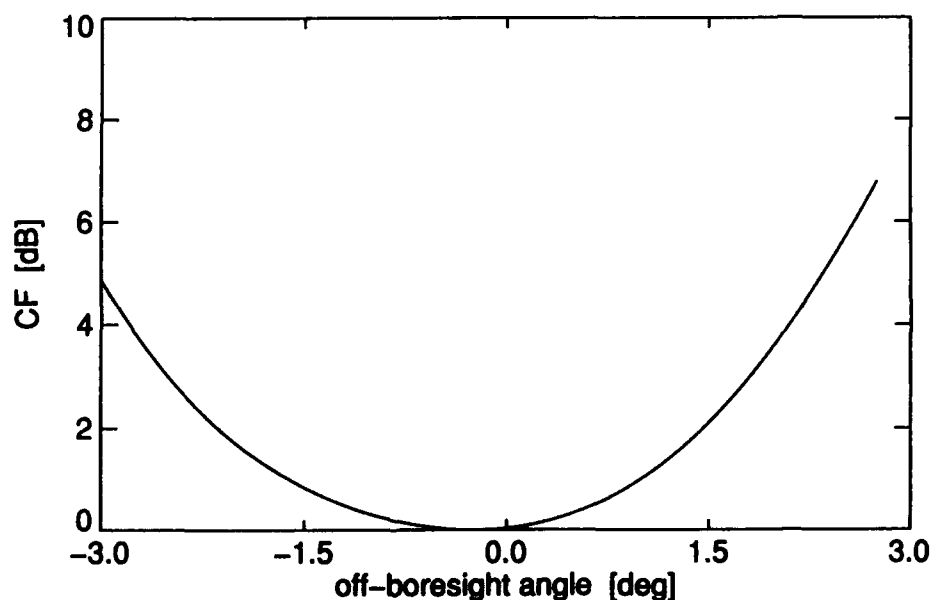


Fig. 2 Correction function CF across the swath. Near range is on the left, far range on the right; boresight angle of antenna is 0° .

The computed correction function CF across the swath within the HPBW is shown in Fig. 2. The asymmetric shape is caused by the illumination geometry.

4. INFLUENCE OF BORESIGHT ERRORS DUE TO UNKNOWN ATTITUDE ERROR IN ROLL DIRECTION

For known antenna pointing and given (or measured) pattern shape in elevation, it is possible to ap-

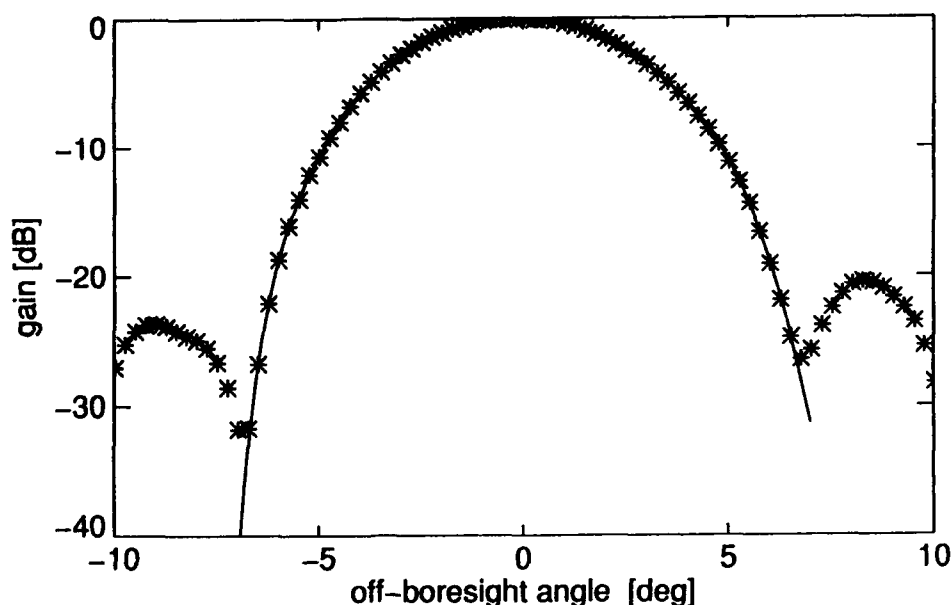


Fig. 3 Predetermined X-SAR elevation pattern.

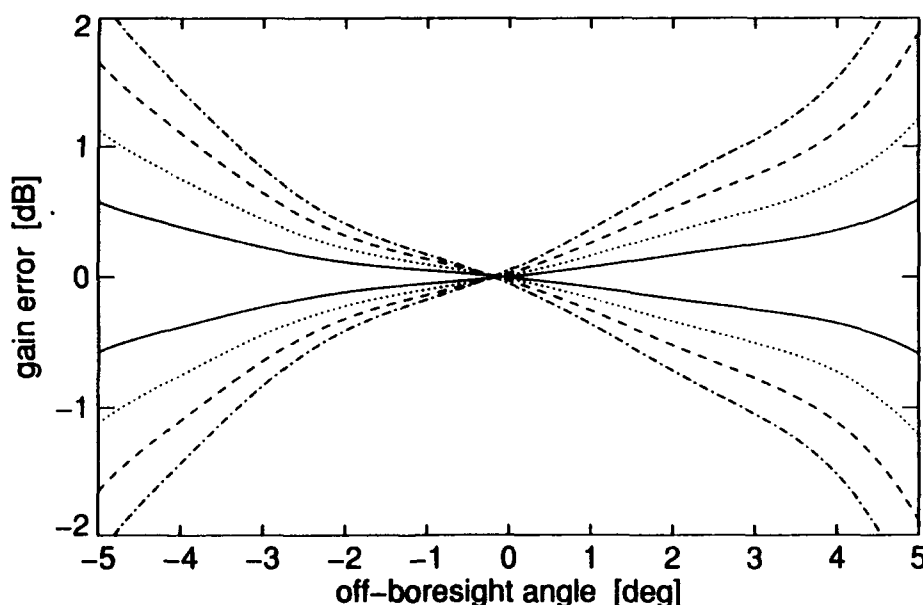


Fig. 4 Gain error function for various boresight angle errors; solid line $\pm 0.3^\circ$, and dashed-dotted line $\pm 0.4^\circ$.

ply equation (2) to correct the image amplitude.

In case the pointing error is unknown, a radiometric error will be produced which, in most cases, cannot be corrected.

For instance, the predetermined X-SAR elevation pattern (Fig. 3) is used to compute a gain error function (Fig. 4) for various boresight uncertainties (0.1° to 0.4° angle deviations). An HPBW of about $\pm 3^\circ$ (in Fig. 4) is relevant for the swath width of X-SAR.

The gain error function has to be squared to show its impact on image amplitudes (grey levels of SAR image).

5. ANTENNA PATTERN MEASUREMENT

As mentioned in part 3 of this paper, the antenna pattern must be known for precise radiometric correction. In view of strong mechanical stress during launch, possible deployment errors and thermal effects, the actual inflight antenna pattern should be used to achieve the highest quality results. In our institute, we use a large number of high precision calibration receivers, aligned in the cross-track direction (see Fig. 5) to measure the azimuth cuts of the actual antenna pattern. Every receiver digitizes and stores each received radar pulse as 16 samples. In parallel, UTC is co-registered with high precision (10^{-7}), so that the measured azimuth-cuts can later be time-correlated and the required elevation main cut of the antenna pattern can be reconstructed. Of course, the precise location of the SAR-sensor vs. time must be known to convert the time of pulse receipt

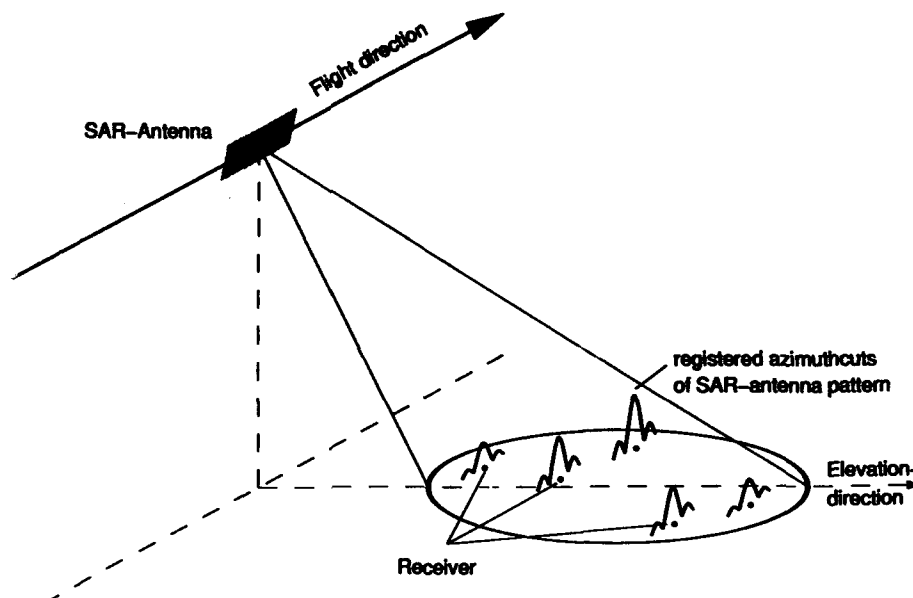


Fig. 5: Schematic experiment set-up.

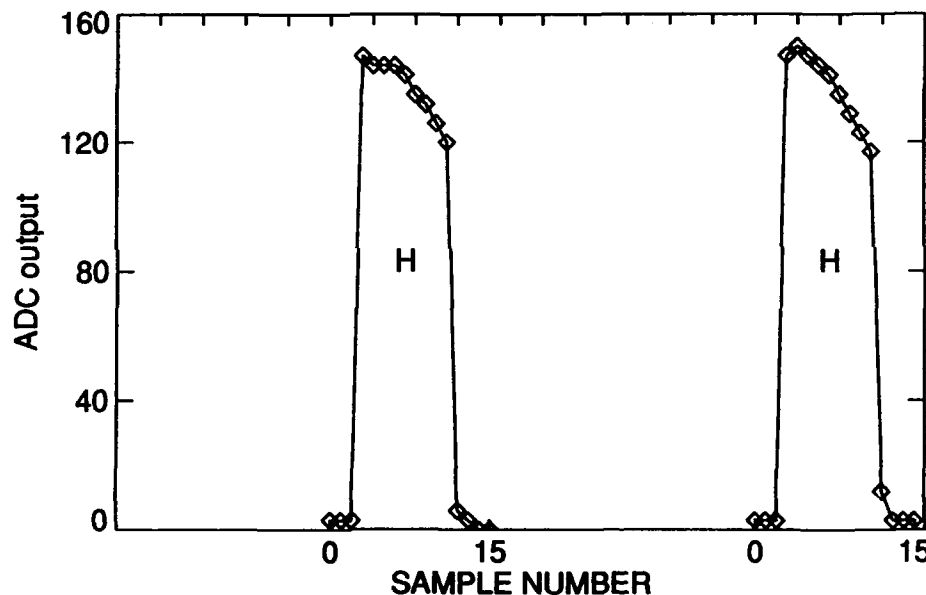


Fig. 6: Registered pulseshapes from NASA/JPL's C-band HH DC-8 SAR.

into antenna angles. It is also mandatory to precisely know the attitude data of the platform as well as the location of each receiver.

In the 1991 NASA/JPL airborne SAR-campaign over our test site, we had a first opportunity to test our measuring system [9].

Fig. 6 shows registered radar pulses from the C-band SAR of NASA/JPL's DC-8 (horizontal polarization). Slight distortions, i.e. decreasing power from begin to end of the pulse can be seen, probably due to the wide chirp used and the relatively small antenna bandwidth.

An azimuth cut can be obtained, by integrating the pulse energies and plotting them against time. The time-correlation of all azimuth cuts gives the main cut of the antenna elevation pattern (see Fig. 7).

The relatively large deviations of the measured points from the fitted curve in Fig. 7 can be explained by 3 facts:

- 1) precise flight and attitude data have not yet been received from,
- 2) the positions of the receivers were only known to about $\pm 100\text{m}$,
- 3) at the time of the experiment not all of our equipment was fully calibrated.

These drawbacks will be eliminated in our future experiments with spaceborne SAR-sensors (all receivers are fully calibrated now, positions are determined using differential GPS and precise orbit and attitude data are available from the satellite owners).

The co-registration of the time of pulse receipt

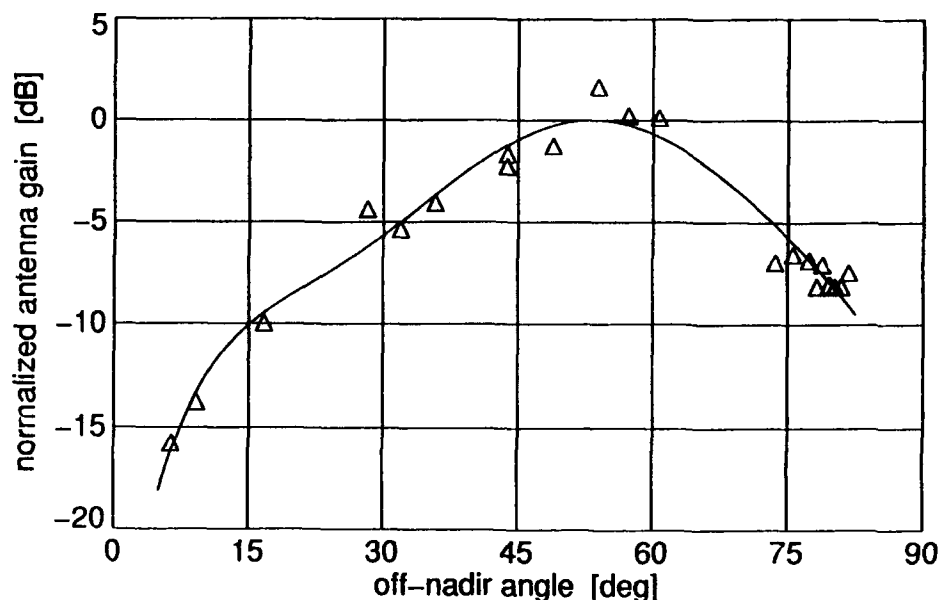


Fig. 7 Reconstructed main cut of the antenna elevation pattern.

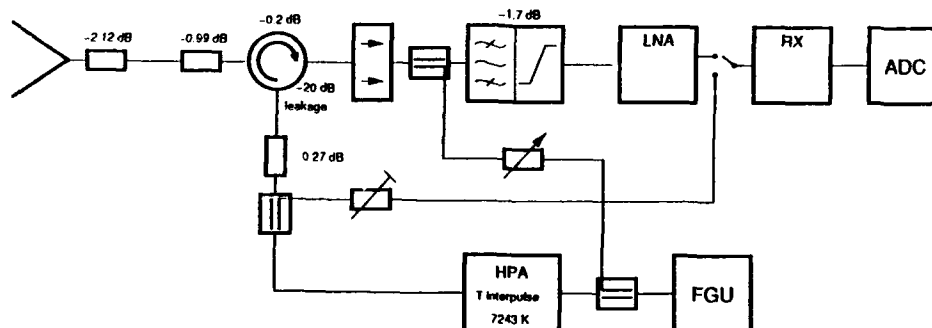


Fig. 8 X-SAR calibration block diagram.

can yield two sets of further information:

Precise measurement of cross-band beam alignment in azimuth and elevation direction (especially suitable in the X-SAR/SIR-C mission) and possible antenna squint angles.

Our system will be used in all present and near-future SAR missions (ERS-1, JERS-1, X-SAR/SIR-C, PRIRODA).

6. INTERNAL CALIBRATION

Spaceborne SAR systems should have life times between 3 and 6 years without too much degradation in performance. Internal calibration loops are advisable to monitor system stability. For the high power output, monitoring can be achieved by measuring a small portion; the measuring point could be a directional coupler between the high power amplifier (HPA) and the antenna.

Receiver gain stability and linearity can be measured by feeding a small part of the radar signal via attenuators through the whole receiver chain. For power leakage problems, the HPA is usually switched off during this test phase and the signal is taken from a low power section.

Furthermore, the actual chirp can be measured be-

fore and after data takes. It can be used to deduce an optimum reference function for processing. The test signal can either be taken from the low power part of the radar transmitter (HPA is switched off) or from the directional coupler between the HPA and antenna. In the latter case, the low noise amplifier (LNA) will be bypassed. These loops are indicated in the block diagram in Fig. 8.

Internal calibration of active array antennae is more complicated due to the large number of transmit/receive modules (T/R modules), which can easily reach several hundred to several thousand.

These T/R modules of the next generation SAR antennae will be designed and manufactured in monolithic microwave integrated circuitry (MMIC) based on GaAs technology. Besides control and monitor units (power, phase shifter, polarization), a time sequential check-out of the transmitter and receiver stages is necessary. Different concepts using separate feeding networks to distribute or collect calibration signals within the active arrays are presently under study at various centres.

For internal calibration, the balance and orthogonality of in-phase and quadrature channel (after demodulation) are important. Error analyses for X-SAR have shown that 5° deviation from orthogonality causes about 0.2 dB amplitude error and 0.2

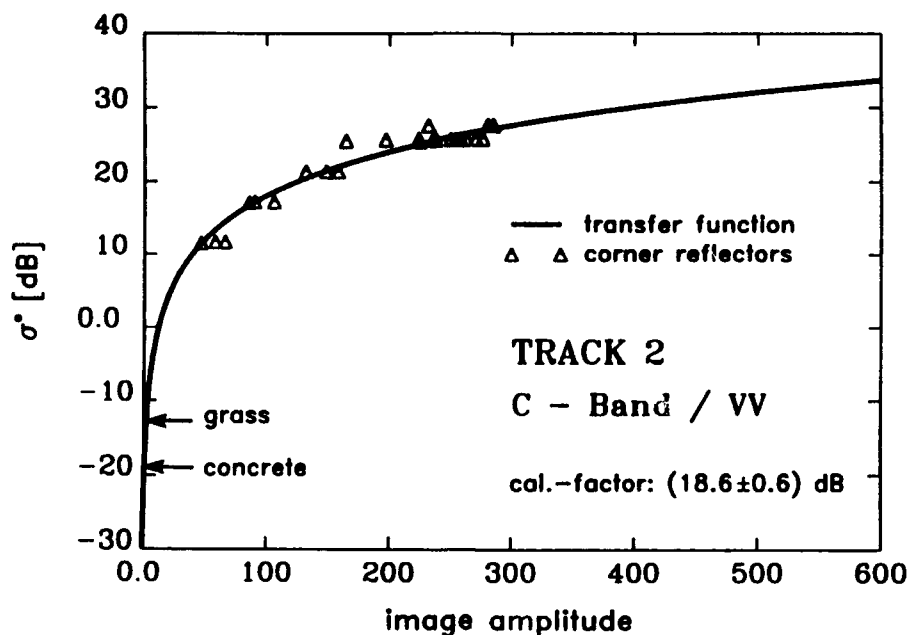


Fig. 9 E-SAR system transfer function.

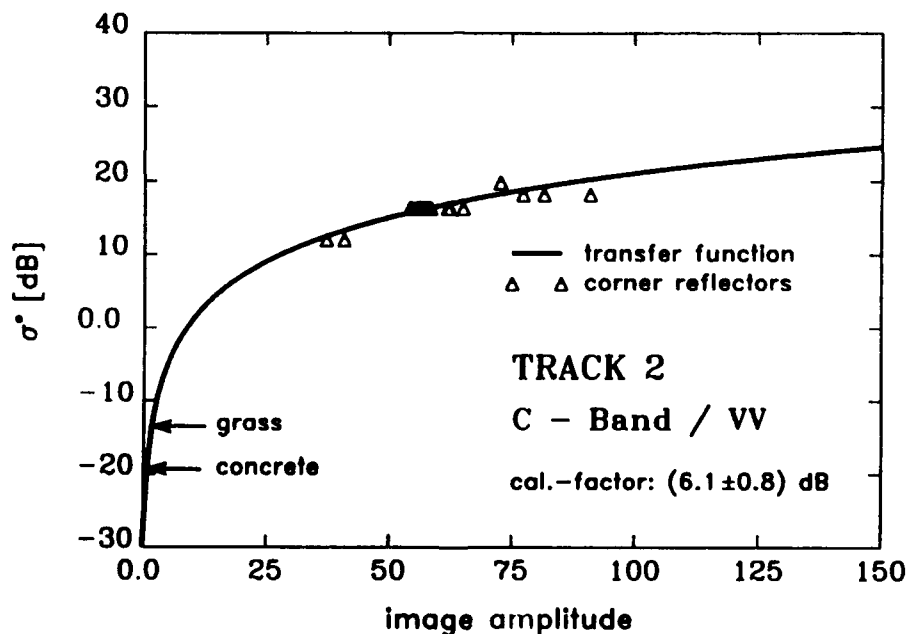


Fig. 10 DC-8 SAR system transfer function.

dB imbalance an additional error of up to 0.2 dB.

Another source of SAR signal contamination is the total system noise. This noise is mainly composed of contributions from the sensor itself (ADC, LNA, ohmic losses) and the earth surface. In the case of the X-SAR system, this quantity is estimated before mission and measured in a receive-only mode during mission. On the raw data stage a noise subtraction takes place by using the resulting noise data.

7. EXTERNAL CALIBRATION

External calibration can only be usefully performed after having accomplished the previously described internal calibration and radiometric corrections. The main objective in the scope of absolute radiometric calibration is the determination of the overall SAR system transfer function relating image amplitudes P_1 to σ° -values, as expressed in the following equation:

$$\sigma^\circ = 10 \cdot \lg(P_1) - 10 \cdot \lg(K') - 10 \cdot \lg(r_A r_R) \quad (3)$$

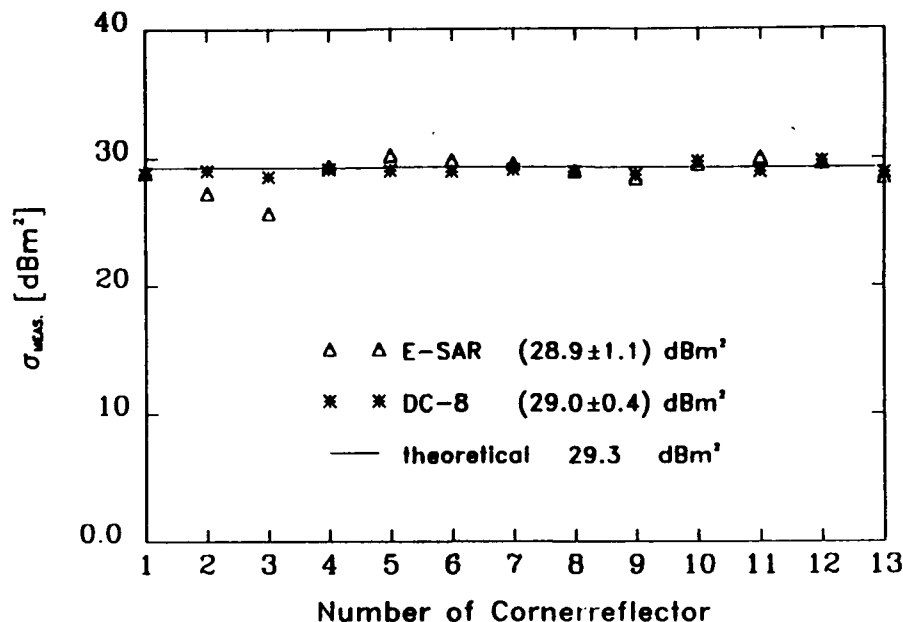


Fig. 11 Amplitude accordance of 13 equally sized corner reflectors.

P_1 is the image power in the case of distributed targets and the impulse response minus an averaged clutter (noise) level for point targets; r_A denotes the azimuth resolution. K' is slightly different to the factor K of equation (1) because of the inclusion of the processing gain which is achieved by forming the synthetic aperture. External reference targets with known RCS-values have to be used in order to determine the calibration factor K' . Corner reflectors and active radar calibrators (ARC) are appropriate tools to fulfil this task for the central and upper parts of the system transfer function, whereas in situ RCS measurements with scatterometers of especially selected area-extended targets are helpful to determine the lower part of the system transfer function.

As an example, results of the 1989 Oberpfaffenhofen airborne SAR calibration campaign are presented in Fig. 9 and 10. These figures show the C-band VV overall system transfer functions of DLR's experimental SAR (E-SAR) and NASA/JPL's DC-8 SAR. Both system transfer functions represent best fits of the corner reflector responses as marked by triangles in the two figures. The calibration factors for both systems could be determined with an accuracy better than 1 dB, showing a fairly good calibration performance for airborne SARs. The σ^0 correspondence due to the SAR systems involved has been determined to be within the 1 dB error bounds for two typical earth surface object classes: grass land and concrete.

Cross-calibration becomes more and more important in order to keep the effort and expenditure on multichannel and multisensor calibration within tolerable limits. This is especially true in view of the upcoming spaceborne missions, such as X-SAR/SIR-C and the follow-on activities. A measure of cross-calibration quality is, for instance, the RCS accordance of equally sized corner reflectors derived from image data from two different SAR systems. Such an example of thirteen 0.9 m corner reflector responses concerning the C-band VV mode of the E-SAR and DC-8 SAR is illustrated in Fig. 11 together with the theoretical RCS value.

The mean values determined were 28.9 dBm² and 29.0 dBm², which are in good mutual agreement and also in good agreement with the theoretical value of 29.3 dBm².

Fully polarimetric SAR sensors, such as the DC-8 SAR and the SIR-C system, additionally require the application of polarimetric calibration procedures. Such procedures imply the elimination of the sensor induced distortions cross-talk and channel imbalance. This can be accomplished by utilizing either different types of corner reflectors or clutter statistics together with trihedral corner reflectors [10].

8. GEOCODING

Due to the sidelooking illumination geometry and the "azimuth-range-imaging" of SAR, mountains seem to bow toward the sensor. This phenomenon is known as foreshortening and, in the worst case, as lay-over. The latter happens in cases when mountain peaks are less distant from the sensor than the valley in front of them.

In Fig. 12 the foreshortening can easily be seen by comparing the projected slope area in front of the mountain S_f , which appears in the SAR image as $(R_2 - R_1)$, and the projected slope area behind the mountain S_b , which appears in the image as $(R_3 - R_2)$.

The power density relationship S_f between $(R_2 - R_1)$ and $(R_3 - R_2)$ can be approximated as follows

$$\frac{S_f}{R_2 - R_1} \frac{R_3 - R_2}{S_b} = \frac{(R_1 + R_2)(R_3 - R_2)(\theta_2 - \theta_1)}{(R_3 + R_2)(R_2 - R_1)(\theta_3 - \theta_2)} \quad (4)$$

The second and third factors in the numerator are larger than in the denominator (see Fig. 12) and, therefore, the power density ratio is $\gg 1$.

This can be seen in SAR images in the form of bright slopes in front of mountains.

Geocoding means precise rectification. For this

purpose, about a dozen control points from maps (scale 1:50.000) will be used (for instance for ERS-1 images).

No additional radiometric correction will be applied (see Fig. 13). A very rough correction would be the inverse application of equation (4), assuming an isotropic scattering behaviour of the slopes.

This assumption is not valid, especially not in the presence of vegetational layers. A tool to include radiometric correction according to the incidence angle could be the incidence angle dependent σ^0 . But again this implies some a priori knowledge about the ground consistency.

REFERENCES

- [1] NASA Shuttle Imaging Radar-C Science Plan.
JPL Publication 86-29, Sept. 1, 1986.
- [2] Öttl, H. The X-SAR Science Plan.
Valdoni, F. DFVLR-Mitt. 85-17.
et al.
- [3] Seifert, P. Preparatory Investigations Concerning the Calibration of Spaceborne SAR-Systems.
Blötscher, H. Proc. IGARSS '91, Helsinki, 3-6 June, 1991.
- [4] Menard, Y. Design and Performance Assessment of an Ultra Stable Calibration Subsystem for a SAR and a Scatterometer.
Oudart, P. Proc. IGARSS '87, Ann Arbor, 18-21 May 1987.
- [5] Hartl, Ph. Radar Calibration Techniques Including Propagation Effects.
Heel, F. Adv. Space Res. Vol. 7, No. 11, pp. (11)259-(11)268, 1987.
Keydel, W.
Kietzmann, H.
- [6] Heel, F. Proc. of the SAR Calibration Workshop, DLR, Oct. 9-11, 1991.
Freeman, A. (Organizers)
- [7] Heel, F. Radiometric Calibration of an Airborne C-band Synthetic Aperture Radar.
Öttl, H. Proc. of The 17th Internat. Symp. on Space Technology and Science, Tokyo, 1990.
Zink, M.
- [8] Zink, M. The Oberpfaffenhofen SAR Calibration Experiment of 1989.
Heel, F. Journal of Electromagn. Waves and Appl., Vol. 5, No. 9, 1991, pp. 935-951.
Kietzmann, H.
- [9] Seifert, P. Ground-based Measurements of Inflight Antenna Patterns for Imaging Radar Systems.
Lentz, H. To be published in IEEE Trans. on Geoscience and Remote Sensing, 1992.
Zink, M.
Heel, F.
- [10] Zink, M. Comparative Investigations of Polarimetric Calibration Methods.
Heel, F. Progress in Electromagnetics Research Symp., PIERS '91, Cambridge (MA., USA), July 1991.
Kietzmann, H.

SAR SIMULATION

by

D. Hounam

Deutsche Forschungsanstalt für Luft- und Raumfahrt e.V.
 Institut für Hochfrequenztechnik
 8031 Oberpfaffenhofen
 Germany

1. SUMMARY

The use of software tools as an investigative method is particularly important in the case of synthetic aperture radar sensors, as the geometry cannot be reproduced in the laboratory. Also, the complete SAR system, from the target via the propagation path, sensor and image processor to the final image, represents a highly complex data chain, which cannot be treated in part.

The lecture discusses different approaches from parametric analysis tools to full-blown simulators capable of analysing all elements of the SAR system. The latter will be illustrated with the aid of the Sarsim simulator, which was used for confirming parameters of the ERS-1 Active Microwave Instrument (AMI).

Particular emphasis will be placed on the simulation of target scattering mechanisms, the understanding of which is essential if the potential of SAR systems is to be fully exploited, and on the modelling of sensor characteristics.

The author would like to thank T. Pike and S. Potter for the use of material and K.-H. Zeller for useful discussions.

2. INTRODUCTION

The term SAR simulation is used for a wide range of software tools to help design and evaluate SAR systems. Clearly, such an approach can be much more economical than performing experiments, bearing in mind the difficulty, and in the case of satellite sensors, impossibility of achieving a realistic geometry.

In this lecture, we will differentiate between analytic tools and simulators. The former term encompasses all purely algorithm based programs, whereas the simulators attempt to mimic as many parts of the SAR system as possible.

In general, an analytic approach to solving a problem is preferable to simulation, because it leads to a more complete understanding of the problem. However, sometimes problems arise which are not accessible to analysis. Experiment or simulation are then the only alternatives. Simulation, like experimentation can also usefully augment analysis and provide valuable confirmation that the understanding of the mechanisms within the system is correct.

It is clearly out of scope of one lecture to discuss the algorithms of such tools in detail and so the emphasis will be placed on architecture and performance.

3. ANALYTIC TOOLS

When confronted with analysing a SAR system, one is faced with a multitude of parameters many of which are strongly interdependent and all of which impact on performance and sensor design.

The first challenge for the SAR engineer is the system design, which requires juggling with the system parameters until the required performance is met. This can be described as a 'bottom up' type of analysis, i.e. starting with a set of performance requirements and external constraints, the engineer attempts to find a set of design parameters to meet his goal. This procedure is often called parametric analysis and culminates in a set of performance specifications.

The second task arises when the system design has firmed up and the engineer needs to monitor whether the performance is being met. This is the top down approach, deriving the performance characteristics from the estimated or measured sensor parameters.

The performance of a SAR sensor is described in terms of imaging parameters [1]. As a SAR image only materializes after considerable data processing, the SAR processor characteristics have also to be considered in the analysis. Clearly, somewhere the engineer has got to put stakes in the ground or his design will never converge. It is probably fortunate that some constraints exist such as physical dimensions, platform flight path (orbit) available power etc., limiting the degrees of freedom. Nevertheless, it will generally be necessary to freeze those parameters which are not part of the design task. For example, the SAR processor characteristics will be fixed when designing the SAR sensor and vice versa.

3.1 Parametric Analysis

Parametric analysis software can be regarded as a suite of software utilities to aid in the design of the SAR system. Because of the large numbers of choices open to the SAR engineer, frequent interaction with the user is necessary. There is no hard and fast rule as to where one starts in designing the system, but the timing scheme, i.e. the choice of pulse repetition frequencies (PRFs) and the position and duration of the received echo need to be defined at an early stage.

3.1.1 Timing

The minimum PRF is determined by the width of the received Doppler spectrum, it needing to be higher to satisfy the Nyquist sampling theory. The steps to arrive at the PRF are as follows:

- The width D (azimuth dimension) of the antenna is derived from the required azimuth resolution. Remember the rule of thumb that the single look azimuth resolution is half the antenna width.
- The antenna beamwidth can be calculated from the physical width:

$$\Theta_B = \frac{k \lambda}{D} \quad (1)$$

k is the broadening factor due to weighting of the antenna aperture and λ is the wavelength. k is 0.886 for an unweighted aperture, which can be shown to be optimum, if the PRF is chosen to just meet the sampling requirement (see below).

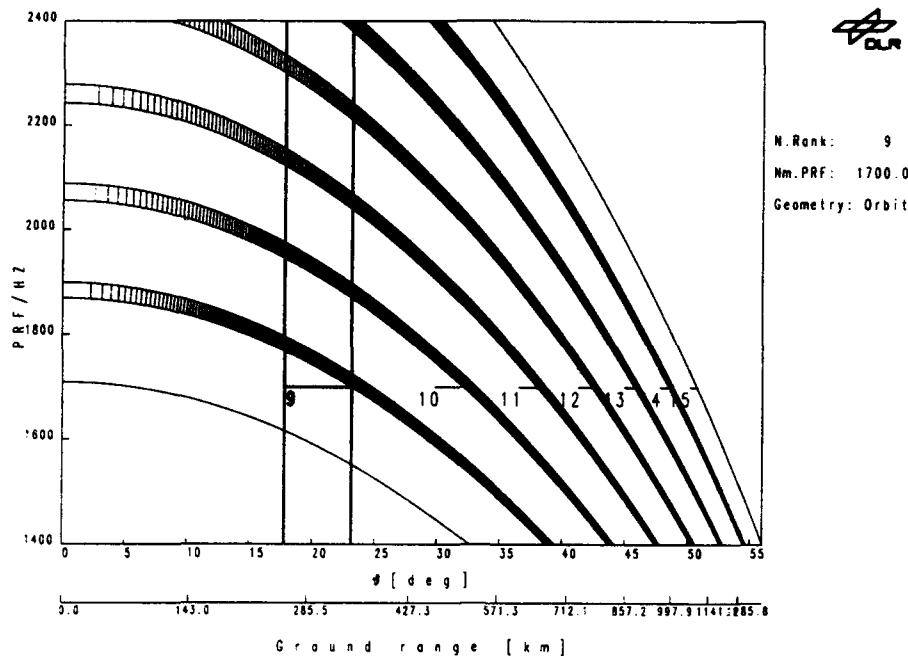


Fig. 1 Timing for the ERS-1 satellite derived by the Cross-track Geometry Program. The wanted echo window is identified by the vertical lines.

- Now the width of the received Doppler spectrum B_D can be calculated:

$$B_D = \frac{2V \phi_B}{\lambda}, \quad (2)$$

where V is the velocity of the sensor platform.

- To satisfy Nyquist, the PRF needs to exceed the bandwidth:

$$PRF > 1.2 B_D. \quad (3)$$

The above steps are simple approaches which can require more sophistication, depending on the case in hand. In effect, a software utility needs to be developed to handle all aspects. For example, the last step, where adequate sampling is considered, ensures that ambiguous responses in azimuth, due to aliasing unwanted energy into the wanted Doppler spectral band, can also be influenced by the characteristics of the azimuth compression routine in the SAR processor. However, the design of many SARs has started down this path.

The timing of the received echoes requires consideration of the cross-track geometry and the pulse characteristics of the radar. The art is to find space between successive transmit pulses for the echo with enough margin for the receiver to settle back to full performance. Another constraint is that the echo from immediately beneath the sensor (nadir) should also not fall close to the echo window. Having an incidence angle of 90° it can be strong enough to overload the receiver. Particularly, for satellite geometries, many pulses may be underway before the echo is received (for ERS-1 9) and just as many nadir echoes exist. These ambiguous echoes interfere with one another and have to be suppressed by the antenna elevation pattern.

An example of a software utility for analysing the timing is the Cross-track Geometry Program developed by the DLR. Fig. 1 shows a typical example for the ERS-1 satellite. The program computes the valid bands where the echo is corrupted by neither the preceding or succeeding transmit pulses, nor the nadir echo. Forbidden areas are shown hatched.

The bands are plotted on a graph of PRF versus off-nadir angle (angle between the target and the vertical) and ground distance (distance between the target and the ground track). The axes can also be swapped around. For the wanted swath, the user can select the PRF, rank (number of transmit pulses after which the echo is received) and the maximum and minimum off-nadir angles, i.e. the limits of the antenna elevation pattern. The program calculates the position of the unwanted ambiguous echoes enabling the requirements on the elevation pattern to be derived.

3.1.2 Link Budget

Once the timing has been defined, the geometry is known and the link budget can be computed according to the radar equation. This is a straight forward task and doesn't require much software sophistication.

The following form of the radar equation can easily be realised with a spreadsheet. Table 1 gives an example with the values for the ERS-1 satellite.

The radar equation for a single look in the final image can be written:

$$S/N_{\text{image}} = \frac{[G_A^2 P]}{[N_o]} \frac{[\tau_p]}{[\tau_{CP}]} \frac{[\tau_i \tau_{CP} PRF]}{[C]} \frac{[\lambda^2]}{[(4\pi)^2 r^4]} \cdot \frac{[\tau_{CP} C_o]}{[2 \sin i]} \frac{[\frac{r \lambda}{2 \tau_i V_s}]}{[F]} \frac{[\sigma_o]}{[G]} \frac{[1]}{[L_{ATM} L_p]} \quad (4)$$

where,

- G_A = one way antenna gain,
- P = transmit power,
- N_o = receiver noise density,
- τ_p = transmit pulse length,
- τ_{CP} = compressed pulse length,
- τ_i = azimuth integration time,
- PRF = pulse repetition frequency,
- λ = wavelength,
- r = slant range,
- C_o = velocity of light,

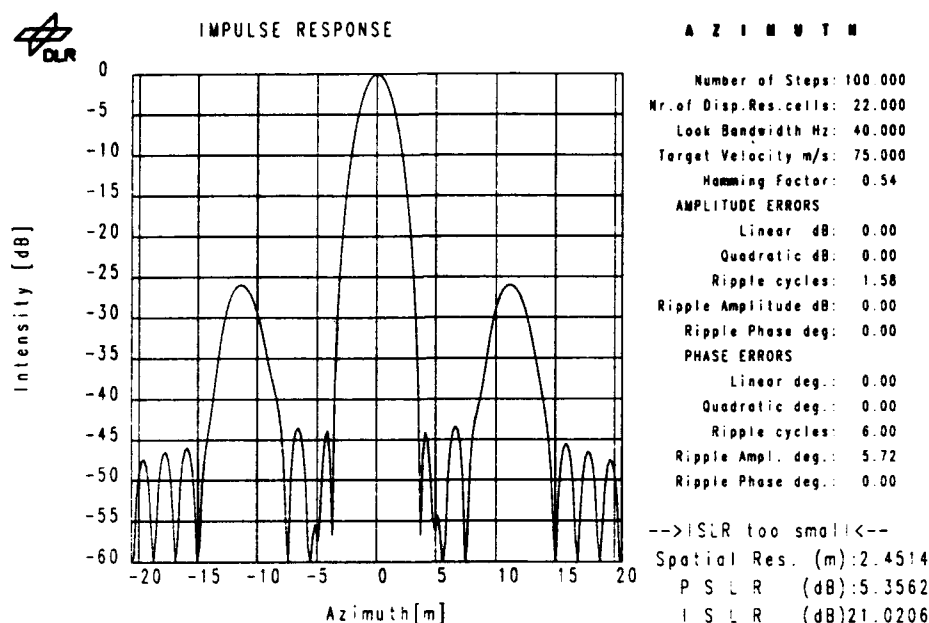


Fig. 2 Azimuth impulse response computed with IMPRES.

i = incidence angle,
 V_s = satellite velocity,
 σ_o = backscatter coefficient,
 L_{ATM} = atmospheric loss,
 L_p = processing loss.

The terms have been grouped to separate the various influences.

[A] = RF sensor parameters, called 'nominal gain' for ERS-1,
 [B] = range compression gain,
 [C] = noise bandwidth,
 [D] = free space loss,
 [E] = range resolution,
 [F] = azimuth resolution,
 [G] = target backscatter coefficient,
 [H] = losses.

The radiometric resolution γ is computed from the expression:

$$\gamma = 10 \log \left[1 + \frac{1}{\frac{S/N_{\text{image}}}{\sqrt{L}}} \right], \quad (5)$$

where L is the effective number of looks.

3.1.3 Impulse Response

The shape of the impulse response of a SAR sensor is dependent on the used weighting functions and the phase and amplitude errors. The latter can be due to sensor imperfections and, in the case of the azimuth response, also due to errors in the knowledge of the flight path. The DLR program IMPRES [2] derives the range impulse response from the chirp characteristic, the range weighting function and amplitude and phase errors. With the azimuth response, instead of the chirp, the Doppler characteristics determine the resolution. The weighting function and errors can either be entered as formulae or from look-up tables. Fig. 2 shows an example of the azimuth response showing panedechoes. Fig. 3 shows an impressive two-dimensional representation, which however, can be difficult to interpret.

IMPRES also evaluates the impulse response and computes resolution, peak sidelobe ratio and inte-

25.7.89	Radar Equation	ERS-1		
[A]	Signal/noise contribution	Antenna gain	38.2 dB	76.4
		Peak power	4800 W	36.8
		Int. losses	4 dB	-4
		Noise figure	5.5 dB	
		or Noise density	-138.48 dBW/Hz	198.5 307.7 dB
[B]	Range comp. gain	Tx pulse length	37.1 us	-44.3
		Comp. pulse	65 ns	71.9 27.6 dB
[C]	Inverse noise bandwidth	Av. integ. time	110 ms	-9.6
		Comp. pulse	65 ns	-71.9
		RF	1640 Hz	32.1 -49.3 dB
[D]	Free space loss	Wavelength	0.0566 m	-24.9
		Altitude	78500 m	
		Off-nadir angle	20.55 deg	
		or Slant range	838347 m	-236.9
		Constant	0.0005	-33.0 -294.9 dB
[E]	Range resolution	Comp. pulse	65 ns	-71.9
		Integ. angle	20.55 deg	4.5
		Constant	1.5e+08	81.8 14.4 dB
[F]	Azimuth resolution	Slant range	838347 m	59.2
		Wavelength	0.0566 m	-12.5
		Av. integ. time	110 ms	9.6
		Sensor velocity	7200 m/s	-36.6
		Constant	0.5	-3.0 14.8 dB
[G]	Backscatter coefficient	(1) Reference	-18 dB	-18.0 -18 dB
		(2) Composite	-30.0 dB	
		(3) Vegetation	0 dB	
		(4) Geology	0 dB	
		(5) Ocean	0 dB	
		Select (1...5)	1	
[H]	Losses	Atmosphere	0.13 dB	-0.1
		Processing	1.5 dB	-1.5 -1.6 dB
Signal/Noise Ratio				0.7 dB
Radiometric resolution		Number of looks	6	2.45 dB

Table 1 Spreadsheet of the link budget using the example of the ERS-1 satellite.

grated sidelobe ratio.

3.1.4 Performance Estimation

The above tools are designed to be quick and easy to use and run fast enough to be able to iterate the design. They can, therefore, be called upon to perform both the top-down and bottom-up design



IMPULSE RESPONSE

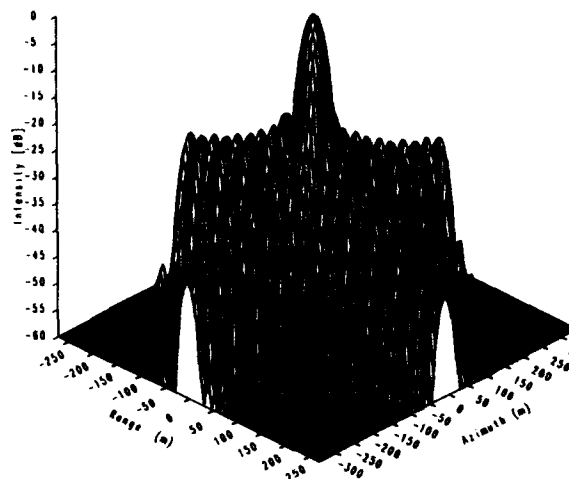


Fig. 3 Two-dimensional impulse response.

tasks mentioned above. Separate utilities like these have the advantage over comprehensive parametric analysis packages that they are easier to master. The DLR Performance Estimator [3] software is such a package which uses more sophisticated versions of the above utilities.

The Performance Estimator was originally developed for the X-SAR sensor to be flown on space shuttle together with the SIR-C sensor in 1993. It grew out of the need to provide the operators during the mission with a tool to ensure that the radar is optimally adjusted before each data take. Experience with the preceding SIR-A and SIR-B missions had shown that the predicted shuttle position and attitude was so inaccurate that relying on preset parameters meant that target sites could be missed. This led to an architecture for the Performance Estimator which has not only fulfilled the requirements of shuttle missions but also of conventional SAR satellites like ERS-1 and airborne SARs like the DLR E-SAR.

Fig. 4 shows a schematic of the Performance Estimator. Its basic architecture follows the approach described above. In the case of satellite platforms, the geometry is calculated from the orbit parameters and the position of the target site. For airborne sensors or cases where the orbit parameters are not known, a fixed geometry can be entered. The radar parameters are stored in two ways, differentiating between those which will eventually be fixed and those which can be changed by the operator, for instance, by means of telecommands from the ground. Examples of the latter are timing parameters, gains antenna pointing, etc. The 'fixed' parameters are stored in the so-called systems file, whereas the parameters under operator control are calculated and ranked by the Estimator, providing the user with a choice. Clearly, the 'fixed' parameters can be changed at any time. Typically the specifications of the radar parameters would be used as fixed parameters in the early phase of sensor design to be replaced by true measured values later.

The algorithms used in the Estimator are coded in the program but in some cases a choice of algorithms is provided. An example of this is the algorithm for choosing the optimum gain setting,

PARAMETER IMPULSE RESPONSE: RANGE

Number of Steps: 100 000
Nr. of Disp Res cells: 22 000
Chirp Bandwidth MHz: 15 550
Incidence Angle deg: 23 000
Hanning Factor: 0.720

AMPLITUDE ERRORS
Linear dB: 1 000
Quadratic dB: -0.600
Ripple cycles: 1 500
Ripple Amplitude dB: 0.400
Ripple Phase deg: 0.000

PHASE ERRORS
Linear deg: 60 000
Quadratic deg: 25 000
Ripple cycles: 1 500
Ripple Amplitude deg: 5 000
Ripple Phase deg: 0.000

PARAMETER IMPULSE RESPONSE: AZIMUTH

Number of Steps: 100 000
Nr. of Disp Res cells: 22 000
Look Bandwidth Hz: 242 000
Target Velocity m/s: 7552.007
Hanning Factor: 0.720

AMPLITUDE ERRORS
Linear dB: 0.000
Quadratic dB: 0.000
Ripple cycles: 1 500
Ripple Amplitude dB: 0.400
Ripple Phase deg: 0.000

PHASE ERRORS
Linear deg: 0.000
Quadratic deg: 0.000
Ripple cycles: 1 500
Ripple Amplitude deg: 5 000
Ripple Phase deg: 0.000

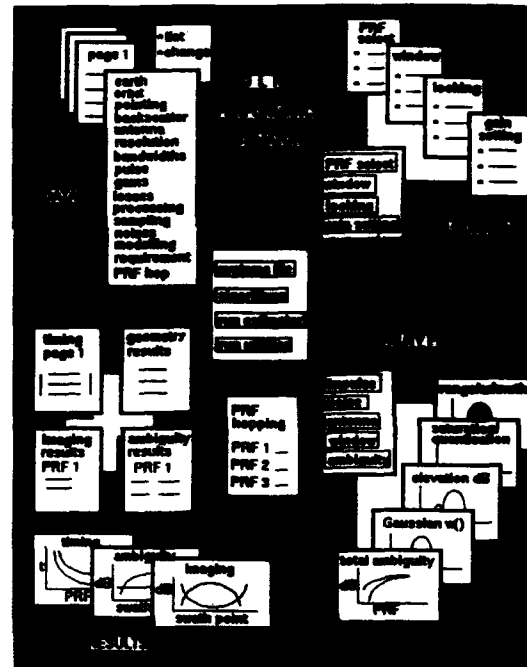


Fig. 4 Schematic diagram of the Performance Estimator.

where different philosophies can be used, depending on the sensor.

The Estimator first calculates the timing parameters by running through all the available PRFs to see which PRFs meet the requirements. Where image quality is affected simple algorithms, as given in Section 3.1.1 are used for the bottom up analysis. The PRFs for which adequate solutions are found are ranked according to criteria, which can be selected by the operator. The solutions are displayed on the timing page (see Table 2). The timing page also lists the performance parameters which are dependent on geometry and timing like swath width and position, and spatial resolution.

PULSE REP FREQ SORT	TIMING					
	1	2	3	4	5	6
PULSE REP FREQ Hz	1702.0	1700.0	1698.0	1696.0	1694.0	1692.0
PULSE REP INT micro	587.5	588.2	589.1	589.6	590.3	591.0
RX WIND LENGTH samp	5616.0	5616.0	5616.0	5616.0	5616.0	5616.0
RX WIND LENGTH micro	296.2	296.2	296.2	296.2	296.2	296.2
SWATH WIDTH micro	259.3	259.3	259.3	259.3	259.3	259.3
SWATH WIDTH km	99.7	99.7	99.7	99.7	99.7	99.7
ASS RX WID DEL mill	5.6	5.6	5.6	5.6	5.6	5.6
ORDER SIGNAL RETURN	9.0	9.0	9.0	9.0	9.0	9.0
START POSITION	42.0	41.0	40.0	39.0	38.0	37.0
REL RX WINDROW micro	279.0	274.5	270.0	265.5	261.0	256.5
NEAR GRD SPAT RES m	25.2	25.1	25.1	25.2	25.1	25.2
FAR GRD SPAT RES m	18.8	18.7	18.7	18.8	18.7	18.8
ORDER RADAR RETURN	8.0	8.0	8.0	8.0	8.0	8.0
RELATIVE RADAR micro	496.9	491.4	485.9	480.3	474.8	469.2
NAMEWIDTH ADEQUATE?	YES	YES	YES	YES	YES	YES
TRX INTERFERENCE?	NO	NO	NO	NO	NO	NO
RADAR CASE 1,2a/b,3	2b	2b	2b	2b	2b	2b
RX WIND OBSERVED	26.4	26.8	27.1	26.0	26.3	25.2
CLOSEST SEPARATE micro	0.0	0.0	0.0	0.0	0.0	0.0

PULSE REP FREQ SORT	TIMING					
	7	8	9	10	11	12
PULSE REP FREQ Hz	1690.0	1688.0	1686.0	1684.0	1682.0	1680.0
PULSE REP INT micro	591.7	592.4	593.1	593.8	594.5	595.2
RX WIND LENGTH samp	5616.0	5616.0	5616.0	5616.0	5616.0	5616.0
RX WIND LENGTH micro	296.2	296.2	296.2	296.2	296.2	296.2
SWATH WIDTH micro	259.3	259.3	259.3	259.3	259.3	259.3
SWATH WIDTH km	99.7	99.7	99.7	99.7	99.7	99.7
ASS RX WID DEL mill	5.6	5.6	5.6	5.6	5.6	5.6
ORDER SIGNAL RETURN	9.0	9.0	9.0	9.0	9.0	9.0
START POSITION	44.0	43.0	42.0	41.0	40.0	39.0
REL RX WINDROW micro	243.0	238.5	234.0	229.5	225.0	221.5
NEAR GRD SPAT RES m	25.2	25.1	25.2	25.1	25.2	25.1
FAR GRD SPAT RES m	18.8	18.7	18.7	18.8	18.7	18.8
ORDER RADAR RETURN	8.0	8.0	8.0	8.0	8.0	8.0
RELATIVE RADAR micro	463.6	458.0	452.3	446.7	441.1	435.4
NAMEWIDTH ADEQUATE?	YES	YES	YES	YES	YES	YES
TRX INTERFERENCE?	NO	NO	NO	NO	NO	NO
RADAR CASE 1,2a/b,3	2b	2b	2b	2b	2b	2b
RX WIND OBSERVED	25.5	25.9	26.3	25.2	24.3	24.4
CLOSEST SEPARATE micro	0.0	0.0	0.0	0.0	0.0	0.0

Table 2 Example Performance Estimator timing page (ERS-1).

The next phase of the Performance Estimator is to calculate the imaging performance for the various PRF solutions. Normally, the three highest ranked PRF solutions will be analysed but the operator can change the ranking or the number of solutions, if he desires.

Imaging performance is displayed on three screens: signal to noise, ambiguity ratios and target detection.

Using built in algorithms for the radar equation digitisation noise, bit error noise and a variety of scenarios for the normalised backscatter coefficient σ_0 , the Estimator computes the signal-to-noise ratios for each selected PRF solution and nine positions across the swath. The S/N at the input to the analogue-to-digital converter, i.e. the video S/N, the S/N for each processed look and the multilook S/N are all calculated. From the latter the radiometric resolution can be computed. The dynamic range is the range of signal powers over which a particular requirement, e.g. radiometric resolution is met. The Estimator searches over a range of σ_0 values until the radiometric resolution goes out of specification. Table 3 shows typical results for the ERS-1 satellite.

SELECTED PRF=1702.0Hz GAIN SETTING=15.0dB											
NEAR			MIDDLE			FAR					
SWT PT (km)	245.9	250.4	270.9	283.4	295.9	308.4	320.8	333.3	345.8		
VIDEO	25.8	25.9	26.0	26.0	25.9	25.6	25.2	24.8	24.3		
ABC	41.1	41.2	41.3	41.2	41.1	41.0	40.8	40.6	40.3		
LOOK 1	-1.6	-1.1	-0.9	-1.0	-1.3	-2.0	-2.7	-3.5	-4.3		
LOOK 2	1.0	1.5	1.7	1.6	1.3	0.7	-0.2	-1.3	-2.6		
LOOK 3	2.3	2.9	3.0	2.9	2.5	1.7	1.0	-0.1	-1.4		
LOOK 4	2.3	2.8	2.9	2.9	2.5	1.9	1.0	-0.1	-1.4		
LOOK 5	1.5	1.7	1.6	1.2	0.6	-0.2	-1.3	-2.7			
LOOK 6	-1.6	-1.1	-0.9	-1.0	-1.4	-2.0	-2.8	-3.9	-5.3		
TOTAL	0.8	1.3	1.5	1.4	1.1	0.5	-0.4	-1.5	-2.8		
RESOLV	2.4	2.4	2.3	2.3	2.4	2.5	2.7	3.0	3.4		
TP SIG	1.9	6.0	5.0	5.0	6.0	14.0	7.0	7.0	7.0		
DT SIG	-14.0	-15.0	-15.0	-15.0	-15.0	-14.0	-13.0	-12.0			
DT SIG	21.9	21.9	20.0	20.0	20.0	21.0	20.0	20.0	20.0		

PERFORMANCE SWATH IS 99.99km. 100.00% OF ILLUMINATED
RADIOMETRIC RESOLUTION FOR NOISE EQUIVALENT SIGNAL = 2.59 dB

Table 3 Example of the Performance Estimator signal-to-noise performance (ERS-1).

The ambiguity performance in range is calculated from the geometry, timing and antenna elevation pattern. Range ambiguities occur when the slant range differs by half the pulse repetition interval (PRI). The ambiguity ratio is computed by integrating the energy in the wanted region and ambiguous regions and dividing. The antenna elevation pattern can be entered as a look-up table or as a weighted pattern with up to seven weighting coefficients.

Azimuth ambiguities occur, due to aliasing of unwanted Doppler frequency bands into the wanted region. The latter are suppressed by the antenna azimuth pattern. The azimuth ambiguity ratio is calculated by integrating the energy in the Doppler band selected by the SAR processor and the energy in the ambiguous bands and dividing. Apart from the azimuth antenna pattern, the processed Doppler bandwidth and the weighting function used for azimuth compression have to be taken into account. A large number of weighting functions can be selected. Again the azimuth antenna pattern can be entered as an analytic function or as a look-up table.

The distributed target ambiguity ratio is calculated by combining range and azimuth ambiguity ratios. Table 4 shows typical values for the ERS-1 satellite.

SELECTED PRF=1702.0Hz GAIN SETTING=15.0dB											
NEAR			MIDDLE			FAR					
SWT PT (km)	245.9	250.4	270.9	283.4	295.9	308.4	320.8	333.3	345.8		
RANGE	38.2	41.6	45.0	48.5	52.1	55.9	59.3	61.4	61.5		
AZIMUTH LOOKS :											
LOOK 1	20.8	20.8	20.8	20.8	20.8	20.8	20.8	20.8	20.8		
LOOK 2	25.5	25.5	25.5	25.5	25.5	25.5	25.5	25.5	25.5		
LOOK 3	29.1	29.1	29.1	29.1	29.1	29.1	29.1	29.1	29.1		
LOOK 4	24.9	24.9	24.9	24.9	24.9	24.9	24.9	24.9	24.9		
LOOK 5	23.6	23.6	23.6	23.6	23.6	23.6	23.6	23.6	23.6		
LOOK 6	13.8	13.8	13.8	13.8	13.8	13.8	13.8	13.8	13.8		
AZIMUTH SUM	21.7	21.7	21.7	21.7	21.7	21.7	21.7	21.7	21.7		
TOTAL	21.6	21.7	21.7	21.7	21.7	21.7	21.7	21.7	21.7		

Table 4 Example of the Performance Estimator ambiguity performance.

The target detection characteristics describe the ability of a SAR sensor to detect point targets above a distributed target background.

Man-made targets generally consist of single or combinations of discrete scatterers and can be regarded as having deterministic properties. Such scatterers, often called point targets, are usually much smaller in extent than the resolution cell size. Although the radiometric resolution can be calculated for such targets, the user is more interested in the ability to detect targets above the system noise or distributed target background (clutter).

To detect a scattering centre or point target successfully it must be brighter than the brightest point in the speckled background.

In principle, the radiometric resolution can be calculated for point targets and this can be a useful parameter if the radar cross section of the target needs to be measured with known precision. The application considered here, to image man-made objects consisting of one or several dominant scattering centres, requires that the weakest scatterer can still be resolved above the background. If sufficient scatterers from the target can be detected, the size and shape of the object can be reconstructed and, hence, the object described.

In the approach described here, two parameters from radar detection theory are used as a measure of the ability to detect a scatterer. The false alarm rate (FAR) is the probability that the intensity of the background in an image pixel is such that it is falsely interpreted as a point target. The detection probability is the probability that a point target can be detected above the background.

A scatterer is considered to be detected in an image pixel if the intensity of that pixel exceeds the intensity of the surrounding pixels by an

amount large enough to meet the required false alarm rate and detection probability.

To analyse the problem quantitatively, assumptions have to be made about the object to be detected and its surroundings. In the following, three scenarios for the analysis have been chosen.

- 1) The first scenario consists of a single stable point target in a background consisting of a distributed target. The assumption is that, although the point target, by definition, is smaller than the resolution cell, only the point target contributes to the energy in the corresponding pixel. This would apply to the case where the point target is surrounded by a surface of low scattering cross section large enough to fill the resolution cell and where the system noise is negligible compared with the background σ_0 . This scenario, is typical for large metallic structures, such as aircraft, where the scatterers are surrounded by large metallic surfaces reflecting the energy away from the sensor.
- 2) The second scenario considers a single point target in a distributed target background where the background, the system noise as well as the point target contribute to the energy in the point target pixel. This is a more general case than the first scenario and would be typical of buildings and small isolated objects.
- 3) In both the above cases it is assumed that the target cross section remains constant. In reality, it will vary according to the aspect angle (glint). For such a variation, a Rice distribution can be used. The third scenario therefore assumes that the energy in the target cell is a combination of a varying target cross section as well as background energy and system noise.

The principle of the model is that a threshold is set according to the background and the required false alarm rate. Fig. 5 shows the position of the threshold for the three detection scenarios with the probability density of the image intensities. The FAR is obtained by integrating the probability density of the background from the threshold to infinity. The detection probability is the area under the probability density curve of the target from the threshold to infinity. For the first scenario it is always one.

With this model the Estimator can calculate FAR and detection probability. Typical results for the ERS-1 satellite are shown in Table 5. Fig. 6 shows the detection probability plotted against swath position with the false alarm rate as a parameter.

The model elements of the Estimator are summarised once more below:

- a GEM6 Earth model which includes Earth rotation,
- a circular orbit (to calculate the platform velocity),
- uncertainties in the height of the platform, nadir and target,
- antenna and platform pointing errors,
- theoretical and measured azimuth and elevation antenna patterns,
- a variety of ground clutter models which represent the expected radar backscatter coef-

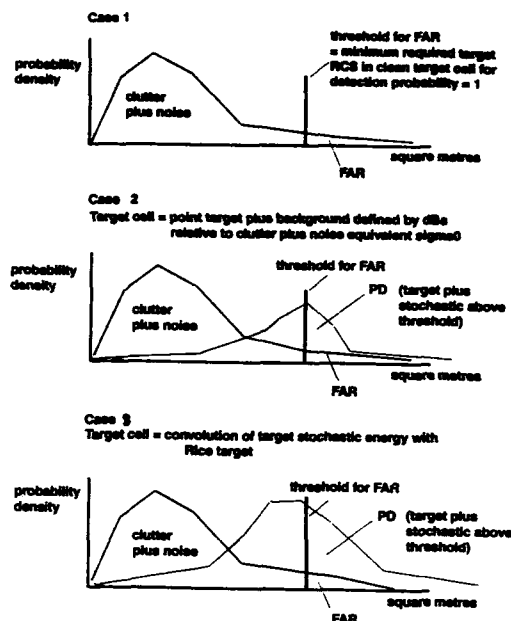


Fig. 5 Representation of the three detection scenarios.

TARGET CASE = 4 NOISE EQUIVALENT SIGNAL = -21.50
TARGET DETECTION PROBABILITIES (%)

	NEAR	MIDDLE	FAR
SWT PT (km)	247.5	259.9	272.4
FAR (dB)	24.4	25.3	26.2
-20.0	0.0	0.0	0.0
-30.0	0.0	0.0	0.0
-40.0	0.0	0.0	0.0
-50.0	0.0	0.0	0.0
-60.0	0.0	0.0	0.0

Table 5 Example of the Performance Estimator detection performance.

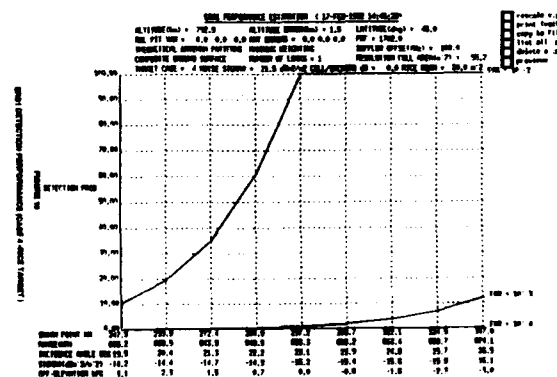


Fig. 6 Detection probability for the ERS-1 satellite as a function of FAR. The object is a large vehicle.

- efficient versus incidence angle,
- a variety of target models (RCS characteristics embedded in noise and clutter) for False Alarm Rate (FAR) detection modelling,
- the prediction of signal attenuation versus rain-rate,
- a variety of ways of selecting the PRFs, as well as user selected,
- the selection of an optimal set of PRFs for PRF hopping,

- a variety of receiver gain setting algorithms which use either centre swath signal, mean swath signal and mean or the minimum/maximum backscatter coefficient, as well as user selected,
- a choice of either fine or coarse range resolution,
- various system hardware gains and losses,
- the possibility of overlapping azimuth looks,
- characterisation of the thermal and Analogue to Digital Converter (ADC) noise sources,
- a variety of amplitude weighting functions, as well as user selected,
- the ability to degrade the range ambiguity ratio due to an expected range of radar backscatter coefficients.

The software characterising these functions has the following features:

- partitions which can be displayed on the screen with descriptions,
- DEC windows designed to allow the user to go forwards and backwards through all the options to make and assess system changes quickly,
- the ability to generate antenna patterns from a Fortran file,
- a facility to examine graphically the manner in which, for example, the antenna patterns and the ADC noise are modelled,
- fast evaluation of a large number of swath points which are split up into their azimuth look components,
- all the timing information that can be paged for all the PRF and includes for example the predicted interference cases,
- tables and graphs of ambiguity, signal to noise and imaging data for all the selected PRFs that are easily copied to a specified printer,
- tables and graphs of required target size for detection or detection probability versus false alarm rate for verification modelling,
- graphs of the components of the video signal to noise ratio and the factors that degrade this,
- the analysis of the effect of changing any system parameter and plotting the change produced in any of the performance measures,
- run information and a series of warning messages when either algorithms are not functioning or when the user has made a mistake,
- graphics software that allows the user to easily select graphs, automatically scales and grids the data, plots requirement curves and, if applicable, fully labels the output and provides a rescale facility for comparisons with other graphs. In addition radar sensitivity data are given under each modelled swath point,
- book-keeping functions for the performance plots which allow the user to keep track of

the system analysis performed to date,

- a listing of all system files available and the switching to other radar systems using function keys.

The Performance Estimator is typical of an algorithm based simulation tool. The software uses DEC windows and allows the user to play with different parameter settings and check the performance. Clearly, the algorithms that are used are tried and tested, so that few major surprises are to be expected in the results. Full-blown simulators, as described below, mimic all the steps in the SAR system and can, hence, be used for scientific investigations.

4. SIMULATION

A simulator attempts to model as many parts of the SAR system without recourse to analytic functions. The advantage of this approach is that genuine data are generated, which can be examined at each stage. Fig. 7 shows the elements of a SAR system which may be simulated and the evaluations which can be performed.

Although all elements contribute to the imaging performance, some may be able to be simplified depending on the application. For instance, if the application is concerned with the investigation of SAR data processors, a very primitive raw data generator with simple targets and ideal sensor may be adequate for the task. For this reason simulators tend to grow, starting off being tailored to a particular application and later being augmented to become a more comprehensive tool.

The first step in simulating a SAR system is to model the target. The target can most easily be simulated, if it is described by a two-dimensional matrix of scatterers each modelled as a complex vector voltage reflection coefficient. Fig. 8 shows such a target model consisting of xy cells. As will be seen, the simulator only has to form the sum of all vectors within the instantaneous field of view (IFOV) of the radar to generate the time domain signal. The latter process is referred to as raw-data generation and the final result is to generate the signal received at the output of the antenna. The raw data generation can be the most complex part of the simulation chain, even exceeding the complexity of the SAR processor.

Generating such a two-dimensional array of vectors assumes that the scattering process lends itself to this representation. Distributed targets with differing normalised reflector coefficients σ_0 can be synthesised with such a model, as can isolated point targets. Mixing distributed and point targets is also possible. The speckle associated with distributed targets can be generated with an appropriate statistical model. Most simulators working in this way include utilities to help the user generate target patterns.

The following description of the DLR simulator SARSIM will be used to illustrate such a simulator.

4.1 The System Simulator, SARSIM

SARSIM was originally developed by Ferranti in the UK in 1977 taking about 15 man-years of effort.

The original software was extensively modified by Ferranti in 1978/79, by Logica (UK) in 1981/82 and currently by the DLR since 1978. Two versions of the program exist, one on the DLR CRAY and more recently on a VAX4000 workstation. SARSIM is described in [4 and 5].

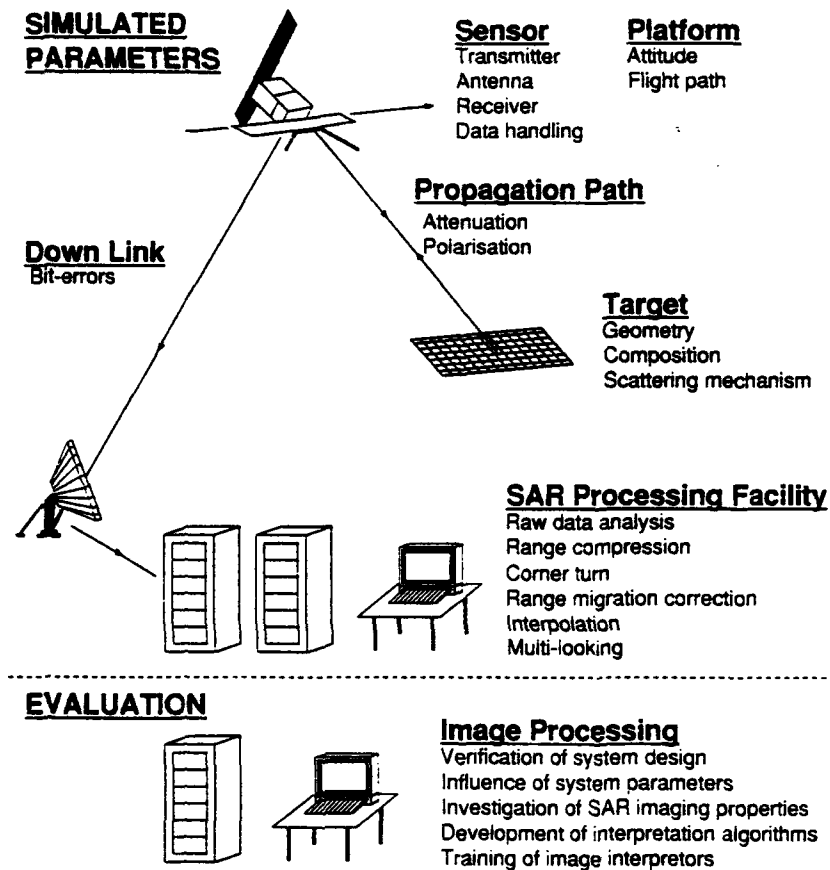


Fig. 7 Simulated elements and evaluation tasks of a comprehensive SAR simulator.

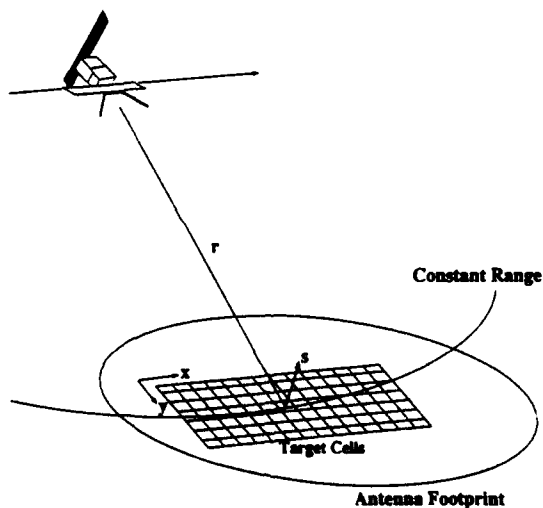


Fig. 8 Representation of the simulator geometry with the target represented by two-dimensional array of complex reflection coefficients.

A schematic of the SARSIM model is given in Fig. 9. SARSIM is an "end-to-end" simulator producing as an output the SAR image of the input target.

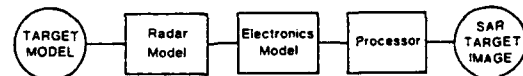


Fig. 9 Schematic of the SARSIM structure.

For each physical element of the system, there is a corresponding software module. These software modules simulate the physical element characteristics with the important exception of the linear gain of the element. This means that the overall model should be seen as a relative, rather than absolute, assessment tool. A more detailed schematic of SARSIM is given in Fig. 10.

Here one can see that the simulator has been divided into two segments. The first segment, signal generation, deals with simulation of the SAR video signal, that is the SAR system up until the point where the analogue signal (in baseband) comes out of the receiver system mounted on the platform. The second segment, data handling and SAR processing, then simulates the remaining on-board electronics, data-link, and SAR processing to produce the SAR target image. Auxiliary programs can then be used to create a hard copy of this image, apply post processing algorithms or to make image quality measurements.

SARSIM has in-built options to generate several

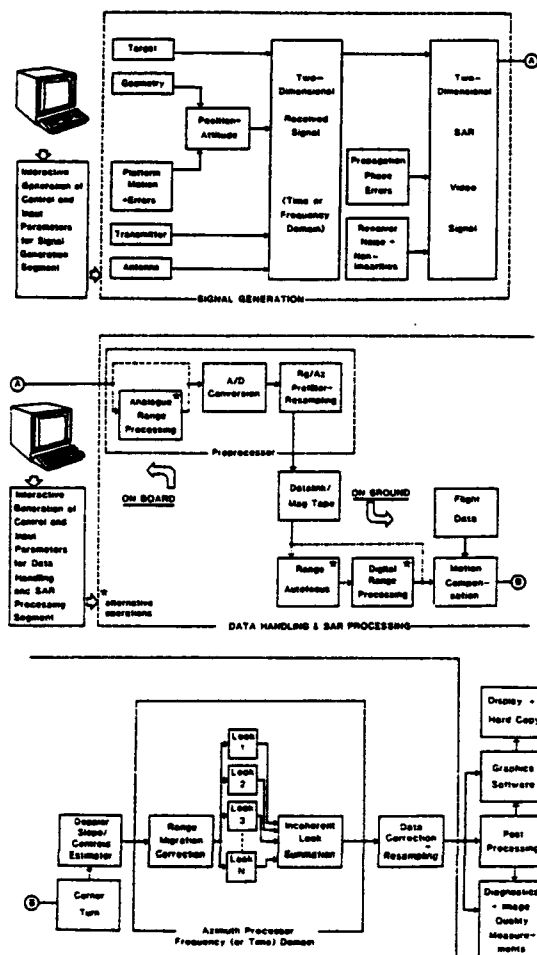


Fig. 10 SRSIM configuration.

standard types of targets. Slope effects, such as layover and shadowing, are not simulated. The basic principle of simulation is a "pulse by pulse" simulation, that is the relative positions of platform and target, together with platform attitude are calculated for each radar pulse and then this is used to calculate the returned signal for each transmitted pulse. The returned signal is represented by a sequence of floating-point (complex) numbers obtained by convolving the transmitted pulse form with the target, weighted by the antenna pattern and taking into account any special receiver chain features.

The sample spacing of the returned signal is chosen to match with the Analogue to Digital Converter (ADC) sampling frequency. As the simulation is performed directly in baseband, RF system element effects must be carefully accounted for. After the ADC, the signal may be prefiltered or resampled if such an option is present in the real radar system.

In Fig. 10, alternative options of on-board analogue range processing or on-ground digital range processing are shown, these simply reflect alternative positions of performing the range processing in the SAR system. The range processing (and azimuth processing) can be performed in the frequency or time domain. After the range processing the data is reordered (corner turn followed by range migration correction) before the azimuth processing. Illustrated in Fig. 10 is multi-look

processing, where the Doppler history of the target is split into N segments, each segment is separately processed and then added incoherently after detection. This technique improves the radiometric resolution at the expense of spatial resolution. Finally the data can be corrected (calibrated) if desired.

As an alternative to the built-in processor, SRSIM data can also be processed with the DLR motion compensation processor.

4.1.1 The Target

The target is represented by a matrix of complex voltage reflection coefficients assumed to lie directly on the earth's surface. Distortions and effects due to local height variations cannot be simulated. Similarly, variations of radar reflectivity with incidence angle and time cannot be simulated. The complex voltage reflection coefficient $V_x + iV_y$ is related to the radar cross-section σ of the corresponding ground element by the following equation,

$$V_x^2 + V_y^2 = k\sigma$$

where k is a constant. The target size is restricted to 192,000 elements.

The target generation segment of SRSIM consists of a two stage algorithm. In the first stage, a matrix of cells is generated according to some pattern corresponding to the ideal radar cross-section of the target. In the second stage, each cell is divided into a number (at least one) of subcells and the value of the reflection coefficient for each sub-cell is derived from the value for the whole cell. This second stage permits the introduction of speckle into the model, by assuming that the amplitude of each sub-cell value is drawn from a Rayleigh distribution. The mean of the Rayleigh distribution is specified by the cell value generated in the first stage algorithm. The phase of each sub-cell value can either be fixed or drawn from a uniform distribution ($-\pi, \pi$). Each sub-cell value can be thought of as representing the reflectivity from a point target located at the centre of the cell. Therefore, the target, even though representing an extended target, consists of a matrix of point targets. This is a standard method for modelling extended targets [6]. Superimposed on this, the user can specify up to 16 deterministic point scatterers.

Fig. 11 illustrates a possible target example. Here, each cell has been split into four sub-cells. The amplitude, A_i of each sub-cell can be determined in one of three ways:

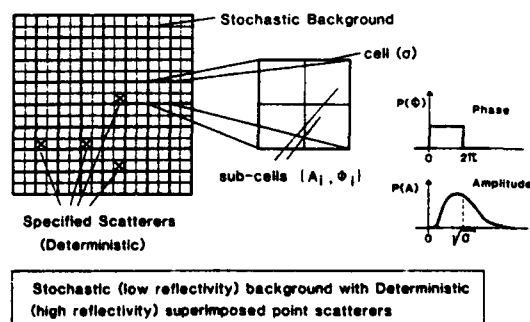


Fig. 11 Target examples.

- 1) A_i is fixed and proportional to $\sqrt{\sigma}$.
- 2) One value per cell is drawn from a Rayleigh

distribution (mean = $\sqrt{\sigma}$) and all A_i within the cell take this value.

- 3) An A_i value for each sub-cell in turn drawn from a Rayleigh distribution. The same distribution is used for all sub-cells within the cell.

Similarly the phase, ϕ of each sub-cell can be determined in one of three ways:

- 1) ϕ_i takes a constant value for every sub-cell in the matrix.
- 2) One value per cell is drawn from a uniform distribution and all ϕ_i within the cell take this value.
- 3) A ϕ_i value for each sub-cell in turn is drawn from a uniform distribution.

In the case where the sub-cell and cell are identical, then options 2 and 3 in both of the above are similarly identical. A cut-off point can also be specified where option 1 is used for all azimuth bins greater than the cut-off point, and options 2/3 are used for the remaining azimuth bins. This is referred to as a semi-diffuse target.

The following options are provided for generation of the (first stage) matrix of cells:

- A) User specified pattern: a two dimensional array of amplitude data is read in from a file provided by the user.
- B) Cyclic pattern: a set of cycles is generated in either the azimuth or range direction. Each cycle consists of an alternating sequence of high reflectivity and low reflectivity amplitudes. The length of the sequences within each cycle is fixed, but increases by one cell between successive cycle-series. An example is given in Fig. 12.

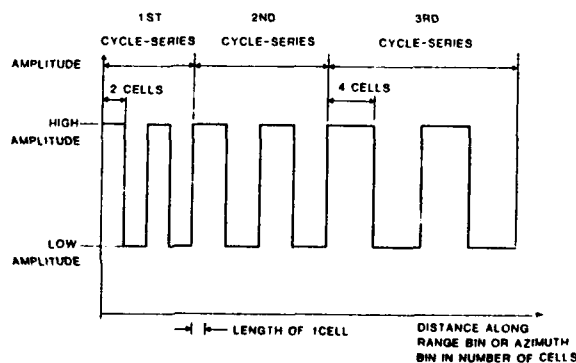


Fig. 12 Cyclic target pattern.

- C) Linear pattern: a set of point targets of linearly increasing amplitudes in one (or more) range bin or azimuth bin.
- D) Two point targets: two point targets of specified amplitudes are placed in either one range bin or one azimuth bin.
- E) Single point target: a point target of specified amplitude at a specified position.
- F) Checkerboard pattern: a pattern of alternating squares/ rectangles of high amplitude and low amplitude.
- G) Square well pattern: a uniform target with a square of zero reflectivity inset.

In options B - E, values not explicitly specified in the pattern are set to a background value.

4.1.2 Geometry

Two models exist for specifying the geometry of the SAR system. The first model uses a flat earth model together with a platform model assuming either constant linear velocity or stepwise constant acceleration components. This is suitable for simulating an airborne SAR. The second model uses an ellipsoidal earth model, together with an ellipsoidal orbit model. The second model is suitable for spaceborne SAR simulations. In both models the platform coordinate origin (x, y) is defined as the platform position when the beam centre and target centre are in alignment. The platform position is expressed in Cartesian coordinates. In the case of the ellipsoidal earth model, a local spherical approximation is made to the earth's surface, and the target is assumed to lie on this spheroid. This assumption is valid so long as only a few seconds of flight time are simulated. Earth rotation is taken into account by combining the earth's surface velocity with the platform velocity to produce a relative velocity vector, and modifying the platform yaw angle.

4.1.3 Platform Position and Attitude

The platform position and attitude are calculated for every pulse in the time interval $[-T/2, T/2]$, that is the simulation is constructed time symmetrically about time zero, time zero being the time when beam and target are in alignment. In the case of the elliptical orbit simulation, the orbit and geometry parameters are sufficient to determine the theoretical position of the platform for every pulse. However, an additional perturbation may be introduced in the form of a constant linear acceleration term. The flat earth simulation, requires instead input data relating to the linear velocity components at time zero and linear acceleration components before the platform position per pulse can be calculated.

The platform attitude per pulse is expressed in yaw, pitch and roll angles. These can either be considered as constant or as conforming to some specified angular motion.

4.1.4 Transmitter

In Sarsim, the transmitter is ideally modelled, with the only feature characterized being the ideal form of the transmitted pulse. It is not possible to simulate any form of noise or distortion in the transmitter system. Mismatch between the up- and down-converters is assumed to result in a residual carrier frequency and this is modelled in the receiver simulation.

The following forms of transmitted pulse can be simulated:

- 1) A pulse with constant frequency.
- 2) A linear FM pulse; the frequency of the transmitted pulse increases/decreases linearly during the pulse transmission.
- 3) A quadratic FM pulse; the frequency variation of the pulse during transmission is a quadratic function of time.
- 4) a binary phase encoded pulse; the frequency of the pulse is constant, but the phase can take two values: 0 and π .

The phase structure of the pulse is specified by a binary string.

In all four forms of the transmitted pulse, the amplitude of the pulse is constant.

4.1.5 Antenna

The antenna is defined by a two-way antenna gain pattern, specified in azimuth and elevation. The antenna gain function is assumed separable, that is the antenna gain in any given direction is obtained by multiplying the appropriate azimuth and elevation gains together. No provision is made for gain variations during the simulation period. The following gain patterns can be used in the simulation:

- 1) Uniform pattern $G = 1$.

- 2) Modified cosine pattern.

$$G = \frac{\cos(x)}{(\frac{\pi}{2})^2 - x^2}, \quad \text{where } x = \frac{\pi D}{\lambda} \sin \theta,$$

where: D is the effective antenna aperture (in azimuth or elevation),
 λ is the radar wavelength,
 θ is the azimuth/elevation offset angle.

- 3) Sinc pattern.

$$G = \frac{\sin(x)}{(x)}, \quad \text{where } x \text{ is defined above.}$$

- 4) User specified pattern. The user must specify a table of gain against azimuth/elevation offset angle.

The beamwidths of the antenna pattern (in azimuth and elevation) must be specified by the user. These values define the extent of the generated antenna pattern.

4.1.6 Propagation

The radar equation is not included in the SRSIM model. Most of the terms in the radar equation are constants (for most system simulator applications), apart from the range gain dependence (r^4). For satellite simulations the lack of range dependent attenuation is thought to be of negligible significance (though of more significance for airborne applications).

Atmospheric distortions are only included in as much as the optional addition of a phase noise term. The noise follows either a uniform, Rayleigh, exponential, or normal distribution; in the case of the normal distribution an auto-correlation function can also be specified. The auto-correlation function can either be linear, quadratic, exponential, Gaussian, or user supplied.

4.1.7 Signal Generation

The primary option for received signal generation generates the returned signal for each pulse in turn in the time domain. The distance to each target element is calculated and then the returns (after weighting by the appropriate antenna gain) from all target elements within a range gate are summed, taking into account the appropriate phases, to give the final return range gate value. This operation is performed for all range gates within the sampled return pulse and for all pulses simulated and is, hence, not an insignificant task. Fig. 13 illustrates the target returns which contribute to the return range gate value.

The exact form of the curved radar range bin depends on the orbit and earth geometry simulated. The width of the bin is determined by the sampling frequency of the ADC, which, together with the receiver gate times, also determines the number of

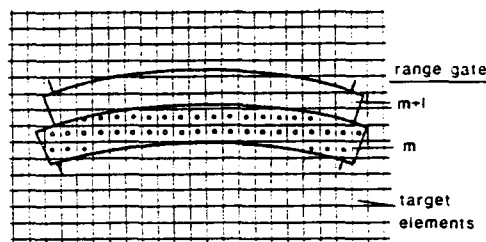


Fig. 13 Target element contributions to the m^{th} range bin return using signal generation primary option (time domain).

range bins. It should be noted here that the target cell range dimensions should be chosen equal to, or smaller than, the range bin width. This is to minimise problems occurring when few target cells happen to fall in a given range bin, a result of the fact that the target is in fact modelled by a number of discrete point scatterers, rather than by a true extended target.

The primary method of signal generation inherently includes all range migration effects due to earth rotation, earth curvature and radar wave front curvature. The simulation of the range modulation can either be performed in the time domain (by convolving the returned signal directly with the transmitted waveform), or in the frequency domain (by multiplying the appropriate Fourier transforms together and then taking the inverse transform).

Two secondary options for received signal generation exist, both of which attempt to reduce the amount of computer time required. The first of these options generates the expected return (phase history) from a point target located at the centre of the target matrix assuming an ellipsoidal, locally spherical, earth's surface and an unperturbed elliptical orbit. Appropriate account is taken of the azimuth antenna pattern. The azimuth modulation is performed in the frequency domain and so the Fourier transform of this phase history is used to calculate the return range gate values. The same phase history is used for all range gate values. Range migration effects are not accounted for in this model. Note that the target element spacing is assumed to be defined by the range bin width in range and the pulse repetition interval in azimuth.

The second option extends the above idea to partly include range migration effects by taking into account that the return from a point target appears in several range gates, or alternatively expressed, that neighbouring target gates contribute to the return from one range gate (Fig. 14). The transition points between neighbouring range/target gates are calculated at the centre of the target (mid-swath) and assumed to apply to all range/target gates. The phase history segments are convolved with the target in the time domain. In both of the secondary options the range modulation can either be performed in the frequency or time domain, as in the primary option signal generation.

4.1.8 Receiver

The receiver system typically consists of a low noise amplifier a down-converter, an IF amplifier, and an IQ detector. The low noise amplifier is assumed to be perfect apart from the addition of thermal noise. The down-converter is similarly assumed perfect apart from the possibility of a residual carrier frequency resulting from a mismatch between the up- and down-converters. This residual frequency produces an additional term in the un-

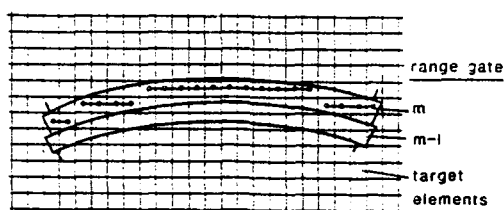


Fig. 14 Target element contribution to the m^{th} range bin return using signal generation secondary option partially accounting for range migration.

compressed radar pulse. The IF amplifier is characterised by a filter response and its non-linearities.

The filter characteristics can either be specified by the user in the form of a gain against input signal amplitude table or by an analytical expression.

After the IF amplifier comes the IQ detector. This is modelled with the following error sources:

- phase and amplitude errors,
- orthogonality error,
- DC offset,
- gain imbalance.

Receiver system phase noise can be introduced immediately prior to the IF amplifier. The receiver noise form (both phase noise and thermal noise from the low noise amplifier) follows either a uniform, Rayleigh, exponential, or normal distribution; in the case of the normal distribution an auto-correlation function can be specified. The auto-correlation function can either be linear, quadratic, exponential, Gaussian, or user supplied.

4.1.9 Analogue to Digital Conversion

The Analogue to Digital Converter (ADC) can be thought of as consisting of sampling and quantising operations. The sampling operation is inherent in the SRSIM model, as the analogue signal is represented by a set of discrete samples, each sample consisting of a (complex) pair of floating point numbers. The quantisation process then converts these floating-point numbers to a finite set of quantisation levels consisting of both positive and negative values. Values exceeding the largest quantisation level (ignoring sign) are set to this level. The number of overflows is counted. Quantisation of both the radar signal and transmitted chirp replica can be simulated. The quantiser itself can be specified in two forms:

1. The user specifies up to 14 threshold values and corresponding output levels.
2. The user specifies the number of bits n , thereby defining the number of quantisation levels $(2n)$. The optimum equally spaced symmetric quantiser is used as shown in Fig. 15.

The quantisation process consists of the following steps:

- 1) Scale the data and add a DC offset, if required. The scaling can either be user-specified or automatic. For automatic scaling, the maximum, mean or mean squared, of the samples in the first pulse, is adjusted (scaled) to be a user-specified fraction of the maximum

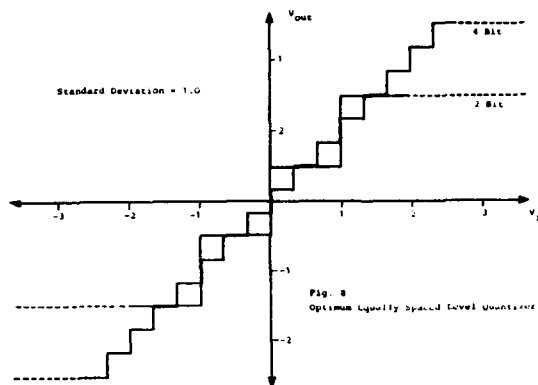


Fig. 15 Optimum equally spaced level quantiser.

quantisation threshold.

- 2) Quantise the data.
- 3) Rescale the data to compensate for scaling introduced in 1), if required.

4.1.10 Prefilter/Presummer

The purpose of the digital prefilter is to reduce the quantity of data to be transmitted or stored. The filter can operate either in the range or azimuth directions, or on the transmitted chirp replica.

The filter can either operate on both channels (full quadrature) or just on one (real) channel (non-quadrature) by setting the remaining (imaginary) channel to zero. The prefilter is assumed perfect apart from errors introduced by the finite word length within the digital filter. Word-length effects (both before and during the filter) may be simulated by specifying the number of bits available in the digital filter registers.

4.1.11 Datalink

The datalink between the on-board system and ground based processor can either take the form of a telemetry link (satellite SAR) or a High Density Digital Tape (aircraft SAR). The model restricts the datalink simulation to allowing the user to specify a link transmission word length and then simulating bit errors over the link. The bit errors can either be stochastic, where the spacing between bit errors is a random variable drawn from an exponential distribution, or deterministic, where a user-specified cyclic table (of up to 50 values) is used to determine the distance between one bit error and the next. The setting of the bit in error is switched. The datalink is simulated by the following algorithm:

1. Scale and quantise the data to the relevant link transmission word length, if necessary. The scaling factor must be defined by the user.
2. Insert bit errors.
3. Rescale the data to compensate for scaling introduced in (1), if required.

4.1.12 Processing

For a frequency modulated or "chirped" pulse, the first step in the SAR processing is to remove the frequency modulation. This is known as range processing and can either be performed on-board in the analogue system using a direct replica of the

transmitted pulse, or, on-ground using either a replica or theoretical values for the reference function generation. As far as the simulation model is concerned, the difference in these two approaches to range processing is apparent only in the fact that the range processing simulation has two possible positions in the radar data chain (Fig. 10). Range processing can either be performed immediately prior to the ADC (on-board analogue range compression), or immediately after the datalink (on-ground digital range compression). It would also be possible to simulate on-board digital range compression if required.

The first step in the range processing is to generate a range reference function or copy of the transmitted pulse form. There are three ways of doing this:

1. Ideal replica. A copy of the transmitted pulse form used in the transmitter segment is generated.
2. Standard reference function. The possible forms of the reference function correspond to those possible for the transmitted pulse, i.e. linear FM, quadratic FM and binary phase encoded. The user must specify the appropriate reference function parameters.
3. User-specified reference function.

Once the range reference function has been generated it is conjugated, and then used in the compression. It is also possible to specify a reference function weighting. Compression can either be performed in the frequency or time domain. For frequency domain compression, the reference function and signal must first both be transformed to the frequency domain, multiplied together, and then inverse transformed back to the time domain.

For time domain compression, it is necessary to directly correlate the reference function with the signal. Two methods of time domain correlation are possible in the simulation model: the overlap add technique and overlap save technique. These techniques are specially designed for the case where one function (reference function) is considerably shorter than the other (range line), and are fully described in [7].

After range processing, the radar data on disk must normally be re-ordered before the range migration correction and azimuth processing can be performed. Up until this point the radar data file has consisted of successive range lines or azimuth bins. The azimuth processing requires the data are ordered so that the data file consists of successive azimuth lines or range bins. This process is called corner turning.

Range migration is caused by the fact that the distance (hence time delay) to a target cell changes as the target cell moves through the beam. This is due to earth rotation, curvature of the earth, and the ellipticity of the orbit. The end result is that the response from one target cell is not in one range bin, but split into bands over several range bins. Therefore, before the radar can be processed in the azimuth direction, it is necessary to re-order the data so that the response from one target cell is observed only in one range bin (Fig. 16). This must be repeated for each pulse and across the swath, and can involve some form of interpolation. Range migration itself can be split into two components: a linear component (range walk) representing the difference in range to a target cell between when it enters the beam and when it leaves the beam, and a higher-order terms component (range curvature). The simulation model has an algorithm to correct for only the linear

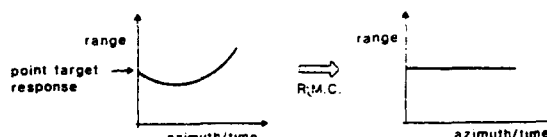


Fig. 16 Range Migration Correction.

migration effects in the time domain.

For each range bin in turn, the range walk for a target cell is calculated and applied. The range walk is calculated by considering the range history used in the azimuth reference function generation, and so the range walk function is updated whenever the azimuth reference is updated.

The feature that distinguishes SAR from other imaging radar systems is its ability to achieve high azimuth resolution through coherent integration of the returned radar signal. As a target cell passes through the beam the phase of the returned signal changes, and this can be picked out by convolving the (azimuth) returned signal with the appropriate reference function. The convolution can be performed in one, or split into segments (subapertures or looks), each segment being convolved separately. The resulting looks are detected (amplitude taken) and summed to give, what is commonly called, a multi-look image. The simulator can perform all these operations, starting with the azimuth reference function generation.

The following reference functions can be generated, either as one reference function (single look processing) or as several subaperture reference functions (multi-look processing):

1. Curved Earth Time Invariant: the same phase history is assumed to apply to all target cells in a given range bin. The user must specify the bin number before the reference function can be calculated.
2. Flat Earth Time Varying: the phase history for an individual target cell is calculated. The user must specify the coordinates of the target cell. This option allows several different azimuth reference functions to be convolved with each range bin, by generating reference functions for target cells with different azimuth coordinates within the bin.
3. Curved Earth Time Varying: as for option 2, but for curved earth geometry.

In all three of the above options the azimuth reference functions are generated for a particular range bin. The reference functions generated though, may be applied to all range bins, or alternatively updated (new reference function generated) every n range bins, as required, where n is specified by the user.

The platform geometry used in the azimuth reference function generation is, in the basic case, the same as that used in the returned radar signal generation, i.e. it is assumed that the platform position and attitude are exactly known. Errors can be simulated by generating a new platform data file, specifying different geometry and/or error values, this is then used for the reference function generation, or, more simply, by specifying geometrical or Doppler errors. In the case of geometric errors, the user specifies slant range and yaw angle errors, which are directly used in the reference function generation. For Doppler errors, it is necessary to convert the Doppler errors to equivalent range and yaw errors. Doppler errors

are specified in terms of a Doppler slope error (slant range error) and a mean Doppler error (yaw angle error). The azimuth reference function can be weighted.

Once the appropriate azimuth reference functions have been generated, it is necessary to convolve them with the range migration corrected signal data. It is possible to perform the azimuth processing in either the frequency or time domain, using exactly the same techniques and algorithms as in the range processing. After azimuth processing, the signal data are detected, that is the moduli (or moduli squared) of the complex values are taken, and, in the case of multi-look processing, the individual looks are summed. Word length effects in the summation can be simulated, and the summation can be weighted (for example to accommodate antenna gain pattern effects).

4.1.13 SARSIM Application Example

In this section an example of a satellite SAR simulation is given. The configuration of the system is based on that for the ESA Remote-Sensing satellite (ERS-1). Errors and noise sources within the system are not simulated in this example.

Fig. 17 shows the radar target used in the example simulation: a single point target on a non-reflecting background. Fig. 18 is a plot of the range compressed SAR data. Fig. 19 shows the final image plot of the single point target.

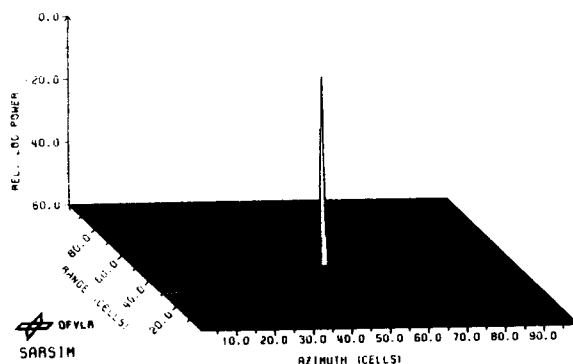


Fig. 17 Simulated point target

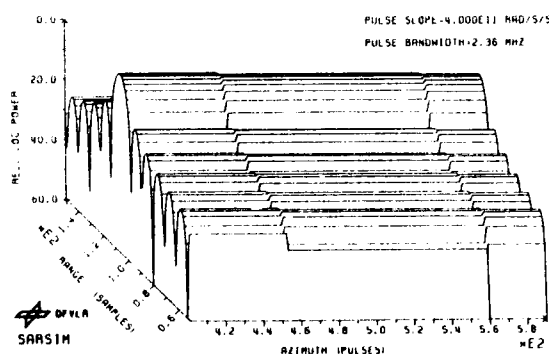


Fig. 18 Signal after range compression.

4.2 Simulator with Facet Backscattering Model

The two-dimensional reflection coefficient target model used in SARSIM is adequate for many applications, for example sensor investigations but it is very limited if scattering mechanisms of complex targets are to be examined. The facet backscattering model used in the SARAS simulator, developed by Naples University [8] models the target as a

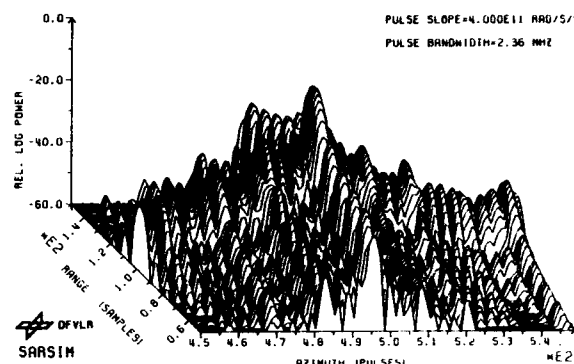


Fig. 19 Signal after azimuth compression.

series of small plates or facets enabling the target to be entered as a complex shape. The model is capable of handling hidden surfaces (radar shadows) and can generate polarimetric signatures, a feature of increasing interest for the next generation of SAR sensors.

5. CONCLUSION

Parametric analysis and simulation software packages for investigating SAR systems have been described and their merits discussed. The usefulness of simulators is often called into question as the cost and manpower invested can be large. It is, therefore, worth considering two applications of the SARSIM simulator.

In 1984, the ERS-1 project was faced with the problem that the coverage of the synthetic aperture radar mode of the Active Microwave Instrument known as the 'wave' mode was found to be marginal for the application it was designed for. The wave mode images small areas of the ocean surface, the data being stored on-board the satellite to achieve global coverage. From the images, the ocean wave spectrum was to be derived by generating the two-dimensional Fourier power spectrum. The limited storage capacity of the recorder meant that the imaged area was limited to approx 2×5 km. This area was found to be too small to detect long waves.

The only practical solution was to reduce the amount of recorded data by halving the number of bits used for quantising each SAR data sample from 4 bits I/4 bits Q to 2 bits I/2 bits Q. Analysis showed that quantisation noise would be acceptable, but would sufficient information be retained to derive the wave spectrum?

The problem was analysed using SARSIM [9]. An ocean scene was simulated (Fig. 20) and the image (Fig. 21) used to generate the power spectrum (Fig. 22). Analysis of the latter showed the wave spectrum was still reproducible. The new quantisation scheme was introduced and today the ERS-1 satellite has a coverage of 5×5 km in the wave mode.

The above example shows how simulation can remove final doubts even if analysis of the problem is successful.

Another example also concerns quantisation noise. When plotted against input signal power, the quantisation noise shows a distinct minimum increasing at low powers, due to the discrete quantisation steps and at high powers, due to saturation (see Fig. 23 and Fig. 24). These curves were derived theoretically [10] (dotted) and SARSIM was used to confirm the results. The simulation results are joined by dashed lines.

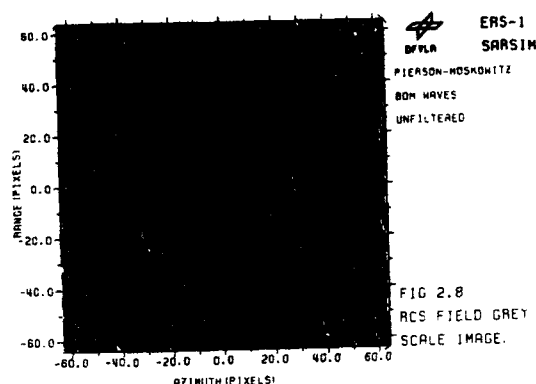


Fig. 20 Simulated ocean wave scene.

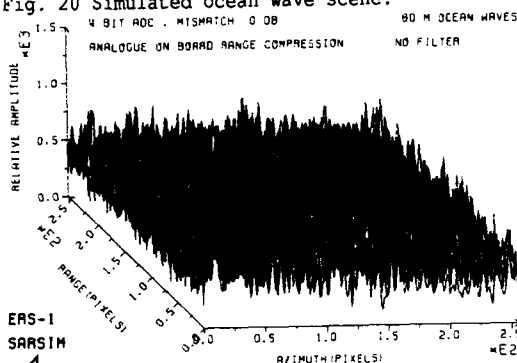


Fig. 21 SAR image of the scene in Fig. 23.

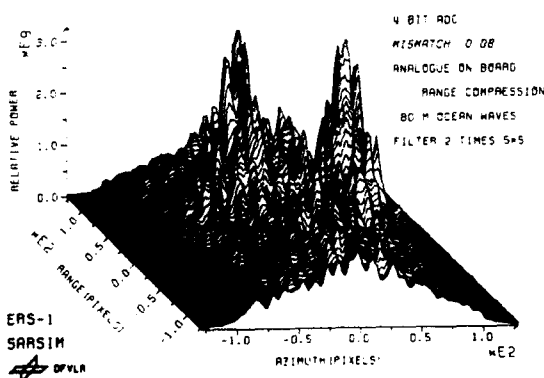


Fig. 22 Fourier spectrum of the image in Fig. 24.

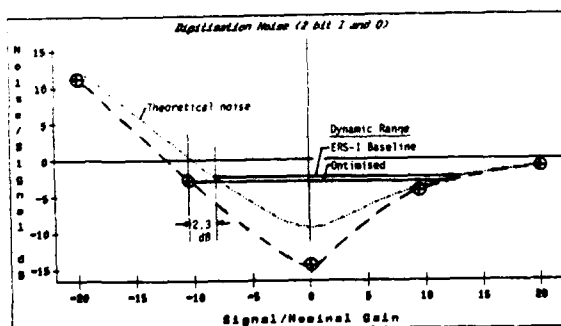


Fig. 23 2-bit quantisation noise curve.

For both the 2 bit case (Fig. 23) and the 5 bit case (Fig. 24), the simulated values are much less than the theoretical results. An at least partial explanation of this is the non-white nature of quantisation noise [11] and the influence of the

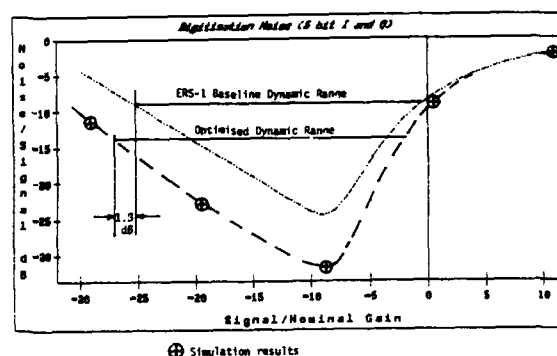


Fig. 24 5-bit quantisation noise curve.

matched filters in the SAR processor. This is an example of simulation throwing up surprises and leading to further investigations.

6. REFERENCES

- [1] Hounam, D. Pierschel, D. Derivation of the Technical Specification of the ERS-1 Active Microwave Instrument to Meet the SAR Image Quality Requirements. Proc. of IGARSS '87 Symp., Ann Arbor, 18-21 May 1987.
- [2] Chorherr, G. Hounam, D. IMPRES, A Program to Generate the Impulse Response of a Synthetic Aperture Radar. DLR-IB 551-3/92.
- [3] Hounam, D. Potter, S. Schmid, R. Algorithms and Software User Guide for the Performance Estimation of Synthetic Aperture Radars. DLR-IB 551-4/92.
- [4] Pike, T.K. SARSIM: A Synthetic Aperture Radar System Simulation Model. DFVLR-Mit. 85-11.
- [5] Pike, T.K. Analysis of ERS-1 SAR Performance through Simulation. Proc. IEEE '86 National Radar Conf., Los Angeles, March 12-13, 1986, pp. 12-18.
- [6] Krul, L. Principles of Radar Measurement. Proc. EARSel Radar Calibration Workshop, Alpbach, Austria, December 1982, ESA SP-193, pp. 11 - 20.
- [7] Rabiner, L.R. Gold, B. Theory and Application of Digital Signal Processing. Englewood Cliffs, NJ: Prentice Hall 1975.
- [8] Franceschetti, G. Migliaccio, M. Riccio, D. Schirinzi, G. SARAS: A Synthetic Aperture Radar (SAR) Raw Signal Simulator. IEEE Transaction on Geoscience and Remote Sensing Vol. 30, No. 1, Jan. 1992.

- [9] Wolfram, A.P.
Pike, T.K.

Quantization Study for ERS-1
Wave Mode.
DFVLR Research Report,
DFVLR-FB 84-39, October
1984.
- [10] Sappl, E.

An Optimal Quantisation of
Coherent Radar Echoes from
Terrain or Sea Surface.
DFVLR, Institut für Hoch-
frequenztechnik, Report,
Sept. 1984.
- [11] Li, F.
Held, D.
Honeycutt, B.
Zebker, H.

Simulation and Studies of
Spaceborne Synthetic Aper-
ture Radar Image Quality
with Reduced Bit Rate.
15th International Sympo-
sium on Remote Sensing of
the Environment, Ann Ar-
bor, May 1981.

Multi-Frequency Multi-Polarization Processing for Spaceborne SAR

J.C. Curlander and C.Y. Chang
 Jet Propulsion Laboratory
 California Institute of Technology
 4800 Oak Grove Drive
 Pasadena, Ca 91109
 United States of America

Abstract

The Shuttle Imaging Radar-C (SIR-C) is the third in a series of space shuttle based synthetic aperture radars (SAR) sponsored by the National Aeronautics and Space Administration (NASA). The SIR-C ground data processing system is to process the playback SAR signal data into a variety of data products for distribution to the science community. This paper presents an overview of the end-to-end ground data processing system with emphasis on the unique characteristics involved in the system design. Included in the discussion are science requirements, radar system specifications, input data format specifications, system operations design, data products design, processing algorithm design, hardware architecture design and software design.

1. INTRODUCTION

The Shuttle Imaging Radar-C (SIR-C) will for the first time provide simultaneous data acquisition of eight radar channels (two radar frequencies: L and C, each comprised of two like-polarized and two cross-polarized channels) from a spaceborne synthetic aperture radar (SAR) [Curlander, 91a], [Curlander, 91b], [Jordan, 91]. This instrument is accompanied by a VV-polarized, X-band SAR (X-SAR) which will operate simultaneously with SIR-C. The SIR-C/X-SAR is currently scheduled for three space shuttle flights, the first being in late 1993. Each flight is planned for a six to eight day data acquisition period. Table 1 summarizes the SIR-C science requirements on the image quality of output products.

Table 1: SIR-C science requirements on the image quality of output data products.

Resolution broadening	$\leq 20\%$
Integrated Sidelobe Ratio	≤ -14 dB
Peak Sidelobe Ratio	≤ -17 dB
Ambiguity to Signal Ratio	≤ -20 dB
Swath Width	15 Km to 90 Km
Radiometric Accuracy (Science Goal)	
- Relative Cross-Swath (1σ)	± 1.0 dB
- Relative Band-to-Band (1σ)	± 1.5 dB
- Relative Channel-to-Channel (1σ)	± 1.0 dB
- Absolute Each Channel (3σ)	± 3.0 dB
- Phase Error	$\leq 10^\circ$
Geometric Accuracy (3σ)	
- Absolute Location	≤ 100 m
- Channel-to-Channel Registration Error	$\leq 1/8$ pixel
- Scale error	$\leq 0.1\%$
- Skew error	$\leq 0.1\%$

ucts. Table 2 shows the orbit characteristics and the radar specifications.

This paper presents the system design of the SIR-C ground data processor, which is being developed at the Jet Propul-

Table 2: SIR-C orbit characteristics and radar specifications.

SAR Orbit	
- Nominal Altitude	215 \pm 25 Km
- Eccentricity	$\leq 0.002^\circ$
- Inclination	57°
Attitude Measurement Error(3σ)	
- Roll	$\pm 1.24^\circ$
- Yaw	$\pm 1.43^\circ$
- Pitch	$\pm 1.78^\circ$
Attitude Drift Rate Error(3σ)	
- Roll	$\pm 0.03^\circ/\text{sec}$
- Yaw	$\pm 0.03^\circ/\text{sec}$
- Pitch	$\pm 0.03^\circ/\text{sec}$
Transmitter frequency	
- L-Band	1.25 GHz
- C-Band	5.30 GHz
Polarization	HH, HV, VH, VV
Pulse bandwidth	20, 10 MHz
Pulse duration	33.8, 16.9, 8.44 μsec
Sampling rate	45, 22.5 MHz
Data quantization format	4-bit, 8-bit, (8,4) BFPQ
Pulse Repetition Frequency	1344, 1395, 1440, 1488, 1512, 1620, 1674, 1736 Hz
Antenna Dimension	
- L-Band	12.1 m x 2.8 m
- C-Band	12.1 m x 0.74 m
Incidence Angle	17° to 63°

sion Laboratory (JPL) under contract with NASA [Curlander, 91b]. There are two European space agencies working on the X-SAR processor development: the German Aerospace Research Establishment (DLR) and the Italian Space Agency (ASI) [Runge, 90].

The major challenge to the SIR-C processor design is to cope with a large number of radar modes. Nominally the SIR-C science team has selected seventeen data acquisition modes from all the possible combinations with eight radar channels (See Table 3), two pulse bandwidths and three data quantization formats. Additionally, data will be collected in two nominal attitudes over incidence angles from 17° to 63° with a variety of antenna elevation patterns controllable to provide beam spoiling at the steep incidence angles. The large number of radar modes complicates the logics in handling different types of data format and increases the scope of testing the integrated processor software.

The second challenge to the SIR-C processor design is to cope with the large attitude uncertainties and high attitude drift rates of the space shuttle platform as shown in Table 2. The large attitude uncertainties create PRF ambiguity problem in Doppler centroid estimation and large Doppler errors for data acquired over high terrain relief areas. Special techniques (multiple PRF technique and attitude steering technique, respectively) are required to resolve the problems [Chang, 92a], [Chang, 92b]. The high attitude drift rates induce fast Doppler drifts in both cross-track and along-track dimensions. Frequent Doppler update is required to maintain the image quality, which complicates the geometric rectification procedure to produce a seamless image.

The third challenge to the SIR-C processor design is to produce radiometrically calibrated and geometrically registered

multi-band, polarimetric SAR image [Freeman, 89], [Klein, 92]. For radiometric calibration, the built-in-test-equipment (BITE) data are designed for probing the health of the antenna, receive only noise data for estimating the noise power, calibration tone signal for monitoring the receiver gain and temperature measurements and T/R module failure information transmitted via the downlink telemetry. These ancillary data and calibration site data are essential to derive radiometric calibration parameters which are applied during the data processing to produce calibrated image product. For geometric registration, special consideration is required in the processor design to ensure that the output images are registered in both cross-track and along-track dimensions.

The remaining paper presents an overview of the SIR-C end-to-end ground data processing system design, which includes input data format specifications, system operations design, data products design, processing algorithm design, hardware architecture design and software design. At the end of the paper, we give a brief summary of the status and plan for the processor development.

2. INPUT DATA FORMAT

The signal data is recorded across four recorder channels on the High Density Digital Cassette (HDDC). The data rate for each recorder channel is 45 Mbps for a total of 180 Mbps. The signal data is quantized into one of three types of format: 4-bit, 8-bit or (8, 4) block floating point quantization (BFPQ). Nominally, the data is collected over a period called data take using the same set of commanded radar parameters. The length of the data take varies from 3 minutes to as long as 15 minutes for ocean site data. The average length is estimated to be between 4 and 5 minutes.

The nominal SIR-C data take consists of a turn-on sequence, followed by the science data collection and a turn-off sequence as shown in Figure 1. The first four seconds of the turn-on sequence consist of (one second each): receive only noise data, caltone scan data, low noise amplifier (LNA) BITE data and high power amplifier (HPA) BITE data. These four second data are used for radiometric calibration. The remainder of the turn-on sequence consists of one second of PRF_A data and one second of PRF_B data which together with the first second of PRF_C data are used for resolving PRF ambiguity in estimating the Doppler centroid frequency [Chang, 92a]. The system remains on PRF_C for collection of the science data. The turn-off sequence is similar to the turn-on sequence in that the science data collection is followed by one second each of PRF_B and PRF_A . The last four seconds of the turn-off sequence are receive only noise data.

Table 3: SIR-C radar data acquisition modes.

MODE	CHANNEL-1	CHANNEL-2	CHANNEL-3	CHANNEL-4
1	LH	LH	LH	LH
2	LV	LV	LV	LV
3	CH	CH	CH	CH
4	CV	CV	CV	CV
5	LH	LH	LV	LV
6	CH	CH	CV	CV
7	LH	LH	CH	CH
8	LV	LV	CV	CV
9	LH	LV	CH	CV
10	LV	LV	CH	CV
11	LH	LV	CH	CV
12	LV	LV	CH	CV
13	LH	LV	CH	CV
14	LH	LV	CH	CV
15	CH	CV	CH	CV
16	LV, LH	LV, LV	CH, CH	CV, CV
23 Tape 1	LH	LV	LH	LV
23 Tape 2	CH	CV	CH	CV

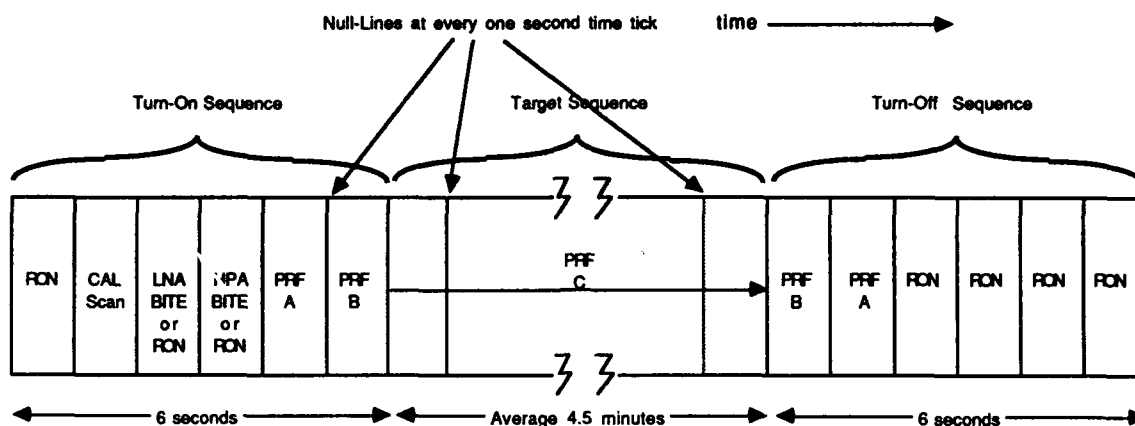


Figure 1: SIR-C input data run format. Each segment in turn-on and turn-off sequence is 1 second duration.

RON: Receive Only Noise, LNA: Low Noise Amplifier, HPA: High Power Amplifier, CAL scan: Caltone Scan.

At every one second time tick, a null-line is inserted. The null-line is obtained by setting a half of the phase array elements with a 180° phase difference to create a null around the center of the antenna elevation pattern. The null-line is used to estimate the shuttle roll angle drift.

A sinusoid waveform, called the calibration tone (caltone) signal, is injected in the receiver electronics and recorded together with the return echo data. The caltone is used to estimate the receiver gain change as the temperature varies.

3. SYSTEM OPERATIONS DESIGN

Operations of the SIR-C processor is comprised of two main phases: phase 1 survey processing and phase 2 standard processing, which last for a total of one year. During the phase 1 operations, a quick-look survey processor is employed to process single-frequency band, single-polarization channel data into low resolution strip images. These survey images will cover all the SIR-C ground sites albeit with a single radar channel. By-products of the survey processor include unambiguous Doppler centroid estimates history and roll angle estimates history. Additionally, during the phase 1 operations, some selected data segments (covering calibration sites) will be processed into single-look, full-resolution complex imagery. These data will be analyzed to derive the parameters used for antenna pattern generation and polarimetric calibration. These parameters will be applied during the phase 2 standard processing to produce phase and amplitude calibrated data products [Freeman, 89], [Klein, 92].

The system operations schedule is planned as follows. Six weeks are allocated for processor check-out upon receipt of the first signal data tape. Phase 1 operations will begin following the completion of the processor system check-out and last for a period of twelve weeks. This is followed by phase 2 operations for a period of forty weeks.

4. DATA PRODUCTS DESIGN

The SIR-C output data products include three image products: survey image, standard multi-look image and standard single-look image; and one reformatted signal data product. The throughput requirements are to produce 24 survey image products per week during the phase 1 operations and to produce 9 standard multi-look image, 1 single-look image and 1 reformatted signal data products per week during the phase 2 operations. The expected processor throughput far exceeds the requirements.

The survey image is a 4-look, single-polarization strip image, stored in the byte amplitude format. The image is deskewed to zero-Doppler and resampled to the ground range domain with a 50 meter pixel spacing. The resolution is approximately 100 meters. The length of the survey image is equal to the length of the data take. The average length is approximately 4.5 minutes or 2000 Km. The survey image will be recorded on Alden thermal prints and CD-ROMs. The CD-ROMs will be distributed to all the principal investigators (PIs).

The standard multi-look image is a multiple look, polarimetric (single-, dual- or quad-polarization) frame image. The image is deskewed to zero-Doppler and resampled to the ground range domain with a 12.5 meter pixel spacing. The azimuth resolution is chosen to be 25 meters. The range resolution is chosen to be 25 meters or the natural resolution if greater than 25 meters. The image data is stored in a compressed cross-product format [Dubois, 89]. The basic frame size is chosen to be 100 Km. The image will be recorded on Kodak prints and CEOS formatted tapes.

The standard single-look complex image is a single-look, polarimetric (single-, dual- or quad-polarization) frame image. The image is processed to full-resolution, deskewed to zero-

Doppler and presented in the slant range domain in natural pixel spacing. The image data is stored in a compressed scattering matrix format. The basic frame size is chosen to be 50 Km. The image will be recorded on CEOS formatted tapes and a reduced, detected image will be printed by the Kodak printer.

The reformatted signal data contains the signal data reformatted in the range line byte format. The signal data together with the decoded radar parameters will be stored on CEOS formatted tapes.

5. PROCESSING ALGORITHM DESIGN

5.1 Survey Processing Algorithm

The SIR-C survey processor utilizes a burst mode processing algorithm [Sack, 85], [Curlander, 91b]. The algorithm flow chart is shown in Figure 2. The survey processor is designed to process an entire data take into a strip image in approximately one-seventh the real time data collection rate. To attain high throughput rate, the data is bursted in azimuth (slow time) with a one-quarter duty cycle factor. The data volume is further reduced by a factor of four in range (fast time) by processing the data using only one-quarter of the range chirp bandwidth. The azimuth compression

is performed using the spectral analysis (SPECAN) algorithm which requires fewer azimuth FFT's than the traditional matched filtering algorithm. Following azimuth compression, radiometric correction is applied to compensate for the along-track radiometric modulation. This is followed by a geometric rectification step that resamples the slant range-Doppler image into the ground range cross-track and along-track domain. The rectified burst images are then overlaid to produce the final multi-look strip image.

For the survey processor, the initial Doppler centroid frequency is determined using a clutterlock routine and a ambiguity resolution technique that requires a multiple PRF data collection at the start of each data take [Chang, 92a]. The unambiguous Doppler centroid frequency is then tracked by a burst mode clutterlock algorithm during the data processing. The Doppler frequency rate is solely derived from the ephemeris parameters. Analysis results show that the accuracy of the ephemeris is sufficient for generation of survey products without employing the autofocus routine.

5.2 Standard Processing Algorithm

Prior to standard processing, preprocessing is employed to iteratively refine the Doppler centroid frequency and the Doppler frequency rate estimates using clutterlock and autofocus techniques [Li, 85]. Doppler centroid frequency is estimated from the azimuth spectrum by locating the energy centroid. Doppler frequency rate is estimated from the look registration error by azimuth cross-correlating the look-1 and look-4 images obtained by spectral division. Identical Doppler parameters are used for processing all polarimetric data channels to ensure the phase coherency required for the polarimetric data analysis. This approach will result in some increase in azimuth ambiguities if the antenna beams are not exactly aligned.

The range-Doppler processing algorithm (i.e., the rectangular algorithm) with secondary range compression and frequency domain range cell migration compensation was selected by SIR-C for standard processing [Wu, 82], [Jin, 84], [Curlander, 91a]. The algorithm flowchart is shown in Figure 3. The range compression and azimuth compression matched filtering operations are performed using the frequency domain fast convolution technique. All the signal data, independent of the final products, are initially processed to single-look, complex imagery using the full azimuth processing bandwidth. This is followed by an azimuth deskew operation where the resulting deskewed, single-look complex image is then radiometrically corrected.

Following standard processing, postprocessing is employed to generate the final image product [Curlander, 91b]. Data

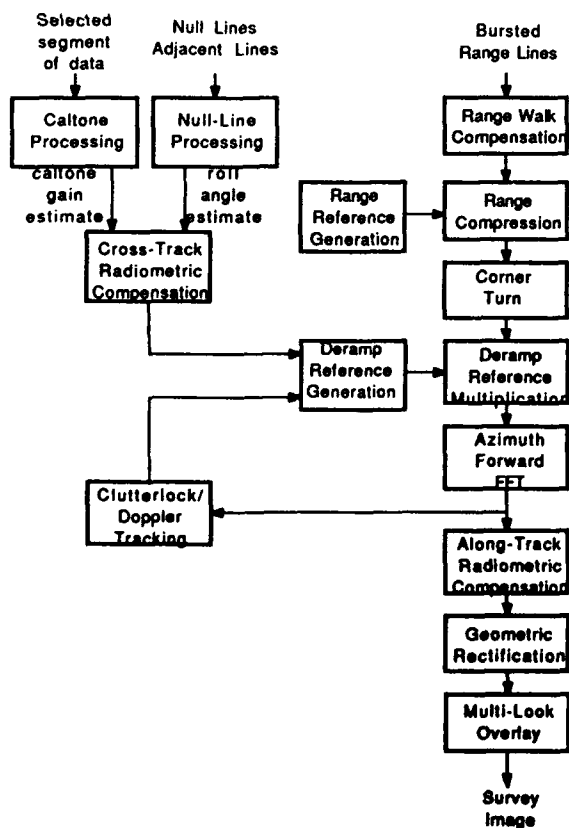


Figure 2: Survey processing algorithm flowchart.

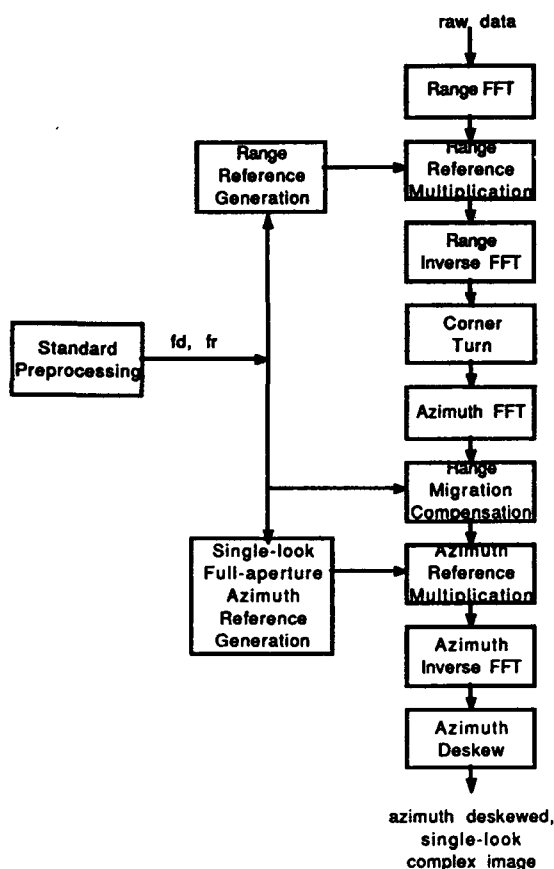


Figure 3a: Standard processing algorithm flowchart.

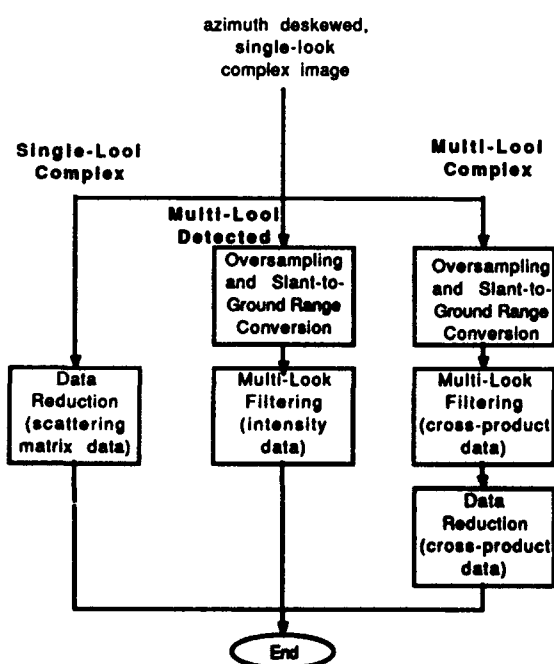


Figure 3b: Standard postprocessing algorithm flowchart.

reduction is the only postprocessing function for generation of single-look image products, where the data reduction function is applied to the scattering matrix. Major postprocessing functions for generation of multi-look image products include cross-product generation, multi-look filtering and data reduction where the multi-look filtering combines multi-looking as well as geometric rectification functions. For SIR-C, all the multi-look images will be filtered to a 25 m resolution in azimuth and a 25 m or natural resolution in range. The pixel spacing is selected to be 12.5 m in both range and azimuth. The filtering is applied to the cross-products. The data reduction function is then applied to the multi-look filtered cross-products data.

6. HARDWARE ARCHITECTURE DESIGN

Figure 4 shows the hardware architecture design of the SIR-C ground data processor. The entire processor system is composed of seven subsystems. The Data Transfer Subsystem (DTS) performs raw data reformatting and line synchronization. The SAR Correlator Subsystem (SCS) processes the SAR signal data into survey and standard image data. The Output Products Subsystem (OPS) performs image data reformatting, recording and display. The Control Processor Executive (CPX) controls the processing sequence of the above three subsystems. The Catalog Subsystem (CAS) stores the information concerning the processing request and processor status into database. The Calibration Subsystem (CAL) is used for generation of calibration parameters and analysis of calibration site image quality. The Radar Data Center (RDC) archives all the output data products.

The SCS consists of a STAR array processor with three computational modules, an Alliant FX/8 mini-supercomputer with eight compute elements and an Alliant FX/2800 mini-supercomputer with twelve i860-based CPU's. The STAR array processor is the main compute engine for survey processor. Its FFT performance is measured at 120 MFLOPS using three computational modules. The Alliant FX/8 is primarily used for standard postprocessing functions. Its aggregate FFT performance nears 20 MFLOPS. Two SKYBOLT accelerator boards are installed to speed up the FX/8 computer, which provide additional 100 MFLOPS compute power. The FX/2800 is the main compute engine for standard processor and standard preprocessor. Its aggregate FFT performance is measured at over 300 MFLOPS. Computational tasks are distributed over computers for concurrency processing in order to provide maximum processor throughput.

The DTS consists of a high density digital recorder, a DEMUX and two data quality analyzers (DQA). The DEMUX is used for selection of recorder channel for data processing. The DQA is used for line synchronization and verifying the

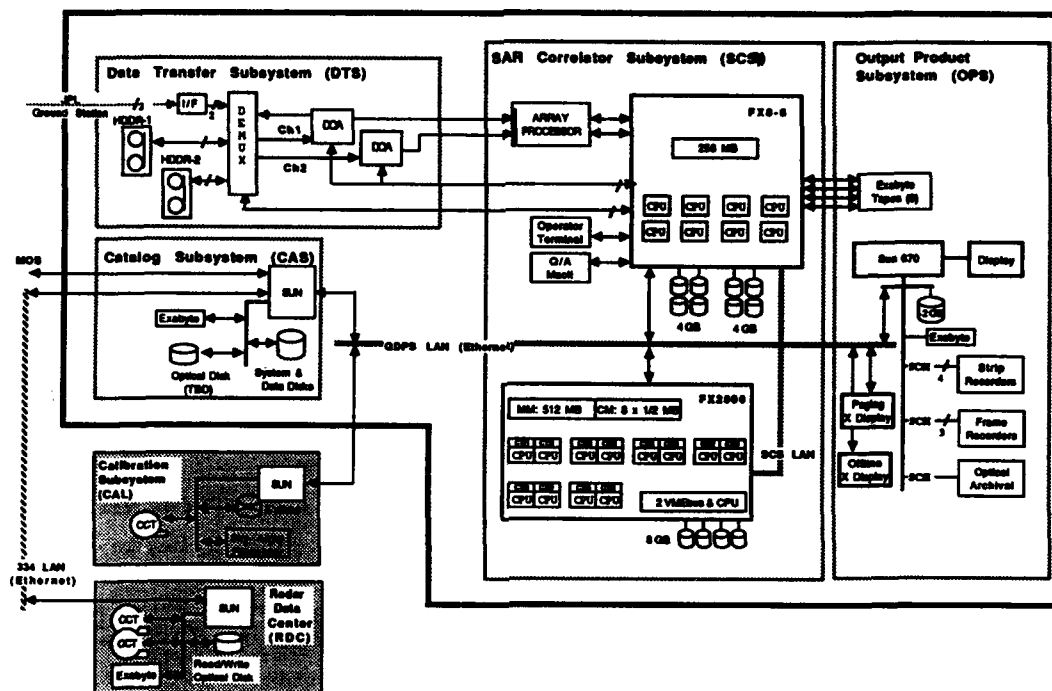


Figure 4: SIR-C ground data processing system hardware architecture.

data quality and integrity. The OPS consists of Exabyte tape drives, Alden thermal printers and Kodak color printers. Three subsystems, OPS, CAS and CAL, run on three separate SUN Sparc workstations. The image display and operator interface display are handled via X-terminals.

7. SOFTWARE DESIGN

There are a variety of software packages used for developing the SIR-C processor due to the need of specific applications. The major part of the signal processing software is written in FORTRAN while the input and output formatting software is written in C. The image display software is developed using X-library routines. The operator interface software is developed using a graphics user interface software called Teleuse which runs on top of MOTIF. The image annotation is created using a commercially available software package called PV-WAVE. The catalog subsystem software uses both FORTRAN and INGRES.

8. SUMMARY

Design and implementation of the SIR-C ground data processing system is quite a challenge due to the large number of radar modes and the large attitude errors/high attitude drift rates. In addition to the correlation software, there are many software programs required for deriving parameters from the ancillary data in order to ensure that the output image products are radiometrically calibrated and geomet-

rically registered. Another challenge to development of this large software based system is its complex interfaces among the many software programs. Clear interface definitions are essential to successfully deliver the operational system on schedule.

Currently, we are in the middle of developing all the processor software. Major computer hardware will be installed by summer 1992. The end-to-end system integration will take place in early 1993. The entire system is scheduled to begin operations in late 1993.

Development of the SIR-C processor inherits a great deal of experience from the previous and existing spaceborne and airborne SAR processors, such as SEASAT, SIR-B, and JPL AIRSAR. Experience accumulated from the SIR-C processor will certainly benefit future processor design and development, such as EOS SAR and RADARSAT.

ACKNOWLEDGEMENTS

The research described in this paper was performed at the Jet Propulsion Laboratory, California Institute of Technology, under the contract with the National Aeronautics and Space Administration.

REFERENCES

- [Chang, 92a] C.Y. Chang and J.C. Curlander, "Applications of the Multiple PRF Technique to Resolve Doppler Centroid

Estimation Ambiguity for Spaceborne SAR, " IEEE Transactions on Geoscience and Remote Sensing, September 1992.

[Chang, 92b] C.Y. Chang and J.C. Curlander, "Attitude Steering for Space Shuttle Based Synthetic Aperture Radar, " Proceedings of 1992 International Geoscience and Remote Sensing Symposium, Houston, May 1992.

[Curlander, 91a] J.C. Curlander and R.N. McDonough, Synthetic Aperture Radar: Systems and Signal Processing, John Wiley and Sons, 1991.

[Curlander, 91b] J.C. Curlander and C.Y. Chang, "Techniques in Processing Multi-Frequency Multi-Pol. Spaceborne SAR Data, " European Transactions on Telecommunications, Vol. 2, No. 6, pp. 605-617, November 1991.

[Dubois, 89] P.C. Dubois, et al, "Data Volume Reduction for Imaging Radar Polarimetry, " IEEE International Symposium on Antennas and Propagation, 1989, Vol III, pp.1354-1357.

[Freeman, 89] A. Freeman and J.C. Curlander, "Radiometric Correction and Calibration of SAR Images, " Photogrammetric Engineering and Remote Sensing, Vol. 55, No. 9, September 1989, pp. 1293-1301.

[Jin, 84] M. Jin and C. Wu, "A SAR Correlation Algorithm which Accommodates Large Range Migration, " IEEE

Transactions on Geoscience and Remote Sensing, Vol. GE-22, No. 6, November 1984, pp. 592-597.

[Jordan, 91] R. Jordan, B. Huneycutt, M. Werner, "SIR-C/X-SAR Synthetic Aperture Radar Systems, " Proceeding of the IEEE, Vol 79, No. 6, pp. 827-838, June 1991.

[Klein, 92] J.D. Klein, "Calibration of Complex Polarimetric SAR Imagery Using Backscatter Correlations, " IEEE Transactions on Aerospace and Electronic System, Vol. 28, No. 1, pp. 183-194, January 1992.

[Li, 85] F. Li, D. Held, J.C. Curlander, and C. Wu, "Doppler Parameter Estimation for Spaceborne Synthetic Aperture Radars, " IEEE Trans. on Geoscience and Remote Sensing, Vol. GE-23, No. 1, January 1985, pp. 47-56.

[Runge, 90] H. Runge and R. Bamler, "X-SAR Precision Processing, " Proceedings of the International Geoscience and Remote Sensing Symposium, College Park, Maryland, May 1990.

[Sack, 85] M. Sack, M.R. Ito, and I.G. Cumming, "Application of Efficient Linear FM Matched Filtering Algorithms to Synthetic Aperture Radar Processing, " IEE Proceedings, Vol. 132, Pt. F, No. 1, February 1985, pp. 45-57.

[Wu, 82] C. Wu, K.Y. Liu, and M. Jin, "Modeling and a Correlation Algorithm for Spaceborne SAR Signals, " IEEE Trans. on Aerospace and Electronic Systems, Vol. AES-18, No. 5, September 1982, pp. 563-575.

INVERSE SYNTHETIC APERTURE RADAR

J.P. Hardange
Thomson-CSF

178, Bd Gabriel Péri
92242 MALAKOFF Cedex
FRANCE

1. OBJECTIVES AND APPLICATIONS

ISAR is a technique, based on time and Doppler frequency analysis, which is used for imaging of targets having rotational motions with regard to the radar. In the sixties, observation of the Moon and planets by a radar located on the Earth was one of the first applications (Ref. 1, 2 chapter 33). Closely derived from these first trials, imaging of objects in terrestrial orbit by ISAR techniques is performed with interesting results (Ref. 3).

However, the most current domains of application of ISAR are now measurements of targets signatures and target recognition.

The objective of the first one is to measure the complex reflectivity of each reflecting point of a target. Although the processing has to compensate for various degrading effects of the image quality, it is in general the most simple case, as far as the conditions of the experiment can be perfectly mastered. This happens if the target can be put on a turntable for the analysis (Ref. 5). The result of the analysis is a two dimensional (2-D) image of the distribution of the reflecting points. The two dimensions are range and cross-range in a fixed plan.

The second application has been subject to numerous studies and experiments in the field of aircraft classification from a ground based radar (Ref. 4, 7, 8, 13, 14). 1-D (cross-range only) and 2-D principles have been tested. ISAR has been envisaged to equip air defence radars and eventually airborne fire control radars with a non-cooperative target recognition mode.

In the same domain, the most demanding configuration is obtained when the radar and the target are moving simultaneously, and when their relative position and velocity can be described only with the help of an analysis of the returned radar signal itself. This is the case of ship imaging with an airborne radar (Ref. 11, 16). In this case, the particular behaviour of ships at sea allows the production of 3-D images: range, azimuth and height.

2. HOW TO GET THE IMAGE ?

Let us consider a conventional radar, in which the receiver is matched to a single pulse return, that is to say to a very short observation time. In this case, it is

well known that the resolution in range is inversely proportional to the bandwidth of the received waveform. The coherent processing is too short in time to allow any resolution in Doppler frequency (Ref. 2 p. 3-18).

If several targets are located in the beam in the same range cell, they cannot be resolved. Furthermore, there is no information at all about their range rate, acceleration, rotational motions, etc... The conventional radar is basically a mono-dimensional range-only sensor. Specific means have to be added to give to the radar the ability to provide the position in azimuth and height of the target, and all the parameters listed above.

To try to get all these informations, the principle is to realize a filter which is matched to a long time observation of the target. In these conditions, the Doppler frequency can be analysed, providing an additional dimension to the image.

One question is here to recognize the axis which corresponds to this Doppler analysis: Is it the azimuth? Is it the height? Is it something other? This requires some knowing about the conditions of observation. If the axis of rotation of the target is known, like in the case of an object put on a turntable, it is shown in paragraph 4 that the dimension which is measured by the

Doppler analysis is a cross-range axis, in a plane orthogonal to the axis of rotation of the target.

Generalizing this remark, one can realize a reception filter which is matched to a longer and longer analysis. Several terms of the conventional ambiguity function, which are negligible for a short or medium analysis time, become preponderant. The output of the filter is not only a function of time and Doppler frequency, but also of derivatives of the Doppler frequency: Doppler rate, Doppler acceleration, etc... It is a generalized ambiguity function (Ref. 2 pp. 3-14 and 3-15).

The output of this long time matched filter is a function depending of 2, 3 or more parameters. Through an a priori knowing of the behaviour of the target, it can be possible, in some particular cases, to establish a relation between each parameter of the ambiguity function and an axis of analysis of the target: Range, azimuth, height. As an example, a relation between the parameters of the generalized ambiguity

function and the two cross-range axis of a target is established in paragraph 6 in the case of ship classification.

2.1. Doppler Frequency

The expression of the Doppler frequency is well-known, but is established again in this paragraph, as an introduction to further developments. These developments lead to the estimation of the resolution that can be obtained for the different parameters of the generalized ambiguity function. The computation of the resolution in range, using a Taylor development of the correlation function of the received signal, is not performed. But the computation of the resolution in Doppler is done, and then the computation of the resolution in Doppler rate, by the same method.

Let us consider a radar, transmitting a constant frequency continuous wave. The phase of the transmitted signal is linked to the time and the carrier frequency by the expression:

$$\phi_e(t) = 2 \pi f_c t + \phi_0 \quad (1)$$

ϕ_0 : Initial phase

The signal is reflected by a target, located at a range R . The signal which is transmitted at instant t , is received at:

$$t_r = t + \frac{2R}{c} \quad (2)$$

Approximation: We consider that the velocity of the target is far lower than the velocity of light. As a consequence, we admit that the range of the target doesn't vary between the time of transmission of the signal and the time of reception.

At this time, the phase of the received signal is the one which had been transmitted at instant t :

$$\phi_r(t_r) = \phi_e(t) \quad (3)$$

Taking the instant of reception as reference time, equation (3) becomes:

$$\phi_r(t) = \phi_e(t - \frac{2R}{c}) \quad (4)$$

Using equation (1), we get:

$$\phi_r(t) = 2 \pi f_c (t - \frac{2R}{c}) + \phi_0 \quad (5)$$

$$\phi_r(t) = 2 \pi f_c t - \frac{4 \pi R f_c}{c} + \phi_0 \quad (6)$$

Introducing the wavelength:

$$\lambda = \frac{c}{f_c} \quad (7)$$

Equation (6) becomes:

$$\phi_r(t) = 2 \pi f_c t - \frac{4 \pi R}{\lambda} + \phi_0 \quad (8)$$

R is in fact a function of time. $R(t)$ can be developed, using its successive derivatives (up to the third order, in the above example), around its value at an initial reference time ($t=0$):

$$R(t) = R_0 - u_0 t - \gamma_0 \frac{t^2}{2} - \gamma_0' \frac{t^3}{6} \quad (9)$$

$$u_0 = - \left. \frac{dR}{dt} \right|_{t=0} \quad \begin{array}{l} \text{initial velocity of the} \\ \text{target, relative to the} \\ \text{radar (positive when} \\ \text{closing)} \end{array} \quad (10)$$

$$\gamma_0 = - \left. \frac{d^2R}{dt^2} \right|_{t=0} \quad \begin{array}{l} \text{initial acceleration of the} \\ \text{target, relative to the} \\ \text{radar} \end{array} \quad (11)$$

$$\gamma_0' = - \left. \frac{d^3R}{dt^3} \right|_{t=0} \quad \begin{array}{l} \text{derivative of the} \\ \text{acceleration of the target} \\ \text{relative to the radar} \end{array} \quad (12)$$

Substituting (9) in (8), we obtain:

$$\begin{aligned} \phi_r(t) = 2 \pi f_c t - \frac{4 \pi R_0}{\lambda} + \phi_0 \\ + \frac{4 \pi}{\lambda} u_0 t \\ + \frac{4 \pi}{\lambda} \gamma_0 \frac{t^2}{2} \\ + \frac{4 \pi}{\lambda} \gamma_0' \frac{t^3}{6} \end{aligned} \quad (13)$$

The three last terms of equation (13) are characteristic of the motion of the target. We can define a "Doppler phase", which is the phase that remains after demodulation of the received signal by the transmitted signal:

$$\phi_D(t) = \frac{4 \pi}{\lambda} u_0 t + \frac{4 \pi}{\lambda} \gamma_0 \frac{t^2}{2} + \frac{4 \pi}{\lambda} \gamma_0' \frac{t^3}{6} \quad (14)$$

The Doppler frequency is deduced, being a derivative of the Doppler phase:

$$f_D(t) = \frac{1}{2 \pi} \frac{d\phi_D}{dt} \quad (15)$$

$$f_D(t) = \frac{2 u_0}{\lambda} + \frac{2 \gamma_0}{\lambda} t + \frac{\gamma_0'}{\lambda} t^2 \quad (16)$$

We have obtained an expression of the Doppler frequency and phase, depending of the parameters which are describing the motions of the target. It can be useful to settle the expression of the Doppler phase as a function of the Doppler frequency and its derivatives:

$$f_D(t) = f_D + \dot{f}_D t + \frac{\ddot{f}_D}{2} t^2 \quad (17)$$

$$f_D = \frac{2 u_0}{\lambda} \quad \text{Average Doppler frequency} \quad (18)$$

$$\dot{f}_D = \frac{2 \gamma_0}{\lambda} \quad \text{Doppler slope} \quad (19)$$

$$\ddot{f}_D = \frac{2 \ddot{\gamma}_0}{\lambda} \quad \text{Doppler acceleration} \quad (20)$$

$$\Phi_D(t) = 2\pi f_D t + \pi \dot{f}_D t^2 + \pi \frac{\ddot{f}_D}{6} t^3 \quad (21)$$

2.2. Received signal

We consider now that the signal which is transmitted, $s(t)$, is no more a continuous wave at constant frequency, but a narrow bandwidth waveform on a carrier frequency. To simplify the notations, the amplitude is normalized to 1. Expression of the received signal:

$$s_r(t) = s(t) \exp [j \Phi_D(t)] \quad (22)$$

$$s_r(t) = s(t) \exp [j 2\pi (f_D t + \frac{\dot{f}_D}{2} t^2 + \frac{\ddot{f}_D}{6} t^3)] \quad (23)$$

2.3. Matched Filter

The filter, which is matched to a signal of Doppler parameters f_a , \dot{f}_a , \ddot{f}_a , has the following impulse response:

$$h(t) = s^*(-t) \exp [-j 2\pi (f_a t + \frac{\dot{f}_a}{2} t^2 + \frac{\ddot{f}_a}{6} t^3)] \quad (24)$$

Notations:

$$f = f_D - f_a \quad (25)$$

$$\dot{f} = \dot{f}_D - \dot{f}_a \quad (26)$$

$$\ddot{f} = \ddot{f}_D - \ddot{f}_a \quad (27)$$

Output of the matched filter:

$$X(\tau, f, \dot{f}, \ddot{f}, \dot{f}_a, \ddot{f}_a) = \int_{-\infty}^{\infty} h(\tau-t) s_r(t) dt \quad (28)$$

$$X(\tau, f, \dot{f}, \ddot{f}, \dot{f}_a, \ddot{f}_a) = \int_{-\infty}^{\infty} s(t) s^*(t-\tau) e^{j\Phi} dt \quad (29)$$

with:

$$\Phi = 2\pi [f_D t + \frac{\dot{f}_D}{2} t^2 + \frac{\ddot{f}_D}{6} t^3 - f_a (t-\tau) - \frac{\dot{f}_a}{2} \frac{(t-\tau)^2}{2} - \frac{\ddot{f}_a}{6} \frac{(t-\tau)^3}{6}] \quad (30)$$

$$X(\tau, f, \dot{f}, \ddot{f}, \dot{f}_a, \ddot{f}_a) = \int_{-\infty}^{\infty} s(t) s^*(t-\tau) dt \quad (31)$$

$$\exp j 2\pi [(f + \dot{f}_a \tau - \frac{\ddot{f}_a \tau^2}{2}) t + (\dot{f} + \ddot{f}_a \tau) \frac{t^2}{2} + \frac{\ddot{f}}{6} t^3] dt$$

2.4. Ambiguity function

$|X(\tau, f, \dot{f}, \ddot{f}, \dot{f}_a, \ddot{f}_a)|^2$ is the generalized ambiguity function of the waveform.

3- RESOLUTION

3.1. Resolution in Doppler frequency

To evaluate the resolution in Doppler frequency, we suppose that the derivatives of the Doppler frequency are null. That is to say, we use the range-Doppler ambiguity function.

The ambiguity function is a correlation function. Its maximum is at the origin.

To estimate the width of the correlation peak on the frequency axis, we perform a Taylor development around the position of the peak (0,0):

$$|X(0, f)|^2 = |X(0, 0)|^2 + f \frac{d|X(0, f)|^2}{df} \Big|_{f=0} + \frac{f^2}{2!} \frac{d^2|X(0, f)|^2}{df^2} \Big|_{f=0} \quad (32)$$

The first derivative of the ambiguity function at (0,0) is equal to zero, because at this point, the function is reaching its maximum:

$$\frac{d|X(0, f)|^2}{df} \Big|_{f=0} = 0 \quad (33)$$

The second derivative can be computed, as a function of the value of the ambiguity function at (0,0):

$$\frac{d^2|X(0, f)|^2}{df^2} \Big|_{f=0} = -2(2\pi)^2 \int_{-\infty}^{\infty} t^2 |s(t)|^2 dt |X(0, 0)|^2 \quad (34)$$

f_0 is the half width of the peak on the Doppler axis, at 3 dB:

$$\frac{|X(0, f_0)|^2}{|X(0, 0)|^2} = \frac{1}{2} \quad (35)$$

The width of the peak is then:

$$2 f_0 = \frac{\sqrt{2} (\int_{-\infty}^{\infty} |s(t)|^2 dt)^{1/2}}{2\pi (\int_{-\infty}^{\infty} t^2 |s(t)|^2 dt)^{1/2}} = \frac{1}{T_e} \quad (36)$$

T_e is the "equivalent duration" of the signal. For the signals of finite duration, which are considered in our application, T_e is very near from the duration of the signal.

Example:

For an observation during an aperture time T_a , the resolution of equation (36) gives:

$$2 \dot{f}_0 = \frac{\sqrt{6}}{\pi T_a} = \frac{0.78}{T_a} \quad (37)$$

3.2. Resolution in Doppler acceleration

We make now the hypothesis that the Doppler frequency is null, and we use the same principle to evaluate the resolution in \dot{f} .

The Taylor development of the ambiguity function around $(0,0,0)$ is done hereafter:

$$|X(0,0,\dot{f})|^2 = \left| \int_{-\infty}^{\infty} |s(t)|^2 e^{j\pi \dot{f} t^2} dt \right|^2 \quad (38)$$

$$= |X(0,0,0)|^2 + \dot{f} \frac{d|X(0,0,\dot{f})|^2}{d\dot{f}} \bigg|_{\dot{f}=0} + \frac{\dot{f}^2}{2} \frac{d^2|X(0,0,\dot{f})|^2}{d\dot{f}^2} \bigg|_{\dot{f}=0} \quad (39)$$

$$= |X(0,0,0)|^2 - \frac{\pi^2}{2} \dot{f}^2 \int_{-\infty}^{\infty} t^4 |s(t)|^2 dt \quad (40)$$

\dot{f}_0 is the half width of the peak on the Doppler derivative axis, at 3 dB:

$$\frac{|X(0,0,\dot{f}_0)|^2}{|X(0,0,0)|^2} = \frac{1}{2} \quad (41)$$

$$\pi^2 \dot{f}^2 \int_{-\infty}^{\infty} t^4 |s(t)|^2 dt = |X(0,0,0)|^2 \quad (42)$$

The width of the peak is then:

$$2 \dot{f}_0 = \frac{2 \left(\int_{-\infty}^{\infty} |s(t)|^2 dt \right)^{1/2}}{\pi \left(\int_{-\infty}^{\infty} t^4 |s(t)|^2 dt \right)^{1/2}} \quad (43)$$

Example:

For an observation during an aperture time T_a , the resolution of equation (43) gives:

$$2 \dot{f}_0 = \frac{8\sqrt{5}}{\pi T_a^2} = \frac{5.7}{T_a^2} \quad (44)$$

4- BASIC ISAR

4.1. Description

The radar is fixed (point A of figure 1). The target is rotating at a constant rate ω . The center of rotation is C. The range between the radar and the center of rotation is R.

We consider one reflecting point of the target (point M of figure 1), which is located at coordinates $(x,y,0)$, at initial time ($t=0$). x and y are small compared to R.

The coordinates of M at each time are $(u,v,0)$:

$$u = x \cos \omega t - y \sin \omega t \quad (45)$$

$$v = x \sin \omega t + y \cos \omega t \quad (46)$$

The range of the reflecting point is:

$$R_M^2 = (R + u)^2 + v^2 \quad (47)$$

$$R_M^2 = (R + x \cos \omega t - y \sin \omega t)^2 + (x \sin \omega t + y \cos \omega t)^2 \quad (48)$$

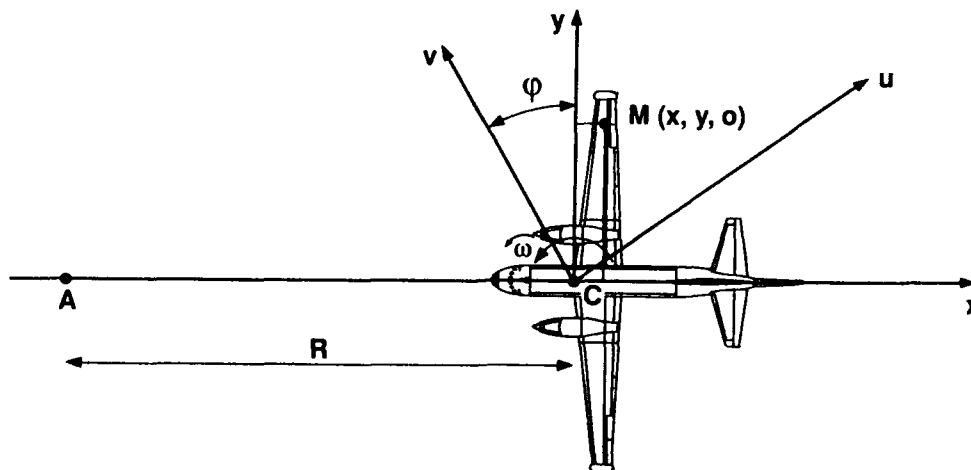


Figure 1: Basic ISAR geometry

$$R_N^2 = R_0^2 + 2 R x \cos \omega t - 2 R y \sin \omega t \quad (49)$$

with $R_0 = R_N$ at $t = 0$

$$R_N \sim R_0 \left(1 + \frac{R x \cos \omega t}{R_0^2} - \frac{R y \sin \omega t}{R_0^2} \right) \quad (50)$$

The Doppler frequency of M is then:

$$f_D \sim \frac{2}{\lambda} \omega (y \cos \omega t + x \sin \omega t) \quad (51)$$

For a short observation time T_a around $t=0$, the Doppler frequency is depending only on the y coordinate:

$$f_D = \frac{2 y \omega}{\lambda} \quad (52)$$

We have established a direct relation between the Doppler frequency and the position of the reflecting point on a cross-range axis, relative to the center of rotation.

We can note that the reception filter has to be matched to signals of constant frequency and finite duration. As a consequence, the ISAR processing is reduced to a simple Fourier transform.

4.2. Resolution

As a result of equation (36), the resolution in Doppler frequency, for an observation time T_a , is:

$$r_{fD} = \frac{k}{T_a} \quad (53)$$

where the value of k is near to 1. This result is well-known for every conventional spectral analysis. It could be possible to achieve a better resolution, by the mean of estimation methods. Unfortunately, these methods require a high signal-to-noise ratio and a large amount of computation. They are not currently used in this field of application.

The resolution on the cross-range axis is then:

$$r_y = \frac{\lambda r_{fD}}{2 \omega} = \frac{\lambda}{2 \omega T_a} \quad (54)$$

$$r_y = \frac{\lambda}{2 \phi_a} \quad (55)$$

with

$$\phi_a = \omega T_a \quad (56)$$

ϕ_a is the angle of rotation of the target during the observation time (figure 1). It is interesting to note that the resolution

is a function of only one parameter ϕ_a .

4.3. Projection plan

It comes from previous developments that the resolution of ISAR processing is obtained on a cross-range axis, which is orthogonal to the axis of rotation of the target.

The image is a projection in a plan containing the radar-to-target axis (range axis) and the cross-range axis which is orthogonal to the axis of rotation.

Figure 2 gives several examples of basic projections.

- In figure 2a, the target is oriented to the radar and has a pitch motion. The range resolution is on the length axis of the target, and the cross-range resolution is the height of the target. The projection plan is a range-height vertical plan.
- In figure 2b, the target is oriented perpendicular to the radar range axis and has a roll motion. The range resolution is on the width axis of the target, and the cross-range resolution is still the height. The projection plan is a width-height vertical plan.
- In figure 2c, the target is oriented to the radar and has a yaw motion. The range resolution is on the length axis of the target, and the cross-range resolution is the width. This case is comparable to SAR. The projection plane is a length-width horizontal plan.

In several applications, the configuration is not so simple. The target principal axis are any possible orientation compared to the range axis. There can be simultaneously pitch, roll and yaw motions. The orientation of the instantaneous axis of rotation is not known. Consequently, the position of the projection plan is not known either.

5- RELATIONS WITH SAR, REAL APERTURE, AND TOMOGRAPHY

5.1. Relation with SAR

Figure 3 shows a typical SAR configuration. The radar is flying at constant speed, u, and height on a straight line. It is observing a first reflecting point designed by M_1 . The azimuth of the target is ϕ_1 . The Doppler frequency is:

$$f_{D1} = \frac{2 u}{\lambda} \cos \phi_1 \quad (57)$$

There is a second reflecting point, M_2 , which is at the same range, but with a slightly different azimuth:

$$\phi_2 = \phi_1 + \delta \phi \quad (58)$$

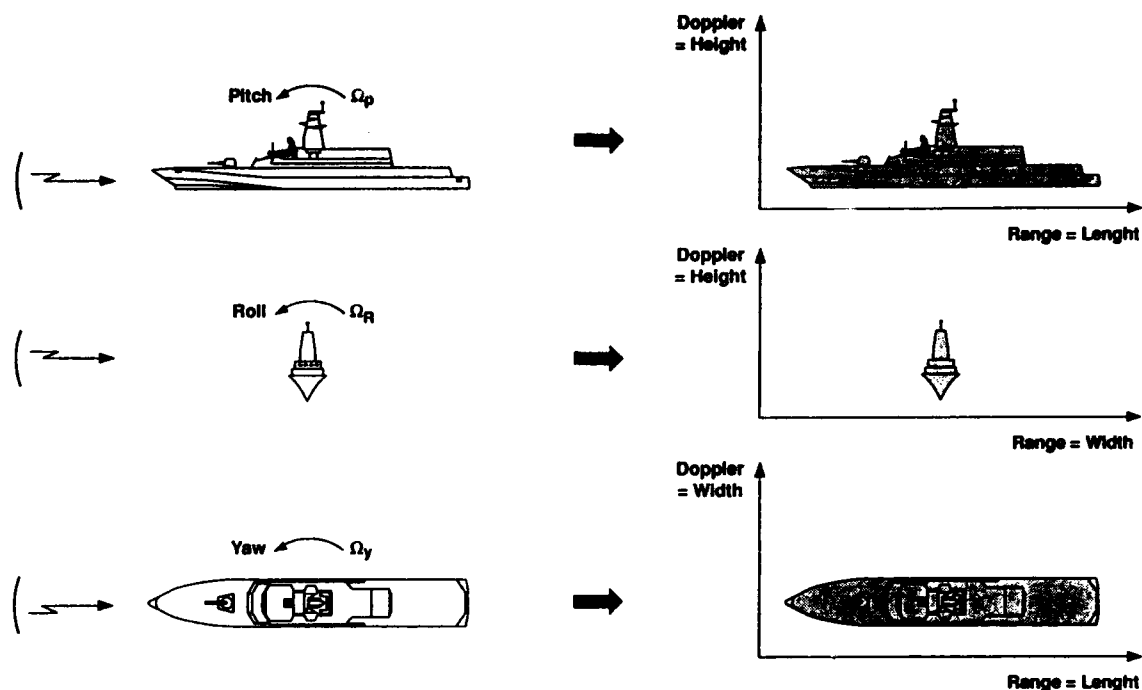


Figure 2: Projection plan of the image

The Doppler frequency of the second reflecting point is:

$$f_{D2} = \frac{2u}{\lambda} \cos(\phi_1 + \delta\phi) \quad (59)$$

At the first order:

$$f_{D1} - f_{D2} = \frac{2u}{\lambda} \sin \phi_1 \delta\phi \quad (60)$$

For a short observation time T_a , ϕ_1 can be considered as a constant. In this case, the signals received from the targets are pure constant frequencies, and the matched processing is done by Fourier transform. The resolution in Doppler frequency is $1/T_a$. The associated angular resolution in azimuth is derived:

$$\frac{2u}{\lambda} \sin \phi_1 r_\phi = \frac{1}{T_a} \quad (61)$$

$$r_\phi = \frac{\lambda}{2u T_a \sin \phi_1} \quad (62)$$

The projection of this angular resolution at the range of the target is:

$$r_y = \frac{\lambda R}{2u T_a \sin \phi_1} \quad (63)$$

During the observation time, the displacement of the radar is the length of the synthetic aperture:

$$L = u T_a \quad (64)$$

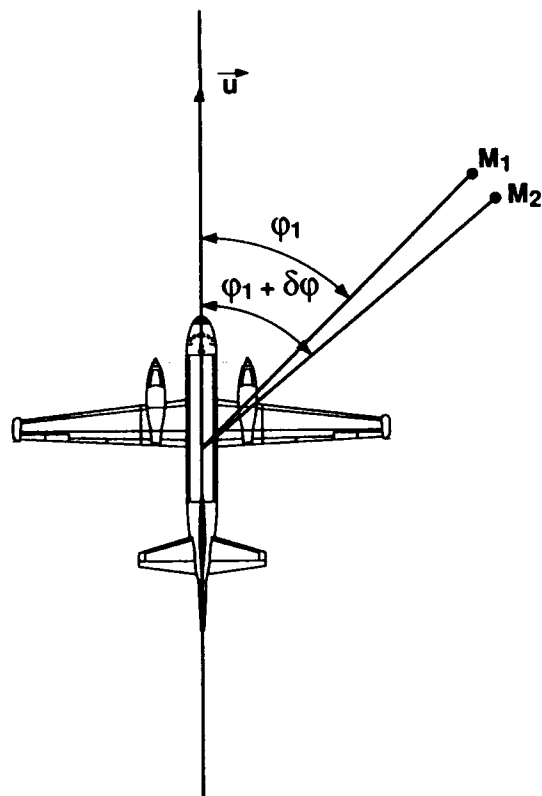


Figure 3: SAR geometry

The variation of attitude angle of the target relative to the radar is:

$$\phi_a = \frac{L}{R} = \frac{u T_a}{R} \quad (65)$$

The resolution r_y can be written as a function of ϕ_a :

$$r_y = \frac{\lambda}{2 \phi_a \sin \phi_1} \quad (66)$$

The best resolution is achieved for $\phi_1 = 90^\circ$ (side-looking radar). In this case:

$$r_y = \frac{\lambda}{2 \phi_a} \quad (67)$$

This equation is identical to equation 55.

SAR and ISAR are identical. In both cases, the parameter, which fixes the resolution, is the variation of attitude angle of the target, relative to the radar. To change from SAR to ISAR is only a change of reference:

- Rotation angle referred to the radar: SAR
- Rotation angle referred to the target: ISAR

We have established this result, considering a short observation time. We have limited the computations to first order developments:

- In SAR technics, it is the hypothesis of the unfocused SAR. The processing is the same (Fourier transform), whatever the range of the target is: it is focused at infinite range.
- In ISAR technics, the equivalent name "unfocused ISAR" is not usual. But the principle is the same: second and higher order terms in the variation of the range are neglected.

For a longer aperture time, there is a difference between SAR and ISAR:

- In a pure ISAR configuration, the range between the radar and the center of rotation of the target is constant.
- In a SAR configuration, this range is varying following a quadratic law. However, the effect of this range variation can be compensated through an appropriate demodulation of the received signal.

5.2. Relation with the real aperture

For SAR and ISAR, the length of the synthetic aperture is:

$$L = \phi_a R \quad (68)$$

The real aperture providing the same resolution is:

$$1 = \frac{\lambda}{r_\phi} \quad (69)$$

$$1 = 2 L \quad (70)$$

5.3. Relations with tomography

It can be shown that some kind of ISAR can be interpreted as a tomographic reconstruction problem (Ref. 10).

Computer-aided tomography (CAT) is a technique for providing a two- or three-dimensional image of an object through digital processing of many 1-D projectional views taken from different look angles. It is used in the medical field for imaging with X-ray scanners.

The projection-slice theorem, that is used in this technique, can be applied to ISAR processing.

5.3.1. Tomography principle, projection-slice theorem and backprojection reconstruction method

Let $\sigma(x,y)$ be the function to map.

The measurement are made by the mean of several 1-D projections on different directions. The direction of the line-of-sight for one projection is ϕ . The value of the projection at each range u is:

$$p_\phi(u) = \int_{-\infty}^{\infty} \sigma[x(u,v,\phi), y(u,v,\phi)] dv \quad (71)$$

with notations of figure 1:

$$x(u,v,\phi) = u \cos \phi - v \sin \phi \quad (72)$$

$$y(u,v,\phi) = u \sin \phi + v \cos \phi \quad (73)$$

The projection function has a Fourier transform:

$$P_\phi(U) = \int_{-\infty}^{\infty} p_\phi(u) e^{-j2\pi u U} du \quad (74)$$

The Fourier transform of the projection function is one slice of the 2-D Fourier transform of the image $\sigma(x,y)$ (projection-slice theorem). The orientation of the slice is given by the angle ϕ :

$$P_\phi(U) = I(U \cos \phi, U \sin \phi) \quad (75)$$

$I(X,Y)$ is linked to $\sigma(x,y)$ by the relation:

$$I(X,Y) = \int_{-\infty}^{\infty} \int_{-\infty}^{\infty} \sigma(x,y) e^{-j2\pi(xX + yY)} dx dy \quad (76)$$

$\sigma(x,y)$ can be reconstructed by the use of a 2-D inverse Fourier transform:

$$\sigma(x,y) = \int_{-\infty}^{\infty} \int_{-\infty}^{\infty} I(X,Y) e^{j2\pi(xX + yY)} dX dY \quad (77)$$

Generally, the reconstruction is not made by the mean of an inverse Fourier transform, because the value of $I(X,Y)$, in rectangular coordinates is not known. It has to be computed, using interpolations. Another method is used, based on filtering and backprojection in polar coordinates.

The measurements are obtained in polar coordinate. Let us write equation (77) as a function of these polar coordinates:

$$X = U \cos \phi, Y = U \sin \phi \quad (78)$$

$$\sigma(x,y) = \int_{-\pi}^{\pi} \int_0^{\infty} I(U \cos \phi, U \sin \phi) e^{j2\pi U(x \cos \phi + y \sin \phi)} |U| dU d\phi \quad (79)$$

$$\sigma(x,y) = \int_{-\pi}^{\pi} \int_0^{\infty} P_{\phi}(U) |U| e^{j2\pi U(x \cos \phi + y \sin \phi)} dU d\phi \quad (80)$$

The integral over U is identified as an inverse Fourier transform of variable $(x \cos \phi + y \sin \phi)$:

$$\sigma(x,y) = \int_{-\pi}^{\pi} [P_{\phi} * k](x \cos \phi + y \sin \phi) d\phi \quad (81)$$

where k is the inverse Fourier transform of $|U|$.

The processing is made of the following successive steps:

- . a high-pass filter, $H(f) = |U|$, which is producing a contrast enhancement,
- . a sum for all the values of ϕ

Other reconstruction methods are existing and are listed in Ref. 12.

5.3.2. ISAR as a tomographic reconstruction problem

We consider now a radar which is transmitting several continuous waves at constant frequencies. The different frequencies are regularly spaced and can be addressed simultaneously or sequentially. This type of observation is repeated for several values of the angle of view ϕ of the target.

The signal received for a given frequency and a given angle of view, after demodulation, is proportional to:

$$s(f,\phi) = \int_{-L}^{+L} P_{\phi}(u) e^{j2\pi 2f/c u} du \quad (82)$$

where $2L$ is the dimension of the target along the line of sight, and $P_{\phi}(u)$ is defined by equation (71).

$s(f,\phi)$ is the Fourier transform of the projection $p_{\phi}(u)$:

$$s(f,\phi) = P_{\phi}(U), \text{ with } U = -\frac{2f}{c} \quad (83)$$

The back-projection algorithm can be used, following equations (80) and (81):

- . Multiplication by $|U|$
- . Inverse Fourier transform. At this step the signal is compressed on the range axis.
- . Spreading of each point (amplitude and phase) of each profile on a line which is orthogonal to the line of sight of the profile, and sum of the resulting signal at each point (x,y) .

6- EXAMPLE OF APPLICATION: IMAGING OF SHIPS AT SEA

6.1. Modelization

Imaging of ships at sea is a complex application of ISAR. It is interesting, because it is a case where the discriminating parameters are not only the time and the Doppler frequency, but also the derivative of the Doppler frequency.

Figure 4 is a geometrical representation. The radar is flying on-board an aircraft, at velocity u_r . Its initial position is O and its average course is along the X-axis.

The antenna is oriented toward the ship, defining an x-axis. The angle between X and x is the azimuth of the target, ϕ .

The center of rotation of the target is located initially at point O'. Its velocity is u_t and its course makes an angle α relative to the x-axis. Two cross-range axis are defined: y-axis, in the horizontal plan, orthogonal to x, and z-axis, which is the height.

We consider a reflecting point M on the ship. Its position, relative to O', is $(0, y, z)$.

The ship is supposed to have sinusoidal pitch and roll motions. The angular velocity in pitch and roll are:

$$\Omega_p = \omega_p \sin(2\pi f_p t + \phi_p) \quad (84)$$

$$\Omega_r = \omega_r \sin(2\pi f_r t + \phi_r) \quad (84)$$

The Doppler frequency of the signal reflected by point M, and its derivative, are:

$$f_D = -\frac{1}{\lambda} \left(u_x \sin \phi - u_x \sin \alpha + \Omega_p z \sin \alpha + \Omega_r x \cos \alpha \right)^2 \quad (86.1)$$

$$- \frac{u_x \sin \phi - u_x \sin \alpha}{R} y \quad (86.2)$$

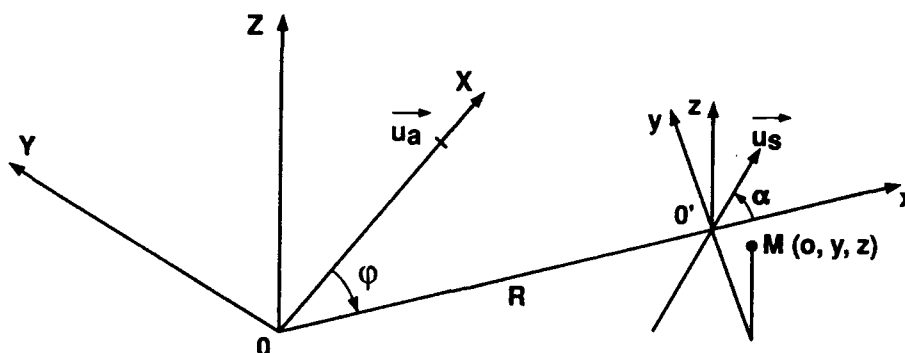


Figure 4: Ship imaging by an airborne radar

$$+ (\dot{\Omega}_r(t) \sin \alpha + \dot{\Omega}_t(t) \cos \alpha) z \quad (86.3)$$

$$+ u_a \cos \phi + u_s \cos \alpha \quad (86.4)$$

$$+ f_{D_a}(t) \quad (86.5)$$

The terms in $\dot{\Omega}_t$ and $\dot{\Omega}_r$ of equation (86.1) are negligible.

f_{D_a} is the effect of spurious aircraft motion.

$$f_D = -\frac{2}{\lambda} \left[-\frac{(u_a \sin \phi - u_s \sin \alpha)^2}{R} \right] \quad (87.1)$$

$$+ (\dot{\Omega}_r(t) \sin \alpha + \dot{\Omega}_t(t) \cos \alpha) y \quad (87.2)$$

$$+ f_{D_a}(t) \quad (87.3)$$

Let us give an interpretation of each term of equations (86) and (87) and explain their interest:

86.1: It is a linear term, which does not depend on y and z . It is identical for each reflecting point. It brings no discriminating information. The parameters u_a , u_s , ϕ and α can be estimated, by the use of tracking or other method (Ref. 16). This term is eliminated by Doppler compensation.

86.2: This term is proportional to y . It establishes the link between the Doppler frequency and the position of the reflecting point in azimuth. It is depending only on the displacement of the aircraft. It is in fact a SAR effect.

86.3: This term is proportional to z . It establishes the link between the Doppler frequency and the position of the reflecting point in height. It is depending on the rotation of the ship. It is an ISAR effect.

86.4: This term is proportional to the velocity of the ship relative to the aircraft. It brings no discriminating information. It is eliminated by the same way than (86.1).

86.5: The spurious Doppler frequency due to aircraft motion is supposed to be sufficiently small to have no coupling effect with other terms. It is evaluated by inertial means, to allow a compensation of Doppler frequency before any further processing.

Equation (86) could permit to resolve the ambiguity between y and z , if the aperture time is sufficiently large. But this also can be done, considering equation (87), in which only z is mentioned:

87.1: It is a constant Doppler acceleration term, which is identical for every reflecting points. It is eliminated by the same way than term (86.1).

87.2: This term is proportional to z . It allows the measurement of z .

87.3: Effect of aircraft spurious motion, which is corrected by the same way than term (86.5).

To simplify the problem, we make an additional hypothesis: The ship has only a roll motion, and $\phi_r = 0$. After correction of non discriminating terms, equations (86) and (87) become:

$$f_D = -\frac{2}{\lambda} \left[-\frac{u_a \sin \phi - u_s \sin \alpha}{R} y + \omega_r \sin(2\pi f_r t) \sin \alpha z \right] \quad (88)$$

$$f_D = -\frac{2}{\lambda} \omega_r \cos(2\pi f_r t) \sin \alpha z \quad (89)$$

We come here to a fundamental property of ISAR applied to ship imaging (figure 5):

- The Doppler frequency is a sinusoidal function. The average value of the function is proportional to the azimuth of the reflecting point. The amplitude of variation is proportional to the height of the reflecting point. The use of a time-frequency transform is very interesting to visualise the evolution of the Doppler frequency of each scatterer during the observation time. It can be

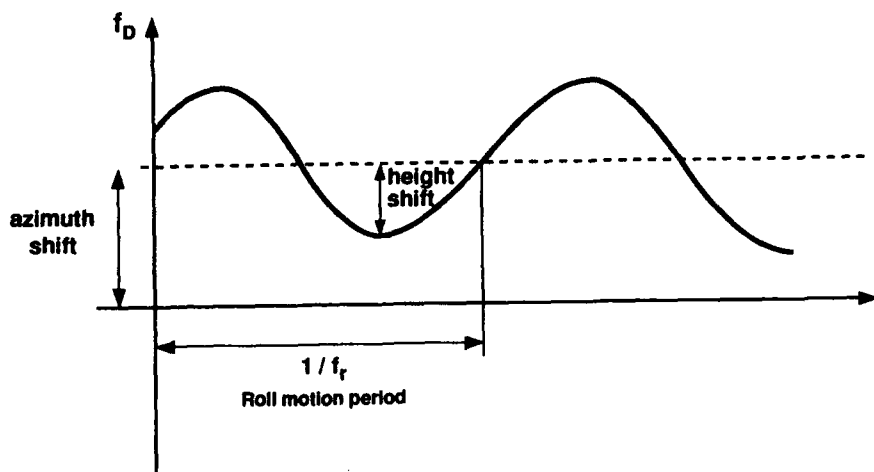


Figure 5: Evolution and interpretation of the Doppler frequency

either a wavelet transform (Ref. 17.) or a Wigner-Ville transform (Ref. 12).

- The derivative of the Doppler frequency is a sinusoidal function, centered on zero. Its amplitude is proportional to the height of the reflecting point.

6.2. Characteristics of the image

If we realize the filter described by equation (31), the resolutions in azimuth and height can be estimated using equations (37) and (44), (88) and (89).

The best result will be obtained around $t=0$. At this time, the Doppler frequency in equation (88) is due only to y (the term in z is null). Considering $u_a \gg u_s$ (velocity of the aircraft greater than the velocity of the ship) the resolution in azimuth is:

$$r_y = r_{yD} \frac{\lambda R}{2 u_a \sin \phi} = \frac{\sqrt{6} \lambda R}{2 \pi T_a u_a \sin \phi} \quad (91)$$

Considering the height, starting from equation (89), at first order we can write:

$$f_D = -\frac{2}{\lambda} \omega_r \sin \alpha z \quad (92)$$

$$r_{yD} = -\frac{2}{\lambda} \omega_r \sin \alpha r_z \quad (93)$$

$$= \frac{8\sqrt{5}}{\pi T_a^2} \quad (94)$$

$$r_z = \frac{4\sqrt{5} \lambda}{\pi T_a^2 \omega_r \sin \alpha} \quad (95)$$

Example:

$$\lambda = 3 \text{ cm (X-band)}$$

$$u_a = 150 \text{ m/s}$$

$$R = 100 \text{ km}$$

$$\phi = 90^\circ$$

$$\omega_r = 3^\circ/\text{s}$$

$$T_a = 1,5 \text{ s}$$

$$\alpha = 45^\circ$$

$$\text{Resolution in azimuth: } r_y = 5,2 \text{ m}$$

$$\text{Resolution in height: } r_z = 1 \text{ m}$$

Taking into account all the approximations that have been done to come to this result, these values are to be considered only as orders of magnitude.

The resolution in azimuth is not so good than the resolution in height, because it is proportional to the range. At far range, it is useless to try to have an exploitable top-view of a ship.

7- SPURIOUS EFFECTS

The spurious effects are identical to spurious effect in SAR, but interpretation can be different. The most important are listed hereafter.

7.1. Range-cell migration

7.1.1. Description

Due to its rotation relative to the radar, the aspect of the target is changing during the aperture time.

The range of each reflector is changing, providing the Doppler effect. If the change of range becomes greater than the range

resolution (or the range-cell), the reflector does not appear any more as a point scatterer on the image. There is a degradation of the range resolution.

Furthermore, the processing is most of the time organized in two successive steps:

- . First step: range processing, performing a matched filtering on a short time.
- . Second step: Cross-range processing, performing a further matching on a long time. This processing is usually made on signals at constant range of the radar, that is to say, independantly for each range cell.

If there is a migration of the echo, greater than the range resolution cell, the processing in cross-range is mismatched. The aperture time is reduced to the time of presence of the echo in one range cell. The resolution in cross-range is degraded.

7.1.2. Compensation methods

To compensate for this effect, the principle is to perform the cross-range processing at variable ranges. There are two possibilities:

- . to shift, in time, the received signal,
- . to shift, in time, the impulse response of the cross-range matched filter.

The main problem is that the range-cell migration is not the same for every scatterer. It is proportional to the distance between the scattering point and the center of rotation, that is to say, to its Doppler frequency.

7.2. Unknown radar and target motions

7.2.1. Modelization

The modelization is made for the basic case of ISAR: Short aperture time, developments limited to first order.

The signal received from a point reflector is:

$$s_r(t) = s(t) e^{j\phi(t)} e^{j2\pi f_D t} \quad (96)$$

where $\phi(t)$ is the phase generated by unknown spurious motion.

The output of the matched filtering is deduced from equation (31):

$$X(\tau, f) = \int_{-\infty}^{+\infty} s(t) s^*(t-\tau) e^{j\phi(t)} e^{j2\pi f t} dt \quad (97)$$

If $s(t)$ is supposed to be a signal of constant amplitude and frequency during the aperture time, then equation (97) can be considered as the Fourier transform of:

$$e^{j\phi(t)} \quad (98)$$

It is usual, in the study of spurious aircraft motion for SAR processing, to distinguish low frequency motion and high frequency motion.

7.2.2. Low frequency motions

Two main situation can happen:

- . Error on the rotation rate
It is evident, from equation (52), and without making any computation, that this error will modify the scale factor on the cross-range axis.

If the value of the rotation rate is not known, the scale factor is anyhow unknown to.

- . Slow variation of the rotation rate. This will cause a change of the value of the Doppler frequency during the aperture time. We can make the hypothesis of a linear variation. It is equivalent to introduce a quadratic phase shift.

The result is a degradation of the cross-range resolution.

$$\omega(t) = \omega_0 + k_\omega t \quad (99)$$

$$k_\omega = \frac{\delta\omega}{T_a} \quad (100)$$

The corresponding variation of Doppler frequency during the aperture time is:

$$\delta f = \frac{2 \delta\omega y}{\lambda} \quad (101)$$

A good approximation is to consider that the linear variation of the frequency, δf , provides a widening of the peak, at the output of the Fourier transform, according to the expression:

$$r_{fD} = (r_{fD0}^2 + \delta f^2)^{1/2} \quad (102)$$

$$r_{fD} = (r_{fD0}^2 + \frac{4 \delta\omega^2 y^2}{\lambda^2})^{1/2} \quad (103)$$

$$r_y = (r_{y0}^2 + \frac{2 \delta\omega^2 y^2}{\omega_0^2})^{1/2} \quad (104)$$

7.2.3. High frequency motions

It is the domain of periodic motion, having several periods during the aperture time: Vibrations.

A reflector can have a vibration motion on the target. For example, on a ship, objects located on the mast are vibrating with frequencies depending on the natural frequencies of the mast and the engines.

The spurious motion on the range axis is:

$$x(t) = x_0 \sin(2\pi f_m t) \quad (105)$$

The spurious phase is:

$$\phi(t) = \frac{4\pi}{\lambda} x_0 \sin(2\pi f_m t) \quad (106)$$

Writing (106) in equation (97), it comes:

$$X(0, f) = \int_{-\infty}^{+\infty} \exp\left(j\frac{4\pi x_0}{\lambda} \sin(2\pi f_m t)\right) e^{j2\pi f t} dt \quad (107)$$

$$X(0, f) \sim \delta(f) + \frac{2\pi x_0}{\lambda} [\delta(f - f_m) + \delta(f + f_m)] \quad (108)$$

The usefull echo is bordered with two side-lobes, located at Doppler frequencies f_m and $-f_m$ (figure 6).

The position of the false echos is:

$$y = \pm \frac{\lambda f_m}{2\omega} \quad (109)$$

The level of these echos is:

$$|X(0, f_m)| = \frac{2\pi x_0}{\lambda} \quad (110)$$

(with $|X(0, 0)| = 1$, level of the peak)

7.2.4. Random motions

Random motions is a generalization of high frequency motions. Instead of one vibration frequency, there is a complete spectrum, creating a continuous level of side-lobes.

$x(t)$ is the spurious displacement, X^2 is the variance of x .

The spurious phase is:

$$\phi(t) = \frac{4\pi}{\lambda} x(t) \quad (111)$$

The variance of the phase of the spurious signal is:

$$\phi^2 = \left(\frac{4\pi}{\lambda}\right)^2 X^2 \quad (112)$$

The output of the processing filter is:

$$X(0, f) = \int_{-\frac{T_0}{2}}^{\frac{T_0}{2}} e^{j[2\pi f t + \phi(t)]} dt \quad (113)$$

$$|X(0, f)|^2 = \int_{-\frac{T_0}{2}}^{\frac{T_0}{2}} \int_{-\frac{T_0}{2}}^{\frac{T_0}{2}} e^{j[2\pi f u + \phi(u)]} e^{-j[2\pi f v + \phi(v)]} du dv \quad (114)$$

$$|X(0, f)|^2 = \int_{-\frac{T_0}{2}}^{\frac{T_0}{2}} \int_{-\frac{T_0}{2}}^{\frac{T_0}{2}} e^{j[\phi(u) - \phi(v)]} e^{-j2\pi f(v-u)} du dv \quad (115)$$

Variable change:

$$w = v - u \quad (116)$$

$$|X(0, f)|^2 = \int_{-\frac{T_0}{2}}^{\frac{T_0}{2}} \int_{-\frac{T_0}{2}}^{\frac{T_0}{2}} e^{j[\phi(u) - \phi(w+u)]} e^{-j2\pi f w} du dw \quad (117)$$

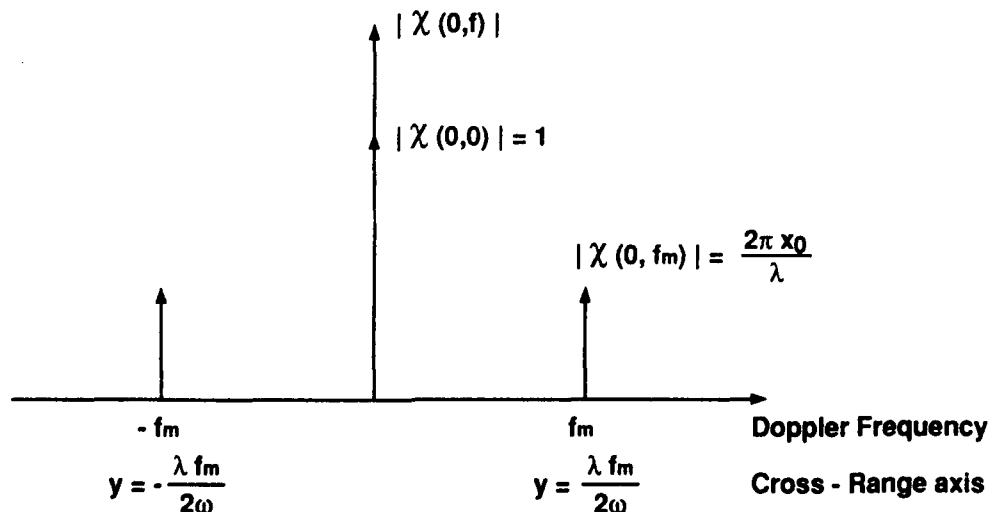


Figure 6: Side-lobes due to vibrations of the target or the radar

$$\int_{-\frac{T_a}{2}}^{\frac{T_a}{2}} e^{j[\phi(u)-\phi(w+u)]} du = \int_{-\frac{T_a}{2}}^{\frac{T_a}{2}} \frac{1+j[\phi(u)-\phi(w+u)] - \frac{[\phi(u)-\phi(w+u)]^2}{2}} du \quad (118)$$

$$= T_a - T_a \phi^2 + R_{\phi\phi}(w) \quad (119)$$

$$|X(0,f)|^2 = T_a \delta(f) - T_a \phi^2 \delta(f) + S_{\phi}(f) \quad (120)$$

with:

$$S_{\phi}(f) = \int_{-\infty}^{\infty} R_{\phi\phi}(w) e^{-j2\pi fw} dw \quad (121)$$

The average power of signal at the output of the processing is:

$$E(|X(0,f)|^2) = T_a \delta(f) - T_a \phi^2 \delta(f) + E\{S_{\phi}(f)\} \quad (121)$$

$$E(|X(0,f)|^2) = T_a (1 - \phi^2) \delta(f) + \frac{\phi^2}{B_{df}} \quad (122)$$

The peak-to-sidelobe ratio is:

$$S/L \sim \left(\frac{4\pi}{\lambda}\right)^2 X^2 \frac{1}{B_{df} T_a} \quad (123)$$

7.3. Spectral purity of the radar

7.3.1. Modelization

The effect of local oscillator (L.O.) instability is identical to the effect of spurious radar and target motions:

- . Low rate frequency drifts: Degradation of the resolution
- . Spurious lines: Side-lobes, isolated
- . Phase noise: Average level of side-lobes

The local oscillator frequency is used for up-conversion at transmission and down-conversion at reception (figure 7).

This operation is equivalent to a single delay filtering of the local oscillator signal. It is performing a weighting of the phase noise spectrum:

$$E_r(f) = 4 \sin^2(\pi f T_t) E(f) \quad (125)$$

$T_t = 2 r/c$ is the time corresponding to the range of the target.

The effect of this weighting is an enhancement of the high frequency noise power, by a factor of 2, and an attenuation of the low frequency noise power, by a factor:

$$\rho(f) = 4 \pi^2 f^2 T_t^2 \quad (126)$$

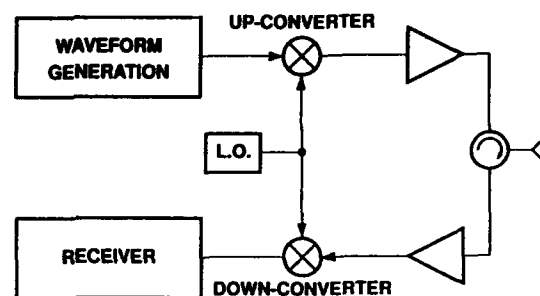


Figure 7: Transmission/Reception bloc-diagram

7.3.2. Effect of local oscillator phase noise

The same calculation than in paragraph 7.2.4. provides the average peak-to-sidelobe ratio:

$$S/L = 2 \frac{\int_{-\frac{B_{df}}{2}}^{\frac{B_{df}}{2}} 4 \sin^2(\pi f T_t) E(f) df}{B_{df} T_a} \quad (127)$$

8- REFERENCES (unclassified publications only)

1. Brown W.M., Fredricks R.J., "Range-Doppler Imaging with Motion through Resolution Cells", IEEE Trans. Aerospace and Electronics Systems, VOL. AES-5, N°1, Jan. 1969, pp. 98-102.
2. Skolnik M., "Radar Handbook", Mc Graw-Hill Book Company, 1970.
3. Gniss H., Krucker K., Magura K., Perkuhn D., "Problems of Signal Processing in a high Resolution Radar - Synthetic Aperture Imaging of rotating Targets with narrowband and broadband Signals", SEE 1978 International Conference on Radar, Paris, Dec. 1978, pp. 243-250.
4. Chen C.C., Andrews H.C., "Target Motion Induced Radar Imaging", IEEE Trans. Aerospace and Electronics Systems, VOL. AES-16, N°1, Jan. 1980, pp. 1-14.
5. Chen C.C., Andrews H.C., "Multifrequency Imaging of Radar Turntable Data", IEEE Trans. Aerospace and Electronics Systems, VOL. AES-16, N°1, Jan. 1980, pp. 15-22.
6. Walker J.L., "Range Doppler Imaging of Rotating Objects", IEEE Trans. Aerospace and Electronics Systems, VOL. AES-16, N°1, Jan. 1980, pp. 23-53.
7. Dike G., Wallenberg R., "Inverse SAR and its Application to Aircraft Classification", IEEE 1980 International Radar Conference Record, Arlington, April 1980, pp. 161-167.

8. Prickett M.J., Chen C.C., "Principles of Inverse Synthetic Aperture Radar (ISAR) Imaging", IEEE EASCON'80 Record, Sep. 1980, pp. 340-345.
9. Mensa D.L., Dean L., "High Resolution Target Imaging", Artech House, 1981.
10. Munson D.C.Jr., O'Brien J.D., Jenkins W.K., "A Tomographic Formulation of Spotlight-Mode Synthetic Aperture Radar", Proceedings of the IEEE, Vol. 71, n°8, August 1983, pp. 917-925.
11. Wehner D.R., "High Resolution Radar", Artech House, 1987, pp. 273-339.
12. D'Addio E., Farina A., Morabito C., "The applications of multidimensional processing to radar systems", International Conference on Radar 1989, Paris, April 1989, pp. 62-78.
13. Bethke K.H., Röde B., "A fast ISAR-imaging Process and its inherent degrading Effect on Image Quality", AGARD CP-459, The Hague, 8-12 May 1989, pp. 31-1 to 31-12.
14. Ender J., "1D-ISAR imaging of manoeuvring Aircraft", AGARD CP-459, The Hague, 8-12 May 1989, pp. 33-1 to 33-9.
15. Marini S., Pardini S., Prodi F., "Radar Target Image by ISAR Case Study", AGARD CP-459, The Hague, 8-12 May 1989, pp. 35-1 to 35-14.
16. Fenou M., "L'Imagerie de Cibles marines à la Frontière entre le SAR et l'ISAR", AGARD CP-459, The Hague, 8-12 May 1989, pp. 28-1 to 28-10.
17. Daubechies I., "The Wavelet Transform, Time-Frequency Localization and Signal Analysis", IEEE Transactions on Information Theory, Vol. 36, n°5, Septembre 1990.

Special SAR Techniques and Applications

R. Keith Raney
Canada Centre for Remote Sensing

1. SUMMARY

SAR systems as considered in these lectures are fully coherent, and are characterized by large time/bandwidth signal structure in both range and azimuth. These properties allow additional and specialized performance to be achieved through innovative system variations.

Using *one signal sequence*, resolution may be improved in azimuth through increased target Doppler bandwidth. Broad beam and Spotlight SAR are techniques used. For the Spotlight mode, high resolution in azimuth is achieved at the expense of image size, so that the Stretch range bandwidth reduction technique is useful to allow increased resolution in both dimensions. A subset of these methods is the Squint mode, whereby the side-looking antenna is pointed forward (or aft) of the zero-Doppler direction, leading to increased complexity for image processing. Wave domain or polar format techniques are required.

The requirements, capabilities, and limitations of single beam moving target indication (MTI) for a SAR are reviewed. Special processing for multi-look SARs to enhance SAR ocean wave imagery contrast and directional spectral estimation is highlighted.

Since the SAR signal is coherent, signal phase comparison is possible between *pairs of signals*. For *spatial separation* of the signal pair, interferometric signal combina-

tion leads to the possibility of terrain height estimation, with a precision on the order of the system resolution. Differential interferometric techniques allow observation of changes in the scene on the order of the radar wavelength. For *time separation* of the signal pair, the full potential of SAR MTI may be realized. Implementation in the time domain and in the frequency domain is described. Airborne versus spaceborne constraints are compared. The principle of conservation of energy of moving targets is presented, and used to estimate target velocity.

2. INTRODUCTION

The special techniques considered in this lecture depend upon the coherent characteristics of SAR signals, and often of greater importance, on coherence properties encountered in the complex image domain. This section introduces the main concepts.

2.1. Coherent Signal Structure

Signals encountered in SAR analysis have phase as their most important attribute, and thus must be coherent over each sequence of received samples. Coherence in the azimuth dimension may be exploited to achieve remarkably good resolution, and may be used for special techniques as well. The classic treatment of SAR analysis is that of Harger [1], who makes the usual assumption for most of his treatment that the two SAR dimensions, range and azimuth, are uncoupled, and that the antenna

beam is so narrow that range curvature is not an important consideration.

For most advanced techniques, detailed treatment of two-dimensional coupling must be included in the model. One such analysis may be found in [2], which is based on the generic signal received from a point scatterer as observed in a wide beam geometry. In studying the azimuth resolution capability, looking at the Doppler properties, or analyzing methods of preserving phase in the derived (complex) image space, an expression for the range signal, azimuth image domain is essential. Such an expression opens our review of special topics.

Consider a large time-bandwidth signal $ss(x,y)$ from a scatterer at $(x=0, y=R_n)$ observed in signal space (x azimuth, and y range) having wavenumber $k=2\pi/\lambda$, and two-dimensional pulse envelope $a[x,y - R_n(x)]$ according to

$$ss(x,y) = a[x, y - R_n(x)] \cdot \exp\{-j2kR_n(x)\} \exp\{-jb[y - R_n(x)]^2\} \quad (1)$$

where

$$R_n(x) = \sqrt{R_n^2 + x^2} \quad (2)$$

Then the azimuth Fourier transform

$$Ss(\omega_x, y) = \int ss(x, y) \exp\{-j\omega_x x\} dx \quad (3)$$

of the signal is given by

$$Ss(\omega_x, y) = C a\left(-\frac{R_n \omega_x}{2k}, y - R_n(\omega_x)\right) \cdot \exp\{-jb'[y - R_n(\omega_x)]^2\} \cdot \exp\left\{-j2kR_n\left(1 - \frac{\omega_x^2}{4k^2}\right)^{1/2}\right\} \quad (4)$$

where C is a complex "constant",

$$R_n(\omega_x) = \frac{R_n}{\left(1 - \frac{\omega_x^2}{4k^2}\right)^{1/2}} \quad (5)$$

and

$$b' = \frac{b}{1 + \frac{bR_n\omega_x^2}{4k^3(1 - \omega_x^2/4k^2)^{3/2}}} \quad (6)$$

The key result is the generalized Doppler domain expression of Eq. 4, derived in [2].

Range curvature refers primarily to the range/azimuth coupling found in the range delay term of the envelope of Eq. 1 and the locus of Eq. 5 in the Doppler domain of Eq. 4. This coupling is itself range dependent. (This little subtlety is at the heart of processor design for this class of imaging systems.) Doppler properties are set by the width and angular position of the envelope, both of which are range dependent.

Whether or not significant range curvature is present, the signal expression may be transformed and processed to derive an image. In its most fundamental form the

image is *complex*, having a phase structure that may be exploited for certain applications. Ideally, the complex image is simply a linear transformation of the input signal, and has no phase errors introduced by operations in the processor. (Note that very few SAR processors in use today satisfy this objective.) Selected advantages of the complex image domain for calibration purposes are explored in [3]. Considerations essential to arriving at a complex image with robust phase is considered further in section 2.3 below.

2.2. Comments on Resolution

A nice discussion of resolution restraints for a SAR may be found in [1]. For the present purposes, we highlight the central result, presented in a form rather more general than that usually found in the literature. Resolution is generally (but loosely) defined as the width of the "point spread function", the "Green's function", or the "impulse response function", depending on whether one has an optics, a physics, or an electronic systems background. More properly, "resolution" refers to the ability of a system to differentiate two image features corresponding to two closely spaced small objects in the illuminated scene when the brightnesses of the two objects in question are comparable (according to Lord Rayleigh [1879]).

A SAR is distinguished due to its ability to achieve "high resolution" (by which is meant, small response function width, and therefore "good") in the azimuth direction, which is parallel to the sensor platform velocity vector.

General case: It follows from Eq. 4 that azimuth resolution is determined only by the wavelength and the span of angles over which the object is viewed. For a moving

platform, these are sufficient to establish the Doppler bandwidth of the signal. The class of sensors includes SAR, certain SONAR devices, Spotlight SAR, tomography, inverse SAR as used for imaging Earth satellite and nearby planets, etc. The azimuth resolution is given by the inverse (spatial) bandwidth, which leads to

$$\rho_{az} = \frac{\lambda}{2 (\sin \beta_1 + \sin \beta_2)} \quad (7)$$

where the angles of observation are defined in Figure 1.

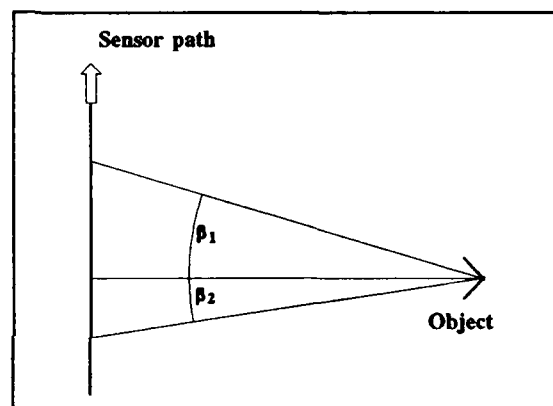


Figure 1. Geometry of viewing angles, general case.

Extremum: The minimum (limiting best or finest) resolution is obtained for an effective field of view of 180°. The limiting value is readily seen to be

$$\lim_{\beta_1, \beta_2 \rightarrow 90^\circ} \rho_{az} = \frac{\lambda}{4} \quad (8)$$

which might seem unrealistic. However, it should be noted that results approaching this value have been achieved in certain applications such as active seismics.

SAR Application: For a SAR, the subtended angles of view are generally very small, and, furthermore, are oriented nominally at right angles to the velocity vector of the sensor. In this case the small angle sine approximation applies, and one obtains

$$\rho_{SAR_{Az}} = \frac{\lambda}{2 \beta_{eff}} \quad (9)$$

where the angle expresses the total *effective* viewing angle. It should be noted for satellite radar systems, where one should account for the sphericity of the viewing geometry [4], that

$$\beta_{eff} = \frac{V_{S/C}}{V_{Beam}} \beta_{Beam} \quad (10)$$

which expresses the fact that the angle over which the object is viewed in a satellite setting is increased over the azimuth (free space) beamwidth of the antenna pattern due to the rotation of the spacecraft as it progresses along its orbit. (The parameters $V_{S/C}$ and V_{Beam} refer to the velocity of the spacecraft along its orbit, and the velocity of the antenna beam footprint over the surface of the Earth, respectively.) Note that in virtually all available literature this factor is not included.

A common approximation, familiar to SAR people, is that

$$\beta_{Beam} \approx \frac{\lambda}{D_h} \quad (11)$$

where D_h is the (azimuth) aperture size of the antenna. Thus, from Eq. 3, we reach the famous representation

$$\rho_{SAR_{az}} \approx \frac{D_h}{2} \quad (12)$$

in which there is no dependence on range or wavelength! This is a fundamental characteristic of SAR systems, and makes them well suited to spacecraft platforms. NB: The magnitude of expression of Eq. 12 is an approximation only, as it violates the correct diffraction limited result that follows from Eq. 7, and it does not account for the benefits of orbital geometry. It is this subtlety that justifies revisiting SAR resolution in this lecture. Although the best known of the "SAR facts" to be found in the open literature, Eq. 12 remains an unacceptable approximation for many space based SAR considerations.

2.3. Comments on Processing

Means of handling the coupling in the context of range curvature correction in a SAR processor are well reviewed by Bamler [5]. The several cases discussed in that reference differ primarily by the method and scope of approximations employed. The consequence of most limitations used to date is to restrict applicability of any given method to narrow beamwidth around zero Doppler offset, or to narrow beamwidth about a given Doppler offset. Implementation of several traditional techniques is covered more extensively in [6].

For phase sensitive applications, particularly as encountered in interferometry (see section 4 below), requirements on phase precision in the derived complex image surpasses the ability of most traditional processing algorithms. In response, Cafforio, Prati, and Rocca [7] introduced seismic wave domain techniques to the field of radar. In the context of seismic inversion problems, typically characterized by rather large angular fields of view, and hence severe range/azimuth signal coupling, Stolt [8] had developed an effective change of variables in the two-dimensional frequency

domain. A practical difficulty is that the Stolt change of variables requires an interpolator for its implementation, which leads to increased cost and decreased precision impacting particularly phase fidelity in the complex image. Improvements have been demonstrated (e.g., [9]), although until recently interpolators are still required. The main difficulty arises from the range dependence of the range curvature parameter, a quantity not available in the two-dimensional frequency or "wave-number" domain.

For phase precision, it is desirable to be able to cope with large angular field and range depth without the need for an interpolator. There have now been processors demonstrated that satisfy this objective ([10], [11], and [12]). In future, the coherent structure inherent to the complex image of SAR and related system data sets should not be limited by processor fidelity. The remainder of this lecture assumes that complex image data is available with sufficient phase accuracy to satisfy processing requirements.

3. ONE SIGNAL SEQUENCE

Specialized systems have been demonstrated that depend on coherent properties of a single sequence of signals in order to improve resolution, or to derive information about moving targets.

3.1. Squint Mode

In many applications, particularly for tactical systems, it is desirable for the radar to look forward (or aft) of the zero Doppler plane by a significant amount. The attainable azimuth resolution for such a "squint mode" SAR follows from Eq. 7 and Figure 1. With suitable processing, azimuth

resolution may be maintained to within about a factor of two over "perfect" side-looking SAR resolution out to squint angles on the order of 45° , and certain systems support squint up to 80° and more.

In squint mode geometry, since the range and azimuth coordinate systems are no longer orthogonal, targets appear to move through many range resolution cells during their time of radar illumination. For narrow beam systems, this "range walk" may usually be approximated by a linear phase term. Processing adapted to squint mode radars is covered in [6] usually implemented digitally using interpolation. A more recent wave domain contribution described in [9] has been demonstrated at squint angles in excess of 45° .

A second complexity arises in squint mode geometry. Recall that the radar is a sampled system in the azimuth dimension. According to the Nyquist sampling criterion (see, for example, [1]), the Doppler spectrum of the signal sequence must be sampled with sufficiently high radar pulse repetition frequency (*PRF*) so that spectral aliases, or ambiguities, are avoided. The mean Doppler frequency is set by the squint angle of the antenna according to the terms of Eq. 7. It is in general *not desirable* to increase the *PRF* in proportion to squint, since that would reduce the unambiguous range interval available to the system.

Fortunately, the bandpass version of the Nyquist sampling theorem applies, so that the *PRF* must be greater than only the Doppler bandwidth of the signal sequence. This leaves open the question of estimating the *Doppler centroid* which may be many times larger than the *PRF*, a common challenge in most SAR systems. (Doppler centroid estimation is covered in another lecture in this series.)

3.2. Spotlight Mode

If one attempts to sharpen azimuth resolution in a conventional SAR, either in a squint or side looking mode, a smaller azimuth antenna aperture must be used. This is the "ground rule" for any strip mapping mode SAR. Unfortunately, the effective gain of the antenna is reduced by the square of its aperture, so a severe and usually unacceptable penalty must be paid to push the antenna aperture to very small dimensions.

The fundamental resolution expression of Eq. 7 may be exploited in another way, however. Resolution for a given illuminated region is determined primarily by the set of angles over which the data sequence is gathered. A *Spotlight SAR* is designed to observe a selected patch of terrain with dynamic angular pointing of the antenna pattern steered so as to maintain illumination of the desired area as the sensor passes by. Azimuth resolution much smaller than the antenna half-aperture may be achieved for one area, with the trade-off being that other adjacent areas are not imaged at all.

Antenna size for a Spotlight SAR is governed by the desired size of illuminated area, and by the required signal-to-noise ratio of the received signal sequence. Both of these objectives are range dependant, leading to *larger* antenna size for larger ranges, all else equal. Phased array antenna technology is highly desirable for such systems, although impressive performance may be obtained with rather modest scan angles. For example, from Eq. 7, one may find that resolutions on the order of only 5 times the wavelength (15 cm at X-band) may be achieved with an illumination angle of about 3° (in the nominally side-looking Spotlight geometry). For an N-look image,

proportionally more Doppler bandwidth must be obtained.

Processing for Spotlight SARs tends to be specifically designed for the task. A so-called "polar format" is often employed [13]. This had its roots in the days of optical processing, and creates a data format analogous to the polar coordinate system in which the Spotlight SAR naturally observes its target. The first unclassified work on the subject was [13], and an interesting interpretation may be found in [14]. Treatment of Spotlight SAR in the general context of SAR processing is included in [6]. Modern systems use on-board real time processing.

3.3. The Stretch Technique

Having achieved very fine azimuth resolution through the Spotlight technique, it is natural to seek comparable resolution in the range direction. This is not easily done by direct means. For example, for 15 cm range resolution (symmetrical with the azimuth example above), the range bandwidth required is on the order of 1 GHz. It is desirable to maintain fine range resolution without paying such a penalty.

In the early 1970's the "stretch" technique was demonstrated [15]. For a linear frequency modulated (linear fm) signal, demodulation of the received signal by a delayed replica of the original results in a difference signal of constant frequency. The frequency is proportional to the relative delay of the received and reference signals. Useful results occur only when the signals overlap substantially.

Stretch is perfect for the Spotlight application. It reduces the bandwidth requirements needed for all portions of the system following demodulation. It does this by a trade-off between range and bandwidth, a

convenient consequence of the linear fm waveform. It is thus restricted to scenes with relatively small range extent, which fits the Spotlight requirement. Stretch modulation applied to the Spotlight SAR case is described by Walker in [13].

3.4. MTI

An ability for moving target indication (MTI) has been for many years an objective of both strategic and tactical radar systems. It is of interest to explore the ability of a SAR in this application. Early work in this area may be found in [1], and especially [16], both of which are restricted to rates rather small compared to that of the radar platform. For larger motions, the problem rapidly gets more complicated [17].

Attempting to simultaneously achieve both fine spatial resolution and spectral resolution flies in the face of physical principals (e.g. [18]). The general formulation of this principle is through the *ambiguity function*. These fundamental limits apply to the conventional SAR configuration, suggested in Figure 2.

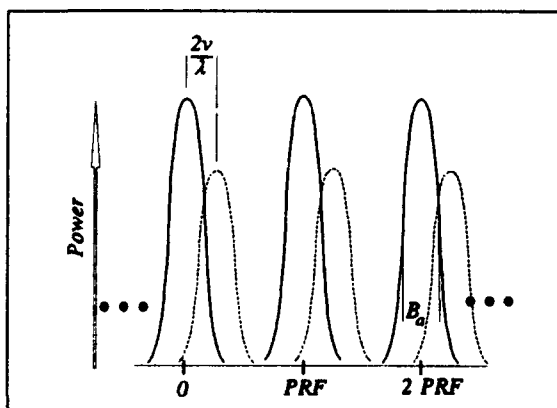


Figure 2. SAR Doppler space in the presence of a moving target. (Two ambiguities explicitly shown.)

The solid lines in the figure represent the (two-way) power profile of stationary scatterer return as limited by the azimuth pattern of the radar antenna. The zero order Doppler response is shown together with two of the ambiguous spectra each centered on a multiple of the *PRF*. The width of the clutter spectrum is $B_a = 2\beta V/\lambda$, where β is the two-way half-power angular width of the antenna pattern, and V is the radar vehicle speed.

The dotted lines represent the envelope returned from a single target having radial velocity v with respect to the radar line of sight, leading to a Doppler frequency shift $2v/\lambda$ which appears as an additional phase term (normalized to azimuth spatial frequency by V^1) in Eq. 4. (This may be derived from from Eq. 1 by using $R_n = R_n + vt$.)

We are interested in describing the way a slowly moving target appears in a SAR image, and in the possibility of detection of moving targets.

For a SAR, the small (coherent) radial velocity component of a scatterer leads to a shift Δx in the mapped azimuth position of its image. This is a natural consequence of the fact that the azimuth coordinate system is derived from Doppler information, and the processor has no way of knowing that the target itself might have a Doppler component. For the aircraft case [16], this argument leads to $\Delta x = R_n v/V$. Since the range to a scatterer is relatively large, there is often a shift in scatterer position many times the azimuth resolution. However, unless there are tell-tale signs of where the object *should* be located (such as the wake of a ship), it is impossible to identify the return as being associated with a moving target. This is an example of the spatial-Doppler ambiguity inherent in the problem.

In order for a signal to be detected as moving, its Doppler shift (see Figure 2) must be greater than the Doppler bandwidth of the return from stationary scatterers, which, for satellite SARs, may be many km/h. Furthermore, in order to detect a small moving target against a larger clutter background, and to guard against false alarms, usually the Doppler shift must be much larger than the system Doppler bandwidth.

In order to achieve such a result, the Doppler MTI passband, defined as the space between ambiguous Doppler spectra free from clutter energy, must be made large, requiring a larger than normal *PRF*. Normal motions from vehicles and other moving targets of potential interest are usually more complicated than these simple results consider. In general, defocusing arises when all velocity components are included and the possibility of range acceleration is allowed [16]. More complex motions and vehicle vibrations may lead to loss of signal coherence. These considerations argue against effective adaptation of a conventional SAR as an MTI device. (More may be done, however, as noted below.)

3.5. Imaging Ocean Waves

The most subtle of "conventional" SAR imaging applications is that of ocean waves. A SAR observes essentially only the surface layer of salt water which under typical circumstances is constantly in motion. Ships moving on the surface may reasonably be expected to follow the "rules" outlined in the preceding section, but what about the water itself? The question has value in that SARs are promoted as potential sources of global wave climatology data. Today this promise has yet to be fulfilled.

A qualitative prediction of SAR wave imaging appeared in 1978 [19]. Most quantitative analysis was concerned with the effect on a SAR image by the advection of each scattering cell on the ocean's surface by the passage of longer waves such as swell [20], [21]. Since motion coherently sensed by the SAR causes image shift, systematic motions from the waves' orbital velocities leads to "velocity bunching", actually helpful (within limits) for forming a wave-like contrast pattern in a SAR ocean image. However, the detailed structure of a wave changes with time, sometimes rapidly, so that there are coherence time limitations on image formation that lead to inherent azimuth resolution constraints, the so-called "azimuth cut-off". The state of the art of ocean SAR imaging at that time is summarized in [22].

Independent investigations, both theoretical [23] and experimental [24], raised the importance of non-coherent aspects of SAR wave imaging. Since waves move, and since they are imaged from a platform itself in motion, both phase sensitive and position sensitive motions should be of importance.

For the time scales encountered in airborne SAR systems, the two types of wave motion may be exploited. The separate looks normally created from a SAR data set are spectrally separable in the Doppler domain. Since the azimuth signal is of large time-bandwidth product, the Doppler spectrum, for any reference time, is proportional to the time of actual data collection with respect to the reference time. It follows that looks may be separately processed, relative image shift between looks compensated, and then the shifted looks combined [23]. Properly done, this leads to an "optimum" SAR image of ocean waves, and, of more importance, to an optimized directional spectrum derived from the SAR data [25]. Furthermore, the technique naturally

leads to removal of the 180° ambiguity of wave propagation direction so typical of wave imaging systems.

Imaging ocean waves from satellite altitudes and velocities is in general less than optimum. The time variable aspect of the geometry is scaled to first order by h/V which assume less favourable values for most orbits than for most aircraft SARs. Ocean wave imaging is an active area of research.

4. SEQUENCE PAIRS

One could visualize a SAR as simply one example of a classical coherent imaging system. It is well known that such systems reach their pinnacle of precise performance when used in an interferometric mode, *i.e.*, one in which the scene observed is made to yield its secrets at scales of the wavelength of illumination. This is the objective of SAR configurations designed to use a pair of signal sequences, either spatially or temporally.

4.1. Spatial Interferometry

A SAR image of terrain is a two-dimensional mapping of a three-dimensional surface. Unless more information is available, there is no way to quantitatively estimate terrain height. Of course, as with aerial photographs, a pair of SAR images each taken from a different point of view could be used as a stereo pair, but as a coherent system, SAR has much more to offer than that.

In the early 1970's, Goodyear introduced a SAR system [26] that carried two antennas designed to function simultaneously.

The two received signals were coherently combined analogous to an optical interferometer. The main elements of the

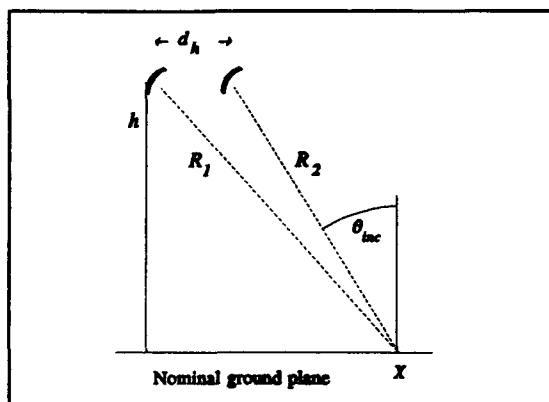


Figure 3. Basic geometry for topographic interferometric imaging radars.

geometry are shown in Figure 3. The essential feature is that, for known antenna separation d_h , and known slant ranges R_1 and R_2 to a scattering centre, then its relative height may be estimated from the phase information in the interference pattern.

In the mid-1980's, a brilliant innovation was introduced by Goldstein of JPL [27]. He suggested that an interferometric pair could be created by two relatively closely spaced but *separate* passes of a (single antenna) SAR satellite. Two pass interferometry was proven using selected passes of existing Seasat data, from which interference fringes were generated, and relative terrain height estimated.

Large area image interferometry placed a great strain on the SAR processing capabilities then available. In response, the "wave-domain" algorithm and its derivatives were introduced: collaboration between Rocca and Goldstein led to better phase performance of SAR processors, and proliferation of SAR interferometric work to Europe and elsewhere.

The underlying assumption of two pass interferometry is that the terrain being observed is essentially unchanged (with respect to phase characteristics) in the time interval between observations. The condition may be inverted, since the absence of interference fringes is an indication of (randomly) changed phase in the affected area.

The basic SAR interferometric principle leads to terrain height estimation with a precision on the order of the resolution of the SAR [28]. Its accuracy, however, is very sensitive to the value of the baseline d_n . For applications in which a known "level" terrain feature is present, such as a shoreline, then the elevation contours may be calibrated. In principle, the technique may be used with any satellite SAR.

The measurement capability of interferometric SARs has been extended through the use of differential techniques [29], [30], [31]. Through this approach, one looks for differences in the fringe pattern between two pairs of observation opportunities. In effect, in each case, one of the signal pair establishes a reference phase for each element in the scene, and the other signal provides an estimate of phase change with respect to the reference. In principle, the method is sensitive to physical changes in position of a reflecting element to less than $\lambda/4$, which has been demonstrated [29]. It has been proposed as a method for estimating crustal movement either before or after an earthquake [30].

Interferometry is not without its problems. One of the most challenging is "phase unwrapping" [31], [32]. Interferometry rests on phase estimation, which, unless other information is implicitly or explicitly available, is multiple valued. Current techniques in effect rely on an assumption

of slope continuity through which progressive phase shift may be integrated across changes in excess of 2π . Use of low resolution methods such as "shape from shading" is also helpful.

Within the last decade, interferometry for SAR is one of the two most significant developments. (Quadrature polarimetry is the other one.) The topic remains an area of very active research, and may reasonably be expected to offer valuable quantitative results to the user community in the years to come.

4.2. Temporal Interferometry

There is an alternative way in which to build an interferometer. For a SAR on a moving platform, a pair of antennas could be arranged to lie along the flight vector, thus providing essentially identical views of the illuminated field, but at slightly different times. The basic geometry is illustrated in Figure 4.

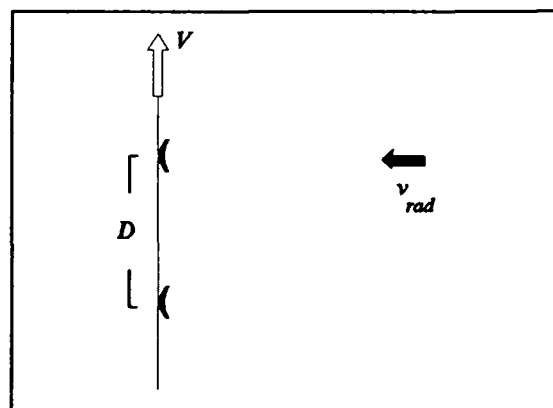


Figure 4. Dual antenna time-sequential interferometry.

The time delay δt between the pair of received signals is D/V if the antennas are operated separately as transmitter and receiver. The time delay is $D/2V$ if, as is usually the case, only one antenna is used for transmission and both are used for reception.

Scene elements having radial motion v_{rad} cause a differential phase shift

$$\Delta\phi = 4\pi \frac{v_{rad}}{\lambda} \delta t \quad (13)$$

which may be detected by interferometric combination of the signals from the two channels. For area extensive motion, such as ocean surface currents, the detection technique normally employed is correlation [33], from which excellent results have been obtained. The technique has been extended to wave spectral estimation through a variation on the basic theme [34].

4.3. MTI and Velocity Estimation

When most of the imaged field is expected to be unchanged, the more direct processing strategy of "delay and subtract" applies. This is the case for MTI. It has been known for many years that the dual antenna configuration offers a way around the Doppler lower limit imposed by the clutter spectrum [35]. Performance estimates for the SAR case are available in [16].

If $ss_1(t)$ is the signal from the front antenna, and $ss_2(t)$ is the signal from the rear antenna, and $mm(t)$ is the signal from a slowly moving target with radial velocity v_{rad} , then

$$m_{\Delta}(t) = ss_2(t) - ss_1(t - \delta t) \quad (14)$$

where, neglecting noise, one may show that

$$m_{\Delta}(t) = mm(t) \left[1 - \exp \left(-j4\pi \frac{v_{rad}}{\lambda} \delta t \right) \right] \quad (15)$$

as the indication of the presence of a moving target. The detected difference image will contain only moving targets (plus differential clutter and noise), each weighted by the squared magnitude of the radially dependent phase term of Eq. 15.

Implementation of this algorithm using digital techniques in general requires interpolation since there must be continuous adaptation to variations in aircraft velocity V . There is a neat way around this objection, however, by taking the (azimuth) Fourier transform, yielding a domain characterized by a pair of signals such as given by Eq. 4. The delay operator becomes simply a phase multiply

$\exp(-jD\omega_x/2)$ when written in spatial

frequency, and under the assumptions that only one antenna is used for transmission, and that the *PRF* is maintained proportional to ground speed.

The companion operation on the signal pair of Eq. 14 is to form their sum. Thus

$$m_{\Sigma}(t) = 2ss_1(t) + mm(t) \left[1 + \exp \left(-j4\pi \frac{v_{rad}}{\lambda} \delta t \right) \right] \quad (16)$$

in which the effective common mode (complex) signal is doubled, and the phase modulated term is present as the complement to the differential channel. One may show [36] that an effective doubling of the image SNR follows from the first effect.

The two components of the moving target are shared proportionately between the two channels, with $\sin^2(k v_{rad} \delta t)$ in the difference channel, and $\cos^2(k v_{rad} \delta t)$ in the sum channel, where $k = 2\pi/\lambda$. These expressions show that there is a "blind speed" $v_{rad, B}$, at which the target motion is through one (round-trip) wavelength between observations, and thus not detectable by phase shift. Blind speeds are characteristic of MTI radar systems.

Energy partitioning of the moving target signal between the sum and the difference channel may be used for target velocity estimation, analogous to the same technique used for calibration of dual channel polarimetric radars [36].

Extrapolation of this principle to orbital velocities shows that along track antenna separations of several hundred metres would be required for detection of targets with small components of velocity towards the radar.

5. ADDITIONAL COMMENTS

This lecture has attempted to suggest ways in which the basic capabilities of a SAR system may be stretched to new and sometimes almost unbelievable domains. The discussion has been far from complete. Some closing comments are offered here.

One of the richest areas for SAR system advanced technology is in quadrature polarimetry. This topic is covered by other lectures in this series. One should note in passing, however, that the underlying coherence of the SAR channels is required to achieve full polarimetric synthesis either in the signal domain or the image domain.

Improvement of image quality, both through summation of extra non-coherent looks, and through coherent integration in special circumstances, has been demonstrated using separate data sets, available, for example, from nearly spatially coincident orbits.

By taking the two-pass topographic interferometric geometry to the limit, in principle one could generate multiple range offset data sets sufficient to create full holographic (three dimensional) images of the illuminated surface. In fact, this was demonstrated nearly 20 years ago using aircraft based radars, but has certain physical limitations when presented as an optical analog. It could have value in the modern era of digital imaging, however.

Both spatial- and time-delay interferometry have been implemented using a SAR. The classic (partially coherent) field analysis tool, however, is the *mutual coherence function* which utilizes simultaneous application of a spatial and a temporal interferometric baseline. Such a tool in the SAR context should have value, for example, in deeper analysis of SAR ocean wave imaging.

Most of the techniques described above, and the underlying capability to form a basic SAR image, all have their "bistatic" counterparts. A bistatic system is one for which the transmitter and the receiver are in different locations, sometimes widely separated. We have restricted the discussion to the case for which the radar transmitter and receiver have the same physical location, the so-called mono-static case. The fundamental requirement for bistatic configurations, just as for the conventional case, is that there be "system coherence". In each situation a means of maintaining phase robustness is required for all signals to be utilized.

Under the constraint that phase of the signal ensemble is available, then there are many varied measurement possibilities open to the clever inventor. One may reasonably expect that in the forthcoming years, more special SAR techniques will be developed, and be adopted as needed for specific applications of this exciting device.

6. REFERENCES

- [1] R. O. Harger, *Synthetic Aperture Radar Systems: Theory and Design*, Academic Press, New York, 1970.
- [2] R. K. Raney, A New and Fundamental Fourier Transform Pair, *Proceedings of the International Geoscience and Remote Sensing Symposium*, 26-29 May 1992, Houston, Tx.
- [3] R. Touzi, K. Raney, and A. Lopes, On the Use of Complex SAR Data for Calibration, *Proceedings of the International Geoscience and Remote Sensing Symposium*, 26-29 May 1992, Houston, Texas.
- [4] R. K. Raney, Conceptual Design of Satellite SAR, *Proceedings of the International Geoscience and Remote Sensing Symposium*, Strasbourg, ESA Publication SP-215, 27-30 Aug, 1984, pp. 801-807.
- [5] R. Bamler, A Systematic Comparison of SAR Focusing Algorithms, *Proceedings of the International Geoscience and Remote Sensing Symposium*, Espoo, Finland, June 1991, pp. 1005-1009.
- [6] D. A. Ausherman, A. Kozma, J. L. Walker, H. M. Jones, and E. C. Poggio, Developments in Radar Imaging, *IEEE Trans. on Aerospace and Electronic Systems*, Vol. AES-20, No. 4, July 1984, pp 363-400.
- [7] C. Cafforio, C. Prati, and F. Rocca, Full Resolution Focusing of Seasat SAR Images in the Frequency-Wavenumber Domain, *International Journal of Remote Sensing*, Vol. 12, 1991, pp. 491-510.
- [8] R. Stolt, Migration by Fourier Transform Techniques, *Geophysics*, Vol. 43, 1978, pp. 49-76.
- [9] R. K. Raney and P. W. Vachon, A Phase Preserving SAR Processor, *Proceedings of the International Geoscience and Remote Sensing Symposium*, Vancouver, Canada, July, 1989, pp. 2588-2591.
- [10] R. K. Raney, An Exact Wide Field Digital Imaging Algorithm, *International Journal of Remote Sensing*, Vol. 13, No. 5, 1992, pp. 991-998.
- [11] I. Cumming, F. Wong, and R. K. Raney, A SAR Processing Algorithm with No Interpolation, *Proceedings of the International Geoscience and Remote Sensing Symposium*, Houston, Tx., 26-29 May 1992.
- [12] H. Runge and R. Bamler, A Novel High Precision SAR Processing Algorithm Based on Chirp Scaling, *Proceedings of the International Geoscience and Remote Sensing Symposium*, Houston, Tx., 26-29 May 1992.
- [13] J. L. Walker, Range-Doppler Imaging of Rotating Objects, *IEEE Transactions on Aerospace and Electronic Systems*, AES-16, No. 1, Jan 1980, pp 23-52.
- [14] D. C. Munson, J. D. O'Brien, and W. K. Jenkins, A Tomographic Formulation of Spotlight-mode Synthetic Aperture Radar, *Proceedings of the IEEE*, No. 7, Aug 1983, pp 917-925.

- [15] W. J. Caputi, Jr, Stretch: A Time-Transformation Technique, *IEEE Transactions on Aerospace and Electronic Systems*, Vol. AES-7, No.2, Mar 1971, pp. 269-278.
- [16] R. K. Raney, Synthetic Aperture Radar and Moving Targets, *IEEE Transactions on Aerospace and Electronic Systems*, Vol. AES-7, No. 3, May 1971, pp. 499-505.
- [17] E. J. Kelly and R. P. Wishner, Matched Filter Theory for High-velocity Accelerating Targets, *IEEE Transactions on Military Electronics*, Vol. MIL-9, Jan 1965, pp. 56-59.
- [18] J. R. Klauder, The Design of Radars Having Both High Range Resolution and High Velocity Resolution, *Bell System Technical Journal*, July 1960, pp. 745-808.
- [19] R. K. Raney and R. A. Shuchman, SAR Mechanisms for Imaging Ocean Waves, *Proceedings 5th Canadian Symposium on Remote Sensing*, Victoria, B.C., 1978, pp. 495-505.
- [20] C. T. Swift and L. R. Wilson, Synthetic Aperture Radar Imaging of Ocean Waves, *IEEE Transactions on Antennas and Propagation*, Vol. 27, No. 6, 1979, pp. 725-729.
- [21] W. R. Alpers and C. L. Rufenach, The Effect of Orbital Motions on Synthetic Aperture Radar Imagery of Ocean Waves, *IEEE Transactions on Antennas and Propagation*, Vol. 27, No. 5, 1979, pp. 685-690.
- [22] K. Hasselmann, R. K. Raney, W. J. Plant, W. Alpers, R. A. Shuchman, D. R. Lyzenga, C. L. Rufenach, and M. J. Tucker, Theory of Synthetic Aperture Radar Ocean Imaging: A MARSEN View, *Journal of Geophysical Research*, Vol. 90, No. C3, May 1985, pp. 4659-4686.
- [23] R. K. Raney and P. W. Vachon, Synthetic Aperture Radar Imaging of Ocean Waves from an Airborne Platform: Focus and Tracking Issues, *Journal of Geophysical Research*, Vol. 93, No. C10, 1988, pp. 12,475-12,486.
- [24] P. W. Vachon and J. C. West, Spectral Estimation Techniques for Multilook SAR Images of Ocean Waves, *IEEE Transactions on Geoscience and Remote Sensing*, to appear, 1992.
- [25] P. W. Vachon and R. K. Raney, Ocean Waves and Optimal SAR Processing: Don't Adjust the Focus!, *Transactions of the IEEE Geoscience and Remote Sensing Society*, to appear, 1992.
- [26] L. C. Graham, Synthetic Interferometers for Topographic Mapping, *Proceedings of the IEEE*, Vol. 62, No. 6, 1974, pp. 763-768.
- [27] H. A. Zebker and R. M. Goldstein, Topographic Mapping from Interferometric Synthetic Aperture Radar Observations, *Journal of Geophysical Research*, Vol. 91, No. B5, 1986, pp. 4993-4999.
- [28] C. Prati, F. Rocca, and A. M. Guarnieri, Effects of Speckle and Additive Noise on the Altimetric Resolution of Interferometric SAR (ISAR) Surveys, *Proceedings of the International Geoscience and Remote Sensing Symposium*, Vancouver, Canada, July 1989, pp. 2469-2472.
- [29] A. L. Gray and P. Farris-Manning, Two-Pass Interferometry with Airborne Synthetic Aperture Radar, *IEEE Transactions on Geoscience and Remote Sensing*, to appear, 1992.

[30] A. K. Gabriel, R. M. Goldstein, and H. A. Zebker, Mapping Small Elevation Changes over Large Areas: Differential Radar Interferometry, *Journal of Geophysical Research*, Vol. 94, No. B7, July 1989, pp. 9183-9191.

[31] F. K. Li and R. M. Goldstein, Studies of Multibaseline Spaceborne Interferometric Synthetic Aperture Radars, *IEEE Transactions on Geoscience and Remote Sensing*, Vol. 28, No. 1, Jan 1990, pp. 88-97.

[32] C. Prati, M. Giani, and N. Leuratti, SAR Interferometry, A 2D Phase Unwrapping Technique based on Phase and Absolute Value Information, *Proceedings of the International Geoscience and Remote Sensing Symposium*, Washington, D.C., May 1990, pp. 2043-2046.

[33] R. M. Goldstein and H. A. Zebker, Interferometric Radar Measurements of Ocean Surface Currents, *Nature*, Vol. 328, 1987, pp. 707-709.

[34] D. R. Lyzenga and J. R. Bennet, Estimation of Ocean Wave Spectra using Two-Antenna SAR Systems, *IEEE Transactions on Geoscience and Remote Sensing*, Vol. 29, No. 3, May 1991, pp. 463-465.

[35] H. Urkowitz, The Effect of Antenna Pattern on the Performance of Dual-antenna Radar Airborne Moving Target Indicators, *IEEE Transactions on Aerospace and Naval Electronics*, Vol. ANE-11, December 1964, pp. 218-223.

[36] R. K. Raney, A "Free" 3-dB in Cross-Polarized SAR Data, *IEEE Transactions on Geoscience and Remote Sensing*, Vol. 26, No. 5, Sept 1988, pp. 700-702.

Review of Spaceborne and Airborne SAR Systems

R. Keith Raney
Canada Centre for Remote Sensing

1. SUMMARY

This Lecture provides a concise summary of the state of the art in SAR systems, both spaceborne and airborne. The first civilian SAR mission in space was the United States' SEASAT (L-band), operating July-September 1978. It was followed by two Shuttle missions of one week duration each, SIR-A (L-band, November 1981) and SIR-B (L-band, October 1984). The 1990's is witnessing a flurry of orbital SAR activity, with Almaz (USSR, S-band, March 1991), ERS-1 (ESA, C-band, July 1991), J-ERS-1 (Japan, L-band, February 1992), SIR-C/X-SAR (USA/Germany and Italy, L-, C-, and X-bands, three launches planned after 1993), ERS-2 (ESA, repeat mission), and RADARSAT (Canada, C-band, 1995) taking place in the decade. System parameters are included in Tables, and general characteristics of these radars are compared and contrasted. The lecture also provides an overview of airborne SAR systems, including those of NASA (USA), CCRS (Canada), Intera/MDA (Canada), DLR (Germany), and TUD (Denmark), among others. Acronyms are defined in appropriate sections of the text.

2. INTRODUCTION

After decades of development since the concept of "synthetic aperture radar" was published in 1951, the 1990's is witnessing an unprecedented level of technical (and financial) activity in imaging radar techniques based on Carl Wiley's original

idea. This lecture describes the current state of system development. All civilian Earth observing synthetic aperture radar (SAR) satellites are reviewed: past, present, and future. The current status of representative airborne SAR systems is outlined, and several other airborne systems mentioned. The discussion includes more than twenty SARs, hardly an exclusive field as of this writing! Taken together, the implied financial support is on the order of 5 billion dollars.

There are several published sources that are more complete than this brief lecture is able to be. The reader is referred to a special issue of the *Proceedings of the IEEE* [1] for articles that describe currently operating and approved future satellite SAR systems in some detail. Those papers include planetary missions as well as the Earth orbital radars of interest here. In the context of preparation for the EOS SAR mission of NASA, an excellent review article [2] has been prepared that covers several airborne SAR systems as well as orbital ones.

For satellite SARs, this lecture is organized according to epoch: previous missions; present missions; planned missions; and proposed missions. The airborne systems, typically in a constant state of change, are described in terms of present known capabilities.

As is the case for any area in which many sources might be found, there is not always agreement in those sources on the detailed specifications for any given

system. This is understandable, particularly when technical change as well as language and terminology confound the issue. In this review, primary sources are used whenever available. Furthermore, when there is an important conflict in published data, comments are included in the text to help clarify the matter for the interested reader.

3. PREVIOUS ORBITAL SAR SYSTEMS

For some individuals, history hinges on the wisdom of Lao Tzu (1st century, China), and for others on the inspiration of Jesus Christ (1st century, Judea). For those interested in synthetic aperture radar, however, history hinges on Seasat (20th century, North America). Virtually all Earth observing SAR satellite systems in this lecture owe both their inspiration and baseline performance standards to Seasat, and by implication its design and science teams. Of course, there are solid logical reasons for the technical similarities, but the fact remains, Seasat led the way. Seasat was initiated by an inter-agency study team, and its implementation was managed by the Jet Propulsion Laboratory (JPL) (of the California Institute of Technology in Pasadena, California) funded by NASA. Seasat was a magnificent achievement [1].

Principle parameters of Seasat are sketched in Table 1, abstracted from [3], also available from a widely distributed literature. As in the remainder of this lecture, most comments in the discussion on this SAR are keyed to entries in pertinent columns of tables.

The design lifetime of Seasat was two years. Unfortunately, the spacecraft failed after three months of SAR operation due

to a massive short circuit in the slip ring assembly of the solar panel primary power system. (There are system evaluation reports available from the committees charged with investigating this event, should any reader be interested in hardware and programmatic details.) Data provided by Seasat proved to be of high quality and immense interest to the science and applications communities, and still appears as prime material for recent papers in the professional literature.

In the Table, the antenna is described as "corporate". This is a shorthand notation for a passive antenna using power dividing techniques to distribute the signal to be transmitted to a network of radiating elements. In the case of Seasat, the antenna was a flat microstrip array, built on eight panels. The size of the antenna for Seasat is of interest. Its long length, and large aspect ratio, is "typical" of "standard" (satellite) SAR antennas. The reasons for this may be found in [3], and in other lectures in this series.

Typical parameter values important for image quality for satellite SAR systems, in particular resolution and number of looks, were firmly established by Seasat. Unless one is willing to give up other image aspects such as swath width, there is rather little flexibility available.

The NASA objective for Seasat was digital processing, but NASA ran out of money (after the potential processor contractor had been selected, but before the contract had been awarded!). The project was launched, literally, with optical processing as the baseline. In parallel, Charles Wu at JPL (and MDA, Canada) developed digital processing techniques for Seasat. Seasat was a resounding success largely because of digital processing, as the

TABLE 1. Previous Orbital SAR Systems

	Seasat	SIR-A	SIR-B	(Kosmos 1870)
General				
Country	USA	USA	USA	USSR
Agency	NASA	NASA	NASA	Glavkosmos
Spacecraft	Seasat	Shuttle	Shuttle	Salyut
Launch date	26 Jun 78	12 Nov 81	5 Oct 84	25 Jul 87
Lifetime	3 mos	2.5 days	8 days	2 years
Radar				
Band [wavelength (cm)]	L [23.5]	L [23.5]	L [23.5]	S [10]
Frequency (GHz)	1.275	1.278	1.282	3.0
Antenna	corporate	corporate	corporate	waveguide
Size (m), length x height	10.7x2.16	9.4x2.16	10.7x2.16	1.5x15 (2)
Polarization	HH	HH	HH	HH
Incidence angle (°)	23	50	15 - 64	30 - 60
Range resolution (m)	25	40	25	(~30)
Azimuth resolution (m)	25	40	58 - 17	(~30)
Looks	4	6	4	(4)
Swath width (km)	100	50	10 - 60	20 - 45
Recorder on board?	N	Y	Y	Y
Processing (Optical, Digital)	O,D	O	O,D	O
Noise equivalent σ^0 (dB)	-24	-32	(-28)	
Mission				
Nominal altitude (km)	800	260	350, 225	250-280
Inclination (°)	108	38	57	71.5
Sun synchronous?	N	N	N	N
Down-link data rate (MB/sec)	110	(none)	30	analog
Repeat cycle (days)	17, 3	nil	nil	variable
Operation time per orbit (min)	10	-	-	3 min/tape

remainder of the Tables will support.

Seasat used an analog downlink with a bandwidth of 20 MHz. The data was recorded, thence a/d converted (5 bits, I and Q, fixed point) to an effective data rate of 110 MB/sec.

The Shuttle SAR missions extended the foundations established by Seasat in the dimension of incidence angle. Both SIR-A and SIR-B [2] provided valuable results, but with technical limitations. SIR-A used only optical processing, depending on airborne film recorders adapted to the Shuttle mission. (SIR-A was an achievement in its own right, however, as it was the first payload to fly aboard a space Shuttle platform.) For SIR-B, two problems interfered with the SAR data quality, including a partial failure of the signal line connector to the antenna (with severe increase in noise level), and failure of the data downlink system (TDRS antenna tracking system) so that the data recovery originally planned was curtailed. Never-the-less, much valuable data was collected within the constraints of the flight mission.

For two years at the close of the decade, the USSR operated the Kosmos 1870 radar [4] [5], at the time a classified system. Kosmos 1870 was one of three satellite SARs built in the late 1970's built by NPO Machinostroenye. (The other two are known at present by the name of Almaz, discussed below.) The Soviets had a series of well known real aperture radars in space (the Kosmos 1500 series), but Kosmos 1870, in addition to Venera 16 and 17 to Venus, was its first publicized orbital SAR. Kosmos 1870 and its Almaz relatives are the only space radars with two antenna assemblies, directed to opposite sides of the orbital plane.

After the conclusion of the Kosmos 1870 mission, Glavkosmos started to advertize its SAR products on the international market, using agreements with such organizations as Space Commerce Corporation (USA). Kosmos 1870 was a radar limited in several regards by its "analog" foundations. Image products from that radar appeared to be far inferior to expectations based on paper specifications. Optical processing in series with analog data links seem to have significantly reduced the effective bandwidth of the data, leading to fewer looks and more coarse resolution than the radar itself should have provided. (N.B. "Digital" image products available from Kosmos 1870 are digitized optically processed SAR data, not to be confused with digitally processed SAR data.)

4. PRESENT SAR SATELLITES

In contrast to the almost total absence of (civilian) space radar capability in the ten years following Seasat, the present decade is witnessing substantial activity. All known space based SARs presently in service are listed in Table 2.

4.1. Lacrosse

Although a classified mission, there have been several open literature publications (e.g. [6] and [7]) from which the entries in the table for Lacrosse have been gleaned. The key items include resolution, down to one metre [7], and the antenna size, which may be estimated from an illustration published in [6] and *Paris Match* (date unknown). These two facts lead to the conclusion that Lacrosse uses the Spotlight SAR technique in its high resolution mode. This requires a steerable antenna pattern, so it follows that the rather large

TABLE 2. Present SAR Satellites

	(Lacrosse)	Almaz	ERS-1	J-ERS-1
General				
Country	USA	USSR	Europe	Japan
Agency	USAF	Glavkosmos	ESA	MITI/NASDA
Spacecraft	(Atlantis)	Salyut	ERS-1	J-ERS-1
Launch date	13 Dec 88	31 Mar 91	16 Jul 91	11 Feb 92
Lifetime (design)	-	2 years	2-3 years	2 years
Radar				
Band [wavelength (cm)]	X [3.0]	S [10]	C [5.7]	L [23.5]
Frequency (GHz)	9.5	3.0	5.25	1.275
Antenna	array	waveguide	waveguide	corporate
Size (m), length x height	(~8x2)	15x1.5 (2)	10x1	11.9x2.4
Polarization	HH	HH	VV	HH
Incidence angle (°)	steerable	30 - 60	23	38
Range resolution (m)	> 1	15 - 30	26	18
Azimuth resolution (m)	> 1	15	28	18
Looks	variable	> 4	6	3
Swath width (km)	variable	20 - 45	100	75
Recorder on board?	-	Y	N	Y
Processing (Optical, Digital)	D	D	D	D
Noise equivalent σ^0 (dB)	-	-	-24	-20.5
Mission				
Nominal altitude (km)	~275	300	~780	568
Inclination (°)	57	73	98.5	97.7
Sun synchronous?	N	N	Y	Y
Down-link data rate (MB/sec)	-	-	105	30 (x2)
Repeat cycle (days)	-	nil	3, 35, 176	44
Operation time per orbit (min)	-	3 min/tape	10	20

antenna must be a phased array. Orbital parameters are based on the capability of the Shuttle Atlantis launched from Cape Kennedy, for which 57° is the limiting inclination. (Lacrosse is manoeuvrable [7], however, so that current values of inclination and altitude may differ from those in the Table.) The press reports at least two other Lacrosse systems awaiting operations, one of which may already have been launched. Imagery from Lacrosse is not available.

4.2. Almaz

Almaz ([1], [4], [5]), or "diamond in the rough", is very similar to Kosmos 1870, but up-graded in several regards. Data is stored onboard in four parallel video recorders whose capacity limit the length of each data take. The data downlink is analog for both realtime data and recorded data. The most significant improvements in the Almaz signal chain followed from conversion to digital data handling and processing. The standard processor is patterned after a VAX 780, and uses the conventional range/Doppler algorithm. Image quality is variable, but some excellent examples are available.

From an applications point of view, Almaz is a very interesting system. Its S-band wavelength and selectable incidence angle make it a good choice for certain Earth resource issues. An example of Almaz imagery may be found in Figure 1.

4.3. ERS-1

After extensive studies and preparations from about 1975, the European Space Agency launched ERS-1 in 1991. The primary payload [8], [9] onboard ERS-1 ("European Remote Sensing" satellite) is the Active Microwave Instrument (AMI),

the heart of which is a SAR whose parameters are listed in the table. After several months in the three day repeat orbit used for system verification and data validation, the orbit was changed. The first two weeks of April 1992 used the "roll tilt" mode in a 35 day repeat pattern. The "roll tilt" accomplishes a change in incidence angle to about 35° . After mid-April, ERS-1 resumed normal operations, still in the 35 day repeat orbit. The 176 day repeat orbit will be used for an extended period later in the mission to support altimetric experiments. Data is downlinked when within range of a receiving station on X-band at 105 MB/sec using 5 bit quantization (fixed point) on the I and Q channels. Image quality from ERS-1 is excellent.

With two operational SARs in orbit, it is interesting to compare their respective views of the Earth. Figure 1 shows an area near Whitecourt, Alberta as seen by both Almaz and ERS-1. The contrast between these two images is striking. ERS-1 appears to be more sensitive to topographic effects, and less sensitive to differences in vegetation. Almaz, on the other hand, easily displays the clear-cuts in the forest, but is less sensitive to the terrain relief.

4.4. J-ERS-1

The Japanese launched J-ERS-1 ("Earth Resources Satellite") early in 1992. After early difficulty with the mechanism, the SAR antenna was successfully deployed on 9 April. At this writing, the SAR system is still undergoing inflight checkout; the initial imagery is excellent. J-ERS-1 is a joint development of the Ministry of International Trade (MITI) and the Science and Technology Agency of the National Space Development Agency

© ESA 1991

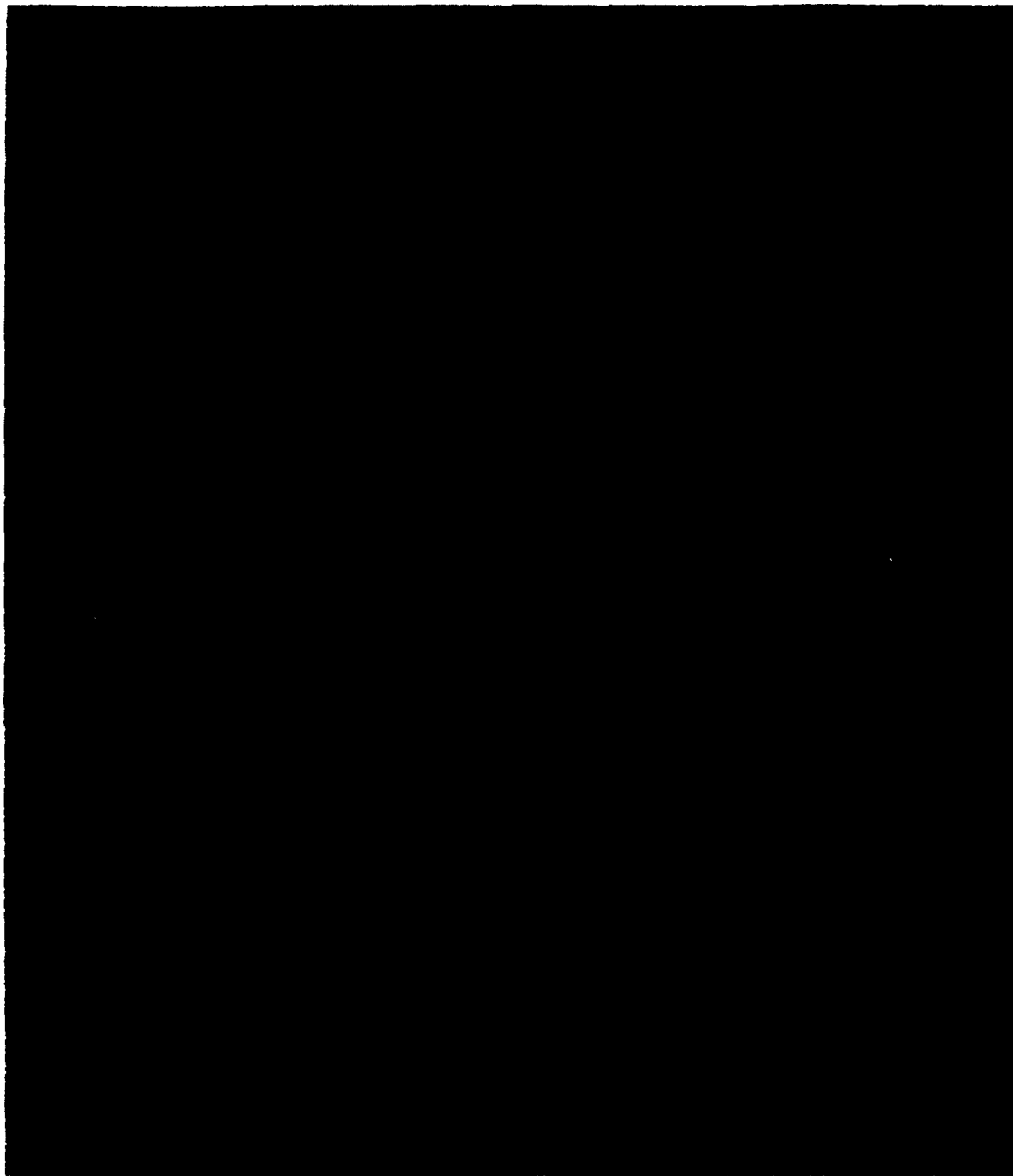


Figure 1. Satellite Imagery of the Forest Test Site in Whitecourt, Alberta.
Top: ERS-1 image (C-band, 23° incidence angle)
Bottom: ALMAZ image (S-band, 44° incidence angle)
(Processing courtesy Canada Centre for Remote Sensing)

(NASDA) of Japan [10].

J-ERS-1 is like Seasat SAR in many ways. In fact, its original performance specifications were identical to those of Seasat. It turned out that two things combined leading to the present parameters (Table 2). First, the test results for the solid state power amplifiers showed much better output power than had been thought possible in early design stages. Thus, greater range could be accepted. Second, the driving application for J-ERS-1 is global economic geology, for which larger incidence angles are desirable in order to reduce image distortions from terrain relief. The nominal incidence angle for J-ERS-1 was changed accordingly, now at 38° , rather than the nominal 23° of Seasat. (Note that the literature almost always quotes a "look angle" of 35° for J-ERS-1, which refers to the angle of the antenna beam at the spacecraft, and does not include Earth curvature. Incidence angle is the preferred specification for the antenna effective viewing angle.)

As a consequence of the larger incidence angle, the ground range resolution is reduced from 25 metres to 18 metres, with no change in system range bandwidth. Having a range resolution of 18 metres, the azimuth resolution was chosen to be the same, achieved by a simple adjustment in the processor. Finally, the number of looks available is reduced by about 25%, leading to 3 looks, or $(18/25) \times 4$. Conclusion? Although the specifications for J-ERS-1 look different from Seasat, the imagery with respect to image quality should be about the same. The increased incidence angle should be of value.

5. PLANNED ORBITAL SAR MISSIONS

In the sense used here, planned orbital missions are those for which the sponsoring agencies have committed the necessary resources, and the flight systems are under construction. The "approved" systems are outlined in Table 3. They include: SIR-C/X-SAR, a series of Shuttle-based missions each of relatively short duration; ERS-2, identical in most regards to ERS-1 (see above); and RADARSAT, the first remote sensing satellite mission of Canada.

5.1. SIR-C/X-SAR

The SIR-C/X-SAR mission represents a major milestone in space-based radar. Principal features of interest are suggested by the entries in Table 3 which guide the comments in this section. More details may be found in [2] and [11].

SIR-C/X-SAR is a joint venture between the United States (NASA-/JPL), and a European consortium of Deutsche Forschungsanstalt für Luft- und Raumfahrt e.V. (the German Aerospace Research Establishment known as DLR) and the Agenzia Spaziale Italiana (ASI, Italy). JPL is responsible for the C- and L-band systems, and DLR/ASI is responsible for the X-band system. Through extensive collaborative efforts, these radars have been harmonized so that they may be operated simultaneously, clearly a "first" at both organizational and technical levels. Since the Shuttle has limited orbital duration, each of the three planned missions are expected to last for about 10 days, although an extended (16 day) Shuttle capability remains a possibility for the later launches.

TABLE 3. Planned Orbital SAR Systems

	SIR-C/X-SAR	ERS-2	RADARSAT
General			
Country	(See text)	Europe	Canada
Agency	NASA/DLR/DARA	ESA	CSA/USA
Spacecraft	Shuttle	ERS-2	(dedicated)
Launch date	'93, '94, '96	1994	1995
Design lifetime	10 days	2-3 years	5 years
Radar			
Band [wavelength (cm)]	L,C; X	C [5.25]	C [5.7]
Frequency (GHz)	1.25, 5.3, 9.6	5.3	5.3
Antenna	arrays + WG(X)	WaveGuide	WG array
Size (m), length x height	12x(3, 0.75, 0.4)	10x1	15x1.5
Polarization	quad-pol L+C; X _{VV}	VV	HH
Incidence angle (°)	15 - 55	23	< 20 - > 50
Range resolution (m)	10 - 30	26	10 - 100
Azimuth resolution (m)	30	28	9 - 100
Looks	~4	6	1 - 8
Swath width (km)	15 - 60	100	10 - 500
Recorder on board?	Y (+ D/L)	N	Y
Processing (Optical, Digital)	D	D	D
Noise equivalent σ^0 (dB)	-40 < -28	-24	-23
Mission			
Altitude (km)	225	~780	~800
Inclination (°)	57	98.5	98.6
Sun synchronous?	N	Y	Y
Down-link data rate (MB/sec)	45 (TDRS)	105	74 - 105
Repeat cycle (days)	nil	TBD	24
Operation time per orbit (min)	(60 h, total)	10	20

The radar bands selected represent orbital SAR heritage (L), current operational preference (C), and extension to a new (civilian) orbital wavelength (X). The antennas required have been matched in two regards. First, in order to allow the same PRF for all three bands, dictated by the requirement to have simultaneous multi-frequency operation, each of the antennas should have the same length. Second, in order to have nominally the same elevation beamwidth, the height of the antennas must be scaled in proportion to their wavelength. The size of the total array is about 12m by 4.1m. The three antennas will be mounted on one common structure in the cargo bay of the Shuttle, vertically stacked.

Antenna technology for the X-band system is slotted waveguide, horizontally polarized. Elevation steering is by physical rotation of the antenna radiating surface about its longitudinal axis.

Antennas for both the C- and L-band radars use active phased array technology. There are 18 panels for each antenna, each one consisting of transmit/receive (T/R) modules for H and V polarizations. By using phase control of the individual T/R modules, the antenna patterns can be steered in both elevation and azimuth.

The H and V phased arrays, backed up by parallel receiver and data recording chains, may be cycled to achieve reception of the complex scattering matrix of the scene, the so-called quadrature polarization technique (described in another lecture in this series). SIR-C/X-SAR will be the first time that this capability is available from space.

Clearly, with choice of polarizations and frequencies, nearly 20 modes are available

from this radar system. These, coupled with a degree of freedom in bandwidth and incidence angle selection, lead to very complex planning for the operations of SIR-C/X-SAR. In addition, there are options in the number of bits to be included in the signal data path, and allowance for experimental passes in the ScanSAR format (see RADARSAT below), and for squinted beam data collection. (At this time, however, there is no plan to support data processing for these special imaging geometries.)

Processing for SIR-C, and particularly for X-SAR, poses its own challenges. Normal Shuttle angular motions, in combination with Earth rotation, lead to relatively large and time varying Doppler centroid variations in the received SAR signals. For the Shuttle, pitch, roll, and yaw are allowed to vary within 1.5° . (The attitude control system for the Shuttle is not "proportional", but depends on angular momentum impulses from gas-jet thrusters to correct angular position when the design "dead-zone" is exceeded.) Tolerance by the coherent radar signal to (yaw) attitude is determined primarily by azimuth antenna beamwidth. For a given aperture size, the beamwidth of the antenna pattern decreases in proportion to wavelength. For example, the azimuth beamwidth for X-SAR is about 0.15° , which is ten times smaller than the Shuttle attitude uncertainty. It follows that Doppler centroid estimation and tracking, and its compensation in time and range, is the most challenging SAR processing task among all others represented by the mission. This circumstance has led DLR to new frontiers in SAR data processing techniques, *i.e.*, [12] and [13].

5.2. RADARSAT

On 13 September 1989, the Government of Canada announced full commitment to build and operate RADARSAT, Canada's first Earth resources remote sensing satellite [14]. It is being prepared for a launch in 1995, and is designed for five years of service in orbit. The only imaging instrument is a SAR. A variety of resolution, image swath width, and incidence angle parameters are available that may be selected through ground command. The designated agency responsible for RADARSAT is the Canadian Space Agency (CSA). The mission is the result of more than a decade of work and initiative by the Canada Centre for Remote Sensing (CCRS).

The nominal configuration of the spacecraft has the SAR pointing to the north side of the orbital plane. This makes possible regular coverage of the Arctic up to the pole, but coverage of the central Antarctic region is not possible with this geometry. However, for two periods during the first two years of the mission, the satellite will be rotated 180° about its yaw axis so as to direct the radar antenna beam to the south side of the orbital plane. Each such yaw manoeuvre is expected to be maintained for two weeks. The purpose of this manoeuvre is to obtain a complete SAR map of Antarctica at the times of maximum and minimum ice cover. (To the extent that spacecraft thermal budgets allow, this will also allow opposite side viewing for selected regions north of the Equator during these periods.) Optical sensors such as Landsat have no access to regions closer to the poles than 81°, and are further compromised by clouds and darkness. Other space radars such as

ERS-1 have no ability to look to the south, or, in the case of Almaz, have orbital inclinations such that Antarctic coverage is incomplete.

NASA is a major partner in the RADARSAT mission contributing services for the planned 1995 launch from Vandenberg AFB using a medium-class expendable vehicle (McDonnell Douglas Delta II 7920-10). The satellite payload will consist of the SAR and its associated downlink transmitters, tape recorders, and command and control computer. The spacecraft is being procured from Ball Aerospace (United States), while SPAR Aerospace (Canada) has prime system responsibility under contract with the Canadian Space Agency.

Data downlink for RADARSAT is at X-band, with the maximum data rate chosen to be compatible with the ERS-1 data rate. RADARSAT will use 4 bit floating point quantization, I and Q. There are two downlink channels, required to support simultaneous readout of the onboard tape recorder together with "live" data. There are three downlink transmitters, a "3 for 2" redundancy approach.

For a satellite using a radar sensor, good solar illumination of the spacecraft is more important than sunlight on the Earth's surface. For this reason, RADARSAT will use a sun synchronous *dawn-dusk* orbit. In this orbit, the spacecraft is illuminated by the sun throughout each orbit. (There are short periods at southern latitudes during the Austral winter during which the spacecraft is in eclipse.) Perhaps the greatest operational advantage of this orbit is that the SAR can be fully dependent on solar derived rather than stored battery power,

which means that there is no limiting distinction between ascending and descending passes from an applications point of view. Thus, nearly twice as many viewing opportunities are available to the mission than would otherwise be available. Another operational advantage is that the ground station data downlink periods for RADARSAT will not conflict with other remote sensing satellites, most of which use near mid-day orbit timing.

RADARSAT will carry tape recorders with sufficient capacity for more than ten minutes of full quality SAR data. As a consequence of the orbit yaw manoeuvre and the onboard recorders, RADARSAT will be the first fine resolution satellite system capable of complete global coverage. This feature of RADARSAT is relevant to global environmental monitoring as well as being of scientific value.

5.2.1. Modes

RADARSAT has been designed in response to user requirements that demand a variety of incidence angles (from about 20° to 50°) in the standard imaging modes. An antenna with electronic elevation beam steering is part of the baseline RADARSAT design. Although this enables user requirements to be met, it does add further complexity to the entire system. In order to provide a (nominally) constant ground range resolution over the range of incidence angles, three different pulse bandwidths are needed. It also follows that very fine control of the transmitter pulse repetition frequency (PRF) is required.

Having moved to build in an antenna and control system with the flexibility (and complexity) necessary to support standard

imaging modes at a variety of incidence angles, several additional imaging modes become available at rather small marginal cost. The design philosophy for these extra modes has been to base the system specifications on the standard imaging modes, and to optimize the performance of the additional modes within the design envelope determined by the standard modes. Image quality in the additional modes is predicted to be comparable to that of the standard modes.

Imaging modes for RADARSAT include Standard, Wide Swath, Fine Resolution, Extended, and ScanSAR (see Figure 2 and Table 4). In each mode, data are collected continuously along a swath parallel to the sub-satellite path. Swath length is limited only by the duration of continuous radar operation, and may be thousands of kilometres long. Swath widths and positions are determined by the antenna elevation beam patterns (and the radar range gate control), and have been chosen for the standard modes so that there is at least 10% overlap between adjacent swaths. Range resolution when projected onto the Earth's surface varies with incidence angle and hence ground range. Three range bandwidths are available (11.6, 17.3, and 30.0 MHz) to allow choice in ground range resolution achieved at each incidence angle. Nominal range resolution for the standard beams has been specified at ground ranges of 400 km and 675 km from the sub-satellite locus.

The additional modes are generated by appropriate choices of antenna beam and range pulse bandwidth. The fine resolution mode, for example, is achieved by selecting the widest available bandwidth, and using a narrow beam in elevation at incidence angles larger than

TABLE 4. RADARSAT Imaging Modes

Mode	Resolution (R ¹ x A, m)	Looks ²	Width (km)	Incidence (degrees)
Standard	25 x 28	4	100	20 - 49
Wide (1)	48-30 x 28	4	165	20 - 31
Wide (2)	32-25 x 28	4	150	31 - 39
Fine resolution	11-9 x 9	1	45	37 - 48
ScanSAR (N)	50 x 50	2-4	305	20 - 40
ScanSAR (W)	100 x 100	4-8	510	20 - 49
Extended (H)	22-19 x 28	4	75	50 - 60
Extended (L)	63-28 x 28	4	170	10 - 23

¹ Nominal; ground range resolution varies with range.

² Nominal; range and processor dependent.

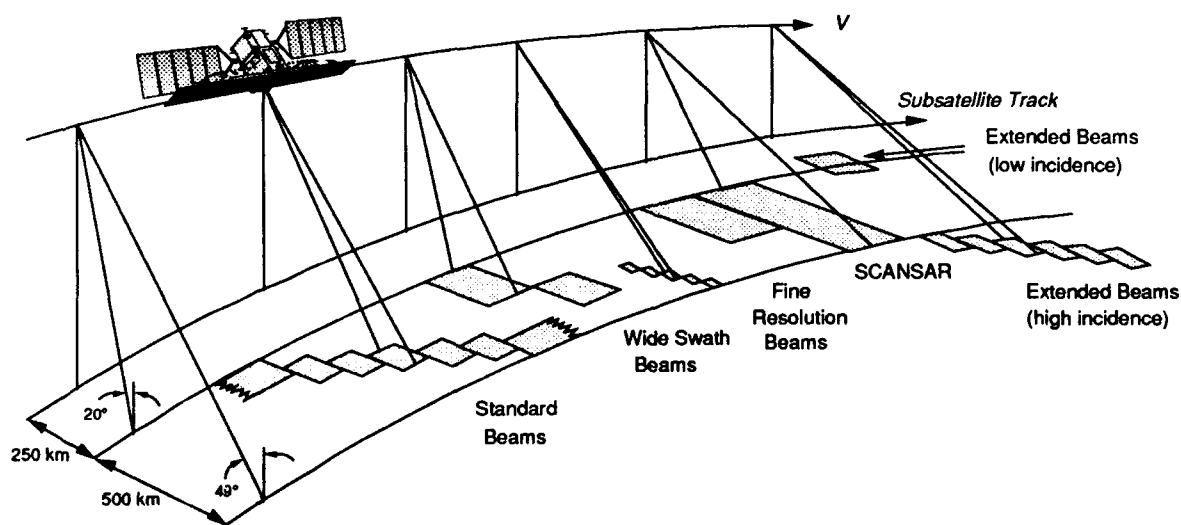


Figure 2. RADARSAT Imaging Modes

(nominally) 45° . A narrow swath results from the requirement to minimize beamwidth in order to maintain good signal to noise ratio, and also from the necessity to maintain data rates consistent with downlink channel capacity. Wide swath modes are supported by wider antenna beam widths than normal at steeper incidence angles, and use of the smallest available range pulse bandwidth leading to more coarse ground range resolution. Signal to noise ratio and data bandwidth arguments apply in these modes that are counterparts to those for the fine resolution modes, but with the result of broadening the usable swath width. Extended modes result from selection of beams outside of the nominal 500 km accessibility region, either closer to nadir (steeper incidence), or further away (more shallow or grazing incidence angle).

5.2.2. *ScanSAR*

In order to allow imaging of a swath much wider than ambiguity limits would normally allow, the RADARSAT system has been designed to incorporate an alternative and less conventional mode ([15] and [16]) known as ScanSAR. In this mode, for which rapid steering of the elevation beam pattern of the antenna is essential, extended range coverage can be obtained using a set of contiguous beams, enabling images of total swath width up to about 500 km to be produced. This is accomplished at no increase in mean data rate from the radar, but at the cost of degraded resolution of the resulting image.

The principle of ScanSAR is to share radar operational time between two or more separate sub-swaths in such a way as to obtain full image coverage over their combined swath. The set of returns used

to image a section of one sub-swath must be from consecutive pulses in order to provide adequate sampling, and must be of sufficient length to allow formation of the synthetic aperture needed for the sub-swath at the required resolution. The imaging operations are therefore split up into a series of blocks of pulses, each block providing returns from one of the sub-swaths. Each block is processed to provide an image of a section of the corresponding sub-swath. The imaging operations cycle around the full set of sub-swaths sufficiently rapidly that the imaged sections in any one sub-swath are adjoining or over-lapping.

RADARSAT will be the first operational satellite radar system to implement the ScanSAR technique.

6. AIRBORNE SAR SYSTEMS

This section provides a glimpse at civilian airborne SAR systems now in service. Since most of these radars are meant for technology development as well as applications experiments, the hardware is frequently changed. The parameters listed in Table 5 are thought to be an accurate representation of the basic performance of those systems. Additional comments, and a resume of other airborne SARs are included in the following sub-sections.

6.1. Comparison of Selected Systems

The most widely deployed airborne SAR, and the one having the most modes, is that of NASA which carries the radar of JPL (the Jet Propulsion Laboratory). This radar, known as AirSAR ([2] and [19]), is relatively new, having been designed and built to replace its predecessor which was destroyed in an aircraft fire in 1985. The

TABLE 5. Current Status of Selected Airborne SAR Systems

	AirSAR	C/X SAR	E-SAR	KRAS	STAR-1
General					
Country	USA	Canada	Germany	Denmark	Canada
Agency	JPL/NASA	CCRS	DLR	TUD	Intera
Aircraft	DC-8	CV-580	DO-228	Gulfstream	Cessna
Nominal altitude (km)	8	6	3.5	12.5	10
Nominal airspeed (m/sec)		130	70	300	175
Purpose	exp'l	exp'l	exp'l	exp'l	operat'l
Radar					
Band	C, L, P	X, C	X, C, L	C	X
Frequency (GHz)	5.3, 1.25, 0.44	9.3, 5.3	9.6, 5.3, 1.3	5.3	9.6
Antenna length (m)	1.3, 1.6, 1.8	~1.2	0.15, 0.24, 0.85	1.2	~0.8
Antenna motion controller ?	N	Y	N	Y	Y
Polarization diversity	Y	Y	HH, VV	VV	HH
Quadrature polarization	C, L, P	C	No	No	No
Incidence angle (°)	20-60	0 - 85	15 - 60	20 - 80	45 - 80
Range resolution (m) (Slant)	7.5 (S)	6 - 20	2 (S)	2,4,8	6, 12
Range cells		4096	2048	8192	4096
Azimuth resolution (m)	2	< 1 - 10	2	2,4,8	6
Looks	4	1 - 7	1 - 8	2 - 16	7
Swath width (km) (Slant)	7-13	18 - 63	3 (S)	9 - 48 (S)	40, 60 (S)
STC ?		Y	Y	Y	N
Processor on board ?	Y (1 ch)	Y	Y (QL)	(Y)	Y
Noise equivalent σ^0 (dB)		-30, -40	-40, -30, -35	-42	-30
Special modes	InSAR, Δt	InSAR			

quadrature polarimetric capability at the three frequencies of this radar offers a unique and very rich data source that is made available by NASA to investigators around the world. AirSAR also offers two other special modes that merit attention, as noted in the Table. InSAR is an interferometric mode created by using data from two antennas, one mounted above the other on the side of the aircraft. The interference pattern between them may be used to deduce terrain height information. For AirSAR, this capability is at C-band only. The other special mode also requires two separate antennas, this time spaced along the line of flight. Interferometric measurements with these two antennas may be used to observe phenomena in the scene that change over the short interval Δt between observations, such as currents on the ocean's surface.

The SAR flown by CCRS (the Canada Centre for Remote Sensing) is on a Convair-580. Both X- and C-bands are fully supported by onboard real time digital processors [20], and have a variety of modes and data combinations available. The standard image products are produced at seven looks. The system has recently been modified to incorporate full quadrature polarimetry on C-band, and may be operated in an InSAR mode. Signal data is recorded so that ground processing may be used for specific experimental purposes, such as investigations requiring access to separate looks for optimized oceanographic SAR wave imagery.

The airborne radar of DLR (defined in section 5.1) continues to be upgraded with new modes and capabilities [21], [22], and [23]. It is designed primarily for high resolution and technology development, hence it has a narrower swath width than

do the previous two systems. Its recent extension to X-band is in support of DLR's vested interest in X-band for the X-SAR radar. The system includes a quick-look (QL) onboard processor having 50 m x 50 m resolution.

The radar of the Technical University of Denmark (TUD) has been designed to offer a variety of incidence and image parameter values within the constraint of being a single polarization C-band system [24], [25]. Within the limits set by their respective imaging geometries, the radar is matched to the ERS-1 SAR, aided by the use of an aircraft capable of high speed and high altitude.

The leading civilian SAR that is used for mapping surveys is STAR-1, owned and operated by Intera, of Calgary, Alberta [26]. This X-band system has performed more than 75% of all of the airborne radar mapping done for commercial clients world-wide since 1986. Data products from this system are digitally rectified to map accuracy standards, and, with the recent use of GPS, allows accurate mapping with no need for surveyed control points. Under satellite navigation control, the radar map itself is the most accurate source.

6.1. Overview of Other Systems

There are several other airborne SARs that deserve mention. The Netherlands for many years has been supporting the development of an advanced system known as PHARS [27]. Currently, PHARS is a C-band SAR mounted in a Swaeringen Metor II, a twin engined business plane. Early results meet or exceed specifications. Nominal resolution is about 5 metres with about 6 looks. The antenna is VV polarized to support

experiments with ERS-1. The program is committed to implementing a full quadrature polarimetric version within a few years.

One of the pioneers in the field of SAR is the Environmental Research Institute of Michigan (ERIM), whose civilian experimental SAR is managed by the United States Navy Air Development Center (NADC), and is mounted on a P-3 aircraft. The radar operates at X-, C-, and L-bands, and is fully polarimetric [28]. Nominal resolution is in the 3 metre range.

The French have been actively involved in SAR for many years. Their SAR (a civilian version of a former Thomson-CSF classified X-band system) is known as VARAN-S [29], and has supported several remote sensing experiments in Europe. Polarizations are HH and VV. Nominal resolution is on the order of 5 meters, with four looks, nominal.

In addition to these relative well known systems, others might be mentioned for completeness. The Chinese Academy of Sciences developed their own X-band SAR several years ago. The system is called CASSAR, and has seen limited deployment in the Far East. The USSR maintained an airborne SAR capability as a test-bed for satellite programs, both Earth oriented and planetary. India has developed its own airborne SAR as well as an indigenous digital SAR data processing capability.

7. PROPOSED SAR SATELLITES

There are three SAR satellites likely to be approved for completion and launch in the next decade, as noted in Table 6. Almaz

II has already been built, and is virtually a twin to Almaz. There is an intention to launch and operate this radar, but the changing infra-structure of the former USSR space segment places the future of Almaz II in doubt. Programmatic responsibility has been assumed by Russia for PRIRODA ("nature"), a complex payload that includes a SAR as one of several instruments [17], [18]. Much of the hardware for the PRIRODA payload has already been built.

The EOS-SAR (Earth Observing System SAR) [2] is at a different stage. There is an active design and science team at work at JPL on EOS-SAR, but the program has yet to receive funding approval from NASA. The Proposal by the EOS-SAR team to NASA is to be in 1993.

The EOS-SAR as presently conceived would be a most ambitious system. It would carry the multi-frequency, quadrature polarization capability of SIR-C/X-SAR into a long design life satellite implementation.

In addition to these SARs, there are other initiatives being developed. France for several years has been promoting SAR-2000, an X-band space radar intended to complement the SPOT program. Recently, France and Canada have entered a bilateral agreement to do joint studies of a combined satellite radar system building on the SAR-2000 and the RADARSAT III planning. RADARSAT II, essentially a replacement for RADARSAT, is under consideration by the Canadian government. The European Space Agency has sponsored several studies of SAR concepts that look beyond ERS-2. Undoubtedly, other space agencies have exploratory space radar studies under way.

TABLE 6. Proposed SAR Satellites

	ALMAZ II	EOS-SAR	PRIRODA
General			
Country	(TBD)	USA	Russia
Agency	TBD	NASA	TBD
Spacecraft	Salyut	(dedicated)	MIR
Launch date	(1994?)	2000 +	(1994?)
Lifetime	2 years	15 years	-
Radar			
Band	S	L, C, X	L, S
Antenna	WaveGuide	arrays	WG, array
Polarization	HH	quad-pol	VV or HH
Incidence angle (°)	30 - 50	15 - 45	35
Range resolution (m)	15 - 30	20 - 250	100
Azimuth resolution (m)	15	8 - 250	50, 150
Looks	> 4	1 - 10	-
Swath width (km)	20 - 45	30 - 360	80
Recorder on board?	Y	TBD	Y

8. REFERENCES

- [1] F. L. Li and R. K. Raney, Prolog to Special Section on Spaceborne Radars for Earth and Planetary Observations, *Proceedings of the IEEE*, Vol. 79, No. 6, June 1991, pp. 773-776.
- [2] J. Way and E. A. Smith, The Evolution of Synthetic Aperture Radar Systems and their Progression to the EOS SAR, *IEEE Transactions on Geoscience and Remote Sensing*, Vol. 29, No. 6, November 1991, pp. 962-985.
- [3] R. L. Jordan, The Seasat-A Synthetic Aperture Radar System, *IEEE Journal of Oceanic Engineering*, Vol. OE-5, No. 2, April 1980, pp. 154-163.
- [4] W. B. Wirin and R. A. Williamson, Satellite Remote Sensing in the USSR: Past, Present, and Future, *Remote Sensing Yearbook 1990*, Chapter 3, Burgess Scientific Press, Basingstoke, UK, pp. 49-64.
- [5] S. Chenard, Soviet Earth Observation gets Less Remote, *Interavia Space Markets*, Vol. 6, No. 1, January/February 1990, pp. 17-22.
- [6] *USA Today*, 14 December 1988.
- [7] J. T. Richelson, The Future of Space Reconnaissance, *Scientific American*, Vol. 264, No. 1, January 1991, pp. 38-45.
- [8] ERS-1 Special Issue, *ESA Bulletin*, European Space Agency, 8-10 rue Mario-Nikis, 75738 Paris Cedex 15, No. 65, February 1991.
- [9] E. P. W. Attema, The Active Microwave Instrument on-Board the ERS-1 Satellite, *Proceedings of the IEEE*, Vol. 79, No. 6, June 1991, pp. 791-799.
- [10] Y. Nemoto, H. Nishino, M. Ono, H. Mizutamari, K. Nishikawa, and K. Tanaka, Japanese Earth Resources Satellite-1 Synthetic Aperture Radar, *Proceedings of the IEEE*, Vol. 79, No. 6, June 1991, pp. 800-809.
- [11] R. L. Jordan, B. L. Huneycutt, and M. Werner, The SIR-C/X-SAR Synthetic Aperture Radar System, *Proc. of the IEEE*, Vol. 79, No. 6, June 1991, pp. 827-838.
- [12] H. Runge, Benefits of Antenna Yaw Steering for SAR, *Proceedings of the International Geoscience and Remote Sensing Symposium, IGARSS '91*, Espoo, Finland, 3-6 June 1991, pp. 257-261.
- [13] R. Bamler and H. Runge, PRF-Ambiguity Resolving by Wavelength Diversity, *IEEE Transactions on Geoscience and Remote Sensing*, Vol. 29, No. 6, Nov 1991, pp. 997-1003.
- [14] R. K. Raney, A. P. Luscombe, E. J. Langham, and S. Ahmed, RADAR-SAT, *Proceedings of the IEEE*, Vol. 79, No. 6, June 1991, pp. 839-849.
- [15] R. K. Moore, J. P. Claasen, and Y. H. Lin, Scanning Spaceborne Synthetic Aperture Radar with Integrated Radiometer, *IEEE Transactions on Aerospace and Electronic Systems*, Vol. AES-17, No. 3, 1981, pp. 410-421.
- [16] K. Tomiyasu, Conceptual Performance of a Satellite Borne, Wide Swath Synthetic Aperture Radar, *IEEE Transactions on Geoscience and Remote Sensing*, Vol. GE-19, No. 2, April 1981, pp. 108-116.
- [17] Glavkosmos, Orbital Station "MIR": Complex of Remote Sensing of the Earth "PRIRODA", Moscow, 1990.

- [18] N. A. Armand, A. A. Kalinkevich, B. G. Kutuza, and S. M. Popov, SAR Facilities for the "PRIRODA" Mission, *Proceedings of the International Geoscience and Remote Sensing Symposium, IGARSS'91*, Espoo, Finland, 3-6 June 1991, pp. 1790-1792.
- [19] J. J. van Zyl *et al.*, *AIRSAR Reference Manual*, Jet Propulsion Laboratory, California Institute of Technology, 1991.
- [20] C. E. Livingstone, A. L. Gray, R. K. Hawkins, and R. B. Olsen, CCRS C/X-Airborne Synthetic Aperture Radar: an R and D Tool for the ERS-1 Time Frame, *IEEE AES Magazine*, October, 1988, pp. 11-16.
- [21] R. Horn, M. Werner, and B. Mayr, Extension of the DLR Airborne Synthetic Aperture Radar, E-SAR, to X-band, *Proceedings of the International Geoscience and Remote Sensing Symposium, IGARSS'90*, Washington, DC, 20-24 May 1990, p. 2047.
- [22] R. Horn, C-Band SAR Results Obtained by an Experimental Airborne SAR System, *Proceedings of the International Geoscience and Remote Sensing Symposium, IGARSS'89*, Vancouver, Canada, 10-14 July 1989, pp. 2213-2216.
- [23] C. Dahme, R. Horn, D. Hounam, H. Öttl, and R. Schmid, Recent Achievements of DLR's Airborne Experimental SAR System and Image Processing Equipment, *Proceedings of the International Geoscience and Remote Sensing Symposium, IGARSS'91*, Espoo, Finland, 3-6 June 1991, pp. 245-246.
- [24] S. N. Madsen, E. L. Christensen, N. Skou, and J. Dall, The Danish SAR System: Design and Initial Tests, *IEEE Transactions on Geoscience and Remote Sensing*, Vol. 29, No. 3, May 1991, pp. 417-426.
- [25] J. Dall, J. H. Jørgensen, E. L. Christensen, and S. N. Madsen, A Real-time Processor for the Danish C-Band SAR, *Proceedings of the International Geoscience and Remote Sensing Symposium, IGARSS'91*, Espoo, Finland, 3-6 June 1991, pp. 279-282.
- [26] A. D. Nichols, J. W. Wilhelm, T. W. Gaffield, D. R. Inkster, and S. K. Leung, A SAR for Real-time Ice Reconnaissance, *IEEE Transactions on Geoscience and Remote Sensing*, Vol. GE-24, No. 3, May 1986, pp. 383-389.
- [27] P. Hoozeboom, P. J. Koomen, H. Pouwels, and P. Snoeij, First Results from The Netherlands SAR Testbed "PHARS", *Proceedings of the International Geoscience and Remote Sensing Symposium, IGARSS'91*, Espoo, Finland, 3-6 June 1991, pp. 241-244.
- [28] A. D. Kozma, A. D. Nichols, R. F. Rawson, S. J. Shackman, C. W. Haney, and J. J. Shanne Jr., Multi-frequency, -polarization SAR for Remote Sensing, *Proceedings of the International Geoscience and Remote Sensing Symposium, IGARSS'86*, Zurich, Switzerland, 8-11 September 1986, ESA Publication SP-254, pp. 715-719.
- [29] R. Albrizio, P. Blonda, A. Mazzone, F. Pasquali, G. Pasquariello, F. Posa, and N. Veneziana, Digital Processing of X-Band VARAN-S Airborne SAR Images, *Proceedings of the International Geoscience and Remote Sensing Symposium, IGARSS'89*, Vancouver, Canada, 10-14 July 1989, pp. 2203-2208.

BIBLIOGRAPHY

This Bibliography was compiled to support Lecture Series 182 by the Fachinformationszentrum, Karlsruhe, D-7514 Eggenstein-Leopoldshafen 2 (Fiz Karlsruhe), Germany, in association with the Lecture Series Director, Dr W. Keydel.

TYPE 1/4/1

Quest Accession Number : 91A52169

91A52169 NASA IAA Journal Article Issue 22

Radarsat

(AA)RAMEY, R. K.; (AB)LUSCOMBE, ANTHONY P.; (AC)LANGHAM, E. J.; (AD)JAMEER, SHADEER
(AA)(Canada Centre for Remote Sensing, Ottawa); (AB)(Spar Aerospace, Ltd., Sainte-Anne-de-Bellevue, Canada); (AD)(Canadian Space Agency, Ottawa, Canada)
IEEE, Proceedings (ISSN 0018-9219), vol. 79, June 1991, p. 839-849.
910600 p. 11 refs 32 In: EN (English) p.3832

Radarsat, the first Canadian remote-sensing spacecraft, is designed to provide earth observation information for five years. The satellite is scheduled for launch in 1994. The only payload instrument is a 5.6-cm-wavelength (C-band) synthetic aperture imaging radar (SAR). Radarsat will gather data on command for up to 28 min during each cycle of its 800-km (nominal) near-polar orbit. Image resolutions from 10 to 100 m at swath widths of 45 to 500 km will be available. The Radarsat mission is reviewed, and the design, characteristics, and implementation of the radar are introduced. Technical problems addressed include calibration, rapid data processing, the phased array antenna that provides controlled beam steering, and the first satellite implementation of a special radar technique known as ScanSAR.
I.E.

TYPE 1/4/3

Quest Accession Number : 91A52166

91A52166 NASA IAA Journal Article Issue 22

Japanese Earth Resources Satellite-1 synthetic aperture radar

(AA)NEMOTO, YOSHIAKI; (AB)NISHINO, HIDEO; (AC)ONO, MAKOTO; (AD)WIZUTAMARI, HITOSHI; (AE)NISHIKAWA, KATSUHIKO; (AF)TANAKA, KAORU
(AB)(Japan Resources Observation System Organization, Technical Dept., Tokyo); (AD)(Mitsubishi Electric Corp., Kanakura Works, Japan); (AE)(NEC Corp., Space and Laser Communications Development Div., Yokohama, Japan); (AF)(NEC Corp., Guidance and Electro-Optics Div., Tokyo, Japan)
IEEE, Proceedings (ISSN 0018-9219), vol. 79, June 1991, p. 800-809.
910600 p. 10 refs 8 In: EN (English) p.3832

The spaceborne L-band SAR to be launched on the Japanese Earth Resources Satellite-1 is described. The mission is mainly dedicated to geological applications. The ground resolution of the processed image is designed as 18 m, and the off-nadir angle required to meet geological applications is 35 deg. The design and performance of the key system parameters are discussed, along with the reasons for choosing such design parameters. The antenna is a thin-flat-foldable configuration that has a 11.9-m by 2.2-m aperture when extended in orbit. The transmitter, receiver, and signal processor are all of the solid-state type to achieve high reliability of operation. They transmit an 1100-W peak (minimum) chirp pulse and receive the return echos and process the echo signals into in-phase and quadrature data streams.
I.E.

TYPE 1/4/2

Quest Accession Number : 91A52168

91A52168* NASA IAA Journal Article Issue 22

The SIR-C/X-SAR synthetic aperture radar system
(AB)JORDAN, RANDO L.; (AB)HUNEYCUIT, BRYAN L.; (AC)WERNER, MARIAN
(AB)(JPL, Pasadena, CA); (AC)(DLR, Institut fuer Hochfrequenztechnik, Oberpfaffenhofen, Federal Republic of Germany)
Jet Propulsion Lab., California Inst. of Tech., Pasadena. (J3574450)
IEEE, Proceedings (ISSN 0018-9219), vol. 79, June 1991, p. 827-838.
Research supported by DLR. 910600 p. 12 refs 16 In: EN (English) p.3832

SIR-C/X-SAR, a three-frequency radar to be flown on the Space Shuttle in September 1993, is described. The SIR-C system is a two-frequency radar operating at 1250 MHz (L-band) and 5300 MHz (C-band), and is designed to get four-polarization radar imagery at multiple surface angles. The X-SAR system is an X-band imaging radar operating at 9600 MHz. The discussion covers the mission concept; system design; hardware; RF electronics; digital electronics; command, timing, and telemetry; and testing.
I.E.

TYPE 1/4/4

Quest Accession Number : 91A52164

91A52164* NASA IAA Journal Article Issue 22

Magellan imaging radar mission to Venus

(AA)JOHNSON, WILLIAM T. K.
(AA)(JPL, Pasadena, CA)
Jet Propulsion Lab., California Inst. of Tech., Pasadena. (J3574450)
IEEE, Proceedings (ISSN 0018-9219), vol. 79, June 1991, p. 777-790.
910600 p. 14 refs 21 In: EN (English) p.3831

The Magellan imaging-radar mapping mission has collected and processed data from the spacecraft in an elliptical orbit around Venus. A brief description is given of the mission and the spacecraft, followed by a more detailed description of the radar system design, which used earth-orbiting SAR experience and several innovations in its design to operate from an orbit around another planet. The radar sensor, ground processing, and data products are described. This multimode radar is the only science instrument on the mission and has the objective of mapping at least 70 percent of the planet surface. It has three modes: SAR, altimetry, and passive radiometry. The radar system has produced maps of almost all of the Venusian surface with a resolution better than 600-m equivalent optical line pair, and the best resolution obtained is equivalent to less than 300 m. Some of the early radar images are shown.
I.E.

TYPE 1/4/5

Quest Accession Number : 91A49343

91A49343 NASA IAA Journal Article Issue 21

Speckle reduction in multipolarization, multifrequency SAR imagery

(AA)LEE, JONG-SEN; (AB)GRUNES, MITCHELL R.; (AC)WANGO, STEPHEN A.

(AC)(U.S. Navy, Naval Research Laboratory, Washington, DC)

(IGARSS '90 - IEEE International Geoscience and Remote Sensing Symposium

on Remote Sensing Science for the Nineties, 10th, University of Maryland,

College Park, May 20-24, 1990) IEEE Transactions on Geoscience and Remote

Sensing (ISSN 0196-2892), vol. 29, July 1991, p. 535-544. 910700 p. 10

refs 12 In: EN (English) p.3728

An algorithm to take advantage of this polarization diversity to suppress the speckle effect with much less resolution broadening than using spatial filtering is discussed. The coupling between polarization channels is minimized by using local intensity ratios. The degree of speckle reduction is similar to two-look or three-look processing. The same algorithm can also be used to process multifrequency polarimetric SAR. For three-frequency aircraft SAR data speckle reduction equivalent to six-look processing can be achieved, and further reduction is possible by applying speckle filters in the spatial domain. A vector speckle filter which operates simultaneously in the polarization and spatial domains is also tested. Experimental results with simulated polarimetric SAR as well as one-look and multilook parametric SAR data demonstrate the effectiveness of these speckle reductions, with minimum resolution broadening and coupling between polarimetric and frequency channels. I.E.

TYPE 1/4/7

Quest Accession Number : 91A43129

91A43129 NASA IAA Conference Paper Issue 18

Complex phase error and motion estimation in synthetic aperture radar imaging

(AA)SOURDIS, M.; (AB)YANG, H.

(AB)(State University of New York at Buffalo, Amherst)

NSF NIP-90-04996 In: Image processing algorithms and techniques II;

Proceedings of the Meeting, San Jose, CA, Feb. 25-Mar. 1, 1991 (A91-43127

18-35). Bellingham, WA, Society of Photo-Optical Instrumentation

Engineers, 1991, p. 104-113. 910000 p. 10 refs 7 In: EN (English) p.

3116

Attention is given to a SAR wave equation-based system model that accurately represents the interaction of the impinging radar signal with the target to be imaged. The model is used to estimate the complex phase error across the synthesized aperture from the measured corrupted SAR data by combining the two wave equation models governing the collected SAR data at two temporal frequencies of the radar signal. The SAR system model shows that the motion of an object in a static scene results in coupled Doppler shifts in both the temporal frequency domain and the spatial frequency domain of the synthetic aperture. The velocity of the moving object is estimated through these two Doppler shifts. It is shown that once the dynamic target's velocity is known, its reconstruction can be formulated via a squint-mode SAR geometry with parameters that depend upon the dynamic target's velocity. O.G.

TYPE 1/4/6

Quest Accession Number : 91A47233

91A47233 NASA IAA Journal Article Issue 20

Measurement of surface microtopography

(AA)WALL, S. D.; (AB)FARR, T. G.; (AC)MULLER, J.-P.; (AD)LEWIS, P.; (AE)LEBERL, F. W.

(AB)(JPL, Pasadena, CA); (AD)(University College, London, England);

(AE)(Vexcel Corp., Boulder, CO)

Jet Propulsion Lab., California Inst. of Tech., Pasadena. (J3574450)

Photogrammetric Engineering and Remote Sensing (ISSN 0099-1112), vol.

57, Aug. 1991, p. 1075-1078. Research supported by NASA, University

College London, and Vexcel Corp. 910800 p. 4 refs 24 In: EN (English)

p.3472

Acquisition of ground truth data for use in microwave interaction modeling requires measurement of surface roughness sampled at intervals comparable to a fraction of the microwave wavelength and extensive enough to adequately represent the statistics of a surface unit. Sub-centimetric measurement accuracy is thus required over large areas, and existing techniques are usually inadequate. A technique is discussed for acquiring the necessary photogrammetric data using twin film cameras mounted on a helicopter. In an attempt to eliminate tedious data reduction, an automated technique was applied to the helicopter photographs, and results were compared to those produced by conventional stereogrammetry. Derived root-mean-square (RMS) roughness for the same stereo-pair was 7.5 cm for the automated technique versus 6.5 cm for the manual method. The principal source of error is probably due to vegetation in the scene, which affects the automated technique but is ignored by a human operator. Author

TYPE 1/4/8

Quest Accession Number : 91A42468

91A42468 NASA IAA Journal Article Issue 17

Estimation of ocean wave spectra using two-antenna SAR systems

(AA)LYZENGA, D. R.; (AB)BENNETT, J. R.

(AB)(Michigan, Environmental Research Institute, Ann Arbor)

N00014-90-C-0071 IEEE Transactions on Geoscience and Remote Sensing

(ISSN 0196-2892), vol. 29, May 1991, p. 463-465. 910500 p. 3 refs 9

In: EN (English) p.2983

Data from synthetic aperture radar (SAR) systems can be used to estimate ocean wave directional spectra, but the method is limited by nonlinearities associated with the velocity bunching mechanism and the azimuth falloff effect, which reduces the range of azimuth wavelengths that can be observed. A theoretical analysis which suggests that the use of two or more receive antennas, spaced in the along-track direction, may reduce these limitations is presented. Specifically, the band of azimuth wavenumbers is shifted by an amount proportional to the antenna spacing, so that a broader range of wavenumbers can be covered by combining the spectrum obtained from the two-antenna signals with the conventional image spectrum. The angular dependence of the velocity modulation mechanism is also modified to include purely range-traveling waves in the two-antenna case. I.E.

TYPE 1/4/9

Quest Accession Number : 91A42467

91A42467 NASA IAA Journal Article Issue 17

Terrain influences in SAR backscatter and attempts to their correction

(AA)BAVER, THOMAS; (AB)WINTER, RUDOLF; (AC)SCHREIER, GUNTER

(AC)(DLR, Oberpfaffenhofen, Federal Republic of Germany)

IEEE Transactions on Geoscience and Remote Sensing (ISSN 0196-2892),
vol. 29, May 1991, p. 451-462. 910500 p. 12 refs 19 In: EN (English)
p. 2970

SAR images reveal radiometric image distortions that are caused by terrain undulations. The authors present the results of a study extracting and investigating the various components of these terrain influences. An imaging model is set up for the geometric rectification of the SAR image and for a reconstruction of the imaging geometry. A prerequisite for the setup of this model is the use of a digital elevation model. Eight different geometric parameters are derived and investigated for their influence on grey-value variations in the geocoded SAR image. Image grey-value variations of three major land-use classes-forest, agricultural land, and urban/suburban areas-are examined. Empirical models of the SAR-backscatter variations are used to describe the relations between image grey values and various geometric parameters. The models are used for a numerical estimation of the terrain influence on the backscatter variations in the SAR image. The models allow the derivation of 13 different functions for the correction of the relief-induced radiometric image distortions. These functions are applied to test areas within the SAR scene under investigation, and their correction effects are described and compared numerically as well as visually.
I.E.

TYPE 1/4/11

Quest Accession Number : 91A42461

91A42461 NASA IAA Journal Article Issue 17

Doppler frequency estimation and the Cramer-Rao bound

(AA)BANKEN, RICHARD

(AA)(DLR, Oberpfaffenhofen, Federal Republic of Germany)

IEEE Transactions on Geoscience and Remote Sensing (ISSN 0196-2892),
vol. 29, May 1991, p. 385-390. 910500 p. 6 refs 19 In: EN (English)
p. 2909

The authors address the problem of Doppler frequency estimation in the presence of speckle and receiver noise. An ultimate accuracy bound for Doppler frequency estimation is derived from the Cramer-Rao inequality. It is shown that estimates based on the correlation of the signal power spectra with an arbitrary weighting function are approximately Gaussian-distributed. Their variance is derived in terms of the weighting function. It is shown that a special case of a correlation-based estimator is a maximum-likelihood estimator that reaches the Cramer-Rao bound. These general results are applied to the problem of Doppler centroid estimation from SAR (synthetic aperture radar) data. Different estimators known from the literature are investigated with respect to their accuracy. Numerical examples are presented and compared with experimental results.
I.E.

TYPE 1/4/10

Quest Accession Number : 91A42463

91A42463* NASA IAA Journal Article Issue 17

The Danish SAR system - Design and initial tests

(AA)MADSEN, SOREN N.; (AB)CHRISTENSEN, ERIK L.; (AC)SKOU, NIELS;

(AD)DALL, JORGEN

(AA)(JPL, Pasadena, CA); (AD)(Technical University of Denmark, Lyngby)
Jet Propulsion Lab., California Inst. of Tech., Pasadena. (J3574450)
IEEE Transactions on Geoscience and Remote Sensing (ISSN 0196-2892),
vol. 29, May 1991, p. 417-426. Research supported by Thomas B. Thriges
Foundation. 910500 p. 10 refs 15 In: EN (English) p. 2909

In January 1986, the design of a high-resolution airborne C-band SAR started at the Electromagnetics Institute of the Technical University of Denmark. The initial system test flights took place in November and December 1989. The authors describe the design of the system, its implementation, and its performance. They show how digital technology has been utilized to realize a very flexible radar with variable resolution, swath-width, and imaging geometry. The motion-compensation algorithms implemented to obtain the high resolution and the special features built into the system to ensure proper internal calibration are outlined. The data processing system, developed for image generation and quality assurance, is sketched, with special emphasis on the flexibility of the system. Sample images and a preliminary performance evaluation are presented, demonstrating that the design goals have been met. The ongoing system upgrades and the planned scientific utilization of the C-band SAR are described.
I.E.

TYPE 1/4/12

Quest Accession Number : 91A41831

91A41831 NASA IAA Conference Paper Issue 17

Detection of slowly moving targets with airborne radar
Entdeckung langsam bewegter Ziele mit luftgetragenen Radar

(AA)ENDER, JOACHIM; (AB)KLEMM, RICHARD

(AA)(Forschungsgesellschaft fuer angewandte Naturwissenschaften,
Forschungsinstitut fuer Funk und Mathematik, Wachtberg-Werthhoven, Federal
Republic of Germany)

IN: Radar Symposium, 7th, Ulm, Federal Republic of Germany, Oct. 10-12,
1989, Reports (A91-41822 17-32). Duesseeldorf, Deutsche Gesellschaft fuer
Ordnung und Navigation, 1989, p. 161-186. In German. 890000 p. 26 refs
17 In: GM (German) p. 2902

It is shown here that recent airborne radar systems can detect moving targets amid clutter by using optimal filtering with an order of magnitude improvement over previous systems. One-channel and multichannel methods are compared in terms of theoretical limits. The optimal clutter suppression method in multichannel systems is investigated by analysis in the frequency and time regions. Methods for obtaining suboptimal filter procedures with reduced computational expense are determined.
C.D.

TYPE 1/4/13

Quest Accession Number : 91A41830

91A41830 NASA IAA Conference Paper Issue 17

Calibration of SAR systems for remote sensing using X-SAR/SIR-C as an example

Die Kalibrierung von Synthetik-Apertur-Radar-Systemen der Fernerkundung am Beispiel des X-SAR/SIR-C

(AA)KIETZMANN, H.; (AB)BLOETSCHER, H.

(AA)DLR, Institut fuer Hochfrequenztechnik, Oberpfaffenhofen, Federal Republic of Germany

In: Radar Symposium, 7th, Ulm, Federal Republic of Germany, Oct. 10-12, 1989, Reports (A91-41822 17-32). Duesseldorf, Deutsche Gesellschaft fuer

Ortung und Navigation, 1989, p. 147-159. In German. 890000 p. 13 refs 9

In: GM (German) p.2902

Calibration of an SAR system for quantitative signature analysis in remote sensing is illustrated here in step-by-step fashion for the X-SAR/SIR-C sensor. Both internal and external calibration are addressed. The determination of operational antenna diagrams is shown.

C.D.

TYPE 1/4/15

Quest Accession Number : 91A41828

91A41828 NASA IAA Conference Paper Issue 17

Concept and results of the Azimuth Quick-Look Processor for aircraft SAR of the DLR

Konzept und Ergebnisse des Azimut Quick-Look Prozessors fuer das Flugzeug Synthetik Apertur Radar der DLR

(AA)MOREIRA, ALBERTO

(AA)DLR, Institut fuer Hochfrequenztechnik, Wessling, Federal Republic of Germany

In: Radar Symposium, 7th, Ulm, Federal Republic of Germany, Oct. 10-12, 1989, Reports (A91-41822 17-32). Duesseldorf, Deutsche Gesellschaft fuer

Ortung und Navigation, 1989, p. 113-126. In German. 890000 p. 14 refs 11

In: GM (German) p.2861

A real time azimuth processor has been built for the aircraft-borne E-SAR system (Experimental Radar System with Synthetic Aperture). The processor uses an unfocused correlation procedure which greatly simplifies the data processing and permits operation in real time without much use of hardware. A new algorithm has been developed which improves image parameters except for resolution and is comparable with available focused processor procedures. A number of real time images with postprocessing are shown which meet expectations and validate the algorithm.

C.D.

TYPE 1/4/14

Quest Accession Number : 91A41829

91A41829 NASA IAA Conference Paper Issue 17

Specification of an inertial navigation system for experimental SAR

Spezifikation eines inertialen Navigationssystems fuer das experimentelle Synthetik Apertur Radar

(AA)BUCKREUSS, STEFAN

(AA)DLR, Institut fuer Hochfrequenztechnik, Oberpfaffenhofen, Federal Republic of Germany

In: Radar Symposium, 7th, Ulm, Federal Republic of Germany, Oct. 10-12, 1989, Reports (A91-41822 17-32). Duesseldorf, Deutsche Gesellschaft fuer

Ortung und Navigation, 1989, p. 135-146. In German. 890000 p. 12 refs 7

In: GM (German) p.2862

An experimental radar system with SAR which will be operated in the L, C and X bands is discussed. The determination of allowable uncompensated disturbing motions by the system is examined, and the ways in which the strapdown inertial navigation system works are outlined. Sources of error in the motion compensation are considered, and the results of testing of an INS associated with the SAR are summarized.

C.D.

TYPE 1/4/16

Quest Accession Number : 91A41826

91A41826 NASA IAA Conference Paper Issue 17

Results of a first test of the ROSAR procedure

Ergebnisse einer ersten Erprobung des ROSAR-Verfahrens

(AA)KLAUSING, H.; (AB)BARTSCH, N.

(AA)DLR, Institut fuer Hochfrequenztechnik, Oberpfaffenhofen, Federal Republic of Germany

In: Radar Symposium, 7th, Ulm, Federal Republic of Germany, Oct. 10-12, 1989, Reports (A91-41822 17-32). Duesseldorf, Deutsche Gesellschaft fuer

Ortung und Navigation, 1989, p. 65-92. In German. 890000 p. 28 refs 12

In: GM (German) p.2902

The realizability of an SAR based on a rotating antenna (ROSAR) is investigated. The ROSAR theory is analytically reviewed, emphasizing its lateral resolution. The results of ROSAR applications to the imaging of individual, strongly reflecting objects with defined radar backscattering cross sections and known surroundings are discussed.

C.D.

TYPE 1/4/17

Quest Accession Number : 91A41825

91A41825 NASA IAA Conference Paper Issue 17

Experimental X-band synthetic aperture radar in aircraft

(AA)HORN, RALF; (AB)WERNER, MARIAN

(AB)(DLR, Institut fuer Hochfrequenztechnik, Oberpfaffenhofen, Federal

Republic of Germany)

IN: Radar Symposium, 7th, Ulm, Federal Republic of Germany, Oct. 10-12,

1989, Reports (A91-41822 17-32). Duesseldorf, Deutsche Gesellschaft fuer

Ordnung und Navigation, 1989, p. 59-63. In German. 890000 p. 5 In: GM

(German) p.2861

An experimental aircraft SAR for the X-band is described. The overall system, technical specifications, and experimental results are briefly reported. A block switching diagram of the system is shown.

C.D.

TYPE 1/4/19

Quest Accession Number : 91A38977

91A38977# NASA IAA Conference Paper Issue 16

Present and future imaging radar systems

(AA)RAMEY, R. KELTH

(AA)(RADARSAT Project Office, Ottawa, Canada)

IN: Space commercialization: Satellite technology: Symposium on Space

Commercialization: Roles of Developing Countries, Nashville, TN, Mar.

5-10, 1989, Technical Papers (A91-38976 16-12). Washington, DC, American

Institute of Aeronautics and Astronautics, Inc., 1990, p. 1-10. 900000

p. 10 In: EM (English) p.2677

Synthetic aperture radar (SAR) systems available for the use of planners in developed and developing countries for the purpose of meeting future resource-observation requirements are reviewed, and attention is given to nominal image parameters, global system development, and access to data. Focus is placed on such airborne SAR systems available for civilian use as the STAR 1 (Canada), and Varan-3 (France). Expected SAR-carrying spacecraft including ERS-1 (ESA), J-ERS-1 (Japan), and Radarsat (Canada), as well as research-oriented SAR systems to be flown on the Shuttle and on polar-orbiting platforms. It is noted that SAR data is well suited for the quantitative observation of critical national and global resources such as tropical forests and will be a primary source of information for many resource-monitoring and analysis responsibilities.

V.T.

TYPE 1/4/18

Quest Accession Number : 91A39775

91A39775 NASA IAA Journal Article Issue 16

An efficient SAR parallel processor

(AA)FRANCESCETTI, GIORGIO; (AB)SCHIRINZI, GIUDA; (AC)PASCAZIO, VITO;

(AB)MAZZEO, ANTONINO; (AE)MAZZOCCA, NICOLA

(AB)(CNR, Istituto di Ricerca per l'Elettromagnetismo e i Componenti

Elettronici, Naples, Italy); (AC)(Istituto Universitario Navale, Naples,

Italy); (AE)(Napoli, Universita, Naples, Italy)

IEEE Transactions on Aerospace and Electronic Systems (ISSN 0018-9251),

vol. 27, March 1991, p. 343-353. 910300 p. 11 refs 16 In: EN (English)

p.2703

A parallel architecture especially designed for a synthetic-aperture-radar (SAR) processing algorithm based on an appropriate two-dimensional fast Fourier transform (FFT) code is presented. The algorithm is briefly summarized, and the FFT code is given for the one-dimensional case, although all results can be immediately generalized to the double FFT. The computer architecture, which consists of a toroidal net with transputers on each node, is described. Parametric expressions for the computational time of the net versus the number of nodes are derived. The architecture allows drastic reduction of the processing time, preserving elaboration accuracy and flexibility.

I.E.

TYPE 1/4/20

Quest Accession Number : 91A33211

91A33211# NASA IAA Journal Article Issue 13

The unveiling of Venus - Magellan's synthesis radar penetrates the cloud

cover

Die Entschleierung der Venus - Magellans Syntheseradar durchdringt die

Wolkendecke

(AA)FISCHER, DANIEL

Sterne und Weltraum (ISSN 0039-1263), vol. 30, April 1991, p. 226-230,

232, 233. In German. 910400 p. 7 In: GM (German) p.2255

The revelation of the surface of Venus by the Magellan synthetic radar is discussed. The highlights of the discoveries are shown and described, including the long strips called 'noodles', the complex geological formation called the Phoebe region, the mountainous Lakshmi region which contains evidence of plate tectonics, and the Thetis Regio highland region, which may have formed by processes analogous to those which made the Hawaiian islands. Mysterious phenomena, like the apparent youth of many of the craters, are addressed.

C.D.

TYPE 1/4/21

Quest Accession Number : 91A32322

91A32322 NASA IAA Journal Article Issue 12

The modified beta density function as a model for synthetic aperture radar clutter statistics

(AA)WAPPELT, ANDREW L.; (AB)WACKERMAN, CHRISTOPHER C.

(AB)(Michigan, Environmental Research Institute, Ann Arbor)

IEEE Transactions on Geoscience and Remote Sensing (ISSN 0196-2892), vol. 29, March 1991, p. 277-283. 910300 p. 7 refs 17 In: EN (English) p.2019

The authors show that the modified beta distribution function is an adequate model for the underlying distribution function of the random variable used to model SAR image data. The model represents a range of SAR returns from different ice types by using a simple change in its parameter. The ability is explained by describing the distribution functions in width, modified skewness space where the modified beta function covers a region, while the other, more common, distribution functions cover only a curve. A procedure for comparing simple distribution functions with analytical functions specifically for digitized SAR data is presented, and the modified beta model is tested on 166 subsets drawn from three SAR collections over different ice types and over open water. The modified beta function can model essentially all of the SAR subtypes, where the other more common densities cannot. Some classification of ice types using the parameters from the modified beta function are provided.

I.E.

TYPE 1/4/23

Quest Accession Number : 91A29141

91A29141 NASA IAA Journal Article Issue 11

Accuracy of using point targets for SAR calibration

(AA)JULANDER, LARS M. H.

(AA)(Canada Centre for Remote Sensing, Ottawa)

IEEE Transactions on Aerospace and Electronic Systems (ISSN 0018-9251), vol. 27, Jan. 1991, p. 139-148. Research supported by Swedish Board for Space Activities. 910100 p. 10 refs 22 In: EN (English) p.1744

The peak and integral methods for radiometric calibration of a synthetic aperture radar (SAR) using reference point targets are analyzed. Both calibration methods are shown to be unbiased, but the peak method requires knowledge of the equivalent rectangle system resolution which is sensitive to system focus. Exact expressions for the RMS errors of both methods are derived. It is shown that the RMS error resulting from the peak method is always smaller than or equal to that from the integral method for a well-focused system. However, for robust radiometric calibration of SAR, or when nonlinear phase errors are present, the integral method is recommended, because it does not require detailed knowledge of the impulse response and the resulting RMS error is not dependent on system focus.

I.E.

TYPE 1/4/22

Quest Accession Number : 91N30395

91N30395# NASA STAR Technical Report Issue 22

Cross-calibration between airborne SAR sensors

(AA)ZINK, MANFRED

(Germany, F.R.). (DO776452) Abt. HF-Systeme.

DLR-FB-91-10; ISSN-0939-2963; ETN-91-99791 910200 p. 57 In: EN

(English) Avail: NTIS HC/MF A04; DLR, Wissenschaftliches Berichtswesen,

VB-PL-DO, Postfach 90 60 58, 5000 Cologne, Fed. Republic of Germany, HC 22

DM p.3663

As synthetic Aperture Radar (SAR) system performance and experience in SAR signature evaluation increase, quantitative analysis becomes more and more important. Such analyses require an absolute radiometric calibration of the complete SAR system. To keep the expenditure on calibration of future multichannel and multisensor remote sensing systems (e.g., X-SAR/SIR-C) within a tolerable level, data from different tracks and different sensors (channels) must be cross calibrated. The 1989 joint E-SAR/DC-8 SAR calibration campaign gave a first opportunity for such an experiment, including cross sensor and cross track calibration. A basic requirement for successful cross calibration is the stability of the SAR systems. The calibration parameters derived from different tracks and the polarimetric properties of the uncalibrated data are used to describe this stability. Quality criteria for a successful cross calibration are the agreement of alpha degree values and the consistency of radar cross sections of equally sized corner reflectors. Channel imbalance and cross talk provide additional quality in case of the polarimetric DC-8 SAR.

ESA

TYPE 1/4/24

Quest Accession Number : 91A25943

91A25943 NASA IAA Journal Article Issue 09

The radiometric quality of AGRISAR data

(AA)QUEGAN, S. J.

(AE)SIEBER, A. J.

(AB)(Sheffield, University, England); (AE)(CEC, Joint Research Centre,

Ispra, Italy)

(Remote Sensing Society, Workshop on SAR Processing and Information

Extraction from SAR Images, University of Sheffield, England, Mar. 22,

1989) International Journal of Remote Sensing (ISSN 0143-1161), vol. 12,

Feb. 1991, p. 277-302. Research sponsored by the Conselho Nacional de

Desenvolvimento Cientifico e Tecnologico. 910200 p. 26 refs 21 In: EN

(English) p.1418

The AGRISAR '86 data set for the Feltwell, U.K. test site is assessed for its ability to provide information on the spatial and temporal variation of backscatter from growing crops. The image data is shown to contain several sources of radiometric distortion which affect any attempt at image calibration. Of these, the simplest to correct is that caused by range interpolation in the amplitude data. All interpolated pixels should be discarded from the amplitude data supplied by CNES. Correction from slant range to ground range is comparatively straightforward. Effects due to variations in antenna pattern, in the range and azimuth direction, require assumptions about the angular variation of the backscatter of crops and statistical homogeneity of ground cover before they can be removed. The properties of system noise appear complicated and are not yet properly characterized, but interfere with corrections for the antenna pattern. Offsets in the two channels of the complex data also interfere adversely with antenna pattern corrections. The size of these offsets cannot be estimated reliably from the AGRISAR amplitude data, and complex data, and complex data should be supplied as a standard product. No sound basis for inter-image comparison has been found.

Author

TYPE 1/4/25

Quest Accession Number : 91A25942

91A25942 NASA IAA Journal Article Issue 09

SAR motion compensation using autofocus

(AA)BLACKWELL, D.; (AB)QUEGAN, S.

(AA)GEC-Marconi Research Centre, Chelmsford, England); (AB)(Sheffield, University, England)

(Remote Sensing Society, Workshop on SAR Processing and Information Extraction from SAR Images, University of Sheffield, England, Mar. 22, 1989) International Journal of Remote Sensing (ISSN 0143-1161), vol. 12, Feb. 1991, p. 253-275. Research supported by the Ministry of Defence Procurement Executive. 910200 p. 23 refs 19 In: EN (English) p.1370

Conventional motion compensation schemes correct for unwanted synthetic aperture radar (SAR) platform motions using information from an inertial measurement unit (IMU). Autofocus techniques, which focus SAR images, produce an 'autofocus parameter' which is related to the platform motion. In this paper, strong evidence is presented to support the assumption that the contrast optimization autofocus algorithm behaves as a least-squares quadratic fitting to the SAR platform trajectory. Using this assumption, the relationship between the autofocus parameter and across-track accelerations of the SAR platform is derived. This allows the SAR platform motion to be estimated from the autofocus parameter measurements and incorporated in a motion compensation instead of IMU measurements. Three implementations of motion compensation using autofocus are compared and the achievable image quality is quantified.

Author

TYPE 1/4/27

Quest Accession Number : 91A25413

91A25413 NASA IAA Conference Paper Issue 09

Estimating the residual error of the reflectivity displacement method for aircraft motion error extraction from SAR raw data

(AA)MOREIRA, JOAO

(AA)(DLR, Institut fuer Hochfrequenztechnik, Oberpfaffenhofen, Federal Republic of Germany)

IN: IEEE 1990 International Radar Conference, Arlington, VA, May 7-10, 1990, Record (A91-25401 09-32). New York, Institute of Electrical and Electronics Engineers, Inc., 1990, p. 70-75. 900000 p. 6 refs 9 In: EN (English) p.1320

The performance of the reflectivity displacement method is reported. The reflectivity displacement method extracts all the necessary motions of the aircraft from the radar backscatter signal using a new radar configuration and new methods for evaluating the azimuth spectra of the radar signal. Hence, an inertial navigation system is unnecessary for many applications. An error analysis of this method is carried out, and a comparison of two processed images with and without motion compensation is shown, proving the estimated performance.

I.E.

TYPE 1/4/26

Quest Accession Number : 91A25941

91A25941 NASA IAA Journal Article Issue 09

A new approach to range-Doppler SAR processing

(AA)SMITH, A. M.

(AA)(SD-Scicon, London, England)

(Remote Sensing Society, Workshop on SAR Processing and Information Extraction from SAR Images, University of Sheffield, England, Mar. 22, 1989) International Journal of Remote Sensing (ISSN 0143-1161), vol. 12, Feb. 1991, p. 235-251. Research supported by the Ministry of Defence. 910200 p. 17 refs 6 In: EN (English) p.1370

This paper presents a general analysis of frequency-domain SAR processing based on the relationship between the phase of the two-dimensional Fourier transform of a point response to its range-time history. The paper demonstrates how this provides an appropriate basis for the design of a coherent strip-mode processor, free of geometric or phase distortion and artefacts, and without excessive computational cost. The relevance of the analysis to ambiguity estimation and the processing of very long-integration-time SAR data is indicated.

Author

TYPE 1/4/28

Quest Accession Number : 91A25411

91A25411 NASA IAA Conference Paper Issue 09

An improved multi-look technique to produce SAR imagery

(AA)MOREIRA, ALBERTO

(AA)(DLR, Institut fuer Hochfrequenztechnik, Oberpfaffenhofen, Federal Republic of Germany)

IN: IEEE 1990 International Radar Conference, Arlington, VA, May 7-10, 1990, Record (A91-25401 09-32). New York, Institute of Electrical and Electronics Engineers, Inc., 1990, p. 57-63. 900000 p. 7 refs 20 In: EN (English) p.1361

A multilook technique for improving the radiometric resolution in SAR image formation without altering the geometric resolution of the impulse response is proposed. This technique is based on the formation of looks with different bandwidths. The final image is formed by giving each look a proper size and weighting and then adding them incoherently. The looks with larger bandwidth contribute to an improvement of the overall geometric resolution, while the looks with smaller bandwidth improve the overall radiometric resolution. The equivalent number of looks is more than 2.3 times the number of independent looks and is superior to conventional multilook processing with overlapping. An algorithm for efficient processing using the proposed technique is presented, and its validity is proved by image comparison and analysis.

I.E.

TYPE 1/4/29

Quest Accession Number : 91A25410

91A25410 NASA IAA Conference Paper Issue 09

Feasibility of a synthetic aperture radar with rotating antennas (ROSAR)

(AA)KLAUSING, HELMUT; (AB)KEYDEL, WOLFGANG

(AA)HBS GmbH, Otterbrunn, Federal Republic of Germany; (AB)DLR,

Institut fuer Hochfrequenztechnik, Weesling, Federal Republic of Germany

IN: IEEE 1990 International Radar Conference, Arlington, VA, May 7-10,

1990, Record (A91-25401 09-32). New York, Institute of Electrical and

Electronics Engineers, Inc., 1990, p. 51-56. Research sponsored by DLR and

NBS GmbH. 900000 p. 6 refs 5 In: EN (English) p.1360

ROSAR (rotor-SAR) is a synthetic aperture radar concept for pilot sight target detection and target localization with high resolution. ROSAR is based on illuminating/receiving antennas placed at the tips of helicopter rotor blades. The ROSAR concept has potential benefits for civil and military helicopter-borne imaging applications. The concept has two main potential benefits: the imaging field of view is 360 deg, and there is no need for a forward velocity of the carrier platform. As opposed to SAR systems based on linear movement of the antenna, ROSAR imaging is based on synthetic apertures of a circular shape. Thus, the image formation process requires a polar format processing architecture.

I.E.

TYPE 1/4/31

Quest Accession Number : 91A15997

91A15997 NASA IAA Conference Paper Issue 04

Further results of radiometric calibration of a multifrequency airborne SAR system

(AA)KASISCHKE, ERIC S.; (AB)GINERIS, DENISE J.

(AB)Michigan, Environmental Research Institute, Ann Arbor

IN: Quantitative remote sensing: An economic tool for the Nineties;

Proceedings of IGARSS '89 and Canadian Symposium on Remote Sensing, 12th,

Vancouver, Canada, July 10-14, 1989. Volume 5 (A91-15476 04-43). New York,

Institute of Electrical and Electronics Engineers, 1989, p. 2897-2900.

890000 p. 4 refs 7 In: EN (English) p.500

Further results from field experiments to radiometrically correct a multifrequency airborne SAR system are presented. Three frequencies of SAR data (X-, C-, and L-band) at VV polarization were collected over a target array of calibrated trihedral corner reflectors over a 2-week period in summer 1988. For all three frequencies, data collected on one date are utilized to absolutely calibrate data on a second date. The rms errors for this calibration procedure are shown to be less than 1 dB for all three frequencies. In addition, for the L-VV channel, it is shown that the system stability over the entire period of calibration flights (which is the limiting factor for absolute and relative between-scene calibration) was also less than 1 dB.

I.E.

TYPE 1/4/30

Quest Accession Number : 91A20526

91A20526* NASA IAA Journal Article Issue 07

Multiple image SAR shape-from-shading

(AA)THOMAS, J.; (AB)KOBBER, W.; (AC)LEBERL, F.

(AC)Vexcel Corp., Boulder, CO

(AC)Vexcel Corp., Boulder, CO. (V0987612)

JPL-957955; JPL-958594 Photogrammetric Engineering and Remote Sensing

(ISSN 0099-1112), vol. 57, Jan. 1991, p. 51-59. 910100 p. 9 refs 26

In: EN (English) p.1068

A technique for combining radar image shape-from-shading with stereo radiogrammetry to produce terrain surface models using multiple SAR images is described. This technique is expected to be of use to reconstruct surface shape from Magellan images of planet Venus, and to refine the results of terrestrial radar measurements. Local variation in pixel shading is an indicator of terrain slope changes. This variation in pixel shading offers an opportunity for increasing the detail of terrain mapping over that which is available from stereo radiogrammetry alone. Shape-from-shading can potentially provide a relative change in height at each pixel. This leads to a dense set of height measurements and a more faithful rendition of the local terrain shapes. However, shape-from-shading needs some type of boundary values or external terrain low-frequency information to succeed. These can be obtained from stereo or from altimeter measurements.

Author

TYPE 1/4/32

Quest Accession Number : 91A15996

91A15996* NASA IAA Conference Paper Issue 04

Calibration of quadpolarization SAR data using backscatter statistics

(AA)KLEIN, JEFFREY D.

(AA)JPL, Pasadena, CA

IN: Quantitative remote sensing: An economic tool for the Nineties;

Proceedings of IGARSS '89 and Canadian Symposium on Remote Sensing, 12th,

Vancouver, Canada, July 10-14, 1989. Volume 5 (A91-15476 04-43). New York,

Institute of Electrical and Electronics Engineers, 1989, p. 2893-2896.

890000 p. 4 refs 11 In: EN (English) p.500

A new technique is described for calibration of complex multipolarization SAR imagery. Scatterer reciprocity and lack of correlation between like- and cross-polarized radar echoes for natural targets are used to remove cross-polarized contamination in the radar data channels without the use of known ground targets. If known targets are available, all data channels can be calibrated relative to one another and absolutely as well. The method is verified with airborne SAR data.

I.E.

TYPE 1/4/33

Quest Accession Number : 91A15994

91A15994 NASA IAA Conference Paper Issue 04

Comparison of SAR polarimetric calibration techniques using clutter

(AA)SHEEN, D. R.; (AB)KASISCHKE, E. S.

(AB)(Michigan, Environmental Research Institute, Ann Arbor)

IN: Quantitative remote sensing: An economic tool for the Nineties; Proceedings of IGARSS '89 and Canadian Symposium on Remote Sensing, 12th, Vancouver, Canada, July 10-14, 1989. Volume 5 (A91-15476 04-43). New York, Institute of Electrical and Electronics Engineers, 1989, p. 2885-2888. Research supported by the Environmental Research Institute of Michigan. 890000 p. 4 refs 8 In: EN (English) p.500

Polarimetric calibration can require several reference targets. The polarimetric scattering properties of clutter can be exploited in calibration. Because of the cost of reference targets and the effort required to deploy them, using clutter data is desirable for some aspects of calibration if it can be readily used. Polarimetric L-band imagery collected by the MADC/ERIM P-3/SAR system over a forested region is examined. Reference reflectors deployed for calibration included trihedrals, dihedrals at a variety of orientations, and active radar calibrators. The imaged areas consisted of forest and grassy fields, as well as some crop land. Phase calibration methods using these clutter regions can be verified by comparison to methods using reference targets. Once verified, the clutter statistics are used to extend calibration spatially over the image. After the image is calibrated, the signatures of various targets are compared to expected signatures, showing good agreement.

I.E.

TYPE 1/4/35

Quest Accession Number : 91A15937

91A15937* NASA IAA Conference Paper Issue 04

Doppler centroid estimation ambiguity for synthetic aperture radars

(AA)CHANG, C. Y.; (AB)CURLANDER, J. C.

(AB)(JPL, Pasadena, CA)

Jet Propulsion Lab., California Inst. of Tech., Pasadena. (JJ574450)

IN: Quantitative remote sensing: An economic tool for the Nineties; Proceedings of IGARSS '89 and Canadian Symposium on Remote Sensing, 12th, Vancouver, Canada, July 10-14, 1989. Volume 4 (A91-15476 04-43). New York, Institute of Electrical and Electronics Engineers, 1989, p. 2567-2571. 890000 p. 5 refs 7 In: EN (English) p.499

A technique for estimation of the Doppler centroid of an SAR in the presence of large uncertainty in antenna bore-sight pointing is described. Also investigated is the image degradation resulting from data processing that uses an ambiguous centroid. Two approaches for resolving ambiguities in Doppler centroid estimation (DCE) are presented: the range cross-correlation technique and the multiple-PRF (pulse repetition frequency) technique. Because other design factors control the PRF selection for SAR, a generalized algorithm is derived for PRFs not containing a common divisor. An example using the SIR-C parameters illustrates that this algorithm is capable of resolving the C-band DCE ambiguities for antenna pointing uncertainties of about 2-3 deg.

I.E.

TYPE 1/4/34

Quest Accession Number : 91A15942

91A15942 NASA IAA Conference Paper Issue 04

A phase preserving SAR processor

(AA)RANEY, R. KEITH; (AB)VACHON, PARIS W.

(AB)(Canada Centre for Remote Sensing, Ottawa)

IN: Quantitative remote sensing: An economic tool for the Nineties; Proceedings of IGARSS '89 and Canadian Symposium on Remote Sensing, 12th, Vancouver, Canada, July 10-14, 1989. Volume 4 (A91-15476 04-43). New York, Institute of Electrical and Electronics Engineers, 1989, p. 2588-2591. 890000 p. 4 refs 6 In: EN (English) p.499

SAR image phase information is necessary to support many advanced SAR applications. The phase information in the complex image for conventional range Doppler processors is not a robust estimate of scene phase. A SAR processor specifically designed to preserve phase information is being developed at the Canada Centre for Remote Sensing. In addition to preserving vital phase information, this processor can support large degrees of range curvature and range migration. Therefore, it is possible, in principle, to use this processor for satellite SAR data, high-resolution airborne SAR data, and both squint-mode and spotlight-mode SAR data. The theory is summarized, and early results are presented.

I.E.

TYPE 1/4/36

Quest Accession Number : 91A15882

91A15882 NASA IAA Conference Paper Issue 04

C-band SAR results obtained by an experimental airborne SAR sensor

(AA)HORN, R.

(AA)(DLR, Institut fuer Hochfrequenztechnik, Oberpfaffenhofen, Federal Republic of Germany)

IN: Quantitative remote sensing: An economic tool for the Nineties; Proceedings of IGARSS '89 and Canadian Symposium on Remote Sensing, 12th, Vancouver, Canada, July 10-14, 1989. Volume 4 (A91-15476 04-43). New York, Institute of Electrical and Electronics Engineers, 1989, p. 2213-2216. 890000 p. 4 In: EN (English) p.498

Described is an airborne experimental SAR currently under development by the DLR. It allows the study of the SAR method and its problems, such as motion error correction and overall system calibration. The sensor is designed to operate aboard a DO 228 aircraft in either L- or C-band. A first series of flight experiments in L-band was completed successfully in spring 1988. The C-band system installation onboard the aircraft was completed in October 1988, and first flight experiments were carried out over test areas in southern Germany. The C-band front-end represents a first step towards an active array. The amount of quantization and saturation noise is minimized by adapting the received-signal power variation to the dynamic range of the A/D converters. Platform-attitude and navigation data are collected and recorded on high-density tape. The ground-based data processing and the results obtained with the radar are examined.

I.E.

TYPE 1/4/37

Quest Accession Number : 91A15831

91A15831 NASA IAA Conference Paper Issue 04
Discrete target recognition in polarimetric SAR data
(AA)HEAL, J. RUSSELL; (AB)CUMMING, IAN G.
(AB)(British Columbia, University, Vancouver, Canada)

IN: Quantitative remote sensing: An economic tool for the Nineties; Proceedings of IGARSS '89 and Canadian Symposium on Remote Sensing, 12th, Vancouver, Canada, July 10-14, 1989. Volume 3 (A91-15476 04-43). New York, Institute of Electrical and Electronics Engineers, 1989, p. 1836-1840. Research supported by NSERC, Science Council of British Columbia, and MacDonald Detteller and Associates, Ltd. 890000 p. 5 refs 13 In: EN (English) p.498

Whether the extra information content in polarimetric features will overcome the difficult problems of target recognition in SAR (synthetic aperture radar) imagery is examined. In conventional SAR these problems are mainly the result of speckle and receiver noise adversely affecting the single channel of data. To meet this objective, a supervised scheme to classify discrete targets in SAR image utilizing spatial functions of the polarimetric properties of scatterers has been implemented. Target classes are defined by their polarization signature and available ground truth data. The authors examined a large number of polarimetric features and were able to determine a set that gives good classification performance. Comparing these results with trials performed on single-channel SAR data synthesized from the same data set clearly demonstrates a significant performance benefit of polarimetric radar.
I.E.

TYPE 1/4/39

Quest Accession Number : 91A15794

91A15794 NASA IAA Conference Paper Issue 04
Value added geocoded SAR products
(AA)SCHREIER, G.; (AB)KNOEPFLE, M.; (AC)KOSMANN, D.
(AC)(DLR, Oberpfaffenhofen, Federal Republic of Germany)

IN: Quantitative remote sensing: An economic tool for the Nineties; Proceedings of IGARSS '89 and Canadian Symposium on Remote Sensing, 12th, Vancouver, Canada, July 10-14, 1989. Volume 3 (A91-15476 04-43). New York, Institute of Electrical and Electronics Engineers, 1989, p. 1613-1616. 890000 p. 4 refs 11 In: EN (English) p.550

In the framework of the definition of higher-level SAR (synthetic aperture radar) products for the ERS-1 and the SIR-C/X-SAR missions, DLR will deliver to the user geocoded data in several presentations. These data comprise ellipsoid-corrected and terrain-corrected information, as well as additional data sets which will aid the thematic interpretation. In addition to these standard products some investigations have been performed to demonstrate the feasibility and usability of value-added geocoded products, mainly derived from terrain-corrected, one-layer high-precision data. Among these proposed products are three-dimensional views in several presentations, such as perspective and anaglyph views, digital elevation model slope and incidence angle data, simulated SAR views, and vector data overlay. The basic generation algorithms and some examples, mainly performed on Seasat data, are given. The current work on facilities, software, and databases to perform value-added product generation is explained, and an outlook for merging SAR geocoded data with GIS vector data is given.
I.E.

TYPE 1/4/38

Quest Accession Number : 91A15812

91A15812* NASA IAA Conference Paper Issue 04
Squint mode SAR processing algorithms
(AA)CHANG, C. Y.; (AB)JIN, M.; (AC)CURLANDER, J. C.
(AC)(JPL, Pasadena, CA)

IN: Quantitative remote sensing: An economic tool for the Nineties; Proceedings of IGARSS '89 and Canadian Symposium on Remote Sensing, 12th, Vancouver, Canada, July 10-14, 1989. Volume 3 (A91-15476 04-43). New York, Institute of Electrical and Electronics Engineers, 1989, p. 1702-1706. 890000 p. 5 In: EN (English) p.497

The unique characteristics of a spaceborne SAR (synthetic aperture radar) operating in a squint mode include large range walk and large variation in the Doppler centroid as a function of range. A pointing control technique to reduce the Doppler drift and a new processing algorithm to accommodate large range walk are presented. Simulations of the new algorithm for squint angles up to 20 deg and look angles up to 44 deg for the Earth Observing System (EOS) L-band SAR configuration demonstrate that it is capable of maintaining the resolution broadening within 20 percent and the ISLR within a fraction of a decibel of the theoretical value.
I.E.

TYPE 1/4/40

Quest Accession Number : 91A15781

91A15781 NASA IAA Conference Paper Issue 04
Absolute calibration of the CCRS C-band SAR during BEPERS-88
(AA)ULANDER, L.
(AA)(Chalmers Tekniska Hogskola, Goteborg, Sweden)

IN: Quantitative remote sensing: An economic tool for the Nineties; Proceedings of IGARSS '89 and Canadian Symposium on Remote Sensing, 12th, Vancouver, Canada, July 10-14, 1989. Volume 3 (A91-15476 04-43). New York, Institute of Electrical and Electronics Engineers, 1989, p. 1528-1531. Research supported by the Swedish Board of Space Activities and ESA. 890000 p. 4 refs 7 In: EN (English) p.497

A procedure for calibrating the real-time processed image data from the CCRS C-band synthetic aperture radar (SAR) is presented. Measurements made during the Bothnian experiment in preparation for ERS-1 (BEPERS-88) of the returned signal from radar reflectors, of injected noise to confirm STC (sensitivity time control) operation, and of image noise are analyzed and discussed. The maximum total error is estimated to be ± 3.0 dB for absolute calibration and ± 2.0 dB and ± 0.6 dB for relative calibration across and along track, respectively. The calibration procedure is illustrated by computing the backscatter coefficient between 20 and 70 deg of incidence angle for data obtained over two sea-ice classes in the Gulf of Bothnia.
I.E.

TYPE 1/4/41

Quest Accession Number : 91A15667

91A15667* NASA IAA Conference Paper Issue 04

Recent advances in airborne terrestrial remote sensing with the NASA airborne visible/infrared imaging spectrometer (AVIRIS), airborne synthetic aperture radar (SAR), and thermal infrared multispectral scanner (TINS)

(AA)VAME, GREGG; (AB)EVANS, DIANE L.; (AC)KAHLE, ANNE B.

(AC)(JPL, Pasadena, CA)

IN: Quantitative remote sensing: An economic tool for the Nineties;

Proceedings of IGARSS '89 and Canadian Symposium on Remote Sensing, 12th, Vancouver, Canada, July 10-14, 1989. Volume 2 (A91-15476 04-43). New York, Institute of Electrical and Electronics Engineers, 1989, p. 942, 943. 890000 p. 2 In: EN (English) p.479

Significant progress in terrestrial remote sensing from the air has been made with three NASA-developed sensors that collectively cover the solar-reflected, thermal infrared, and microwave regions of the electromagnetic spectrum. These sensors are the airborne visible/infrared imaging spectrometer (AVIRIS), the thermal infrared mapping spectrometer (TINS) and the airborne synthetic aperture radar (SAR), respectively. AVIRIS and SAR underwent extensive in-flight engineering testing in 1987 and 1988 and are scheduled to become operational in 1989. TINS has been in operation for several years. These sensors are described.

I.E.

TYPE 1/4/43

Quest Accession Number : 91A15557

91A15557* NASA IAA Conference Paper Issue 04

Linear '87 ice surface characteristics and their effect upon C-band SAR signatures

(AA)DRINKWATER, MARK R.

(AC)(JPL, Pasadena, CA)

IN: Quantitative remote sensing: An economic tool for the Nineties;

Proceedings of IGARSS '89 and Canadian Symposium on Remote Sensing, 12th, Vancouver, Canada, July 10-14, 1989. Volume 1 (A91-15476 04-43). New York, Institute of Electrical and Electronics Engineers, 1989, p. 390-393. 890000 p. 4 refs 11 In: EN (English) p.587

Ice surface characterization data were recorded during March 1987 in the Labrador Sea marginal ice zone, at the onset of spring melt. Measured data are used as input parameters in a simple scattering model to simulate the effects of temporal variations in material properties upon C-band scattering signatures. Snow moisture and surface roughness have a significant effect upon sigma(0) and large differences are predicted between undeformed ice surfaces and deformed or rubble ice areas. The model reproduces a calibrated synthetic-aperture-radar (SAR)-derived signature obtained during the experiment with a reasonable degree of certainty. Predictions also simulate a trend observed in SAR images of increasing backscatter contrast between deformed and undeformed ice over period of surface warming.

I.E.

TYPE 1/4/42

Quest Accession Number : 91A15628

91A15628* NASA IAA Conference Paper Issue 04

Ice classification algorithm development and verification for the Alaska SAR Facility using aircraft imagery

(AA)HOLT, BENJAMIN; (AB)KWOK, RONALD; (AC)RIGNOT, ERIC

(AC)(JPL, Pasadena, CA)

IN: Quantitative remote sensing: An economic tool for the Nineties;

Proceedings of IGARSS '89 and Canadian Symposium on Remote Sensing, 12th, Vancouver, Canada, July 10-14, 1989. Volume 2 (A91-15476 04-43). New York, Institute of Electrical and Electronics Engineers, 1989, p. 751-754. 890000 p. 4 In: EN (English) p.588

The Alaska SAR Facility (ASF) at the University of Alaska, Fairbanks is a NASA program designed to receive, process, and archive SAR data from ERS-1 and to support investigations that will use this regional data. As part of ASF, specialized subsystems and algorithms to produce certain geophysical products from the SAR data are under development. Of particular interest are ice motion, ice classification, and ice concentration. This work focuses on the algorithm under development for ice classification, and the verification of the algorithm using C-band aircraft SAR imagery recently acquired over the Alaskan arctic.

I.E.

TYPE 1/4/44

Quest Accession Number : 91A15529

91A15529* NASA IAA Conference Paper Issue 04

Results of the 1988 NASA/JPL airborne SAR calibration campaign

(AA)FREMANN, A.; (AB)WERNER, C.; (AC)KLEIN, J. D.

(AC)(JPL, Pasadena, CA)

IN: Quantitative remote sensing: An economic tool for the Nineties;

Proceedings of IGARSS '89 and Canadian Symposium on Remote Sensing, 12th, Vancouver, Canada, July 10-14, 1989. Volume 1 (A91-15476 04-43). New York, Institute of Electrical and Electronics Engineers, 1989, p. 249-253. 890000 p. 5 refs 7 In: EN (English) p.537

During the spring of 1988, the NASA/JPL multifrequency, multipolarization SAR (synthetic aperture radar) flew in series of calibration experiments over the Goldstone dry lake bed. An array of calibration devices was deployed, including dihedral and trihedral corner reflectors, polarimetric active radar calibrators, passive receivers, and CW (continuous wave) tone generators. The aim of the campaign was to calibrate both amplitude and phase of the resulting SAR images, over long and short time scales. The results of the analysis of the calibration data collected in the spring of 1988 are presented. Trihedral corner reflector signatures and certain image background measures are used to externally calibrate relative amplitude and phase between polarizations at a given frequency, and to calibrate across frequencies. Assessments are made of the calibration accuracy as a function of image frame position for each frequency, and the stability of the radar calibration over long and short time-scales.

I.E.

TYPE 1/4/45

Quest Accession Number : 91A15527

91A15527 NASA IAA Conference Paper Issue 04
Calibration for airborne SAR(AA)HARRIS, R. K.; (AB)LUKOWSKI, T. I.; (AC)GRAY, A. L.;
(AD)LIVINGSTONE, C. E.

(AD)(Canada Centre for Remote Sensing, Ottawa)

IN: Quantitative remote sensing: An economic tool for the Nineties;
Proceedings of IGARSS '89 and Canadian Symposium on Remote Sensing, 12th,
Vancouver, Canada, July 10-14, 1989. Volume 1 (A91-15476 04-43). New York,
Institute of Electrical and Electronics Engineers, 1989, p. 238-242.
890000 P. 5 refs 28 In: EN (English) p.537

Relative and absolute radiometric calibration of the CCRS (Canada Center for Remote Sensing) airborne SARs (synthetic aperture radars) is discussed. It is noted that airborne SAR has unique calibration difficulties due to its large swath/height ratio when compared with the satellite-borne case. This manifests itself in strongly varying terms in the radar equation, with important implications for image interpretation and analysis. Calibration for airborne SARs may therefore lead to data products dissimilar from their satellite counterparts. Recommendations for data acquisition and calibration using the CCRS facility are presented, along with CCRS plans for continuing calibration strategy, which emphasize the implications of calibration on data utility.

I.E.

TYPE 1/4/47

Quest Accession Number : 91M15451

91M15451# NASA STAR Conference Paper Issue 07
Antenna subarrays and GaAs T/R modules for X-SAR on EOS

(AA)BRUNNER, A.; (AB)LANGER, E.

Siemens A.G., Munich (Germany, F.R.). (SK032012) Radio and Radar
Systems/Semiconductors.In DLR, Symposium on Applications of Multifrequency/Multipolarization
SAR in View of X-EOS (X-SAR for EOS) CGS p.259-271 (SEE N91-15434 07-32)
900500 P. 13 Original contains color illustrations In: EN (English)
Avail: NTIS HC/NP A12; DLR, VB-PL-DO, Postfach 90 60 58, 5000 Cologne,
Fed. Republic of Germany, NC 105 Deutsche Marks p.993

An alternative antenna concept to the printed patch principle is proposed for the X-SAR (Synthetic Aperture Radar) quad polarization mission. The active phased array system consists of a doubly polarized slotted waveguide array fed via active antenna modules. The high polarization purity required is achieved by orthogonal slots in the broad side of two integrated groups of rectangular waveguides. A waveguide section of 10 (20) slots can be used as a subarray for one active module. That means 64 (32) subarrays along the 16 m of the flight direction and 18 along the 0.38 m in range. The 1152 (576) subarrays or 1152 (576) active modules fill out the 6 sq m aperture. A number of 1152 active modules corresponds with 4.3 W output RF-power per module, for 5 kW peak power is to be radiated. Because of a better efficiency of a 4.3 W module compared to a 8.6 module out of 576 active modules for 576 subarrays, the 4.3 W output power module is recommended. Light weight structures for module boxes and substrates are discussed. Principles of module components like Low Noise Amplifier (LNA) or Single-Pole-Double Through (SPDT) switches are explained and shown.

ESA

TYPE 1/4/46

Quest Accession Number : 91A15525

91A15525# NASA IAA Conference Paper Issue 04
The need for SAR calibration

(AA)FREEMAN, A.

(AA)(JPL, Pasadena, CA)

IN: Quantitative remote sensing: An economic tool for the Nineties;
Proceedings of IGARSS '89 and Canadian Symposium on Remote Sensing, 12th,
Vancouver, Canada, July 10-14, 1989. Volume 1 (A91-15476 04-43). New York,
Institute of Electrical and Electronics Engineers, 1989, p. 230-233.
890000 P. 4 refs 17 In: EN (English) p.537

TYPE 1/4/48

Quest Accession Number : 91M15446

91M15446# NASA STAR Conference Paper Issue 07
SAR interferometry can give 1 meter altitude resolution

(AA)PRATI, C.; (AB)ROCCA, P.; (AC)MONTIGNIERI, A.

(AC)(Consiglio Nazionale delle Ricerche, Florence, Italy)

Politecnico di Milano (Italy). (PX565076) Dipt. di Elettronica.

In DLR, Symposium on Applications of Multifrequency/Multipolarization
SAR in View of X-EOS (X-SAR for EOS) CGS p.197-212 (SEE N91-15434 07-32)
900500 P. 16 In: EN (English) Avail: NTIS HC/NP A12; DLR, VB-PL-DO,
Postfach 90 60 58, 5000 Cologne, Fed. Republic of Germany, NC 105 Deutsche
marks p.992

In Synthetic Aperture Radar (SAR) interferometry, the altimetric information of the terrain can be obtained from the phase difference of two focused complex images. These images can be gathered by the same sensor in two passes along different orbits or by two sensors mounted on the same platform. The altimetric resolution of such a system improves when the sensors displacement is increased in the cross track direction. The maximum allowed displacement, limited by speckle noise, increases with the spatial resolution of the SAR image. Excluding the additive noise, it is shown that the achievable vertical resolution is better than the slant range resolution. As an example, an altimetric map of the Panamint Valley area is calculated using repeated passes of the Seasat satellite. The effect of the additive noise is visible only when the cross track distance of the two orbits is low.

ESA

TYPE 1/4/49

Quest Accession Number : 91N15441

91N15441# NASA STAR Conference Paper Issue 07
 Multiparametric radar data for land applications

(AA)MÄRKER, W.; (AB)WITTHACK, J.
 (AB)Deutsche Forschungsgemeinschaft fuer Luft-
 Oberpfaffenhofen, Germany, F.R.)
 Freiburg Univ. (Germany, F.R.).

In DLR, Symposium on Applications of Multifrequency/Multipolarization
 SAR in View of X-BOS (X-SAR for EOS) CGS p 115-138 (SEE N91-15434 07-32)
 900500 P. 24 Original contains color illustrations In: EN (English)
 Avail: NTIS HC/NF A12; DLR, VB-PL-DO, Postfach 90 60 58, 5000 Cologne,
 Fed. Republic of Germany, HC 105 Deutsche marks p.992

The influence of different sensor parameters and different surface
 conditions on the backscattering of the microwaves are studied. Campaigns
 conducted within the member countries both of ESA and the European
 community are described. The AGRISAR '86 campaign, the first European
 campaign to study the temporal change of backscattered signal of
 agricultural units in the X-band using an imaging SAR (Synthetic Aperture
 Radar) system, the AGRISCART '87 and '88 campaigns, multiband
 scatterometer-campaigns, flown to study the influence of a variety of
 recording parameters on the backscattering signal are described. All three
 campaigns are flown over a test site west of the city of Freiburg in the
 upper Rhine valley.
 ESA

TYPE 1/4/51

Quest Accession Number : 91N15439

91N15439# NASA STAR Conference Paper Issue 07

Applications of Multifrequency (MF) SAR images in hydrology
 (AA)CAMUZI, P.; (AB)CHIARAMONTI, L.; (AC)MORETTI, S.

(AB)Science for Environment Foundation, Florence, Italy)
 Florence Univ. (Italy). (P7392165) Dept. of Earth Science.

In DLR, Symposium on Applications of Multifrequency/Multipolarization
 SAR in View of X-BOS (X-SAR for EOS) CGS p 77-94 (SEE N91-15434 07-32)
 900500 P. 18 In: EN (English) Avail: NTIS HC/NF A12; DLR, VB-PL-DO,
 Postfach 90 60 58, 5000 Cologne, Fed. Republic of Germany, HC 105 Deutsche
 marks p.991

Although various forms of remote sensing have been used extensively for
 several decades, it is only recently that, through the development of new
 instruments and techniques, the versatility and potential of microwave
 remote sensing for the qualitative and quantitative measurements of
 hydrological processes have shown considerable improvements. Particularly,
 Multifrequency (MF), Multipolarization (MP), Multi-incidence Angles (MA)
 SAR (Synthetic Aperture Radar) systems provided for EOS (Earth Observation
 System) polar platforms will open new applicative horizons in the study of
 hydrological processes over large areas in a wide range of environmental
 conditions. Decisive contributions to applicative perspectives and system
 requirements have come out of international experimental activities
 carried out in the last decade, and from multidisciplinary evaluation of
 the collected data. SAR campaigns planned for the next few years, and
 further evaluation of SAR images to match quantitative estimations
 required for hydrological process-based modeling are discussed.
 ESA

TYPE 1/4/50

Quest Accession Number : 91N15440

91N15440# NASA STAR Conference Paper Issue 07

Applicability of radar data for geoscientific purposes and expected
 improvements by use of multifrequency and multipolarization data

(AA)JASKOLLA, F.; (AB)BODECHTEL, J.

Technische Univ., Munich (Germany, F.R.). (U492950) Inst. for General
 and Applied Geology.

In DLR, Symposium on Applications of Multifrequency/Multipolarization
 SAR in View of X-BOS (X-SAR for EOS) CGS p 95-114 (SEE N91-15434 07-32)
 900500 P. 20 Original contains color illustrations In: EN (English)
 Avail: NTIS HC/NF A12; DLR, VB-PL-DO, Postfach 90 60 58, 5000 Cologne,
 Fed. Republic of Germany, HC 105 Deutsche marks p.991

Application of synthetic aperture radar data in the field of geoscience
 is discussed. High potential especially for mapping purposes in geology is
 demonstrated. The differentiation possibilities of lithological units are
 recognized as poor due to small variations of dielectric properties of
 rocks and the poor availability of multiparameter radar data. Ways in
 which the interpretation of structural features, could be significantly
 improved are outlined. Delineation of surface morphology, delineation of
 structural features surface and subsurface phenomena and determination of
 surface moisture content are areas in which feature interpretation can be
 improved. These subjects include manifold parameters which are
 indispensable for an optimized inclusion of radar data to different fields
 of interest. The most significant and promising applications besides
 classical applications (e.g., lithological and structural mapping) are
 identified.
 ESA

TYPE 1/4/52

Quest Accession Number : 91N15438

91N15438# NASA STAR Conference Paper Issue 07

Application of multifrequency and multipolarization SAR systems in
 remote sensing for agriculture

(AA)KUEHBAUCH, W.

Bonn Univ. (Germany, F.R.). (BT209639)

In DLR, Symposium on Applications of Multifrequency/Multipolarization
 SAR in View of X-BOS (X-SAR for EOS) CGS p 58-76 (SEE N91-15434 07-32)
 900500 P. 19 Original contains color illustrations In: EN (English)
 Avail: NTIS HC/NF A12; DLR, VB-PL-DO, Postfach 90 60 58, 5000 Cologne,
 Fed. Republic of Germany, HC 105 Deutsche marks p.991

The deficiencies of remote sensing as applied in agriculture are
 discussed. They are due to the fact that optical sensors depend on day
 light and on cloudfree coverage and, even under suitable weather
 conditions, miss important characters of the plant canopy that are related
 to crop species and yield. The all weather capability of radar especially
 in humid regions offers considerable advantages in agricultural
 application. SAR (Synthetic Aperture Radar) potential for species
 recognition and yield prediction of agricultural crops is reviewed both as
 related to multitemporal single frequency and single temporal
 multifrequency-multipolarization observations. The potential of variable
 SAR systems and of combined optical and microwave sensors is discussed.
 ESA

TYPE 1/4/53

Quest Accession Number : 91A14841

91A14841* NASA IAA Journal Article Issue 03

Incorporation of polarimetric radar images into multisensor data sets
(AA)EVANS, DIANE L.; (AB)VAN ZYL, JAKOB J.; (AC)BURNETTE, CHARLES F.
(AC)(JPL, Pasadena, CA)

Jet Propulsion Lab., California Inst. of Tech., Pasadena. (JJ574450)

IEEE Transactions on Geoscience and Remote Sensing (ISSN 0196-2892),
vol. 28, Sept. 1990, p. 932-939. 900900 p. 8 refs 12 In: EN (English)
p.390

A technique is presented for registering polarimetric SAR data to other aircraft and spaceborne data sets. Resampling is done on the full Stokes matrix, allowing full polarization synthesis on the coregistered data set. Analysis of data acquired over Pissgah Crater in the Mojave Desert, CA, as part of the Mojave Field Experiment shown that the resampling does not seriously affect the pedestal heights of polarization signatures or affect estimates of RMS heights for smooth to moderately rough surfaces.
I.E.

TYPE 1/4/54

Quest Accession Number : 91A14839

91A14839 NASA IAA Journal Article Issue 03

Determination of antenna elevation pattern for airborne SAR using the rough target approach

(AA)HAWKINS, ROBERT K.

(AA)(Canada Centre for Remote Sensing, Ottawa)

IEEE Transactions on Geoscience and Remote Sensing (ISSN 0196-2892),
vol. 28, Sept. 1990, p. 896-905. 900900 p. 10 refs 23 In: EN (English)
p.358

Data from a forested region of northern Ontario are analyzed to yield an estimate of the antenna elevation pattern for the Canada Centre for Remote Sensing airborne SAR. The method relies on the imaged area being uniform on an average basis but not necessarily uniform on a pixel-scale basis. The extended uniform area was imaged as a series of short-flight segments in which the antenna depression angle was systematically stepped, keeping all other acquisition parameters of the aircraft and SAR essentially fixed. Subsequent analysis of the real-time imagery was then performed, dividing average image powers for discrete bands of pixels across the swath to yield the relative gain of the antenna corresponding to the antenna angles for the center of these bands. Combining the total set of these measurements generates the entire elevation pattern. Results are given for the C-band, HH-pattern over an angular range of 50 deg and dynamic range of over 30 dB and compared to antenna range measurements taken before installation. It is concluded that this method has good potential for airborne SARs with dynamic antenna pointing capability.
I.E.

TYPE 1/4/56

Quest Accession Number : 91N14642

91N14642* NASA SPAR Issue 06

Method for detecting surface motions and mapping small terrestrial or planetary surface deformations with synthetic aperture radar / Patent
(AA)GABRIEL, ANDREW K.; (AB)GOLDSTEIN, RICHARD M.; (AC)ZEBKER, HOWARD A.
(AA)inventor (to NASA); (AB)inventor (to NASA); (AC)inventor (to NASA)
(AC)(Jet Propulsion Lab., California Inst. of Tech., Pasadena.)
National Aeronautics and Space Administration, Pasadena Office, CA. (NDS94694)

NASA-CASE-NPO-17831-1-CU; US-PATENT-4,975,704; US-PATENT-APPL-SN-470665;
US-PATENT-CLASS-342-25; INT-PATENT-CLASS-G01S-13/90 901204 p. 9 Filed
26 Jan. 1990 In: EN (English) Avail: US Patent and Trademark Office p. 840

A technique based on synthetic aperture radar (SAR) interferometry is used to measure very small (1 cm or less) surface deformations with good resolution (10 m) over large areas (50 km). It can be used for accurate measurements of many geophysical phenomena, including swelling and buckling in fault zones, residual, vertical and lateral displacements from seismic events, and prevolcanic swelling. Two SAR images are made of a scene by two spaced antennas and a difference interferogram of the scene is made. After unwrapping phases of pixels of the difference interferogram, surface motion or deformation changes of the surface are observed. A second interferogram of the same scene is made from a different pair of images, at least one of which is made after some elapsed time. The second interferogram is then compared with the first interferogram to detect changes in line of sight position of pixels. By resolving line of sight observations into their vector components in other sets of interferograms along at least one other direction, lateral motions may be recovered in their entirety. Since in general, the SAR images are made from flight tracks that are separated, it is not possible to distinguish surface changes from the parallax caused by topography. However, a third image may be used to remove the topography and leave only the surface changes.

Official Gazette of the U.S. Patent and Trademark Office

TYPE 1/4/55

Quest Accession Number : 91A14838

91A14838 NASA IAA Journal Article Issue 03

SAR observations and modeling of the C-band backscatter variability due to multiscale geometry and soil moisture

(AA)BERARDINO, A.; (AB)CHV, Q. R. J.; (AC)LE TOAN, THUY

(AB)(Sherbrooke, Universite, Canada); (AC)(Centre d'Etude Spatiale des

Rayonnements, Toulouse, France)
IEEE Transactions on Geoscience and Remote Sensing (ISSN 0196-2892),
vol. 28, Sept. 1990, p. 886-895. Research supported by NSERC. 900900 p.
10 refs 15 In: EN (English) p.377

The effect of the multiscale surface geometry on the sensitivity of C-band synthetic aperture radar (SAR) data to soil moisture is studied. The experimental data consist of C-band SAR images of an agricultural site. The backscatter variability due to surface roughness has been analyzed. The effect of random roughness associated with soil clods is never less than 2 dB, and the effect of a row pattern can be as strong as 10 dB. In addition, the periodic drainage topography induces a backscatter variability due to soil moisture variation and drainage relief. Parameters accounting for multiscale geometry have been modeled and used in theoretical surface scattering models. Good agreement was found between theoretical results and experimental data for the backscatter angular variation due to random roughness and row structure. The validated models have been used to extend the observations beyond the available range of incidence and azimuth angles provided by airborne SARs. The results indicate clearly that airborne C-band SAR data cannot be easily inverted into soil moisture data. However, with ERS-1 or Radarsat data at an incidence angle of about 20 deg, the effect of random and periodic roughness can be reduced to about 2 dB if the look angle is less than 50 deg.
I.E.

TYPE 1/4/57

Quest Accession Number : 91NI14638

91NI14638# NASA STAR Technical Report Issue 06

Multiband radar characterization of forest biomes / Final Report, 1 Mar. 1985 - 28 Feb. 1990

(AA)DOBSON, M. CRAIG; (AB)ULABY, FAWAZ T.

Michigan Univ., Ann Arbor. (NK270710) Radiation Lab.

NASA-CR-185101; NAS 1.26:185101; UN-022486-1-P NAGW-733 900200 p. 12

In: EN (English) Avail: NTIS HC/MF A03 p.839

The utility of airborne and orbital SAR in classification, assessment, and monitoring of forest biomes is investigated through analysis of orbital synthetic aperture radar (SAR) and multifrequency and multipolarized airborne SAR imagery relying on image tone and texture. Preliminary airborne SAR experiments and truck-mounted scatterometer observations demonstrated that the three dimensional structural complexity of a forest, and the various scales of temporal dynamics in the microwave dielectric properties of both trees and the underlying substrate would severely limit empirical or semi-empirical approaches. As a consequence, it became necessary to develop a more profound understanding of the electromagnetic properties of a forest scene and their temporal dynamics through controlled experimentation coupled with theoretical development and verification. The concatenation of various models into a physically-based composite model treating the entire forest scene became the major objective of the study as this is the key to development of a series of robust retrieval algorithms for forest biophysical properties. In order to verify the performance of the component elements of the composite model, a series of controlled laboratory and field experiments were undertaken to: (1) develop techniques to measure the microwave dielectric properties of vegetation; (2) relate the microwave dielectric properties of vegetation to more readily measured characteristics such as density and moisture content; (3) calculate the radar cross-section of leaves, and cylinders; (4) improve backscatter models for rough surfaces; and (5) relate attenuation and phase delays during propagation through canopies to canopy properties. These modeling efforts, as validated by the measurements, were incorporated within a larger model known as the Michigan Microwave Canopy Scattering (MIMICS) Model.

Author

TYPE 1/4/58

Quest Accession Number : 91NI13595

91NI13595# NASA STAR Issue 05

Pipeline synthetic aperture radar data compression utilizing systolic binary tree-searched architecture for vector quantization / Patent Application

(AA)CHANG, CHI-YUNG; (AB)FANG, WAI-CHI; (AC)CURLANDER, JOHN C.

(AA)inventor (to NASA); (AB)inventor (to NASA); (AC)inventor (to NASA)

(AC)(Jet Propulsion Lab., California Inst. of Tech., Pasadena.)

National Aeronautics and Space Administration. Pasadena Office, CA. (ND894694)

NASA-CASE-NPO-17941-1-CU; NAS 1.71:NPO-17941-1-CU; US-PATENT-APPL-SN-55-

0775 NAS7-918 900710 p. 37 In: EN (English) Avail: NTIS HC/MF A03

p.648

A system for data compression utilizing systolic array architecture for Vector Quantization (VQ) is disclosed for both full-searched and tree-searched. For a tree-searched VQ, the special case of a Binary Tree-Search VQ (BTSVQ) is disclosed with identical Processing Elements (PE) in the array for both a Raw-Codebook VQ (RCVQ) and a Difference-Codebook VQ (DCVQ) algorithms. A fault tolerant system is disclosed which allows a PE that has developed a fault to be bypassed in the array and replaced by a spare at the end of the array, with codebook memory assignment shifted one PE past the faulty PE of the array.

NASA

TYPE 1/4/60

Quest Accession Number : 90A51385

90A51385# NASA IAA Journal Article Issue 23

Synthetic-aperture-radar imaging of the ocean surface using the slightly-rough facet model and a full surface-wave spectrum JULIAN C. (AA)WEST, JAMES C.; (AB)MOORE, RICHARD K.; (AC)HOLTZMAN, JULIAN C.

(AC)(University of Kansas Center for Research, Inc., Lawrence)

Kansas Univ. Center for Research, Inc., Lawrence. (KF728369)

N00014-79-C-0533; NAGW-1278 International Journal of Remote Sensing

(ISSN 0143-1161), vol. 11, Aug. 1990, p. 1451-1480. 900800 p. 30 refs

48 In: EN (English) p.3771

A new model of synthetic-aperture-radar (SAR) imaging of ocean waves is described. The model is based on mapping individual, slightly-rough surface facets through the SAR processor into the image and responses of the facets in the image domain are added together coherently to give the composite image. A windowing technique allows both the orbital motion and the phase velocity of the long waves to be included. It is determined that the azimuthal cut-off is due to a smearing of the response of the facets in the image induced by the random orbital motion of the intermediate large-scale waves and that the focus adjustment that gives the greatest image contrast is half the phase velocity of the dominant long wave. The optimal processing technique, however, may consist of spatially offsetting the multiple looks on the image domain to compensate the propagation of long waves during the integration time of the SAR.

I.K.S.

TYPE 1/4/59

Quest Accession Number : 91NI13594

91NI13594# NASA STAR Issue 05

Method for providing a polarization filter for processing synthetic aperture radar image data / Patent Application

(AA)DUBOIS, PASCAL C.; (AB)VANZYL, JAKOB J.

(AA)inventor (to NASA); (AB)inventor (to NASA)

(AB)(Jet Propulsion Lab., California Inst. of Tech., Pasadena.)

National Aeronautics and Space Administration. Pasadena Office, CA. (ND894694)

NASA-CASE-NPO-17904-1-CU; NAS 1.71:NPO-17904-1-CU; US-PATENT-APPL-SN-54-

4293 NAS7-918 900625 p. 27 In: EN (English) Avail: NTIS HC/MF A03

p.648

A polarization filter can maximize the signal-to-noise ratio of a polarimetric synthetic aperture radar (SAR) and help discriminate between targets or enhance image features, e.g., enhance contrast between different types of target. The method disclosed is based on the Stokes matrix/ Stokes vector representation, so the targets of interest can be extended targets, and the method can also be applied to the case of bistatic polarimetric radars.

NASA

TYPE 1/4/61

Quest Accession Number : 90A50723

90A50723 NASA IAA Journal Article Issue 23

Synthetic aperture radar imaging of ship wakes in the Gulf of Alaska

(AA)SHENGIN, OMAR H.

(AA)(Ocean Research and Engineering, Pasadena, CA)

Journal of Geophysical Research (ISSN 0148-0227), vol. 95, Sept. 15,

1990, p. 16319-16338. Research supported by the U.S. Navy. 900915 p. 20

refs 11 In: EN (English) p.3704

The Gulf of Alaska SAR experiment was conducted during March 9-14, 1984 to investigate SAR imaging of narrow-v wakes in a deep mixed layer environment so that surface manifestations of ship-generated internal waves would be made small. Five SAR flights were executed over large ships of opportunity in deep water where the mixed layer depth exceeded 100 m in all cases. SAR images were obtained in sea states 1-4. Range and azimuthally traveling ships were imaged. The incidence angles of azimuthally traveling ships ranged from 24 to 53 deg. The following results are reported: (1) the half angles associated with narrow-v wakes are consistent with first-order Bragg surface wave theory described by Case et al. (1984); (2) the decay rate along the bright arms of the narrow-v wake is consistent with the combined viscous and radiation decay of short surface waves with first-order Bragg wavelengths; (3) narrow-v wakes are observed in sea states 1-3 at incidence angles less than 45 deg, with the longest narrow-v wakes bright-arm observed being 3.3 km; (4) turbulent wakes (dark band between the bright arms) are observed in sea states 1-4 at incidence angles less than 53 deg, with the longest turbulent wake length observed being 41 km; and (5) bright boundaries along one side of the turbulent wake are observed.

Author

TYPE 1/4/63

Quest Accession Number : 90A50487

90A50487 NASA IAA Journal Article Issue 23

Incidence-angle dependence in forested and non-forested areas in Seasat

SAR data

(AA)RAUSTE, YRJO

(AA)(Technical Research Centre of Finland, Espoo)

(CEC and JPL, International Forest Signature Workshop, Ispra, Italy,

Sept. 7-9, 1988) International Journal of Remote Sensing (ISSN 0143-1161),

vol. 11, July 1990, p. 1267-1276. Research supported by the Technical

Research Centre of Finland, Academy of Finland, and Neste, Ltd. 900700

p. 10 refs 19 In: EN (English) p.3754

Quantitative evaluation of the topography-induced variation in a Seasat SAR scene is presented. Variations in the slope of the backscatter curve (sensitivity of radar to alterations in incidence angle) between spruce-dominated mixed forests, pine-dominated mixed forests, deciduous forests, and regenerated (pine plantations) areas are defined. The contribution of the corner reflector backscatter mechanism to the total backscatter is analyzed. Analytical results show that 65 percent of the total variation in land pixels can be attributed to terrain topography.

R.E.P.

TYPE 1/4/62

Quest Accession Number : 90A50720

90A50720 NASA IAA Journal Article Issue 23

Cross sections and modulation transfer functions at L and Ku bands measured during the Tower Ocean Wave and Radar Dependence Experiment

(AA)KELLER, WILLIAM C.; (AB)PLANT, WILLIAM J.

(AA)(U.S. Navy, Naval Research Laboratory, Washington, DC); (AB)(Woods

Hole Oceanographic Institution, MA)

Journal of Geophysical Research (ISSN 0148-0227), vol. 95, Sept. 15,

1990, p. 16277-16289. Research supported by the U.S. Navy. 900915 p. 13

refs 26 In: EN (English) p.3771

Normalized radar cross sections and modulation transfer functions (MTFs) for microwave backscattering from the sea surface have been measured at both L- and Ku-bands during the Tower Ocean Wave and Radar Dependence Experiment. Long waves during the experiment were usually not generated by the local wind, so a unique opportunity was afforded to investigate the effects of arbitrary wind, wave, and antenna angles on the backscatter. Cross sections at L-band are shown to be isotropic with respect to wind-antenna angle and nearly independent of wind speed except at the lowest wind speeds. Ku-band cross sections, on the other hand, show the expected wind-antenna angle anisotropy and wind speed dependence. The Ku-band cross sections agree well in magnitude with previous wave-tank and satellite measurements, casting doubt on the dependence of cross section on antenna height which has been suggested in the literature. At both frequencies the data suggest that cross sections may be lowered slightly when long waves propagate at large angles to the wind.

Author

TYPE 1/4/64

Quest Accession Number : 90A50479

90A50479* NASA IAA Journal Article Issue 23

The effect of changing environmental conditions on microwave signatures

of forest ecosystems - Preliminary results of the March 1988 Alaskan

aircraft SAR experiment

(AA)WAV, JOBEA; (AB)PARIS, JACK; (AC)KASISCHKE, ERIC; (AD)SLAUGHTER,

CHARLES; (AE)VIERECK, LESLIE

(AB)(JPL, Pasadena, CA); (AC)(Michigan, Environmental Research

Institute, Ann Arbor); (AE)(Institute of Northern Forestry, Fairbanks, AK)

Jet Propulsion Lab., California Inst. of Tech., Pasadena. (JUS74450)

(CEC and JPL, International Forest Signature Workshop, Ispra, Italy,

Sept. 7-9, 1988) International Journal of Remote Sensing (ISSN 0143-1161),

vol. 11, July 1990, p. 1119-1144. 900700 p. 26 refs 29 In: EN

(English) p.3753

In preparation for the ESA ERS-1 mission, a series of multitemporal, multifrequency, multipolarization aircraft SAR data sets were acquired near Fairbanks in March 1988. P-, L-, and C-band data were acquired with the NASA/JPL Airborne SAR on five different days over a period of two weeks. The airborne data were augmented with intensive ground calibration data as well as detailed simultaneous in situ measurements of the geometric, dielectric, and moisture properties of the snow and forest canopy. During the time period over which the SAR data were collected, the environmental conditions changed significantly; temperatures ranged from unseasonably warm (1 to 9 C) to well below freezing (-8 to -15 C), and the moisture content of the snow and trees changed from a liquid to a frozen state. The SAR data clearly indicate the radar return is sensitive to these changing environmental factors, and preliminary analysis of the L-band SAR data shows a 0.4 to 5.8 dB increase (depending on polarization and canopy type) in the radar cross section of the forest stands under the warm conditions relative to the cold. These SAR observations are consistent with predictions from a theoretical scattering model.

Author

TYPE 1/4/65

Quest Accession Number : 90A49700

90A49700+ NASA IAA Journal Article Issue 22

Assessment of tropical forest stand characteristics with
multipolarization SAR data acquired over a mountainous region in Costa
Rica

(AA)NU, SHIH-TSENG

(AA)NASA, John C. Stennis Space Center, Bay Saint Louis, MS)
National Aeronautics and Space Administration. John C. Stennis Space
Center, Bay Saint Louis, MS. (ND103456)(IEEE, Canadian Remote Sensing Society, URSI, et al., Quantitative
remote sensing: An economic tool for the Nineties - 1989 International
Symposium on Remote Sensing and Canadian Symposium on Remote
Sensing, 12th, (IGARSS'89), Vancouver, Canada, July 10-14, 1989) IEEE
Transactions on Geoscience and Remote Sensing (ISSN 0196-2892), vol. 28,
July 1990, p. 752-755. 900700 p. 4 refs 8 In: EN (English) p.3571A digital terrain elevation data set was coregistered with radar data
for assessing tropical forest stand characteristics. Both raw and
topographically corrected L-band polarimetric radar data acquired over the
tropical forests of Costa Rica were analyzed and correlated with
field-collected tree parameter data to study the stand characteristics.
The results of analyses using 18 out of 81 plots for sites A and B
indicated that per-plot bole volume and tree volume are related to SAR
data, particularly at site A. The topographically corrected SAR data
appear to produce the same findings as those of uncorrected data.
I.E.

TYPE 1/4/67

Quest Accession Number : 90A49681

90A49681+ NASA IAA Journal Article Issue 22

Finding curvilinear features in speckled images

(AA)RAMADANI, RAMIN; (AB)VESECKY, JOHN F.

(AB)(Stanford University, CA)

Stanford Univ., CA. (S0380476)

MAC2W-419 (IEEE, Canadian Remote Sensing Society, URSI, et al.,
Quantitative remote sensing: An economic tool for the Nineties - 1989
International Symposium on Remote Sensing and Canadian Symposium on Remote
Sensing, 12th, (IGARSS'89), Vancouver, Canada, July 10-14, 1989) IEEE
Transactions on Geoscience and Remote Sensing (ISSN 0196-2892), vol. 28,
July 1990, p. 669-673. Research supported by the
Center for Aeronautics and Space Information Sciences and U.S. Navy.
900700 p. 5 refs 11 In: EN (English) p.3602A method for finding curves in digital images with speckle noise is
described. The solution method differs from standard linear convolutions
followed by thresholds in that it explicitly allows curvature in the
features. Maximum a posteriori (MAP) estimation is used, together with
statistical models for the speckle noise and for the curve-generation
process, to find the most probable estimate of the feature, given the
image data. The estimation process is first described in general terms.
Then, incorporation of the specific neighborhood system and a
multiplicative noise model for speckle allows derivation of the solution,
using dynamic programming, of the estimation problem. The detection of
curvilinear features is considered separately. The detection results allow
the determination of the minimal size of detectable feature. Finally, the
estimation of linear features, followed by a detection step, is shown for
computer-simulated images and for a SAR image of sea ice.
I.E.

TYPE 1/4/66

Quest Accession Number : 90A49694

90A49694 NASA IAA Journal Article Issue 22

Textural filtering for SAR image processing

(AA)WANG, Li; (AB)HE, DONG-CHEN; (AC)FABRI, ANDREA

(AB)(Sherbrooke, Université, Canada); (AC)International Institute for
Aerospace Survey and Earth Sciences, Enschede, Netherlands)(IEEE, Canadian Remote Sensing Society, URSI, et al., Quantitative
remote sensing: An economic tool for the Nineties - 1989 International
Symposium on Remote Sensing and Canadian Symposium on Remote
Sensing, 12th, (IGARSS'89), Vancouver, Canada, July 10-14, 1989) IEEE
Transactions on Geoscience and Remote Sensing (ISSN 0196-2892), vol. 28,
July 1990, p. 735-737. 900700 p. 3 refs 12 In: EN (English) p.3571Examples of the application of a new approach to the textural filtering
and enhancing of digital images are presented. Satisfactory results are
obtained in processing images from both natural textures and airborne SAR
scenes. Textural filtering of SAR images can be useful in improving the
discrimination between lithologic units with different surface-roughness
characteristics. One application example is discussed in which textural
features show different discrimination performances before and after
textural filtering.
I.E.

TYPE 1/4/68

Quest Accession Number : 90A49680

90A49680+ NASA IAA Journal Article Issue 22

Coastline detection and tracing in SAR images

(AA)LEE, JONG-SEN; (AB)JURKEVICH, IGOR

(AB)(U.S. Navy, Naval Research Laboratory, Washington, DC)

(IEEE, Canadian Remote Sensing Society, URSI, et al., Quantitative
remote sensing: An economic tool for the Nineties - 1989 International
Symposium on Remote Sensing and Canadian Symposium on Remote
Sensing, 12th, (IGARSS'89), Vancouver, Canada, July 10-14, 1989) IEEE
Transactions on Geoscience and Remote Sensing (ISSN 0196-2892), vol. 28,
July 1990, p. 662-668. 900700 p. 7 refs 12 In: EN (English) p.3570An algorithm for the global detection of coastlines based on a sequence
of basic image-processing procedures and a new edge-tracing algorithm is
described. The application of the proposed procedure to Seasat SAR and
Shuttle Imaging Radar B images demonstrates that with only a modest
computational burden it produces a good visual match between the detected
coastline and the coastline of the original image. Additionally, the
separation of land from water achieved by this algorithm permits clean
pseudocoloring of coastal area images.
I.E.

TYPE 1/4/69

Quest Accession Number : 90A49677

90A49677 NASA IAA Journal Article Issue 22
Interpolation and sampling in SAR images

(AA)GURCAN, SHAUM

(AA)Sheffield, University, England

(IEEE, Canadian Remote Sensing Society, URSI, et al., Quantitative remote sensing: An economic tool for the Nineties - 1989 International Geoscience and Remote Sensing Symposium and Canadian Symposium on Remote Sensing, 12th, (IGARSS'89), Vancouver, Canada, July 10-14, 1989) IEEE Transactions on Geoscience and Remote Sensing (ISSN 0196-2892), vol. 28, July 1990, p. 641-646. 900700 p. 6 refs 8 In: EN (English) p.3604

The implications of interpolation and resampling for the statistics of SAR images are analyzed. Interpolation of the complex data conserves the statistical distribution and all moments if a condition involving the autocorrelation functions of the SAR and the interpolating filter is met; in the ideal case (uncorrelated samples) this reduces to the requirement that the interpolating filter has unit energy. Interpolation of the intensity data does not conserve the distribution. Expressions for moments up to the fourth for an arbitrary interpolation scheme applied to correlated exponential data are derived, and conditions for conservation of these moments displayed. Any finite resampling or interpolation scheme (other than nearest neighbor) will change the autocorrelation functions of the complex and intensity data and may introduce nonstationarity. I.E.

TYPE 1/4/71

Quest Accession Number : 90A49673

90A49673 NASA IAA Journal Article Issue 22
Performance of a proposed spaceborne synthetic aperture radar with variable antenna height

(AA)TOMIVASU, KIVO

(AA)GE Valley Forge Space Center, Philadelphia, PA

(IEEE, Canadian Remote Sensing Society, URSI, et al., Quantitative remote sensing: An economic tool for the Nineties - 1989 International Geoscience and Remote Sensing Symposium and Canadian Symposium on Remote Sensing, 12th, (IGARSS'89), Vancouver, Canada, July 10-14, 1989) IEEE Transactions on Geoscience and Remote Sensing (ISSN 0196-2892), vol. 28, July 1990, p. 609-613. 900700 p. 5 refs 5 In: EN (English) p.3509

Broadside mapping with high area rates over a wide range of grazing angles is possible with a variable antenna area for a spaceborne SAR. The rectangular antenna length is fixed by the azimuth resolution, and the antenna area must exceed a minimum value to avoid ambiguous responses in both range and Doppler. The minimum antenna height is established by the ambiguity constraint for each mapping geometry, and then perhaps increased in height to meet an SAR power limit. With a variable-height antenna, mapping area rates up to 2142 sq km/s were computed for a 5.3-GHz SAR in an 800-km-altitude orbit. Hardware design issues are addressed, and an active-element phased array with discrete heights is suggested. I.E.

TYPE 1/4/70

Quest Accession Number : 90A49675

90A49675 NASA IAA Journal Article Issue 22
A new method of aircraft motion error extraction from radar raw data for real-time motion compensation

(AA)MOREIRA, JOAO R.

(AA)DLR, Institut fuer Hochfrequenztechnik, Oberpfaffenhofen, Federal Republic of Germany

(IEEE, Canadian Remote Sensing Society, URSI, et al., Quantitative remote sensing: An economic tool for the Nineties - 1989 International Geoscience and Remote Sensing Symposium and Canadian Symposium on Remote Sensing, 12th, (IGARSS'89), Vancouver, Canada, July 10-14, 1989) IEEE Transactions on Geoscience and Remote Sensing (ISSN 0196-2892), vol. 28, July 1990, p. 620-626. 900700 p. 7 refs 12 In: EN (English) p.3491

A method for real-time motion compensation is presented. The method extracts all the necessary motions of the aircraft from the radar backscatter signal using a new radar configuration and new methods for evaluating the azimuth spectra of the radar signal. Hence an inertial navigation system becomes unnecessary for many applications. The motion-compensation parameters for real-time motion error correction are the range delay, the range-dependent phase shift, and the pulse repetition frequency. The motions of the aircraft to be extracted are the displacement in line-of-sight direction, the aircraft's yaw and drift angle, and the forward velocity. Results show that a three-look image with an azimuth resolution of 3 m in L-band using a small aircraft is achievable, and the implementation of this method in real time using an array processor is feasible. I.E.

TYPE 1/4/72

Quest Accession Number : 90A45352

90A45352 NASA IAA Journal Article Issue 20
A state-of-the-art review in radar polarimetry and its applications in remote sensing

(AA)BOERNER, WOLFGANG-M.; (AB)YAMAGUCHI, YOSHIO

(AB)Illinois, University, Chicago

(1989 International Symposium on Noise and Clutter Rejection in Radars and Imaging Sensors, Kyoto, Japan, Nov. 14-16, 1989) IEEE Aerospace and Electronic Systems Magazine (ISSN 0885-8985), vol. 5, June 1990, p. 3-6. 900600 p. 4 refs 8 In: EN (English) p.3195

The authors assess the state of the art, focusing on their own contributions. Covered areas are the electromagnetic inverse problem in radar polarimetry, coherent polarization radar theory, partially coherent polarization radar theory, vector (polarization) inverse scattering approaches, the polarimetric matched filter approach, polarimetric Doppler radar applications in meteorology and oceanography, and image fidelity in microwave vector diffraction tomographic imaging. I.E.

TYPE 1/4/73

Quest Accession Number : 90A44319

90A44319 NASA IAA Journal Article Issue 20

The role of spaceborne synthetic aperture radar in global wave forecasting

(AA)BEAL, ROBERT C.

(AA)(Johns Hopkins University, Laurel, MD)

Johns Hopkins Univ., Laurel, MD. (JS767253)

1990, P. 54-62. Research supported by Johns Hopkins University, NOAA, ESA, NASA, and U.S. Navy. 900600 p. 9 refs 14 In: EN (English) p.3234

The importance of improved global directional wave forecasts is outlined, and the contingency of these forecasts upon improvements in global wind fields, model physics, and global directional wave measurements and related assimilation schemes is stressed. Information for global numerical models must come from satellite platforms and synthetic aperture radar (SAR) is the only radar technique potentially useful for remote ocean wave monitoring which has actually flown in space. The geometry and functions of a spaceborne SAR are discussed and research highlights of the past decade are reviewed. Future plans for global ocean spectral sampling to be conducted by the NASA SIR-C and subsequent experiments in the areas of ecology, geology, hydrology, oceanography, radar calibration, and electromagnetic scattering theory are outlined. The development of an experimental on-board SAR processor to produce nearly continuous real-time ocean wave spectra from the C-band channel is described.

L.R.S.

TYPE 1/4/75

Quest Accession Number : 90A41054

90A41054 NASA IAA Conference Paper Issue 18

Improved filters for moving target indication with synthetic aperture radar

(AA)MEDLIN, GREGORY W.; (AB)ADAMS, JOHN W.

(AA)(South Carolina, University, Columbia); (AB)(Hughes Aircraft Co.,

Radar Systems Group, Los Angeles, CA)

IN: International Conference on Radar 89, Paris, France, Apr. 24-28, 1989, Proceedings. Volume 2 (A90-40951 18-32). Boulogne-Billancourt, France, RADAR 89, 1989, p. 392-397. 890000 p. 6 refs 6 In: EN (English) p.2882

A digital filter design technique is proposed for the pre-filter moving target indication (MTI) method for synthetic aperture radar (SAR) systems. The filters have exactly linear phase and are based on a multiple stopband design where the integrated aliasing error is minimized and the filter passband is maximally flat. The proposed filters show significant improvement in clutter cancellation and overlap between MTI bands when compared to previous designs. A design example is included which demonstrates the effectiveness of the technique.

Author

TYPE 1/4/74

Quest Accession Number : 90A41671

90A41671 NASA IAA Journal Article Issue 18

Synthetic aperture radar calibration using reference reflectors

(AA)GRAY, A. LAURENCE; (AB)VACHON, PARIS W.; (AC)LIVINGSTONE, CHARLES E.

(AD)LUKOWSKI, TOM I.

(AD)(Canada Centre for Remote Sensing, Ottawa)

IEEE Transactions on Geoscience and Remote Sensing (ISSN 0196-2892), vol. 28, May 1990, p. 374-383. 900500 p. 10 refs 23 In: EN (English) p.2879

A simple expression for the terrain backscatter coefficient is derived in terms of the integrated power of an adjacent known radar reflector in an SAR image. It is shown that this SAR image-calibration technique is independent of the radar system focus or partial coherence and thereby possesses an important advantage over the usual technique, which relies on an estimate of the peak of the reflector impulse response. Results from airborne SAR overflights of corner reflectors and active radar calibrators are used to demonstrate the validity and consistency of the method and to show that the method is robust under defocus caused by an incorrect FM rate or inadequate motion compensation of data collected during turbulence. It is also shown that the fading errors associated with the integral method are comparable to or slightly worse than those associated with the peak estimation method. However, this small disadvantage is outweighed by the fact that the integral method is independent of actual resolution.

I.E.

TYPE 1/4/76

Quest Accession Number : 90A41044

90A41044 NASA IAA Conference Paper Issue 18

Autofocusing synthetic aperture radar images

(AA)PRATI, CLAUDIO

(AA)(Milano, Politecnico, Milan, Italy)

IN: International Conference on Radar 89, Paris, France, Apr. 24-28, 1989, Proceedings. Volume 2 (A90-40951 18-32). Boulogne-Billancourt, France, RADAR 89, 1989, p. 314-319. Research supported by the Stanford Exploration Project. 890000 p. 6 refs 8 In: EN (English) p.2875

The correct focusing of synthetic aperture radar (SAR) relies on knowing precisely the geometric and transmission parameters of the system. Transmission parameters are usually defined specifically, while the geometrical parameters can be derived from the satellite data. The only two geometric parameters involved in the focusing process are the sensor-target relative velocity and the sensor-target nearest approach distance. A technique to extract these two geometrical parameters from the data themselves (autofocusing), in order to achieve the best possible focusing of SAR images, is discussed.

R.E.P.

TYPE 1/4/77

Quest Accession Number : 90A41043

90A41043 NASA IAA Conference Paper Issue 18

Processing of spaceborne and airborne SAR data - An experimental activity

(AA)VINELLI, F.; (AB)MORABITO, C.; (AC)TOMA, M. R.; (AD)D'ADDIO, E.; (AE)FARINA, ALFONSO

(AF)(Selenia S.p.A., Rome, Italy)

IN: International Conference on Radar 89, Paris, France, Apr. 24-28, 1989, Proceedings. Volume 2 (A90-40951 18-32). Boulogne-Billancourt, France, RADAR 89, 1989, p. 301-308. 890000 p. 8 refs 11 In: EN (English) p.2875

A test-bed for processing recorded and simulated SAR data is studied. The SAR processor, which synthesizes images from spaceborne and airborne SAR sensors, is based on the range-Doppler algorithm. The process used to simulate SAR data is described. The SAR processor is evaluated using recorded and simulated data. The automation feature extraction algorithms based on the Hough transform technique are examined. I.F.

TYPE 1/4/79

Quest Accession Number : 90A41000

90A41000 NASA IAA Conference Paper Issue 18

Parallel DFT algorithms for radar signal processing

(AA)SORAGHAM, JOHN J.; (AB)GREEN, RICHARD C.

(AC)Strathclyde, University, Glasgow, Scotland;

(AD)Technology, Reading, England

IN: International Conference on Radar 89, Paris, France, Apr. 24-28, 1989, Proceedings. Volume 1 (A90-40951 18-32). Boulogne-Billancourt, France, RADAR 89, 1989, p. 323-327. 890000 p. 5 refs 7 In: EN (English) p.2925

DFT implementation on a distributed array of processors is studied. A mapping strategy is presented and its complexity analyzed. Synthetic Aperture Radar (SAR) azimuth compression is chosen as a radar problem that demands significant computational capabilities. It is shown that the AMT DAP-510 not only matches this computational requirement but also that it efficiently copes with the range migration associated with SAR. Example processing times are given for simulated SEASAT and ERS-1 SAR data. Author

TYPE 1/4/78

Quest Accession Number : 90A41042

90A41042 NASA IAA Conference Paper Issue 18

3D synthetic aperture radar surveys

(AA)PRATI, CLAUDIO

(AB)(Milano, Politecnico, Milan, Italy)

IN: International Conference on Radar 89, Paris, France, Apr. 24-28, 1989, Proceedings. Volume 2 (A90-40951 18-32). Boulogne-Billancourt, France, RADAR 89, 1989, p. 295-300. Research supported by the Stanford Exploration Project. 890000 p. 6 refs 5 In: EN (English) p.2875

It is shown that by utilizing multiple passes of a SAR system, terrain elevation can be measured. For greater altimetric resolution, the satellite's displacement in the cross-track direction is adapted to the slope of the terrain. A coarse altimetric map of the Panamint Valley area in Eastern California is constructed by utilizing three repeated passes of the Seasat SAR satellite. The technique avoids the foreshortening effect which is clearly visible on hilly areas. The interference fringe images presented show an acceptably high signal-to-noise ratio. It is pointed out that the same analysis may be applied to tethered-satellite SAR systems, thereby avoiding the effects of the changing of the observed areas with respect to time. S.A.V.

TYPE 1/4/80

Quest Accession Number : 90A39952

90A39952 NASA IAA Conference Paper Issue 17

Target cluster detection in cluttered synthetic aperture radar imagery

(AA)LANDOWSKI, JAMES G.; (AB)LOE, RICHARD S.

(AB)(Lockheed Research and Development Laboratories, Palo Alto, CA)

IN: Advances in image compression and automatic target recognition; Proceedings of the Meeting, Orlando, FL, Mar. 30, 31, 1989 (A90-39951 17-63). Bellingham, WA, Society of Photo-Optical Instrumentation Engineers, 1989, p. 9-16. 890000 p. 8 refs 9 In: EN (English) p.2766

A technique for detecting clusters of objects in noisy, cluttered, moderate resolution imagery is discussed. The algorithm is demonstrated on synthetic aperture radar (SAR) data. The approach is based on the use of a nonlinear spatial highpass or 'antimedian' filter, the complement of the median filter. The filter is coarsely tuned to produce maximum response for structures the size of or smaller than the expected object size. The filter is followed by histogram thresholding and connected region processing. Knowledge about the object's shape and the cluster deployment patterns is then used to eliminate false detections. This detection technique is suitable for any imagery where the objects of interest produce sensor responses that form contiguous regions. False clusters due to edge leakage are discussed and a solution formulated. Author

TYPE 1/4/81

Quest Accession Number : 90A38345

90A38345 NASA IAA Journal Article Issue 16

The slightly-rough facet model in radar imaging of the ocean surface

(AA)WEST, JAMES C.; (AB)MOORE, RICHARD K.; (AC)HOLTZMAN, JULIAN C.

(AC)University of Kansas Center for Research, Inc., Lawrence)

N00014-79-C-0533 International Journal of Remote Sensing (ISSN

0143-1161), vol. 11, April 1990, p. 617-637. 900400 p. 21 refs 49 In:

EN (English) p.2591

The slightly-rough facet model of the ocean surface, an extension of the two-scale radar scattering model, is well suited for investigating SAR imaging of the surface. Several statistical properties of the facets that are important in an imaging model are derived. The two-scale scattering model is extended to include both first-order and second-order large-scale effects (tilt and curvature) using physical optics, showing that a spectrum of small-scale ripples, rather than a single ripple given by the Bragg resonance condition, contributes to the backscatter from a facet. The bandwidth of the resonant ripple spectrum depends on the radar wavelength, large-scale curvature and illumination widths. The resonant ripple spectra of adjacent facets overlap, so the backscatter from adjacent facets is correlated. The backscatter from individual facets temporally decorrelates due to dispersion of the ripples in the resonant spectrum. Depending on the conditions, the decorrelation time may be on the order of the integration times of SAR processors.

Author

TYPE 1/4/82

Quest Accession Number : 90A38343

90A38343* NASA IAA Journal Article Issue 16

Global digital topography mapping with a synthetic aperture scanning radar altimeter

(AA)ELACHI, C.; (AB)IM, K. E.; (AC)RODRIGUEZ, E.

(AC)JPL, Pasadena, CA)

Jet Propulsion Lab., California Inst. of Tech., Pasadena. (JJ574450)

International Journal of Remote Sensing (ISSN 0143-1161), vol. 11, April

1990, p. 585-601. 900400 p. 17 refs 11 In: EN (English) p.2580

Global digital topography data of the land surface is of importance in a variety of geoscientific and application disciplines. Such a database, with a spatial resolution of 150 to 500 m and height accuracy of 5 m or better can be acquired from an orbiting platform using a synthetic aperture scanning radar altimeter. Near-global coverage can be achieved within 14 days from an orbiting platform in a polar or near-polar orbit.

Author

TYPE 1/4/83

Quest Accession Number : 90A37750

90A37750 NASA IAA Journal Article Issue 16

Motion compensation of airborne synthetic aperture radars using

autofocus

(AA)BLACKWELL, D.; (AB)QUEGAN, S.

(AA)(General Electric Company, PLC, Marconi Research Centre, Chelmsford,

England); (AB)(Sheffield, University, England)

GEC Journal of Research (ISSN 0264-9187), vol. 7, no. 3, 1990, p.

168-182. Research supported by the Ministry of Defence Procurement

Executive. 900000 p. 15 refs 18 In: EN (English) p.2530

Conventional motion compensation schemes correct for unwanted SAR platform motions using information from an inertial measurement unit (IMU). Autofocus techniques, which focus SAR images, produce an 'autofocus parameter' which is related to the platform motion. In this paper, strong evidence is presented to support the assumption that the contrast optimization autofocus algorithm behaves as a least-squares quadratic fitting to the SAR platform trajectory. Using this assumption, the relationship between the autofocus parameter and across-track accelerations of the SAR platform is derived. This allows the SAR platform motion to be estimated from the autofocus parameter measurements and incorporated in a motion compensation scheme, instead of IMU measurements. Three implementations of motion compensation using autofocus are compared, and the achievable image quality is quantified.

Author

TYPE 1/4/84

Quest Accession Number : 90A34922

90A34922# NASA IAA Journal Article Issue 14

Radio and optical remote sensing: Satellite and ground observations. II

- SIR-C/X-SAR experimental plan

(AA)FUJITA, MASA HARU; (AB)MASUKO, HARUNOBU; (AC)OKAMOTO, KEN'ICHI;

(AD)URATSUKA, SEIHO

Communications Research Laboratory, Review (ISSN 0914-9279), vol. 35,

Dec. 1989, p. 515-521. In Japanese, with abstract in English. 891200 p.

7 refs 14 In: JA (Japanese) p.2141

In June 1986, NASA/DFVLR/PGN issued an announcement of opportunity for using the SIR-C/X-SAR, which will be launched in early 1992 on the Space Shuttle. In response, two experimental proposals were submitted and were accepted in 1988. The titles of the proposals are 'Like- and cross-polarization calibration, topographic mapping and rice field experiments by SIR-C/X-SAR' and 'Remote sensing of sea pollution and sea ice by SIR-C/X-SAR'. This paper gives a brief explanation of both of the experiments together with an outline of the SIR-C/X-SAR hardware.

Author

TYPE 1/4/85

Quest Accession Number : 90A34147
90A34147 NASA IAA Conference Paper Issue 14
Synthetic aperture radar - A Kelvin wake image artifact
(AA)HARGER, ROBERT O.

(AA)(Maryland, University, College Park)
IN: Millimeter wave and synthetic aperture radar; Proceedings of the Meeting, Orlando, FL, Mar. 27, 28, 1989 (A90-34126 14-32). Bellingham, WA, Society of Photo-Optical Instrumentation Engineers, 1989, p. 225-234. Research supported by the Environmental Research Institute of Michigan. 890000 p. 10 refs 10 In: EN (English) p.2212

A possible physical basis is presented for some of the narrow-vee artifacts occurring in SAR images of ship wakes. It is suggested that this pattern will emerge when the ship and SAR platform directions are nearly parallel; when these directions are less well aligned, one arm of the narrow-vee pattern artifact will be missing. Then, when the directions have become sufficiently misaligned, no image artifact will be visible. Other curious artifacts in SAR images, such as parallel lines, have been observed in SAR images but appear to require a different physical mechanism.
O.C.

TYPE 1/4/87

Quest Accession Number : 90A33035

90A33035 NASA IAA Journal Article Issue 13
Wind and ocean swell measurements from space using microwaves
Wind- und Seegangsmessungen mit Mikrowellen vom Weltraum aus
(AA)ALPERS, WERNER
(AA)(Bremen, Universitaet, Federal Republic of Germany)
(Deutsche Meteorologen-Tagung ueber Atmosphaere, Ozeane, Kontinente, Kiel, Federal Republic of Germany, May 16-19, 1989) Annalen der Meteorologie (ISSN 0072-4122), no. 26, 1989, p. 63-66. In German. 890000 p. 4 refs 8 In: GM (German) p.2058

Satellite-based measurements of wind and ocean swell using active microwaves are reported. The scatterometer and the SAR used to make the measurements are described. Normalized radar cross sections are shown as a function of wind direction for various wind velocities.
C.D.

TYPE 1/4/86

Quest Accession Number : 90A34145
90A34145* NASA IAA Conference Paper Issue 14
The Earth Observing System (EOS) SAR ground data system
(AA)CURLANDER, JOHN C.

(AA)(JPL, Pasadena, CA)
Jet Propulsion Lab., California Inst. of Tech., Pasadena. (JJ574450)
IN: Millimeter wave and synthetic aperture radar; Proceedings of the Meeting, Orlando, FL, Mar. 27, 28, 1989 (A90-34126 14-32). Bellingham, WA, Society of Photo-Optical Instrumentation Engineers, 1989, p. 210-220. 890000 p. 11 refs 7 In: EN (English) p.2143

NASA, in association with ESA and NASDA, will launch the Space Station Freedom in 1993. As a complement to the Space Station, several unmanned Polar-Orbit Platforms (POPs) will be developed, built and launched with suites of instruments devoted to remote-sensing for earth surface and atmosphere observations or to planetary and deep-space studies. Attention is presently given to the POPs-associated Earth Observing System SAR Ground Data System, which encompasses a SAR processor, a postprocessing subsystem, a geophysical processor, and a data management and control O.C.

TYPE 1/4/88

Quest Accession Number : 90A31297

90A31297# NASA IAA Journal Article Issue 12
Theoretical studies for ERS-1 wave mode
(AA)CORDEY, R. A.; (AB)MACKLIN, J. T.; (AC)GUIGNARD, J.-P.; (AD)ORIOL-PIBERNAT, E.
(AB)(GEC-Marconi Research Centre, Chelmsford, England); (AC)(ESTEC, Noordwijk, Netherlands); (AD)(ESA, European Space Research Institute, Frascati, Italy)
ESA Journal (ISSN 0379-2285), vol. 13, no. 4, 1989, p. 343-362. Research supported by ESA. 890000 p. 20 refs 30 In: EN (English) p.1886

The theory of how the sea surface is imaged by synthetic-aperture radar (SAR) and inverse methods for recovering quantitative information about ocean waves are considered, with emphasis on the operation of the wave mode of ERS-1. The two-scale representation of radar backscattering from the sea surface and its limitations are discussed. The description of the sea surface is reviewed, covering short-wave spectra, wave/wave interactions (hydrodynamic modulations), and breaking waves. Linear and nonlinear descriptions of ocean-wave imaging are examined. A new inverse method using complex imagery is developed and is shown to offer improved prediction of the speckle component in SAR-image power spectra. Azimuthal smearing from random wave motions imposes a fundamental limitation on the recovery of wave information under nonlinear imaging conditions. Recommendations for ERS-1 wave mode, including the requirements for validating the imaging theory, are discussed.
Author

TYPE 1/4/89

Quest Accession Number : 90A30653

90A30653* NASA IAA Journal Article Issue 12

Phase calibration of imaging radar polarimeter Stokes matrices

(AA)ZEBKER, HOWARD A.; (AB)LOU, YUNLING

(AB)(JPL, Pasadena, CA)

Jet Propulsion Lab., California Inst. of Tech., Pasadena. (JJ574450)

IEEE Transactions on Geoscience and Remote Sensing (ISSN 0196-2892),

vol. 28, March 1990, p. 246-252. 900300 p. 7 refs 11 In: EN (English)

p. 1829

It is shown that the Stokes matrices measured by an imaging radar polarimeter provide enough information for the accurate phase calibration of the observed polarimetric characteristics of a surface. This is important because it allows the data to be reduced in volume in an operational synthetic aperture radar correlator with no prior knowledge of the conditions at the surface, and the end user can later select the particular region where he or she is comfortable with making an assumption regarding the relative phases of the hh and vv signals. No ground calibration equipment is necessary, as all important parameters are derived from the data themselves.

I.E.

TYPE 1/4/91

Quest Accession Number : 90A30503

90A30503* NASA IAA Journal Article Issue 12

An automated system for mosaicking spaceborne SAR imagery

(AA)KROK, RONALD; (AB)CURLANDER, JOHN C.; (AC)PANG, SHIRLEY S.

(AC)(JPL, Pasadena, CA)

Jet Propulsion Lab., California Inst. of Tech., Pasadena. (JJ574450)

International Journal of Remote Sensing (ISSN 0143-1161), vol. 11, Feb.

1990, p. 209-223. 900200 p. 15 refs 9 In: EN (English) p. 1827

An automated system has been developed for mosaicking spaceborne synthetic aperture radar (SAR) imagery. The system is capable of producing multiframe mosaics for large-scale mapping by combining images in both the along-track direction and adjacent cross-track swaths from ascending and descending passes. The system requires no operator interaction and is capable of achieving high registration accuracy. The output product is a geocoded mosaic on a standard map grid such as UTM or polar stereographic. The procedure described in detail in this paper consists essentially of remapping the individual image frames into these standard grids, frame-to-frame image registration and radiometric smoothing of the seams. These procedures are directly applicable to both the Magellan Venus Mapper and a scanning SAR design such as Radarsat, Eos SAR in addition to merging image frames from traditional SAR systems such as Seasat and SIR-B. With minor modifications, it may also be applied to spaceborne optical sensor data to generate large-scale mosaics efficiently and with a high degree of accuracy. The system has been tested with Seasat, SIR-B and Landsat TM data. Examples presented in this paper include a 38-frame mosaic of the Yukon River basin in central Alaska, a 33-frame mosaic of southern California and a three-frame terrain-corrected geocoded mosaic of the Wind River basin in Wyoming.

Author

TYPE 1/4/90

Quest Accession Number : 90A30648

90A30648 NASA IAA Journal Article Issue 12

SAR image statistics related to atmospheric drag over sea ice

(AA)BURNS, BARBARA A.

(AA)(Alfred-Wegener-Institut fuer Polar- und Meeresforschung,

Bremerhaven, Federal Republic of Germany)

N00014-81-C-0295; N00014-83-C-0404 IEEE Transactions on Geoscience and

Remote Sensing (ISSN 0196-2892), vol. 28, March 1990, p. 158-165. 900300

p. 8 refs 31 In: EN (English) p. 1884

The possibility of using SAR data to distinguish sea-ice regions with different atmospheric drag is explored. Both the amplitude of the radar return and statistics derived from SAR image data are examined. Roughness statistics data from several pack-ice areas are used in a backscatter model to predict the return from surfaces with measured drag coefficients. The results suggest that the scattering coefficient for typical radar wavelengths is insensitive to the roughness elements responsible for the observed drag coefficient variations over pack ice free of major ridges. For marginal ice zones, where ice concentration and floe deformation contribute to atmospheric drag, a simple model for the atmospheric boundary layer is used to provide qualitative relationships between drag coefficient and regional ice properties (ice concentration, floe size distribution, floe edge density) derivable from SAR data. Simple algorithms to produce maps of ice concentration and edge density are outlined and applied to 23.5-cm SAR digital image data.

I.E.

TYPE 1/4/92

Quest Accession Number : 90A26668

90A26668* NASA IAA Journal Article Issue 10

An ice-motion tracking system at the Alaska SAR facility

(AA)KROK, RONALD; (AB)CURLANDER, JOHN C.; (AC)PANG, SHIRLEY S.

(AD)MCCONNELL, ROSS

(AC)(JPL, Pasadena, CA); (AD)(Vexcel Corp., Boulder, CO)

Jet Propulsion Lab., California Inst. of Tech., Pasadena. (JJ574450)

IEEE Journal of Oceanic Engineering (ISSN 0364-9059), vol. 15, Jan.

1990, p. 44-54. 900100 p. 11 refs 18 In: EN (English) p. 0

An operational system for extracting ice-motion information from synthetic aperture radar (SAR) imagery is being developed as part of the Alaska SAR Facility. This geophysical processing system (GPS) will derive ice-motion information by automated analysis of image sequences acquired by radars on the European ERS-1, Japanese ERS-1, and Canadian RADARSAT remote sensing satellites. The algorithm consists of a novel combination of feature-based and area-based techniques for the tracking of ice floes that undergo translation and rotation between imaging passes. The system performs automatic selection of the image pairs for input to the matching routines using an ice-motion estimator. It is designed to have a daily throughput of ten image pairs. A description is given of the GPS system, including an overview of the ice-motion-tracking algorithm, the system architecture, and the ice-motion products that will be available for distribution to geophysical data users.

I.E.

TYPE 1/4/93

Quest Accession Number : 90N25096

90N25096# NASA STAR Technical Report Issue 19

Concepts for high resolution space based SAR/ISAR systems

(AA)BOESSWETTER, CLAUD; (AB)WOLFRAMM, ARIBERT PAUL; (AC)PIKE, TIMOTHY

KEVIN; (AD)HERMER, JEAN MICHEL

(AD)(Thomson-CSF, Montrouge, France)

Messerschmitt-Boelkow-Blohm G.m.b.H.,

MT620643) Unternehmensegruppe Raumfahrt.

MBB-UK-0057/89-PUB In its Research and Development: Technical and

Scientific Publications 1989 p 261-270 (SEE N90-25075 19-01) 890000 p.

10 Presented at AGARD Avionics Panel Symposium on High Resolution Air and

Spaceborne Radar, The Hague, Netherlands, 8-12 May 1989 In: EN (English)

Avail: NTIS HC A15/MF A02 p.2652

Different beam pointing techniques, such as monobeam, multibeam in azimuth/elevation are addressed for strip mapping SAR modes as well as for MTI/ISAR modes. Basic requirements for selection of orbits are also discussed. The MTI/ISAR modes is intended to detect and classify from space clusters of fast moving small targets against the clutter background of the earth surface. High along-track resolution is achieved by using an antenna as short as possible in the along-track direction, collecting a large number of return echoes and processing these, according to the regular SAR principle. But the antenna technology and the realtime processing technology necessary to handle the large amount of data generated by multimode resolution systems create difficulties.

TYPE 1/4/95

Quest Accession Number : 90N24257

90N24257# NASA STAR Technical Report Issue 18

Synthetic aperture radar imagery of airports and surrounding areas:

Denver Stapleton International Airport / Final Report, 31 Aug. 1987 - 30

Nov. 1989

(AA)ONSTOTT, ROBERT G.; (AB)GINERIS, DENISE J.

Environmental Research Inst. of Michigan, Ann Arbor. (E0356283)

NASA-CR-4305; NAS 1.26:4305; DOT/FAA/DS-89/16 NAS1-18465 505-67-41-57

Washington 900700 p. 385 In: EN (English) Avail: NTIS HC A17/MF A02

P.2495

This is the third in a series of three reports which address the statistical description of ground clutter at an airport and in the surrounding area. These data are being utilized in a program to detect microbursts. Synthetic aperture radar (SAR) data were collected at the Denver Stapleton Airport using a set of parameters which closely match those which are anticipated to be utilized by an aircraft on approach to an airport. These data and the results of the clutter study are described. Scenes of 13 x 10 km were imaged at 9.38 GHz and HH-, VV-, and HV-polarizations, and contain airport grounds and facilities (up to 14 percent), cultural areas (more than 50 percent), and rural areas (up to 6 percent). Incidence angles range from 40 to 84 deg. At the largest depression angles the distributed targets, such as forest, fields, water, and residential, rarely had mean scattering coefficients greater than -10 dB. From 30 to 80 percent of an image had scattering coefficients less than -20 dB. About 1 to 10 percent of the scattering coefficients exceeded 0 dB, and from 0 to 1 percent above 10 dB. In examining the average backscatter coefficients at large angles, the clutter types cluster according to the following groups: (1) terminals (-3 dB), (2) city and industrial (-7 dB), (3) warehouse (-10 dB), (4) urban and residential (-14 dB), and (5) grass (-24 dB).

Author

TYPE 1/4/94

Quest Accession Number : 90N24489

90N24489# NASA STAR Conference Paper Issue 18

Analysis and test interaction in the development of a hold down and release mechanism

(AA)LUHMANN, H.-J.; (AB)ETZLER, C.-CH.

Dornier System G.m.b.H., Friedrichshafen (Germany, F.R.). (D0272085)

In ESA, Fourth European Space Mechanisms and Tribology Symposium p

181-186 (SEE N90-24462 18-31) 900300 p. 6 In: EN (English) Avail: NTIS

HC A14/MF A02 p.2539

The features of the hold-down and release mechanism used to hold the folded synthetic aperture radar antenna onboard the ESA Remote Sensing Satellite (ERS-1) during launch are described. Six hinged clamps are released in orbit via a system of springs and cables connected to a pyrotechnical device. Improvements in the mechanism introduced during the early design stage on the basis of analytical investigations and component tests are highlighted. Special emphasis is given to the interaction between analysis and test results. Results from subsystem tests are considered.

ESA

TYPE 1/4/96

Quest Accession Number : 90A24232

90A24232 NASA IAA Book/Monograph Issue 09

Synthetic aperture radar stations with digital processing (Russian book

) Radiolokatsionnye stantsii s tsifrovym sintezirovaniem apertury anteny

(AA)ANTIPOV, VLADIMIR N.; (AB)GORIAINOV, VLADIMIR T.; (AC)KULIN,

ANATOLII N.; (AD)MANSUROV, VLADIMIR V.; (AE)OKHONSKII, ALEKSANDR G.

Moscow, Izdatel'stvo Radio i Sviaz', 1988, 304 p. In Russian. 880000

p. 304 refs 77 In: RU (Russian) p.1297

The principles underlying SAR with digital processing are examined.

Particular attention is given to structural and logical schemes of basic

radar systems, aspects of moving target indication, the digital simulation

of radar operation, and trajectory-signal simulation. It is noted that

digital signal processing makes possible the optimal unification of SAR

units, the automated design and development of SAR systems, and a

reduction in SAR weight and size.

B.J.

TYPE 1/4/97

Quest Accession Number : 90A23504

90A23504* NASA IAA Journal Article Issue 08

A signal processing view of strip-mapping synthetic aperture radar

(AA)MURSON, DAVID C., JR.; (AB)VISENTIN, ROBERT L.

(AB)(Illinois, University, Urbana)

Illinois Univ., Urbana. (1B647432)

DAL03-86-R-0111; JPL-957927; N00014-84-C-0149 IEEE Transactions on

Acoustics, Speech, and Signal Processing (ISSN 0096-3518), vol. 37, Dec.

1989, p. 2131-2147. 891200 p. 17 refs 49 In: EN (English) p.1136

The authors derive the fundamental strip-mapping SAR (synthetic aperture radar) imaging equations from first principles. They show that the resolution mechanism relies on the geometry of the imaging situation rather than on the Doppler effect. Both the airborne and spaceborne cases are considered. Range processing is discussed by presenting an analysis of pulse compression and formulating a mathematical model of the radar return signal. This formulation is used to obtain the airborne SAR model. The authors study the resolution mechanism and derive the signal processing relations needed to produce a high-resolution image. They introduce spotlight-mode SAR and briefly indicate how polar-format spotlight processing can be used in strip-mapping SAR. They discuss a number of current and future research directions in SAR imaging.

I.E.

TYPE 1/4/98

Quest Accession Number : 90A23347

90A23347* NASA IAA Journal Article Issue 08

Opening and closing of sea ice leads - Digital measurements from synthetic aperture radar

(AA)FILI, M.; (AB)ROTHROCK, D. A.

(AA)(Grenoble, Universite, Saint-Martin-d'Herès, France); (AB)(Washington, University, Seattle)

Grenoble-1 Univ., Saint Martin d'Herès (France). (G5963195)

MAGW-412 Journal of Geophysical Research (ISSN 0148-0227), vol. 95,

Jan. 15, 1990, p. 789-796. Research supported by the U.S. Navy and ESA.

900115 p. 8 refs 16 In: EN (English) p.1191

An algorithm that uses two sequential SAR digital images to measure the opening and closing of sea ice leads is introduced. The methods used to analyze the SAR images is described, including the mesh of tie points and the classification of leads and ice. The results of the analysis are compared with independent manual measurements, showing that the cells covering each lead are best interpreted as opening or closing in a group, rather than individually. Also, consideration is given to an automated algorithm for grouping cells, the possibility of simplifying the method, and the relationship between the opening and closing measurements and the theory of their parametric relation to mean deformation.

R.B.

TYPE 1/4/99

Quest Accession Number : 90N22826

90N22826# NASA STAR Technical Report Issue 16

Spaceborne radar observations: A guide for Magellan radar-image analysis
(AA)FORD, J. P.; (AB)BLOM, R. G.; (AC)CRISP, J. A.; (AD)ELACHI, CHARLES;
(AE)PARR, T. G.; (AF)SAUNDERS, R. STEPHEN; (AG)THEILIG, E. E.; (AH)WALL,
S. D.; (AI)YEMELL, S. B.

Jet Propulsion Lab., California Inst. of Tech., Pasadena. (J3574450)

NASA-CR-184998; JPL-PUBL-89-41; NAS 1:26:184998 NAS7-918

844-20-00-30-02 891200 P. 132 Original contains color illustrations

In: EN (English) Avail: NTIS HC A07/MF A01; 25 functional color pages

p.2249

Geologic analyses of spaceborne radar images of Earth are reviewed and summarized with respect to detecting, mapping, and interpreting impact craters, volcanic landforms, eolian and subsurface features, and tectonic landforms. Interpretations are illustrated mostly with Seasat synthetic aperture radar and shuttle-imaging-radar images. Analogies are drawn for the potential interpretation of radar images of Venus, with emphasis on the effects of variation in Magellan look angle with Venutian latitude. In each landform category, differences in feature perception and interpretive capability are related to variations in imaging geometry, spatial resolution, and wavelength of the imaging radar systems. Impact craters and other radially symmetrical features may show apparent bilateral symmetry parallel to the illumination vector at low look angles. The styles of eruption and the emplacement of major and minor volcanic constructs can be interpreted from morphological features observed in images. Radar responses that are governed by small-scale surface roughness may serve to distinguish flow types, but do not provide unambiguous information. Imaging of sand dunes is rigorously constrained by specific angular relations between the illumination vector and the orientation and angle of repose of the dune faces, but is independent of radar wavelength. With a single look angle, conditions that enable shallow subsurface imaging to occur do not provide the information necessary to determine whether the radar has recorded surface or subsurface features. The topographic linearity of many tectonic landforms is enhanced on images at regional and local scales, but the detection of structural detail is a strong function of illumination direction. Montopographic tectonic lineaments may appear in response to contrasts in small-surface roughness or dielectric constant. The breakpoint for rough surfaces will vary by about 25 percent through the Magellan viewing geometries from low to high Venutian latitudes. Examples of anomalies and system artifacts that can affect image interpretation are described.

Author

TYPE 1/4/100

Quest Accession Number : 90A21604

90A21604# NASA IAA Journal Article Issue 07

High-performance SAR processors for mission planning and control
(AA)SCHOTTER, ROLAND; (AB)FRITSCH, BRUNO

Dornier Post (ISSN 0012-5563), no. 3, 1989, p. 13-15. 890000 p. 3 In:
EN (English) p.925

Pipeline-architecture image processors have been devised for real-time SAR operation whose operational modules perform FFT, correlation, complex arithmetic, lowpass/bandpass filtering, and two-dimensional memory functions. All modules have been implemented in power-saving MOS technology to facilitate the use of real-time SAR processors in such limited power dissipation conditions as those of mobile ground stations. Attention is given to the ERS-1 'Quicklook' processor for a mobile Antarctic ground station; the Do-SAR experimental airborne SAR system, and the FLEX-SAR processor that is being implemented for the Do-SAR program. O.C.

TYPE 1/4/101

Quest Accession Number : 90N21246

90N21246# NASA STAR Conference Paper Issue 14

SAR image coding

CODAGE D'IMAGES SAR

(AA)TOURTIER, P.

Thomson-CSF, Paris (France). (TV609526)

In AGARD, High Resolution Air- and Spaceborne Radar 6 p (SEE N90-21223 14-32) 891000 p. 6 In: FR (French) Avail: NTIS HC A10/MF A02; Non-NATO Nationals requests available only from AGARD/Scientific Publications Executive p.1964

The Synthetic Aperture Radar imagery causes a very large flow rate, to the extent that the data flow is at a record level. The image coding technique reduces the flow rate so that the original quality is preserved. This permits the reduction of the transmission channel capacity and improves the flow rate. A different technique is presented for data flow compression. The technique performs best at low cosine transform and is described in detail. The results obtained by Thomson-CSF show that a compression rate of the magnitude of 4 or 5 is possible without visible image degradation.

Transl. by E.R.

TYPE 1/4/102

Quest Accession Number : 90N21245

90N21245# NASA STAR Conference Paper Issue 14

Image simulation of geometric targets for synthetic aperture radar

SIMULATION D'IMAGES DE CIBLES GEOMETRIQUES POUR RADAR A OUVERTURE

SYNTHETIQUE

(AA)NASR, J. M.

Aerospatiale, Les Mureaux (France). (AG943352) Dept. Mesures.

In AGARD, High Resolution Air- and Spaceborne Radar 7 p (SEE N90-21223

14-32) 891000 p. 7 In: FR (French) Avail: NTIS HC A10/MF A02; Non-NATO

Nationals requests available only from AGARD/Scientific Publications

Executive p.1964

A new technique for image simulation which comes from a synthetic aperture radar is presented. The method is based on the embedding of an artificially simulated target in a real radar image captured by an operational antenna window on a satellite (SEASAT or SIR-B). A 1 and C band was used for the capture. The target dimensions studied were large enough for use with long waves provided the calculation techniques used with high frequencies were for an equivalent area radar (SER). The calculation of SER allows the capture of a raw signal received from the antennas. So that the possibility of simulation is low, some restrictions are made. The results are sufficiently interesting enough to let the study of the behavior of a particular target become of use to civilians or the military, in the functional bounds of radar waves.

Transl. by E.R.

TYPE 1/4/104

Quest Accession Number : 90N21242

90N21242# NASA STAR Conference Paper Issue 14

Radar target image by ISAR case study

(AA)WARTINI, S.; (AB)PARDINI, S.; (AC)PRODI, F.

Selenia S.p.A., Rome (Italy). (SF408204) Dept. of Radar.

In AGARD, High Resolution Air- and Spaceborne Radar 14 p (SEE N90-21223

14-32) 891000 p. 14 In: EN (English) Avail: NTIS HC A10/MF A02;

Non-NATO Nationals requests available only from AGARD/Scientific

Publications Executive p.1963

Target imaging based on Inverse Synthetic Aperture Radar techniques are described. Theoretical and experimental results are presented. Theoretical topics illustrate the set of processing functions needed to obtain the target image starting from the radar echoes. Key processing steps include motion compensation and reconstruction of the reflectivity function. An experimental setup based on a currently available tracking radar, a data recorder and off-line processing facilities are illustrated. A high cross range resolution image of a MB-339 aircraft was obtained by processing recorded radar echoes from a Selenia X band tracking radar.

Author

TYPE 1/4/103

Quest Accession Number : 90N21244

90N21244# NASA STAR Conference Paper Issue 14

Concept and results of the DLR realtime SAR processor

(AA)MOREIRA, ALBERTO

Deutsche Forschungs- und Versuchsanstalt fuer Luft- und Raumfahrt, Oberpfaffenhofen (Germany, F.R.). (D0699060) Inst. for Radio Frequency Technology.

In AGARD, High Resolution Air- and Spaceborne Radar 6 p (SEE N90-21223

14-32) 891000 p. 6 In: EN (English) Avail: NTIS HC A10/MF A02;

Non-NATO Nationals requests available only from AGARD/Scientific

Publications Executive p.1963

A real time azimuth processor was developed for the airborne E-SAR system (Experimental Synthetic Aperture Radar). The processor works with an unfocused compression method. This method greatly simplifies the data processing and is easily implemented by a moving average approach. A SAR image processed by a traditional unfocused processing method has a lower contrast, higher sidelobes, and worse resolution than in the focused case. A new algorithm was developed, so that a triangular amplitude weighting could be implemented into the unfocused processing method without additional complications. Images processed in real time are presented. They show good contrast and strong suppression of the sidelobes. The processor hardware can be implemented with reduced costs in small aircraft and is suitable for several applications such as the detection of oil pollution over the sea.

Author

TYPE 1/4/105

Quest Accession Number : 90N21239

90N21239# NASA STAR Conference Paper Issue 14

A fast ISAR-imaging process and its inherent degrading effects on image quality

(AA)BETHKE, K.-H.; (AB)ROEDE, B.

Deutsche Forschungs- und Versuchsanstalt fuer Luft- und Raumfahrt, Oberpfaffenhofen (Germany, F.R.).

Hochfrequenztechnik. (D0699060) Inst. fuer

In AGARD, High Resolution Air- and Spaceborne Radar 12 p (SEE N90-21223

14-32) 891000 p. 12 In: EN (English) Avail: NTIS HC A10/MF A02;

Non-NATO Nationals requests available only from AGARD/Scientific

Publications Executive p.1963

A method for a fast 2-D inverse synthetic aperture radar (ISAR) imaging process is presented. A coherent short pulse radar is used to sample amplitude and phase of the backscattered field from a continuously rotating object. This is being done while a narrow range gate is sweeping in range steps of 15 cm across the target plane at a typical speed of 150 m/s. Applying fast SAR principles, in an off-line process for each range cell, an acceptable good cross range resolution can be obtained when processing angle intervals of less than 30 deg. The influence of analytical approximations as well as the effect of moving scattering centers through several range resolution cells during the process interval can cause severe image degradations. Two methods for partial and complete compensation of these effects under the aspect of minimum loss in processing speed were developed and are presented.

TYPE 1/4/106

Quest Accession Number : 90N21238

90N21238# NASA STAR Conference Paper Issue 14

Problems in ISAR processing with range resolution by stepped frequency bursts

(AA)KRAEMER, GERD

Forschungsinstitut fuer Hochfrequenzphysik, Werthhoven (Germany, F.R.). (F1944607)

In AGARD, High Resolution Air- and Spaceborne Radar 5 p (SEE N90-21223 14-32) 891000 p. 5 In: EN (English) Avail: NTIS HC A10/MF A02; Non-NATO Nationals requests available only from AGARD/Scientific Publications Executive p.1962

If a target image is reconstructed from an ISAR (Inverse Synthetic Aperture Radar) measurement by immediate application of the Discrete Fourier Transform, the image becomes blurred with increasing distance from its center. It is shown that with an ISAR sensor applying stepped frequency bursts, samples of the 2-D Fourier Transform of a 2-D scatterer density are measured and how a target image can be reconstructed.

Author

TYPE 1/4/108

Quest Accession Number : 90N21235

90N21235# NASA STAR Conference Paper Issue 14

A motion compensation study for the PHARUS project

(AA)OTTEZ, M. P. G.

Organisatie voor Toegepast Natuurwetenschappelijk Onderzoek, The Hague (Netherlands). (01465661) Radar and Communications Div.

In AGARD, High Resolution Air- and Spaceborne Radar 12 p (SEE N90-21223 14-32) 891000 p. 12 In: EN (English) Avail: NTIS HC A10/MF A02; Non-NATO Nationals requests available only from AGARD/Scientific Publications Executive p.1962

In the PHARUS project, a polarimetric C band SAR is being developed, which will be preceded by a polarimetric test system called PHARS. A motion compensation study is also part of preparatory studies for the final PHARUS design. A SAR data simulator was developed as a tool for the study of the effects of aircraft motion on the SAR image. From the SAR mapping geometry, a terrain description, the radar parameters, and detailed trajectory and attitude data of a non-maneuvering aircraft, the simulator generates raw data with a given range resolution. This can be processed, by azimuth compression, into the SAR image. A secondary purpose of the simulation is to determine the impact of several design parameter choices, and to provide well defined test input for SAR processing software. The results of test runs with real flight data were verified theoretically, and have shown the need for motion compensation. It was also shown that a major advantage of simulation, in that it can take many factors into account at the same time, including for instance the SAR processing method, which is hard to do theoretically.

Author

TYPE 1/4/107

Quest Accession Number : 90N21236

90N21236# NASA STAR Conference Paper Issue 14

A solution for real time motion compensation for SAR without using inertial navigation systems

(AA)MOREIRA, JOAO R.

Deutsche Forschungs- und Versuchsanstalt fuer Luft- und Raumfahrt, Wesseling (Germany, F.R.). (D0705482) Inst. for Radio Frequency Technology.

In AGARD, High Resolution Air- and Spaceborne Radar 6 p (SEE N90-21223 14-32) 891000 p. 6 In: EN (English) Avail: NTIS HC A10/MF A02; Non-NATO Nationals requests available only from AGARD/Scientific Publications Executive p.1962

A new solution is given for real time motion compensation. The main idea is to extract all the necessary motions of the aircraft from the radar backscatter signal using a new radar configuration and new methods for evaluating the azimuth spectra of the radar signal. Hence an inertial navigation system becomes unnecessary for many applications. The motion compensation parameters for real time motion error correction are the range delay, the range dependent phase shift and the pulse repetition frequency. The motions of the aircraft to be extracted are the displacement in line of sight direction, the aircraft's yaw and drift angle and forward velocity. Results show that a three look image with an azimuth resolution of 3m in the L-band using a small aircraft is achievable and the implementation of this method in real time using an array processor is feasible.

Author

TYPE 1/4/109

Quest Accession Number : 90N21234

90N21234# NASA STAR Conference Paper Issue 14

Concept for a spaceborne Synthetic Aperture Radar (SAR) sensor based on active phased array technology

(AA)BRUNNER, A.; (AB)LANGER, E.; (AC)OETTL, H.; (AD)ZELLER, K. H.

(AD)Deutsche Forschungs- und Versuchsanstalt fuer Luft- und Raumfahrt, Oberpfaffenhofen, Germany, F.R.)

Siemens A.G., Munich (Germany, F.R.). (SK032012)

Telecommunication/Semiconductors.

In AGARD, High Resolution Air- and Spaceborne Radar 10 p (SEE N90-21223 14-32) 891000 p. 10 In: EN (English) Avail: NTIS HC A10/MF A02; Non-NATO Nationals requests available only from AGARD/Scientific Publications Executive p.1962

For surveillance with spaceborne remote sensing systems, quite often a spatial resolution of 1 m or less is requested. A SAR concept is presented for a low flying satellite. Assuming a peak power of 5 kW and using active phased array technology, a swath width of about 30 km at an off nadir angle of 35 deg is considered to be reasonable. A wide swath width combined with a high resolution can only be achieved if a fixed antenna beam is used for transmitting which illuminates the whole swath width, while a very narrow antenna beam scans the swath in the manner as the reflected pulse travels from the near range to the far range across the swath width. For the active antenna system, a high efficiency of the transmit/receive modulus, low losses in the feeding network and doubly polarized radiating elements with high polarization purity are considered of utmost importance. An antenna based on the slotted waveguide principle is described. The technology of the GaAs based modules with special respect to space requirement resulting in an economic solution of the power generation below 3 W per module is described.

Author

TYPE 1/4/110

Quest Accession Number : 90N21233

90N21233# NASA STAR Conference Paper Issue 14

Real-time adaptive radiometric correction for imaging radars systems

(AA)MOREIRA, JOAO R.; (AB)PORTZSCH, WINFRIED

Deutsche Forschungs- und Versuchsanstalt fuer Luft- und Raumfahrt, Messel, Germany, F.R.). (00705482) Inst. for Radio Frequency Technology.

In AGARD, High Resolution Air- and Spaceborne Radar 6 p (SEE N90-21223

14-32) 891000 p. 6 In: EN (English) Avail: NTIS HC A10/MF A02;

Non-NATO Nationals requests available only from AGARD/Scientific

Publications Executive p.1962

A new solution is given of a real time radiometric image correction that also minimizes the quantization and saturation noise introduced by the process of analog-to-digital conversion of raw data of coherent and noncoherent imaging radar systems. The implementation of this procedure was successfully performed with the experimental SAR System (E-SAR) of the DLR.

Author

TYPE 1/4/111

Quest Accession Number : 90N21229

90N21229# NASA STAR Conference Paper Issue 14

ROSAR (Helicopter-Rotor based Synthetic Aperture Radar)

(AA)KLAUSING, HELMUT; (AB)KALTSCHMIDT, HORST; (AC)KEYDEL, WOLFGANG

(AC)Deutsche Forschungs- und Versuchsanstalt fuer Luft- und Raumfahrt, Messel, Germany, F.R.)

Messerschmitt-Boelkow-Blohm G.m.b.H., Ottobrunn (Germany, F.R.). (

WT620643)

In AGARD, High Resolution Air- and Spaceborne Radar 12 p (SEE N90-21223

14-32) 891000 p. 12 In: EN (English) Avail: NTIS HC A10/MF A02;

Non-NATO Nationals requests available only from AGARD/Scientific

Publications Executive p.1961

ROSAR is a synthetic aperture radar concept based on rotating antennas of a helicopter for pilot sight target detection and target localization with high resolution. The ROSAR concept has potential benefits for civil and military helicopterborne imaging applications, if the antennas are mounted at the tips of the rotor blades. The concept has two main potential benefits, the imaging field of view is 360 deg and there is no need for a forward velocity of the carrier platform. As opposed to SAR systems based on linear movement of the antenna, ROSAR imaging is based on synthetic aperture of a circular shape. Thus, the image formation process requires a polar format processing architecture. The ROSAR principle is also applicable for other radar mapping systems with rotating antennas, not only for helicopters.

Author

TYPE 1/4/112

Quest Accession Number : 90N21223

90N21223# NASA STAR Conference Proceedings Issue 14

High Resolution Air- and Spaceborne Radar

Advisory Group for Aerospace Research and Development, Neuilly-Sur-Seine

(France). (AD455458) Avionics Panel.

AGARD-CP-459; ISBN-92-835-0530-1 891000 p. 224 Symposium held in The

Hague, Netherlands, 8-12 May 1989 In ENGLISH and FRENCH In: AA (Mixed)

Avail: NTIS HC A10/MF A02; Non-NATO Nationals requests available only from

AGARD/Scientific Publications Executive p.1960

Imaging techniques are important sources of information in military operations. They may serve for purposes such as target detection and location, reconnaissance, classification and identification of fixed or moving objects as well as for orientation over unknown terrain. Despite considerable advances in electro-optical imaging systems the radar sensor has become an attractive alternative for several reasons: large range performance, penetration of weather, smoke, dust and foliage, day and night operation. On the other hand high resolution radar techniques such as synthetic aperture radar (SAR) and inverse synthetic aperture radar (ISAR) promise geometrical resolution of about 1 m and less. For individual titles, see N90-21224 through N90-21246.

TYPE 1/4/113

Quest Accession Number : 90N18371

90N18371# NASA STAR Technical Report Issue 11

Synthetic aperture radar imagery of airports and surrounding areas:

Archived SAR data / Final Report, 31 Aug. 1987 - 30 Nov. 1989

(AA)ONSTOTT, ROBERT G.; (AB)GINERIS, DENISE J.

Environmental Research Inst. of Michigan, Ann Arbor. (E0356283)

NASA-CR-4275; NAS 1.26:4275; DOT/FAA/DS-89/14 NAS1-18465 505-67-41-57

NASA Washington 900200 p. 214 In: EN (English) Avail: NTIS HC A10/MF

A02 p.1453

The statistical description of ground clutter at an airport and in the surrounding area is addressed. These data are being utilized in a program to detect microbursts. Synthetic aperture radar (SAR) data were acquired from the ERIM SAR data archive and were examined for utility to this program. Eight digital scattering coefficient images were created of five airports. These data are described along with the results of the clutter study. These scenes were imaged at 9.38 GHz and HH- and VV-polarizations and contained airport grounds and facilities, industrial, residential, fields, forest, and water. Incidence angles ranged from 12 to 72 deg. Even at the smallest incidence angles, the distributed targets such as forest, fields, water, and residential rarely had mean scattering coefficients greater than -10 dB. Eighty-seven percent of the image had scattering coefficients less than -17.5 dB. About 1 percent of the scattering coefficients exceeded 0 dB, with about 0.1 percent above 10 dB. Sources which produced the largest cross sections were largely confined to the airport grounds and areas highly industrialized. The largest cross sections were produced by observing large buildings surrounded by smooth surfaces.

Author

TYPE 1/4/114

Quest Accession Number : 90A17853

90A17853* NASA IAA Journal Article Issue 05

Phase calibration of polarimetric radar images

(AA)SHEEN, DAN R.; (AB)KASISCHKE, ERIC S.; (AC)FREEMAN, ANTHONY

(AB)(Michigan, Environmental Research Institute, Ann Arbor); (AC)(JPL, Pasadena, CA)

Environmental Research Inst. of Michigan, Ann Arbor. (E0356283)

MO0014-87-C-07262; MAG-1101 (Remote Sensing Society, IEEE, URSI, et al., International Geoscience and Remote Sensing Symposium /IGARSS '88/ on Remote Sensing: Moving Towards the 21st Century, Scotland, Sept. 12-16, 1988) IEEE Transactions on Geoscience and Remote Sensing (ISSN 0196-2892), vol. 27, Nov. 1989, p. 719-731. 891100 p. 13 refs 14 In: EN (English) p.663

The problem of phase calibration between polarization channels of an imaging radar is studied. The causes of various types of phase errors due to the radar system architecture and system imperfections are examined. A simple model is introduced to explain the spatial variation in phase error as being due to a displacement between the phase centers of the vertical and horizontal antennas. It is also shown that channel leakage can cause a spatial variation in phase error. Phase calibration using both point and distributed ground targets is discussed and a method for calibrating phase using only distributed targets is verified, subject to certain constraints. Experimental measurements using the MADC/ERIM P-3 synthetic-aperture radar (SAR) system and NASA/JPL DC-8 SAR, which operates at C-, L-, and P-bands, are presented. Both of these systems are multifrequency, polarimetric, airborne, SAR systems.

I.E.

TYPE 1/4/116

Quest Accession Number : 90A17851

90A17851* NASA IAA Journal Article Issue 05

Estimation of the SAR system transfer function through processor defocus

(AA)VACHON, PIERRE W.; (AB)RANEY, R. KEITH

(AB)(Canada Centre for Remote Sensing, Ottawa)

(Remote Sensing Society, IEEE, URSI, et al., International Geoscience and Remote Sensing Symposium /IGARSS '88/ on Remote Sensing: Moving Towards the 21st Century, Edinburgh, Scotland, Sept. 12-16, 1988) IEEE Transactions on Geoscience and Remote Sensing (ISSN 0196-2892), vol. 27, Nov. 1989, p. 702-708. 891100 p. 7 refs 12 In: EN (English) p.651

It is generally accepted that in order to derive wave directional spectra from synthetic-aperture radar (SAR) image data, the system transfer function (STF) must be removed from the raw SAR image spectrum. The STF, very nearly equivalent to the magnitude of the Fourier transform of the N-look perfect-focus impulse response, can be estimated from actual SAR image data as the magnitude of the Fourier transform of the autocorrelation function of the speckle in a low-contrast scene. The authors outline and demonstrate a novel approach for estimating the STF based on the observation that system defocus, to the first order, does not impact speckle statistics. Therefore, a speckle pattern suitable for STF estimation is produced from typical SAR data, including ocean waves, by operating the processor out of focus. Processor defocus does not 'blur' the speckle, but it does blur the wave image, thus reducing the image correlation function, and hence the image spectrum to be essentially that of the STF desired.

I.E.

TYPE 1/4/115

Quest Accession Number : 90A17852

90A17852* NASA IAA Journal Article Issue 05

Multitemporal and dual-polarization observations of agricultural vegetation covers by X-band SAR images

(AA)LE TOAN, THUY; (AB)MOUGIN, ERIC; (AC)LOPES, ARMAND; (AD)LAUR, HENRI

(AC)(Centre d'Etude Spatiale des Rayonnements, Toulouse, France); (AD)(ESA, European Space Research Institute, Frascati, Italy)

(Remote Sensing Society, IEEE, URSI, et al., International Geoscience and Remote Sensing Symposium /IGARSS '88/ on Remote Sensing: Moving Towards the 21st Century, Edinburgh, Scotland, Sept. 12-16, 1988) IEEE Transactions on Geoscience and Remote Sensing (ISSN 0196-2892), vol. 27, Nov. 1989, p. 709-718. 891100 p. 10 refs 18 In: EN (English) p.684

A study is presented of synthetic-aperture (SAR) images which aims to demonstrate the capability of radar to identify vegetation types and to determine the vegetation canopy parameters. The investigations, performed on bitemporal and dual-polarization (HH and VV) X-band SAR images of an agricultural scene, included all the steps involved from SAR images to applications: (1) radar backscatter values were retrieved from SAR images, using external references targets; (2) the polarization and temporal responses of the vegetation covers were analyzed, highlighting the particular behavior of flooded rice fields; (3) the observations of rice fields were interpreted by a theoretical model. During an extended period of rice plant growth, the model, in agreement with the observations, suggests a possible use of both HH and VV images for rice field mapping and monitoring. An example of rice field mapping with an algorithm based on the above results is also presented.

I.E.

TYPE 1/4/117

Quest Accession Number : 90A17846

90A17846* NASA IAA Journal Article Issue 05

Complex SAR imagery and speckle filtering for wave imaging

(AA)CORDEY, RALPH A.; (AB)MACKLIN, J. TREVOR

(AB)(CEC Research, Ltd., Marconi Research Centre, Great Baddow, England)

(Remote Sensing Society, IEEE, URSI, et al., International Geoscience and Remote Sensing Symposium /IGARSS '88/ on Remote Sensing: Moving Towards the 21st Century, Edinburgh, Scotland, Sept. 12-16, 1988) IEEE Transactions on Geoscience and Remote Sensing (ISSN 0196-2892), vol. 27, Nov. 1989, p. 666-673. Research supported by ESA and Royal Aerospace Establishment. 891100 p. 8 refs 13 In: EN (English) p.694

A method is described to predict the wavenumber dependence of the speckle component in spectra of synthetic aperture radar intensity images. Filtering of this component is an important step in recovering waveheight spectra for synthetic-aperture radar (SAR) images of the ocean, and an effective means of doing so is required for the 'wave mode' of the European satellite ERS-1. The method uses the correlation function of the corresponding complex images and has been tested using a variety of airborne and spaceborne imagery obtained over both land and sea. Examples are shown of both successful and unsuccessful applications of the method. The successes show a great improvement in speckle filtering over previous techniques, while the failures can possibly be explained in terms of artifacts of particular SAR processors.

I.E.

TYPE 1/4/118

Quest Accession Number : 90N17744
 90N17744# NASA STAR Conference Paper Issue 10
 Power conditioning for active array SAR antennas
 (AA)SCHAEFER, W.

Dornier System G.m.b.H., Friedrichshafen (Germany, F.R.). (D0272085)
 In ESA, European Space Power, Volume 1 p 457-461 (SEE N90-17678 10-20)
 890800 p. 5 In: EN (English) Avail: NTIS HC A19/MF A03 p.1338

A trade off between different overall concepts rather than circuit details, in designing active array SAR (synthetic aperture radar) antenna power conditioning and distribution subsystems, is presented. A hierarchically structured system employing ac distribution is shown to be favorable. Active antennas are shown to be failure tolerant to a certain extent. Special attention is paid to particular reliability aspects. Breadboard hardware is presented. A discussion of further improvement of pulse energy storage is included.

ESA

TYPE 1/4/120

Quest Accession Number : 90N11218
 90N11218# NASA STAR Technical Report Issue 02

Simulation of synthetic aperture radar 1: Feature density and accuracy requirements / Final Report, Jan. 1986 - Jan. 1988

(AA)CRANE, PETER M.; (AB)BELL, HERBERT H.; (AC)KALINYAK, ROBERT G.; (AD)DOOLEY, JOHN; (AE)HUBBARD, DAVID C.

(AB)(Dayton Univ., OH.)
 Air Force Human Resources Lab., Brooks AFB, TX. (A1169445)
 AD-A211019; AFHRL-TR-88-42 890700 p. 37 In: EN (English) Avail: NTIS
 HC A03/MF A01 p.213

Simulations of ground mapping radar are generated from Defense Mapping Agency Digital Feature Analysis Data (DFAD) products which were developed to support real beam ground mapping radar. Criteria for inclusion of an object within a given level of DFAD are radar significance, height, and size. In general, level 1 includes objects 100m and larger and level 2 includes objects 30m and larger. A prototype DFAD incorporating features as small as 10m (level X) was developed to support the higher resolution Synthetic Aperture Radar (SAR); however, the minimum data base requirements for simulating SAR have not been determined. The present report describes three studies conducted to determine these requirements. In the first study, B-1B and P-15E radar operators rated SAR simulations produced from level 2 DFAD (30m) and level X (10m), plus two experimental data bases with 15m and 20m capture criteria. Eighty-two percent of SAR-experienced subjects found the 15m data acceptable. Simulations produced from level 2 depicted areas of high reflector density as a single feature with uniform brightness and were acceptable to only 18 percent of the subjects. A study of the Radar Scope Interpretation (RSI) cues used by B-1B Offensive Systems Officers (OSOs) found that roads and rivers were critical cues, whereas individual structures were used only in the immediate vicinity of the aimpoint. A third study compared B-1B OSO performance on a navigation update task using 10m and 15m feature data and generically enhanced 30m (level 2) and 100m (level 1) data.

GRA

TYPE 1/4/119

Quest Accession Number : 90N16112

90N16112# NASA STAR Technical Report Issue 08
 Necessity and benefit of the X-SAR Space Shuttle experiment
 (AA)KEYDEL, WOLFGANG; (AB)OETTL, HERWIG

(AB)(Deutsche Forschungs- und Versuchsanstalt fuer Luft- und Raumfahrt, Oberpfaffenhofen, Germany, F.R.)

European Space Agency, Paris (France). (Z6854803)

ESA-TT-1164; DFVLR-MIT-88-29; ETN-90-96192 Transl. into ENGLISH of Notwendigkeit und Nutzen des X-SAR-Space-Shuttle-Experiments 891000 p. 38 Original language document was announced as N89-24698 In: EN (English) Avail: NTIS HC A03/MF A01; original German version available from DFVLR, VB-PL-DO, Postfach 90 60 58, 5000 Cologne, Federal Republic of Germany, 26.50 deutsche marks p.1057

The X-band (9.6 GHz) Synthetic Aperture Radar (X-SAR) is studied. It is the first space qualified SAR in X-band. The X-SAR is to be flown on several Shuttle missions as part of the U.S. Radarlab program for Earth observation. The examples shown clearly indicate that the X-band is an extremely valuable and important frequency range for areas of remote sensing. X-band measurements supply valuable additions to measurements in the L- and C-bands. It can be applied to the classification of cultivated land surfaces and of ice and snow and for finding pollution in rivers, lakes and on the seas.

ESA

TYPE 1/4/121

Quest Accession Number : 90A10187

90A10187 NASA IAA Conference Paper Issue 01

Speckle statistics in synthetic aperture radar (SAR) imagery with correlated looks

(AA)APRIL, G. V.; (AB)HARVEY, E. R.

(AB)(Universite Laval, Quebec, Canada)

In: Statistical optics: Proceedings of the Meeting, San Diego, CA, Aug. 18, 19, 1988 (A90-10186 01-35). Bellingham, WA, Society of Photo-Optical Instrumentation Engineers, 1988, p. 2-7. 880000 p. 6 refs 10 In: EN (English) p.26

The high resolution in synthetic aperture radar (SAR) systems is reduced by the speckle appearing in the images. This speckle noise is generated by the coherent processing of radar signals and exists in all types of coherent imaging systems. The statistical properties of speckle noise in a four-look Seasat SAR image are studied to show evidence of correlation between underlying looks resulting in correlated values for adjacent pixels in the final image. Concentrating on homogeneous areas of the image, experimental determination of the SNR and of the probability density of the recorded intensity is performed. It is shown that the intensity fluctuations due to speckle noise in homogeneous areas are not gamma distributed. A model incorporating the empirical correlation coefficient is extracted from experimental data.

Author

TYPE 1/4/123

Quest Accession Number : 89A53785

89A53785* NASA IAA Journal Article Issue 24
Radiometric correction and calibration of SAR images

(AA)FREMAM, ANTHONY; (AB)CURLANDER, JOHN C.
(AB)(California Institute of Technology, Jet Propulsion Laboratory,
Pasadena)

Jet Propulsion Lab., California Inst. of Tech., Pasadena. (JJ574450)

Photogrammetric Engineering and Remote Sensing (ISSN 0099-1112), vol.
55, Sept. 1989, p. 1295-1301. 890900 p. 7 refs 13 In: EN (English)
p.3831

A technique for producing radiometrically calibrated SAR image products is described. The output imagery is corrected to represent a measurement of the ground reflectivity or radar cross section. The sources of calibration errors are discussed and the appropriate forms of the radar equation as applied to SAR-image data are reviewed. A key result is the radar equation dependence on the azimuth reference function used in processing. A radiometric correction algorithm for use in an operational SAR correlator is presented. This algorithm has the characteristic that it is fully reversible. Additionally, it can be applied equally to detected or complex SAR images, and it allows for the subtraction of the estimated noise floor in the image but does not require this procedure.

Author

TYPE 1/4/124

Quest Accession Number : 89A48128

89A48128 NASA IAA Journal Article Issue 21

A statistical approach for determining radiometric precisions and accuracies in the calibration of synthetic aperture radar imagery

(AA)KASISCHKE, ERIC S.; (AB)FOWLER, GARY W.

(AA)(Michigan, Environmental Research Institute, Ann Arbor);
(AB)(Michigan, University, Ann Arbor)

IEEE Transactions on Geoscience and Remote Sensing (ISSN 0196-2892),
vol. 27, July 1989, p. 416-427. 890700 p. 12 refs 18 In: EN (English)
p.3318

A model that estimates a relative error bound for the radiometric calibration of SAR imagery is presented. This model is based on a statistical coefficient of variation of error model, which produces a relative error bound by propagating the measured or estimated uncertainties in the radar-system parameters used to correct digitally processed SAR image intensity values. Using this model, algorithms are generated for absolute and relative radiometric calibration of SAR imagery. These algorithms are demonstrated using parameters from an existing airborne SAR system to determine the relative error bound. It is found that the antenna gain pattern has the greatest influence on the relative error bound. When incidence angles of less than 20 deg were encountered or the target signal-to-radar system noise ratio was less than 6 dB, significant increases (1 dB or greater) in the relative error bound also occur. The actual errors are within 0.3 dB of the model predicted errors.

I.E.

TYPE 1/4/123

Quest Accession Number : 89A48310

89A48310* NASA IAA Journal Article Issue 21
Aberrations in the SAR image of a moving object

(AA)FRANCESCHETTI, GIORGIO; (AB)TATOIAN, JAMES Z.; (AC)DUTT, BIRENDRA
(AA)(CNR, Istituto di Ricerca per l'Elettromagnetismo e i Componenti
Elettronici, Naples, Italy); (AC)(Research and Development Laboratories,
Culver City, CA)

NO0024-83-C-5301 Alta Frequenza (English Edition) (ISSN 0002-6557),
vol. 58, Mar.-Apr. 1989, p. 175-183. 890400 p. 9 refs 12 In: EN
(English) p.3319

Spacecraft imaging of a moving object by means of SAR is studied. It is reviewed how the radial velocity component is responsible for the azimuthal displacement from the correct image location, and how the full velocity components are responsible for image defocusing. A full parametric study elucidating the resulting aberrations in SAR imagery of a moving object is presented.

Author

TYPE 1/4/125

Quest Accession Number : 89A48126

89A48126* NASA IAA Journal Article Issue 21

Block adaptive quantization of Magellan SAR data

(AA)KWOK, RONALD; (AB)JOHNSON, WILLIAM T. K.

(AB)(California Institute of Technology, Jet Propulsion Laboratory,
Pasadena)

Jet Propulsion Lab., California Inst. of Tech., Pasadena. (JJ574450)
IEEE Transactions on Geoscience and Remote Sensing (ISSN 0196-2892),
vol. 27, July 1989, p. 375-383. 890700 p. 9 refs 14 In: EN (English)
p.3289

A report is presented on a data compression scheme that will be used to reduce the SAR data rate on the NASA Magellan mission to Venus. The spacecraft has only one scientific instrument, a radar system for imaging the surface, for altimetric profiling of the planet topography, and for measuring radiation from the planet surface. A straightforward implementation of the scientific requirements of the mission results in a data rate higher than can be accommodated by the available system bandwidth. A data-rate-reduction scheme which includes operation of the radar in burst mode and block-adaptive quantization of the SAR data is selected to satisfy the scientific requirements. Descriptions of the quantization scheme and its hardware implementation are given. Burst-mode SAR operation is also briefly discussed.

I.E.

TYPE 1/4/126

Quest Accession Number : 89A19617
89A19617* NASA IAA Journal Article Issue 16
Geometric accuracy in airborne SAR images
(AA)BLACKWELL, D.; (AB)QUEGAN, S.; (AC)WARD, I. A.; (AD)FREEMAN, A.; (AE)FINLEY, I. P.
; (AC)GEC Research, Ltd., Marconi Research Centre, Great Baddow, England)
Pasadena: GEC Research, Ltd., Marconi Research Centre, Great Baddow, England); (AE)Royal Signals and Radar Establishment, Malvern, England)
GEC-Marconi Electronics Ltd., Chelmsford (England). (GB135511)
IEEE Transactions on Aerospace and Electronic Systems (ISSN 0018-9251),
vol. 25, March 1989, p. 241-258. Research supported by the Royal Signals
Radar Establishment. 890300 p. 18 refs 11 In: EN (English) p.

corrected across-track motions of a synthetic aperture radar (SAR) platform can cause both a severe loss of azimuthal positioning accuracy in the defocusing of the resultant SAR image. It is shown how the results of an autofocus procedure can be incorporated in the azimuth processing to produce a fully focused image that is geometrically accurate in azimuth. Range positioning accuracy is also discussed, leading to a comprehensive treatment of all aspects of geometric accuracy. The system considered is an X-band SAR.
I.E.

TYPE 1/4/128

Quest Accession Number : 89A18341
89A18341 NASA IAA Conference Paper Issue 16
Preparatory microwave remote sensing activities in view of the forthcoming X-SAR/SIR-C missions
(AA)OETTL, HERMIG; (AB)HEEL, FRANZ; (AC)KEYDEL, WOLFGANG
(AC)(DFVLR, Messling, Federal Republic of Germany)
IN: International Symposium on Space Technology and Science, 16th, Sapporo, Japan, May 22-27, 1988, Proceedings. Volume 2 (A89-38031 16-12). Tokyo, ASEE Publishing, Inc., 1988, p. 2271-2276. 890000 p. 6 refs 7 In: EN (English) p.2455

Current developments regarding airborne SAR-sensors in DFVLR are described as well as radiometric calibration activities. The characteristics of the L-band and C-band SAR are presented as well as those of airborne X-band SAR. It is concluded that a high radiometric resolution and a calibration in all frequency ranges used as well as interchannel stability of all sensors is necessary for the operational interpretation of SAR images.
K.K.

TYPE 1/4/127

Quest Accession Number : 89A39609
89A39609 NASA IAA Journal Article Issue 16
Estimating the Doppler centroid of SAR data
(AA)MADSEN, S. NOKVANG
(AA)(Danmarks Tekniske Højskole, Lyngby, Denmark)
IEEE Transactions on Aerospace and Electronic Systems (ISSN 0018-9251),
vol. 25, March 1989, p. 134-140. 890300 p. 7 refs 13 In: EN (English) p.2482

After reviewing frequency-domain techniques for estimating the Doppler centroid of synthetic-aperture radar (SAR) data, the author describes a time-domain method and highlights its advantages. In particular, a nonlinear time-domain algorithm called the sign-Doppler estimator (SDE) is shown to have attractive properties. An evaluation based on an existing SEASAT processor is reported. The time-domain algorithms are shown to be extremely efficient with respect to requirements on calculations and memory, and hence they are well suited to real-time systems where the Doppler estimation is based on raw SAR data. For offline processors where the Doppler estimation is performed on processed data, which removes the problem of partial coverage of bright targets, the DeltaE estimator and the CDE (correlation Doppler estimator) algorithm give similar performance. However, for nonhomogeneous scenes it is found that the nonlinear SDE algorithm, which estimates the Doppler-shift on the basis of data signs alone, gives superior performance.
I.E.

TYPE 1/4/129

Quest Accession Number : 89A35334
89A35334# NASA IAA Journal Article Issue 14
Stochastic processes in microwave remote sensing
Stochastische Prozesse in der Mikrowellenfernerkundung
(AA)KEYDEL, W.
(AA)(DFVLR, Institut fuer Hochfrequenztechnik, Oberpfaffenhofen, Federal Republic of Germany)
(UKSI and Informationsstechnische Gesellschaft, Gemeinsame Tagung, Kleinheubach, Federal Republic of Germany, Oct. 3-7, 1988) Kleinheubacher Berichte (ISSN 0343-5725), vol. 32, 1989, p. 151-151h. In German. 890000 p. 9 refs 8 In: GW (German) p.2144

Stochastic processes and their significance for the efficiency of systems and remote sensing procedures in the microwave radiometry and radar are discussed. Fluctuation problems in remote sensing, image effects, and speckle are addressed, and the influence of system components and eigennoise in SAR are considered. The geometry and radiometric resolution power, measurement accuracy, and the calibration of microwave remote sensing systems are examined.
C.D.

TYPE 1/4/130

Quest Accession Number : 89A31944
89A31944 NASA IAA Journal Article Issue 12
X-SAR specification, design, and performance modeling (synthetic aperture radar for shuttle mission)
(AA)MILLER, DAVID
(AA)(Dornier System GmbH, Friedrichshafen, Federal Republic of Germany)
IEEE Transactions on Geoscience and Remote Sensing (ISSN 0196-2892),
vol 27, March 1989, p. 170-176. 890300 p. 7 refs 5 In: EN (English)
p.1800

The detailed design and development phase of the X-SAR 9.6-GHz vertical polarization segment of the Shuttle Radar Lab (SRL) mission, started in Spring 1987, is discussed. The design incorporates a planar array antenna based on metallized carbon-fiber-reinforced plastic technology, a traveling-wave-tube amplifier, and a dual-channel receiver using surface acoustic wave devices. Several radar parameters are controllable from ground to achieve high performance over a wide range of measurement geometries. Definitions of image performance parameters and modeling algorithms developed in support of instrument specification and performance monitoring during hardware development are presented. The algorithms have been implemented as a software tool to perform sensitivity analysis and generate interesting graphical results to support top-level instrument verification.
I.E.

TYPE 1/4/132

Quest Accession Number : 89N28942
89N28942# NASA STAR Technical Report Issue 23
The Archimedes 2a Experiment on oil slick detection over the North Sea, April 1988: Measurement Results obtained by the E-SAR System of the Aerospace Research Establishment
(AA)HORN, RALF; (AB)MOREIRA, ALBERTO
Deutsche Forschungs- und Versuchsanstalt fuer Luft- und Raumfahrt, Oberpfaffenhofen (West Germany). (D0699060) Abteilung Hochfrequenzsysteme.
DFVLR-WITT-89-08; ISSN-0176-7739; ETN-89-95299 890200 p. 46 In: EN (English) Avail: NTIS HC A03/MF A01; DFVLR, VB-PL-DO, Postfach 90 60 58, 5000 Cologne, Fed. Republic of Germany, 18.50 DM p.3319

The results of the Archimedes 2a experiment on oil slick detection over the North Sea obtained by the experimental airborne SAR System E-SAR (synthetic aperture radar) are presented. This system is part of the research program at the Institute for Radio Frequency Technology of the German Aerospace Research Establishment. During the experiment carried out on 21 April 1988 the system was operated in L-band at 1.29 GHz. The report discusses briefly some problems with oil slick detection by SAR. It gives an overview of the E-SAR system configuration and system performance. SAR data and image processing procedures are described as well. SAR images of an oil slick of 5 cubic meters of crude oil and corresponding image analysis results are presented.
ESA

TYPE 1/4/131

Quest Accession Number : 89A29428
89A29428 NASA IAA Journal Article Issue 11
Airborne MTI via digital filtering
(AA)ENDER, J.; (AB)KLEMM, R.
(AB)(Forschungsgesellschaft fuer angewandte Naturwissenschaften, Forschungsinstitut fuer Funk und Mathematik, Wachtberg-Werthhoven, Federal Republic of Germany)
IEE Proceedings, Part F: Radar and Signal Processing (ISSN 0143-7070), vol. 136, pt. F, no. 1, Feb. 1989, p. 22-28. 890200 p. 7 refs 9 In: EN (English) p.1594

A simple clutter suppression technique for airborne moving target indicators (MTIs) is proposed which exploits the special properties of a linear equispaced array antenna aligned in the flight direction. In the present method, equidistant pulses are transmitted, and the temporal and spatial samples are equivalent. The method is found to provide better target detection than airborne MTI techniques based on oversampling. It is suggested that the inverse clutter filter can be employed as an output for SAR imaging with improved SNR.
R.R.

TYPE 1/4/133

Quest Accession Number : 89N28911
89N28911# NASA STAR Conference Paper Issue 23
Real time SAR processing techniques
(AA)SCHOTTER, ROLAND
Joint Publications Research Service, Arlington, VA. (J1957394)
In its JPRS Report: Science and Technology. USSR: Space. 16th International Congress of the International Society for Photogrammetry and Remote Sensing, Volume 2 p 75-82 (SEE N89-28903 23-43) Transl. into ENGLISH from International Archives of Photogrammetry and Remote Sensing (Kyoto, Japan), v. 27, pt. B9, 1988 p 184-190 890131 p. 8 In: EN (English) Avail: NTIS HC A09/MF A01 p.3314

Spaceborne synthetic aperture radar (SAR) systems provide raw radar data information at high data rates of 10 Mwords per second. Real time SAR processors, therefore, must perform more than 1 giga-operations (multiplications, additions) per second in order to generate images from the raw data. Since conventional computer systems are not able to cope with these requirements Dornier has developed real time SAR processors on the basis of a modular pipeline concept. The processing pipeline is built up to standardized hardware modules which are required for digital signal processing of two-dimensional data. These modules show identical electrical and mechanical interfaces so that each hardware module can be used in any place of the pipelines. The basic principles are presented for the real time modular pipeline concept and its processing rate requirements for real time SAR processing applications. The implementation of some of the most important modules like Fast Fourier Transformation, correlation, interpolation, and data memory is described. Finally, a short outlook on further applications of the pipeline processing concept is given.
Author

TYPE 1/4/134

Quest Accession Number : 89N28890

89N28890# NASA STAR Conference Paper Issue 23

EXAS: Experiment on Autonomous SAR processor calibration

(AA)RUNGE, H.; (AB)POPELA, A.; (AC)NOACK, W.

Joint Publications Research Service, Arlington, VA. (J1957394)

In its JPRS Report: Science and Technology. USSR: Space. 16th International Congress of the International Society for Photogrammetry and Remote Sensing, Volume 1 p 132-140 (SEE N89-28876 23-43) Transl. into ENGLISH from International Archives of Photogrammetry and Remote Sensing (Kyoto, Japan), v. 27, 1988 p 369-377 890130 p. 9 In: EN (English) Avail: NTIS HC A12/MF A01 p.1311

Future synthetic aperture radar (SAR) missions like the SIR-C with the German X-band radar will acquire multifrequency and multipolarization data with various incidence angles. In order to exploit the mission's full scientific potential DFVLR is going to calibrate both its Intelligent SAR Processor (ISAR) and the final image products. The idea of the EXAS proposal is to use the extra data gained from an independent Doppler measurement. These data will be gathered at a geolocated receiver in order to tune and finally calibrate the ISAR processor. The receiver will be adjusted to the sensor carrier frequency, the signals will be mixed down to baseband, be digitalized and transferred to the ISAR hardware system. This can be performed in parallel for three frequencies with two different polarizations. Immediately after the fly-over the data will be analyzed. The azimuth antenna pattern will be computed and fed back into the processing chain. The replica of the chirps radiated by the sensor will be recorded by the ground receiver. Therefore, the exact range reference function is known and can be used for the processing. The calibrated processor will produce images with a very accurate absolute pixel location. In order to verify this, a cluster of geolocated point reflectors shall be positioned over the swath and the SAR image will be compared with a cartographic map. The experiment plan and the contributions of the three institutes are described.

Author

TYPE 1/4/135

Quest Accession Number : 89N28882

89N28882# NASA STAR Conference Paper Issue 23

KRAS: A Danish high resolution airborne SAR

(AA)MADSEN, SOREN NORVANG; (AB)CHRISTENSEN, ERIK LINTZ; (AC)SKOU, NIELS
Joint Publications Research Service, Arlington, VA. (J1957394)

In its JPRS Report: Science and Technology. USSR: Space. 16th International Congress of the International Society for Photogrammetry and Remote Sensing, Volume 1 p 48-57 (SEE N89-28876 23-43) Transl. into ENGLISH from International Archives of Photogrammetry and Remote Sensing (Kyoto, Japan), v. 27, 1988 p 90-97 890130 p. 10 In: EN (English) Avail: NTIS HC A12/MF A01 p.3309

A C-band high resolution airborne synthetic aperture radar (SAR) is presently being constructed. The main purpose of the project, which is called KRAS, is to develop the knowledge base required to build advanced coherent radars. The design rationale is presented. The design of the radar is based on digital technology to the largest possible degree. This results in a very flexible radar system, with most of the system parameters being software controlled. Variable waveforms of bandwidths larger than 100 MHz and durations up to 20 microsec can be generated. Calibration of the system was also given much consideration, and design principles usually applied in radiometers were implemented. The significant flexibility and the calibration is of major importance since the system is intended for applications ranging from medium resolution wide swath mapping, i.e., sea ice mapping or oil pollution surveillance, to high resolution narrow swath mapping for cartography or reconnaissance.

Author

TYPE 1/4/136

Quest Accession Number : 89A26846

89A26846# NASA IAA Journal Article Issue 10

A simulation for spaceborne SAR imagery of a distributed, moving scene

(AA)VACHON, PARIS W.; (AB)RANEY, R. KEITH; (AC)EMERY, WILLIAM J.

(AA)(Canada Centre for Remote Sensing, Ottawa); (AB)(Radsat Project Office, Ottawa, Canada); (AC)(Colorado, University, Boulder)

IEEE Transactions on Geoscience and Remote Sensing (ISSN 0196-2892), vol. 27, Jan. 1989, p. 67-78. 890100 p. 12 refs 37 In: EN (English) p.1510

A computer simulation that is designed to represent aspects of spaceborne synthetic-aperture radar (SAR) imagery of the ocean surface is presented. The simulation is unique in that a scatterer density (per resolution cell) is explicitly included, thus allowing the incorporation of various scattering natures, from purely specular to purely diffuse. The simulation may be applied to ocean surface wave imaging since velocity bunching and scene coherence times are also included. Certain assumptions inherent in the velocity bunching formulation limit the applicability of the simulation in its present form to spaceborne SAR systems only. Two experiments based on this simulation are considered: (1) the effect of varying the target density; and (2) the effect of the mean scene coherence time in the imaging of a ocean swell system. In each case, the simulation outputs are compared with actual SEASAT SAR imagery. On the basis of certain statistics derived from the simulated scenes, it is shown that specular statistics are quantitatively correct for scenes that may appear diffuse in hard copy form. This observation suggests that quantitative norms be used (rather than intuitive opinion or appearance) for investigating ocean scattering statistics, for example.

I.E.

TYPE 1/4/137

Quest Accession Number : 89N24688

89N24688# NASA STAR Technical Report Issue 18

Necessity and benefit of the X-SAR space shuttle experiment

(AA)KEYDEL, WOLFGANG; (AB)JOETTL, HERWIG
Deutsche Forschungs- und Versuchsanstalt fuer Luft- und Raumfahrt,
Oberpfaffenhofen (West Germany). (DO699060)

DFVLR-MTT-88-29; ISSN-0176-7736; ETN-89-94375 881000 p. 41 Original
contains color illustrations In GERMAN; ENGLISH summary In: AA (Mixed)
Avail: NTIS HC A03/MF A01; DFVLR, VB-PL-DO, Postfach 90 60 58, 5000
Cologne, Federal Republic of Germany, 26.50 deutsche marks p.2582

The X, L, and C-band synthetic aperture radars (SAR) planned to fly in
1992 on space shuttle missions are investigated for their effectiveness in
Earth surface vegetation classification and recognition. The scattering of
electromagnetic waves by twigs, leaves, branches, and trunks permits
vegetation growth length estimation. Earth surface roughness is analyzed
by Rayleigh criterion. The SAR sensors are well adapted to Earth surface
observation independently of daylight and atmospheric conditions.

ESA

TYPE 1/4/139

Quest Accession Number : 89N18953

89N18953# NASA STAR Conference Paper Issue 11

The impacts of quantisation noise on the ERS-1 synthetic aperture radar
performance

(AA)RICHARDS, B. E.; (AB)LANCASHIRE, D. C.

Marconi Space Systems Ltd., Portsmouth (England). (MF879009)

In ESA, Proceedings of the 1988 International Geoscience and Remote
Sensing Symposium (IGARSS) '88 on Remote Sensing: Moving Towards the 21st
Century, Volume 2 p 1159-1160 (SEE N89-18836 11-43) 880800 p. 3 In: EN
(English) Avail: NTIS HC A99/MF A01; ESA Publications Div. ESTEC,
Noordwijk, Netherlands, \$120 US or 250 Dutch guilders p.1552

The contribution of digitizing errors to system resolution is
considered. It is often described as an additional quantization noise
power given by $\Delta/2$ where Δ is the digitizer step size. In a
real system, this is an oversimplification and if the less obvious effects
of digitizing are not included, then system performance can be seriously
degraded. A qualitative description is given of possible effects and the
tradeoff necessary between relevant system parameters. The quantizing
principles as applied to the ERS-1 SAR are presented and the treatment of
system imperfections described. Numerical examples for an ideal case of a
perfect receiver and for a more realistic receiver are given.

ESA

TYPE 1/4/138

Quest Accession Number : 89A22586

89A22586# NASA IAA Journal Article Issue 07

Validation of a synthetic aperture radar ocean wave imaging theory by
the Shuttle Imaging Radar-B experiment over the North Sea

(AA)BRUENING, CIAUS; (AB)ALPERS, WERNER; (AC)ZAMBRESKY, LIANA F.;
(AD)TILLEY, DAVID G.

(AA)(European Centre for Medium Range Weather Forecasts, Reading, England);
(AB)(Bremen, Universitaet, Federal Republic of Germany);
(AC)(European Centre for Medium Range Weather Forecasts, Reading, England);
GKSS-Forschungszentrum Geesthacht GmbH, Federal Republic of Germany);
(AD)(Johns Hopkins University, Laurel, MD)

BMFT-01-QS-86174; N00014-83-G-0126 Journal of Geophysical Research
(ISSN 0148-0227), vol. 93, Dec. 15, 1988, p. 15403-15425. 881215 p. 23
refs 26 In: EN (English) p.1029

SAR image intensity spectra measured during the SIR-B mission (October 6
and October 8, 1984) over the North Sea were compared with an ocean wave
spectra hindcast by a third-generation wave prediction model (WAMODEL). It
was found that, while the hindcast ocean wave spectra had only single
peaks, most of the measured SAR image spectra of October 6 showed double
peaks. It is shown that the double peaks are generated by the SAR imaging
mechanism, when the SAR MTF consisting of the sum of the complex real
aperture radar (RAR) MTF and the velocity bunching MTF has a strong
minimum near the range direction, by which the wave spectrum is cut into
two. The azimuth angle at which this minimum occurs depends strongly on
the phase of the RAR MTF.

I.S.

TYPE 1/4/140

Quest Accession Number : 89N18949

89N18949# NASA STAR Conference Paper Issue 11

Change detection in AGRISAR images

(AA)QUEGAN, S.; (AB)YANASSE, C.; (AC)BLACK, S.; (AD)DANSON, M.
Sheffield Univ. (England). (S1380652)

In ESA, Proceedings of the 1988 International Geoscience and Remote
Sensing Symposium (IGARSS) '88 on Remote Sensing: Moving Towards the 21st
Century, Volume 2 p 1139-1140 (SEE N89-18836 11-43) 880800 p. 2 In: EN
(English) Avail: NTIS HC A99/MF A01; ESA Publications Div. ESTEC,
Noordwijk, Netherlands, \$120 US or 250 Dutch guilders p.1552

Synthetic aperture radar (SAR) data at four dates spanning the growing
season over a UK site was used to derive multitemporal crop radar cross
section signatures. This involves measuring and correcting variations due
to the SAR system within single images, and calibrating images gathered at
different times. Calibration based on use of point targets, fields of
particular crop types, and global measures assuming statistical
homogeneity are evaluated. No basis for multitemporal calibration is
apparent.

ESA

TYPE 1/4/141

Quest Accession Number : 89N18948

89N18948# NASA STAR Conference Paper Issue 11

Extraction of agricultural plant parameters from multitemporal Thematic Mapper (TM) and X-SAR data

(AA)MAUSER, W.; (AB)RIEG, A.

Freiburg Univ. (Germany, F.R.). (F6817510) Inst. for Physical Geography and Hydrology.

BMFT-01-QS-86090; BMFT-01-QS-87033 In ESA, Proceedings of the 1988 International Geoscience and Remote Sensing Symposium (IGARSS) '88 on Remote Sensing: Moving Towards the 21st Century, Volume 2 p 1133-1137 (SEE N89-18836 11-43) In: EN (English) Avail: NTIS HC A99/MF A01; ESA Publications Div. ESTEC, Noordwijk, Netherlands, \$120 US or 250 Dutch guilders p.1551

Within the AGRISAR'86 campaign, 4 SAR images were produced of an agricultural area using the VARIAN-S X-band SAR. Three TM-scenes were analyzed. Ground truth was gathered on an area of 48 sqkm and the field boundaries were digitized to produce images of the measured plant parameters. After geometric registration, regressions were calculated between sensor data and measured biomass, plant height, and water content of different plant species. Land use classifications were carried out. Results show strong correlations between plant parameters and the ratio between bands 4 and 5 of TM. For the SAR data a separation between cereals and corn is possible using a multitemporal approach.

ESA

TYPE 1/4/143

Quest Accession Number : 89N18924

89N18924# NASA STAR Conference Paper Issue 11

E-SAR: The experimental airborne L/C-band SAR system of DFVLR

(AA)HORN, R.

Deutsche Forschungs- und Versuchsanstalt fuer Luft- und Raumfahrt, Wesseling (Germany, F.R.). (D0705482) Inst. for Radiofrequency Technology.

In ESA, Proceedings of the 1988 International Geoscience and Remote Sensing Symposium (IGARSS) '88 on Remote Sensing: Moving Towards the 21st Century, Volume 2 p 1025-1026 (SEE N89-18836 11-43) 880800 p. 2 In: EN (English) Avail: NTIS HC A99/MF A01; ESA Publications Div. ESTEC, Noordwijk, Netherlands, \$120 US or 250 Dutch guilders p.1548

The E-SAR system was developed to study the SAR method and its problems, such as motion error correction and overall system calibration. The sensor is designed to operate on board DO 228 aircraft in either L- or C-band. The system features stripline active array antennas, built in test equipment for system calibration, real time motion error correction, and quicklook data processing.

ESA

TYPE 1/4/142

Quest Accession Number : 89N18925

89N18925# NASA STAR Conference Paper Issue 11

Taking a broader view: Radarsat adds ScansAR to its operations (AA)LUSCOMBE, A. P.

Spar Aerospace Ltd., Ste-Anne-de-Bellevue (Quebec). (SV029037)

In ESA, Proceedings of the 1988 International Geoscience and Remote Sensing Symposium (IGARSS) '88 on Remote Sensing: Moving Towards the 21st Century, Volume 2 p 1027-1032 (SEE N89-18836 11-43) Sponsored in part by the Canadian government 880800 p. 6 In: EN (English) Avail: NTIS HC A99/MF A01; ESA Publications Div. ESTEC, Noordwijk, Netherlands, \$120 US or 250 Dutch guilders p.1548

ScansAR operations were added to Radarsat SAR capabilities to enable very wide swaths to be imaged. The principle of ScansAR is outlined and the criteria used in defining the operations are explained. The major implications of ScansAR for the SAR system, in the instrument on-board the satellite and in the processor on the ground, are identified. The definition of 2 standard forms of ScansAR operation, providing coverage respectively of swaths of over 300 and 500 km, is described. These swath widths compare with the maximum of 150 km previously available with Radarsat using conventional SAR imaging. The ScansAR operations are not restricted to these two standard forms, however; the SAR can also image with a variety of other combinations of beams on command from the ground.

ESA

TYPE 1/4/144

Quest Accession Number : 89N18923

89N18923# NASA STAR Conference Paper Issue 11

X-SAR: A new spaceborne synthetic aperture radar

(AA)VELTEN, E. H.

Dornier-Werke G.m.b.H., Friedrichshafen (Germany, F.R.). (D0425275)

In ESA, Proceedings of the 1988 International Geoscience and Remote Sensing Symposium (IGARSS) '88 on Remote Sensing: Moving Towards the 21st Century, Volume 2 p 1021-1024 (SEE N89-18836 11-43) 880800 p. 4 In: EN (English) Avail: NTIS HC A99/MF A01; ESA Publications Div. ESTEC, Noordwijk, Netherlands, \$120 US or 250 Dutch guilders p.1547

The X-synthetic aperture radar (SAR) instrument design is described, including mechanical and electrical layout, operation modes, and interfaces to Shuttle and SIR-C, as well as major design parameters of the subsystems. The configuration of the ground segment is illustrated. The X-SAR design is determined by the selection of the resonant slotted waveguide CRPP antenna working at a center frequency of 9.6 GHz and the high power amplifier using a 3 kW traveling wave tube. The radio frequency electronics comprises the frequency and chirp generation, up- and down-conversion, and filtering. The digital instrument control and data handling electronics provides high speed A/D conversion with selectable bandwidth, buffering, and conversion to serial format for onboard storage on tape or direct transmission to ground. The X-SAR includes an onboard calibration system with two different loops.

ESA

TYPE 1/4/145
 Quest Accession Number : 89N18885
 89N18885# NASA STAR Conference Paper Issue 11
 Engineering calibration of the ERS-1 active microwave instrumentation in orbit

(AA)ATTEMA, E.
 European Space Agency. European Space Research and Technology Center, ESTEC, Noordwijk (Netherlands). (E6889478)
 In its Proceedings of the 1988 International Geoscience and Remote Sensing Symposium (IGARSS) '88 on Remote Sensing: Moving Towards the 21st Century, Volume 2 p 859-862 (SEE N89-18836 11-43) 880800 p. 4 In: EN (English) Avail: NTIS HC A99/MF A01; ESA Publications Div. ESTEC, Noordwijk, Netherlands, \$120 US or 250 Dutch guilders p.1541

The ESA baseline plan for radiometrical calibration of the output of the synthetic aperture radar and the scatterometer that constitute a sensor known as Active Microwave Instrument (AMI) onboard the ERS-1 satellite, is outlined. On the basis of a nonlinear, time-variant system model for the AMI, a composite strategy is described consisting of a prelaunch instrument characterization and postlaunch instrument monitoring, using internal stimuli, as well as external reference targets.

ESA

TYPE 1/4/147
 Quest Accession Number : 89N18850
 89N18850# NASA STAR Conference Paper Issue 11
 New architecture for a real-time SAR processor

(AA)APARMBEPOLA, B.
 GEC-Marconi Electronics Ltd., Chelmsford (England). (GB135511)
 In ESA, Proceedings of the 1988 International Geoscience and Remote Sensing Symposium (IGARSS) '88 on Remote Sensing: Moving Towards the 21st Century, Volume 2 p 691-694 (SEE N89-18836 11-43) 880800 p. 4 In: EN (English) Avail: NTIS HC A99/MF A01; ESA Publications Div. ESTEC, Noordwijk, Netherlands, \$120 US or 250 Dutch guilders p.1536

A processor architecture for real-time SAR azimuth processing is presented. It consists of a linear or circular array of identical processing modules. Hardware design is simplified by having a regular array of modules with nearest neighbor connectivity. Architecture is expandable to meet a variety of swath width, resolution, and throughput requirements. There is no explicit corner-turning. Input and output are in range line order. Memory requirements are minimized.

ESA

TYPE 1/4/146
 Quest Accession Number : 89N18851
 89N18851# NASA STAR Conference Paper Issue 11
 The Alaska SAR processor

(AA)CARANDE, R. E.; (AB)CHARNY, B.
 Jet Propulsion Lab., California Inst. of Tech., Pasadena. (JJ574450)
 In ESA, Proceedings of the 1988 International Geoscience and Remote Sensing Symposium (IGARSS) '88 on Remote Sensing: Moving Towards the 21st Century, Volume 2 p 695-698 (SEE N89-18836 11-43) 880800 p. 4 In: EN (English) Avail: NTIS HC A99/MF A01; ESA Publications Div. ESTEC, Noordwijk, Netherlands, \$120 US or 250 Dutch guilders p.1536

The Alaska SAR processor was designed to process over 200 100 km x 100 km (seasat like) frames per day from the raw SAR data, at a ground resolution of 30 m x 30 m from ERS-1, J-ERS-1, and Radarsat. The near real time processor is a set of custom hardware modules operating in a pipelined architecture, controlled by a general purpose computer. Input to the processor is provided from a high density digital cassette recording of the raw data stream as received by the ground station. A two pass processing is performed. During the first pass clutter-lock and auto-focus measurements are made. The second pass uses the results to accomplish final image formation which is recorded on a high density digital cassette. The processing algorithm uses fast correlation techniques for range and azimuth compression. Radiometric compensation, interpolation and deskewing is also performed by the processor. The standard product of the ASP is a high resolution four-look image, with a low resolution (100 to 200 m) many look image provided simultaneously.

ESA

TYPE 1/4/148
 Quest Accession Number : 89N18716
 89N18716# NASA STAR Conference Paper Issue 11
 Multitemporal and dual polarization of agricultural crops by X-band SAR images

(AA)LETOAN, T.; (AB)LAUR, H.
 Centre d'Etude Spatiale des Rayonnements, Toulouse (France). (CK523228)
 In ESA, Proceedings of the 1988 International Geoscience and Remote Sensing Symposium (IGARSS) '88 on Remote Sensing: Moving Towards the 21st Century, Volume 3 p 1291-1294 (SEE N89-18704 11-43) 880800 p. 4 In: EN (English) Avail: NTIS HC A99/MF A01; ESA Publications Division, ESTEC, Noordwijk, Netherlands, \$120 US or 250 Dutch guilders p.1513

X-band SAR images on agricultural crops were analyzed, emphasizing the differences between two parallel polarizations HH and VV, observed on cover types at two dates. The most striking feature is the singular behavior of flooded ricefields, which differs from the early to fully growth stage. The behavior, explained by backscattering models on vegetation canopy with highly reflecting underlying surface, suggests the use of the polarization ratio between HH and VV for ricefield monitoring.

ESA

TYPE 1/4/149

Quest Accession Number : 89N18710

89N18710/ NASA STAR Conference Paper Issue 11

Adaptive speckle filtering for SAR images

(AA)LOPES, A.; (AB)TOUZI, R.

Centre d'Etude Spatiale des Rayonnements, Toulouse (France). (CK523228)
 In ESA, Proceedings of the 1988 International Geoscience and Remote
 Sensing Symposium (IGARSS) '88 on Remote Sensing: Moving Towards the 21st
 Century, Volume 3 P 1263-1266 (SEE N89-18704 11-43) 880800 p. 4 In: EN
 (English) Avail: NTIS HC A99/MF A01; ESA Publications Division, ESTEC,
 Noordwijk, Netherlands, \$120 US or 250 Dutch guilders p.1512

A generalized adaptive filter is developed which can be adapted to
 preserve any kind of information characterized by the appropriate index.
 Filters are tested on a 4 look SAR 580 image. The best known adaptive
 filters are optimized such that they average well homogeneous areas and
 preserve edge and textural information (with less noise smoothing) at the
 same time. However, such filters do not smooth well the noise in textured
 areas and much work must be done to develop filters which, by taking into
 account all the properties of the speckle, reduce it as well within
 homogeneous areas as in the textured ones without loss of information.
 ESA

TYPE 1/4/151

Quest Accession Number : 89A15915

89A15915/ NASA IAA Journal Article Issue 04

Radar Polarimetry - Analysis tools and applications

(AA)EVANS, DIANE L.; (AB)FARR, TOM G.; (AC)VAN ZYL, JAKOB J.;

(AD)ZERKER, HOWARD A.

(AD)California Institute of Technology, Jet Propulsion Laboratory,
 Pasadena)

Jet Propulsion Lab., California Inst. of Tech., Pasadena. (J3574450)
 IEEE Transactions on Geoscience and Remote Sensing (ISSN 0196-2892),

vol. 26, Nov. 1988, p. 774-789. 881100 p. 16 refs 22 In: EN (English)
 p.561

The authors have developed several techniques to analyze polarimetric
 radar data from the NASA/JPL airborne SAR for earth science applications.
 The techniques determine the heterogeneity of scatterers with subregions,
 optimize the return power for each pixel in a radar image. These techniques
 scattering mechanisms for each pixel in a radar image. These techniques
 are applied to the discrimination and characterization of geologic
 surfaces and vegetation cover, and it is found that their utility varies
 depending on the terrain type. It is concluded that there are several
 classes of problems amenable to single-frequency polarimetric data
 analysis, including characterization of surface roughness and vegetation
 structure, and estimation of vegetation density. Polarimetric radar remote
 sensing can thus be a useful tool for monitoring a set of earth science
 parameters.
 I.E.

TYPE 1/4/150

Quest Accession Number : 89A16980

89A16980/ NASA IAA Journal Article Issue 04

Comparisons of simulated and actual synthetic aperture radar gravity
 wave images

(AA)HARGER, ROBERT O.; (AB)KORMAN, CAN E.

(AB)Maryland, University, College Park)

Journal of Geophysical Research (ISSN 0148-0227), vol. 93, Nov. 15,
 1988, p. 13867-13882. Navy-supported research. 881115 p. 16 refs 23
 In: EN (English) p.509

A series of SAR images obtained with an L band system during the Tower
 Ocean Wave and Radar Dependence experiment have been compared with
 simulations of an SAR ocean imaging model based on two-scale hydrodynamic
 and electromagnetic scattering models. The best focus parameter is
 estimated using a subimage cross-correlation technique. Results show a
 magnitude increase with an increase in magnitude of the angle between the
 dominant long wave and the SAR axes, and illustrate the independence of
 the altitude and the range-to-velocity ratio.
 R.R.

TYPE 1/4/152

Quest Accession Number : 89A15914

89A15914/ NASA IAA Journal Article Issue 04

A statistical and geometrical edge detector for SAR images

(AA)TOUZI, RIDHA; (AB)LOPES, ARMAND; (AC)BOUSQUET, PIERRE

(AC)Centre d'Etude Spatiale des Rayonnements, Toulouse, France)

IEEE Transactions on Geoscience and Remote Sensing (ISSN 0196-2892),
 vol. 26, Nov. 1988, p. 764-773. 881100 p. 10 refs 11 In: EN (English)
 p.528

A constant-false-alarm-rate (CFAR) edge detector based on the ratio
 between pixel values is described. The probability distribution of the
 image obtained by applying the edge detector is derived. Hence, the
 decision threshold can be theoretically determined for a given probability
 of false alarm as a function of the number of looks of the image under
 study and the size of the processing neighborhood. For a better and finer
 detection, the edge detector operates along the four usual directions over
 windows of increasing sizes. A test performed, for a given direction, on a
 radar image of an agricultural scene shows good agreement with the
 theoretical study. The operator is compared with the CFAR edge detectors
 suitable for radar images.
 I.E.

TYPE 1/4/153

Quest Accession Number : 89A15913
89A15913# NASA IAA Journal Article Issue 04
A digital calibration method for synthetic aperture radar systems
(AA)LARSON, RICHARD W.; (AB)JACKSON, P. L.; (AC)KASISCHKE, ERIC S.
(AC)(Michigan, Environmental Research Institute, Ann Arbor)
Environmental Research Inst. of Michigan, Ann Arbor. (E0356283)
IEEE Transactions on Geoscience and Remote Sensing (ISSN 0196-2892),
vol. 26, Nov. 1988, p. 753-763. USAF-NASA-supported research. 881100 p.
11 refs 29 In: EN (English) p.507

A basic method to calibrate imagery from synthetic aperture radar (SAR) systems is presented. SAR images are calibrated by monitoring all the terms of the radar equation. This procedure includes the use of both external (calibrated reference reflectors) and internal (system-generated calibration signals) sources to monitor the total SAR system transfer function. To illustrate the implementation of the procedure, two calibrated SAR images (X-band, 3.2-cm wavelength) are presented, along with the radar cross-section measurements of specific scenes within each image. The sources of error within the SAR image calibration procedure are identified.
I.E.

TYPE 1/4/155

Quest Accession Number : 89N13032
89N13032# NASA STAR Conference Paper Issue 04
Estimating aircraft SAR response characteristics and approximating ocean wave spectra in the Labrador Sea
(AA)TILLEY, D. G.
Johns Hopkins Univ., Laurel, Md. (JS767253) Applied Physics Lab.
In ESA, Proceedings of the 1988 International Geoscience and Remote Sensing Symposium (IGARSS 1988) on Remote Sensing: Moving Towards the 21st Century, Volume 1 p 399-402 (SEE N89-12936 04-42) Sponsored by NASA and the ONR 880800 p. 4 In: EN (English) Avail: NTIS HC A99/NF E03; ESA Publications Div., ESTEC, Noordwijk, Netherlands, 120 US dollars or 250 Dutch guilders p.511

The data processing methods employed to compute estimates of two-dimensional wave height-variance spectra from the ocean imagery obtained in the Labrador Sea by a C-band airborne SAR system are described. The SAR spectra are compared for high and low altitude geometries with large and small elevation angles. A surface contour radar and a radar ocean wave spectrometer aboard an aircraft are used to verify the surface wave spectrum.
ESA

TYPE 1/4/154

Quest Accession Number : 89N13033
89N13033# NASA STAR Conference Paper Issue 04
Phase versus orbital velocity in SAR wave imaging: Paradox lost
(AA)RANEY, R. K.; (AB)VACHON, P. W.
Canada Centre for Remote Sensing, Ottawa (Ontario). (CE390486)
RADARSAT Project Office.
In ESA, Proceedings of the 1988 International Geoscience and Remote Sensing Symposium (IGARSS 1988) on Remote Sensing: Moving Towards the 21st Century, Volume 1 p 405-406 (SEE N89-12936 04-42) 880800 p. 2 In: EN (English) Avail: NTIS HC A99/NF E03; ESA Publications Div., ESTEC, Noordwijk, Netherlands, 120 US dollars or 250 Dutch guilders p.511

The focus paradox in ocean wave SAR imaging from the air is reconciled. Improved wave imagery from an airborne SAR is possible by compensating individual looks (in a multilook data set) for wave movement prior to look summation. By observing the direction of wave motion between looks, the omnipresent 180 deg ambiguity (in wave direction estimation through spectral analysis) may be resolved using only the SAR data from one pass of the sensor. (There are known methods for resolution of the directional ambiguity for a single mode sea using two opposed passes). Approximation of the required image shift by focus adjustment is not recommended because the azimuth impulse response is degraded in the process, the method by definition is tuned to only one wave component, and the resulting image shift is in the azimuthal direction only and thus not necessarily in the direction of wave propagation. For directional spectral calculations, Fourier transformation of individual looks by magnitude summation leads to better results than the normal method of Fourier transformation of the look summed wave image. These results do not depend on invocation of any particular wave imaging mechanism.
ESA

TYPE 1/4/156

Quest Accession Number : 89N13029
89N13029# NASA STAR Conference Paper Issue 04
Complex SAR imagery and speckle filtering for ERS-1 wave mode
(AA)CORDEY, R. A.; (AB)MACKLIN, J. T.
GEC-Marconi Electronics Ltd., Chelmsford (England). (GB135511)
In ESA, Proceedings of the 1988 International Geoscience and Remote Sensing Symposium (IGARSS 1988) on Remote Sensing: Moving Towards the 21st Century, Volume 1 p 387-390 (SEE N89-12936 04-42) 880800 p. 4 In: EN (English) Avail: NTIS HC A99/NF E03; ESA Publications Div., ESTEC, Noordwijk, Netherlands, 120 US dollars or 250 Dutch guilders p.510

A method to predict the wavenumber dependence of the speckle component in spectra of SAR intensity images is described. Filtering of this component is an important step in recovering wave height spectra from SAR images of the ocean, and an effective means of doing so is required for the wave mode of ERS-1. The method uses the correlation function of the corresponding complex images and was tested using airborne and spaceborne imagery obtained over land and sea. Examples of successful and unsuccessful applications of the method are shown. The successes show a great improvement in speckle filtering over previous techniques, while the failures can be explained in terms of artefacts of an individual SAR processor or too coarse a digitization of complex pixel amplitudes.
ESA

TYPE 1/4/157

Quest Accession Number : 89N13021

89N13021# NASA STAR Conference Paper Issue 04

Formulation of the proper equations for developing standards in coherent dual polarisation SAR imaging

(AA)BOERNER, W.-M.; (AB)KOSTINSKI, A. B.

Illinois Univ., Chicago. (18525400) Communications Lab.

In ESA, Proceedings of the 1988 International Geoscience and Remote Sensing Symposium (IGARSS 1988) on Remote Sensing: Moving Towards the 21st Century, Volume 1 p 351-353 (SEE N89-12936 04-42) 880800 p. 3 In: EN (English) Avail: NTIS HC A99/MF E03; ESA Publications Div., ESTEC, Noordwijk, Netherlands, 120 US dollars or 250 Dutch guilders p.509

Crucial inconsistencies in the basic equations of radar polarimetry which are common in the literature were detected. The formulations of the polarization state definitions given in the IEEE/ANSI Standards 149-1979 are in error. These and other inconsistencies and conceptual errors are discussed. The correct formulae for the proposed revision of the polarimetric standards together with a well-defined and consistent procedure for measuring target scattering matrices in monostatic and bistatic arrangements are given. The proposed procedure can be applied to an arbitrary measurement process in any general elliptical polarization basis.
ESA

TYPE 1/4/159

Quest Accession Number : 89N13018

89N13018# NASA STAR Conference Paper Issue 04

Calibration of multipolarisation imaging radar

(AA)FREEMAN, A.; (AB)WERNER, C.; (AC)SHEN, YUHSHEN

Jet Propulsion Lab., California Inst. of Tech., Pasadena. (JJ574450)

In ESA, Proceedings of the 1988 International Geoscience and Remote Sensing Symposium (IGARSS 1988) on Remote Sensing: Moving Towards the 21st Century, Volume 1 p 335-339 (SEE N89-12936 04-42) 880800 p. 5 In: EN (English) Avail: NTIS HC A99/MF E03; ESA Publications Div., ESTEC, Noordwijk, Netherlands, 120 US dollars or 250 Dutch guilders p.509

An experiment was designed to calibrate airborne imaging radar (AIR) images, in terms of relative and absolute backscatter, and relative phase between polarization channels. The calibration uses measurements made within the radar system itself (internal calibration) and using ground-based corner reflectors and transponders (external calibration). The techniques developed for the AIR calibration campaign will form the basis of the calibration approach for SIR-C.
ESA

TYPE 1/4/158

Quest Accession Number : 89N13020

89N13020# NASA STAR Conference Paper Issue 04

The NASA/JPL multifrequency, multipolarisation airborne SAR system

(AA)HELD, D. N.; (AB)BROWN, W. E.; (AC)FREEMAN, A.; (AD)KLEIN, J. D.;

(AE)ZEBKER, H. A.; (AF)SATO, T.; (AG)MILLER, T.; (AH)NGUYEN, Q.; (AI)LOU, Y.

Jet Propulsion Lab., California Inst. of Tech., Pasadena. (JJ574450)

In ESA, Proceedings of the 1988 International Geoscience and Remote Sensing Symposium (IGARSS 1988) on Remote Sensing: Moving Towards the 21st Century, Volume 1 p 345-349 (SEE N89-12936 04-42) 880800 p. 5 In: EN (English) Avail: NTIS HC A99/MF E03; ESA Publications Div., ESTEC, Noordwijk, Netherlands, 120 US dollars or 250 Dutch guilders p.509

Polarimetric synthetic aperture radars, operating at L-, C- and P-band, were designed to replace and upgrade a system destroyed in an aircraft accident. Ground and flight tests were conducted, and the radar was flown over a calibration site in a sequence of experiments designed to calibrate the system. The radar also took part in science campaigns.
ESA

TYPE 1/4/160

Quest Accession Number : 89N13015

89N13015# NASA STAR Conference Paper Issue 04

Phase calibration of polarimetric SAR

(AA)SHEN, D. R.; (AB)KASISCHKE, E. S.; (AC)SHUCHMAN, R. A.

Environmental Research Inst. of Michigan, Ann Arbor. (E0356283) Radar Science Lab.

In ESA, Proceedings of the 1988 International Geoscience and Remote Sensing Symposium (IGARSS 1988) on Remote Sensing: Moving Towards the 21st Century, Volume 1 p 323-326 (SEE N89-12936 04-42) 880800 p. 4 In: EN (English) Avail: NTIS HC A99/MF E03; ESA Publications Div., ESTEC, Noordwijk, Netherlands, 120 US dollars or 250 Dutch guilders p.508

Techniques to measure the phase characteristics of a polarimetric imaging SAR were developed. Techniques to calibrate the phase portion of the radar signature from an airborne, polarimetric SAR system, targets (dihedral and trihedral corner reflectors) with known characteristics were deployed, and several passes of polarimetric data collected. The techniques used to reduce and analyze these data are presented. The radar-measured scattering matrix is compared to the theoretical scattering matrix. The results of this calibration are discussed in the context of the rms phase errors achieved for the SAR system utilized in the experiment.
ESA

TYPE 1/4/161

Quest Accession Number : 89N13014

89N13014# NASA STAR Conference Paper Issue 04

Design considerations for advanced multi-polarisation SAR

(AA)KLEIN, J. D.; (AB)FREDMAN, A.

Jet Propulsion Lab., California Inst. of Tech., Pasadena. (JJ574450)

In ESA, Proceedings of the 1988 International Geoscience and Remote Sensing Symposium (IGARSS 1988) on Remote Sensing: Moving Towards the 21st Century, Volume 1 p 317-321 (SEE N89-12936 04-42) 880800 p. 5 In: EN (English) Avail: NTIS HC A99/MF E03; ESA Publications Div., ESTEC, Noordwijk, Netherlands, 120 US dollars or 250 Dutch guilders p.508

System design and verification of an airborne imaging radar (AIR) system are discussed. Issues of importance to multipolarization systems (e.g., mutual coherence and amplitude balance between channels) are emphasized. Methods of detecting and correcting channel imbalances are discussed, and AIR test results are presented.

ESA

TYPE 1/4/163

Quest Accession Number : 89N12956

89N12956# NASA STAR Conference Paper Issue 04

The effects of undersampling on multipolarization SAR images

(AA)FREDMAN, A.; (AB)DUBOIS, P. C.; (AC)KLEIN, J. D.

Jet Propulsion Lab., California Inst. of Tech., Pasadena. (JJ574450)

In ESA, Proceedings of the 1988 International Geoscience and Remote Sensing Symposium (IGARSS 1988) on Remote Sensing: Moving Towards the 21st Century, Volume 1 p 75-78 (SEE N89-12936 04-42) 880800 p. 4 In: EN (English) Avail: NTIS HC A99/MF E03; ESA Publications Div., ESTEC, Noordwijk, Netherlands, 120 US dollars or 250 Dutch guilders p.498

The scattering matrix and Stokes matrix formats for multipolarization synthetic aperture radar (SAR) images are introduced. The effects of converting to the Stokes matrix format, without first doubling the sampling rate to allow for the conversion from a complex to an intensity format is quantified and discussed. It is shown that for most applications the Stokes matrix format is acceptable, since errors introduced by undersampling tend to average out when large numbers of pixels are averaged. For those applications requiring analysis of single image pixels, the scattering matrix format is recommended.

ESA

TYPE 1/4/162

Quest Accession Number : 89N12971

89N12971# NASA STAR Conference Paper Issue 04

SAR-seen multimode waves in ice: Evidence of imaging nonlinearities

(AA)RANEY, R. K.; (AB)VACHON, P. W.

Canada Centre for Remote Sensing, Ottawa (Ontario). (CE390486)

RADARSAT Project Office.

In ESA, Proceedings of the 1988 International Geoscience and Remote Sensing Symposium (IGARSS 1988) on Remote Sensing: Moving Towards the 21st Century, Volume 1 p 141-144 (SEE N89-12936 04-42) 880800 p. 4 In: EN (English) Avail: NTIS HC A99/MF E03; ESA Publications Div., ESTEC, Noordwijk, Netherlands, 120 US dollars or 250 Dutch guilders p.501

A two dimensional wave field analytic model based on the synthetic aperture radar (SAR) velocity bunching mechanism that is extended to the multi-modal case and includes the effects of wave component translation between looks is discussed. Using this model, directional spectra results are presented for a bimodal sea. As significant wave height is increased, the image spectra evolve from the correct bimodal form through suppression of the correct modes to creation of a new and dominant spectral artifact propagating at approximately 90 deg to the true wave direction. The simulated wave images compare favorably to actual imagery of waves in ice from the LIMEX/LEMEX 87 EXPERIMENT using similar radar, viewing geometry, and wave parameters. It is concluded that coherence time limitation is beneficial, as it expands the effective linear domain of the SAR imaging process.

ESA

TYPE 1/4/164

Quest Accession Number : 89N12954

89N12954# NASA STAR Conference Paper Issue 04

On the concept of the polarimetric matched filter in high resolution radar imaging: An alternative for speckle radiation

(AA)BOERNER, W.-M.; (AB)KOSTINSKI, A. B.; (AC)JAMES, B. D.

Illinois Univ., Chicago. (IB525400) Communications Lab.

In ESA, Proceedings of the 1988 International Geoscience and Remote Sensing Symposium (IGARSS 1988) on Remote Sensing: Moving Towards the 21st Century, Volume 1 p 69-72 (SEE N89-12936 04-42) 880800 p. 4 In: EN (English) Avail: NTIS HC A99/MF E03; ESA Publications Div., ESTEC, Noordwijk, Netherlands, 120 US dollars or 250 Dutch guilders p.498

The potential of an exclusively polarimetric image filtering approach, i.e., filtering which takes full advantage of the POL-SAR matrix data provided on a pixel-by-pixel basis and which complements the existing scalar speckle reduction techniques, was assessed. The three stage polarimetric optimization procedure search for optimal polarizations on a pixel-by-pixel basis is combined with a subsequent statistical analysis of polarization eigenvectors (versus surface category), and the digital adjustment of polarimetric variables. Results are encouraging. In order to improve the efficiency of the polarimetric filtering method, it must be combined with other image processing and statistically communication theory techniques. Filter efficiency depends critically on peak sharpness of the histograms, and multilook incoherent averaging, block discretization, and nonuniform quantization can be used to improve peakedness.

ESA

TYPE 1/4/165

Quest Accession Number : 89N12953

89N12953# NASA STAR Conference Paper Issue 04

Statistical properties of phase difference between two orthogonally-polarised SAR signals

(AA)EOM, H. J.; (AB)BOERNER, W.-M.
Illinois Univ., Chicago. (IB525400) Dept. of Electrical Engineering and Computer Science.

In ESA, Proceedings of the 1988 International Geoscience and Remote Sensing Symposium (IGARSS 1988) on Remote Sensing: Moving Towards the 21st Century. Volume 1 p 65-66 (SEE N89-12936 04-42) 880800 p. 2 In: EN (English) Avail: NTIS HC A99/WF E03; ESA Publications Div., ESTEC, Noordwijk, Netherlands, 120 US dollars or 250 Dutch guilders p.498

The theoretical behavior of two linearly polarized (VV and HH polarization states) radar backscattered fields is examined statistically. The coherency between two polarized signals is studied in terms of their statistical behavior on phase difference between two signals. The probability density function corresponding to the phase difference between two signals is derived and studied in terms of the degree of polarization, and the variance of each polarized signal. The phase difference is considered with respect to the polarimetric SAR data collected over rugged terrain and ocean. It is found that the phase coherency between two copolarized channels (VV and HH polarizations) strongly depends upon the degree of terrain roughness structure. The degree of polarization is also found to be closely related to terrain/oceanic surface roughness and anisotropy.

ESA

TYPE 1/4/167

Quest Accession Number : 89A10938

89A10938# NASA IAA Conference Paper Issue 01

SAR image data compression for an on-line archive system

(AA)CHANG, C. Y.; (AB)KWOK, R.; (AC)CURLANDER, J. C.

(AC)California Institute of Technology, Jet Propulsion Laboratory, Pasadena

Jet Propulsion Lab., California Inst. of Tech., Pasadena. (J574450)

In: International Symposium on Remote Sensing of Environment, 21st, Ann Arbor, MI, Oct. 26-30, 1987, Proceedings. Volume 1 (A89-10926 01-43). Ann Arbor, MI, Environmental Research Institute of Michigan, 1987, p. 171-182. 870000 p. 12 refs 10 In: EN (English) p.92

This paper summarizes the investigation of SAR image data compression for an on-line archive data distribution system. This system is planned for the ground processing system of Alaska SAR Facility (ASF) and Shuttle Imaging Radar (SIR-C). The objective of the SAR image data compression is to enable the data archive system to provide the remote users a large data base with good image quality, short response time, low transfer cost, and minimal decoding complexity. The requirements and limitations of the on-line archive data distribution system are presented. The effects of SAR image data characteristics on data compression are addressed. The users' survey results suggest that compression ratios between 10:1 and 20:1 appear suitable. Based on the algorithm evaluation results, the two-level tree-searched vector quantization technique has been recommended as the SAR image data compression algorithm for the on-line archive data distribution system.

Author

TYPE 1/4/166

Quest Accession Number : 89A12173

89A12173 NASA IAA Journal Article Issue 02

Synthetic aperture radar imaging of ocean waves from an airborne platform - Focus and tracking issues

(AA)RANEY, R. K.; (AB)VACHOW, P. W.

(AA)Radarsat Project Office, Ottawa, Canada); (AB)Canada Centre for Remote Sensing, Ottawa)

Journal of Geophysical Research (ISSN 0148-0227), vol. 93, Oct. 15, 1988, p. 12475-12486. 881015 p. 12 refs 19 In: EN (English) p.167

This paper addresses the aspects of focus and tracking in the process of SAR imaging of ocean waves from an airborne platform. It is demonstrated that there is a direct relationship between focus and wave phase velocity through purely noncoherent consequences of the SAR response to the translating reflectivity density envelope of the wave field. It is also shown that the orbital velocity affects the phase of the received signal, leading to velocity bunching, and is scaled by the ratio of sensor altitude to sensor velocity. It is suggested that better performance can be obtained by compensating individual looks for wave movement before look summation, while using nominal perfect focus.

I.S.

TYPE 1/4/168

Quest Accession Number : 89N10315

89N10315# NASA STAR Conference Paper Issue 01

The use of the complex correlation function in the recovery of ocean wave spectra from SAR images

(AA)CORDEY, R. A.; (AB)MACKLIN, J. T.

Marconi Co. Ltd., Great Baddow (England). (MF831696)

ESA-6878/87-HGE-I(SC) In ESA, Proceedings of the 4th International Colloquium on Spectral Signatures in Remote Sensing p 63-67 (SEE N89-10305 01-43) 880400 p. 5 In: EN (English) Avail: NTIS HC A23/MF A01; ESA Publications Division, ESTEC, Noordwijk, Netherlands 80 Dutch guilders p.58

A method to predict the wavenumber dependence of the speckle component in spectra of synthetic-aperture radar intensity images was tested using data from VARAN-S and Seasat systems. The method uses the correlation function of the corresponding complex images and assumes that pixel statistics are Gaussian. It is expected that such a technique will be of use in the routine recovery of ocean wave height spectra from SAR imagery. Results from the Agrisar campaign with VARAN-S over land and sea are good, with speckle spectra being well matched by their predicted forms. Ocean spectra from Seasat are, however, poorly matched in their dependence on azimuth wavenumber. This is not thought to be caused by any sea surface or propagation effect but rather to be an artifact of signal processing.

ESA

TYPE 1/4/169

Quest Accession Number : 88A53680

88A53680* NASA IAA Journal Article Issue 23

Spatial compression of Seasat SAR imagery

(AA)CHANG, C. Y.; (AB)KOK, RONALD; (AC)CURLANDER, JOHN C.

(AC)(California Institute of Technology, Jet Propulsion Laboratory, Pasadena)

Jet Propulsion Lab., California Inst. of Tech., Pasadena. (JJ574450)

(IEEE, URSI, NASA, et al., IGARSS '87 - International Geoscience and

Remote Sensing Symposium, University of Michigan, Ann Arbor, May 18-21,

1987) IEEE Transactions on Geoscience and Remote Sensing (ISSN 0196-2892),

vol. 26, Sept. 1988, p. 673-685. 880900 p. 13 refs 25 In: EN (English)

p.3812

The results of a study of techniques for spatial compression of synthetic-aperture-radar (SAR) imagery are summarized. Emphasis is on image-data volume reduction for archive and online storage applications while preserving the image resolution and radiometric fidelity. A quantitative analysis of various techniques, including vector quantization (VQ) and adaptive discrete cosine transform (ADCT), is presented. Various factors such as compression ratio, algorithm complexity, and image quality are considered in determining the optimal algorithm. The compression system requirements are established for electronic access of an online archive system based on the results of a survey of the science community. The various algorithms are presented and their results evaluated considering the effects of speckle noise and the wide dynamic range inherent in SAR imagery. The conclusion is that although the ADCT produces the best signal-to-distortion-noise ratio for a given compression ratio, the two-level tree-searched VQ technique is preferred due to its simplicity of decoding and near-optimal performance.

I.E.

TYPE 1/4/171

Quest Accession Number : 88A46766

88A46766* NASA IAA Journal Article Issue 19

Multisensor classification of sedimentary rocks

(AA)EVANS, DIANE

(AA)(California Institute of Technology, Jet Propulsion Laboratory, Pasadena)

Jet Propulsion Lab., California Inst. of Tech., Pasadena. (JJ574450)

Remote Sensing of Environment (ISSN 0034-4257), vol. 25, July 1988, p.

129-144. 880700 p. 19 refs 29 In: EN (English) p.3242

A comparison is made between linear discriminant analysis and supervised classification results based on signatures from the Landsat TM, the Thermal Infrared Multispectral Scanner (TMS), and airborne SAR, alone and combined into extended spectral signatures for seven sedimentary rock units exposed on the margin of the Wind River Basin, Wyoming. Results from a linear discriminant analysis showed that training-area classification accuracies based on the multisensor data were improved an average of 15 percent over TM alone, 24 percent over TMS alone, and 46 percent over SAR alone, with similar improvement resulting when supervised multisensor classification maps were compared to supervised, individual sensor classification maps. When training area signatures were used to map spectrally similar materials in an adjacent area, the average classification accuracy improved 19 percent using the multisensor data over TM alone, 2 percent over TMS alone, and 11 percent over SAR alone. It is concluded that certain sedimentary lithologies may be accurately mapped using a single sensor, but classification of a variety of rock types can be improved using multisensor data sets that are sensitive to different characteristics such as mineralogy and surface roughness.

Author

TYPE 1/4/170

Quest Accession Number : 88A52625

88A52625* NASA IAA Journal Article Issue 23

Satellite radar interferometry - Two-dimensional phase unwrapping

(AA)GOLDSTEIN, RICHARD M.; (AB)ZEBKER, HOWARD A.; (AC)WERNER, CHARLES L.

(AC)(California Institute of Technology, Jet Propulsion Laboratory, Pasadena)

Jet Propulsion Lab., California Inst. of Tech., Pasadena. (JJ574450)

Radio Science (ISSN 0048-6604), vol. 23, July-Aug. 1988, p. 713-720.

880800 p. 8 refs 8 In: EN (English) p.3775

Interferometric synthetic aperture radar observations provide a means for obtaining high-resolution digital topographic maps from measurements of amplitude and phase of two complex radar images. The phase of the radar echoes may only be measured modulo 2π ; however, the whole phase at each point in the image is needed to obtain elevations. An approach to 'unwrapping' the 2π ambiguities in the two-dimensional data set is presented. It is found that noise and geometrical radar layover corrupt measurements locally, and these local errors can propagate to form global phase errors that affect the entire image. It is shown that the local errors, or residues, can be readily identified and avoided in the global phase estimation. A rectified digital topographic map derived from the unwrapped phase values is presented.

Author

TYPE 1/4/172

Quest Accession Number : 88A44651

88A44651* NASA IAA Journal Article Issue 18

An effect of coherent scattering in spaceborne and airborne SAR images

(AA)RANEY, R. K.; (AB)GRAY, A. L.; (AC)PRINCZ, J. G.

(AA)(Radar Project Office, Ottawa, Canada); (AC)(Canada Centre for Remote Sensing, Ottawa)

International Journal of Remote Sensing (ISSN 0143-1161), vol. 9, May

1988, p. 1039-1049. 880500 p. 11 refs 10 In: EN (English) p.3091

Radar imagery obtained by the Shuttle Imaging Radar-B (SIR-B) is compared to high resolution aircraft imagery of the same urban and agricultural areas close to the city of Montreal, Canada. It is clear that the SIR-B radar is more sensitive than the aircraft radar to reflections from extended, along-track radar targets. The effect is evident for both urban and agricultural areas in which the street or field orientation is near parallel to the radar azimuth direction. It is likely that such reflectivity enhancement is due to coherent combination of the scattered field from appropriate scattering centers. The paper considers the observed phenomena and probes potential scattering models to explain the results.

Author

TYPE 1/4/173

Quest Accession Number : 88A42786

88A42786 NASA IAA Conference Paper Issue 17
A basis for SAR oceanography: Theory and experiment

(AA)WARGER, ROBERT O.; (AB)KORMAN, CAN
(AB)Maryland, University, College Park)

IN: IEEE National Radar Conference, 3rd, Ann Arbor, MI, Apr. 20, 21, 1988, Proceedings (A88-42751 17-32). New York, Institute of Electrical and Electronics Engineers, Inc., 1988, p. 200-203. 880000 p. 4 refs 18 In: EN (English) p.2904

A comparison of synthetic-aperture radar (SAR) sea images generated by a simulation program implementing a two-scale theory and by the Jet Propulsion Laboratory L-band SAR flow in the TOWARD oceanographic experiment is discussed. A subimage cross-correlation technique estimates the best image focus. The sea surface imagery is composed of two scales, a long-wave ensemble and a short-wave ensemble, and both gravity waves. The appropriate two-scale hydrodynamic and electromagnetic scattering approximate models are combined with a model for SAR imaging of a time-variant, extended scene. The resulting model is complicated and generally requires a simulation, which generates the complex, high-resolution SAR image to reveal its full nature. The two-scale theory's predictions agree well with the actual measurements, including the discriminating prediction that the best focus correction is proportional to the long wave's phase velocity.

I.E.

TYPE 1/4/175

Quest Accession Number : 88A42755

88A42755 NASA IAA Conference Paper Issue 17

CCRS C/X-airborne synthetic aperture radar: An R and D tool for the ERS-1 time frame

(AA)LIVINGSTONE, C. E.; (AB)GRAY, A. L.; (AC)HAWKINS, R. K.; (AD)OLSEN, R. B.

(AD)(Canada Centre for Remote Sensing, Ottawa)

IN: IEEE National Radar Conference, 3rd, Ann Arbor, MI, Apr. 20, 21, 1988, Proceedings (A88-42751 17-32). New York, Institute of Electrical and Electronics Engineers, Inc., 1988, p. 15-21. 880000 p. 7 In: EN (English) p.2826

The airborne synthetic-aperture radar (SAR) system developed for the Canada Centre for Remote Sensing is discussed. The SAR consists of two radars at C- and X-bands. Each radar incorporates dual-channel receivers and dual-polarized antennas; a high quality, seven-look, real-time processor; a sensitivity time control for range-dependent gain control; a motion compensation system for antenna steering in azimuth and elevation; and baseband I- and Q-signal phase rotation. The system features a high-power transmitter with a low-power backup and can map to either side of the aircraft, at high or low resolution, at incidence angles which in high resolution span of 0 to 80 deg. The radar operating parameters, data products, key specifications and the motion-compensation scheme used are given. Properties of the real-time imagery are discussed and examples of C-band SAR data in the three operating modes are presented.

I.E.

TYPE 1/4/174

Quest Accession Number : 88A42771

88A42771 NASA IAA Conference Paper Issue 17

A statistical model for prediction of precision and accuracies of radar scattering coefficient measurements derived from SAR data

(AA)KASISCHKE, ERIC S.; (AB)FOWLER, GARY W.; (AC)WACKERMAN, CHRISTOPHER C.

(AC)(Michigan, Environmental Research Institute, Ann Arbor)

IN: IEEE National Radar Conference, 3rd, Ann Arbor, MI, Apr. 20, 21, 1988, Proceedings (A88-42751 17-32). New York, Institute of Electrical and Electronics Engineers, Inc., 1988, p. 111-117. 880000 p. 7 refs 11 In: EN (English) p.2827

A model is presented to estimate a relative error-bound associated with radiometric calibration of the scattering coefficient derived from synthetic-aperture radar (SAR) data. This error bound is based on a statistical coefficient-of-variation error model. The error model was exercised parametrically to determine what factors most significantly influence radiometric errors from SAR systems. It was found that errors in the measurement of the antenna elevation gain-pattern resulted in the most dramatic increases in the statistical error bound. The results from this analysis can be utilized in both the design of SAR systems and measurements programs needed to calibrate SAR systems to minimize the error bounds associated with radiometric calibration.

I.E.

TYPE 1/4/176

Quest Accession Number : 88A42753

88A42753* NASA IAA Conference Paper Issue 17

Preliminary results from the NASA/JPL multifrequency, multipolarization synthetic aperture radar

(AA)HELD, DANIEL N.; (AB)BROWN, WALTER E.; (AC)MILLER, TIMOTHY W.

(AC)(California Institute of Technology, Jet Propulsion Laboratory, Pasadena)

IN: IEEE National Radar Conference, 3rd, Ann Arbor, MI, Apr. 20, 21, 1988, Proceedings (A88-42751 17-32). New York, Institute of Electrical and Electronics Engineers, Inc., 1988, p. 7, 8. 880000 p. 2 In: EN (English) p.2826

A brief description is given of the three-frequency polarimetric synthetic-aperture radar built and tested at the Jet Propulsion Laboratory. The radar has the capability to simultaneously acquire fully polarimetric data at P-, L-, and C-bands from a DC-8 airborne platform. The radar has an instantaneous data rate of approximately 2.1 Gb/s and has selectable record rates between 80-240 Mb/s. The system has a wide dynamic range featuring 8-b analog-to-digital converters and full digital floating-point processing. The processing is accomplished offline on a minicomputer system assisted by an array processor. Sample images are presented.

I.E.

TYPE 1/4/177

Quest Accession Number : 88A37288

88A37288# NASA IAA Journal Article Issue 15

SAR swath-widening techniques

(AA)WALTER, WINFRED; (AB)BRAUN, HANS MARTIN

Dornier-Post (English Edition) (ISSN 0012-5563), no. 1, 1988, p. 24-27.
880000 p. 4 In: EN (English) p.2442

The possible ways of expanding the swath illuminated by SAR antennas used in space-based imaging encompass antenna lengthening, the positioning of two parallel beams, and the use of electronic beam steering in a phase-controlled active array. Attention is presently given to the comparative results of a study that considered these alternatives, mechanical, thermal, structural, and electrical requirements and characteristics. The passive antennas are found to be mechanically only insignificantly different from the active phased array antenna, in such matters as panel arrangement, launcher stowage, mechanical and thermal stability, and pointing accuracy.
O.C.

TYPE 1/4/179

Quest Accession Number : 88A27829

88A27829# NASA IAA Journal Article Issue 10

DFVLR's intelligent SAR-processor - ISAR

(AA)WOACK, W.; (AB)RUNGE, H.

(AB)(DFVLR, Oberpfaffenhofen, Federal Republic of Germany)

(COSPAR, WMO, URSI, et al., Plenary Meeting, 26th, Symposium 3, Workshop V, and Topical Meeting A2 on Remote Sensing from Space, Toulouse, France, June 30-July 11, 1986) Advances in Space Research (ISSN 0273-1177), vol. 7, no. 11, 1987, p. 273-279. 870000 p. 7 refs 8 In: EN (English) p. 1514

The fact that future SAR sensors like ERS-1 and X-SAR will be operational systems requires a processor system design which is significantly different from existing SAR correlators. Future systems require highest throughput and reliability. In addition, more attention must be paid to the user community needs in terms of various product levels and adequate production and organization schemes. This paper presents the design of the ISAR system which is identified by a distributed processor architecture using a high speed array processor, enhanced by a two-dimensional accessible memory, a front-end processor and a knowledge engineering workstation. An expert system will support a human system operator for the mass production of SAR images and the detection and correction of system malfunctions. As a result the system will be accessible and comprehensive for both experts and operators.
Author

TYPE 1/4/178

Quest Accession Number : 88A27831

88A27831# NASA IAA Journal Article Issue 10

Simulation of bit-quantization influence on SAR images

(AA)WOLFRAM, A. P.; (AB)PIKE, T. K.

(AB)(DFVLR, Institut fuer Hochfrequenztechnik, Oberpfaffenhofen, Federal Republic of Germany)

(COSPAR, WMO, URSI, et al., Plenary Meeting, 26th, Symposium 3, Workshop V, and Topical Meeting A2 on Remote Sensing from Space, Toulouse, France, June 30-July 11, 1986) Advances in Space Research (ISSN 0273-1177), vol. 7, no. 11, 1987, p. 285-288. 870000 p. 4 refs 10 In: EN (English) p. 1546

The influence of two-bit and four-bit quantization schemes on the ocean wave spectra obtained in the wave imaging mode of the first European Remote Sensing Satellite ERS-1 is analyzed. The SAR images utilized were obtained through simulation using a static ocean-wave radar model and a comprehensive software SAR system simulation model. The results indicate that spectra produced by the four-bit quantization are not significantly degraded from the optimum, but that the two-bit quantization requires some gain adjustment for optimal spectral reproduction. The conclusions are supported by images and spectral plots covering the various options simulated.
C.D.

TYPE 1/4/180

Quest Accession Number : 88A27827

88A27827# NASA IAA Journal Article Issue 10

Radar calibration techniques including propagation effects

(AA)HARTL, PH.; (AB)KEYDEL, W.; (AC)KIETZMANN, H.; (AD)HEEL, F.

(AA)(Stuttgart, Universitaet, Federal Republic of Germany); (AC)(DFVLR, Institut fuer Hochfrequenztechnik, Wessling, Federal Republic of Germany)

(COSPAR, WMO, URSI, et al., Plenary Meeting, 26th, Symposium 3, Workshop V, and Topical Meeting A2 on Remote Sensing from Space, Toulouse, France, June 30-July 11, 1986) Advances in Space Research (ISSN 0273-1177), vol. 7, no. 11, 1987, p. 259-268. 870000 p. 10 refs 13 In: EN (English) p.1514

This paper outlines the extent and difficulties associated with absolute calibration procedures of SAR systems. The calibration principles of SAR systems are reviewed, and the calibration concepts of several SAR systems are described. Accuracy considerations are addressed.
C.D.

TYPE 1/4/181

Quest Accession Number : 88N26541

88N26541# NASA STAR Issue 20

Data volume reduction for imaging radar polarimetry / Patent Application

(AA)ZEBKER, HOWARD A.; (AB)HELD, DANIEL N.; (AC)VANZYL, JAKOB J.;

(AD)DUBOIS, PASCALE C.; (AE)MORIKANE, LYNE

(AA)inventor (to NASA); (AB)inventor (to NASA); (AC)inventor (to NASA);

(AD)inventor (to NASA); (AE)inventor (to NASA)

(AE)(Jet Propulsion Lab., California Inst. of Tech., Pasadena.)

National Aeronautics and Space Administration. Pasadena Office, Calif.

(N0894694)

NASA-CASE-NPO-17184-1-CU; NAS 1.71:NPO-17184-1-CU; US-PATENT-APPL-SN-19-

5225 MAS7-918 880405 p. 26 In: EN (English) Avail: NTIS HC A03/MP A01

p. 2788

Two alternative methods are presented for digital reduction of synthetic aperture multipolarized radar data using scattering matrices, or using Stokes matrices, of four consecutive along-track pixels to produce averaged data for generating a synthetic polarization image.

NASA

TYPE 1/4/183

Quest Accession Number : 88N23357

88N23357 NASA STAR Technical Report Issue 16

Investigation of the imaging of ocean surface waves using a synthetic aperture radar

UNTERSUCHUNG DER ABBILDUNG VON OZEANOBERFLAECHEWELLEN DURCH EIN

SYNTHETIC APERTURE RADAR

(AA)BRUENING, CLAUS

Max-Planck-Inst. fuer Meteorologie, Hamburg (West Germany). (MN457760)

SER-A-WISS-ABHANDL-84; ETN-88-91470 870000 p. 98 In: GM (German)

Avail: FachInformationszentrum Karlsruhe, 7514 Eggenstein-Leopoldshafen

2, Fed. Republic of Germany, 20 DM p. 2236

The imaging of long, wind-induced ocean waves by a SAR using a two-dimensional Monte Carlo simulation model was investigated. It is shown that the nonlinear distortions in the SAR-imaging are essentially due to phase modulation and Doppler broadening of the SAR-signal by the sub-scale orbital velocities of backscattered SAR-signal. The pronounced azimuthal decay of the spectral energy density in the SAR-variance spectrum is due to the Doppler-broadening-induced reduction of the azimuthal resolution, and limits the signal-to-noise ratio of the signal. The validity of the SAR-simulation model was demonstrated by comparison with SAR-variance spectra taken by the Shuttle Imaging Radar.

ESA

TYPE 1/4/182

Quest Accession Number : 88A23547

88A23547 NASA IAA Journal Article Issue 08

Interpretation of Seasat radar-altimeter data over sea ice using near-simultaneous SAR imagery

(AA)ULANDER, LARS M. H.

(AA)Chalmers Tekniska Hogskola, Goteborg, Sweden)

ESA-6617/85/F/FL/(SC) International Journal of Remote Sensing (ISSN

0143-1161), vol. 8, Nov. 1987, p. 1679-1686. Research supported by the

Swedish Board for Space Activities. 871100 p. 8 refs 20 In: EN

(English) p. 0

The backscatter properties of Seasat altimeter data in the Beaufort Sea on October 3, 1978 show distinct zones, which are interpreted in terms of geophysical characteristics. An overlapping and near-simultaneous synthetic-aperture radar image shows regions of open water, new ice, and multi-year sea ice which correspond to the different zones. It is found that the altimeter signal is sensitive to the ocean-ice boundary and that it indicates the ice type. The pulse-echo waveforms also suggest that several scattering components are present in the returned power over sea ice.

Author

TYPE 1/4/184

Quest Accession Number : 88A15372

88A15372 NASA IAA Journal Article Issue 04

Spectral properties of homogeneous and nonhomogeneous radar images

(AA)MADSEN, SOREN NORVANG

(AA)(Danmarks Tekniske Højskole, Lyngby, Denmark)

IEEE Transactions on Aerospace and Electronic Systems (ISSN 0018-9251),

vol. AES-23, July 1987, p. 583-588. 870700 p. 6 refs 13 In: EN

(English) p. 0

On the basis of a two-dimensional, nonstationary white noise model for the complex radar backscatter, the spectral properties of a one-look synthetic-aperture radar (SAR) system is derived. It is shown that the power spectrum of the complex SAR image is scene independent. It is also shown that the spectrum of the intensity image is in general related to the radar scene spectrum by a linear integral equation, a Fredholm's closed-form equation of the third kind. Under simplifying assumptions, a SAR image spectrum can be derived.

Author

TYPE 1/4/185

Quest Accession Number : 88N15284

88N15284# NASA STAR Technical Report Issue 07
SAR (Synthetic Aperture Radar). Earth observing system. Volume 2F:
Instrument panel report
National Aeronautics and Space Administration. Goddard Space Flight
Center, Greenbelt, Md. (NC999967)
NASA-TM-89701; NAS 1.15:89701 870000 p. 260 Original document
contains color illustrations In: EN (English) Avail: NTIS HC A12/MF A01
p.871

The scientific and engineering requirements for the Earth Observing System (EOS) imaging radar are provided. The radar is based on Shuttle Imaging Radar-C (SIR-C), and would include three frequencies: 1.25 GHz, 5.3 GHz, and 9.6 GHz; selectable polarizations for both transmit and receive channels; and selectable incidence angles from 15 to 55 deg. There would be three main viewing modes: a local high-resolution mode with typically 25 m resolution and 50 km swath width; a regional mapping mode with 100 m resolution and up to 200 km swath width; and a global mapping mode with typically 500 m resolution and up to 700 km swath width. The last mode allows global coverage in three days. The EOS SAR will be the first orbital imaging radar to provide multifrequency, multipolarization, multiple incidence angle observations of the entire Earth. Combined with Canadian and Japanese satellites, continuous radar observation capability will be possible. Major applications in the areas of glaciology, hydrology, vegetation science, oceanography, geology, and data and information systems are described.

J.P.B.

REPORT DOCUMENTATION PAGE													
1. Recipient's Reference	2. Originator's Reference AGARD-LS-182	3. Further Reference ISBN 92-835-0683-9	4. Security Classification of Document UNCLASSIFIED										
5. Originator	Advisory Group for Aerospace Research and Development North Atlantic Treaty Organization 7 rue Ancelle, 92200 Neuilly sur Seine, France												
6. Title	FUNDAMENTALS AND SPECIAL PROBLEMS OF SYNTHETIC APERTURE RADAR (SAR)												
7. Presented on	5th—6th October 1992 in Bad Neuenahr, Germany, 8th—9th October 1992 in Gebze-Kocaeli (near Istanbul), Turkey and 26th—27th October 1992 in Ottawa, Canada												
8. Author(s)/Editor(s) Various	9. Date August 1992												
10. Author's/Editor's Address Various	11. Pages 198												
12. Distribution Statement	This document is distributed in accordance with AGARD policies and regulations, which are outlined on the back covers of all AGARD publications.												
13. Keywords/Descriptors													
<table border="0"> <tbody> <tr> <td>Airborne radar</td> <td>Remote sensing</td> </tr> <tr> <td>Algorithms</td> <td>Simulation</td> </tr> <tr> <td>Digital techniques</td> <td>Spaceborne equipment</td> </tr> <tr> <td>Inverse synthetic aperture radar</td> <td>Synthetic aperture antennas</td> </tr> <tr> <td>Polarization (waves)</td> <td>Synthetic aperture radar</td> </tr> </tbody> </table>				Airborne radar	Remote sensing	Algorithms	Simulation	Digital techniques	Spaceborne equipment	Inverse synthetic aperture radar	Synthetic aperture antennas	Polarization (waves)	Synthetic aperture radar
Airborne radar	Remote sensing												
Algorithms	Simulation												
Digital techniques	Spaceborne equipment												
Inverse synthetic aperture radar	Synthetic aperture antennas												
Polarization (waves)	Synthetic aperture radar												
14. Abstract													
<p>The Lecture Series will cover the field of airborne and spaceborne SAR with respect to its technical realisation in order to convey the participants' ideas and know-how on SAR, on its capabilities and on the technology necessary for the successful construction and application of airborne and spaceborne SAR systems.</p> <p>The basic principles of SAR will be explained and SAR will be compared to airborne and spaceborne radar with real aperture.</p> <p>The influence of the antenna parameters on specification and capabilities of SAR and the advantages, necessities and limits will be considered.</p> <p>Digital SAR processing is indispensable for SAR. Theories and special algorithms will be given along with basic processor configurations and different processing techniques on a hardware and software basis.</p> <p>The simulation of SAR-systems as well as SAR-products will also be a topic of the Lecture Series. A presentation of the present state of the art, giving examples of presently planned and realised airborne and spaceborne SAR with its foreseen applications will conclude the Lecture Series.</p> <p>This Lecture Series, sponsored by the Avionics Panel of AGARD, has been implemented by the Consultant and Exchange Programme.</p>													

<p>AGARD Lecture Series 182 Advisory Group for Aerospace Research and Development, NATO FUNDAMENTALS AND SPECIAL PROBLEMS OF SYNTHETIC APERTURE RADAR (SAR) Published August 1992 198 pages</p> <p>The Lecture Series will cover the field of airborne and spaceborne SAR with respect to its technical realisation in order to convey the participants' ideas and know-how on SAR, on its capabilities and on the technology necessary for the successful construction and application of airborne and spaceborne SAR systems.</p> <p>The basic principles of SAR will be explained and SAR will be compared to airborne and spaceborne radar with real aperture.</p> <p>P.T.O.</p>	<p>AGARD-LS-182</p> <p>Airborne radar Algorithms Digital techniques Inverse synthetic aperture radar Polarization (waves) Remote sensing Simulation Spaceborne equipment Synthetic aperture antennas Synthetic aperture radar</p>	<p>AGARD Lecture Series 182 Advisory Group for Aerospace Research and Development, NATO FUNDAMENTALS AND SPECIAL PROBLEMS OF SYNTHETIC APERTURE RADAR (SAR) Published August 1992 198 pages</p> <p>The Lecture Series will cover the field of airborne and spaceborne SAR with respect to its technical realisation in order to convey the participants' ideas and know-how on SAR, on its capabilities and on the technology necessary for the successful construction and application of airborne and spaceborne SAR systems.</p> <p>The basic principles of SAR will be explained and SAR will be compared to airborne and spaceborne radar with real aperture.</p> <p>P.T.O.</p>	<p>AGARD-LS-182</p> <p>Airborne radar Algorithms Digital techniques Inverse synthetic aperture radar Polarization (waves) Remote sensing Simulation Spaceborne equipment Synthetic aperture antennas Synthetic aperture radar</p>
<p>AGARD Lecture Series 182 Advisory Group for Aerospace Research and Development, NATO FUNDAMENTALS AND SPECIAL PROBLEMS OF SYNTHETIC APERTURE RADAR (SAR) Published August 1992 198 pages</p> <p>The Lecture Series will cover the field of airborne and spaceborne SAR with respect to its technical realisation in order to convey the participants' ideas and know-how on SAR, on its capabilities and on the technology necessary for the successful construction and application of airborne and spaceborne SAR systems.</p> <p>The basic principles of SAR will be explained and SAR will be compared to airborne and spaceborne radar with real aperture.</p> <p>P.T.O.</p>	<p>AGARD-LS-182</p> <p>Airborne radar Algorithms Digital techniques Inverse synthetic aperture radar Polarization (waves) Remote sensing Simulation Spaceborne equipment Synthetic aperture antennas Synthetic aperture radar</p>	<p>AGARD Lecture Series 182 Advisory Group for Aerospace Research and Development, NATO FUNDAMENTALS AND SPECIAL PROBLEMS OF SYNTHETIC APERTURE RADAR (SAR) Published August 1992 198 pages</p> <p>The Lecture Series will cover the field of airborne and spaceborne SAR with respect to its technical realisation in order to convey the participants' ideas and know-how on SAR, on its capabilities and on the technology necessary for the successful construction and application of airborne and spaceborne SAR systems.</p> <p>The basic principles of SAR will be explained and SAR will be compared to airborne and spaceborne radar with real aperture.</p> <p>P.T.O.</p>	<p>AGARD-LS-182</p> <p>Airborne radar Algorithms Digital techniques Inverse synthetic aperture radar Polarization (waves) Remote sensing Simulation Spaceborne equipment Synthetic aperture antennas Synthetic aperture radar</p>

<p>The influence of the antenna parameters on specification and capabilities of SAR and the advantages, necessities and limits will be considered.</p> <p>Digital SAR processing is indispensable for SAR. Theories and special algorithms will be given along with basic processor configurations and different processing techniques on a hardware and software basis.</p> <p>The simulation of SAR-systems as well as SAR-products will also be a topic of the Lecture Series. A presentation of the present state of the art, giving examples of presently planned and realised airborne and spaceborne SAR with its foreseen applications will conclude the Lecture Series.</p> <p>This Lecture Series, sponsored by the Avionics Panel of AGARD and the Consultant and Exchange Programme of AGARD, presented on 5th-6th October 1992 in Bad Neuenahr, Germany, 8th-9th October 1992 in Gebze-Kocaeli (near Istanbul), Turkey and 26th-27th October 1992 in Ottawa, Canada.</p> <p>ISBN 92-835-0683-9</p>	<p>The influence of the antenna parameters on specification and capabilities of SAR and the advantages, necessities and limits will be considered.</p> <p>Digital SAR processing is indispensable for SAR. Theories and special algorithms will be given along with basic processor configurations and different processing techniques on a hardware and software basis.</p> <p>The simulation of SAR-systems as well as SAR-products will also be a topic of the Lecture Series. A presentation of the present state of the art, giving examples of presently planned and realised airborne and spaceborne SAR with its foreseen applications will conclude the Lecture Series.</p> <p>This Lecture Series, sponsored by the Avionics Panel of AGARD and the Consultant and Exchange Programme of AGARD, presented on 5th-6th October 1992 in Bad Neuenahr, Germany, 8th-9th October 1992 in Gebze-Kocaeli (near Istanbul), Turkey and 26th-27th October 1992 in Ottawa, Canada.</p> <p>ISBN 92-835-0683-9</p>
<p>The influence of the antenna parameters on specification and capabilities of SAR and the advantages, necessities and limits will be considered.</p> <p>Digital SAR processing is indispensable for SAR. Theories and special algorithms will be given along with basic processor configurations and different processing techniques on a hardware and software basis.</p> <p>The simulation of SAR-systems as well as SAR-products will also be a topic of the Lecture Series. A presentation of the present state of the art, giving examples of presently planned and realised airborne and spaceborne SAR with its foreseen applications will conclude the Lecture Series.</p> <p>This Lecture Series, sponsored by the Avionics Panel of AGARD and the Consultant and Exchange Programme of AGARD, presented on 5th-6th October 1992 in Bad Neuenahr, Germany, 8th-9th October 1992 in Gebze-Kocaeli (near Istanbul), Turkey and 26th-27th October 1992 in Ottawa, Canada.</p> <p>ISBN 92-835-0683-9</p>	<p>The influence of the antenna parameters on specification and capabilities of SAR and the advantages, necessities and limits will be considered.</p> <p>Digital SAR processing is indispensable for SAR. Theories and special algorithms will be given along with basic processor configurations and different processing techniques on a hardware and software basis.</p> <p>The simulation of SAR-systems as well as SAR-products will also be a topic of the Lecture Series. A presentation of the present state of the art, giving examples of presently planned and realised airborne and spaceborne SAR with its foreseen applications will conclude the Lecture Series.</p> <p>This Lecture Series, sponsored by the Avionics Panel of AGARD and the Consultant and Exchange Programme of AGARD, presented on 5th-6th October 1992 in Bad Neuenahr, Germany, 8th-9th October 1992 in Gebze-Kocaeli (near Istanbul), Turkey and 26th-27th October 1992 in Ottawa, Canada.</p> <p>ISBN 92-835-0683-9</p>

NATO  OTAN
7 RUE ANCELLE · 92200 NEUILLY-SUR-SEINE
FRANCE

Telephone (1)47.38.57.00 · Telex 610 176
Telefax (1)47.38.57.99

**DISTRIBUTION OF UNCLASSIFIED
AGARD PUBLICATIONS**

AGARD does NOT hold stocks of AGARD publications at the above address for general distribution. Initial distribution of AGARD publications is made to AGARD Member Nations through the following National Distribution Centres. Further copies are sometimes available from these Centres (except in the United States), but if not may be purchased in Microfiche or Photocopy form from the Sales Agencies listed below.

NATIONAL DISTRIBUTION CENTRES

BELGIUM

Coordonnateur AGARD — VSL
Etat-Major de la Force Aérienne
Quartier Reine Elisabeth
Rue d'Evere, 1140 Bruxelles

LUXEMBOURG

See Belgium

NETHERLANDS

Netherlands Delegation to AGARD
National Aerospace Laboratory, NLR

CAN



DEN

National Aeronautics and
Space Administration

FRA

Washington, D.C. **SPECIAL FOURTH CLASS MAIL**
20546 **BOOK**

GER

LE 001 AG-LS-182 92091489026720
DEPT OF DEFENSE
DEFENSE TECHNICAL INFORMATION CENTER
ATTN DTIC-DCP/JOYCE CHIRAS
CAMERON STATION BLDG 5
ALEXANDRIA VA 223046145

GRE

Naval Air Force Base
Dekelia, Athens TGA 1010

ICELAND

Director of Aviation
c/o Flugrad
Reykjavik

ITALY

Aeronautica Militare
Ufficio del Delegato Nazionale all'AGARD
Aeroporto Pratica di Mare
00040 Pomezia (Roma)

Postage and Fees Paid
National Aeronautics and
Space Administration
NASA-451

Official Business
Penalty for Private Use \$300



Establishment

for to AGARD
nas

Ankara

UNITED KINGDOM

Defence Research Information Centre
Kentigern House
65 Brown Street
Glasgow G2 8EX

UNITED STATES

National Aeronautics and Space Administration (NASA)
Langley Research Center
M/S 180
Hampton, Virginia 23665

**THE UNITED STATES NATIONAL DISTRIBUTION CENTRE (NASA) DOES NOT HOLD
STOCKS OF AGARD PUBLICATIONS, AND APPLICATIONS FOR COPIES SHOULD BE MADE
DIRECT TO THE NATIONAL TECHNICAL INFORMATION SERVICE (NTIS) AT THE ADDRESS BELOW.**

SALES AGENCIES

National Technical
Information Service (NTIS)
5285 Port Royal Road
Springfield, Virginia 22161
United States

ESA/Information Retrieval Service
European Space Agency
10, rue Mario Nikis
75015 Paris
France

The British Library
Document Supply Centre
Boston Spa, Wetherby
West Yorkshire LS23 7BQ
United Kingdom

Requests for microfiches or photocopies of AGARD documents (including requests to NTIS) should include the word 'AGARD' and the AGARD serial number (for example AGARD-AG-315). Collateral information such as title and publication date is desirable. Note that AGARD Reports and Advisory Reports should be specified as AGARD-R-*nnn* and AGARD-AR-*nnn*, respectively. Full bibliographical references and abstracts of AGARD publications are given in the following journals:

Scientific and Technical Aerospace Reports (STAR)
published by NASA Scientific and Technical
Information Division
NASA Headquarters (NTI)
Washington D.C. 20546
United States

Government Reports Announcements and Index (GRA&I)
published by the National Technical Information Service
Springfield
Virginia 22161
United States
(also available online in the NTIS Bibliographic
Database or on CD-ROM)



Printed by Specialised Printing Services Limited
40 Chitwell Lane, Loughton, Essex IG10 3TZ

ISBN 92-835-0683-9